The Telecommunications and Data Acquisition Progress Report 42-116

October–December 1993

Joseph H. Yuen
Editor

February 15, 1994

National Aeronautics and
Space Administration

Jet Propulsion Laboratory
California Institute of Technology
Pasadena, California

The research described in this publication was carried out by the Jet Propulsion Laboratory, California Institute of Technology, under a contract with the National Aeronautics and Space Administration.

Preface

This quarterly publication provides archival reports on developments in programs managed by JPL's Office of Telecommunications and Data Acquisition (TDA). In space communications, radio navigation, radio science, and ground-based radio and radar astronomy, it reports on activities of the Deep Space Network (DSN) in planning, supporting research and technology, implementation, and operations. Also included are standards activity at JPL for space data and information systems and reimbursable DSN work performed for other space agencies through NASA. The preceding work is all performed for NASA's Office of Space Communications (OSC). The TDA Office also performs work funded by another NASA program office through and with the cooperation of OSC. This is the Orbital Debris Radar Program with the Office of Space Systems Development.

The TDA Office is directly involved in several tasks that directly support the Office of Space Science (OSS), with OSC funding DSN operational support. In radio science, *The TDA Progress Report* describes the spacecraft radio science program conducted using the DSN. For the High-Resolution Microwave Survey (HRMS), the report covers implementation and operations for searching the microwave spectrum. In solar system radar, it reports on the uses of the Goldstone Solar System Radar for scientific exploration of the planets, their rings and satellites, asteroids, and comets. In radio astronomy, the areas of support include spectroscopy, very long baseline interferometry, and astrometry.

Finally, tasks funded under the JPL Director's Discretionary Fund and the Caltech President's Fund that involve the TDA Office are included.

This and each succeeding issue of *The TDA Progress Report* will present material in some, but not necessarily all, of the following categories:

- OSC Tasks:
  - DSN Advanced Systems
    - Tracking and Ground-Based Navigation;
    - Communications, Spacecraft–Ground; Station Control and System Technology;
    - Network Data Processing and Productivity
  - DSN Systems Implementation
    - Capabilities for Existing Projects; Capabilities for New Projects;
    - New Initiatives; Network Upgrade and Sustaining
  - DSN Operations
    - Network Operations and Operations Support;
    - Mission Interface and Support; TDA Program Management and Analysis
  - Ground Communications Implementation and Operations
  - Data and Information Systems
  - Flight–Ground Advanced Engineering
  - Long-Range Program Planning

- OSC Cooperative Tasks:
  - Orbital Debris Radar Program

- OSS Tasks:
  - Radio Science; High-Resolution Microwave Survey;
  - Goldstone Solar System Radar; Radio Astronomy

- Discretionary Funded Tasks

Contents

OSC TASKS
DSN Advanced Systems
TRACKING AND GROUND-BASED NAVIGATION

COMMUNICATIONS, SPACECRAFT–GROUND

DSN Systems Implementation
CAPABILITIES FOR EXISTING PROJECTS

CAPABILITIES FOR NEW PROJECTS

NETWORK UPGRADE AND SUSTAINING

DSN Operations

GROUND COMMUNICATIONS IMPLEMENTATION AND OPERATIONS

N94-29653

Toward Astrometric Tracking With the Infrared Spatial Interferometer

R. N. Treuhaft
Radar Science and Engineering Section

M. Bester, W. C. Danchi, and C. H. Townes
Space Sciences Laboratory, University of California at Berkeley

Infrared interferometric demonstrations with the University of California, Berkeley's infrared spatial interferometer (ISI) on Mt. Wilson explore the potential of infrared and optical astrometry for deep space tracking, reference frame development, and DSN science. Astrometric data taken and analyzed over the last 5 years from the ISI have shown that instrumental and atmospheric effects limit current demonstrations. The benefits of sensitivity upgrades, which were performed in 1991 and 1992, have been demonstrated by comparing point-to-point phase fluctuations for the fall 1989 and fall 1992 observing epochs. This comparison showed that point-to-point phase fluctuations due to tropospheric and quantum noise, for optimal integration times of 0.2 sec, are approaching the 0.1-cycle level needed to reliably connect the interferometric phase. The increase in sensitivity, coupled with that arising from very recent hardware upgrades, will greatly enhance phase-connection capabilities necessary for astrometry in the presence of atmospheric refractivity fluctuations. The current data set suggests that atmospheric fluctuations on Mt. Wilson during the best seeing are dominated by a low-lying component, approximately 25 m high, which may be minimized with in situ calibration in the future. During poor seeing conditions that currently prohibit the interferometric phase connection necessary for astrometry, fluctuations seem to be generated by atmospheric inhomogeneities at much higher altitudes above Mt. Wilson. Data taken over the last year suggest that the ISI will soon be able to achieve 50- to 100-nrad astrometry in a single observing session, employing current ground-based laser distance interferometer calibrations to minimize atmospheric effects.

I. Introduction

Infrared and optical astrometry support three areas of potential interest to the Deep Space Network (DSN): tracking of laser-carrying spacecraft; reference frame development, including locating solar system objects in infrared/optical, radio, and planetary reference frames; and DSN astrometric science of the future. Because optical telemetry is being considered for high data-rate transmission within the next few decades [1], development of an infrared or optical metric tracking capability will reduce or eliminate the need for bulky radio equipment on laser-carrying spacecraft. Even in the absence of optical telemetry, the development of infrared and optical reference frames, and the location of solar system objects in those frames, will enable more accurate target-relative tracking with radio systems utilizing radio-optical frame ties. Optical measurements of Global Positioning System (GPS) satellites constitute one example of a radio-optical frame-tie technique. Such measurements are planned for the Table Mountain Ronchi telescope in the near future. Current DSN science frequently involves the measurement of electromagnetic phase or amplitude at radio wavelengths. Similar measurements at infrared and optical wavelengths—such as solar deflection experiments, free of charged-particle effects, and asteroid imaging—will probably be performed by the DSN of the future.

Stellar astrometric demonstrations with the University of California, Berkeley's infrared spatial interferometer (ISI) bear on each of the three areas of DSN interest mentioned above. ISI astrometric demonstrations, which help to determine the limiting accuracy of ground-based infrared or optical astrometry, provide a valuable assessment of the limiting accuracy of tracking, reference frame work, and science at infrared and optical wavelengths. For example, atmospheric refractivity fluctuations studied with ISI are likely to be the dominant astrometric error for tracking spacecraft, galactic, or solar system targets. Refractivity fluctuations are similar in spatiotemporal characteristics at infrared and optical wavelengths. In the presence of refractivity fluctuations, interferometry at the longer infrared wavelengths enables larger apertures than those practical at optical wavelengths. On the other hand, two-color methods at optical wavelengths may help to reduce atmospheric effects [2]. Data from the ISI have already helped to characterize the Mt. Wilson atmosphere, as will be discussed in Section III. Descriptions of Mt. Wilson atmospheric behavior may well apply to other mountain-top astronomical sites.

In addition to the description of atmospheric fluctuation errors, tracking the trajectories of asteroids is another potential application of infrared interferometry in the DSN. Asteroid astrometry benefits both reference frame development and science [3]. Figure 1 shows the approximate flux of an asteroid located at 1 astronomical unit (AU) from the Sun. Various simplifications regarding the angular distribution of thermal flux from the asteroid make the figure approximate at the 30-percent level, but the illustrated wavelength dependence of the radiation is much better than that. The figure applies to the two cases noted, a 10-km-diam asteroid at 0.05 AU from the Earth or a 200-km-diam asteroid at 1 AU from the Earth. The ISI operates at 11 μm and, with recent sensitivity upgrades, should be able to make astrometric measurements of objects with flux in the 1000-Jy range. Optical or infrared measurements of GPS satellites will help to locate the asteroids in the radio VLBI frame used for angular spacecraft tracking. Astrometry of asteroid trajectories will also help to determine their masses [3].

Ground-based demonstrations with the ISI will suggest improvements to the infrared and optical astrometric techniques, as well as the nature of future space-based tracking systems. This article describes recent ISI data acquisition and analysis that help to establish an instrumental and atmospheric error budget. In the next section, the current instrumental characteristics of the ISI and the restrictions they impose on astrometric performance will be discussed. Section III shows characteristics of the Mt. Wilson atmosphere that must be addressed in future demonstrations, and Section IV describes the potential for upgrading both the instrumentation and analysis algorithms to achieve astrometry below the 50-nrad level.

II. Instrumental Sensitivity and Systematics

A single telescope of the ISI is shown in Fig. 2. Each of the two telescopes consists of a steerable flat mirror (on the right), a focusing parabolic mirror, optics, and electronics that detect the infrared signal and convert it to a 2-GHz-wide radio signal for cross-correlation. Helium-neon laser distance interferometers (HeNe LDI's) in each telescope monitor the path lengths between the flat and parabolic mirrors and behind the flat mirror to the optics table. The sensitivity of the ISI for infrared astrometry is limited by the noise in the output of the heterodyne receivers, which is about twice the quantum limit, or equivalent to a single-sideband system temperature of approximately 2600 K. An ISI interferometric time series for the star Alpha Orionis is shown in Fig. 3. These data were taken on September 8, 1992, on a 13-m baseline. There are points in the time series when a cycle may have been incorrectly assigned, but by and large the phase seems properly connected.

A general requirement on the sensitivity of astrometric devices is that the white (quantum or thermal) noise be low enough to allow short integration times as compared to those characteristic of appreciable propagation media effects. For interferometric devices, both white noise and low-frequency-peaked propagation noise [4,5] contributions to the phase must be small enough to allow phase connection. Usually rms phase variations ≤ 0.1 cycle guarantee reliable phase connection. These qualitative statements are illustrated quantitatively in Fig. 4, which shows the point-to-point rms phase variation as a function of integration time for data taken from Fig. 3 and from Alpha Orionis on October 12, 1989. Between the two epochs shown in Fig. 4, a number of sensitivity enhancements were made, including the installation of an improved heterodyne detector in one telescope of the ISI. Low-frequency-peaked atmospheric effects increase as the integration interval increases. Quantum noise from the heterodyne detectors, on the other hand, is white or frequency independent and should therefore average and produce smaller rms phase variations with increased integration time. The decreasing trend with increasing integration times until about 0.2 sec is presumably due to quantum noise, while the increasing trend from 0.2 sec on is associated with atmospheric refractivity fluctuations. The minimum rms phase fluctuation—i.e., the point at which the system noise and atmospheric trends cross—determines the optimal integration time. As can be seen from the figure, sensitivitity upgrades improve performance by lowering the point-to-point fluctuation associated with the optimal integration time between about 0.2 and 0.13 cycle. If there were no rise in Fig. 4 due to atmospheric fluctuations, then integration times could be extended indefinitely and poor sensitivity could be tolerated. During nights of excellent seeing, for example on October 10, 1989, integration times of 1 sec or more were used to connect phase. Figure 4 thus illustrates the relationship between sensitivity and atmospheric fluctuations. Based on Fig. 4, "good seeing" will be defined from here on as atmospheric phase fluctuations less than 0.1 infrared cycle on 0.2-sec time scales. Reliable phase connection requires slightly better sensitivity than that evidenced in Fig. 4 for typical Mt. Wilson observing conditions. Future hardware upgrades, including installation of a new heterodyne detector in the other telescope of the ISI, should improve the potential for phase connection and therefore for infrared astrometry.

In addition to ISI sensitivity, systematic instrumental effects were studied by examining HeNe LDI path delay time series. They revealed resonances that may originate from the movement of the telescopes while tracking, or from resonances in the power supply. The resonances were at about 7 Hz, but sometimes multiple resonances between 1 and 10 Hz were found. The amplitudes of those resonances are such that they just barely contribute to infrared phase instability, but because they occur at frequencies which might cause additional problems with phase connection, we will attempt to identify and minimize them when analyzing data taken this past summer and fall.

III. Atmospheric Limitations in Current ISI Astrometric Demonstrations

The discussion of atmospheric errors in this section assumes that phase-connection problems will be solved by improved ISI sensitivity, as mentioned above. With reliable phase connection, the atmosphere still limits astrometric accuracy by causing different path-length changes between the two telescopes of the ISI. This section discusses the optimal use of HeNe LDI data to minimize atmospheric effects and the altitude dependence of the fluctuations as derived from model calculations.

In Fig. 5, the Alpha Orionis data from September 8, 1992, are shown again, plotted with the telescope-differenced HeNe LDI path lengths, scaled to infrared cycles, and multiplied by three to demonstrate the approximate 0.6 correlation. This correlation suggests that simple subtraction of the telescope-differenced HeNe LDI path delays from the interferometric delays is suboptimal [4]. The time series in Fig. 5 prompted a model calculation to explore the optimal utilization of the HeNe LDI data in the astrometric analysis and to assess the resulting astrometric accuracy. A calculation of the expected level of correlation between HeNe LDI and interferometric path delays was performed using the formalism of [5], and implemented with the numerical techniques of [6]. The total interferometric path length due to nonzero tropospheric refractivity $\tau_{trop}(\theta,\phi,t)$ at elevation angle θ, azimuth ϕ relative to the orientation of the ISI trailers, and time t is given by

$$\tau_{trop}(\theta,\phi,t) \;=\; \tau_{atm}(\theta,\phi,t) \;+\; 2\tau_{HeNe}(t) \qquad (1)$$

where $\tau_{atm}(\theta,\phi,t)$ is the contribution to the interferometric path delay from the differences in atmospheric refractivity along the electromagnetic paths from the observed object to each of the two telescopes of the ISI, and $\tau_{HeNe}(t)$ is the ground-based, one-way, telescope-differenced HeNe LDI path delay due to nonzero refractivity. The HeNe LDI path lengths are defined to lie along the x-axis at $(\theta,\phi) = (0,0)$. The factor of 2 in Eq. (1) accounts for the double traversal of the HeNe LDI path by the infrared interferometric signal: once from the flat mirror to the parabola (propagating to the left in Fig. 2) and once from the parabola through the cat's eye to the optics table in back of the flat mirror (propagating to the right in Fig. 2).

The atmospheric and HeNe LDI path delay terms in Eq. (1) are

$$\begin{aligned}\tau_{atm}(\theta,\phi,t) &= \frac{1}{c\sin\theta}\int_0^h [\chi(\vec{r}_{2,atm}(\theta,\phi,z,t)) \\ &- \chi(\vec{r}_{1,atm}(\theta,\phi,z,t))]dz \\ \tau_{HeNe}(t) &= \frac{1}{c}\int_0^l [\chi(\vec{r}_{2,HeNe}(x)) - \chi(\vec{r}_{1,HeNe}(x))]dx\end{aligned} \tag{2}$$

where $\chi(\vec{r}_{i,atm})$ is the refractivity at the point denoted by the vector $\vec{r}_{i,atm}$ along the line of sight at height z above the ith telescope. For the HeNe LDI delay, $\chi(\vec{r}_{i,HeNe}(x))$ is the refractivity at the vector position a distance x along the HeNe path for the ith telescope. In Eq. (2), h is the height of the turbulent atmosphere, l is the length of the HeNe LDI path (which is 5 m), and c is the speed of light in a vacuum. Using these expressions, the correlation ρ plotted in Fig. 6 is

$$\rho = \frac{<\tau_{trop}\tau_{HeNe}>}{\sqrt{<\tau_{trop}^2><\tau_{HeNe}^2>}} \tag{3}$$

where $<>$ means ensemble average. The abscissa of Fig. 6 is h in Eq. (2). The ensemble averages of refractivity were evaluated using Kolmogorov–Taylor structure functions as in [5], with a structure constant of $4 \times 10^{-7} m^{-1/3}$, an atmospheric height of 25 m, a wind speed of 1 m/sec, and a saturation scale of 10 m. These parameters were chosen because they produce temporal structure functions similar to those of the data of Fig. 5. The line-of-sight coordinates $(\theta,\phi) = (37.6, 71$ deg) were taken from the data of Fig. 5, and the horizontal line in Fig. 6 is ρ derived from the data of Fig. 5, assuming that a temporal average of ρ over a single scan is equal to an ensemble average over many scans (ergodicity). From Fig. 6, a 25-m height is inferred for the turbulent atmosphere. This is a model-dependent result, and the sensitivity of the result to departures from the Kolmogorov–Taylor assumptions will be discussed in future articles.

The above atmospheric modelling can be used to construct an optimal least-squares estimator for the interferometric delay at the middle of an observation interval, which is the fundamental quantity of astrometric interest. The observed interferometric delay is modelled as

$$\begin{aligned}\tau_{int}(\theta,\phi,t) &= \tau_0(\theta,\phi,t_0) + (t-t_0)\dot{\tau}(\theta,\phi,t_0) \\ &+ \tau_{trop}(\theta,\phi,t)\end{aligned} \tag{4}$$

where $\tau_0(t_0)$ is the delay at the reference time t_0, and the changes in θ and ϕ due to sidereal tracking have been ignored. The τ_0 delay and the linear delay rate $\dot{\tau}$ include contributions due to baseline and celestial source coordinates that differ from those used in the lobe rotator model of the ISI correlator. An optimal estimator for τ_0 can be formed [7], and its error standard deviation calculated using the covariance of τ_{trop} between all times t_i and t_j, which, suppressing the θ and ϕ arguments, is given by

$$\begin{aligned}\mathrm{cov}\,(\tau_{\mathrm{trop}}(\mathrm{t_i}),\tau_{\mathrm{trop}}(\mathrm{t_j})) &= <\tau_{trop}(t_i)\tau_{trop}(t_j)> \\ &- <\tau_{trop}(t_i)><\tau_{trop}(t_j)>\end{aligned} \tag{5}$$

The two ensemble averages in the second term on the right of Eq. (5) are nearly zero for an interferometer with both telescopes at the same site. Again, the formalism of [5] can be used to evaluate the ensemble averages that result after inserting expressions from Eq. (2) into the first term on the right of Eq. (5). Figure 7 shows the calculated, troposphere-limited, error standard deviation for angular astrometry, which is c/B times the standard deviation for τ_0 for a 13-m baseline length B as a function of scan integration time. The upper curve shows the effect of the refractivity fluctuations in the absence of HeNe LDI calibration, and the lower curve shows the improvement if the current HeNe LDI calibrations are optimally used. For 1000-sec scans, an approximate 100-nrad accuracy seems attainable for interferometry with optimal HeNe LDI calibration. For azimuths along the HeNe LDI path, the HeNe LDI-calibrated accuracy is improved by about 20 percent.

It should be noted that estimation procedures, which are calculationally simpler that the optimal procedure described above, may be used in actual data analysis; a negligible loss in astrometric accuracy may result. The formulation using Eqs. 1–5 was presented to give insight into the turbulent atmospheric distance scales, the nature of ρ, and the reduction in astrometric error using HeNe LDI calibration.

In addition to the optimal analysis of the HeNe LDI and interferometric path delays, the results of Fig. 6 suggest that local measurements of refractivity in the first 25 m of the atmosphere may yield better than 100-nrad astrometry for observations when the HeNe LDI correlation is high. These local measurements could be meteorological or could consist of additional HeNe LDI's that sample the vertical paths above the ISI. It is very important to note that the above approaches, which exploit the high correlation between the HeNe LDI and atmospheric path delays, may have limited utility. On many nights in the fall of 1992, with poorer seeing than that of September 8, 1992, HeNe LDI fluctuation levels not much different from those of Fig. 5 were observed, while the interferometric fluctuations were much larger than those of Fig. 5. Because the large fluctuations prevented reliable interferometric phase connection on those nights, the width of the power spectrum of the fringe amplitudes coming from the ISI correlator was used as the measure of the fluctuation level. The fact that the interferometer signal was correlated with the HeNe LDI delays on nights of good seeing and much less so on nights of poorer seeing suggests the following picture characterizing the Mt. Wilson atmosphere: During relatively good seeing, the atmospheric fluctuations are fairly low to the ground (within the first 25 m) and optimal incorporation of HeNe LDI data and/or other ground-based calibration strategies may yield 100-nrad-or-better infrared astrometry. During poor seeing, atmospheric fluctuations occur much higher than 25 m above the ISI and neither HeNe LDI data nor ground-based calibration schemes will be of much help. In that case, laser guide star technology [8] may be of use. This hypothesis is consistent with the picture of the atmosphere in [4], in which larger lateral saturation scales are attributed to nights of poorer seeing. The validity of this description of the atmosphere above Mt. Wilson and the ultimate astrometric accuracy of the ISI will be explored with data taken in the summer and fall of 1993.

IV. Summary and Future Directions

Applications of infrared astrometry to DSN tracking include research into techniques for tracking infrared or optical space-borne lasers, reference frame development, and astrometric science at infrared or optical wavelengths. The commonality of atmospheric problems at infrared and optical wavelengths and the capability of larger apertures at infrared wavelengths make infrared interferometry a good tool for studying atmospheric astrometric limitations. Asteroid astrometry and the measurement of gravitational deflection close to the Sun are examples of reference frame development and science that may be enabled by infrared interferometry in the DSN.

By comparing astrometric data from 1989 and 1992, we have verified that instrumental upgrades have indeed improved interferometric phase determination at short time scales. The point-to-point phase scatter on 0.2-sec time scales is about 0.13 infrared cycle for good seeing conditions. A factor of 2 improvement in the point-to-point phase scatter would greatly increase the reliability of interferometric phase connection. This factor of 2 may be realized with additional hardware sensitivity upgrades. Resonances have also been identified in the instrumental HeNe LDI calibration path lengths. These resonances are mainly at 7 Hz and are just barely strong enough to affect the infrared astrometric phase.

Analysis and modelling of ISI data taken in the fall of 1992 suggest a two-component model for the turbulent atmosphere above Mt. Wilson. For good seeing conditions, a 25-m turbulent atmospheric height has been inferred, based on the correlation between HeNe LDI and interferometric path-length fluctuations. A small saturation scale of 10 m was also inferred from the ISI data for good seeing. For poorer seeing conditions, the HeNe LDI–interferometric correlation is weaker, suggesting that the turbulent atmosphere has substantial components above 25 m. This modelling was also used to determine that the atmosphere-limited astrometric accuracy on an ISI 13-m baseline during good seeing, with optimal HeNe LDI calibration, was about 100 nrad for a 1000-sec scan. Accuracy at this level would be a factor of 4 better than previous infrared astrometric results [9]. This level of astrometric accuracy has yet to be demonstrated on multiple sources with the ISI. Single-source phase traces and atmospheric modelling have been used to infer the potential accuracy of the ISI.

Reliable phase connection, optimal application of HeNe LDI calibration, and the resulting 100-nrad single-source astrometry will be demonstrated with data taken in the next observing season. Multiple-source astrometry will also be attempted. This will require developing acquisition or analysis techniques to resolve cycle ambiguities between observations of multiple sources. Future astrometric improvements may include local monitoring of atmospheric effects to improve accuracy on nights of good seeing. Such monitoring could involve a combination of meteorological sensors and new HeNe LDI paths. In the more distant future, the development of an infrared reference frame and asteroid astrometry will be pursued. A direct-detection (as opposed to heterodyne) system is being considered for the ISI on 5-year time scales. Direct detection would greatly increase the usable ISI bandwidth and sensitivity, enabling astrometry in a much wider variety of seeing conditions.

It should be noted that because of the apparent small saturation scale during periods of good seeing, increases in baseline length will yield almost proportionate improvements in accuracy. Data taken on azimuths closer to that of the HeNe LDI will be more effectively calibrated by optimal application of HeNe LDI data. Considering these factors, astrometric accuracy of the order of 50–100 nrad is probably characteristic of future ISI single-observation performance in the absence of the above-mentioned meteorological calibrations. Because of the small saturation scales, troposphere-induced errors for observations from the same session, or from different sessions, should be uncorrelated. By averaging results over many observations, astrometric accuracies of much better than 50–100 nrad should be possible.

References

[1] J. R. Lesh, L. J. Deutsch, and W. J. Weber, "A Plan for the Development and Demonstration of Optical Communications for Deep Space," *The Telecommunications and Data Acquisition Progress Report 42-103, vol. July–September 1990*, Jet Propulsion Laboratory, Pasadena, California, pp. 97–109, November 15, 1990.

[2] M. Colavita, M. Shao, and D. H. Staelin, "Two-Color Method for Optical Astrometry: Theory and Preliminary Measurements with the Mark III Stellar Interferometer," *Applied Optics*, vol. 26, pp. 4113–4122, 1987.

[3] M. Hoffmann, "Asteroid Mass Determination: Present Situation and Perspectives," in *Asteroids II*, edited by R. P. Binzel, T. Gehrels, and M. S. Matthews, Tucson: University of Arizona Press, pp. 228–239, 1989.

[4] M. Bester, W. C. Danchi, C. G. Degiacomi, L. J. Greenhill, and C. H. Townes, "Atmospheric Fluctuations: Empirical Structure Functions and Projected Performance of Future Instruments," *Ap. J.*, vol. 392, p. 357, 1992.

[5] R. N. Treuhaft and G. E. Lanyi, "The Effect of the Dynamic Wet Troposphere on Radio Interferometric Measurements," *Radio Science*, vol. 22, p. 251, 1987.

[6] G. J. Bierman, *Factorization Methods for Discrete Sequential Estimation*, Orlando: Academic Press, 1977.

[7] W. C. Hamilton, *Statistics in Physical Science*, New York: Ronald Press, 1964.

[8] R. K. Tyson, *Principles of Adaptive Optics*, Boston: Academic Press, Inc., 1991.

[9] E. C. Sutton, S. Subranmanian, and C. H. Townes, *Astronomy Astrophysics*, vol. 110, pp. 324–331, 1982.

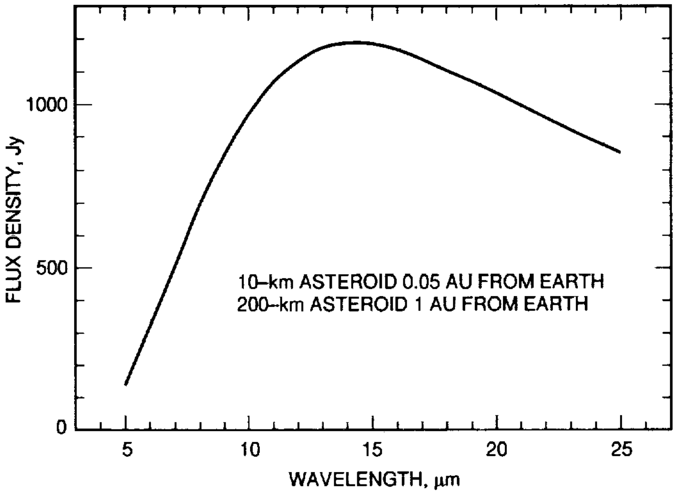

Fig. 1. Black-body calculation of approximate flux density for an asteroid located 1 AU from the Sun, as a function of wavelength.

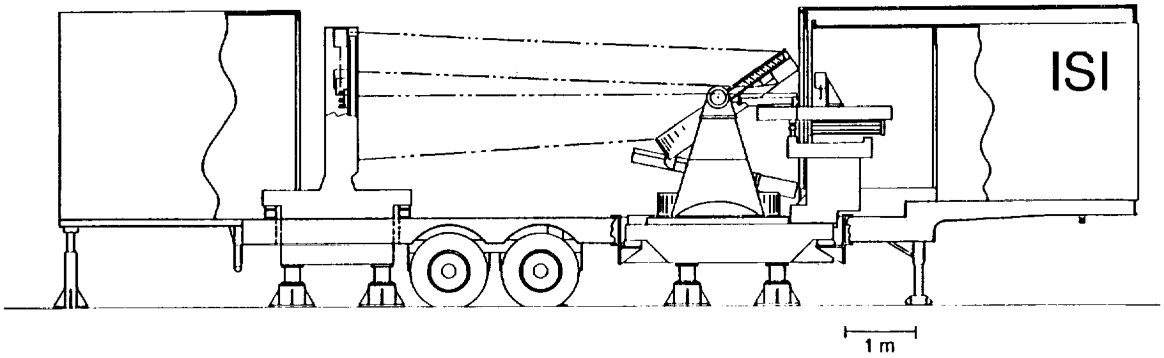

Fig. 2. A single telescope of the ISI, showing the flat mirror, parabolic mirror, and optics table.

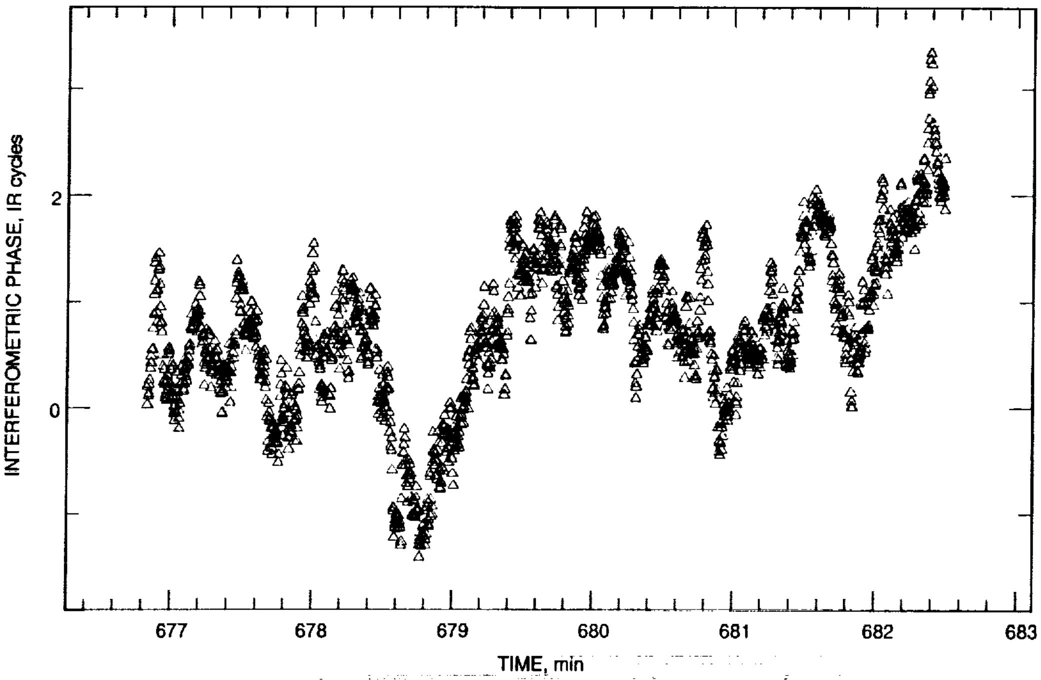

Fig. 3. Infrared interferometric phase as a function of time for the star Alpha Orionis on September 8, 1992.

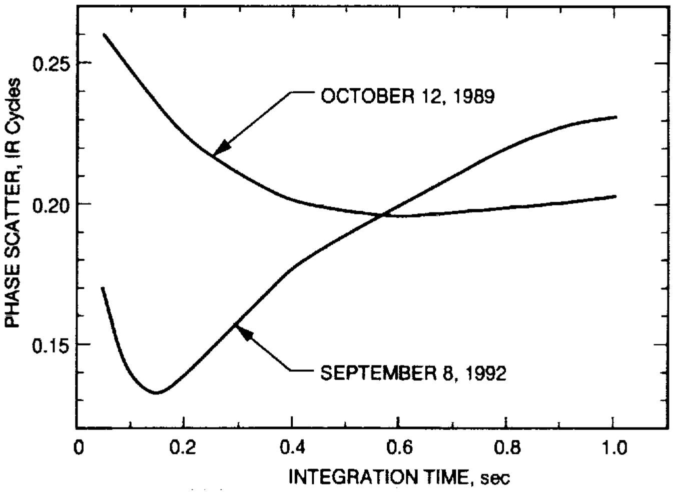

Fig. 4. The point-to-point rms phase scatter as a function of integration time for the data of Fig. 3.

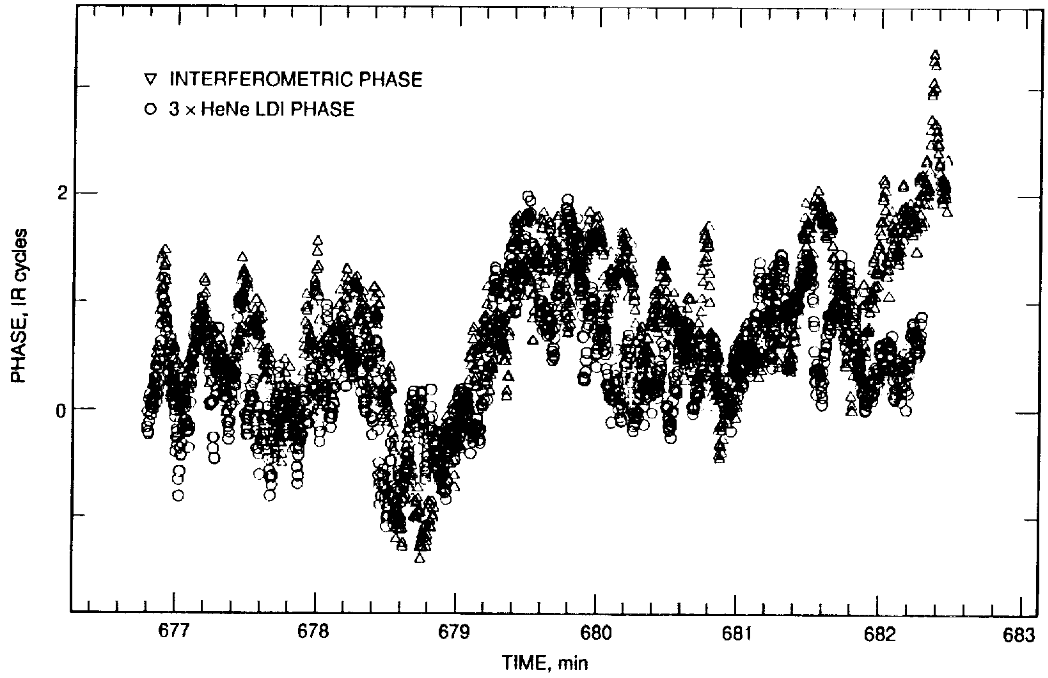

Fig. 5. The phase time series of Fig. 3 with HeNe LDI phases, scaled to infrared cycles, differenced between telescopes, and multiplied by 3.

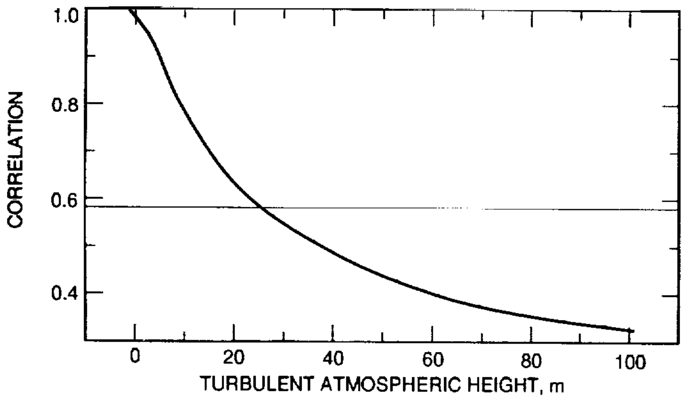

Fig. 6. The calculated correlation between telescope-differenced HeNe LDI data and interferometric data for the conditions of the data in Figs. 3–5. The horizontal line is the actual correlation from the data of Fig. 5.

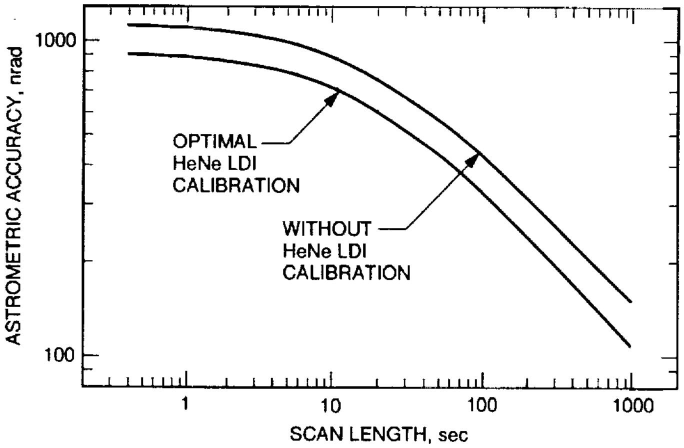

Fig. 7. The calculated astrometric accuracy, as a function of scan length, with and without optimal HeNe LDI calibration, for the conditions of Figs. 3–5.

N94-29654

Line-of-Sight Tropospheric Calibration From Measurements in Arbitrary Directions

J. Z. Wilcox
Tracking Systems and Applications Section

Tropospheric inhomogeneities limit the accuracy with which a path delay in an arbitrary direction can be estimated from calibration measurements in different directions. This article demonstrates a mathematical procedure that has the potential for minimizing errors in the estimated geometrical and tropospheric path delays. The error is minimized by applying least-squares estimation to a combined set of observables in the calibration directions and the direction to be calibrated. A simulated test of this procedure was conducted using a model set of error-free calibration measurements. In the absence of geometrical delay mismodeling, the simulation yielded delay errors which vary from about 1 mm at zenith to about 1 cm at 10 deg. The main principles of how this procedure could be applied to improve accuracy of deep space tracking using Global Positioning System (GPS) data are also discussed.

I. Introduction

Uncertainties in tropospheric path delays are a major source of error in deep space tracking. Inhomogeneities in tropospheric water vapor can result in zenith path delay calibration errors at about the 1-cm level, and inhomogeneities in the dry troposphere at about the 1- to 3-mm level, over a period of several hours [1]. The 1-cm error limits the tracking accuracy of DSN-based very long baseline interferometry (VLBI) to about 1 nrad for the angular position (at the intercontinental baselines of about 10,000 km) and to 2×10^{-14} sec/sec for the delay rate (at zenith) for a 1000-sec scan [1]. Future missions would benefit from troposphere calibration at the 1-mm level.

The error in the estimated path delay is determined by a variety of error sources whose relative importance depends on the calibration instrument. For example, for instruments which measure radio emission, such as water vapor radiometers (WVRs), the error is limited by the accuracy with which path integrals involving the imaginary part of the index of refraction can be related to integrals which involve the real part of the refraction index [2]. Whereas WVRs may be pointed in the direction to be calibrated, this may not be true in general for other instruments. If off-line-of-sight measurements are used in the calibration process, the error will inevitably be affected by tropospheric inhomogeneities, and its magnitude will depend on mathematical analysis of calibration data.

This article suggests and illustrates a mathematical procedure that minimizes the tropospheric inhomogeneity-induced error for path delays inferred from observables in other directions. The procedure involves the application of least-squares estimation to a combined set of observables in the calibration directions and the direction to be calibrated, and the use of the observable variance–covariance matrix during estimation. In order to demonstrate the procedure simply, this article makes the following assumptions: The calibration instrument is error-free (i.e., no other error source besides tropospheric inhomogeneities is present), and it detects path delays. These assumptions are used for clarity of the presentation; the method may be generalized to other types of measurements. An example of how it can be adopted to more realistic (noisy) data is discussed in Section IV of this article. If all other error sources are neglected, the calculated error determines the maximum achievable accuracy for path delay estimates using observables in other directions. Another (more commonly used) procedure determines the delay in the zenith direction by averaging over delays projected into the zenith from many calibration directions. This technique will be referred to in this article as "zenith mapping." Strictly speaking, zenith mapping produces minimal error only for a horizontally homogeneous troposphere. This article will quantify the error reduction obtained from the use of the present technique for an inhomogeneous troposphere. Since the technique's principal intended application is to improve the accuracy of deep space tracking, the direction to be calibrated will be sometimes referred to in this article as the DSN antenna pointing direction.

Section II describes the mathematical procedure used to minimize the estimated delay error. The procedure is exemplified in Section III for a model set of calibration directions (assuming error-free instrumentation) that coincides with directions of lines between a ground-based receiver and Global Positioning System (GPS) satellites visible at Goldstone.[1] These directions were selected as a matter of convenience and because they are known with great accuracy.[2] Tropospheric inhomogeneities were assumed to be generated by Kolmogorov turbulence and transported past the observer by the wind [1]. Section IV discusses the possibility of adapting the procedure to GPS data. Section V is a summary with recommendations for further studies.

II. Mathematical Approach

This section outlines the main principles of the mathematical procedure that minimizes the estimated delay error in an arbitrary direction. The main principle of the procedure is the application of least-squares estimation to a combined set of observables in the calibration directions and the direction to be calibrated (also referred to as the pointing direction of the DSN antenna), and the use of the covariance–variance matrix of observables to weight the quadratic form of observable residuals during estimation. To simplify the illustration, all measurements are assumed to be error-free and to have produced path delays.

The coordinate system is shown in Fig. 1. A calibration instrument, located at the distance $\vec{R}$ from the axis of the DSN antenna, measures tropospheric path delays $L_{tr,i}$ in N different directions (E_i, ϕ_i), where E_i and ϕ_i are elevations and azimuths, respectively, and $i = 1, ..., N$. A DSN antenna (the direction to be calibrated) points in the direction of the elevation, E_s, and azimuth, ϕ_s. By assuming that the ionospheric delay has been calibrated (e.g., by using two frequency measurements), the DSN antenna-measured delay is $L_{tot,s} = L_{g,s} + L_{tr,s}$, where $L_{tot,s}$, $L_{g,s}$, and $L_{tr,s}$ are the total, geometric, and tropospheric delays, respectively. The combined set of observables in the DSN antenna and calibration directions is:

$$L_{tot,s} = L_{tr,s} + L_{g,s} \tag{1a}$$

$$L_i = L_{tr,i} \quad i = 1, ..., N \tag{1b}$$

where the symbol L_i designates the observable $L_{tr,i}$. The delay of interest for deep space tracking is the geometrical delay $L_{g,s}$. To obtain the best estimate $\hat{L}_{g,s}$, we (1) note that $L_{tr,s}$ and $L_{tr,i}$'s are related through tropospheric correlations, (2) parameterize Eqs. (1a) and (1b) with the help of the statistically averaged zenith delay $L_{tr,z}$ (that is, $L_{tr,z}$ is not the instantaneous zenith delay, but rather a delay averaged over all possible tropospheric patterns for the site [1]), and (3) apply least-squares estimation to the parameterized Eqs. (1a) and (1b). Assuming that long-range refraction gradients [6] are absent,[3] the parameterized $L_{tr,s} = \langle L_{tr,s}\rangle + \epsilon_{tr,s}$ and $L_{tr,i} = \langle L_{tr,i}\rangle + \epsilon_{tr,i}$, where $\langle L_{tr,s}\rangle = A_s L_{tr,z}$ and $\langle L_{tr,i}\rangle = A_i L_{tr,z}$, $\langle \ldots \rangle$ designates the expectation value, A_s and A_i are air masses, and $\epsilon_{tr,s}$ and $\epsilon_{tr,i}$ represent tropospheric inhomogeneities in (E_s, ϕ_s) and (E_i, ϕ_i) directions, respectively. Note that because of (2) above, correlations of $\epsilon_{tr,s}$ and $\epsilon_{tr,i}$ can be evaluated in the statistical sense. By defining the observable, parameter, and tropospheric inhomogeneity column vectors $F \equiv [L_{tot,s}/A_s,\ L_i/A_i]$, $X \equiv [L_{tr,z},\ L_{g,s}/A_s]$,

---

[1] Listings of GPS coordinates were provided by G. Purcell, Tracking and System Application Section, Jet Propulsion Laboratory, Pasadena, California, October 1992.

[2] Other off-line-of-sight measurements to which the method may be adapted include microwave temperature profiler [3], lidar [4], radio acoustic sounding [5], and tracking using a number of proposed communication satellites systems, such as Motorola's IRIDIUM constellation.

[3] Unmodeled horizontal gradients may be on the 1-cm level for dry delays at 10-deg elevation [6]; the error can be reduced by gradient modeling during estimation.

and $\epsilon \equiv [\epsilon_{tr,s},\ \epsilon_{tr,i}]$, respectively, and by assuming that $\epsilon_{tr,i}$'s have zero means and a variance–covariance matrix W^{-1}, the parametrized Eqs. (1a) and (1b) are solved by minimizing the quadratic form of the weighted residuals $(F - \mathcal{A}\hat{X})^T\ W\ (F - \mathcal{A}\hat{X})$, where $\mathcal{A}$ is the mapping matrix in $F = \mathcal{A}\ X + \epsilon$,

$$\mathcal{A} = \begin{pmatrix} 1 & 1 \\ 1 & 0 \\ \vdots & \vdots \\ 1 & 0 \end{pmatrix} \tag{2}$$

The result is [7]

$$\hat{X}\ =\ (\mathcal{A}^T W \mathcal{A})^{-1} \mathcal{A}^T W\ F \tag{3}$$

where $\hat{X}$ is the column vector $\hat{X} \equiv [\hat{L}_{tr,z},\ \hat{L}_{g,s}/A_s]$, and the superscript T designates the transpose matrix. The error in $\hat{L}_{g,s}$ is given by the square root of the matrix element $(\sigma^2_{\hat{X}})_{2,2}$ of the variance $\sigma^2_{\hat{X}}$:

$$\begin{aligned} \sigma^2_{\hat{X}} &\equiv \left\langle (\hat{X} - X)(\hat{X} - X)^T \right\rangle \\ &= B^{-1} \mathcal{A}^T W\ \mathrm{cov}\,(F, F^T)\ W\ \mathcal{A}\ B^{-1} \end{aligned} \tag{4}$$

where cov (F, F^T) is the observable covariance–variance matrix, and $B \equiv \mathcal{A}^T\ W\ \mathcal{A}$.

The above-described procedure yields the best estimate $\hat{L}_{g,s}$ and $\hat{L}_{tr,z}$. Note, however, that once $\hat{L}_{g,s}$ has been estimated, Eq. (1a) can also be used to estimate the actual line-of-sight tropospheric delay $L_{tr,s}$. By using Eq. (1a), the estimate $\hat{L}_{tr,s}\ \equiv\ L_{tot,s}\ -\ \hat{L}_{g,s}$. $\hat{L}_{tr,s}$ is the best estimate for $L_{tr,s}$ because $\hat{L}_{g,s}$ is the best estimate for $L_{g,s}$, and because the measured $L_{tot,s}$ contains the effect of line-of-sight inhomogeneities (note that $\hat{L}_{tr,s}$ differs from $\hat{L}_{tr,z} A_s$, which is the best estimate for the statistically averaged delay). Note also that in the absence of other error sources, the error in $\hat{L}_{tr,s}$ is equal to the error in $\hat{L}_{g,s}$.

It will be useful for the ensuing discussion to explicitly write $\hat{L}_{tr,s}$ as[4]

$$\hat{L}_{tr,s} \equiv L_{tot,s} - \hat{L}_{g,s} = L_{tot,s} - A_s \hat{X}_2 = \sum_{i=1}^{N} c_i L_{tr,i} \tag{5}$$

where $c_i \equiv -(A_s/A_i)\ ((\mathcal{A}^T W \mathcal{A})^{-1} \mathcal{A}^T W)_{2,i+1}$ represents contributions from the ith calibration direction. By using Eq. (5), the estimated delay error can be expressed as follows:

$$\begin{aligned} \sigma^2_{\hat{L},tr,s} = \sigma^2_{\hat{L},g,s}\ &=\ \left\langle \left(L_{tr,s} - \sum_{i=1}^{N} c_i L_{tr,i} \right)^2 \right\rangle \\ &= \left\langle L^2_{tr,s} \right\rangle - 2 \sum_{i=1}^{N} c_i \left\langle L_{tr,s}\ L_{tr,i} \right\rangle \\ &\quad + \sum_{i,j=1}^{N} c_i c_j \left\langle L_{tr,i}\ L_{tr,j} \right\rangle \end{aligned} \tag{6}$$

Equation (6) displays an explicit dependence on the coefficients c_i's and on correlations between tropospheric path delays. When c_i's are determined by using some assumed W^{-1} (the so-called consider analysis [1]), the error will be bigger than the error obtained by using the actual observable W^{-1} [7]. A W^{-1} often used during the estimation procedure is the diagonal matrix, $W^{-1}_{i,j} = \delta_{i,j}$ (where $\delta_{i,j}$ is the Kronecker delta). The use of a diagonal W^{-1} corresponds to assuming that observable errors are uncorrelated, and Eq. (3) yields[5] $c_i = A_s/(N A_i)$, which are the same c_i's as those which would be obtained if one set $\hat{L}_{tr,z} \equiv \sum_{i=1}^{N} L_{tr,i}/(A_i\ N)$, and mapped $\hat{L}_{tr,z}$ from the zenith to the (E_s, ϕ_s) direction by using the air mass A_s. The use of zenith mapping will minimize the error only for a horizontally homogeneous troposphere. For an inhomogeneous troposphere, the error is minimized by using the observable $W^{-1} = \mathrm{cov}\,(F, F^T)$; c_i's will then depend on the full (in elevation and azimuth) angular separations between the observed and calibration directions (including the offset $\vec{R}$). By setting $W^{-1} = \mathrm{cov}\,(F, F^T)$, Eq. (4) reduces to $\sigma^2_{\hat{X}} = (\mathcal{A}^T W\ \mathcal{A})^{-1}$

III. Results for an Error-Free Calibration Instrument

Equation (6) was evaluated for a model set of calibration directions assumed to coincide with directions of lines between a ground-based receiver and GPS satellites visible at Goldstone. These directions were selected because there are between 6 and 10 satellites visible from any ground-based site, and the satellite trajectories are known with

---

[4] The proportionality coefficient between $\hat{L}_{g,s}$ and $L_{tot,s}$ is equal to 1 because no other observable depends on $L_{g,s}$.

[5] For elevation-independent correlations, $W^{-1}_{i,j} = \delta_{i,j}/A_i A_j$, the coefficients would become $c_i = A_s A_i / \sum_{i=1}^{N} A_i^2$.

great accuracy. Other directions could be selected; conclusions similar to those derived here will apply to all other selections. The error was quantified by using the Kolmogorov turbulence model for the evaluation of correlations between wet troposphere inhomogeneities, with numerical constants given in [1] (see also Appendix A of this article). The inhomogeneities were frozen into the troposphere slab transported past the observer with the wind velocity $\vec{v} = 10$ m/sec. The structure function constant $C = 1.1 \times 10^{-7} m^{-1/3}$ corresponds to average DSN observation conditions of about a 6-cm zenith wet delay for h_v = 2-km-thick wet troposphere slab [8]; in more humid weather, the structure constant will be greater, depending on turbulence. The dry fluctuation was assumed to be 30 percent of the wet fluctuation [1], which for uncorrelated fluctuations contributes less than 10 percent of the total error for correlations added in quadrature. The error evaluated with the optimized c_i's was compared to the zenith mapping error; the zenith mapping error was greater, especially at low elevations, as expected. The error was quantified for a number of directions (E_s, ϕ_s), for satellite constellations stepped by 6 min during an 8-hr period following 12:00 a.m., July 23, 1992, and for four values of the separation $R = 0$, 200, 500, and 1000 m. The biggest contribution to the estimated delay comes from a calibration direction nearest to the direction to be calibrated; the error vanishes when the two lines coincide. In the absence of a clearly nearest direction, all calibration lines contribute, increasing the error.

A. Delay Error

The error was found to depend in a relatively well-defined manner on the elevation E_s, but not (because the satellites are distributed over the azimuth fairly uniformly) on ϕ_s nor on satellite constellation. Figures 2(a) and 2(b) plot the azimuthally averaged error (dashed line) versus E_s for $R = 0$ and 1000 m. The error spread due to (1) a 360-deg range in ϕ_s, (2) a 360-deg range in the azimuth of $\vec{R}$, and (3) changes in the satellite constellation is also shown. The spread's lower bound is 0 for all E_s in Fig. 2(a) (E_s extends from 10 deg in Fig. 2(a) because the satellites were cut off at 10 deg). The bound is 0 because at $R = 0$, any direction E_s will, for some combination of ϕ_s and satellite constellation, eventually coincide with one of the calibration lines, in which event the tropospheric inhomogeneity-induced error vanishes. Note that the average error is closer to the error upper bound than to the lower bound, indicating that the error is nearly equal to the error upper bound in the majority of observations. Comparing Figs. 2(a) and 2(b), the average error has increased only very little, while the lower bound has become nonzero by increasing R from 0 to 1 km. The average error has increased little because the DSN-observed and calibration lines intersect (and thus probe the same sky region) even when $R = 1$ km; the lower bound has become nonzero because there are no coincident lines when $R > 0$. The average error is fairly flat (about 1 mm) for all E_s between zenith and 40 deg, and it increases rapidly with decreasing E_s at lower elevations; the error is about 1.6 and 12 mm at $E_s = 30$ and 10 deg, respectively.

Figure 3 illustrates how close the calibration and DSN line must be for the error to be less than some desired value. The error (the solid-line curve) will be less than 0.5 mm when the angular separation between the DSN and the nearest calibration line ($R = 0$ in Fig. 3) is less than 3 deg. How small the angular separation must be depends on elevation: modeling results suggest that for the error to be less than 1 mm, the separation must be less than 5 and 2 deg when $E_s = 30$ and 20 deg, respectively. Many estimation strategies estimate zenith delays by averaging over all calibration directions. The zenith mapping error (the dash-dot line) is bigger than the optimized, azimuthally averaged error (the dashed line) by an amount which decreases monotonically with increasing elevation, until, near zenith, the errors are nearly the same (because the mapping distance is short there).

Signal integration averages out the tropospheric inhomogeneity-induced error as the inhomogeneities are carried by wind. Figure 4 shows the effect of the signal integration time T and wind velocity v on the error.[6] The error decreases and its spread (due to different wind directions) increases slowly with increasing T. Note that the average integration time, $T_{1/2}$, required to reduce the error to one-half of its instantaneous value is (for $v = 10$ m/sec) less than 8 min for all $E_s > 30$ deg, and it increases to about 12 min at $E_s = 10$ deg. To minimize the error, c_i's used for Fig. 4 were optimized for the wind. A similar calculation using c_i's optimized for zero wind has produced curves (not shown) that look the same as those in Fig. 4 except that the error was approximately 10 to 30 percent higher (depending on elevation). This relatively small increase is good news, since the determination and inclusion of wind distribution in the estimation procedure could be nontrivial.

The use of more than one calibration instrument will (in principle) increase the probability that one calibration line will be close to the observed line. Figure 5 shows the minimum error for three instruments positioned in corners

---

[6] $R = 200$ m is used in most figures in this article, since the azimuthally averaged errors do not differ too much for all R's < 1 km, and since mounting a calibration instrument in the center of the DSN antenna is nontrivial.

of an equilateral triangle around the DSN antenna. Compared to one instrument (positioned at $R = 0$ and 200 m), the error is smaller by up to 50 percent at high elevations (where it is already small), but only by several percent at low elevations (where it would be needed the most because the error is big there). The result suggests that multiple on-site instruments will be of limited use.

B. Delay Rate Error

Figures 6 and 7 show the inhomogeneity-induced delay rate error. Rate measurements are used for navigation and gravitational wave searches; it is desirable that the inhomogeneity-induced rate error not dominate the total error on any time scale. The rate error was evaluated as the square root of the variance $\sigma^2_{\dot{B}}(T_{sc})$,

$$\sigma^2_{\dot{B}}(T_{sc}) \equiv \left\langle \left(\dot{B}(T_{sc}) - \hat{\dot{B}}(T_{sc}) \right)^2 \right\rangle \tag{7}$$

where $\hat{\dot{B}}(T_{sc})$ and $\dot{B}(T_{sc})$ are the estimated and actual delay rates, respectively, over the scan duration T_{sc} (see [1] and Appendix B). The variance was evaluated by using a linear fit to three equally spaced points[7] within T_{sc}. Figure 6 shows the error evaluated by using the optimized c_i's, and compares it with the uncalibrated error and the error evaluated by using zenith mapping for two elevations, $E_s = 10$ and 60 deg. All three errors decrease with increasing T_{sc} (as they should). However, whereas the optimized error is actually slightly bigger than the uncalibrated and zenith mapping errors for extremely short scans ($T_{sc} <$ 10 sec), the optimized error decreases with increasing T_{sc} more rapidly than the other errors, becoming smaller at a T_{sc} that depends on E_s. For example, at $E_s = 10$ and 60 deg, the error becomes smaller at $T_{sc} = 500$ and 30 sec, respectively. For the error to be reduced by using the optimized c_i's, the scan must be longer than some critical T_{sc}, which is longer at low E_s than at high E_s. At $T_{sc} = 1000$ sec ($R = 200$ m), the average error is about 4×10^{-15} sec/sec and 7×10^{-14} sec/sec at $E_s = 60$ and 10 deg, respectively.

The rate error can also become very small when the angular separation between the observed and nearest calibration line is sufficiently small; however, the condition for the separation smallness is tighter than that for the delay error. This is illustrated in Fig. 7 for $R = 0$. For the error to be less than 10^{-15} sec/sec, the angular separation must be less than about 0.5 deg when $T_s = 1000$ sec and less than about 0.05 deg when $T_s = 100$ sec.

IV. Application to GPS

This section discusses how the mathematical procedure described in Section III could be adapted to path delay estimation using GPS data. GPS tracking depends directly on path delays.[8] However, because of the complexities of GPS delay modeling and data reduction, the present approach to GPS data analyses, driven by the requirement to eliminate or estimate clock errors and geometrical parameter uncertainties,[9] entails estimation of instantaneous zenith delays [9]. Parameter estimation is performed without the use of the tropospheric covariance–variance matrix. The zenith tropospheric delay is constructed by spatial averaging over all satellites. This zenith delay could be used to estimate tropospheric delays in the direction of the DSN antenna by scaling it (using the air mass) into the DSN antenna direction. This article suggests that in the absence of other error sources, line-of-sight delays could be estimated more accurately by modifying the estimation strategy to include the tropospheric correlations between different lines of sight and by applying the estimation procedure to the combined GPS and DSN data.

The coordinate system is the same as in Fig. 1 except that receivers (which are a part of a large global network consisting of about 40 continuously operating receivers set up to estimate the geometrical parameters and to determine the clock uncertainties with the best possible accuracy) are separated by large (several hundred-km) distances. For M receivers, one can introduce M statistically averaged, mutually uncorrelated zenith delays, $L_{tr,j,z}$, where $j = 1, ..., M$. The DSN antenna is assumed to be at the site $j = 1$. At its completion, the GPS constellation will include 24 navigation satellites at about a 20,000-km altitude and equally spaced in six orbit planes. A receiver at any ground-based site will track between 6 and 10 satellites distributed more or less uniformly in azimuth and typically above 10 deg in elevation. The collected data set covers a time period long enough for the number of data in the set to exceed the number of solve-for parameters. Including the delay for the radio signal received by the DSN antenna, the observables are

$$L_{tot,s} = L_{tr,s} + L_{g,s} \tag{8a}$$

---

[7] It can be shown that as the number of fitted points increases to infinity, the rate error changes by only about 20 percent [1].

[8] GPS receivers are used in an automated operating mode, work in all weather conditions, and sense the total (wet and dry) path delays. The satellites transmit carrier signals at two L-band frequencies (1.227 GHZ and 1.575 GHz), so that the ionospheric delay can be calibrated.

[9] S. M. Lichten, personal communication, Tracking Systems and Applications Section, Jet Propulsion Laboratory, Pasadena, California, October 1992.

$$L_{tot,i,j} = L_{tr,i,j} + L_{g,i,j} + L_{cl,i,j} \qquad i = 1, ..., N \quad j = 1, .., M \tag{8b}$$

where N is the total number (assumed to be the same for all receivers) of calibration data at one receiver site (the subindex i counts both the visible satellites and the data sequence for each satellite), and $L_{cl,i,j}$ is a delay caused by clock estimate errors at both the satellite and the receiver. All other symbols are the same as in Section II, and the ionospheric delays have been assumed to be calibrated. Similar to Eqs. (1a) and (1b), Eqs. (8a) and (8b) can be parameterized by setting $\langle L_{tr,s}\rangle = A_s\ L_{tr,1,z}$ and $\langle L_{tr,i,j}\rangle = A_i\ L_{tr,j,z}$, where $L_{tr,j,z}$ are the statistically averaged tropospheric delays in the zenith direction at jth site. By assuming that the observable errors have zero means and a variance–covariance matrix W^{-1}, the parameterized Eqs. (8a) and (8b) can be solved by least-squares estimation for the geometrical delays $L_{g,s}$ and $L_{g,i,j}$ (or rather, by using geometrical delay modeling for parameters which determine $L_{g,s}$ and $L_{g,i,j}$), clock errors $L_{cl,i,j}$, and zenith delays $L_{tr,j,z}$. As was discussed in Section II, it is this parameterization, accompanied by the statistical evaluation of W^{-1}, that allows the solution to produce best estimates. Note also that once $L_{g,s}$ has been estimated, the best estimate for line-of-sight $L_{tr,s}$ can in principle be obtained as the difference $\hat{L}_{tr,s} = L_{tot,s} - \hat{L}_{g,s}$.

For real data, the accuracy of path delay estimates, in addition to tropospheric inhomogeneities, will be affected by other error sources, including instrument and multipathing noise and uncertainties in geometrical delay modeling. Neglecting the specifics of geometrical delay modeling and error statistics, the effect of an overall uncertainty level contributed by various error sources has been modeled by adding to each cov $(L_{tr,i}, L_{tr,i})$ a term assumed to be uncorrelated between different directions and proportional to the air mass. Figure 8 shows the effect of the assumed 0.1-, 0.3-, and 1-cm uncertainty levels.[10] Note that these levels exceed the tropospheric inhomogeneity-induced errors at $E_s = 50$, 22, and 12 deg, respectively. That is, to achieve the tropospheric inhomogeneity-limited accuracy at some elevation, the additional uncertainty must be reduced below the inhomogeneity-induced error at that elevation. The dashed curves in Fig. 8 show the error resulting from the use of c_i's which were optimized for zero measurement and modeling uncertainty. The errors are bigger than for the optimized c_i's by about 15 percent, which is sufficiently small to argue that the use of c_i's optimized for zero additional uncertainty will not significantly increase the total error.

V. Conclusions and Recommendations

This article has outlined a mathematical procedure which has the potential for minimizing the tropospheric inhomogeneity-induced mapping error for estimated path delays along arbitrary lines of sight by using observables from different directions. The main principle of the procedure is the application of least-squares estimation to the combined set of observables in the calibration directions and the direction to be calibrated, and the use of an observable variance–covariance matrix during estimation. A numerical example was given for a set of calibration directions assumed to coincide with directions from a ground-based receiver to GPS satellites visible at Goldstone. For these directions, assuming an error-free calibration instrument and zero geometrical delay mismodeling, and using the Kolmogorov turbulence model, the azimuthally averaged error is found to be about 1 mm in the elevation range from about 40 deg to zenith. At elevations less than 40 deg, the error increases with decreasing elevation, reaching about 1.2 cm at 10 deg. Because of its stochastic origin, the inhomogeneity-induced error cannot be removed by improved modeling or instrument design, and represents the ultimate accuracy for line-of-sight estimates.

The minimum error was compared to the error obtained by using zenith delays which were averaged over many calibration directions, and to error obtained by using line-of-sight estimates optimized for zero wind. The zenith mapping error is nearly twice as large (in the absence of other error sources) as the minimum error, indicating that the effort spent to minimize the error is worthwhile. On the other hand, the error increase resulting from the use of zero wind was less than 30 percent, indicating that it may not be necessary to include the wind in the estimation procedure. Signal integration reduces the error; the integration time required to halve the instantaneous error is less than 8 min for elevations between 30 deg and zenith, reaching about 12 min at 10 deg. The use of multiple on-site receivers will not help to reduce the error at low elevations where it would be needed the most.

The suggested procedure could be used to estimate path delays in the direction of the DSN antenna by using GPS data. The present strategy for GPS data analyses entails construction of a tropospheric zenith delay by averaging over all satellites; the estimated zenith delay error is at the 1-cm level due to the combined effect of tropo-

---

[10] Analysis of recent GPS data shows that assumption of uncorrelated errors is not entirely correct. Efforts to understand the error statistics are under way.

spheric inhomogeneities, uncertainties in geometrical delay modeling, and measurement (thermal noise and multipathing) uncertainties [9]. The combined effect of additional uncertainties has been modeled by adding to the tropospheric variances a term assumed to be uncorrelated between various measurements. As expected, the accuracy of the estimate was limited by this additional term whenever it exceeded the tropospheric inhomogeneity-induced level. Further work should be performed to establish levels and statistics of additional error sources, incorporate their correlations into the analysis, and, if possible, reduce their effect on path delay estimates.

In spacecraft tracking, observing epochs and scan lengths are specified by mission considerations, and the tracked directions differ from satellite directions. However, experiments could be designed in which the direction to be calibrated coincides with one of the satellite directions. For example, by directing WVRs towards satellites, the WVRs themselves could be calibrated.

Acknowledgments

The author is grateful to R. N. Treuhaft for encouragement, many valuable suggestions, and discussions; to G. Purcell for providing the listings of GPS constellations; and to S. M. Lichten and G. M. Resch for discussions and critical reading of the manuscript.

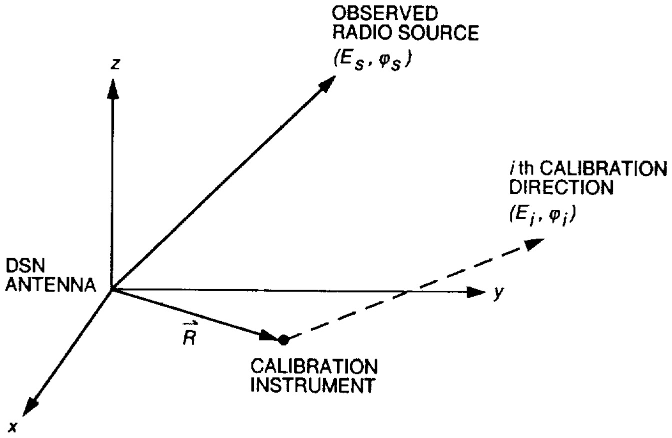

Fig. 1. The coordinate system for DSN and calibration directions.

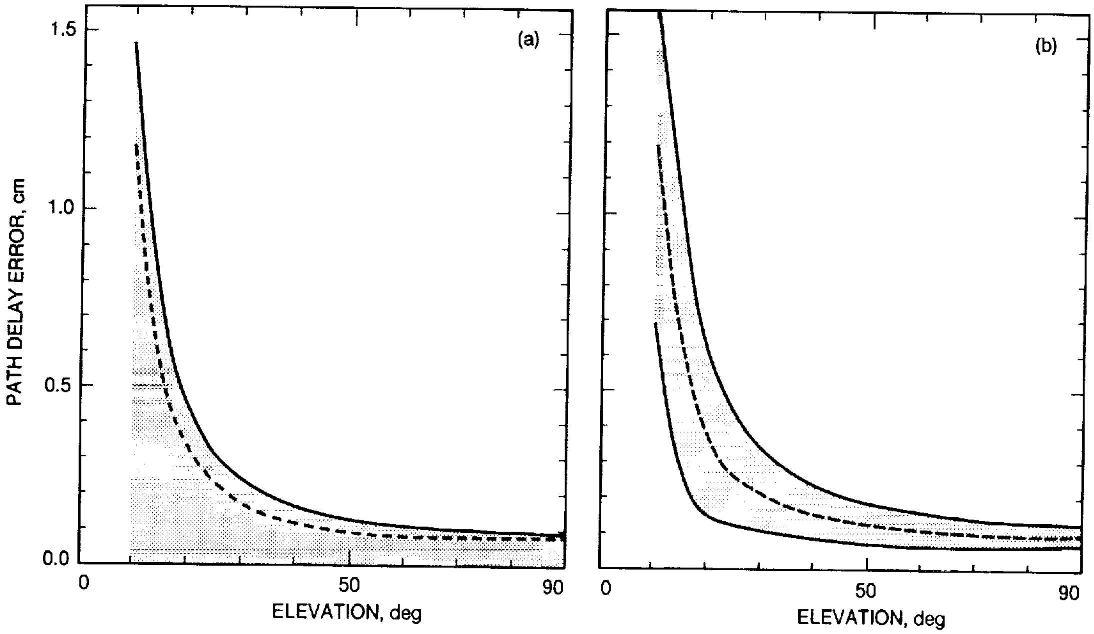

Fig. 2. The instantaneous, tropospheric fluctuation-induced path delay error versus the observed elevation, for (a) $R = 0$ m and (b) $R = 1000$ m. The error range is due to the 360-deg range in the observed azimuth, the azimuth of $\vec{R}$, and satellite constellations. The dashed curves are the azimuthally averaged error.

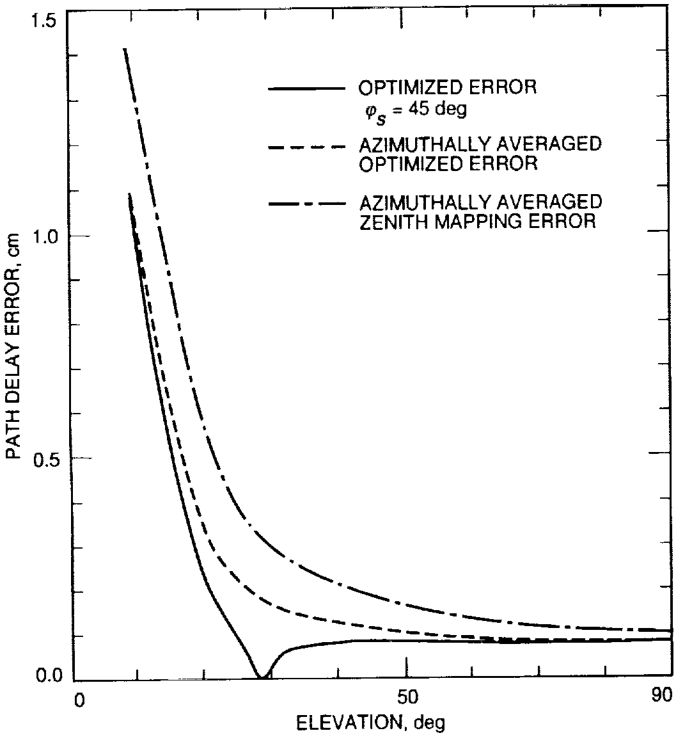

Fig. 3. The tropospheric fluctuation-induced error for one calibration line pointed in the ϕ_l = 45-deg, E_l = 28.4-deg direction (R = 0, error-free calibration instrument). The error with optimized c_l's (solid and dashed-line curves) is less than the zenith mapping error (dash–dot curve) by an amount that depends on the elevation.

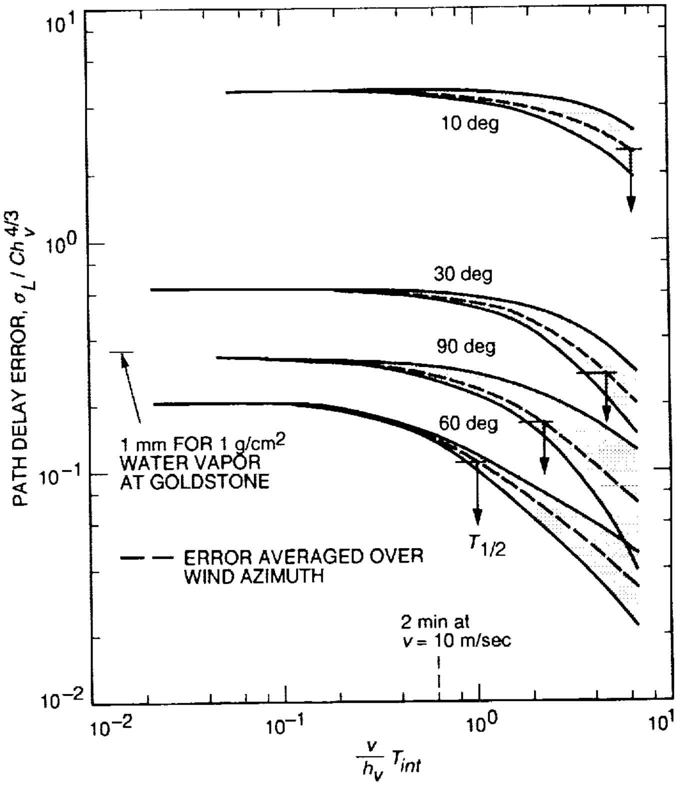

Fig. 4. Tropospheric fluctuation-induced error and the error range (averaged over four principal wind directions) versus the signal integration time T. The azimuth of $\bar{R}$ (R = 200 m) is along the azimuth of ϕ_s, v = 10 m/sec, and the satellite constellation is for 12:00 a.m., July 1, 1992; C is the turbulence strength constant.

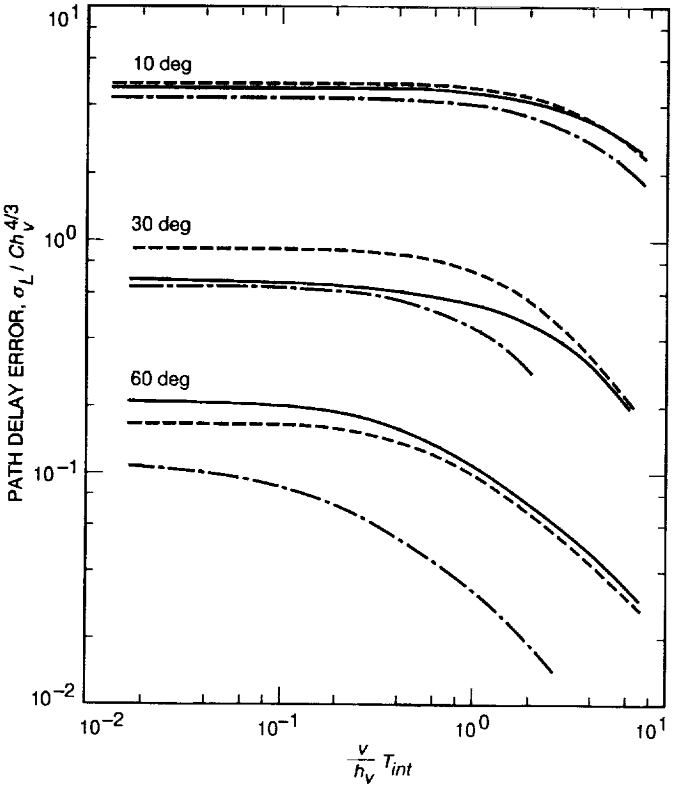

Fig. 5. Tropospheric fluctuation-induced error with c_i's optimized for three calibration instruments positioned at corners of an equilateral triangle centered at R = 200 m around the DSN antenna (dash–dot line); one instrument located at R = 0 (solid line); and one instrument at 200 m (dashed line).

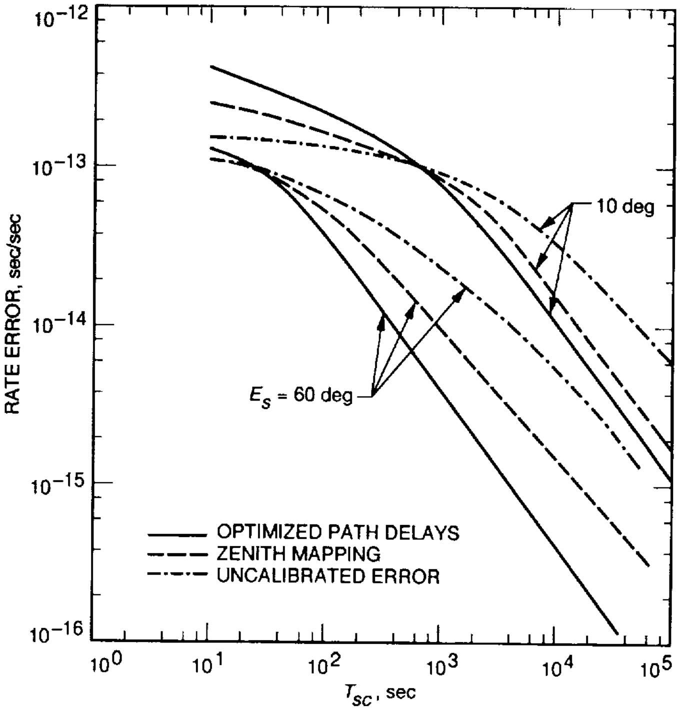

Fig. 6. Tropospheric fluctuation-induced, azimuthally averaged rate error versus scan duration (R = 200 m, v = 10 m/sec). The error calculated by using the optimized c_i's becomes smaller than the uncalibrated error and the error for zenith mapping at a T_{sc} that depends on elevation.

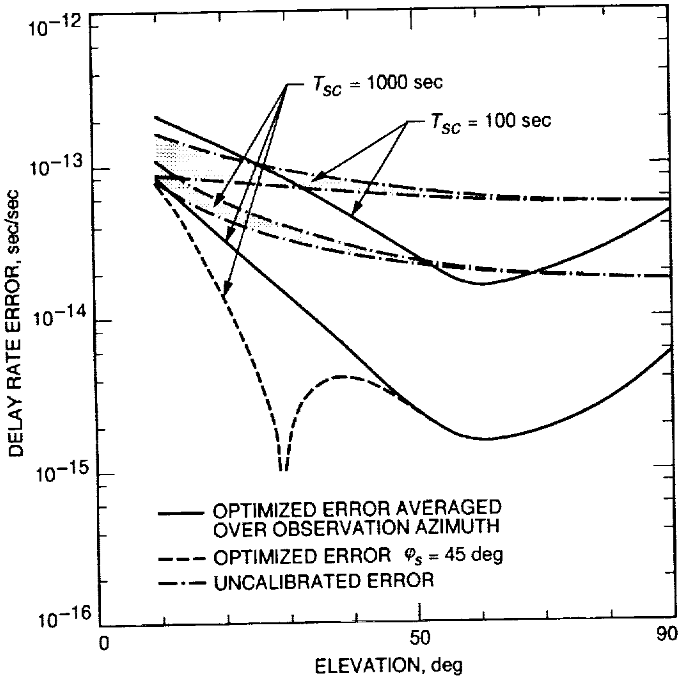

Fig. 7. Tropospheric fluctuation-induced rate error for scan durations T_s = 100 sec and 1000 sec versus E_s when $R = 0$. The satellite constellation used (12:00 a.m., July 1, 1992) has one satellite in the ϕ_i = 45-deg direction.

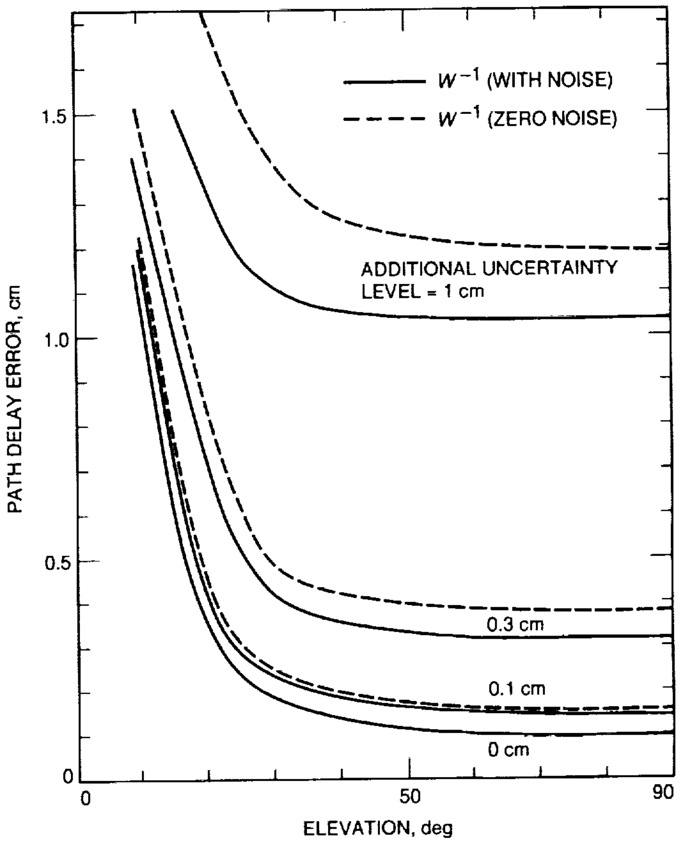

Fig. 8. The combined effect of additional uncorrelated uncertainty levels on the total (azimuthally averaged) error for R = 200 m. The solid-line curves were computed by using c_i's optimized for the additional uncertainty; the dashed lines used c_i's optimized for zero additional uncertainty.

Appendix A

Tropospheric Correlations Using the Kolmogorov Turbulence Model

Path delay correlations are evaluated by writing the path delay at site i and time t as the integral

$$L_{tr,i}(t) = \int_0^{h_v A_i} \chi(\vec{r}_i, t) dr_i \tag{A-1}$$

where the air mass $A_i = 1/\sin E_i$, h_v is the wet troposphere slab height, and $\chi(\vec{r}_i, t)$ is the index of refraction -1 at location $\vec{r}_i$ and time t. For example, the correlation

$$\text{cov}\ (L_{tr,i}(t), L_{tr,j}(t+T)) = (\langle L_{tr,i}(t), L_{tr,j}(t+T)\rangle - \langle L_{tr,i}\rangle \langle L_{tr,j}\rangle) \tag{A-2}$$

is evaluated by substituting Eq. (A-1) and the expression (Eq. (A.3) of [1]):

$$\langle \chi(\vec{r}_i, t)\chi(\vec{r}_j, t+T)\rangle = \langle \chi^2 \rangle - \frac{1}{2} D_\chi(\vec{r}_i - \vec{r}_j + \vec{v}\, T) \tag{A-3}$$

where $\vec{v}$ is the wind velocity, and $D_\chi(\vec{r}_i - \vec{r}_j + \vec{v}\, T) \equiv \left\langle (\chi(\vec{r}_i, t) - \chi(\vec{r}_j, t+T))^2 \right\rangle$ is the structure function for inhomogeneities correlated both spatially and temporally. By interchanging the order of integration and ensemble averaging and setting $dr_i = A_i dz$ and $dr_j = A_j dz'$, Eq. (A-2) becomes

$$\text{cov}\ (L_{tr,i}(t), L_{tr,j}(t+T)) = A_i A_j \int_0^{h_v} dz \int_0^{h_v} dz' \left(\sigma_\chi^2 - \frac{D_\chi(\vec{r}_i - \vec{r}_j + \vec{v}\, T)}{2} \right) \tag{A-4}$$

where the variance $\sigma_\chi^2 \equiv \langle \chi^2 \rangle - \langle \chi \rangle^2$ is independent of spatial coordinates and is obtained by letting the distance R go to infinity in D_χ,

$$\sigma_\chi^2 \equiv \left(\langle \chi^2 \rangle - \langle \chi \rangle^2 \right) = \frac{D_\chi(R = \infty)}{2} \tag{A-5}$$

Assuming that the troposphere is described by the Kolmogorov turbulence model, the structure function for the frozen inhomogeneities is

$$D_\chi(\vec{R} + \vec{v}\, t) \equiv \left\langle \left(\chi(\vec{r}, t) - \chi(\vec{r} + \vec{R} + \vec{v}\, t) \right)^2 \right\rangle = \frac{C^2\ |R + \vec{v}\, t|^{2/3}}{1 + (|R + \vec{v}\, t|/L_s)^{2/3}} \tag{A-6}$$

where $\vec{R}$ is the spatial interval over which the structure function is evaluated, the saturation scale length $L_s \simeq 3000$ km, and the turbulence strength $C = 1.1 \times 10^{-7} \text{m}^{-1/3}$ [1,8] (for the wet slab height $h_v \simeq 2$ km, corresponding to about a 6-cm zenith wet path delay at Goldstone).

Equations of the same type were also used to quantify the effect of dry fluctuations. Assuming that the dry fluctuation is one-third of the wet fluctuation [1] with the scale height $h_d \simeq 8$ km, the dry turbulence strength $C_d \simeq (C_v/3)(h_v/h_d)^{4/3} \simeq 9.2 \times 10^{-9}$. For uncorrelated fluctuations, dry and wet errors add in quadrature.

Appendix B

The Delay Rate Error

The delay rate error was evaluated as the square root of the variance of the estimated delay rate, $\hat{B}(T_{sc})$, which is the slope of the path delay over the scan duration T_{sc} [1]. By dividing T_{sc} into N sections of equal length, and assuming that the time origin is in the middle of T_{sc}, a linear fit to points at the centers of the sections gives the following formula:

$$\hat{B}(T_{sc}) = \frac{\sum_i \hat{L}(t_i)t_i}{\sum_i t_i^2} \qquad \text{(B-1)}$$

where $L(t_i)$ is the delay at the time point t_i at the center of the ith section. By using a similar expression for the actual delay rate, $B(T_{sc})$, the delay rate variance is derived as

$$\sigma_{\hat{B}}^2(T_{sc}) = \left\langle \left(B(T_{sc}) - \hat{B}(T_{sc})\right)^2 \right\rangle$$

$$= \frac{1}{(\sum_i t_i^2)^2} \sum_i \sum_j t_i \; t_j \; \sigma_{\hat{L},tr}^2(t_i - t_j) \qquad \text{(B-2)}$$

where $i, j = 1, ..., N$, and the path delay variance, $\sigma_{\hat{L},tr}^2(t)$, is

$$\sigma_{\hat{L},tr}^2(t) = \left\langle \left(L_{tr,s}(t) - \hat{L}_{tr,s}(t)\right) \left(L_{tr,s} - \hat{L}_{tr,s}\right) \right\rangle \quad \text{(B-3)}$$

where $L_{tr,s}(t)$, $\hat{L}_{tr,s}(t)$, $L_{tr,s}$, and $\hat{L}_{tr,s}$ are the actual and estimated tropospheric path delays in the observed, (E_s, ϕ_s), direction, at times t and o, respectively.

By using $\hat{L}_{tr,s} = \sum_k c_k L_{tr,k}$ (see the discussion following Eq. (5) of the main text), Eq. (B-2) was evaluated by substituting Eq. (B-3) into Eq. (B-2). This yields

$$\sigma_{\hat{B}}^2(T_{sc}) = \frac{1}{(\sum_i t_i^2)^2} \sum_i \sum_j t_i \; t_j \Big[\text{cov}\; (L_{tr,s}(t_i - t_j), L_{tr,s})$$

$$+ \sum_k \sum_l c_k c_l \; \text{cov}\; (L_{tr,k}(t_i - t_j), L_{tr,l})$$

$$- \sum_k c_k (\text{cov}\; (L_{tr,s}(t_i - t_j), L_{tr,k})$$

$$+ \text{cov}\; (L_{tr,k}(t_i - t_j), L_{tr,s}))\Big] \qquad \text{(B-4)}$$

where $L_{tr,k}(t)$ are tropospheric path delays in (E_k, ϕ_k) directions at time t. Eq. (B-4) was evaluated for i =1,..., 3 equally spaced sections within T_{sc} ($t_1 = -T_{sc}/3$, $t_0 = 0$, $t_2 = T_{sc}/3$) by using the Kolmogorov turbulence model described in Appendix A.

References

[1] R. N. Treuhaft and G. E. Lanyi, "The Effect of the Dynamic Wet Troposphere on the Radio Interference Measurements," *Radio Science*, vol. 22, pp. 251–265, March–April 1987.

[2] G. Elgered, J. L. Davis, T. A. Herring, and I. I. Shapiro, "Geodesy by Radio Interferometry: Water Vapor Radiometry for Estimation of Wet Delay," *Journal of Geophysical Research*, vol. 96, no. B4, pp. 6541–6555, April 1991, and references therein.

[3] F. T. Ulaby, R. K. Moore, and A. K. Fung, "Microwave Remote Sensing, Active and Passive," *From Theory to Applications*, vol. 3, Dedham, Massachusetts: Artech House Inc., 1986.

[4] T. Kobayashi, "Techniques for Laser Remote Sensing of the Environment," *Remote Sensing Reviews*, vol. 3, 1987.

[5] W. L. Smith, H. E. Revercomb, H. B. Howell, H.-L. Huang, R. O. Knuteson, E. W. Koenig, D. D. LaPorte, S. Silverman, L. A. Sromovsky, and H. M. Woolf, "GHIS—The GOES High-Resolution Interferometer Sounder," *Journal of Applied Meteorology*, vol. 29, pp. 1189–1204, December 1990.

[6] J. B. Abshire and C. S. Gardner, "Atmospheric Refractivity Corrections in Satellite Laser Ranging," *IEEE Trans. on Geoscience and Remote Sensing*, vol. GE-23, pp. 441–425, July 1985.

[7] W. C. Hamilton, "Statistics in Physical Science," New York: The Ronald Press Company, 1964.

[8] J. Z. Wilcox, "The Effect of Tropospheric Fluctuations on the Accuracy of Water Vapor Radiometry," *The Telecommunications and Data Acquisition Progress Report 42-110, vol. April–June*, Jet Propulsion Laboratory, Pasadena, California, pp. 33–51, August 15, 1992.

[9] D. M. Tralli, S. M. Lichten, and T. A. Herring, "Comparison of Kalman Filter Estimates of Zenith Atmospheric Path Delays Using the Global Positioning System and Very Long Baseline Interferometry," *Radio Science*, vol. 27, no. 6, pp. 999–1007, November–December 1992.

N94- 29655

February 15, 1994

Enhanced Orbit Determination Filter Sensitivity Analysis: Error Budget Development

J. A. Estefan
Navigation Systems Section

P. D. Burkhart
The University of Texas at Austin

An error budget analysis is presented which quantifies the effects of different error sources in the orbit determination process when the enhanced orbit determination filter, recently developed, is used to reduce radio metric data. The enhanced filter strategy differs from more traditional filtering methods in that nearly all of the principal ground system calibration errors affecting the data are represented as filter parameters. Error budget computations were performed for a Mars Observer interplanetary cruise scenario for cases in which only X-band (8.4-GHz) Doppler data were used to determine the spacecraft's orbit, X-band ranging data were used exclusively, and a combined set in which the ranging data were used in addition to the Doppler data. In all three cases, the filter model was assumed to be a correct representation of the physical world. Random nongravitational accelerations were found to be the largest source of error contributing to the individual error budgets. Other significant contributors, depending on the data strategy used, were solar-radiation pressure coefficient uncertainty, random Earth-orientation calibration errors, and Deep Space Network (DSN) station location uncertainty.

I. Introduction

Development of improved navigation techniques which utilize radio Doppler and ranging data acquired from NASA's Deep Space Network (DSN) have received considerable study in recent years, as these data types are routinely collected in tracking, telemetry, and command operations. Furthermore, the availability of high-speed workstation computers has made possible the use of computationally intensive data processing modes for reducing all radio metric data. A new sequential data filtering strategy currently under study is the *enhanced orbit determination filter*, in which most if not all of the major systematic ground system calibration error sources are treated as filter (estimated) parameters, along with the spacecraft trajectory parameters. This strategy differs from the current practice, in which the ground system calibration error sources are represented as unestimated bias parameters, accounted for only when computing the error covariance of the filter parameters.

The motivation behind the enhanced filter is not so much to improve upon the a priori ground system calibrations, but to incorporate a more accurate model of the physical world into the filter [1]. Previous studies suggest that medium-to-high navigation accuracies (40 to 15 nrad in an angular sense) are achievable when the enhanced orbit determination filter is used in conjunction with X-band (8.4-GHz) Doppler and ranging [2]. Studies are also being conducted to demonstrate the utility of this new filtering strategy with actual flight data acquired from the Galileo spacecraft.[1] Critical to understanding the potential benefits and/or deficiencies of this type of orbit determination filter is the development of an *error budget*, which catalogs the contributions of a particular error source or group of error sources to the estimation errors. This form of sensitivity analysis identifies the major sources of error and where future work may need to be focused in order to improve overall navigation system performance.

This article first reviews the fundamental concepts of reduced-order filtering theory, which are essential for sensitivity analysis and error budget development. The theory is then applied to the development of an error budget for a Mars Observer interplanetary cruise scenario in which the enhanced orbit determination filter is used to reduce X-band Doppler and ranging data. The trajectory characteristics of this scenario are reviewed along with the data-acquisition strategies. The filter model is described and error budgets are given for three different data strategies: X-band Doppler only, X-band ranging only, and X-band Doppler plus ranging. For this initial study, the filter model is assumed to be a correct representation of the physical world.

II. Reduced-Order Filtering

In some navigation applications, it is not practical to implement a full-order or truly optimal filter when the system model, with all major error and noise sources, is of high order. This is often the case in applications such as a multisensor avionics navigation system, in which there are memory limitations in the onboard flight computer.[2] Moreover, it is implicitly assumed in the development of the filter equations that exact descriptions of the system dynamics, error statistics, and the measurement process are known; unfortunately, this is rarely true in practice [3]. Use of *reduced-order filtering* techniques allows the analyst to obtain estimates of key parameters of interest, with reduced computational burden and with moderate complexity in the filter model [3,4]. Thus, reduced-order, or, *suboptimal*, filters are the result of design trade-offs in which the designer performs a sensitivity analysis to determine which sources of error are most critical to overall system performance.

In general, the spacecraft orbit determination process is executed entirely on the ground and thus flight computer memory limitations are not a significant factor. Nevertheless, there are reasons for not always using a full-order optimal filter for spacecraft orbit determination. Some of the reasons include: (1) certain parameters, such as fiducial station locations, may be held fixed in order to define a reference frame and/or length scale; (2) there may be a lack of adequate models for an actual physical effect; (3) the existence of computational limitations when attempting to adjust parameters of high order, such as the coefficients in a gravity field; or (4) if estimated, the computed uncertainty in model parameters would be reduced far below the level warranted by model accuracy [5,6].

A. Filter Evaluation Modes

There are a number of error analysis methods which can be used to evaluate filter models and predict filter performance. Reduced-order error analysis techniques enable an analyst to study the effects of using incorrect a priori statistics, data-noise/data-weight assumptions, or process noise models on the filter design. This is usually referred to as the *general filter evaluation mode* and accomplished by establishing a fully detailed reference model (a *truth* model) against which the behavior of a filter can be compared [5]. If the filter is optimal, then the filter and truth models coincide. If the filter is suboptimal, then the filter model is of equal or lower order (i.e., reduced-order) than the truth model and possibly (but not necessarily) represents a subset of the states of the truth model [3]. In practice, a fully detailed truth model may be difficult to develop and thus one typically evaluates a range of "reasonable" truth models to assess whether the filter results are especially sensitive to a particular element(s) of the filtering strategy being used [5]. The objective is to design a filter model to achieve the best possible accuracy, but which is also robust, so that its performance will not be adversely affected by the use of slightly incorrect filter parameters. In the design process, the filter structure and the truth model remain fixed while repeated adjustments are made to the a priori statistics, data noise

---

[1] S. Bhaskaran (personal communication), Navigation Systems Section, Jet Propulsion Laboratory, Pasadena, California, October 1993.

[2] J. Vagners, *Development of the Minimum Variance Reduced Order (MVRO) Estimator Equations in Upper Triangular-Diagonal (U-D) Factored Form*, Boeing report D229-10602-1 (internal document), The Boeing Company, Seattle, Washington, February 21, 1979.

values, or process noise values, until acceptable behavior is achieved [4].

In a special case of reduced-order error analysis, often referred to as a *consider state analysis*, various systematic error sources are treated as unmodeled parameters which are not estimated, but whose effects are accounted for (i.e., "considered") in computing the error covariance of the estimated parameters [7].[3] In a consider state analysis, the sensitivity of the estimated parameter set to various unmodeled consider parameters can be computed via the partial derivatives of the state estimate with respect to the consider parameter set [8]. Depending on the magnitude of the resulting sensitivities, the filter-computed estimation error covariance is modified to account for the unmodeled effects in order to generate a more realistic estimate of predicted navigation performance. The filter has no knowledge about the contribution of the unmodeled parameters to the uncertainty in the state estimate since the modified covariance (the *consider covariance*), which includes effects from both the estimated and consider parameters, is not fed back to the filter. Reduced-order filters of this type have been known to experience *failure modes*, such as cases in which the addition of data yields an increase in the consider covariance, or cases when the consider covariance propagates to an unreasonably large result over time. In these instances, it may be necessary to empirically "tune" the filter (e.g., adjust data weights, model assumptions, etc.) to obtain useful estimates. A mathematical description of these so-called "failure modes" and suggested remedies is described by Scheeres [6].

B. Optimal and Suboptimal Filter Equations

Restricting the discussion to the filter measurement update equations, the mathematical model presented here is the *covariance form* of the measurement update for scalar measurements. Let $\hat{\mathbf{x}}$ represent the state estimate and P represent the error covariance matrix. Using the convention that "(+)" denotes a postmeasurement update value and "(−)" denotes a premeasurement update value, the (optimal) filter measurement update equations for a linear, sequential estimator are given by

$$\text{state estimate} \qquad \hat{\mathbf{x}}_k^{(+)} = \hat{\mathbf{x}}_k^{(-)} + \hat{K}_k \left[\mathbf{z}_k - A_{x_k}\hat{\mathbf{x}}_k^{(-)}\right] \quad (1)$$

$$\text{error covariance} \qquad P_k^{(+)} = \left[I - \hat{K}_k A_{x_k}\right] P_k^{(-)} \quad (2)$$

$$\text{(optimal) gain matrix} \quad \hat{K}_k = \alpha_k^{-1} P_k^{(-)} A_{x_k}^T \quad (3)$$

where $\mathbf{z}_k$ is the observation vector defined by the measurement model, A_{x_k} is the measurement matrix of observation partial derivatives, I is simply the unit or identity matrix, and $\alpha_k = A_{x_k} P_k^{(-)} A_{x_k}^T + W_k^{-1}$ is the innovations covariance. W_k represents the weighting matrix, the inverse of which is taken to be the diagonal measurement covariance R_k; thus, for $i = 1, \ldots, m$ observations, $W_k^{-1} \equiv R_k = \text{diag}\,[r_1, \ldots, r_m]$ for measurement variances r_i.[4] The filter equations described by Eqs. (1) through (3) can be employed without loss of generality, since "whitening" procedures can be used to statistically decouple the measurements in the presence of correlated measurement noise and obtain a diagonal R_k [7]. The gain matrix K_k is used to update estimates of the filter parameters as each measurement is processed. Note that Eq. (2) is valid only for the optimal gain $\hat{K}_k$.

The use of Eq. (2) to compute the error covariance matrix has historically been suspect due to finite computer word length limitations.[5] As a result, a frequently utilized alternative is the *stabilized Joseph form* of the update, expressed as

$$P_k^{(+)} = \left(I - K_k A_{x_k}\right) P_k^{(-)} \left(I - K_k A_{x_k}\right)^T + K_k W_k^{-1} K_k^T \quad (4)$$

Although this form of the covariance measurement update is more stable numerically than Eq. (2), it requires a greater number of computations; however, a further advantage is that it is valid for *arbitrary* gain matrices; therefore, K_k in Eq. (4) need not be optimal.

In some cases, the Joseph form of the update may also be deficient numerically [9]. As a result, factorization methods have been developed to help alleviate the numerical deficiencies of the measurement update algorithms [7,10,11]. Specific details of the factorization procedures will not be discussed here; however, an important observation from the literature and critical to the general evaluation mode of the filter is the observation that Eq. (4) can be written in an equivalent form as

---

[3] This is the more traditional filtering method most often used in practical applications of interplanetary navigation (see introductory remarks), operationally referred to as the *consider option*.

[4] It is assumed that the measurements are corrupted by a vector of independent, zero-mean Gaussian random noise quantities with covariance R_k.

[5] Recall from optimal estimation theory that the error covariance matrix is defined as the expected value of the mean-square estimation error, $P_k \equiv E\left[(\mathbf{x}_k - \hat{\mathbf{x}}_k)(\mathbf{x}_k - \hat{\mathbf{x}}_k)^T\right]$.

$$P_k^{(+)} = \left(I - \hat{K}_k A_{x_k}\right) P_k^{(-)} + \alpha_k \left(K_k - \hat{K}_k\right) \left(K_k - \hat{K}_k\right)^T \tag{5}$$

where K_k is an arbitrary (e.g., suboptimal) gain matrix and $\hat{K}_k$ is the optimal filter gain matrix. This form of the error covariance measurement update is often referred to as the *suboptimal measurement update* since it includes a correction based on the gain difference between the filter evaluation run (which generally assumes an incorrect model) and the original filter (estimation) run. In the general evaluation mode, the filter uses suboptimal gains saved in an evaluation filter from an earlier filter which is run purposely with what is believed to be an incorrect model, in order to generate suboptimal gains [5]. It is this form of the suboptimal measurement update which will be critical to the error budget development described in the following section. In practice, Eq. (5) is typically mechanized in a *U-D* factorized form for numerical stability. A final note about the filter equations: Although the equations for the time update were not presented, it is important to note that the time update in the general filter evaluation mode takes the same form as the original filter time update, except that in the presence of process noise modeling parameters, the original filter stochastic time constants and process noise uncertainties are replaced with evaluation mode time constants and process noise terms [5].[6]

III. Mission Scenario, Data Acquisition, and Filter Modeling Assumptions

A. Mars Observer Interplanetary Cruise Scenario

The Mars Observer spacecraft was launched successfully on September 25, 1992, and was scheduled to initiate the Mars Orbit Insertion (MOI) burn on August 24, 1993; however, communication with the spacecraft was tragically lost just days prior to MOI. Despite the loss of the spacecraft, the interplanetary cruise phase of the mission, which extended from injection to initiation of the MOI burn, represented a challenging navigation scenario, as the declination of the Mars Observer at encounter was within 1 deg of zero. This is a geometry which has historically yielded relatively poor performance with Doppler tracking, due to Doppler data's relative insensitivity to some components of the spacecraft's state in this regime. The Mars Observer was also the first spacecraft to carry an X-band transponder and the first to rely solely on a single-frequency X-band telecommunications system.[7] Thus, this scenario represents a realistic scenario with which to study the relative merits of using the enhanced orbit determination filter to reduce X-band Doppler and ranging data.

The trajectory segment selected for this analysis was taken to be a 182-day time period extending from early February 1993 to early August 1993, which represented the longest leg of the interplanetary cruise, and had the most stringent navigation accuracy requirements in order to support the final maneuver prior to MOI. The trajectory characteristics over the time span of the data arc, which extended from encounter minus 194 (E − 194) days to E − 12 days, are summarized in Table 1.

B. Data-Acquisition Strategy

A fairly sparse DSN data-acquisition schedule was assumed, containing no more than one or two passes of Doppler and ranging data per week. In all cases, the data were assumed to be acquired from the DSN's 34-m high-efficiency (HEF) Deep Space Stations (DSSs) located near Goldstone, California (DSS 15), Canberra, Australia (DSS 45), and Madrid, Spain (DSS 65). This reduced level of coverage is representative of the level anticipated for telemetry acquisition in future missions such as Pathfinder and Cassini. The data schedule consisted of one horizon-to-horizon tracking pass of two-way Doppler and ranging data acquired from the Madrid site on a weekly basis from E − 194 days to E − 90 days, two weekly tracking passes acquired from the Madrid and Canberra sites from E − 90 days to E − 30 days and from E − 30 days to E − 12 days (data cutoff), and a single pass per day from all three DSN sites.

To account for data noise, an assumed one-sigma random measurement uncertainty of 0.0126 mm/sec was chosen for two-way Doppler, and for two-way ranging, the one-sigma random measurement uncertainty was assumed to be 1 m; these noise variances were used in all cases in a manner similar to an earlier study [2]. It should be noted that the data weights quoted here are for the round-trip range-rate and range, respectively. Both data types were collected at a rate of one point every 10 min, and the noise variances were adjusted by an elevation-dependent function for all stations, to reduce the weight of the low-elevation data; furthermore, no data were acquired at elevations of less than 10 deg.

---

[6] The software is described in S. C. Wu, W. I. Bertiger, J. S. Border, S. M. Lichten, R. F. Sunseri, B. G. Williams, P. J. Wolff, and J. T. Wu, *OASIS Mathematical Description*, V. 1.0, JPL D-3139 (internal document), Jet Propulsion Laboratory, Pasadena, California, April 1, 1986.

[7] P. B. Esposito, S. W. Demcak, D. C. Roth, W. E. Bollman, and C. A. Halsell, *Mars Observer Project Navigation Plan*, Project Document 642-312, Rev. C (internal document), Jet Propulsion Laboratory, Pasadena, California, June 15, 1990.

C. Orbit Determination Filter Model

Table 2 summarizes the parameters which make up the enhanced orbit determination filter model, along with a priori statistics, steady-state uncertainties for the Gauss–Markov parameters, and noise densities for the random-walk parameters.[8] All of the parameters were treated as filter (estimated) parameters and grouped into three categories: spacecraft epoch state, spacecraft nongravitational force model, and ground system error model. Effects of uncertainty in the ephemeris and mass of Mars were neglected, as they were believed to be relatively small in this scenario.[9]

The simplified spacecraft nongravitational force model was based on past experience and modeling spacecraft similar to Mars Observer.[10] There were filter parameters representing solar radiation pressure forces as well as small anomalous forces due to gas leaks from valves and pressurized tanks, attitude control thruster misalignments, etc. For processing the two-way ranging data, the filter model included a stochastic bias parameter associated with each ranging pass from each station, in order to approximate the slowly varying, nongeometric delays in ranging measurements that are caused principally by station delay calibration errors and uncalibrated solar-plasma effects. No explicit model parameters were employed for the effect of solar-plasma delays as relatively large (>45 to 60 deg) Sun–Earth–Probe (SEP) angles were assumed for ranging data acquisition, leading to small (<1 m) solar plasma delays.[11]

The station location covariance represents the uncertainty in the station location and pole model solutions developed by Finger and Folkner [13]; this covariance matrix and its associated station location set were used operationally by the Mars Observer Navigation Team during interplanetary cruise.[12] Additionally, three exponentially correlated process noise parameters were included to account for the dynamical uncertainties in the Earth's pole location and rotation period. The tropospheric and ionospheric zenith delay calibration uncertainties were representative of current calibration accuracy. A sequential U-D factorized estimation scheme was employed, in order to track the short-term fluctuations in the transmission media.

IV. Error Budget Calculations

The purpose of developing an error budget is to determine the contribution of individual error sources, or groups of error sources, to the total navigational uncertainty. In general, an error budget is a catalog of the contributions of *all* of the error sources which contribute to errors in the filter estimate at a particular point in time, whether explicitly modeled in the filter or not [3]. For this first analysis, it is assumed that the filter is "optimal," i.e., that the truth model and filter model are the same. This implies that the filter model is an accurate representation of the physical world.

In order to establish an error budget, it is necessary to compute a time history of the filter gain matrix for the *complete* filter model and to subsequently use these gains in the sensitivity calculations [Eq. (4)] during repeated filter evaluation mode runs, in which only selected error sources or groups of error sources are "turned on" in each particular run. In this way, the individual contributions of each error source or group of error sources to the total statistical uncertainty obtained for all of the filter parameters for a given radio metric data set can be established.

Using the reduced data schedule and enhanced filter model derived for the Mars Observer interplanetary cruise scenario described in Section III, orbit determination error statistics were computed for DSN Doppler-only, ranging-only, and Doppler-plus-ranging data sets. The orbit determination statistics were propagated to the nominal time of Mars encounter and expressed as dispersions in a Mars-centered aiming plane, or B-plane, coordinate system;[13]

---

[8] For process noise, first-order Gauss–Markov (exponentialy correlated) random processes were assumed. The process noise covariance is given by $q = (1 - m^2)\sigma_{ss}^2$ where $m = \exp[-(t_{j+1} - t_j)/\tau]$. Here, t_j is the start time for the jth batch and τ is the associated time constant. The term σ_{ss} is the steady-state uncertainty, i.e., the noise level that would be reached if the dynamical system were left undisturbed for a time much greater than τ. For the random walk, both σ_{ss} and τ are unbounded ($\tau = \infty$) and a steady-state is never reached. The noise density for the random walk is characterized by the rate of change of the process noise covariance, $q = \Delta q/\Delta t$ where Δt is the batch size and Δq is the amount of noise added per batch. For this analysis, $\Delta t = 10$ min.

[9] E. M. Standish, "Updated Covariance of Mars for DE234," JPL Interoffice Memorandum 314.6-1452 (internal document), Jet Propulsion Laboratory, Pasadena, California, July 27, 1992.

[10] Esposito, op. cit.

[11] A recent study of a simple solar plasma delay model and its use in the reduction of precision ranging data is presented in [12].

[12] W. M. Folkner, "DE234 Station Locations and Covariance for Mars Observer," JPL Interoffice Memorandum 335.1-92-013 (internal document), Jet Propulsion Laboratory, Pasadena, California, May 26, 1992.

[13] The aiming plane, or B-plane, coordinate system is defined by three unit vectors: $\underline{\mathbf{S}}$, $\underline{\mathbf{T}}$, and $\underline{\mathbf{R}}$; $\underline{\mathbf{S}}$ is parallel to the spacecraft velocity vector relative to Mars at the time of entry into Mars' gravitational sphere of influence, $\underline{\mathbf{T}}$ is parallel to the Martian equatorial plane, and $\underline{\mathbf{R}}$ completes an orthogonal triad with $\underline{\mathbf{S}}$ and $\underline{\mathbf{T}}$. The aim point

specifically, the one-sigma magnitude uncertainty of the miss vector, resolved into the respective miss components **B•R** (normal to Martian equatorial plane) and **B•T** (parallel to Martian equatorial plane), and the one-sigma uncertainty in the *linearized time-of-flight* (LTOF). The LTOF defines the time from encounter (point of closest approach) and specifies what the time of flight to encounter would be if the magnitude of the miss vector were zero. In some cases, the errors were expressed as dispersion ellipses in the B-plane to graphically illustrate the contributions of the most statistically significant groups of error sources.

A. Doppler Only

With the enhanced filter, the Doppler data allowed determination of the **B•R** component of the miss vector to about 22 km and the **B•T** component to about 46 km, with the LTOF determined to approximately 7 sec (~16 km in positional uncertainty). These results are summarized in Table 3, which gives the magnitude of the B-plane dispersions around the nominal MOI aim point (in the form of an error budget) for all groups of truth/filter model error sources to the total statistical uncertainty, in a root-sum-square sense. (Recall that for this analysis, the truth model and filter model are the same.) As seen from the table, the most dominant error source groups were the random nongravitational accelerations, followed by solar radiation pressure coefficient uncertainty, and random Earth-orientation calibration errors. A graphical illustration of these contributions is shown in Fig. 1, in terms of B-plane dispersion ellipses. For this encounter scenario, the direction of the Earth–spacecraft range is closely aligned with the semimajor axis of the B-plane dispersion ellipse. The Doppler data alone were able to determine this component of the solution to only about 50 km.

B. Ranging Only

Orbit solutions computed with ranging data using the enhanced filter are summarized in Table 4, also in error budget format. In this case, the ranging data were able to determine the **B•R** component of the miss vector to about 12 km and the **B•T** component to about 6 km. The LTOF accuracy for this case was not much better than the Doppler-only case, an improvement from 7 sec to approximately 6 sec (~14 km in positional uncertainty). The most dominant error source groups for this data strategy were random nongravitational accelerations, as in the Doppler-only case, followed by measurement (data) noise, and DSN station location uncertainty. Although range bias parameters were included in the ground system error model, they did not adversely affect the performance of the enhanced filter. Figure 2 illustrates these major error sources in terms of B-plane dispersion ellipses along with the full filter-generated root-sum-square uncertainty. The orientation of the full filter dispersion ellipse is rotated about 90 deg from the Doppler-only result, indicating the strength with which the ranging data are able to determine the Earth–spacecraft range component of the trajectory. In this case, the semimajor axis is oriented roughly normal to the Earth–Mars line.

C. Doppler Plus Ranging

For the final case in which both Doppler and ranging data were used, the **B•R** component of the miss vector was determined to about 9 km and the **B•T** component to about 5 km, with the LTOF determined to approximately 4 sec (~9 km in positional uncertainty). Error budget calculations for this case are summarized in Table 5. Similar to the results for the Doppler-only and ranging-only data strategies, random nongravitational accelerations were the dominant error source group. The next two most significant error source groups were Earth-orientation calibration error and DSN station location uncertainty, respectively. As with the ranging-only case, solar radiation pressure coefficient uncertainty and random ranging delay calibration errors were of roughly the same magnitude, but did not contribute to the total error budget as much as the previously cited error sources. B-plane dispersion ellipses are also provided (see Fig. 3), illustrating the contributions of the major error source groups to the total root-sum-square error and the orientation of the ellipses in the aiming plane. In this case, the accuracy with which the Earth–spacecraft range component at encounter was determined was roughly 11 km.

V. Sensitivity Curves

Another benefit of the linearity assumptions used to develop error budgets is that sensitivity curves can readily be generated. *Sensitivity curves* graphically illustrate the effects of using different prescribed values of the error source statistics on the estimation errors, with the assumption that the filter model remains unchanged. The procedure for sensitivity curve development is straightforward and, although described in [3], is repeated here for completeness: (1) subtract the contribution of the error source under consideration from the total mean-square navigation error; (2) to compute the effect of changing the error source by a preset scale factor, multiply its contributions to the mean-square errors by the square of the scale factor value; (3) replace the original contribution to mean-square error

---

for planetary encounter is defined by the miss vector **B**, which lies in the **T** − **R** plane and specifies where the point of closest approach would be if the target planet had no mass and did not deflect the flight path.

by the one computed in the previous step; and (4) take the square root of the newly computed mean-square error to obtain the total root-sum-square navigation error.

Several cases were used to generate sensitivity curves for the major groups of error sources in the filter model; for example, Figs. 4 through 6 give the sensitivity curves for the random nongravitational accelerations and illustrate the sensitivity of this error source group to various scale factor values. Recall that random nongravitational accelerations dominated the error budget in all three data strategy cases considered (c.f., Section IV). As seen from the figures, a quadratic growth in the sensitivity is evident for scale factor values ranging from 1 to 3, and a nearly linear growth is exhibited for scale factor values ranging from 4 to 10. On average, for all three data strategies considered, an order of magnitude increase in the preset scale factor resulted in about a factor of three to six increase in the root-mean-square estimation errors.

VI. Summary and Conclusions

A sensitivity analysis was conducted for a recently developed sequential data filtering strategy referred to as the *enhanced orbit determination filter.* In practice, the enhanced filter attempts to represent all or nearly all of the principal ground system error sources affecting radio metric data types as filter parameters. Reduced-order filtering methods were reviewed and utilized to perform the sensitivity analysis, and, in particular, to develop navigation error budgets for three different data acquisition strategies. The mission scenario assumed for the analysis was based on the Mars Observer interplanetary outer cruise phase. Two-way radio Doppler and ranging were the data types analyzed, with assumed accuracies chosen to reflect actual performance of the DSN's X-band tracking system, as observed in recent interplanetary missions such as Magellan, Ulysses, and Mars Observer.

Error budget computations performed for the assumed mission scenario revealed that the most significant error source for all three data-acquisition strategies studied (i.e., Doppler-only, ranging-only, and Doppler-plus-ranging) was spacecraft random nongravitational accelerations, indicating that, for the reference error model, the enhanced filter is most sensitive to mismodeling of small anomalous forces affecting the spacecraft. Other sources of error which had a significant impact on the overall error budget were, in the case of Doppler-only navigation, solar-radiation pressure coefficient uncertainty and Earth-orientation calibration error. In the case of ranging-only navigation, measurement noise and Earth-orientation calibration error were the other significant contributors to the overall error budget. Earth platform errors, namely DSN station location uncertainty and Earth-orientation calibration error, were the next most significant contributors to the overall error budget for the Doppler-plus-ranging navigation case. These results suggest that if high-precision navigation performance is to be achieved, the error sources requiring the most accurate modeling are spacecraft nongravitational accelerations and Earth platform calibration errors. Future work will focus on the use of Monte Carlo simulation techniques to evaluate the sensitivity of the enhanced orbit determination filter to a variety of truth model assumptions, and will include additional model parameters to account for trajectory-correction maneuver execution errors and uncalibrated solar-plasma delays.

Acknowledgments

The authors would like to thank Sam Thurman of JPL and Robert Bishop of The University of Texas at Austin for their valuable input, support, and review of this article.

References

[1] S. W. Thurman and J. A. Estefan, "Radio Doppler Navigation of Interplanetary Spacecraft Using Different Data Processing Modes," paper AAS 93-163, presented at the AAS/AIAA Spaceflight Mechanics Meeting, Pasadena, California, February 22–24, 1993.

[2] J. A. Estefan, V. M. Pollmeier, and S. W. Thurman, "Precision X-Band Doppler and Ranging Navigation for Current and Future Mars Exploration Missions," paper AAS 93-250, presented at the AAS/GSFC International Symposium on Space Flight Dynamics, Greenbelt, Maryland, April 26-30, 1993.

[3] *Applied Optimal Estimation*, edited by A. Geld, Cambridge, Massachusetts: M.I.T. Press, pp. 229–230 and 260–266, 1974.

[4] P. S. Maybeck, *Stochastic Models, Estimation, and Control: Volume 1*, San Diego, California: Academic Press, Inc., pp. 325–327 and 337–341, 1979.

[5] S. M. Lichten, "Estimation and Filtering Techniques for High-Accuracy GPS Applications," *The Telecommunications and Data Acquisition Progress Report 42-97, vol. January–March 1989*, Jet Propulsion Laboratory, Pasadena, California, pp. 1–20, May 15, 1989.

[6] D. J. Scheeres, "Failure Modes of Reduced-Order Orbit Determination Filters and Their Remedies," *The Telecommunications and Data Acquisition Progress Report 42-114, vol. April–June 1993*, Jet Propulsion Laboratory, Pasadena, California, pp. 34–42, August 15, 1993.

[7] G. J. Bierman, *Factorization Methods for Discrete Sequential Estimation*, San Diego, California: Academic Press, Inc., pp. 162–171, 1977.

[8] S. R. McReynolds, "The Sensitivity Matrix Method for Orbit Determination Error Analysis, With Applications to a Mars Orbiter," *JPL Space Programs Summary 37-56*, vol. 3, January-February 1969, pp. 85–87, March 31, 1969.

[9] G. J. Bierman and C. L. Thornton, "Numerical Comparison of Kalman Filter Algorithms: Orbit Determination Case Study," *Automatica*, vol. 13, pp. 23–35, 1977.

[10] C. L. Thornton, "Triangular Covariance Factorizations for Kalman Filtering," JPL Technical Memorandum 33-798, Jet Propulsion Laboratory, Pasadena, California, October 15, 1976.

[11] C. L. Thornton and G. J. Bierman, "Filtering and Error Analysis Via the UDU^T Covariance Factorization," *IEEE Trans. on Automatic Control*, vol. AC-23, no. 5, pp. 901–907, 1978.

[12] T. P. McElrath, S. W. Thurman, and K. E. Criddle, "Navigation Demonstrations of Precision Ranging with the Ulysses Spacecraft," paper AAS 93-687, presented at the AAS/AIAA Astrodynamics Specialist Conference, Victoria, B.C., Canada, August 16–19, 1993.

[13] M. H. Finger and W. M. Folkner, "A Determination of the Radio-Planetary Frame Tie From Comparison of Earth Orientation Parameters," *The Telecommunications and Data Acquisition Progress Report 42-109, vol. January–March 1992*, Jet Propulsion Laboratory, Pasadena, California, pp. 1–21, May 15, 1992.

Table 1. Mars Observer outer cruise phase trajectory characteristics over an assumed data arc extending from E — 194 days to E — 12 days.

Parameter	Value
Earth-to-spacecraft range, km	80×10^6 to 330×10^6
Geocentric declination, deg	22 to 1
SEP angle, deg	125 to 45

Table 2. Enhanced orbit determination filter with ground-system error model representative of current DSN calibration accuracy.

Estimated parameter set	Uncertainty (1σ)	Remarks
Spacecraft epoch state	A priori,	Constant parameters
Position components	10^5 km	
Velocity components	1 km/sec	
Nongravitational force model		
Solar radiation pressure	A priori,	Constant parameters
Radial (G_r)	10% (= 0.13)	
Transverse (G_x/G_y)	10% (= 0.01)	
Anomalous accelerations	Steady-state,	Markov parameters
Radial (a_r)	10^{-12} km/sec^2	10-day time constant
Transverse (a_x/a_y)	10^{-12} km/sec^2	10-day time constant
Range biases (one per station per pass, ranging data only)	A priori, 4 m	Uncorrelated from pass to pass
Ground system error model		
DSN station locations	A priori,	Constant parameters, relative uncertainty between stations is 1 to 2 cm
Spin radius (r_s)	0.18 m	
Z-height (z_s)	0.23 m	
Longitude (λ)	3.6×10^{-8} rad	
Earth orientation	Steady-state,	Markov parameters,
Pole orientation	1.5×10^{-8} rad	1-day time constant
Rotation period	0.2 msec	12-hr time constant
Transmission media	A priori,	Random walk, 1 cm^2/hr
Zenith troposphere (each station)	5 cm	
Zenith ionosphere (each station)	Steady-state, 3 cm	Markov parameters 4-hr time constant

Table 3. Enhanced-filter error budget for DSN X-band Doppler-only navigation.

Error source group	*B*-plane dispersions		
	B•R, km	**B•T**, km	LTOF, sec
Epoch state	2.92	8.33	0.753
SRP parameters	10.25	27.69	2.164
Nongravitational accelerations	16.52	30.61	4.950
Ionosphere	1.87	3.82	0.891
Troposphere	3.56	6.65	1.500
Station locations	4.29	4.63	1.590
Earth orientation	6.23	14.58	3.428
Measurement noise	3.45	6.41	1.501
Total (root-sum-square)	21.72	45.90	7.024

Table 4. Enhanced-filter error budget for DSN X-band ranging-only navigation.

Error source group	*B*-plane dispersions		
	B•R, km	**B•T**, km	LTOF, sec
Epoch state	0.27	0.13	0.23
SRP parameters	2.26	1.11	0.91
Nongravitational accelerations	7.27	3.54	4.13
Ionosphere	0.78	0.39	0.27
Troposphere	1.54	0.75	0.64
Station locations	5.36	2.63	2.66
Earth orientation	2.47	1.26	0.63
Range biases	2.06	1.00	0.97
Measurement noise	6.59	3.21	3.18
Total (root-sum-square)	11.98	5.86	6.08

Table 5. Enhanced-filter error budget for DSN X-band Doppler-plus-ranging navigation.

Error source group	B-plane dispersions		
	B•R, km	**B•T**, km	LTOF, sec
Epoch state	0.10	0.05	0.10
SRP parameters	1.57	0.76	0.64
Nongravitational accelerations	5.73	2.83	2.87
Ionosphere	0.87	0.41	0.56
Troposphere	1.46	0.69	0.81
Station locations	2.99	1.53	0.97
Earth orientation	2.98	1.50	1.26
Range biases	1.40	0.67	0.68
Measurement noise	5.11	2.46	2.51
Total (root-sum-square)	9.17	4.51	4.35

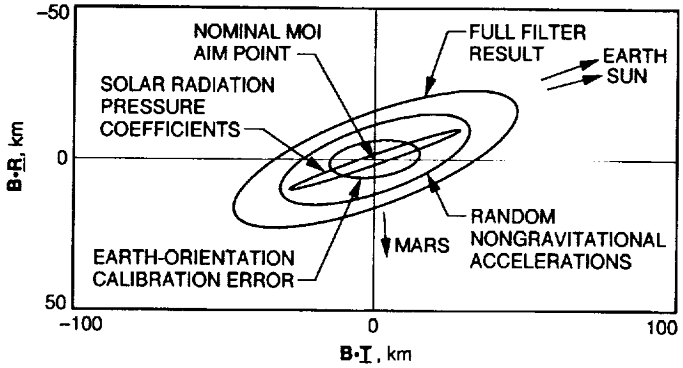

Fig. 1. Mars Observer aiming plane dispersions (one sigma) for DSN X-band Doppler-only navigation.

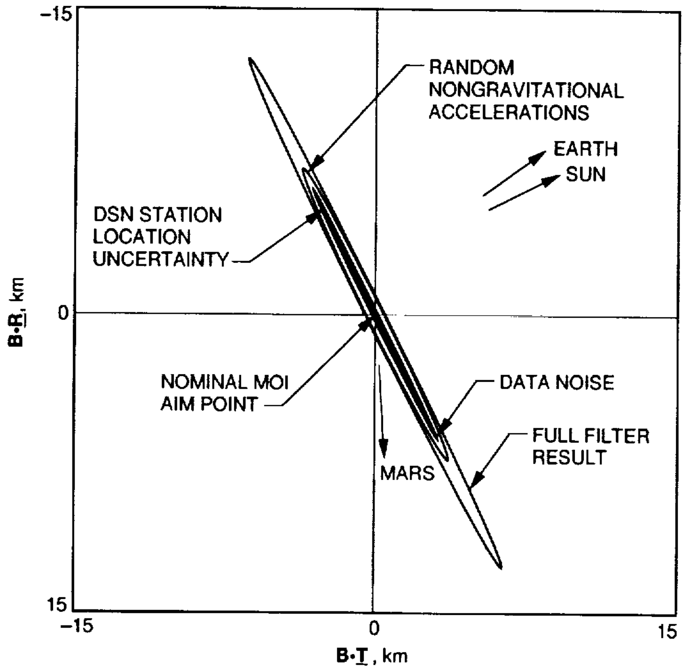

Fig. 2. Mars Observer aiming plane dispersions (one sigma) for DSN X-band ranging-only navigation.

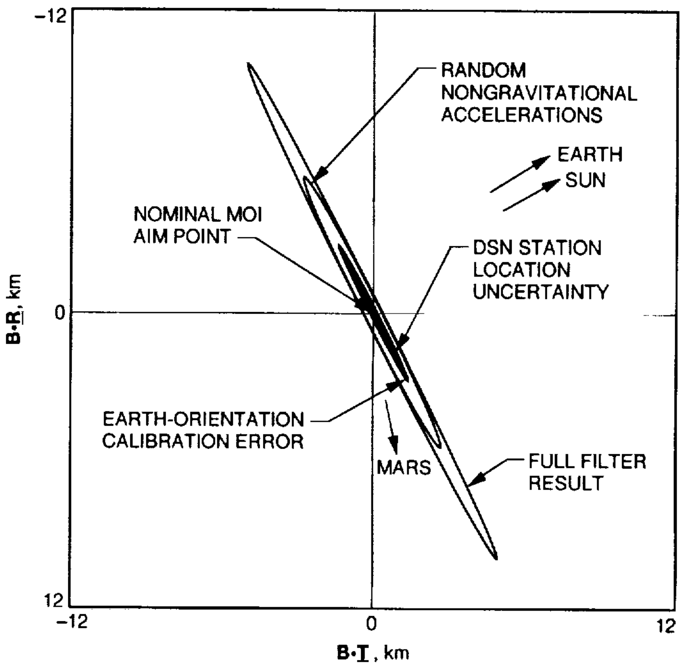

Fig. 3. Mars Observer aiming plane dispersions (one sigma) for DSN X-band Doppler-plus-ranging navigation.

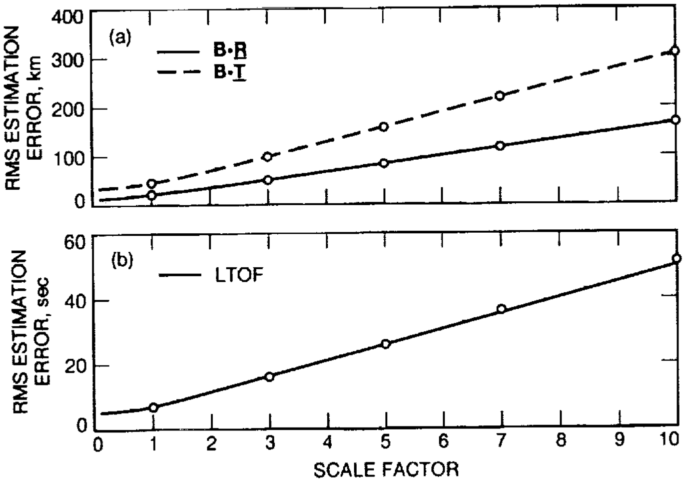

Fig. 4. Sensitivity of root-mean-square estimation error to perturbations of random nongravitational accelerations by preset scale factor (Doppler-only case): (a) B•T and B•R and (b) LTOF.

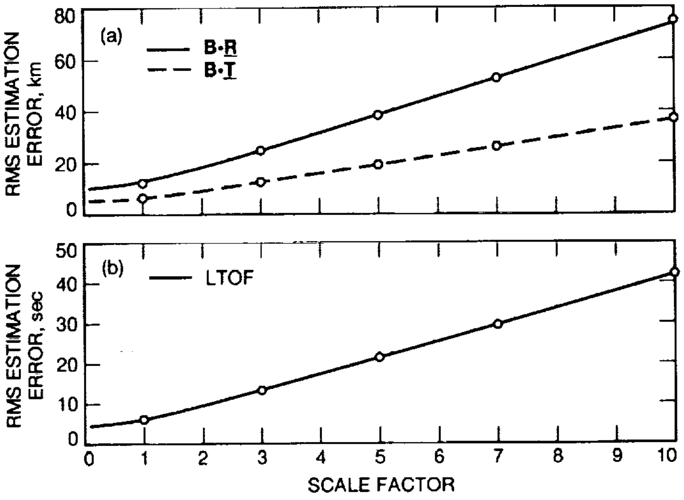

Fig. 5. Sensitivity of root-mean-square estimation error to perturbations of random nongravitational accelerations by preset scale factor (ranging-only case): (a) B•T and B•R and (b) LTOF.

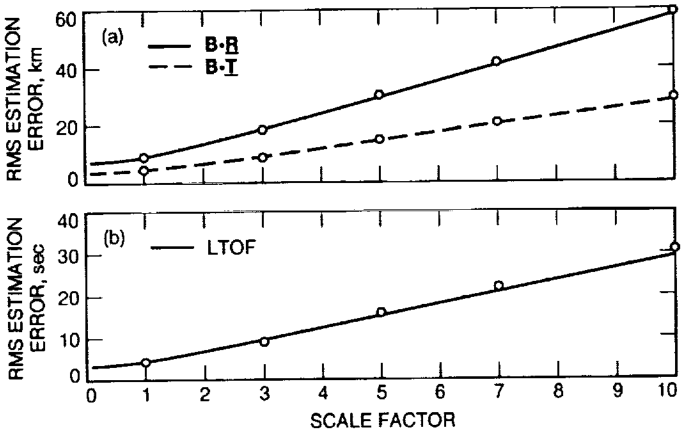

Fig. 6. Sensitivity of root-mean-square estimation error to perturbations of random nongravitational accelerations by preset scale factor (Doppler-plus-ranging case): (a) B•T and B•R and (b) LTOF.

N94-29656

Enhanced Orbit Determination Filter: Inclusion of Ground System Errors as Filter Parameters

W. C. Masters, D. J. Scheeres, and S. W. Thurman
Navigation Systems Section

The theoretical aspects of an orbit determination filter that incorporates ground-system error sources as model parameters for use in interplanetary navigation are presented in this article. This filter, which is derived from sequential filtering theory, allows a systematic treatment of errors in calibrations of transmission media, station locations, and Earth orientation models associated with ground-based radio metric data, in addition to the modelling of the spacecraft dynamics. The discussion includes a mathematical description of the filter and an analytical comparison of its characteristics with more traditional filtering techniques used in this application. The analysis in this article shows that this filter has the potential to generate navigation products of substantially greater accuracy than more traditional filtering procedures.

I. Introduction

In JPL's interplanetary orbit determination process, ground error sources associated with radio metric data, such as station location, Earth orientation, and transmission media calibration errors, are usually treated as unmodelled "consider" parameters in a scheme known as the consider option. This method does not utilize any information pertinent to the consider parameters in computing estimates of the trajectory parameters. Rather, the effects of the consider parameters are accounted for by modifying the computed estimation error covariance with preassigned uncertainties of these parameters. In many cases, this method gives satisfactory results and allows reasonable navigational accuracy. However, the consider option sometimes yields unstable and unpredictable results when used for interplanetary navigation.

Recently, an enhanced orbit determination scheme (which will be referred to throughout this article as the "enhanced" filter) has been developed. The enhanced filter explicitly models ground error sources as random processes simultaneously with the trajectory-related parameters. This method exploits the full information content of the data pertaining to these ground errors in the filtering process and may thereby improve the knowledge of these parameters and the overall accuracy of the estimated flight path.

The enhanced filter has been successfully applied to selected navigation problems in some interplanetary orbit-determination case studies at JPL [1,2]. These studies have shown an increase in orbit-determination accuracy using the enhanced filter method of factors of two to four over the use of more conventional techniques. Interestingly, in the field of Earth satellite orbit determination, similar filtering techniques have been in use for some time. Numerous articles exist in the literature. For example, in the article by Lichten and Border [3], stochastic models for the tropospheric delays are used for problems in Global Positioning System orbit determination.

This article describes the framework of the enhanced filter model and gives an analytical comparison of the enhanced filter with the traditional consider option. Since there are many concepts involved, a quick review of the basic filter model from which the enhanced filter evolved will be given first. A detailed discussion of the consider option will also be presented, so that its characteristics can be compared with those of the enhanced filter.

II. Basic Filter Model

All of the filters discussed herein employ a linear representation of the process dynamics and the measurements. In this formulation, the state space and measurements are described as follows:

$$\mathbf{x}_{j+1} = \Phi(j+1,j)\,\mathbf{x}_j + \mathbf{w}_j \tag{1}$$

$$\mathbf{z}_j = \mathbf{H}_j\,\mathbf{x}_j + \mathbf{v}_j \tag{2}$$

where $\mathbf{x}$ denotes the extended state, which includes the spacecraft state and the dynamic process perturbation parameters. The dynamic process perturbations may be treated as random or deterministic parameters. The transition matrix from time t_j to t_{j+1} is $\Phi(j+1,j)$, and $\mathbf{w}$ represents the state-space modelling errors. The jth data point is $\mathbf{z}_j$, and $\mathbf{v}_j$ is the corresponding data noise. The term $\mathbf{H}_j$ is a matrix that contains the partial derivatives of the jth data point with respect to the extended state.

The computations for the estimate and covariance matrix follow the basic square-root information filtering procedure discussed by Bierman [4]. This procedure can be described as follows: The a priori values and covariance matrix for the estimated parameters are first transformed into the a priori residual and the a priori information matrix. To ensure numerical stability, the Cholesky decomposition is applied to the a priori information matrix to obtain an upper triangular factorization, hence the term "square root" of the matrix. This a priori square-root information matrix is augmented by the a priori residual. Measurements are then included into this augmented matrix using the Householder orthogonal transformations, resulting in the following a posteriori square-root information and residual matrix:

$$\begin{pmatrix} \mathbf{R} & \mathbf{z} \\ & \mathbf{e} \end{pmatrix} \tag{3}$$

where $\mathbf{R}$ denotes the information matrix, $\mathbf{z}$ denotes the residual, and $\mathbf{e}$ denotes the sum of squares of the residual errors as defined in the classical least-squares problem.

The extended state estimate $\hat{\mathbf{x}}$ and the error covariance matrix $\mathbf{P}_x$ for the extended state are computed using the values in the above matrix.

$$\hat{\mathbf{x}} = \mathbf{R}^{-1}\mathbf{z} \tag{4}$$

$$\mathbf{P}_x = \mathbf{R}^{-1}\mathbf{R}^{-T} \tag{5}$$

III. Consider Option

The consider option is based on the assumption that there is a set of parameters that affects the performance of the filter and that it is unnecessary or impractical to model these parameters accurately. These parameters are referred to as consider parameters. Since consider parameters are not included in the model, they are not estimated. Moreover, the estimation and covariance computation process for the extended state is not aware of the presence of these parameters and any errors in their values. Instead, once the state estimation is performed and the error covariance computed, the consider filter modifies the computed error covariance to account for a constant uncertainty in the consider parameters. This new covariance is called the "consider covariance." If $\mathbf{P}_x$ denotes the computed error covariance matrix and $\mathbf{P}_{y_0}$ denotes the a priori covariance of the consider parameters, then the consider covariance, $\mathbf{P}_c$, is computed as follows:

$$\mathbf{P}_c = \mathbf{P}_x + \mathbf{S}\mathbf{P}_{y_0}\mathbf{S}^T \tag{6}$$

The matrix $\mathbf{S}$ above is commonly called the sensitivity matrix and contains the partial derivatives of the estimated state with respect to the consider parameters. In the consider filter, it is a function of the measurements only. More details of the sensitivity matrix can be found in [4].

The consider option is often used to treat ground error sources that affect the measurements. The rationalization is that since these error sources do not affect the spacecraft dynamics, estimating them will not improve the knowledge of the spacecraft state, and therefore it is adequate to just characterize them by their uncertainties. In this approach, the presence of the ground errors is acknowledged in a conservative fashion, which overlooks the important fact that these error sources, since they affect the measurements, do affect the spacecraft state estimates. Note also that this method assumes that the ground error parameters are constants with no dynamics. This simplified modelling does not allow an improvement in knowledge of these parameters to be obtained.

The most obvious disadvantage of the consider option is that when the sensitivity of the state with respect to the ground error parameters increases, the consider covariance increases, as can be seen clearly from Eq. (6). This implies a greater uncertainty in the spacecraft state. When this happens, the only remedy available within the context of the consider option is to decrease the "weight" of the data, i.e., assume that each measurement contains less information than it does in actuality. This and other characteristics of the consider option are discussed by Scheeres [5].

There is, however, a deeper significance here. If the sensitivity of the state with respect to the ground error parameters grows large, then this implies that there is significant information contained in the measurements concerning these parameters. The logical recourse would be to exploit this information in order to learn something about the characteristics of the ground error sources. This implies that the ground error parameters should be incorporated into the filter model.

IV. Enhanced Filter

The enhanced filter provides for the inclusion of the ground error parameters in the filter model so that the estimation process incorporates the information pertinent to the behavior of these parameters. In this treatment, the ground error sources are modelled as dynamic entities. By doing this, an automatic feedback mechanism is created so that no artificial data weighting is needed to keep the covariance of the state estimate from diverging.

A. Enhanced Filter Model

The enhanced filter uses the extended state model for the basic batch sequential model given by Eq. (1). In addition, there are models for ground error parameters and a modified measurement model. The ground error parameters are modelled as a discrete first-order Markov process in a vector form given by

$$\mathbf{y}_{j+1} = \Psi(j+1, j)\,\mathbf{y}_j + \mathbf{u}_j \tag{7}$$

where $\mathbf{y}$ denotes the vector consisting of the ground error parameters, $\Psi(j+1, j)$ accounts for the time dependency of $\mathbf{y}$ from time t_j to t_{j+1}, and $\mathbf{u}$ represents the random driving term.

The measurement model given by Eq. (2) is modified to include information pertaining to the ground error parameters.

$$\mathbf{z}_j = \mathbf{H}_j\,\mathbf{x}_j + \mathbf{G}_j\,\mathbf{y}_j + \mathbf{v}_j \tag{8}$$

where the meanings of $\mathbf{H}_j$ and $\mathbf{v}_j$ are the same as before and $\mathbf{G}_j$ contains the partial derivatives of the jth data point with respect to the ground error parameters.

The enhanced filter model thus consists of Eqs. (1), (7), and (8). The characteristics of this model can be described as follows. Ground error sources are treated as system parameters that can be estimated. The extended spacecraft state space evolves independently from the ground system parameters. The measurements have explicit dependency on the ground system parameters.

B. Estimate and Covariance

In the enhanced filter, estimated parameters include both the extended spacecraft state and the ground system parameters. The computations for the estimate and covariance matrix follow the basic square-root information filtering procedure described in Section II. After processing measurements, the a posteriori information and the residual matrix have the following form:

$$\begin{pmatrix} \mathbf{R}_x & \mathbf{R}_{xy} & \mathbf{z}_x \\ & \mathbf{R}_y & \mathbf{z}_y \\ & & \mathbf{e} \end{pmatrix} \tag{9}$$

In Eq. (9), subscripts are given to show the relationship of the quantities in the matrix with respect to the parameters. Here, $\mathbf{R}_x$ represents the information with respect to the extended state and is the same as $\mathbf{R}$ in Eq. (3); $\mathbf{R}_y$ represents the information with respect to the ground system parameters; $\mathbf{R}_{xy}$ denotes the information concerning the extended state affected by the ground system parameters; and $\mathbf{z}_x$ and $\mathbf{z}_y$ are residual components corresponding to the extended state and ground system parameters, respectively. From this matrix, the extended state and ground system parameter estimates are computed as

$$\hat{\mathbf{x}} = \mathbf{R}_x^{-1}\left[\mathbf{z}_x - \mathbf{R}_{xy}\,\hat{\mathbf{y}}\right] \qquad (10)$$

$$\hat{\mathbf{y}} = \mathbf{R}_y^{-1}\mathbf{z}_y \qquad (11)$$

Equations (10) and (11) show that the information content pertinent to the ground system parameters, $\mathbf{R}_y$ and $\mathbf{z}_y$, is used to estimate these parameters, yielding a new estimate, $\hat{\mathbf{y}}$. This estimate is then used to obtain a new state estimate, $\hat{\mathbf{x}}$, together with the information pertinent to the state, $\mathbf{R}_x$, the state with respect to the ground system parameters, $\mathbf{R}_{xy}$, and the residual, $\mathbf{z}_x$. In the consider option, the state estimate would have used only $\mathbf{R}_x$ and $\mathbf{z}_x$, and no estimate for the ground system parameters would have been computed.

Since all parameters are estimated, the covariance matrix for the extended state is then

$$\hat{\mathbf{P}} = \mathbf{R}_x^{-1}\mathbf{R}_x^{-T} + \left[-\mathbf{R}_x^{-1}\mathbf{R}_{xy}\mathbf{R}_y^{-1}\right]\left[-\mathbf{R}_x^{-1}\mathbf{R}_{xy}\mathbf{R}_y^{-1}\right]^T \qquad (12)$$

Recognizing that $-\mathbf{R}_x^{-1}\mathbf{R}_{xy}$ is the definition of the sensitivity matrix, Eq. (12) may be represented as

$$\hat{\mathbf{P}} = \hat{\mathbf{P}}_x + \mathbf{S}\hat{\mathbf{P}}_y\mathbf{S}^T \qquad (13)$$

In this equation, $\hat{\mathbf{P}}_x = \mathbf{R}_x^{-1}\mathbf{R}_x^{-T}$ and $\hat{\mathbf{P}}_y = \mathbf{R}_y^{-1}\mathbf{R}_y^{-T}$, where $\hat{\mathbf{P}}_x$ and $\hat{\mathbf{P}}_y$ represent the blocks of the computed covariance matrix corresponding to the extended state and the ground system parameters, respectively.

Using the same notations, the full covariance matrix corresponding to the estimate for both the extended state and the ground system parameters is

$$\begin{pmatrix} \hat{\mathbf{P}}_x + \mathbf{S}\hat{\mathbf{P}}_y\mathbf{S}^T & \mathbf{S}\hat{\mathbf{P}}_y \\ \hat{\mathbf{P}}_y\mathbf{S}^T & \hat{\mathbf{P}}_y \end{pmatrix} \qquad (14)$$

Note that the $\hat{\mathbf{P}}_x$ in both Eqs. (13) and (14) is exactly the computed covariance in the consider option. Equation (13) has the same form as Eq. (6), which gives the computation for the consider covariance. But the important difference here is that the covariance for the ground system parameters, $\hat{\mathbf{P}}_y$ in Eqs. (13) and (14), is updated using the measurements and their modelled behavior, while in the consider option only the constant a priori covariance is used.

Further, in the enhanced filter, the full covariance matrix is used to automatically weight the measurement data, thus using the modelled behavior of ground system parameters to control the relative weight given to the measurements. In the consider option, only the computed covariance $\hat{\mathbf{P}}_x$ is used to weight the measurements; therefore, the ground system parameters have no effects on the data weights. In particular, using the enhanced filter formulation, the computed covariance stabilizes as the information contained in $\mathbf{R}_y$ increases. This is transparent since $\hat{\mathbf{P}}_y = \mathbf{R}_y^{-1}\mathbf{R}_y^{-T}$. Thus, there is no need to artificially deweight the data when the information content of the ground system parameters is large. On the other hand, when there is little or no information pertinent to the ground system parameters, the enhanced filter then behaves as in the consider option. In this case, the covariance matrix with respect to the ground system parameters, $\hat{\mathbf{P}}_y$, will consist primarily of the a priori constant covariance for these parameters.

C. Features of the Enhanced Filter

The advantage of modelling measurement error sources as system parameters is that this makes it possible to estimate these parameters. Thus, the knowledge of them may be improved. This approach distinguishes the enhanced filter strategy from other commonly used schemes that treat ground system errors as measurement noise. Many problems arise with such schemes. For example, because of the very assumption that the ground system errors are noise-like, no information regarding these parameters can be extracted from the measurements. Very often, this leads to degenerate covariance matrices; see [6,7] for more discussions on such treatments.

The advantage of modelling the evolution of the ground system parameters independently from the state dynamics is that, while not affecting the state evolution, the ground errors are allowed to evolve according to their own dynamics. This is necessary since some of the error sources, such as Earth orientation and transmission media, are dynamic. This model demonstrates that system parameters do not have to be included in the state dynamics in order to improve the state estimation. Finally, the advantage of modelling the dependency of the measurements on the ground system parameters explicitly is that the best possible weighting of the data can be utilized in the filtering process to generate estimates of the spacecraft trajectory.

The net combination of the above features provides a procedure that fully exploits the information content of the measurements pertaining to the ground system parameters and systematically assigns the proper weight for each measurement according to the modelled behavior. This is achieved in the enhanced filter by using user-input parameters that describe the stochastic nature of the ground system parameters. By choosing the statistics of these parameters properly, accurate estimates of both the ground system parameters and the spacecraft state may be obtained. In addition, the covariance of the ground system parameters may be effectively controlled, ensuring that the estimates for these parameters will be within the accuracy with which they can be modelled.

V. Conclusions

To summarize, the enhanced filter has been shown to offer some advantages over the traditional consider option in the following ways: First, the enhanced filter allows the behavior of the ground system parameters to affect the spacecraft state estimates. This helps to ensure that the spacecraft state is being estimated with a more complete representation of the physical world. Second, the enhanced filter can exploit the information contained in the data pertaining to the ground system parameters, possibly helping to improve the knowledge of these parameters. Moreover, the improved knowledge is fed back into the filtering process automatically, which effectively adjusts the weighting of the data systematically, helping to stabilize the state covariance. Third, the performance of the enhanced filter is no worse than that of the consider option in the case when the information content of the data with respect to the ground system parameters is small.

In reviewing the history and evolution of the sequential filtering techniques, a major motivation for using the consider option in the past was that it was cost effective, in terms of computation time, to deal with a lower dimensional model, even if the accuracy of the filtering product was compromised. With modern computers, this motivation is no longer a valid concern. The enhanced filter model can use this computational power to achieve an unprecedented degree of accuracy and robustness in many orbit determination problems.

References

[1] S. W. Thurman and J. A. Estefan, "Radio Doppler Navigation of Interplanetary Spacecraft Using Different Data Processing Modes," paper AAS 93-163 presented at the AAS/AIAA Spaceflight Mechanics Meeting, Pasadena, California, February 22–24, 1993.

[2] J. A. Estefan, V. M. Pollmeier, and S. W. Thurman, "Precision X-Band Doppler and Ranging Navigation for Current and Future Mars Exploration Missions," paper AAS 93-250 presented at the AAS/GSFC International Symposium on Space Flight Dynamics, NASA Goddard Space Flight Center, Greenbelt, Maryland, April 26–30, 1993.

[3] S. M. Lichten and J. S. Border, "Strategies for High-Precision Global Positioning System Orbit Determination," *Journal of Geophysical Research*, vol. 92, no. B12, pp. 12,751–12,762, November 10, 1987.

[4] G. J. Bierman, *Factorization Methods for Discrete Sequential Estimation*, San Diego, California: Academic Press, 1977.

[5] D. J. Scheeres, "Failure Modes of Reduced-Order Orbit Determination Filters and Their Remedies," *The Telecommunications and Data Acquisition Progress Report 42-114, vol. April–June 1993*, Jet Propulsion Laboratory, Pasadena, California, pp. 34–42, August 15, 1993.

[6] C. K. Chui and G. Chen, *Kalman Filtering with Real-Time Applications*, 2nd ed., Berlin: Springer-Verlag, 1991.

[7] A. H. Jazwinski, *Stochastic Processes and Filtering Theory*, San Diego, California: Academic Press, 1970.

N94- 29657

TDA Progress Report 42-116

February 15, 1994

Determining Noise Temperatures in Beam Waveguide Systems

W. Imbriale, W. Veruttipong, T. Otoshi, and M. Franco
Ground Antennas and Facilities Engineering Section

A new 34-m research and development antenna was fabricated and tested as a precursor to introducing beam waveguide (BWG) antennas and Ka-band (32 GHz) frequencies into the NASA/JPL Deep Space Network. For deep space use, system noise temperature is a critical parameter. There are thought to be two major contributors to noise temperature in a BWG system: the spillover past the mirrors and the conductivity loss in the walls. However, to date, there are no generally accepted methods for computing noise temperatures in a beam waveguide system. An extensive measurement program was undertaken to determine noise temperatures in such a system along with a correspondent effort in analytic prediction. Utilizing a very sensitive radiometer, noise temperature measurements were made at the Cassegrain focus, an intermediate focal point, and the focal point in the basement pedestal room. Several different horn diameters were used to simulate different amounts of spillover past the mirrors. Two analytic procedures were developed for computing noise temperature, one utilizing circular waveguide modes and the other a semiempirical approach. The results of both prediction methods are compared to the experimental data.

I. Introduction

Noise temperature due to a beam waveguide (BWG) system is one of the major contributors to antenna-receive system noise, especially for an ultralow noise system or a system with high spillover power in the BWG shroud. A reasonably accurate prediction of the BWG noise temperature is essential. Direct analytical computation of the noise temperature of elaborate BWG systems, including all mirrors, is an extremely complex problem and, to date, there is no generally accepted method. This article presents two new techniques, one a purely analytical method and the second a semiempirical approach.

The analytical method extends the approach of [1], which computes the waveguide modes that are propagating in the oversized waveguides. Reference [1] describes a physical optics (PO) integration procedure of the currents on the BWG mirrors using a Green's function appropriate to the circular waveguide geometry. Once all the modes in the waveguide are known, it is a simple matter to use standard approximations to determine the attenuation constant and, thus, the conductivity loss if the conductivity of the wall material is known. Also, all energy that propagates toward, but spills past, a BWG mirror is assumed to be lost in the walls of the BWG as well. The noise temperature is computed assuming both loss components see ambient temperature.

The second method uses a technique that combines an analytical approach with data from measurements to construct a specific expression to compute the BWG noise temperature.

To validate both approaches, a series of measurements were made on DSS 13, the recently completed research and development 34-m BWG antenna (see Figs. 1 and 2). The experiments consisted of making very accurate noise temperature measurements for different gain horns located at both the Cassegrain focus (f1) and the BWG focus of the upper portion of the BWG system (f2) (designed to image the horn at the Cassegrain optics focal point). This portion of the BWG optics is enclosed in a 2.44-m-diameter tube. By taking measurements at both focal points, the noise temperature of the BWG portion of the optics can be accurately determined. The results of both computation methods are compared to the measured data.

II. Waveguide Mode Theory

The BWG tube analysis is conceptually similar to the PO analysis used in reflector antenna analysis. Currents induced in the BWG mirror are obtained using a standard PO approximation of $J = 2\hat{n} \times H_{inc}$ where $\hat{n}$ is the surface normal and H_{inc} is the incident field. However, this analysis differs in the methods by which the incident field on a mirror and the scattered field are calculated.

One approach to calculating the scattered field is to use a dyadic Green's formulation [1] where the field scattered from a BWG mirror is computed using the Green's function appropriate to the cylindrical waveguide geometry.

While it is conceptually convenient to use Green's functions to discuss the comparison with PO, the actual computation using this approach is rather cumbersome. Instead, a simpler method is used to calculate waveguide fields, based upon the reciprocity theorem. The basic problem is to find the fields radiated by an arbitrary current (the PO currents on the reflector) in a cylindrical waveguide. The problem is easily solved by expanding the radiated field in terms of a suitable set of normal modes with amplitude coefficients determined by an application of the Lorentz reciprocity theorem.

An arbitrary field in a waveguide can be represented as an infinite sum of the normal modes for the guide. Let the normal modes be represented by

$$\begin{aligned} \overline{E}_n^{(\pm)} &= (\overline{e}_n \pm \overline{e}_{zn})\, e^{\mp\Gamma_n z} \\ \overline{H}_n^{(\pm)} &= (\pm\overline{h}_n + \overline{h}_{zn})\, e^{\mp\Gamma_n z} \end{aligned} \tag{1}$$

where $\overline{E}_n^{(+)}$ represents a mode traveling in the $+z$ direction and $\overline{E}_n^{(-)}$ is a mode traveling in the $-z$ direction. For a basic normal mode description, see [2].

Let the field radiated in the $+z$ direction by the current be represented by

$$\begin{aligned} \overline{E}^{(+)} &= \sum_n a_n \overline{E}_n^{(+)} \\ \overline{H}^{(+)} &= \sum_n \frac{a_n}{Z_n} \overline{H}_n^{(+)} \end{aligned} \tag{2}$$

and the field radiated in the $-z$ direction by

$$\begin{aligned} \overline{E}^{(-)} &= \sum_n b_n \overline{E}_n^{(-)} \\ \overline{H}^{(-)} &= \sum_n \frac{b_n}{Z_n} \overline{H}_n^{(-)} \end{aligned} \tag{3}$$

Recalling the Lorentz reciprocity theorem, if $\overline{E}_1$, $\overline{H}_1$ and $\overline{E}_2$, $\overline{H}_2$ are the fields due to $\overline{J}_1$, $\overline{J}_2$, respectively, then

$$\int_s \hat{n} \bullet \left[\overline{E}_1 \times \overline{H}_2 - \overline{E}_2 \times \overline{H}_1\right] ds =$$

$$\int_v \left[\overline{E}_2 \bullet \overline{J}_1 - \overline{E}_1 \bullet \overline{J}_2\right] dV \tag{4}$$

If we let $\overline{E}_1$, $\overline{H}_1$ be the fields due to the sources J and $\overline{E}_n^{(\pm)}$, and $\overline{H}_n^{(\pm)}$ be the modal (source-free) solutions, substituting in the Lorentz reciprocity theorem gives

$$-\int_s \left[\overline{E}_n^{(\pm)} \times \overline{H}_1 - \overline{E}_1 \times \frac{\overline{H}_n^{(\pm)}}{Z_n} \right] \bullet \hat{n} ds = \int_v \overline{E}_n^{(\pm)} \bullet J dV \tag{5}$$

If we choose a volume bounded by the perfectly conducting guide walls and the two cross-sectional planes S_1 and S_2 (see Fig. 3), then

$$\int_s = \int_{s_1} (-\hat{z}) \bullet \left[\overline{E}^{(-)} \times \frac{\overline{H}_n^{(\pm)}}{Z_n} - \overline{E}_n^{(\pm)} \times H^{(-)} \right] ds$$

$$+ \int_{s_2} (\hat{z}) \bullet \left[\overline{E}^{(+)} \times \frac{\overline{H}_n^{(\pm)}}{Z_n} - \overline{E}_n^{(\pm)} \times H^{(+)} \right] ds \tag{6}$$

Note that the integral along the wall does not contribute because on S_3 $\hat{n} \bullet \overline{E}_1 \times \overline{H}_2 = \overline{H}_2 \bullet \hat{n} \times \overline{E}_1 = \overline{H}_2 \bullet$ tangential $\overline{E} = 0$ for either $E^{(\pm)}$ or $E_n^{(\pm)}$.

Also only transverse fields enter into computations because $\hat{z} \bullet \overline{E} \times \overline{H}$ selects transverse components.

For the normal mode function E_n^+, H_n^+, it is readily found that

$$\int_s = -\frac{2b_n}{Z_n} \tag{7}$$

when the expansion for E^+ and E^- are used in conjunction with the orthogonal property and

$$\int_s (\overline{e}_n \times \overline{h}_m) \bullet \hat{z} ds = \begin{cases} 0 \text{ if } n \neq m \\ 1 \text{ if } m = n \end{cases} \tag{8}$$

Also, if we use the normal mode function $\overline{E}_n^{(-)}$, $\overline{H}_n^{(-)}$, we find that

$$\int_s = -2\frac{a_n}{Z_n} \tag{9}$$

We have therefore shown that

$$a_n = -\frac{1}{2} Z_n \int_v \left[\overline{E}_n^{(-)} \bullet \overline{J} \right] dV$$

$$\tag{10}$$

$$b_n = -\frac{1}{2} Z_n \int_v \left[\overline{E}_n^{(+)} \bullet \overline{J} \right] dV$$

Since we have only surface currents, the integral for the PO currents is over the surface of the reflector. If we let

$$c_n = -\frac{1}{2} \int_s J_s \bullet \overline{E}_n^{(-)} ds \tag{11}$$

where J_s is the PO currents on the mirror, then

$$\overline{H}^+ = \sum_n c_n \overline{H}_n^{(-)}$$

$$\tag{12}$$

$$\overline{E}^+ = \sum_n Z_n c_n \overline{E}_n^{(-)}$$

and the total power contained in the fields is

$$P = \sum_n Z_n |c_n|^2 \tag{13}$$

If the spillover past the mirror is small (i.e., >25 dB edge taper), the PO currents induced on the first mirror are computed in the standard way, by utilizing the free-space near-field radiating H field of the horn and $J_s = 2\hat{n} \times H_{inc}$. Or they may be computed by utilizing a technique similar to the one just described to compute the propagating modes from the horn, radiating in the oversized waveguide and utilizing the appropriate H field derived from these modes as the incident field. On subsequent mirrors, PO currents are computed from the H field derived from the propagating waveguide modes. The technique is summarized in Fig. 4, where it should be noted that

$$H = \int_s \overline{J}_1 \bullet \overline{\overline{G}}_{wg} ds = \sum_n c_n \overline{H}_n^{(-)} \tag{14}$$

Power loss in the conductor is obtained utilizing the standard technique to compute the power dissipated in the conductor per unit length [2] as

$$P_d(Z) = R \int_0^{2\pi} |\overline{H}_t|^2 \, a d\phi \tag{15}$$

where

$$R = \sqrt{\frac{\omega \mu}{2\sigma}} \tag{16}$$

and σ is the wall conductivity, a the radius, and $|\overline{H}_t|^2$ the tangential H field. It should be noted that P_d is a function of Z since $|\overline{H}_t|^2$ is a function of Z (i.e., it is composed of more than one waveguide mode).

Power loss is computed from

$$P = P_o e^{-2\alpha d} \tag{17}$$

where d is the distance from Z_1 to Z_2 and the attenuation constant is computed as

$$\alpha d = \frac{\int_{Z_1}^{Z_2} P_d(z)dz}{2P_f} \tag{18}$$

where P_f is the power flow in the waveguide.

To compute noise temperature, it is convenient to separate the total RF power originating from the horn aperture (viewed in transmission, for convenience) and propagating into two parts

$$P_{BWG} = P_m + P_{spill} \tag{19}$$

where P_{spill} is the portion that spills past the mirrors (since the mirrors do not fill the waveguide). P_{spill} can be computed for each mirror by integrating the total power radiated from the induced mirror currents and comparing it to the incident power. Note that the computation uses the induced currents derived from the waveguide modes. It is then assumed that this spillover power sees ambient temperature since it would be lost in the tube due to multiple bounces in a lossy material.

The total noise temperature then is composed of two parts—the noise due to the spillover power added to the noise from the attenuation of P_m due to the conductivity loss.

III. Semiempirical Approach

The noise temperature of elaborate BWG systems, including mirrors and shroud, can also be computed by using a new technique that combines an analytical approach with data from measurement tests to construct a specific expression. This technique begins by separating total RF power into two parts; that is, the power that originates from a horn aperture and propagates through a BWG shroud (P_{BWG}) (see Fig. 5) is separated by

$$P_{BWG} = P_m + P_{spill} \tag{20}$$

where P_m is the majority of the total power that is always confined inside all BWG mirrors. P_m does not contact the BWG wall and there are no multiple reflection, diffraction, and creeping wave components. P_m can be computed easily and accurately because all BWG wall and mirror interactions are not included. In this analysis, mirrors are assumed to radiate in free space, making the P_{spill} different from the P_{spill} of the waveguide mode theory. P_{spill} is the sum of spillover powers of each mirror. It creeps and bounces around the BWG walls, mirrors, brackets (behind the mirrors), and edges, and suffers dissipation loss and consequent noise. On an average, the P_{spill} power largely dissipates before a small remainder exits the BWG opening near f1 (see Fig. 2). Even though P_{spill} can be computed accurately ($P_{spill} = P_{BWG} - P_m$), its field distribution and its chaotic behavior inside the lossy BWG is virtually impossible to compute analytically.

From Eq. (20), the corresponding noise temperatures are

$$T_{BWG} = T_m + T_{spill} \tag{21}$$

where T_{BWG} is the total noise temperature (in kelvins) due to the BWG system (including the shroud, mirror, brackets, etc.). The values T_m and T_{spill} are the noise temperature contributions from P_m and P_{spill}, respectively. Because of the simplicity of P_m, its corresponding noise temperature T_m can be computed with acceptable accuracy. For 6061T6 aluminum with conductivity of 2.3×10^7 S/m and a 270-K physical temperature, the noise temperature T_m at X-band (8.45 GHz) [3] is

$$T_m = 0.734\frac{P_m}{P_{BWG}} = 0.734\alpha_m \tag{22}$$

where α_m is the P_m fraction of P_{BWG}, dimensionless.

The noise temperature due to spillover power P_{spill} is given in a very simple form as

$$T_{spill} = \left(\frac{P_1}{P_{BWG}}\right)T_1 + \left(\frac{P_2}{P_{BWG}}\right)T_2 = \alpha_1 T_1 + \alpha_2 T_2 \tag{23}$$

where P_1 is the total spillover power of the two mirrors (M5 and M6) in the basement and the value P_2 is the total spillover power of the four mirrors (M1, M2, M3, and M4) above the basement ceiling. The values α_1 and α_2 are the normalized powers (with respect to P_{BWG}) of P_1 and P_2, respectively.

By substituting Eqs. (22) and (23) into Eq. (21), the BWG noise temperature at X-band becomes

$$T_{BWG} = 0.734\alpha_m + \alpha_1 T_1 + \alpha_2 T_2 \tag{24}$$

By performing various measurements at the NASA DSN BWG research station at Goldstone, the coefficients T1 and T2 at X-band have been obtained [3].

$$\text{No basement shroud} \quad \begin{aligned} T_1 &= 300 \pm 10\,\text{K} \\ T_2 &= 240 \pm 45\text{K} \end{aligned} \tag{25}$$

$$\text{Full shroud} \quad \begin{aligned} T_1 &= 280 \pm 20\,\text{K} \\ T_2 &= 230 \pm 45\,\text{K} \end{aligned} \tag{26}$$

Figure 6 shows the comparison between predicted and measured BWG noise temperatures for various total spillover powers at X-band. The results indicate a very good agreement, especially in the operating range (0.5 percent $\leq P_{spill} \leq$ 1.2 percent).

IV. Measurements Program

Figure 1 shows a recent photograph of the 34-m-diameter BWG antenna at the NASA/JPL Goldstone tracking facility near Barstow, California. It is the first BWG antenna built for NASA and is primarily intended for research and development. One of its uses has been to develop and verify theoretical models that can be used as tools for designing future improved BWG antennas.

Focal points f1, f2, and f3 are depicted in Fig. 2. Focal point f1 is the Cassegrain focal point near the main reflector vertex. An intermediate focal f2 lies above the azimuth track, and f3 is the final BWG focal point located in a subterranean pedestal room. Degradations caused by the BWG system mirrors and shrouds were determined from comparisons made of operating system noise temperatures measured at the different focal points.

As discussed earlier, the goal of the experimental technique was to determine the degradations caused by noise temperature contributions from wall losses and mirror spillovers in the BWG system. The experimental technique that was conceived and implemented involved measuring operating system noise temperature at f1, f2, and f3. The difference between noise temperatures at f1 and f2 gives information on total losses from the BWG system that include (1) dissipative losses due to finite conductivity of four mirrors, (2) spillover losses associated with four mirrors, and (3) shroud wall losses between f1 and f2. Similarly, information about total losses from the remaining two mirrors, shroud walls, and unshrouded path between f2 and f3 are determined by measuring the difference in noise temperatures at those focal points.

To obtain information on losses pertaining only to the Cassegrain portion of the BWG antenna, the experimental procedure involved measuring operating system noise temperature with the test package on the ground, and then with the test package installed at f1. The difference between f1 and ground noise temperatures reveals the amount of degradation caused by spillover of power from the horn into the region between the subreflector and main reflector, scattering from the tripod legs, noise contribution from illumination of the ground and sky region as seen from the subreflector focus, and leakage through gaps between panels and perforations in the main reflector surfaces, as well as noise temperature due to illuminating the area between the horn aperture and BWG shroud walls.

To yield the information described above, the experiment required that absolute noise temperature at the different test locations be accurate to about ±0.5 K and be repeatable to about ±0.2 K. The accuracy of values obtained for differential measurements is estimated to be ±0.3 K, which is more accurate than absolute values due to common errors canceling each other out in the differencing process.

To achieve these goals required an ultrastable radiometer and good mechanical stability of the test package at the various focal points after installation. It was shown in a previous article [4] that a number of measurements were made with the test packages installed at the different focal points, then back on the ground, and then back at the focal points. Such repeatability tests confirmed that the X-band test package and radiometric system met the accuracy requirements stated above for making absolute and differential noise temperature measurements.

Figures 7 and 8 show the X-band test package installed at f1 and f2. Horns of different gains at f1 and f2 were easily achieved by beginning with the 29-dBi horn and systematically removing horn sections to produce a lower gain horn. At both f1 and f2, test package adjustments were used to align the phase centers for the different gain horns to the desired geometric focal points.

Special radiometric calibration techniques were employed, such as (1) correcting for changes in atmospheric noise contributions due to changes in air temperature and relative humidity and (2) performing periodic real-time calibrations of the radiometric system for measuring noise temperatures. Further details of the microwave performance of these test packages and radiometric techniques used to achieve the desired stability and precision have been reported elsewhere [5].

V. Results

The measurements described above were made at Cassegrain focus f1, intermediate focus f2, and basement focus f3.

For contrasting the two theories, the most interesting measurements were those made at f2, where the shroud surrounds the mirrors. Since there is no shroud in the pedestal room, both methods give the same result for the basement mirrors.

A horn pattern input at f2 is imaged at f1 so measurements made with the same horn gain at f1 and f2 can be differenced to give the noise temperature due only to the BWG portion of the system. A plot of the measured data for the upper BWG (f2 to f1) is compared to both theories in Fig. 9 for horn gains from 25 to 29.8 dB. Obviously, the lower gain horn spills more energy past the mirrors and has a higher noise temperature contribution. Interestingly, both methods do a fairly good job of predicting noise temperatures. For reference, the BWG system was designed to operate with the 29.8-dB gain horn.

References

[1] A. G. Cha and W. A. Imbriale, "A New Analysis of Beam Waveguide Antennas Considering the Presence of the Metal Enclosure," *IEEE Transactions on Antennas and Propagation*, vol. 40, no. 9, pp. 1041–1046, 1992.

[2] R. F. Harrington, *Time-Harmonic Electromagnetic Fields*, New York: McGraw-Hill, Chapter 8, 1961.

[3] W. Veruttipong and M. Franco, "A Technique for Computation of Noise Temperature Due to a Beam Waveguide Shroud," *1993 IEEE AP-S International Symposium*, The University of Michigan at Ann Arbor, pp. 1659–1662, June 1993.

[4] D. A. Bathker, W. Veruttipong, T. Y. Otoshi, and P. W. Cramer, Jr., "Beam Waveguide Antenna Performance Predictions With Comparisons to Experimental Results," *Microwave Theory and Techniques, Special Issue (Microwaves in Space)*, vol. MTT-40, no. 6, pp. 1274–1285, 1992.

[5] T. Y. Otoshi, S. R. Stewart, and M. M. Franco, "Portable Microwave Test Packages for Beam Waveguide Antenna Performance Evaluations," *Microwave Theory and Techniques, Special Issue (Microwaves in Space)*, vol. MTT-40, no. 6, pp. 1286–1293, 1992.

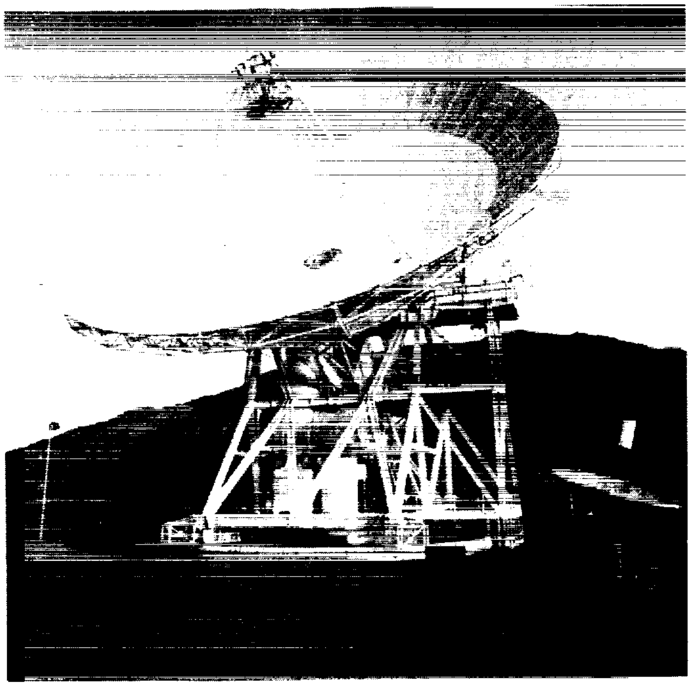

Fig. 1. The DSS-13 34-m BWG antenna.

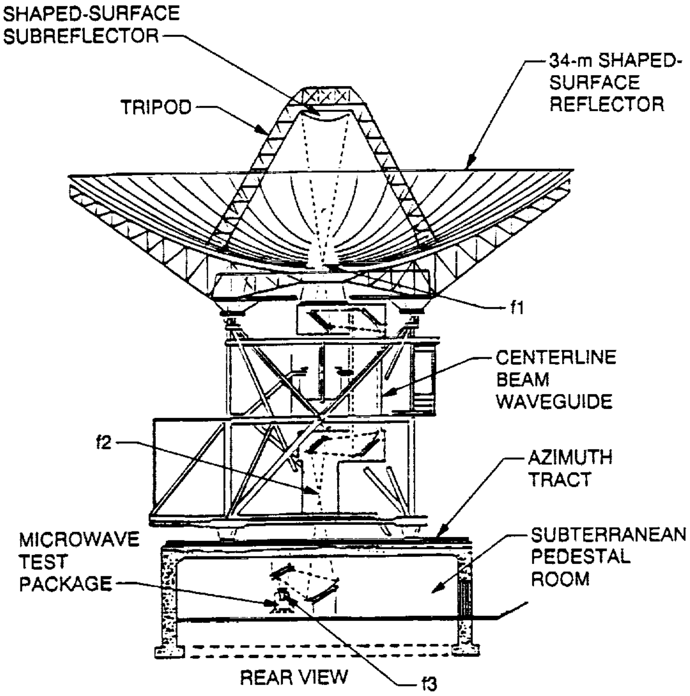

Fig. 2. The 34-m BWG antenna focal points.

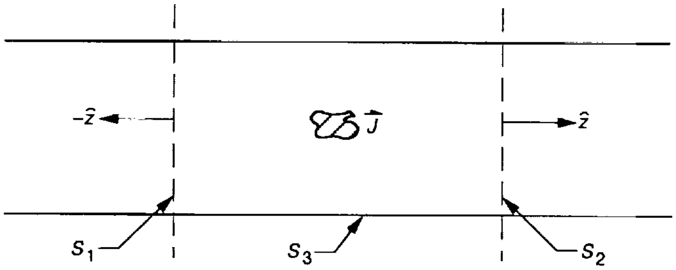

Fig. 3. Geometry for computing waveguide modes.

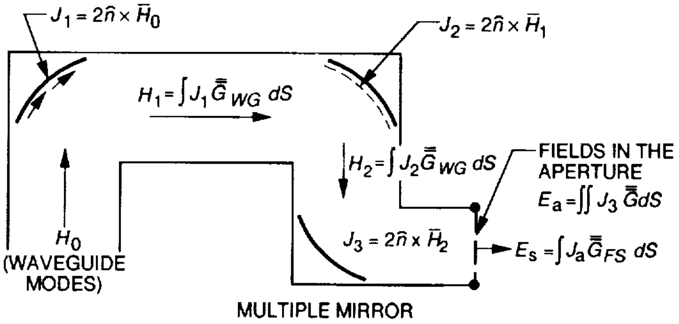

Fig. 4. Computation of fields in the BWG system.

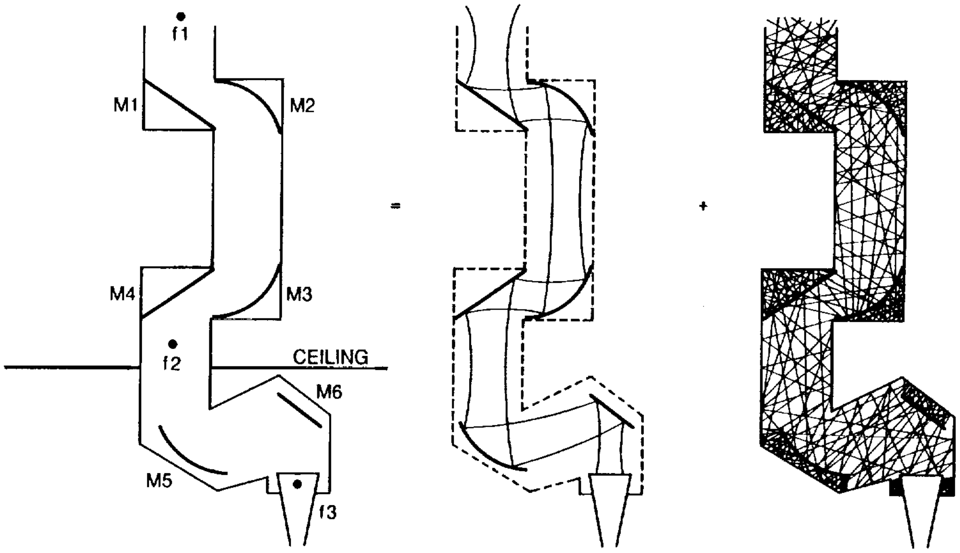

$$P_{BWG} = P_m + P_{spill}$$
$$T_{BWG} = T_m + T_{spill}$$

Fig. 5. Characteristics of the fields inside a BWG shroud and their corresponding noise temperatures.

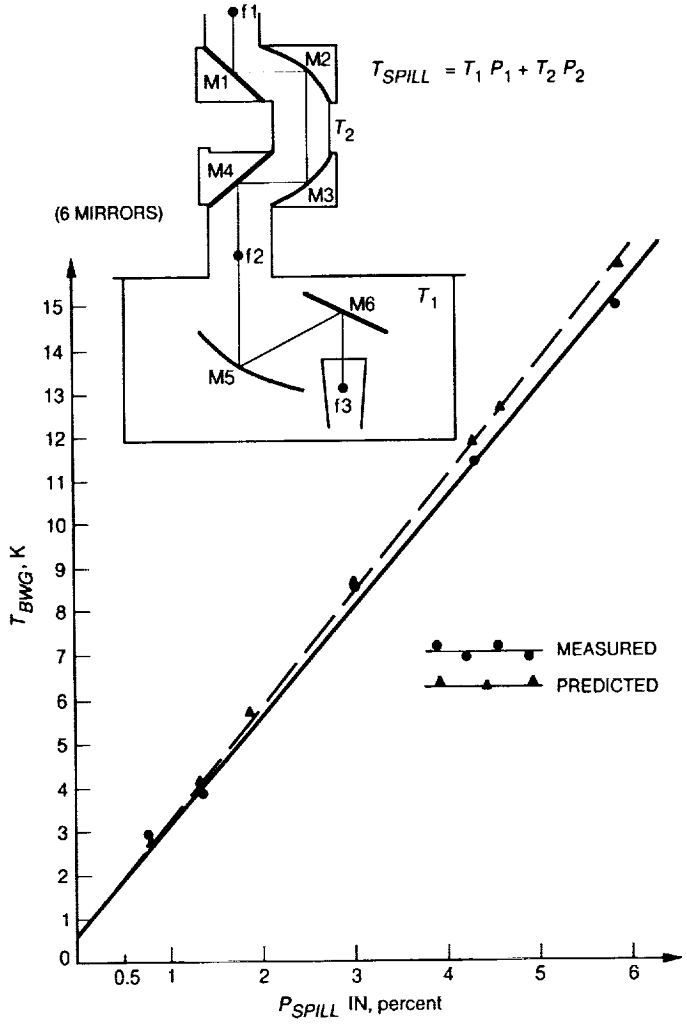

Fig. 6. The comparison between predicted and measured BWG noise temperatures at X-band.

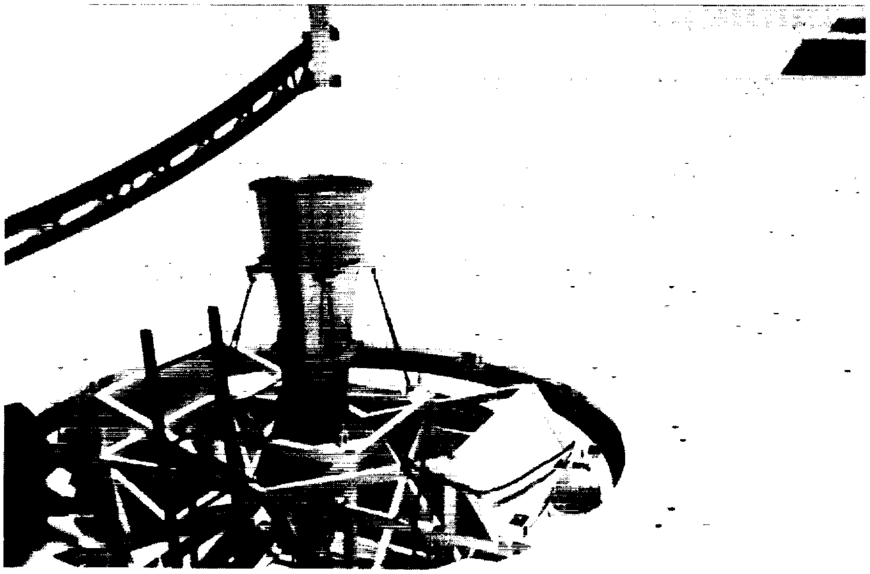

Fig. 7. Partial view of the X-band 29-dBi horn test package and mounting structure installed at the Cassegrain focal point fl.

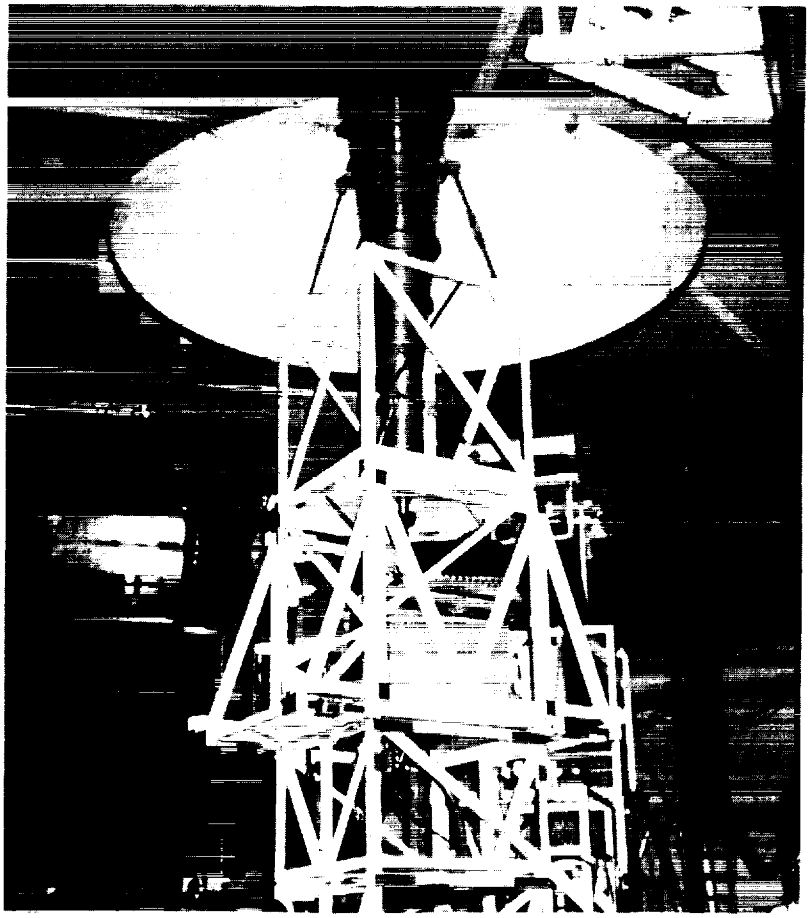

Fig. 8. The 8.45-GHz 22-dBi horn test package and mounting table installed at focal point f2.

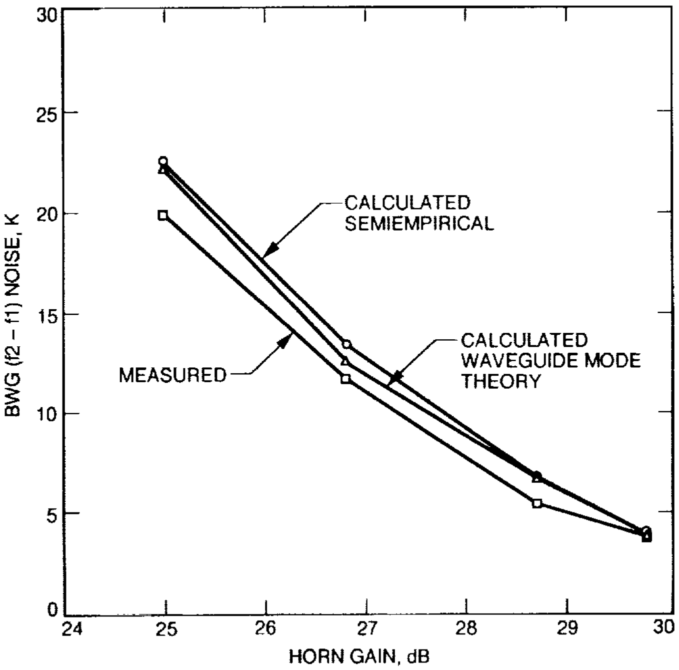

Fig. 9. Comparison of computed and measured noise temperatures with different feedhorn gains at f2.

N94- 29658

A Dual-Cavity Ruby Maser for the Ka-Band Link Experiment

J. Shell and R. B. Quinn
Radio Frequency and Microwave Subsystems Section

A 33.68-GHz dual-cavity ruby maser was built to support the Ka-Band Link Experiment (KABLE) conducted with the Mars Observer spacecraft. It has 25 dB of net gain and a 3-dB bandwidth of 85 MHz. Its noise temperature referred to the cooled feedhorn aperture is 5 K.

I. Introduction

The purpose of this article is to describe the design, construction, and performance of a dual-cavity ruby maser used to support the first Ka-band telemetry downlink demonstration from a spacecraft in deep space. The Ka-band downlink from the Mars Observer spacecraft was at either 33.6709 or 33.6926 GHz. The low transmitted-signal level necessitated that the best possible receiver sensitivity be available. (The link margin for the Ka-band signal was estimated to be 1.6 dB, whereas the margin for the X-band (approximately 8.4-GHz) signal was estimated to be 38.2 dB). Therefore, a low noise temperature for the maser was a primary goal. This was achieved by operating the maser between 1.5 and 1.6 K physical temperature and including the feedhorn and other feed components in the cryogenic package.

Since the two possible downlink frequencies differ by only 22 MHz, a center frequency of 33.68 GHz was selected, and the design goal was to achieve sufficient instantaneous bandwidth to receive either frequency without retuning the maser. Since broad tunability was not a requirement, and the instantaneous bandwidth requirement was fairly narrow, a waveguide cavity design was chosen to give the best performance for the least complexity.

The maser package utilizes superfluid helium in a commercial cryogenic dewar with superinsulation. This package was not intended to tilt and was mounted in a stationary, vertical position in the pedestal room of the 34-m DSS-13 beam waveguide antenna.

II. General Design Considerations

The first parameter to be determined in the design of a cavity maser is the number of cascaded cavities. The total maser gain need only be large enough that the noise contribution from the follow-up high electron mobility transistor (HEMT) amplifier is not significant. For example, with a HEMT amplifier noise temperature of 40 K, a maser net gain of 25 dB results in a HEMT amplifier contribution to the total front-end amplifier noise temperature of 0.13 K. If the maser net gain is 25 dB, the ruby electronic gain will need to be several dB more to overcome losses in the maser cavities, isolators, filters, and connecting waveguide. The estimated necessary ruby electronic gain was approximately 28 dB.

A. Gain Stability

One of the primary concerns in determining the required number of cavities is the gain stability. The fewer the number of cavities, the higher the required gain per cavity. Higher gain implies less stability because, to achieve a power gain of 100 or more in a single cavity, you must operate close to the onset of oscillation.

A rough estimate of the gain stability of the maser as a function of the bath temperature can be obtained in the following way: The temperature dependence of the gain of the maser is determined by the temperature dependence of the magnetic Q, Q_m. The magnetic Q is a useful quality factor in determining the gain of a maser. It quantifies the ability of a maser material, such as ruby, to amplify a signal. In circuit terms, it describes how heavily the "spins" (magnetic moments associated with the chromium ions in the ruby) load the cavity circuit. (For a thorough explanation of the maser process and definitions of terms used to explain the process, the reader should refer to Siegman [1] or other appropiate material.)

Q_m has two temperature dependent factors, the inversion ratio, I, and the thermal equilibrium spin population. (The inversion ratio is the ruby electronic gain in dB divided by the ruby absorption in dB.) For ruby oriented at the push-pull angle of 54.735 deg, the thermal equilibrium spin population is essentially independent of temperature at 1.5 K, and its variation will not be considered. Earlier theoretical work [2] suggests that the temperature dependence of the inversion ratio varies as

$$I \propto T^{-0.7} \tag{1}$$

for $1.5 \text{ K} < T < 2 \text{ K}$. Since Q_m is inversely proportional to the inversion ratio [1], Q_m must vary as

$$Q_m \propto T^{0.7} \tag{2}$$

The power gain ratio of a maser cavity at resonance is given by

$$G = \left| \frac{Q_m + Q_e}{Q_m - Q_e} \right|^2 \tag{3}$$

where Q_e is the external cavity Q. A more general expression will be given later. Solving for the ratio of the Q's gives

$$\frac{Q_e}{Q_m} = \frac{\sqrt{G} - 1}{\sqrt{G} + 1} \tag{4}$$

For example, a single cavity with 28 dB (ratio of 630.96) of gain requires a Q_e/Q_m ratio of 0.9234. Assuming a bath temperature of 1.55 K,

$$\frac{(Q_e/Q_m)_{T=1.54}}{(Q_e/Q_m)_{T=1.55}} = \left(\frac{1.55}{1.54}\right)^{0.7} = 1.00454 \tag{5}$$

Therefore, $(Q_e/Q_m)_{T=1.54}$ will be $(1.00454)(0.92343) = 0.927623$. Putting this new value into Eq. (3) yields a gain of 709.33, or 28.51 dB. Thus, a 0.01-deg bath temperature change will result in a 0.51-dB gain change if all the gain comes from one cavity. Similar calculations have been done for two, three, and four cavities. These results are shown in Table 1. There is a significant reduction in gain variation going from one to two cavities, but further improvement in going to three or four cavities is small. Therefore, a two-cavity design offers significantly better gain stability without adding considerably more complexity.

B. Bandwidth

Siegman [1] has compared the bandwidth of the traveling wave maser and the "ideal" cavity maser. An ideal cavity maser has a magnetic Q much smaller than the atomic Q. (This will be shown shortly to be the case for this maser. In this case, the maser action is strong and the gain-bandwidth product is limited by the magnetic resonance linewidth.) For maser gains of about 14 dB, the ratio of the maser amplifier bandwidth to the magnetic resonance linewidth is approximately 0.5, and is the same for the ideal cavity maser and the traveling wave maser. For larger maser gains, the ideal cavity maser bandwidth is substantially less than the traveling wave maser bandwidth. For smaller maser gains, the ideal cavity maser bandwidth is greater than the traveling wave maser bandwidth. Therefore, a cavity maser with a 14-dB gain or less has good bandwidth potential if the magnetic Q is low.

C. Magnetic Q, Atomic Q, and External Q

The magnetic Q and atomic Q should now be computed to verify that we are in a regime of strong maser action, i.e., $Q_m << Q_a$. The value of magnetic Q can be calculated using

$$\frac{1}{Q_m} = \frac{2g^2\beta^2\mu_o}{h}\frac{I\Delta N\sigma^2\eta}{\Delta f_L} = 1.3\left(10^{-18}\right)\frac{I\Delta N\sigma^2\eta}{\Delta f_L} \qquad (6)$$

where Δf_L is expressed in MHz. A discussion of this equation is given in the Appendix and in [1].

The thermal equilibrium spin density population difference at 1.55 K can be calculated since the spins follow a Boltzmann population distribution. For a 0.05-percent chromium-doped ruby crystal oriented at the push–pull angle, the spin density population difference between levels 2 and 3 is $\Delta N = (0.144)(2.35 \times 10^{19}) = 3.38 \times 10^{18}$ spins/cc. The inversion ratio is approximately 2.0.

The filling factor for the cavity, η, must be estimated. The magnetic susceptibilty of the ruby for the signal transition (2–3) is essentially circularly polarized. The standing wave field in the cavity can be thought of as being half right circularly polarized and half left circularly polarized. Therefore, the maximum filling factor would be 0.50. Since some of the magnetic field extends beyond the ruby, the estimated filling factor is closer to 0.3.

For use in this formula, the signal transition should have a Lorentzian line shape. Since the natural linewidth of ruby is 60 MHz, some artificial broadening of the linewidth is necessary to achieve the goal of 85-MHz instantaneous bandwidth. This is accomplished with both a linear field gradient and single-step staggering. The linear field gradient is achieved by changing the length of the air gap between the hiperco pole pieces where the ruby is located. The single-step staggering is achieved with trim coils placed in the lid of the cavity structure.

Siegman has dicussed how the ratio of the maser amplifier bandwidth to the ruby resonance linewidth is improved with various types of stagger tuning. For a maser gain of 28 dB, the improvement with linear staggering and single-step staggering is comparable. In both cases, the maser bandwidth is approximately 80 percent of the resonance linewidth. Therefore, for an amplifier bandwidth of 85 MHz, the Lorentz equivalent linewidth is about 106 MHz.

The transition probability, $\sigma^2 = 0.9616$, can be determined from the spin Hamiltonian for ruby [3]. Substituting the above values in Eq. (6) gives a magnetic Q of 41. The atomic Q is roughtly 33,700 MHz/106 MHz, or 318. Therefore, $Q_m << Q_a$, as we assumed earlier. Using Eq. (4), the ratio of Q_e/Q_m for a 14-dB gain cavity is 0.66732. A magnetic Q of 41 implies an external Q of 27.

D. Overall Layout

A schematic drawing of the dual-cavity maser is shown in Fig. 1. As seen by the signal, the cavities are one-port reflection cavities with commercial WR-28 waveguide circulators used to separate the ingoing and outgoing signal. There is a waveguide transition between the circulator and the ruby cavities from the WR-28 waveguide to a reduced-height waveguide (WR-30). This was done to increase the coupling to the ruby cavity and will be discussed in the next section. The WR-30 waveguide has cross-sectional dimensions of 0.777 cm (0.306 in.) by 0.127 cm (0.050 in.). The second port of each cavity is beyond cutoff to the signal and is where the pump power (required to invert the ruby) is supplied to the cavity.

Experimentally, a single isolator between cavities did not provide enough isolation to prevent noticeable gain ripple. Therefore, two isolators were used. There are also waffle-iron bandpass filters in the output and input to keep the RF pump energy from reaching the HEMT post amplifier or escaping out the feedhorn. The ruby resonators are contained in the WR-10 waveguide, whose dimensions are 0.254 cm (0.10 in.) by 0.127 cm (0.050 in.). The 69.5-GHz pump energy is normally propagated in the WR-15 waveguide. Therefore, a waveguide transition from the WR-15 to the WR-10 waveguide was necessary. The coupling of the pump energy will be discussed in a later section. A photograph of the maser and HEMT post amplifier is provided as Fig. 2. An early photograph (showing only one interstage isolator) with part of the hiperco magnet return yoke removed is provided as Fig. 3.

III. Cavity Design

The magnetic Q of a cavity maser is determined by the maser material, its orientation relative to the dc magnetic field, the RF pumping scheme employed, the signal linewidth, and the bath temperature. The magnetic Q depends mostly on atomic parameters, and the cavity affects its value only through the polarization. The discrepancy between the desired and the actual polarization is accounted for with a "filling factor." To control the maser mid-band gain, the external Q is adjusted by changing the degree of coupling between the external line and the cavity. For stability, the positive external coupling must load the cavity more heavily than the negative resistance of the spin system [1].

The value of $Q_m = 41$ computed in the prior section indicates that the maser action is fairly strong. A strong external coupling, $Q_e = 27$, will therefore be required. In general, a coupling iris or aperture is used to adjust the degree of coupling of the cavity to an external transmission line. When a cavity filled with a high dielectric-constant maser crystal is coupled to a waveguide, it is difficult to obtain the strong coupling required. The impedance mismatch between the maser crystal dielectric and the helium-filled waveguide may be large enough that sufficiently strong coupling can only be obtained with a coupling aperture consisting of one entire side of the cavity. This was the case with this maser. The role of the aperture is played by the helium-dielectric interface and the change in waveguide width.

The strength of the coupling can fall into one of three categories [4]:

(1) Reflection from the "aperture" dominates over that from the cavity; this is known as undercoupling.

(2) Reflection from the "aperture" cancels that from the cavity at the center frequency, and there is no reflected power; this is known as critical coupling.

(3) Reflection from the cavity dominates that reflected from the "aperture"; this is known as overcoupling.

The impedance locus on a Smith chart for these three cases is shown in Fig. 4. We are interested in the overcoupled case where the impedance locus encircles the origin. Microwave cavities may be considered from either a lumped equivalent circuit viewpoint or from the viewpoint of a transmission line with discontinuities. We will begin with a lumped-equivalent-circuit description, and then give a simple transmission-line equivalent circuit.

The principal advantage of the lumped-element model is that the various Q's are easily identified. We consider the circuit shown in Fig. 5. (The representation of the dielectric-filled cavity by a series resonant circuit and of the ruby spin system by a parallel resonant circuit is discussed in Siegman [1]. We have chosen to use the dual circuit, where the cavity is a parallel resonant circuit and the spin system is a series resonant circuit.) The quantities L, C, and G refer to the cavity inductance, capacitance, and conductance. The quantities L_m, C_m, and G_m refer to the ruby spin system. $G_e(Y_o)$ is the conductance (admittance) of the external transmission line that connects the cavity to the outside world. The reflection coefficient corresponds to the voltage gain and is given by

$$g(w) = \rho(w) = \frac{Y_o - Y_{load}}{Y_o + Y_{load}} \tag{7}$$

The expression for Y_{load} for the circuit of Fig. 5 is given by

$$Y_{load} = G + j\left(wC - \frac{1}{wL}\right) - \frac{1}{\left(\frac{1}{G_m} + j\left(wL_m - \frac{1}{wC_m}\right)\right)} \tag{8}$$

For a series resonance, the Q varies as wLG, and for a parallel resonance, the Q varies as $1/(wLG)$, where w is the angular frequency. The cavity and spin system angular resonance frequencies are denoted by w_o and w_a. The various Q's can now be identified as:

$$\begin{array}{lclcl} \text{magnetic } Q & = & Q_m & = & 1/(G_m w_o L) \\ \text{external } Q & = & Q_e & = & 1/(G_e w_o L) \\ \text{atomic } Q & = & Q_a & = & w_a L_m G_m \\ \text{cavity } Q & = & Q_c & = & 1/(w_o L G) \end{array} \tag{9}$$

Substituting Y_{load} from Eq. (8) into Eq. (7) and using the definitions above, the voltage gain can be written as

$$g(w) = \frac{Q_m + \dfrac{Q_e}{1 + 2j\,Q_a\left(\frac{w - w_o}{w_o}\right)} - 2jQ_mQ_e\left(\frac{w - w_o}{w_o}\right) - \frac{G}{G_m}}{Q_m - \dfrac{Q_e}{1 + 2j\,Q_a\left(\frac{w - w_o}{w_o}\right)} + 2jQ_mQ_e\left(\frac{w - w_o}{w_o}\right) + \frac{G}{G_m}} \tag{10}$$

If $G << G_m$, then all specific admittances will drop out, and the gain is expressed solely in terms of the three quality factors, Q_e, Q_m, and Q_a. At resonance, $w = w_o$, and the voltage gain is given by

$$g(w) = \frac{Q_m + Q_e}{Q_m - Q_e} \qquad (11)$$

The power gain is the square of this and is the result we used earlier as Eq. (3). Since the admittance levels are arbitrary, we set $G_e = 1$ mho ($R_e = 1$ ohm). Since the external Q must be 27, $w_oC = 27$. Therefore, $C = 1.275 \times 10^{-10}$ F. Since the resonant frequency is 33.68 GHz, $L = 1.75 \times 10^{-13}$ H. Since $Q_m = 41 = 1/(w_oLG_m)$, then $G_m = 0.666$ mho ($R_m = 1.5$ ohm). Since the atomic $Q = 33,700$ MHz/106 MHz $= 318 = \omega_a L_m G_m$, then assuming $\omega_a = \omega_o$, $L_m = 1.00 \times 10^{-9}$ H and $C_m = 2.23 \times 10^{-14}$ F. The value of G is unspecified, but must be small compared to the value of G_m. We assume that $G = 0.05$ mho ($R = 20$ ohms), approximately an order of magnitude less than G_m. The values associated with the spin system, L_m, C_m, and G_m, are negative when the spin system is inverted.

A plot of the reflection coefficient using the program Touchstone[1] is shown in Fig. 6. Curve "a" shows the gain performance, and curve "b" shows the ruby absorption. The value of G_m for the absorption is decreased by a factor of 2 since the inversion ratio is about 2 for this frequency, ruby orientation, and RF pumping scheme. The ruby electronic gain is about 12.5 dB. The 3-dB bandwidth is about 82 MHz.

The same calculation can be plotted on a Smith chart to show the phase behavior (Fig. 7). Curve "a," which stays near the periphery of the chart, is the S_{11} behavior of the dielectric-filled cavity. The effect of the ruby spin system in an absorptive state, curve "b," can be seen to be quite strong where it crosses the resistance axis, that is, near resonance. For comparison, experimental data for an early ruby-filled cavity (where the spin system is not resonant) is shown in Fig. 8. (Although the center frequency of 33.0 GHz is slightly low, the frequency span is 2 GHz).

The aperture reflection coefficient can be estimated from a knowledge of the respective wave impedances [5]. In terms of the free space wavelength, λ, the ratio of the wave impedances (for transverse electric modes) for the ruby-filled WR-10 and the helium-filled WR-30 is given by

$$\frac{Z_2}{Z_1} = \left[\frac{\epsilon_1 - (\lambda/\lambda_{c_1})^2}{\epsilon_2 - (\lambda/\lambda_{c_2})^2}\right]^{1/2} = 0.31 \qquad (12)$$

Therefore, the reflection coefficient ρ is given by

$$\rho = \frac{Z_2 - Z_1}{Z_2 + Z_1} = -0.53 \qquad (13)$$

The change in wave impedance gives a substantial reflection coefficient. This was measured experimentally with the test fixture shown in Fig. 9. The tapered section between the alumina and the load material prevented reflection of the wave transmitted through the interface. The effect of the change in waveguide width is probably reduced because the ruby was pulled out 0.356 mm past the plane where the waveguide width changes. The experimental result is shown in Fig. 10. The impedance measurement was 15.9 ohms (relative to 50 ohms). Therefore, from Eq. (13), the corresponding reflection coefficient was −0.52 and essentially frequency-independent from 32 to 35 GHz.

Altman [6] has shown that an equivalent lumped-element resistor-inductor-capacitor (RLC) circuit with normalized parameters can be replaced by a circuit where the R, L, and C represent the intrinsic parameters of the cavity proper, if the effects of the coupling discontinuity are described by a transformer. In this case, the discontinuity or "aperture" is due to the dielectric material and the change in waveguide width. In more conventional cavities, it is due to a thin iris or coupling loop. It is an interesting theoretical experiment to model the present discontinuity as if it were simply a thin iris and to see where it leads. (This approach is not rigorous, and an electromagnetic field analysis is needed to derive the equivalent circuit.) Following the usual analysis for a thin iris in an otherwise homogeneous section of waveguide, the discontinuity can be represented by a transformer with a turns ratio given by

$$n^2 = \frac{1 + \rho}{1 - \rho} \qquad (14)$$

where ρ is the reflection coefficient, assuming the output waveguide is matched. Using the reflection coefficient mentioned above, the turns ratio of the transformer is 0.56. A new lumped-element equivalent circuit incorporating the transformer can be constructed, where the new values of L', C', and R' representing the intrinsic cavity are

$$\begin{aligned} L' &= L/n^2 \\ C' &= n^2 C \\ R' &= R/n^2 \end{aligned} \qquad (15)$$

and the circuit is shown in Fig. 11(a).

---

[1] Touchstone is a trademark of EEsof, Inc., Westlake Village, California.

This new parallel $R'L'C'$ circuit can be formally replaced by an equivalent transmission line. This is discussed in [7] and shown in Fig. 12. The admittance of the line can be determined by equating the susceptance slope parameter of the lumped circuit and the transmission line. The attenuation constant is related to the cavity conductance, G. The appropiate equations are

$$b = w_o C = \frac{1}{(w_o L)} = \frac{n\pi Y_o}{2}\left(\frac{\lambda_{g_o}}{\lambda_o}\right)^2 \tag{16}$$

$$G = Y_o \alpha \ell \ (\alpha \text{ in nepers/unit length})$$

Since the physical transmission-line element in Touchstone is nondispersive, we assume $\lambda_{g_o}/\lambda_o = 1$. This leads to a Y_o of 2.7. Using $G = 0.05$, and $l = 0.2815$ cm, then $\alpha = 0.18$ dB/cm, or 0.051 dB per wavelength. The attenuation of the ruby-filled WR-10 waveguide was measured to be approximately 0.1 dB/cm, or 0.034 dB per guide wavelength at 33.7 GHz. Therefore, an approximate transmission-line equivalent circuit for the cavity can be constructed as shown in Fig. 11(b). A plot of the ruby absorption and gain for this circuit, using Touchstone, is shown in Fig. 6 as curves "c" and "d."

The ruby-filled waveguide is approximately one guide wavelength in length at 33.7 GHz. A full guide wavelength rather than a half was chosen so that the linear magnetic field taper required to broaden the ruby resonance linewidth would not be excessive. The resonant frequency of the cavity was adjusted by varying the length of the ruby crystal. The degree of external coupling was adjusted by pulling the ruby out past the plane where the waveguide changes width. Ruby paramagnetic resonance absorption plots were made at various magnetic field strengths with the cavity cooled to liquid nitrogen temperatures to determine the center frequency of the cavity at cryogenic temperatures. In addition, the tuning range of the maser is indicated by these plots. Such a plot is shown in Fig. 13.

IV. Magnet Design

The decision to build two cavities determined the volume over which the magnetic field must be provided. A circular region of 7.9-cm diameter was required to house the cavity structure and waveguides. The depth of the copper coil form upon which the superconducting wire was wound was estimated to be 19 mm. Therefore, the diameter of the region over which the hiperco yoke would operate is 11.7 cm (see Fig. 14). Assuming a roughly constant field strength of 12,400 G over this region, the total flux would be approximately (12,400 G) x (107.2 cm^2) = 1,329,280 G–cm^2.

If the hiperco annulus that provides the vertical return path for the magnetic field lines is 1.78 cm in the radial direction, the total magnet diameter will be 15.24 cm. The total cross-sectional area of the vertical return path at plane A–A (see Fig. 15) is 75.23 cm^2. Therefore, the field in the hiperco at this point (neglecting flux leakage outside the hiperco) is (1,329,280)/(75.2) = 17,677 G. The top and bottom plates of the hiperco yoke were chosen to be 2.03-cm thick. Therefore, the total cross-sectional area at plane B–B is 74.5 cm^2 and the field is 17,843 G. This is safely below the magnetic saturation for hiperco, which occurs at 23,600 G.

If the flux in the hiperco is 17,677 G, then from the B versus H curve of hiperco 27, the magnetizing force in the hiperco is about 40 Oe. Now the required number of ampere turns can be determined. Looking at a cross-sectional view of the magnet (Fig. 15), we can write Ampere's law for the contour drawn and find

$$\oint \vec{H} \bullet \vec{d\ell} = \frac{4\pi NI}{c} \tag{17}$$

or

$$B(\text{gap})L(\text{gap}) + H(\text{hiperco})L(\text{hiperco}) =$$

$$22{,}854 \text{ G}-\text{cm} = \frac{4\pi NI}{c}$$

therefore

$$NI = \frac{(22{,}854 \text{ G}-\text{cm})(3 \times 10^{10}\text{cm/sec})}{4\pi(3 \times 10^{9} \text{ esu/sec/A})}$$

$$= 18{,}187 \text{ A–turns} \tag{18}$$

The coil form has an inside cross-sectional area of 15.24 mm x 16.51 mm = 2.52 cm^2. Assuming a wire cross-sectional area of 0.0613 mm^2 and a usable area (based on previous experience) of approximately 60 percent of 2.52 cm^2, or 1.51 cm^2, implies a total of (151 mm^2)/(0.0613 mm^2) = 2,462 turns, which means the current required will be I = (18,187)/(2462) = 7.4 A.

The total number of turns of NbTi superconducting wire actually wound on the coil form was 2,850 turns. This implies a current requirement of 6.4 A. The actual current required to charge the magnet is about 6.5 A. The wire was epoxied in place on the coil form under vacuum using Scotchcast 235 epoxy.

The magnetic field over the rubies was broadened by machining a 1.8-deg linear taper in the round hiperco pole piece, which is located directly over the rubies. This taper broadened the ruby line width from 60 to 175 MHz. By rotating the pole piece, each ruby can be placed in a slightly different magnetic field. This technique could be used to achieve broader bandwidth at reduced gain if necessary. In this instance, the amplification bandwidth was set to approximately 85 MHz.

In addition to the main superconducting magnet, a set of four trim coils, two for each cavity, were wound on rexolite cores and placed into holes recessed in the cover of the cavity block. The rexolite cores were rectangular and measured 2.54 mm by 1.27 mm, and each coil was wound with 88 turns of copper wire. In practice, the current used to trim the ruby response is of the order of several hundred mA per coil. With 500 mA per coil, the total power dissipation is about 15 mW.

The main superconducting magnet was operated in the persistent mode by spot welding the free ends of the wire from the coil so the superconductor formed a closed loop. The spot weld was anchored to the negative terminal of a power supply, and the positive terminal was connected to the wire a few inches away. In the superconducting wire between these terminals, a small portion of the copper cladding was etched away, and a small coil of Nichrome heater wire was wound around the exposed NbTi wire. This portion of the wire was covered with Armstrong epoxy for strength and to thermally isolate the wire from the liquid helium. Approximately 60 mW of heater power was required to drive the wire normal. Components of the magnetic circuit can be seen in Figs. 2 and 3.

V. RF Pump Considerations

In order to invert the spin system, RF energy must illuminate the ruby. Since this ruby was oriented at the push–pull angle (c-axis angle of 54.735 deg to the dc magnetic field), a single pump frequency of 69.5 GHz was required. The RF pump energy was supplied by two Hughes solid-state (model 47134H) impact ionization avalanche transit time (IMPATT) oscillators. Each oscillator supplies over 100 mW of RF power. Although each oscillator comes equipped with its own waveguide ferrite isolator, it was found that additional isolators were required to prevent the oscillators from affecting each other.

The pump energy entered the cryostat in the WR-15 waveguide. After passing through an E-plane bend, the energy was passed to the WR-28 waveguide. The oversized waveguide was used to minimize the attenuation of the pump energy as it traveled 0.75 m to the maser. Just before reaching the maser, the waveguide switched back to WR-15. The two WR-15 waveguides were joined at a 3-dB sidewall hybrid coupler. The two outputs of the coupler went to the two cavities. The transitions from WR-15 to WR-28 were accomplished with commercially available cosine taper transitions.

The WR-15 waveguide entered the superconducting magnet and fastened directly to the maser cavity block. The cavity is one wavelength of a ruby-filled channel of WR-10, followed by a section of helium-filled WR-10 that acts as a waveguide beyond cutoff to the signal. A transition from WR-15 to the helium-filled WR-10 was necessary. Careful impedance matching of the pump waveguide to the ruby-filled cavities was necessary to keep the required RF pump power to a minimum.

The design of the quarter-wave step transformers used to impedance match the WR-15 waveguide to the WR-10 waveguide follows standard design [8,9]. The quarter-wavelength steps were first made in the waveguide height and then in the waveguide width. In each case, a two-section quarter-wave transformer was used (Figs. 16 and 17). In this analysis, Z_o and Z_3 are the impedances of the existing waveguides for which the transformers are being designed. The ratio R is given by

$$R = \frac{Z_o}{Z_3} \text{ or } \frac{Z_3}{Z_o} \tag{19}$$

whichever is greater than 1. The impedances of the intermediate quarter-wavelength steps, Z_1 and Z_2, are given by

$$\begin{aligned} Z_1 &= V_1 Z_o \\ Z_2 &= \left(\frac{R}{V_1}\right) Z_o \end{aligned} \tag{20}$$

where V_1 is given by

$$V_1^2 = \left(D^2 + R\right)^{1/2} + D \tag{21}$$

In this expression, D is given by

$$D = \frac{(R-1)\,k^2}{2\,(2-k^2)} \tag{22}$$

where k is given by

$$k = \sin\left(\frac{\pi B}{4}\right) \tag{23}$$

In this expression, B is the fractional bandwidth given by

$$B = \frac{2\,(\lambda_{gH} - \lambda_{gL})}{\lambda_{gH} + \lambda_{gL}} \tag{24}$$

where λ_{gH} and λ_{gL} are the guide wavelengths of the highest and lowest frequencies at which the transformer is to be operated. Using

$$Z_o = \frac{b}{a}\,\frac{\lambda_g}{\lambda_o} \tag{25}$$

for the impedance of a rectangular waveguide, the required height, width, and length (b, a, and L) of the quarter-wave steps can be determined. The length of all steps is one quarter-guide wavelength at 69.5 GHz. The results are shown in Table 2. Finally, a quarter-wavelength transformer of dielectric material with a dielectric constant approximately equal to 3 was used to match the helium-filled WR-10 to the ruby-filled WR-10.

VI. Performance

The electronic gain and ruby absorption of this maser at 1.5 K is shown in Fig. 18. The four magnetic-field trim coils have been adjusted for a flat response. The electronic gain is approximately 28 dB, and the 3-dB bandwidth is 85 MHz. The net gain is approximately 25 dB.

The noise temperature of each cavity can be calculated using [9]

$$T_{cav} = \frac{G-1}{G}\,\frac{hf}{k}\,\frac{G_{el}}{G_{net}}\,\frac{r}{r-1} + \frac{L_o}{G_{net}}\,\frac{1}{e^{hf/kT}-1} \tag{26}$$

where

$G =$ gain of the maser $= 316$

$G_{el} =$ electronic gain $= 28$ dB

$G_{net} =$ net gain $= 25$ dB

$L_o =$ forward loss $= 3$ dB

$h =$ Planck's constant $= 6.626 \times 10^{-34}$ J-sec

$f =$ frequency $= 33.68 \times 10^9$ Hz

$k =$ Boltzmann's constant $= 1.38 \times 10^{-23}$ J/K

$T =$ bath temperature $= 1.5$ K

$r =$ inverted spin population ratio $= 3.76$

where for push-pull pumping, r is given by

$$r = \frac{1 + 2I\left(N_2' - N_3'\right)}{1 - 2I\left(N_2' - N_3'\right)} \tag{27}$$

where

$I =$ inversion ratio $= 2.0$

$N_i' = N_i/N$

where

$N_i =$ number of spins in level i

$N =$ total number of spins in levels 1, 2, 3, and 4

Using the values listed above, the noise temperature of a single cavity is 2.2 K. To calculate the noise temperature of the complete amplifier, the losses and gains and their physical temperatures in the circuit must also be known. These are shown in Fig. 19. We assume all the lines in the circuit are at the bath temperature. The noise contribution from a line with numerical insertion loss $L_i > 1$ referred to the input is given by

$$P_{input} = (L_i - 1)\,P_n(T) \tag{28}$$

where $P_n(T)$ is given by

$$P_n(T) = \frac{hfB}{e^{hf/kT} - 1} \tag{29}$$

If this line is preceeded by a lossy line of insertion loss $L_j > 1$ or an amplifier of gain $G > 1$, then the above expression is modified to

$$P_{input} = \frac{L_j\,(L_i - 1)\,P_n(T)}{G} \tag{30}$$

Therefore, the noise temperature of the complete amplifier can be written as

$$T_{maser} = (L_1 - 1)T_b' + L_1 T_{cav} + \frac{L_1 (L_2 - 1) T_b'}{G_1} + \frac{L_1 L_2 T_{cav}}{G_1} + \frac{L_1 L_2 (L_3 - 1) T_b'}{G_1 G_2} \qquad (31)$$

where T_b' is the effective noise temperature of the 1.5-K bath. It is defined by

$$T_b' = \frac{hf/k}{e^{hf/kT} - 1} \qquad (32)$$

Because of the reduced thermal noise emitted when $hf \approx kT$, the bath really appears to be 0.83 K. The sum of these five contributions yields a maser noise temperature at the cryogenic flange of 3.0 K.

Hot and cold load measurements performed at Goldstone, California, yielded a system T_{op} (outside the antenna) looking at the sky at zenith of 17.5 K. Subtracting 1.9 K for the cosmic background and 9.6–11.6 K for the atmosphere results in a noise temperature at the feedhorn input of 4–6 K. Subtracting 1.7 K for the feedhorn and gas seals and 0.3 K for the cooled waveguide components leads to a noise temperature at the cryogenic input of the maser of 2–4 K. This is consistent with the above calculated value of 3 K.

VII. Conclusion

A dual-cavity ruby maser has been built to support the Ka-Band Link Experiment conducted with the Mars Observer spacecraft. It operated in a superfluid helium bath with a physical temperature between 1.5 and 1.6 K. Its electronic gain was 28 dB; its net gain was 25 dB; the 3-dB instantaneous bandwidth was 85 MHz; and the noise temperature referred to the cooled feedhorn aperture was 5 K. The maser was installed in the pedestal room of the beam waveguide antenna at DSS 13.

Acknowledgments

The authors would like to thank Robert Clauss for many informative discussions during the development and implementation of this maser. Mark Fiore also provided theoretical and experimental support.

References

[1] A. E. Siegman, *Microwave Solid State Masers*, New York: McGraw-Hill Book Company, p. 259, 1964.

[2] J. R. Lyons, "Spin-Lattice Relaxation and the Calculation of Gain, Pump Power, and Noise Temperature in Ruby," *The Telecommunications and Data Acquisition Progress Report 42-98, vol. April–June 1989*, Jet Propulsion Laboratory, Pasadena, California, pp. 63–85, August 15, 1989.

[3] R. W. Berwin, "Paramagnetic Energy Levels of the Ground State of Cr+3 in Al_2O_3 (Ruby)," JPL Technical Memorandum 33-440, Jet Propulsion Laboratory, Pasadena, California, January 15, 1970.

[4] E. L. Ginzton, *Microwave Measurements*, New York: McGraw-Hill Book Company, p. 401, 1957.

[5] C. G. Montgomery, R. H. Dicke, and E. M. Purcell, eds., *Principles of Microwave Circuits*, London: Peter Peregrinus Ltd., p. 369, 1987.

[6] J. L. Altman, *Microwave Circuits*, Princeton, New Jersey: D. Van Nostrand Co., p. 214, 1964.

[7] G. Matthaei, L. Young, and E. M. T. Jones, *Microwave Filters, Impedance-Matching Networks, and Coupling Structures*, Dedham, Massachusetts: Artech House Books, p. 215, 1980.

[8] V. F. Fusco, *Microwave Circuits: Analysis and Computer Aided Design*, London: Prentice-Hall International, p. 306, 1987.

[9] J. S. Shell, R. C. Clauss, S. M. Petty, G. W. Glass, M. S. Fiore, J. J. Kovatch, J. R. Loreman, D. E. Neff, R. B. Quinn, and D. T. Trowbridge, "Ruby Masers for Maximum G/Top," accepted for *Proceedings of the IEEE*, May 1994.

Table 1. Gain stability versus number of cavities with 28-dB fixed total gain.

Number of cavities	Cavity gain, dB	ΔG for ΔT of 0.01 K, dB per cavity	Total ΔG, dB
1	28	0.51	0.51
2	14	0.095	0.19
3	9.33	0.0511	0.15
4	7	0.035	0.14

Table 2. Design parameters and step sizes for the WR-15 to WR-10 transitions.

Parameter	WR-15 to RH WR-15	RH WR-15 to WR-10
R	1.48	2.30
B	0.20	0.20
k	0.156	0.156
D	$2.96(10^{-3})$	$8.00(10^{-3})$
V_1	1.104	1.235
b_1	1.40 mm	1.27 mm
b_2	1.70 mm	1.27 mm
a_1	3.76 mm	3.30 mm
a_2	3.76 mm	2.72 mm
L_1	1.32 mm	1.42 mm
L_2	1.32 mm	1.78 mm

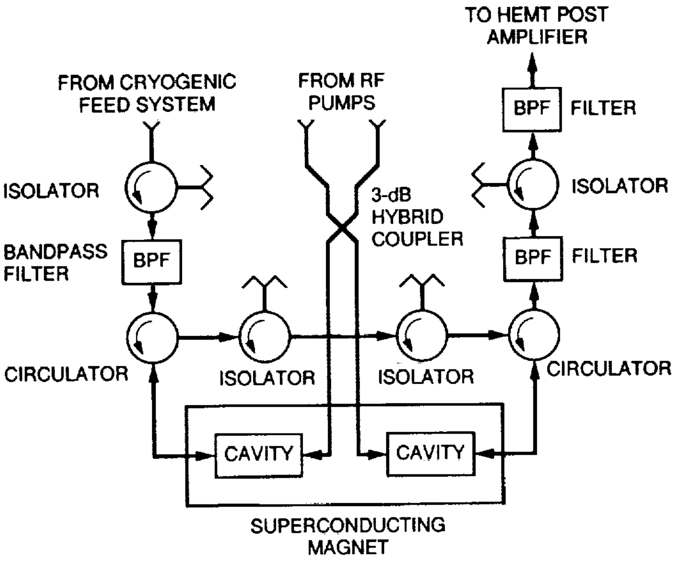

Fig. 1. The dual-cavity maser.

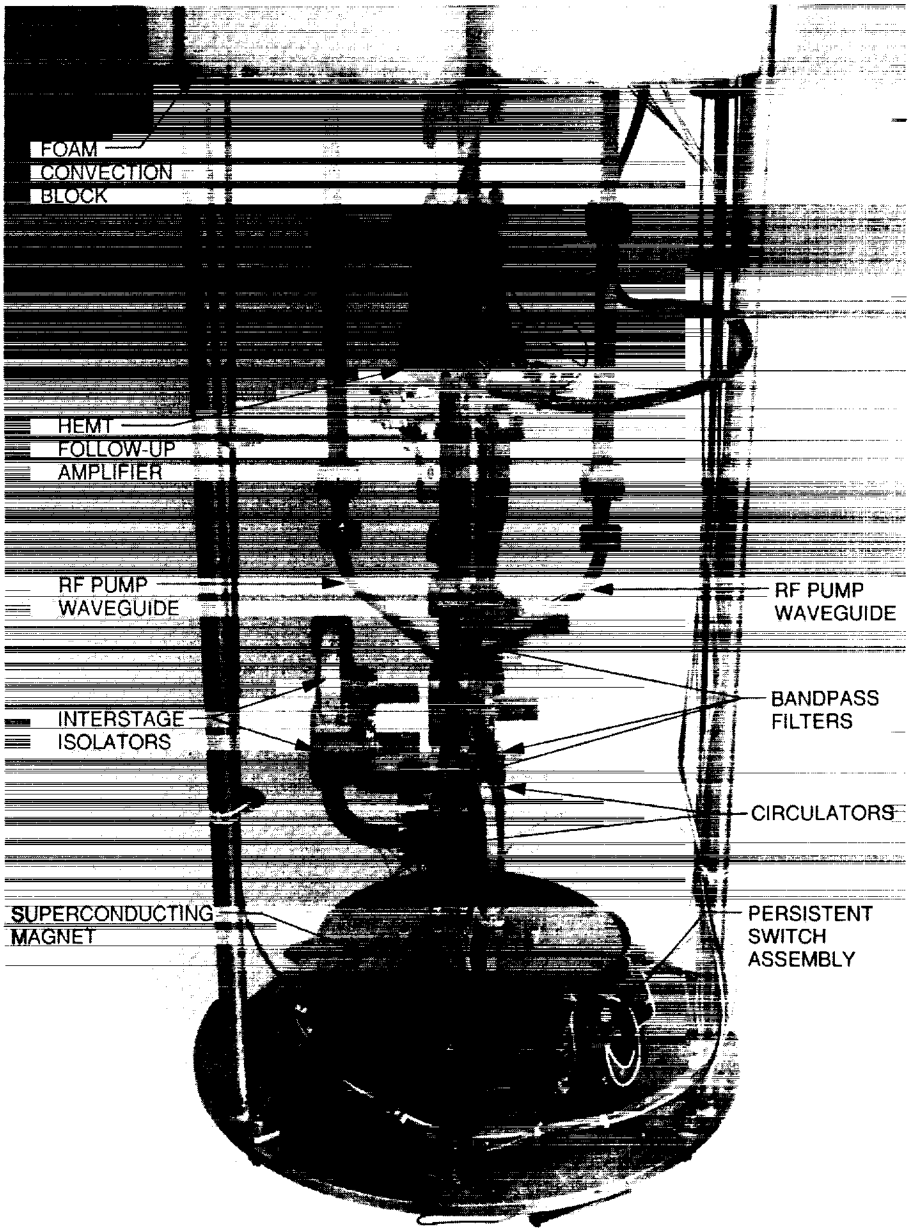

Fig. 2. The cryogenic portion of the completed maser and HEMT post amplifier (the helium dewars and room temperature components are not shown).

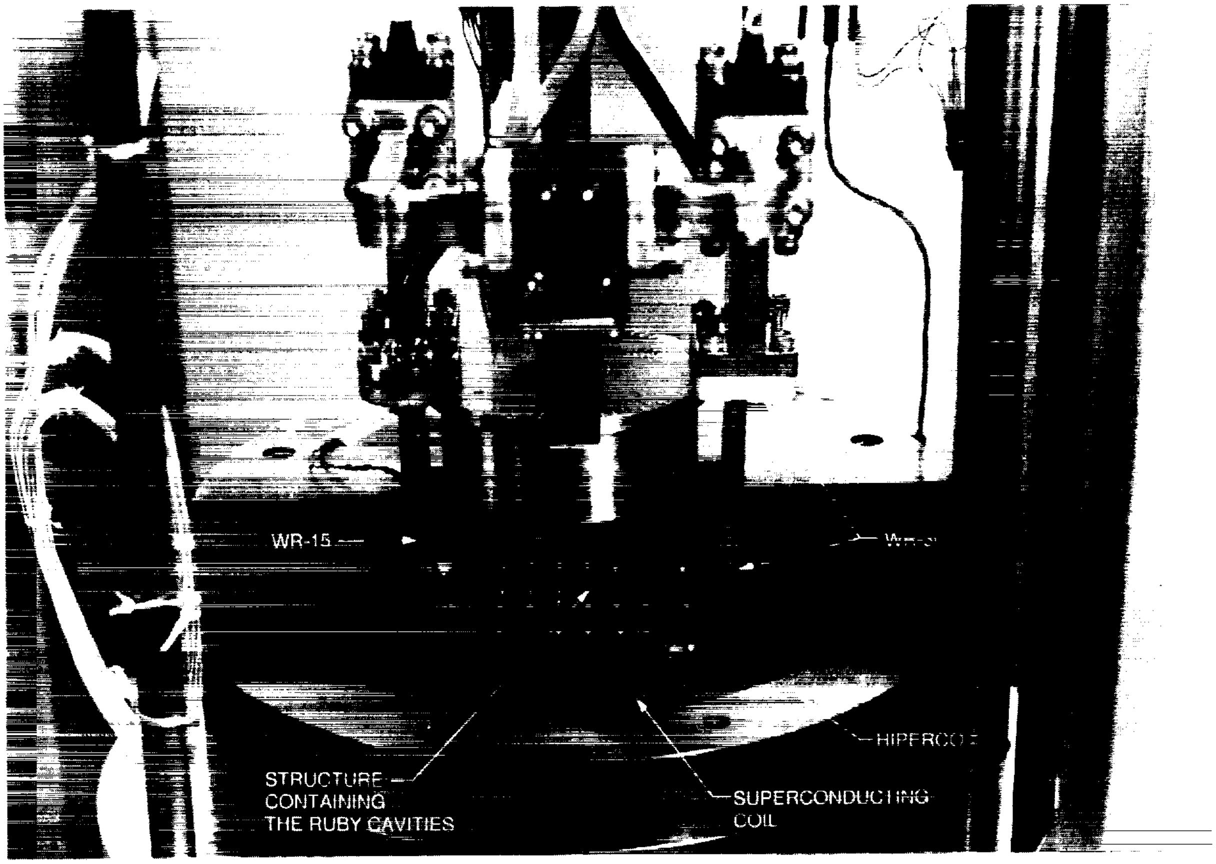

Fig. 3. A view of the maser with half of the top magnet pole piece removed and the round hiperco plug raised to expose the copper superconducting coil form and the structure containing the maser cavities. (At the time of this photograph, only one interstage isolator was present, and the trim coils were not yet installed.)

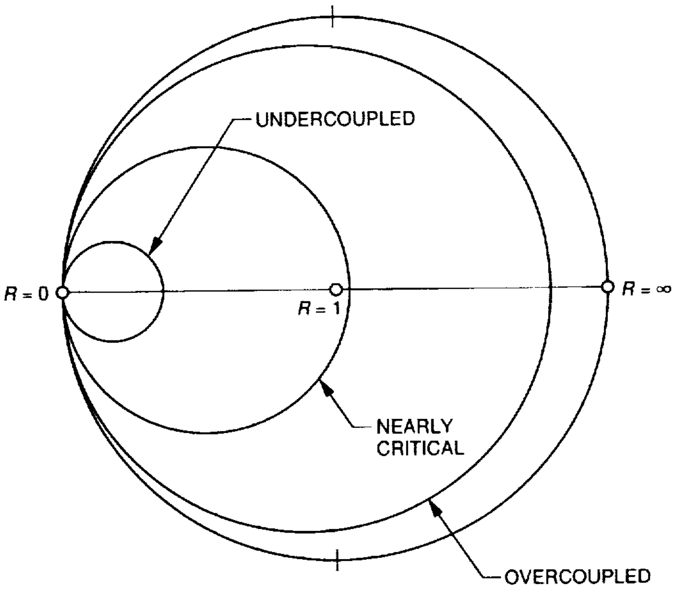

Fig. 4. The reflection coefficient behavior on a Smith chart display of undercoupled, critically coupled, and overcoupled cavities.

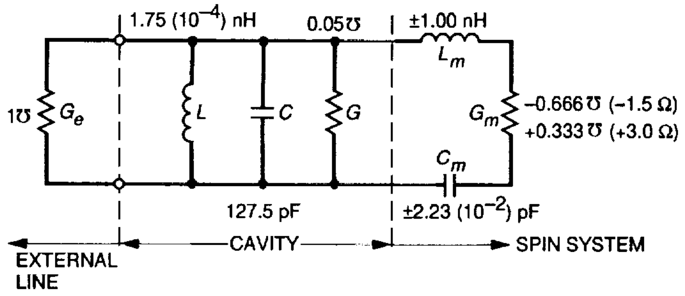

Fig. 5. A lumped-element model of one of the ruby maser cavities.

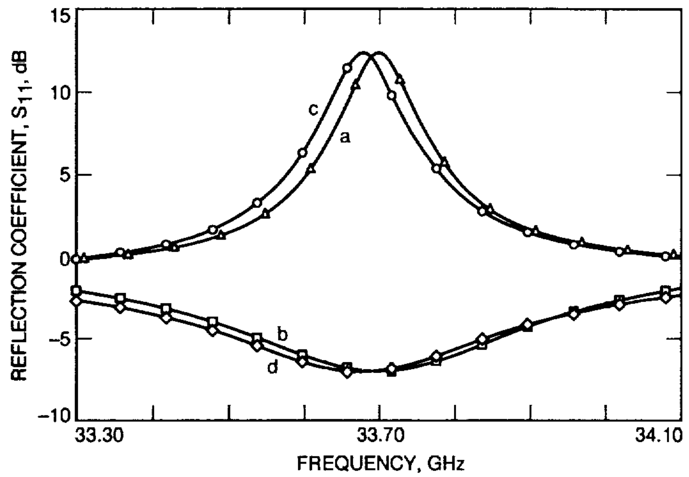

Fig. 6. Calculated ruby absorption and gain in dB versus frequency. Curves "a" and "b" are computed from the lumped-element model of Fig. 5. Curves "c" and "d" are from the transmission-line model of Fig. 11(b).

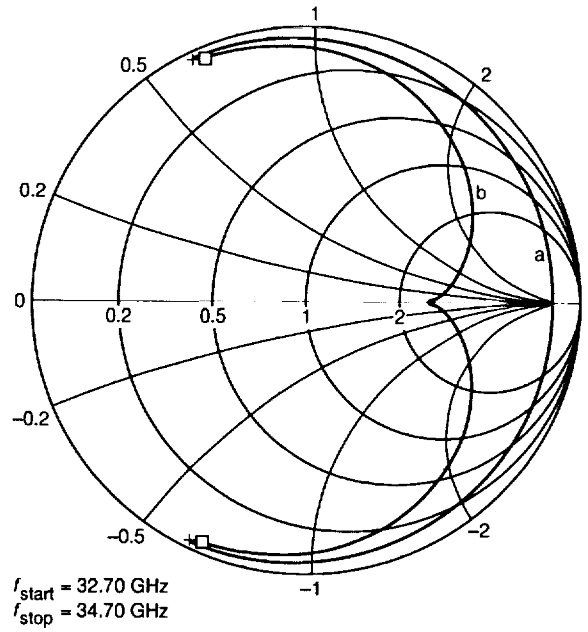

Fig. 7. A Smith chart display of the scattering coefficient (S_{11}) response of the lumped-element parallel RLC cavity model of Fig. 5 (curve "a"), and a similar display with the addition of the series RLC network representing the spin system in a dissipative state (curve "b").

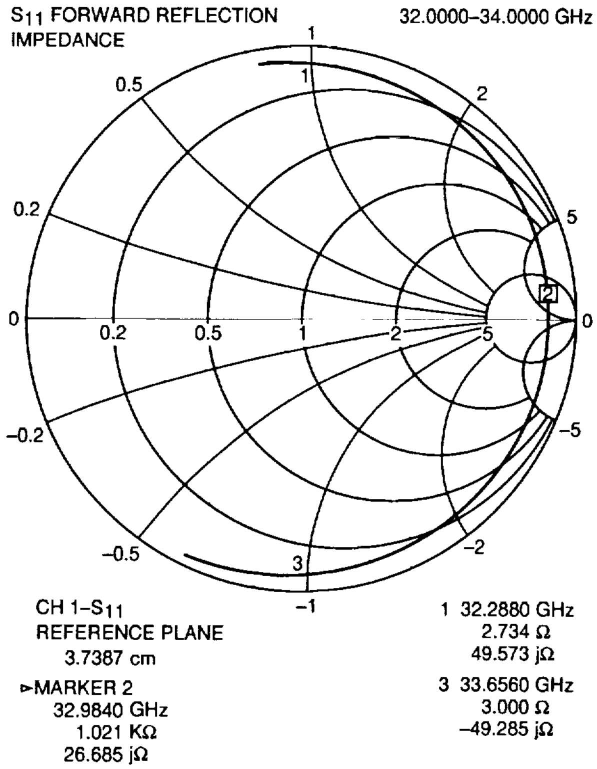

Fig. 8. Measured room temperature reflection coefficient data of one of the ruby cavities (before final adjustment of the resonant frequency).

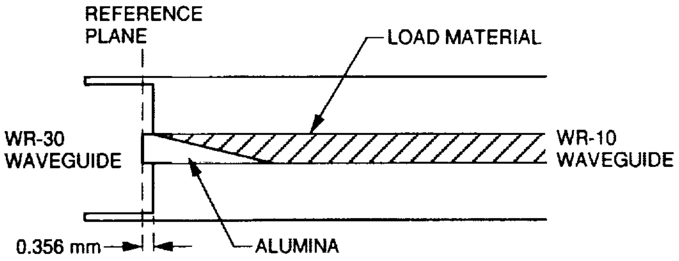

Fig. 9. The test fixture used to measure the reflection coefficient from the cavity aperture (air–ruby interface and WR-30-to-WR-10 transition).

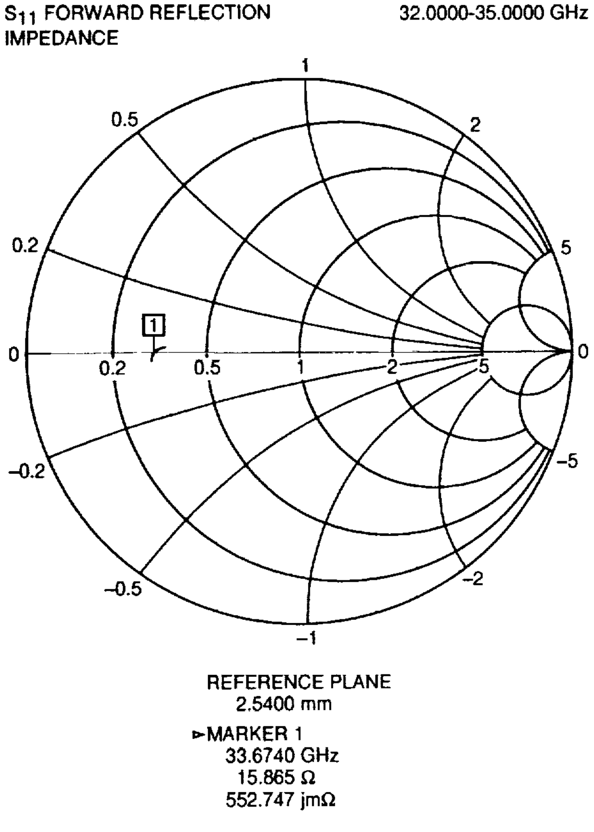

Fig. 10. Measured reflection coefficient, S_{11}, of the test fixture in Fig. 9 from 32 to 35 GHz.

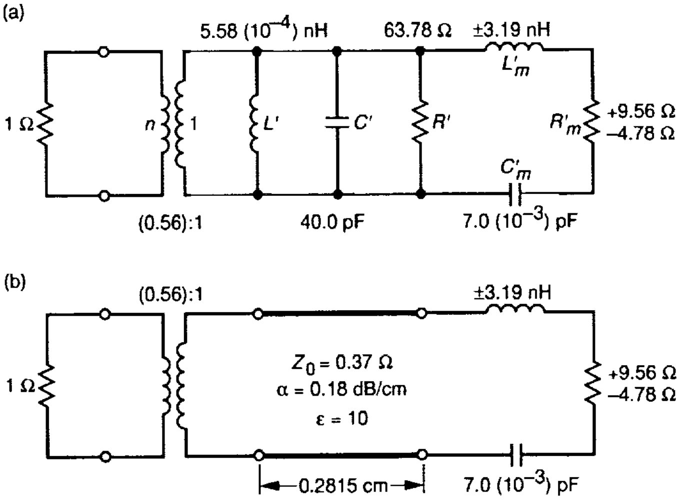

Fig. 11. Modified lumped-element model of the cavity (a) incorporating a transformer to represent the aperture and (b) the same circuit with the parallel RLC circuit replaced by its transmission-line equivalent.

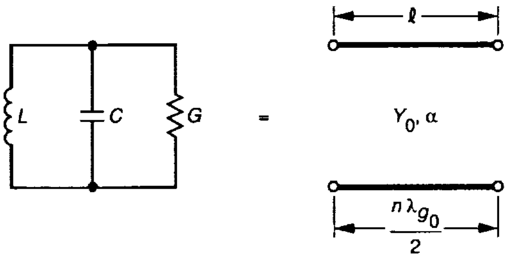

Fig. 12. The equivalence used to replace the parallel RLC lumped-element model of the cavity with a transmission line.

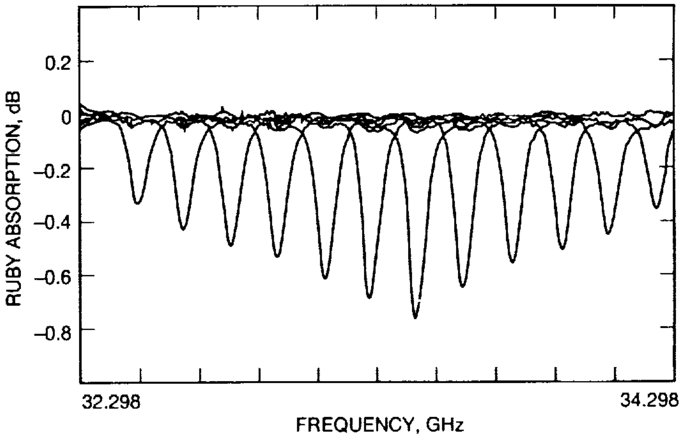

Fig. 13. Ruby absorption versus frequency for different values of the external magnetic field. The cavity was near liquid nitrogen temperatures (77 K).

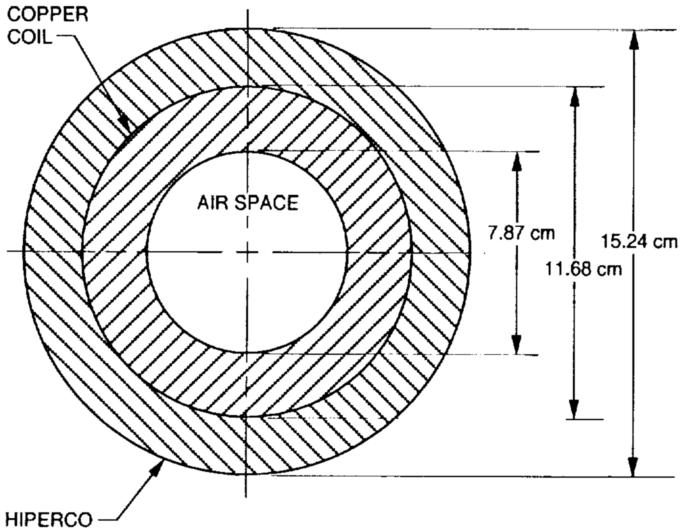

Fig. 14. Cross-sectional view of the magnet assembly, including the hiperco magnet yoke, superconducting coil, and air space for the ruby cavities.

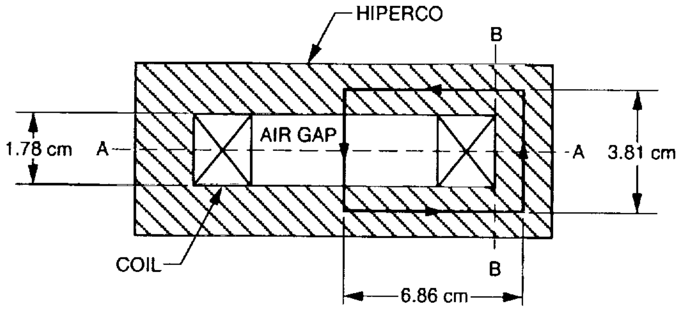

Fig. 15. The transverse dimensions of the magnet assembly, including the contour used for the Ampere's law integration.

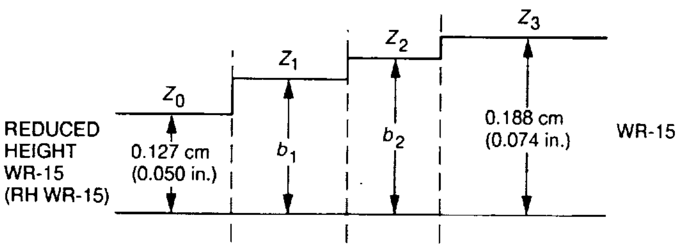

Fig. 16. The impedances and heights to be calculated in the quarter-wave transformer matching of the WR-15 waveguide to the reduced-height WR-15 waveguide. (Height and length values are given in Table 2).

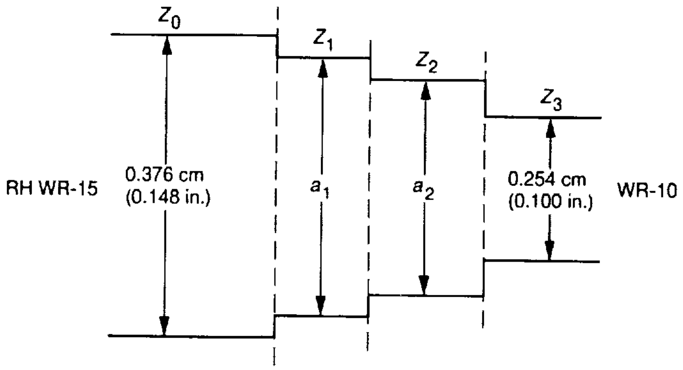

Fig. 17. The impedances and widths to be calculated in the quarter-wave transformer matching of the reduced-height WR-15 waveguide to the WR-10 waveguide. (Width and length values are given in Table 2).

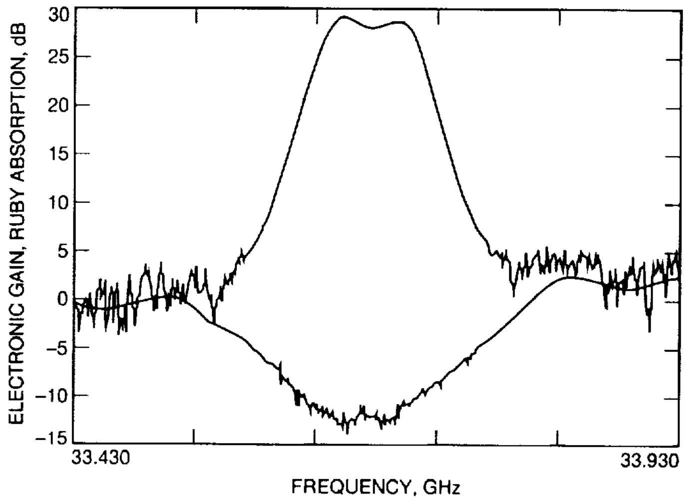

Fig. 18. Ruby gain and absorption versus frequency for the completed dual-cavity maser.

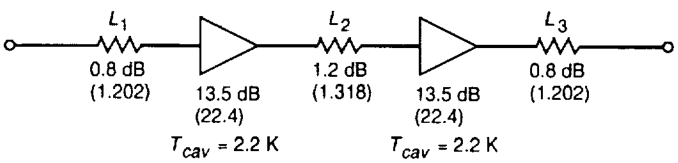

Fig. 19. Loss and gain elements used to estimate the noise temperature of the complete dual-cavity maser at the cryogenic flange.

Appendix

Equation 6 for the magnetic Q is given as

$$\frac{1}{Q_m} = \frac{2g^2\beta^2\mu_o}{h}\frac{I\Delta N\sigma^2\eta}{\Delta f_L} \qquad \text{(A-1)}$$

This expression is correct for m–kg–sec (MKS) units, where

$\beta =$ 9.27 × 10^{-24} J/T (Bohr magneton)

$\mu_o =$ 1.26 × 10^{-6} H/m

$h =$ 6.626 × 10^{-34} J–sec

$g =$ 2.0 (g-factor of the electron)

$\Delta N =$ thermal equilibrium spin density population difference for the signal transition, spins/cc

$\Delta f_L =$ resonance linewidth, MHz

$I =$ inversion ratio (dimensionless)

$\sigma^2 =$ transition probability (dimensionless)

$\eta =$ filling factor (dimensionless)

If the same equation is to be evaluated using cm–g–sec (CGS) units, where

$\beta =$ 9.27 × 10^{-21} ergs/G

$\mu_o =$ 1 G/Oe

$h =$ 6.626 × 10^{-27} erg–sec

then an additional factor of 4π is necessary in the numerator. This is due to the fact that magnetic susceptibility, χ, in MKS and CGS units are given by

$$\chi = \left(\frac{\mu}{\mu_0} - 1\right) \quad MKS \qquad \text{(A-2)}$$

$$\chi = \frac{\mu - 1}{4\pi} \quad CGS \qquad \text{(A-3)}$$

where μ/μ_o is the relative permeability in the MKS case and μ is the relative permeability in the CGS case.

Therefore, setting $\mu_o = 1$ in Eq. (A-2) is not the same as the CGS definition in Eq. (A-3). Since the inverse magnetic Q is essentially the same as the magnetic susceptibility [1], the numerator must have an additional factor of 4π when the other variables are expressed in CGS units. There is an additional factor of 1.0 × 10^{-6} in the numerator for the CGS case when converting from Hz to MHz. This same factor does not appear in the MKS case because the conversion from Hz to MHz is compensated for by the conversion from spins/m^3 to spins per cm^3.

TDA Progress Report 42-116

February 15, 1994

The Rb 780-Nanometer Faraday Anomalous Dispersion Optical Filter: Theory and Experiment

B. Yin, L. S. Alvarez, and T. M. Shay
New Mexico State University, Las Cruces, New Mexico

The Faraday anomalous dispersion optical filter may provide ultra-high background noise rejection for free-space laser communications systems. The theoretical model for the filter is reported. The experimental measurements and their comparison with theoretical results are discussed. The results show that the filter can provide a 56-dB solar background noise rejection with about a 2-GHz transmission bandwidth and no image degradation. To further increase the background noise rejection, a composite Zeeman and Faraday anomalous dispersion optical filter is designed and experimentally demonstrated.

I. Introduction

An important technical issue in free-space laser communications and remote sensing is to effectively reject the optical background while efficiently transmitting the signal through the device. In general, an optical filter with high transmission, narrow bandwidth, wide field of view (FOV), and fast temporal response is needed to extract weak, narrow-bandwidth signals from strong, broadband background radiation, such as the ambient daytime solar illumination (Fig. 1).

We have been exploring a new technology, the Faraday anomalous dispersion optical filter (FADOF) [1–9], that provides a solution to this problem. The performance of the FADOF and other existing state-of-the-art narrow-bandwidth optical filters is summarized in Table 1. The noise rejection factor (NRF) is defined as

$$NRF = 10 \log \left[\frac{T(\lambda_s) \int\limits_0^{\infty} \frac{dP_{noise}}{d\lambda} d\lambda}{\int\limits_0^{\infty} T(\lambda) \frac{dP_{noise}}{d\lambda} d\lambda} \right] \qquad (1)$$

where $T(\lambda)$ represents the filter transmission spectrum, $dP_{noise}/d\lambda$ is the incident noise power spectrum, and λ_s is the signal wavelength. High NRF values of the filter mean high rejection for out-of-passband noise and high transmission in the passband. The wide FOV and image-preserving characteristics make the filter useful for optical tracking in addition to optical communications. The interference filter represents conventional technology and is inexpensive, but it has a broad bandpass at wide FOV. The Lyot [10] filter has a moderate bandpass and moderate FOV, but does not meet the background rejection requirements for free-space laser communications. The atomic resonance optical filter provides a narrow bandpass, wide FOV, and high background noise rejection [11-15]. However, these filters are not image preserving. Therefore, they have limited usefulness in optical tracking. The FADOF clearly shows significant advantages when compared with the other narrow-bandwidth optical filters. In addition to the above advantages, the FADOF is insensitive to mechanical vibrations and misalignment.

This article presents the theoretical and experimental results of studies on the rubidium (Rb) 780-nm FADOF. There is excellent agreement between the theoretical calculation and experimental measurements. The measurements of solar background noise rejection and image quality for the filter are also reported. Finally, a composite filter that has a FADOF and a Zeeman absorption cell is discussed. The background noise rejection of the composite filter is expected to be a factor of 3.5 better than that of the FADOF.

II. Theory

The theoretical framework for resonant Faraday effects has been published by many authors [16-19], so the basic equations are well understood and quite straightforward. However, those articles either lack the treatment for atomic hyperfine structure in the intermediate magnetic-field strength region or are not applied to optical filters. Therefore, a more general formalism using a quantum mechanics treatment of the resonant Faraday effects has been developed [2].

A FADOF consists of an atomic vapor cell placed in a dc magnetic field parallel to the optical path. The cell is situated between 90-deg crossed polarizers (Fig. 2). When linearly polarized light travels along the direction of the magnetic field through the dispersive atomic vapor, a polarization rotation occurs (resonant Faraday effect). Thus, only the narrow frequency band that has a 90-deg polarization rotation will be transmitted with high efficiency.

We assume that (1) optical pumping effects are negligible, because the transmission bands of the FADOF are outside the absorption line centers (for example, the calculated saturation intensity in the filter transmission band of the Rb 780-nm FADOF is about 2 kW/cm^2—4 orders of magnitude higher than the total solar intensity at the Earth's surface) and (2) the magnetic field is homogeneous within the Faraday cell (for inhomogeneous analyses, an integration over the magnetic field along the Faraday cell may be implemented). The FADOF calculation takes into account both Zeeman spectra [20-22] and magneto-optical rotation (Faraday effects). For an atom with a total orbital angular momentum J, nuclear spin I, total angular momentum $F = J + I$, and the projection of the total angular momentum along the direction of the external magnetic field M, the Hamiltonian matrix elements (F, F') for each value of M are

$$\begin{aligned}\langle IJFM|H|IJF'\,M\rangle = {} & \Delta E_F \delta(F,F') \\ & + \Big[\mu B_Z(-1)^{M+J+1+I}(g_J - g_I) \\ & \times \sqrt{J(J+1)(2J+1)(2F+1)(2F'+1)} \\ & \times \begin{Bmatrix} J & 1 & J \\ F' & I & F \end{Bmatrix} \begin{pmatrix} F & 1 & F' \\ -M & 0 & M \end{pmatrix}\Big] \end{aligned} \qquad (2)$$

where the first term represents the hyperfine interaction energy, the second term represents the external magnetic energy, and [11]

$$\Delta E_F = \frac{h}{2}AK + hB \times \left[\frac{\frac{3}{2}K(K+1) - 2I(I+1)J(J+1)}{2I(2I-1)2J(2J-1)}\right] \qquad (3)$$

where $K = F(F+1) - J(J+1) - I(I+1)$, A and B are the magnetic dipole and electric quadruple constants, respectively, for the energy level of interest, μ is the Bohr magneton, B_z is the external magnetic field, and g_J and g_I are the gyromagnetic factors for the total orbital angular momentum and nuclear spin momentum, respectively. The matrix element dependence on M is contained within the 3-J symbol (enclosed by the parentheses), and the matrix element dependence on F is related to a 6-J symbol (enclosed by the curly bracket). These symbols are matrix representations of the spherical coordinate components of the electron wave function for the single atom.

The Zeeman energy levels are readily obtained from the eigenvalues of the Hamiltonian matrix. Figure 3 shows the simplified energy level diagram for the four rubidium transitions in the near infrared and blue. The fine structure energy levels are shown on the left side of the figure. The hyperfine structure energy levels are shown in the middle of the figure and were obtained by adding nuclear spin interaction energy to the fine structure. The magnetic energy levels are shown at the right side of the figure, and show the modification to the hyperfine energy level splittings caused by the addition of the external magnetic field.

Not only do the energy levels split when the magnetic field is applied, but the transition strengths for the different components also change. The Zeeman intensity of each spectral line is proportional to the transition strength denoted by $S_\pm(FM, F'M')$, where the subscripts + and $-$ denote the right-circular and left-circular components of the atomic dipole moment vector $\vec{d}$, respectively.

$$S_\pm^{1/2}(FM, F'M') = \sum_\beta \sum_{\beta'} Y^\gamma_{\beta FM} \times \langle \beta FM | d_\pm | \beta' F' M' \rangle Y^{\gamma'}_{\beta' F' M'} \quad (4)$$

$$\langle \beta FM | d_\pm | \beta' F' M' \rangle = (-1)^{F-M} \times \begin{pmatrix} F & 1 & F' \\ -M & \pm 1 & M' \end{pmatrix} \times \langle \beta F \parallel d \parallel \beta' F' \rangle \quad (5)$$

and

$$\langle \beta F \parallel d \parallel \beta' F' \rangle = (-1)^{J+I+F+1} \sqrt{(2F+1)(2F'+1)} \times \begin{Bmatrix} J & I & F \\ F' & 1 & J' \end{Bmatrix} \langle J \parallel d \parallel J' \rangle \quad (6)$$

where the prime denotes excited states, γ represents perturbed states, β represents diagonalized energy states, Y represents the eigenvector matrix for the Hamiltonian matrix H, and

$$|\gamma FM\rangle = \sum_\beta Y^\gamma_{\beta FM} |\beta FM\rangle \quad (7)$$

The reduced matrix element $\langle J \parallel d \parallel J' \rangle$ is common to all the hyperfine components of the spectral line and is given by the relation

$$\langle J \parallel d \parallel J' \rangle^2 = \frac{3}{64\pi^4}(2J'+1) h \lambda^3 A_{JJ'} \quad (8)$$

where λ and $A_{JJ'}$ are the wavelength and transition probability between levels J' and J, respectively.

The Rb 780-nm transition is between the ground state $5^2S_{1/2}$ and $5^2P_{3/2}$. Natural Rb has two isotopes with an abundance of 72-percent ^{85}Rb and 28-percent ^{87}Rb. The magnetic energy levels of ^{85}Rb $5^2P_{3/2}$ are shown in Fig. 4, and the spectrum of the relative transition intensities is shown in Fig. 5.

The horizontal axis of Fig. 5 represents the transition frequencies, where 0 is the frequency (approximately 3.85 THz) corresponding to 780 nm. The two inside and two outside hyperfine transition groups are from the ^{85}Rb and ^{87}Rb isotopes, respectively. The relative intensity and transition frequency of each hyperfine component depend on the magnetic field.

The observed Zeeman spectrum depends on the viewing direction and the polarization. In our calculations, we assume that the incident radiation is linearly polarized transverse to the magnetic field; therefore, the polarization can be resolved into equal-amplitude left- and right-circularly polarized components.

The Faraday rotation is a direct result of the difference in the frequency dependence of the phase delay between the right- and left-circularly polarized light. The Faraday rotation angle $\phi(\omega)$ is given by

$$\begin{aligned} \phi(\omega) &= \frac{\omega L}{2c} Re[\tilde{n}_+(\omega) - \tilde{n}_-(\omega)] \\ &= \frac{\omega L}{2c}[n_+(\omega) - n_-(\omega)] \end{aligned} \quad (9)$$

where c is the speed of light, $\tilde{n}_+$ and $\tilde{n}_-$ are the complex refractive indices for the right- and left-circularly polarized components, respectively, and $n_\pm$ is the real part of the complex refractive index $\tilde{n}_\pm$. Taking into account the contribution to the refractive indices from each hyperfine component,

$$\tilde{n}_\pm(\omega) = \sum_{F,F',M} \tilde{n}_\pm(\omega, FM, F'M') \quad (10)$$

If $|\tilde{n}_\pm(\omega, FM, F'M') - 1|$ is much less than 1, the complex refractive index for the circularly polarized light is

$$\tilde{n}_\pm(\omega, FM, F'M') - 1 = CS_\pm(FM, F'M')W(\xi_{FM,F'M'}) \tag{11}$$

where $S_\pm(FM, F'M')$ is the line strength given in Eq. (4), $W(\xi_{FM,F'M'})$ is the plasma dispersion function given by

$$W(\xi_{FM,F'M'}) = \frac{1}{\sqrt{\pi}} \int_{-\infty}^{\infty} \frac{e^{-x^2}}{x - \xi_{FM,F'M'}}\, dx \tag{12}$$

$$\xi_{FM,F'M'} = \frac{\sqrt{\ln 2}}{\pi \Delta\nu_D} \left(\omega - \omega_{FM,F'M'} + i\frac{\pi}{\tau}\right) \tag{13}$$

where the transition frequency between the levels FM and $F'M' \omega_{FM,F'M'}$ is calculated from the eigenvalues of the Hamiltonian, and

$$C = \frac{2\pi N(F)}{h(2J+1)(2I+1)\Delta\nu_D} \tag{14}$$

where $\Delta\nu_D$ is the Doppler width, and $N(F)$, the population density of the ground states hyperfine level F (assuming the optical pumping is negligible), is given by

$$N(F) \approx \frac{N e^{-E(F)/KT}}{\sum\limits_F (2F+1) e^{-E(F)/KT}} \tag{15}$$

where $E(F)$ denotes the ground state hyperfine energy level F, k is Boltzmann's constant, T is the cell temperature in Kelvins, and N is the total rubidium ground-state atomic number density.

The absorption coefficients of the atomic vapor are associated with the imaginary part of the complex refractive index,

$$k_\pm(\omega) = \frac{2\omega}{c} Im[\tilde{n}_\pm(\omega)] \tag{16}$$

Therefore, the total attenuation of the linearly polarized incident light intensity due to the absorbing medium is

$$a(\omega) = 0.5\left(e^{-k_+(\omega)L} + e^{-k_-(\omega)L}\right) \tag{17}$$

With the crossed polarizers at the ends of the cell, the transmission of the FADOF can be derived. As shown in Fig. 6, the input polarized radiation $\mathbf{E}_{in}$ can be decomposed into left-circular polarization, $\mathbf{E}_+$, and right-circular polarization, $\mathbf{E}_-$. At the input of the cell, we have

$$\begin{aligned} \mathbf{E}_{in} &= E_0 \hat{x} \\ &= \frac{E_0}{2}(\hat{x} + i\hat{y}) + \frac{E_0}{2}(\hat{x} - i\hat{y}) \\ &= \mathbf{E}_+(0) + \mathbf{E}_-(0) \end{aligned} \tag{18}$$

After traveling through a FADOF cell of length L, the fields are

$$\begin{aligned} \mathbf{E}_+(L) &= \mathbf{E}_+(0)\ \exp\left[i\frac{\tilde{n}_+(\omega)\omega}{c}L\right] \\ &= \frac{E_0}{2}(\hat{x} + i\hat{y}) \\ &\quad \times \exp\left[-\frac{k_+(\omega)}{2}L + i\frac{n_+(\omega)\omega}{c}L\right] \end{aligned} \tag{19}$$

$$\begin{aligned} \mathbf{E}_-(L) &= \mathbf{E}_-(0)\ \exp\left[i\frac{\tilde{n}_-(\omega)\omega}{c}L\right] \\ &= \frac{E_0}{2}(\hat{x} - i\hat{y}) \\ &\quad \times \exp\left[-\frac{k_-(\omega)}{2}L + i\frac{n_-(\omega)\omega}{c}L\right] \end{aligned} \tag{20}$$

The output field is

$$\begin{aligned} \tilde{E}_{out} &= \mathbf{E}_+(L)\hat{y} + \mathbf{E}_-(L)\hat{y} \\ &= i\frac{E_0}{2}\ \exp\left[-\frac{k_+(\omega)}{2}L + i\frac{n_+(\omega)\omega}{c}L\right] \\ &\quad - i\frac{E_0}{2}\ \exp\left[-\frac{k_-(\omega)}{2}L + i\frac{n_-(\omega)\omega}{c}L\right] \end{aligned} \tag{21}$$

The FADOF transmission is given by

$$\begin{aligned} T(\omega) &= \frac{\tilde{E}\tilde{E}^*}{E_0^2} \\ &= \frac{1}{4}\Bigg\{\exp\left[-k_+(\omega)L\right] + \exp\left[-k_-(\omega)L\right] \\ &\quad - 2\cos\left[\frac{n_+(\omega) - n_-(\omega)}{c}\omega L\right] \\ &\quad \times \exp\left[-\frac{k_+(\omega) + k_-(\omega)}{2}L\right]\Bigg\} \\ &= \frac{1}{4}\Bigg\{\exp\left[-k_+(\omega)L\right] + \exp\left[-k_-(\omega)L\right] \\ &\quad -2\cos\left[2\phi(\omega)\right]\exp\left[-\frac{k_+(\omega) + k_-(\omega)}{2}L\right]\Bigg\} \end{aligned} \qquad (22)$$

where $\phi(\omega)$ is defined in Eq. (9).

In order to compare the FADOF with other types of filters, we define the total equivalent noise bandwidth (ENBW) for the FADOF as

$$ENBW = \frac{1}{T_{max}} \int_{-\infty}^{\infty} T(\omega)d\omega \qquad (23)$$

where $T(\omega)$ represents the filter transmission spectrum and T_{max} represents the maximum transmission for the filter. The equivalent noise bandwidth corresponds to the bandwidth of a rectangular notch filter with transmission T_{max} that transmits the same amount of noise as our filter. Using the equivalent noise bandwidth, we can easily compare different filter designs and even different filter technologies.

Figure 7 shows the typical calculated spectrum of Rb 780-nm transmission at a temperature of 100 deg C and a magnetic field of 90 G. The calculations include the contribution from both isotopes. The Rb FADOF shown has an equivalent noise bandwidth of 4.7 GHz, a transmission of 93 percent, and a signal bandwidth of 1.3 GHz.

III. Filter Transmission Spectra Measurements Compared With Theory

The FADOF was characterized using a tunable, narrow-linewidth laser diode source. The tuning of a laser diode is accomplished by varying the injection current or the diode temperature. A single-mode 780-nm laser diode (HL7802E) emitting 10 mW of optical power was used in our experiment. The laser diode current and temperature were controlled by a custom-made diode laser controller. The experimental setup is shown in Fig. 8.

A 12.5-cm-long solenoid coil generated the required magnetic field. The magnetic field was controlled by varying the current through the solenoid. A flexible heater strip was used to heat the Rb vapor cell. Two Glan–Thompson polarizers with extinction ratios of 10^{-5} served as the polarizer-analyzer pair. The Rb vapor cell (2.5-cm long) consisted of a small amount of Rb metal in an evacuated cell. Two PIN detectors, located as shown in Fig. 8, were used to simultaneously measure the transmission spectrum of the Rb cell and of the FADOF.

A small triangle-waveform current ramp was superimposed on the laser diode's direct current to sweep the laser emission wavelength across the FADOF transmission spectrum. Knowledge of the Rb hyperfine absorption spectral features allowed the absolute wavelength calibration from the frequency (energy) differences between the absorption peaks of a Rb cell. A typical measurement of the Rb absorption spectrum is shown in Fig. 9.

The FADOF transmission spectrum was calibrated against the measured absorption of the Rb cell. Figure 10 gives the results of such a comparison.

The absolute FADOF transmission was measured by tuning the diode laser frequency to the center frequency of the transmission peak and then measuring both the power transmitted through, and the power incident upon, the FADOF. The ratio of these power measurements provided the absolute FADOF peak transmission. The experimental results were directly compared to the theoretical calculations after correcting for Fresnel reflection losses.

The Rb 780-nm FADOF transmission spectra are shown in Fig. 11 for different combinations of B-field and temperature. The solid lines in the figures are the measured spectra, and the dashed lines are the theoretical calculations. The spectra show good agreement between theory and experiment for all aspects of the filter, bandwidth, peak transmission, peak center frequency, and spectral response. The theory also predicts the observed 2-GHz tunability of the center frequencies and bandwidths of the FADOF transmission peaks with applied magnetic fields and cell temperatures.

IV. FADOF Imaging and Solar Noise Rejection Measurements

An important advantage of the FADOF over atomic resonance filters is that the FADOF preserves the spatial direction of the signal while filtering out the background noise, but the atomic resonance filter does not [23]. For free-space laser communications applications, this can be used to advantage in the signal acquisition and tracking system. We measured the spatial resolution of the optical system to evaluate its applicability to a signal acquisition and tracking subsystem. A schematic block diagram of the imaging experiment system is shown in Fig. 12.

The target was illuminated by a 3-mW, 780-nm laser diode. A small fraction of the scattered laser light was then incident on both the reference camera and the filtered camera. This system allowed direct comparison of the resolution of images recorded using the unfiltered and filtered cameras. The advantages of the FADOF were demonstrated by comparing the two images as the background light level was changed. The image resolution experiments were performed with the room lights off and using an imaging evaluation test target (Air Force MT-11). The resolution of both cameras was measured to be 170 μrad. Within the 170-μrad resolution limit of our camera, no image degradation resulting from the insertion of the FADOF was observed. Equipment with greater spatial resolution will be needed to measure the resolution limit of the FADOF.

Figure 13 illustrates both the spatial resolution and the background rejection of the FADOF. The solar background rejection was measured at 56 dB. The figure is a photograph of the New Mexico State University (NMSU) logo illuminated by a 3-mW laser diode and a cigarette lighter. Also included in this photograph are the images from both the filtered and unfiltered camera monitors. The unfiltered camera image (upper right) is clearly saturated by the flame of the lighter, while the filtered camera image (lower right) is unaffected by the flame. In addition, the letters "MEX" that are lost in the unfiltered camera image due to the saturation are clearly visible in the filtered camera image. The images were taken with approximately 2-nW/cm^2 of optical power incident on the charge-coupled device (CCD).

V. The Composite Zeeman/FADOF System

The transmission peaks of the FADOF are at the wings of the absorption bands of the atomic vapor. For typical Rb and cesium (Cs) FADOFs, there are four transmission peaks caused by isotopic and hyperfine splitting. Narrowband laser signals are transmitted in one transmission band, and light leakage through the other bands constitutes a source of background noise and adds to the filter's equivalent noise bandwidth. A composite filter system can isolate a single signal transmission band and eliminate the other transmission bands.

In the composite system, a Zeeman absorption cell is placed in series with a FADOF. The Zeeman absorption cell is tuned to absorb three of the four FADOF transmission bands. Optimal operating conditions for the absorption cell were found by calculating the absorption spectra for different combinations of magnetic field and temperature and matching these to the FADOF transmissions.

For right- and left-circularly polarized input, the absorption cell transmission is given as

$$a_{\pm}(\omega) = \exp\left[-k_{\pm}(\omega)L\right] \tag{24}$$

where "+" denotes the right- and "−" denotes the left-circular polarization, k is the absorption coefficient, and L is the cell length. The total transmission of the composite system is

$$T(\omega) = T_{\mathrm{FADOF}}(\omega)a_{\pm}(\omega) \tag{25}$$

where $T_{\mathrm{FADOF}}(\omega)$ is the transmission spectrum of the FADOF.

The block diagram of the composite system for a Rb 780-nm FADOF is shown in Fig. 14. A quarter-wave plate is used to transform the linearly polarized FADOF output to right- or left-circularly polarized input for the absorption cell.

Figure 15 shows the Rb 780-nm FADOF transmission curve at a magnetic field of 60 G and a temperature of 90 deg C. The four transmission peaks of average bandwidth at approximately 0.7 GHz each are characteristic of this FADOF under these conditions. Calculations showed that the absorption of a Rb Zeeman cell at 100 deg C in a 1300-G B-field could be tuned to match the FADOF transmission peaks and results in a single-peak transmission spectrum.

Figure 16 shows the agreement between the theoretical and experimental absorption curves for right-circularly polarized light incident on the Rb Zeeman cell. The resulting composite filter transmission is shown in Fig. 17.

The single-band transmission spectrum in Fig. 17 was obtained by tuning the system so that the right-circularly polarized absorption band of the Zeeman absorption cell overlapped three of the four transmission peaks in the FADOF transmission spectrum and left the transmission of a single peak unchanged. By cascading the filters in this way, the ENBW was reduced by a factor of 3.5, from 3.0 to 0.86 GHz.

With the end application of the filter in mind, we compared the bandwidth of the composite filter to that of a Fourier-transform-limited Gaussian pulse. This is shown in Fig. 18, where it is seen that a transformed 5-nsec Gaussian pulse just fits under the envelope of the filter. Pulse position modulation is the preferred modulation format for deep space optical communications; this experiment shows that the composite filter can provide good background rejection for detection of 5-nsec-wide laser pulses at the optical communications receiver.

VI. Summary

The FADOF has been shown to be able to provide high background noise rejection, high throughput, fast response, and a wide field of view while preserving image information. The general theory for the FADOF was presented in this article. It predicts the FADOF performance for arbitrary magnetic fields and temperatures of the atomic vapors with and without hyperfine structure components. The theory was used to predict the transmission spectrum and performance of a 780-nm Rb FADOF, based on the solved quantum mechanics equations for the atomic levels and transition line strengths for the Rb vapor. The experimental results show very good agreement with theoretical predictions.

A composite Zeeman–FADOF filter has been described and shown to be compatible with a Fourier-transform-limited 5-nsec laser pulse. The filter pair exhibits a single ultra-narrow passband in the transmission spectrum and is expected to reduce the noise rejection factor of the FADOF by 3.5.

Acknowledgments

The authors wish to thank J. Lesh and K. Wilson in the JPL Optical Communications Group for many helpful discussions and suggestions. Thanks are also expressed to D. C. Yuan and Q. C. Liu for their assistance.

References

[1] D. J. Dick and T. M. Shay, "Ultra-High Noise Rejection Optical Filter," *Opt. Lett.*, vol. 16, p. 867, June 1991.

[2] B. Yin and T. M. Shay, "Theoretical Model of Faraday Anomalous Dispersion Optical Filter," *Opt. Lett.*, vol. 16, pp. 1617–1619, October 1991.

[3] B. Yin and T. M. Shay, "A Potassium Faraday Anomalous Dispersion Optical Filter," *Optics Communications*, vol. 94, pp. 30–32, November 1992.

[4] B. Yin and T. M. Shay, "Faraday Anomalous Dispersion Optical Filter of Cs 455 nm," *IEEE Photonics Technology Lett.*, vol. 4, pp. 488–490, May 1992, and addendum, vol. 5, issue 4, April 1993.

[5] T. M. Shay and B. Yin, "Faraday Anomalous Dispersion Optical Filter," *Proceedings of the International Conference on Lasers '91*, San Diego, California, pp. 641–648, December 1991.

[6] B. Yin and T. M. Shay, "Faraday Anomalous Dispersion Optical Filter of Potassium," *Proceedings of the SPIE OE'Laser '92*, Los Angeles, California, pp. 641–648, January 1992.

[7] T. M. Shay, B. Yin, and L. S. Alvarez, "Faraday Anomalous Dispersion Optical Filter," *International Conference on Lasers '92*, Houston, Texas, pp. 829–836, December 1992.

[8] B. Yin and T. M. Shay, "Theoretical Model for a Novel Ultrahigh Optical Background Rejection Optical Filter," *XVIII International Quantum Electronics Conference*, Vienna, Austria, June 1992.

[9] T. M. Shay and B. Yin, "Theoretical Model for a Faraday Anomalous Dispersion Optical Filter Operating at Ca 423-nm," *IEEE Laser and Electro-Optics Society Annual Meeting*, Boston, Massachusetts, November 1990.

[10] A. M. Title and W. J. Rosenberg, "Improvements in Birefringent Filters," *Appl. Optic.*, vol. 18, pp. 3443–3456, October 1979.

[11] T. M. Shay and Y. C. Chung, "An Ultra-High Resolution, Wide Field-of-View Optical Filter for Doubled Nd:YAG," *Optics Lett.*, vol. 13, p. 443, June 1988.

[12] T. M. Shay and D. Garcia, "Theoretical Model for a Background Noise Limited Rb Laser-Excited Optical Filter for Doubled Nd Lasers," *IEEE J. Quantum Electro.*, vol. 26, p. 1135, June 1990.

[13] M. Minden and H. Bruesselbach, "Detection of 532-nm Frequency-Doubled Nd:YAG Radiation in an Active Rubidium Atomic Resonance Filter," *Optics Lett.*, vol. 15, no. 7, p. 384, April 1990.

[14] J. A. Gelbwachs, "Atomic Resonance Filters," *IEEE J. Quant. Electr.*, vol. 24, p. 1266, July 1988.

[15] A. F. Molisch, B. P. Oehry, W. Schupita, and G. Magerl, "Quantum Efficiency and Signal Bandwidth of Thallium Atomic Line Filters," *Opt. Comm.*, vol. 90, pp. 245–250, June 1992.

[16] D. M. Camm and F. L. Curzon, "The Resonant Faraday Effect," *Can. J. Phys.*, vol. 50, p. 2866, November 1972.

[17] G. J. Roberts, P. E. G. Baird, M. W. S. M. Brimicombe, P. G. H. Sandars, D. R. Selby, and D. N. Stacey, "The Faraday Effect and Magnetic Circular Dichroism in Atomic Bismuth," *J. Phys. B: Atom. Molec. Phys.*, vol. 13, p. 1389, April 1980.

[18] P. Yeh, "Dispersive Magneto-Optic Filters," *Applied Optics*, vol. 21, p. 2069, June 1982.

[19] X. Chen, V. L. Telegdi, and A. Wis, "Magneto-Optical Rotation Near the Cesium D2 Line (Macaluso–Corbino Effect) in Intermediate Fields," *J. Phys. B: At.. Mol. Phys.*, vol. 20, p. 5653, November 1987.

[20] R. D. Cowan, *Theory of Atomic Structure and Spectra*, Berkeley, California: University of California Press, p. 497, 1981.

[21] I. I. Sobelman, *Atomic Spectra and Radiative Transition*, New York: Springer–Verlag, p. 194, 1979.

[22] B. W. Shore, *The Theory of Coherent Atomic Excitation*, vol. 2, New York: John Wiley and Sons, p. 1426, 1990.

[23] L. S. Alvarez and T. M. Shay, "High Resolution Imaging Through an Ultra-High Optical Background Rejection Optical Filter," *OSA 1992 Annual Meeting*, Albuquerque, New Mexico, September 1992.

Table 1. The performance of some narrow bandwidth optical filters.

Parameter	Interference	Quartz Lyot	Atomic resonance	FADOF
Throughput	0.5	0.2	0.1–0.5	>0.8
Noise rejection factor, dB	20–30	35	40–60	50–60
Field of view, deg	±2.5–30	±30	±90[a]	±90[b]
Bandwidth, nm	2–20	0.33	0.001–0.01	0.001–0.005
Response time, nsec	0.00004–0.0004	0.005	10–10,000	0.2–1
Imaging	Yes	Yes	No	Yes

[a] The field of view of the atomic resonance filter is limited to ±30 deg by practical considerations.

[b] The field of view is fundamentally ±90 deg. However, the field of view is limited to about ±20 deg by practical considerations.

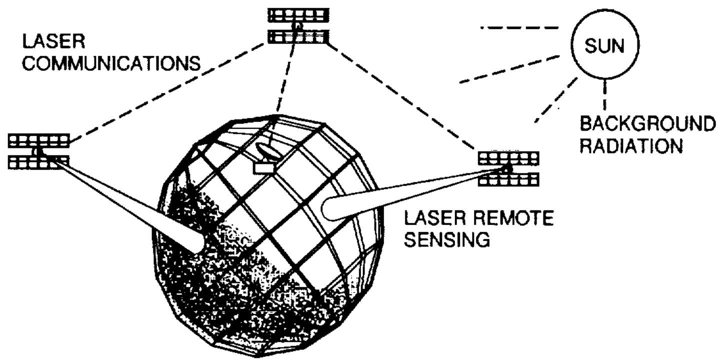

Fig. 1. The broadband, strong solar radiation is the major optical background noise for free-space laser communications and remote sensing.

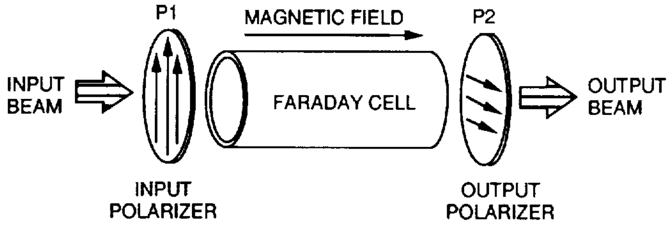

Fig. 2. The Faraday anomalous dispersion optical filter. P1 and P2 are two crossed polarizers.

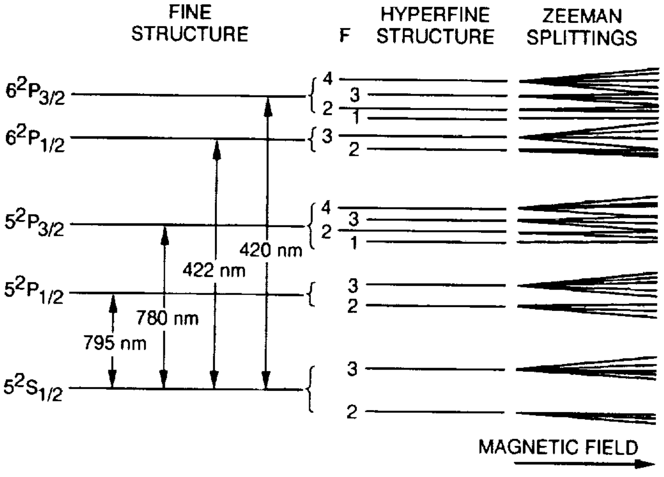

Fig. 3. The simplified energy level diagram for the rubidium near-infrared and blue transitions.

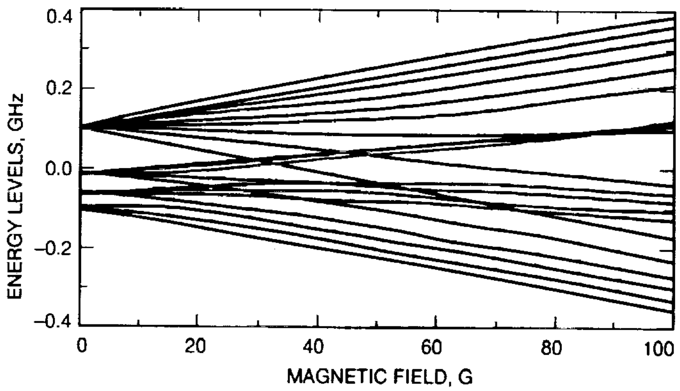

Fig. 4. The calculated ^{85}Rb $5^2P_{3/2}$ energy levels versus the magnetic field.

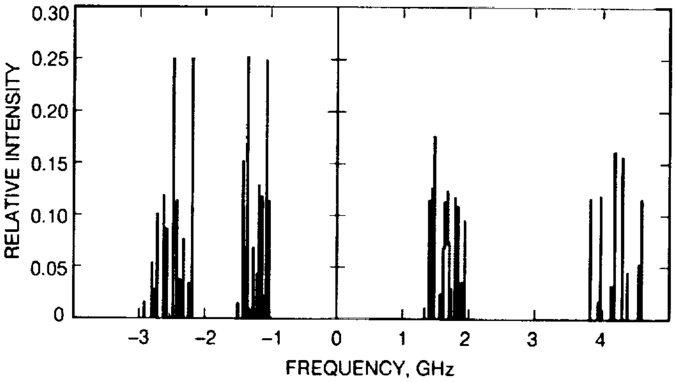

Fig. 5. The ^{85}Rb + ^{87}Rb 780-nm relative hyperfine transition intensities at a magnetic field of 100 G.

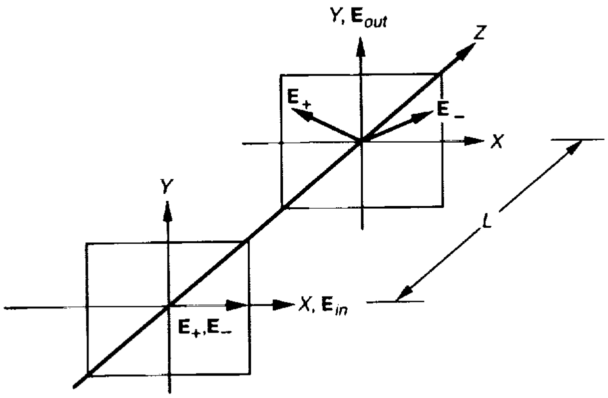

Fig. 6. The rotating fields in the FADOF, where *x* and *y* are the directions of the input and output polarizers and the directions of the input and output polarized radiation, E_{in} and E_{out}, respectively, and *z* is the direction of the magnetic field.

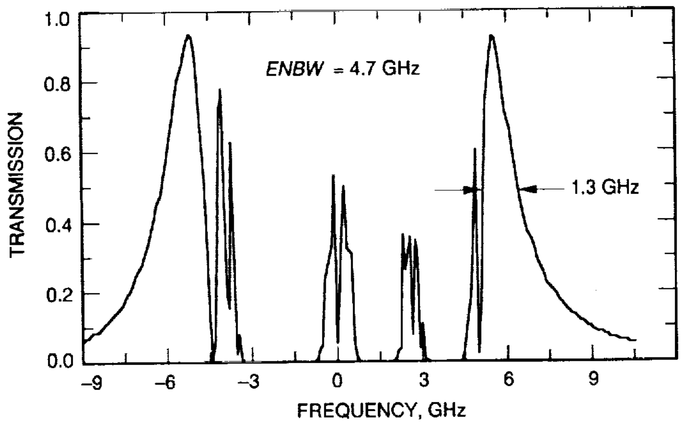

Fig. 7. The calculated Rb 780-nm FADOF transmission at B = 90 G and T = 100 deg C. The maximum transmission is 0.93.

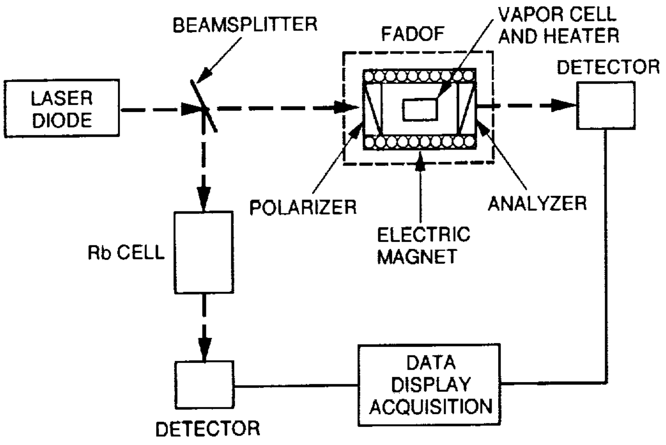

Fig. 8. Experimental setup for the FADOF measurements.

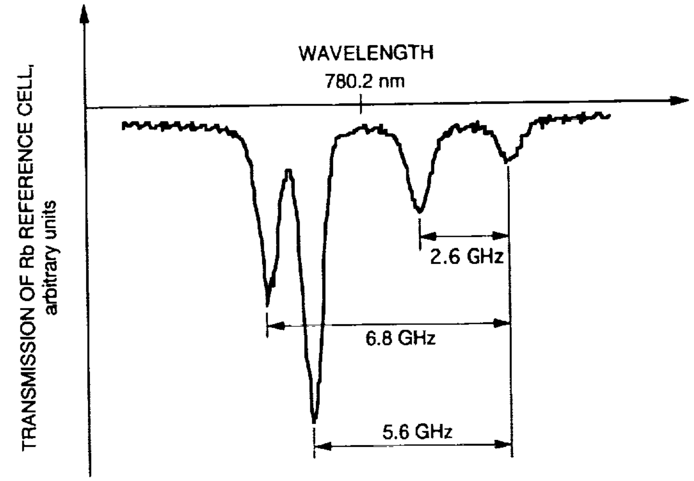

Fig. 9. The transmission spectrum of the absorption cell at a temperature of 300 K .

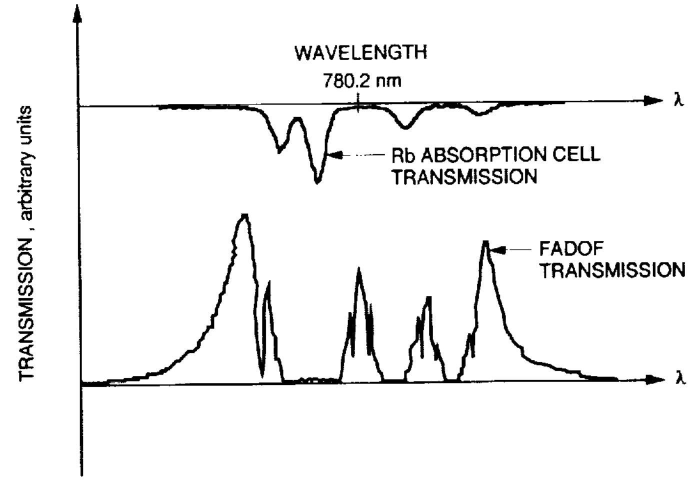

Fig. 10. Experimental measurements of the transmission spectrum of the FADOF. The top curve is measured Rb absorption cell transmission that is used as a frequency reference. The bottom curve is the measured transmission spectrum of the FADOF.

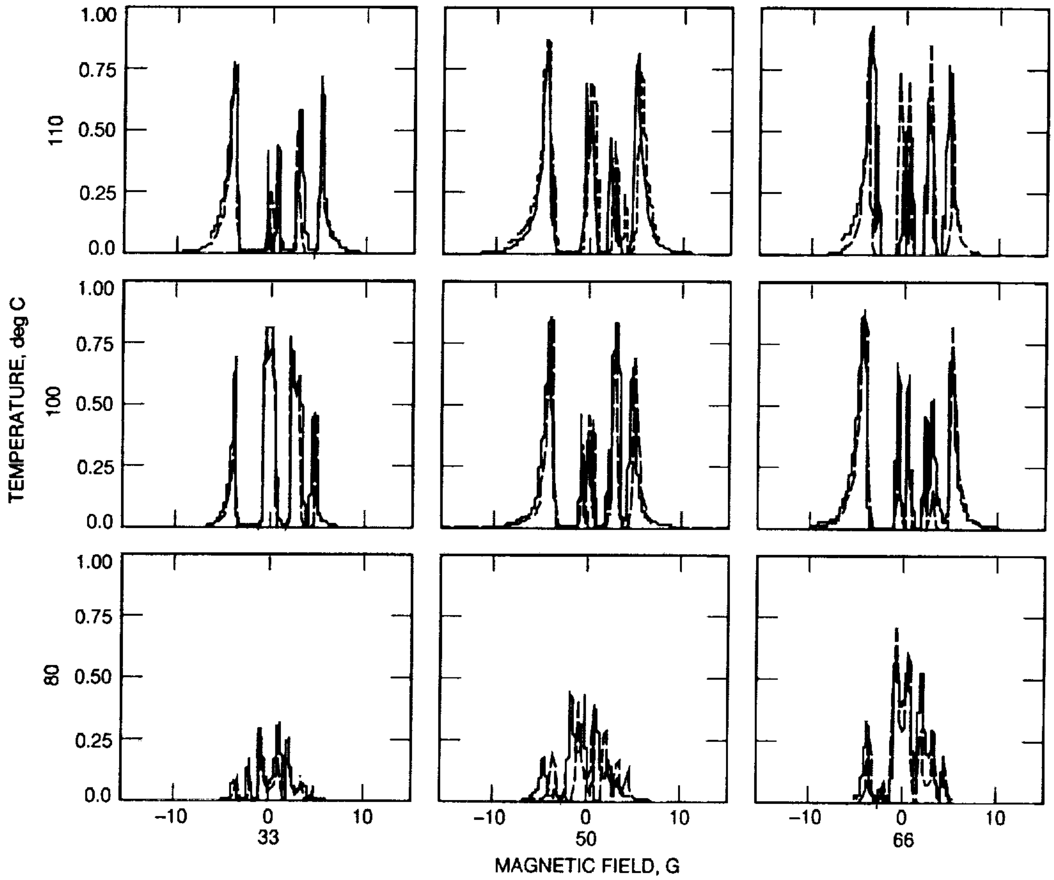

Fig. 11. The transmission curves of the Rb 780-nm FADOF, with the solid lines representing measured transmission and the dashed lines the calculated transmission.

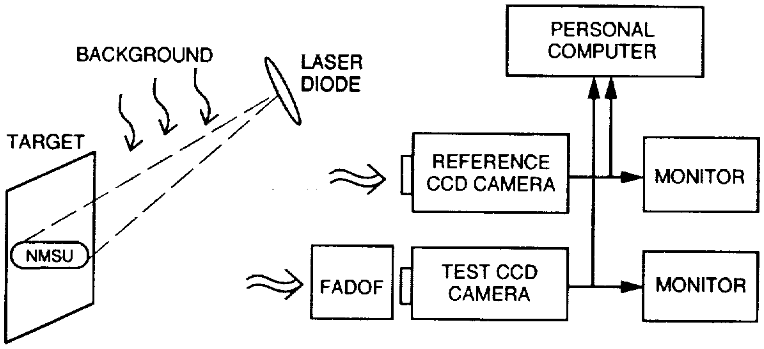

Fig. 12. The FADOF imaging experiment.

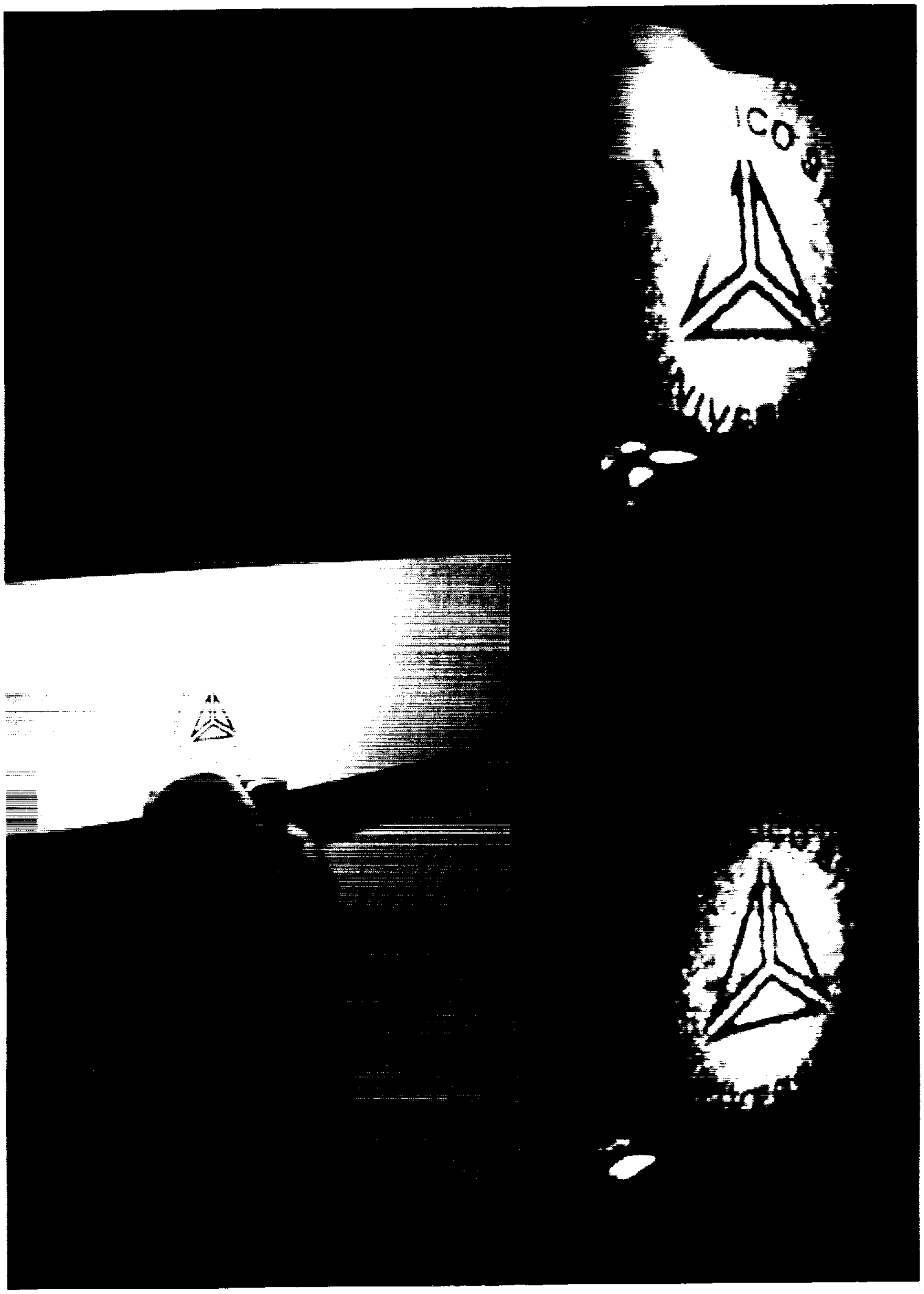

Fig. 13. Images from both filtered and unfiltered camera monitors.

a-2.

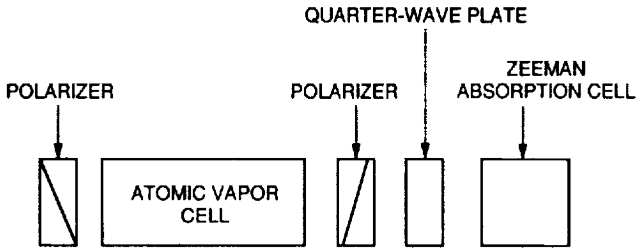

Fig. 14. The composite FADOF/Zeeman system.

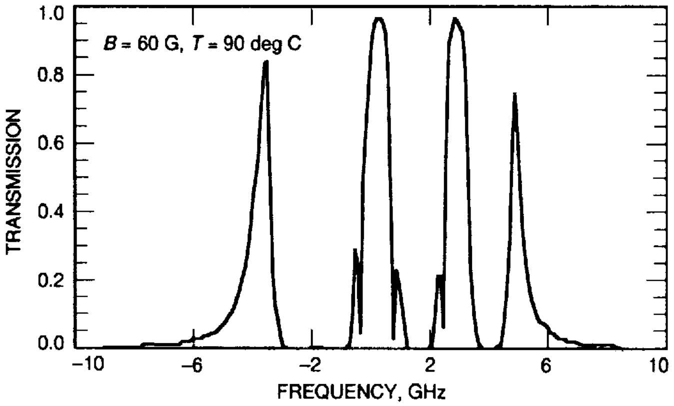

Fig. 15. A Rb 780-nm FADOF transmission with an ENBW of 3.0 GHz.

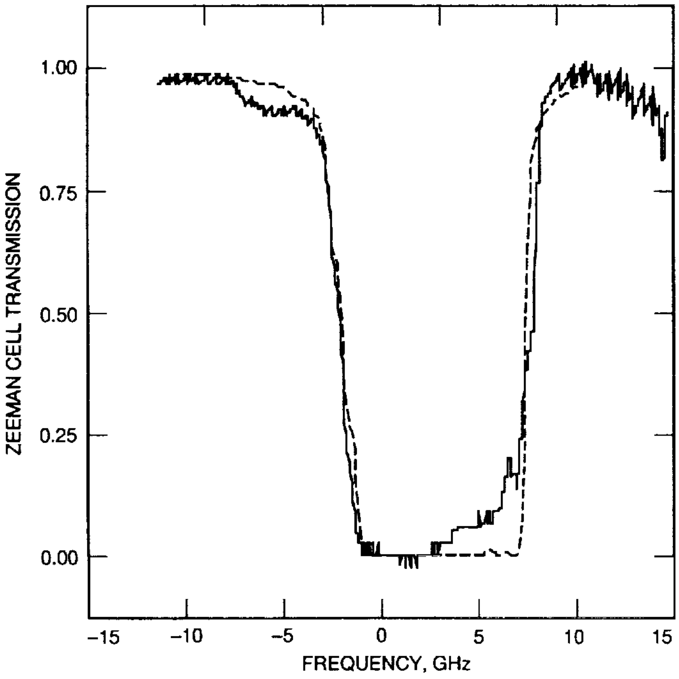

Fig. 16. The transmission spectrum of a Zeeman absorption cell for right-circularly polarized light. The dashed line represents the theoretical curve and the solid line the experimental measurement. The Zeeman cell was operated at a temperature of 100 deg C and a magnetic field of 1300 G.

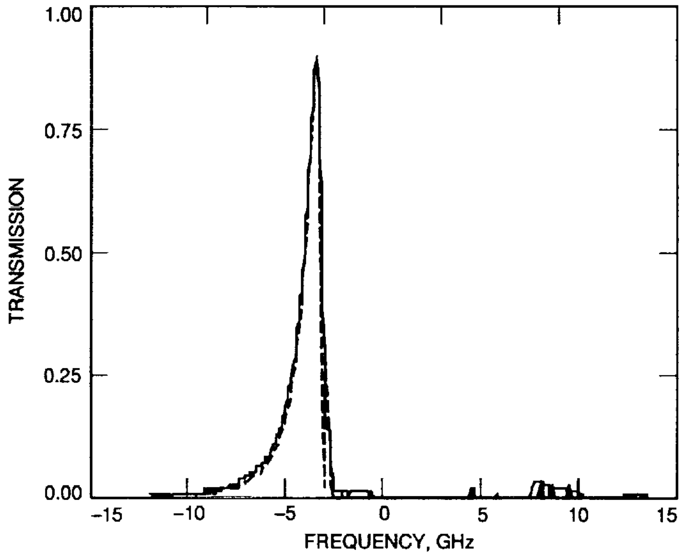

Fig. 17. The transmission spectrum of the Zeeman–FADOF composite filter. The dashed line represents the theoretical curve and the solid line the experimental measurement. The FADOF was operated at a temperature of 100 deg C.

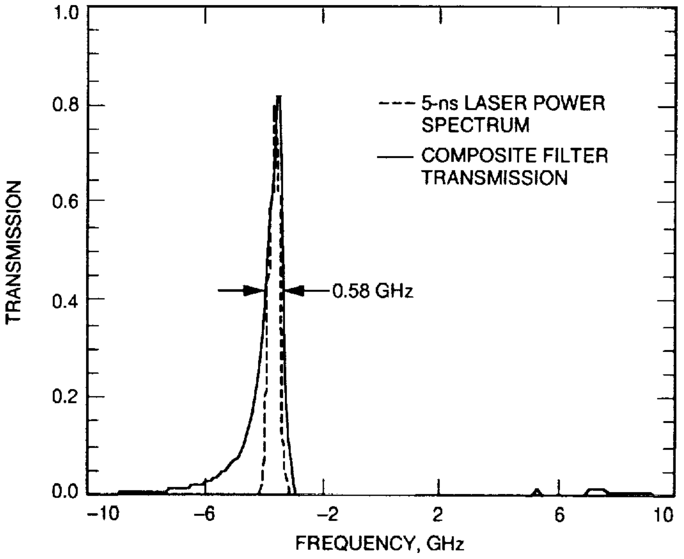

Fig. 18. Total transmission of the Rb composite filter. The ENBW is 0.86 GHz.

N94-29660

TDA Progress Report 42-116 February 15, 1994

A Digital Combining-Weight Estimation Algorithm for Broadband Sources With the Array Feed Compensation System

V. A. Vilnrotter
Communications Systems Research Section

E. R. Rodemich
Robotic Systems and Advanced Computer Technology Section

An algorithm for estimating the optimum combining weights for the Ka-band (33.7-GHz) array feed compensation system has been developed and analyzed. The input signal is assumed to be broadband radiation of thermal origin, generated by a distant radio source. Currently, seven video converters operating in conjunction with the real-time correlator are used to obtain these weight estimates. The algorithm described here requires only simple operations that can be implemented on a PC-based combining system, greatly reducing the amount of hardware. Therefore, system reliability and portability will be improved.

I. Introduction

At the present time, there is considerable interest in operating the DSN at increasingly higher carrier frequencies in order to realize the inherent advantages associated with shorter wavelengths, namely, greater antenna gains, increased useful bandwidth, and reduced sensitivity to plasma effects. Consequently, there is an effort underway to demonstrate the feasibility of using Ka-band (33.7-GHz) carrier frequencies for deep space telemetry. However, there are also disadvantages associated with the use of higher carrier frequencies, such as greater sensitivity to weather effects, increased requirements on pointing accuracy, and reduced antenna gains due to imperfections in the antenna's reflecting surfaces. Such imperfections become particularly noticeable on large receiving antennas, where gravitational distortions, wind-induced vibrations, and collimation problems can seriously degrade antenna performance. Some of these losses can be recovered with a properly designed compensation system employing an array of receiving horns in the focal plane of the antenna; a conceptual design of such a combining system is shown in Fig. 1. Complete descriptions and analyses of a real-time array feed compensation system designed for deep space telemetry can be found in the literature [1–3]. Recently, a seven-element array feed compensation system has been installed at DSS 13 for the purpose of demonstrating combining concepts in real time.

Perhaps the most serious problem encountered during the Ka-band array feed compensation effort was the lack of reliable coherent sources in the antenna's far field. Since this is not an operational frequency band, no spacecraft has yet been built employing Ka-band carrier frequencies (Mars Observer did carry a low-power Ka-band beacon, but this spacecraft ceased to function before reaching its target). However, since only spatial coherence is required to demonstrate the array feed combining concept, it is possible to carry out weighted combining operations using natural radio sources, such as quasars and planets. Since these are always in the antenna's far field, the only additional requirement is that the sources remain unresolved. This article is devoted to the derivation of the optimum combining weights for maximizing he signal-to-noise ratio (SNR) of the combined signal and the estimation of the optimum combining weights in real time from natural radio signals observed in the presence of additive noise.

II. The Received Signal

A functional block diagram of the combining system is shown in Fig. 2. The array horns receive a broadband signal of thermal origin from a distant point source, each with different amplitude and phase introduced by the antenna distortions. An independent noise waveform is added to each signal in every channel, the result of receiver noise plus background radiation received from all directions in space. After passing through narrowband filters of center frequency ω, the received signal can be represented in the kth channel as

$$r_k(t) = s_k(t) + n_k(t) \qquad k = 1,\ 2,\ \dots,\ K \tag{1a}$$

where

$$\begin{aligned} s_k(t) = {} & \sqrt{2}S_k\left\{a_c(t)\cos(\omega t + \theta_k)\right. \\ & \left. + \ a_s(t)\sin(\omega t + \theta_k)\right\} \end{aligned} \tag{1b}$$

$$n_k(t) = \sqrt{2}\left\{n_{ck}(t)\cos(\omega t) + n_{sk}(t)\sin(\omega t)\right\} \tag{1c}$$

Note that the signal components in the various channels differ from each other only in their amplitude and phase, having been generated by the same point source. Thus, the random processes $s_k(t)$ are completely correlated. However, the noise processes $n_k(t)$ are assumed to be uncorrelated in all channels, as these are composed of thermal noise generated within the receivers and background radiation arriving from all directions in space.

The received waveforms are downconverted to baseband in-phase and quadrature signals $r_{Ik}(t)$ and $r_{Qk}(t)$ by premultiplying with local oscillator signals of the form $\sqrt{2}\cos(\omega t)$ and $\sqrt{2}\sin(\omega t)$, and low-pass filtering:

$$r_{Ik}(t) = s_{Ik}(t) + n_{Ik}(t) \tag{2a}$$

$$r_{Qk}(t) = s_{Qk}(t) + n_{Qk}(t) \tag{2b}$$

$$s_{Ik}(t) = S_k\left\{a_c(t)\ \cos(\theta_k) - a_s(t)\ \sin(\theta_k)\right\} \tag{2c}$$

$$s_{Qk}(t) = S_k\left\{a_c(t)\ \sin(\theta_k) + a_s(t)\ \cos(\theta_k)\right\} \tag{2d}$$

$$n_{Ik}(t) = n_{ck}(t) - n_{sk}(t) \tag{2e}$$

$$n_{Qk}(t) = n_{ck}(t) + n_{sk}(t) \tag{2f}$$

After sampling the baseband waveforms, the resulting in-phase and quadrature samples may be treated as complex samples $\tilde{r}_k(i)$, defined as

$$\tilde{r}_k(i) = \tilde{s}_k(i) + \tilde{n}_k(i) \tag{3a}$$

where

$$\tilde{s}_k(i) = s_{Ik}(i) + js_{Qk}(i) \tag{3b}$$

$$\tilde{n}_k(i) = n_{Ik}(i) + jn_{Qk}(i) \tag{3c}$$

In other words, we shall use complex arithmetic to operate on these samples.

Defining the complex coefficient $\tilde{S}_k = S_k e^{j\theta_k}$, Eq. (3b) can also be written as

$$\tilde{s}_k(i) = \tilde{S}_k\left\{a_c(i) + ja_S(i)\right\} = \tilde{S}_k\tilde{a}(i) \tag{4}$$

which shows that the complex channel scaling factors separate from the temporal variations.

The real and imaginary parts of the complex noise sequence are independent random sequences, each with variance σ_k^2. The components of the signal sequence, $a_c(i)$ and $a_s(i)$, are also independent random sequences, being of thermal origin. However, since we are interested in extracting the complex magnitude $\tilde{S}_k$, it is reasonable to let each signal component have variance 1/2, so as not to introduce additional scaling. In the following, the complex signal coefficients and the noise variances will be assumed to be constants independent of time.

III. Combining Weights to Maximize SNR

The goal of the combining operation is to maximize the SNR of the combined sequence. The approach is to multiply each sequence by a complex combining weight with the property that the sum of the weighted sequences achieves the greatest SNR.

Let the kth combining weight be denoted by $\tilde{w}_k$. Multiplying each received sequence by the corresponding complex weight and summing yields the combined sequence $z(i)$:

$$\tilde{z}(i) = \sum_{k=1}^{K} \tilde{r}_k(i)\, \tilde{w}_k(i) \qquad (5)$$

With $\tilde{s}_c(i) = \sum_{k=1}^{K} \tilde{s}_k(i)\, \tilde{w}_k(i)$ denoting the combined signal, the SNR of the combined sequence is defined as

$$\rho_z = \frac{E\left|\tilde{s}_c(i)\right|^2}{\mathrm{var}\left\{\tilde{z}(i)\right\}} = \frac{\left|\sum_{k=1}^{K} \tilde{S}_k \tilde{w}_k\right|^2}{\sum_{k=1}^{K} 2\left|\tilde{w}_k\right|^2 \sigma_k^2} \qquad (6)$$

This is the quantity we wish to maximize by judicious selection of the combining weights.

The optimum combining weights are obtained by means of the Schwarz inequality. Writing the combined sequence as

$$\left|\sum_{k=1}^{K} \tilde{S}_k \tilde{w}_k\right|^2 = \left|\sum_{k=1}^{K} \left(\sqrt{2}\tilde{w}_k \sigma_k\right) \left(\frac{\tilde{S}_k}{\sqrt{2}\sigma_k}\right)\right|^2 \qquad (7)$$

and applying the Schwarz inequality, yields

$$\left|\sum_{k=1}^{K} \left(\sqrt{2}\tilde{w}_k \sigma_k\right) \left(\frac{\tilde{S}_k}{\sqrt{2}\sigma_k}\right)\right|^2 \leq \left(\sum_{k=1}^{K} 2\left|\tilde{w}_k\right|^2 \sigma_k^2\right) \left(\sum_{k=1}^{K} \frac{\left|\tilde{S}_k\right|^2}{2\sigma_k^2}\right) \qquad (8)$$

Dividing both sides by the first term on the right-hand side of Eq. (8), we obtain

$$\frac{\sum_{k=1}^{K} \left(\sqrt{2}\tilde{w}_k \sigma_k\right) \left(\frac{\tilde{S}_k}{\sqrt{2}\sigma_k}\right)}{\sum_{k=1}^{K} 2\left|\tilde{w}_k\right|^2 \sigma_k^2} \leq \sum_{k=1}^{K} \frac{\left|\tilde{S}_k\right|^2}{2\sigma_k^2} \;\underline{\Delta}\; \rho_0 \qquad (9)$$

which shows that for any choice of combining weights, the achievable SNR is bounded from above by the sum of the channel SNRs. Except for an arbitrary complex factor, equality is achieved when we let $\sqrt{2}\tilde{w}_k\sigma_k = \tilde{S}_k^* / \sqrt{2}\sigma_k$, whereby the optimum combining weights are determined in terms of the signal and noise parameters as

$$\tilde{w}_k = \frac{\tilde{S}_k^*}{2\sigma_k^2} \qquad (10)$$

The combined SNR is maximized when each sequence is multiplied by the conjugate of the signal scaling factor and divided by the variance of the additive noise in that channel. Therefore, these quantities have to be estimated in real time to determine the correct combining weights.

IV. Parameter Estimates

The estimator described here is based on the observation that the temporal variation of the signal components is identical in every channel. This implies that the expected value of the product of a received sequence with the complex conjugate of a sequence from any other channel is equal to the product of the complex coefficients. That is,

$$\begin{aligned} E\left[\tilde{r}_\ell^*(i)\tilde{r}_m(i)\right] &= E\left[\left(\tilde{S}_\ell \tilde{a}(i) + \tilde{n}_\ell(i)\right)^* \left(\tilde{S}_m \tilde{a}(i) + \tilde{n}_m(i)\right)\right] \\ &= \tilde{S}_\ell^* \tilde{S}_m \end{aligned} \qquad (11)$$

The last equality follows from the definition $E|\tilde{a}(i)|^2 = 1$, and the assumption that noise sequences are not correlated with other noise sequences or with the signal sequence. If the received sequences are ergodic, then ensemble and time averages are identical, suggesting the following estimates for the coefficient products:

$$\underset{\ell \neq m}{\widehat{\tilde{S}_\ell^* \tilde{S}_m}} = \frac{1}{L} \sum_{i=1}^{L} \tilde{r}_\ell^*(i)\tilde{r}_m(i)$$

$$\ell, m = 1, 2, \ldots, K; \qquad \ell \neq m \qquad (12)$$

As the number of terms grows without bound, the estimation error approaches zero. With the total number of channels equal to K, index the channels according to the SNR, so that channel number 1 contains the greatest SNR, channel number 2 the second-greatest, and so on (in case of equalities, an arbitrary choice can be made). Thus, we may view channel 1 as the "reference channel," as it provides the highest fidelity signal. Consider the estimates of the products $\tilde{S}_1^* \tilde{S}_m$:

$$\widehat{\tilde{S}_1^* \tilde{S}_m} = \frac{1}{L} \sum_{i=1}^{L} \tilde{r}_1^*(i) \tilde{r}_m(i) \quad m = 2, 3, \ldots, K \tag{13}$$

If $\tilde{S}_1^*$ were known, then we could estimate $\tilde{S}_m$, $m = 2, 3, \ldots, K$, by means of the formula

$$\widehat{\tilde{S}_m} = \frac{\widehat{\tilde{S}_1^* \tilde{S}_m}}{\widehat{\tilde{S}_1}} \tag{14}$$

Even if only $|\tilde{S}_1|$ were known (that is, if no phase information could be obtained), we could still determine $\tilde{S}_m e^{-j\theta_1}$, where θ_1 is the argument of $\tilde{S}_1$. Since in our application the combining weights may be multiplied by a complex constant without affecting the combined SNR, the phase of the reference channel need not be estimated. Thus, we turn our attention to the estimation of the signal magnitude in the central reference channel.

An estimate of $|\tilde{S}_1|$ can be obtained in the following manner, using well-established experimental techniques. With the antenna pointing "on-source," we obtain an estimate of the total power P_{t1}, by averaging L independent sample powers:

$$\widehat{P_{t1}} = \frac{1}{L} \sum_{i=1}^{L} \left| \tilde{S}_1 \tilde{a}(i) + \tilde{n}_1(i) \right|^2 \tag{15a}$$

Next, we point the antenna "off-source" and obtain an estimate of the noise power using subsequent samples:

$$\widehat{P_{n1}} = \frac{1}{L} \sum_{i=L+1}^{2L} |\tilde{n}_1(i)|^2 \tag{15b}$$

Since

$$E\left[\widehat{P_{t1}}\right] = \left|\tilde{S}_1\right|^2 + 2\sigma_1^2 \tag{16a}$$

and

$$E\left[\widehat{\tilde{P}_{n1}}\right] = 2\sigma_1^2 \tag{16b}$$

it follows that

$$\widehat{\left|\tilde{S}_1\right|^2} = \begin{cases} \widehat{P_{t1}} - \widehat{P_{n1}}; & \widehat{P_{t1}} \geq \widehat{P_{n1}} \\ \text{not defined}; & \widehat{P_{n_1}} > \widehat{P_{t_1}} \end{cases} \tag{17}$$

is a reasonable estimate of $|\tilde{S}_1|^2$ when the average signal power is large compared to the random variations. When the signal power is not sufficiently great, it is possible for the estimate to become negative, which is meaningless for a power estimate and, therefore, should not be used.

The estimate of $\left|\tilde{S}_1\right|$ follows from Eq. (17) as

$$\widehat{\left|\tilde{S}_1\right|} = \left(\widehat{\left|\tilde{S}_1\right|^2}\right)^{1/2} \tag{18}$$

Using this estimate, the signal coefficients for the outer channels may be obtained from Eqs. (12) and (14), except for a common complex coefficient, as follows:

$$\widehat{\tilde{S}_m e^{-j\theta_1}} = \frac{\widehat{\tilde{S}_1^* \tilde{S}_m}}{\widehat{\left|\tilde{S}_1\right|}} \tag{19}$$

The complex coefficient $e^{-j\theta_1}$ has no effect on the combiner performance, since the combining weights will include this factor, effectively setting the average phase of the combined signal to zero.

V. Statistics of the Weight Estimates

The combining weights that maximize the SNR of the combined samples are defined in Eq. (10), repeated here for convenience:

$$\widehat{\tilde{w}_k} = \frac{\widehat{\tilde{S}_k^*}}{2\widehat{\sigma_k^2}} \tag{20}$$

Each complex weight may be multiplied by a complex constant without affecting combiner performance. Thus, for our purposes, it is sufficient to estimate the "rotated" weights

$$\tilde{w}_k\widehat{e^{-j\theta_1}} = \frac{\widehat{\tilde{S}_k^* e^{-j\theta}}}{2\widehat{\sigma_k^2}} = \frac{\widehat{\tilde{S}_1\tilde{S}_k^*}}{2\widehat{|\tilde{S}_1|}\widehat{\sigma_k^2}} \tag{21}$$

instead, without explicitly determining the phase of the central channel, θ_1.

The denominator of each weight is simply an estimate of the noise variance in that channel. The noise variance in the kth channel, $2\sigma_k^2$, is estimated by means of simultaneous off-source power measurements in all K channels (both real and imaginary noise components have variance σ_k^2, hence the factor of 2 in the variance of the complex noise). If M samples are used, the estimate of the variance in the kth channel is of the form

$$\begin{aligned}\widehat{\sigma_k^2} &= \frac{1}{2M}\sum_{i=1}^{M}|\tilde{n}_k(i)|^2 \\ &= \frac{1}{2M}\left\{\sum_{i=1}^{M} n_R^2(i) + \sum_{i=1}^{M} n_I^2(i)\right\}\end{aligned} \tag{22}$$

Clearly, the expected value of this estimate is the desired quantity,

$$E(\widehat{\sigma_k^2}) = \sigma_k^2 \tag{23}$$

hence the estimator is unbiased. Assuming the underlying processes are Gaussian, the estimate is a scaled central chi-square random variable with $2M$ degrees of freedom and variance

$$\mathrm{var}(\widehat{\sigma_k^2}) = \frac{1}{4M^2}\left(4M\sigma_k^4\right) = \frac{\sigma_k^4}{M} \tag{24}$$

In typical applications, the component of the noise variance due to the receiver remains constant, while the component due to the background changes slowly with elevation and azimuth, but may be considered constant for many weight estimates. The frequency with which off-source measurements must be performed depends on the specific details of the experiment.

The numerator of each rotated weight estimate can be obtained using Eq. (19). In addition to an estimate of the product $\tilde{S}_1\tilde{S}_k^*$ (whose expectation is proportional to the correlation between the first and kth channels), this approach also requires an estimate of the magnitude of the complex scale factor in the central channel. This quantity can be updated with each new weight estimate, using the last noise power measurement, or a separate on-source measurement can be made periodically for the central channel as well. Both cases will be considered. First, assume estimates are made with each update, using the same number of samples as for the weights (L). The estimate of the signal power in the central channel then becomes

$$\widehat{\left|\tilde{S}_1\right|^2} = \frac{1}{L}\sum_{i=1}^{L}\left|\tilde{S}_1\tilde{a}(i) + \tilde{n}_1(i)\right|^2 - \frac{1}{M}\sum_{i=L+1}^{L+M}|\tilde{n}_1(i)|^2 \tag{25}$$

with expectation

$$E\widehat{\left|\tilde{S}_1\right|^2} = \left|\tilde{S}_1\right|^2 \tag{26}$$

and variance

$$\mathrm{var}_L\left(\widehat{\left|\tilde{S}_1\right|^2}\right) = \frac{2}{L}\left(2\sigma_1^2 + \left|\tilde{S}_1\right|^2\right)^2 + \frac{8}{M}\sigma_1^4 \tag{27}$$

Again, we observe from Eq. (26) that an unbiased estimate is obtained. If a separate power measurement is carried out for the central channel using N independent samples, then the signal power estimate becomes

$$\widehat{\left|\tilde{S}_1\right|^2} = \frac{1}{N}\sum_{i=1}^{N}\left|\tilde{S}_1\tilde{a}(i) + \tilde{n}_1(i)\right|^2 - \frac{1}{M}\sum_{i=N+1}^{N+M}|\tilde{n}_1(i)|^2 \tag{28}$$

This estimate is also unbiased; hence, Eq. (26) still holds. However, the variance of the estimate decreases if $N > L$, as shown by comparing the following expression with Eq. (27):

$$\mathrm{var}_N\left(\widehat{\left|\tilde{S}_1\right|^2}\right) = \frac{2}{N}\left(2\sigma_1^2 + \left|\tilde{S}_1\right|^2\right)^2 + \frac{8}{M}\sigma_1^4 \tag{29}$$

The estimate of the signal power can, therefore, be made arbitrarily good by making both N and M sufficiently large, provided the natural time scales of the relevant process variations are not exceeded.

Next consider the statistics of the coefficient product estimates, $\tilde{S}_j\tilde{S}_k^*$. As shown in Eq. (11), the expectation of the product of the received samples between any two channels is the desired coefficient product, implying the unbiased estimator structure defined in Eq. (13).

The variance of this estimate can be obtained by first deriving the second moment of the coefficient product, subtracting the square of the expectation, and dividing the result by the total number of independent sample products averaged to obtain the estimate. If L sample products are averaged, this can be expressed as

$$\text{var}\left(\tilde{S}_j\tilde{S}_k^*\right) = \frac{1}{L}\left\{E\left|\tilde{S}_j\tilde{S}_k^*\right|^2 - \left|E\left(\tilde{S}_j\tilde{S}_k^*\right)\right|^2\right\} \tag{30}$$

Consider the second moment first. Writing the received samples as in Eqs. (3a) and (4), the second moment of the sample products between two distinct channels j and k becomes

$$\begin{aligned}E|\tilde{S}_j\tilde{S}_k^*|^2 &= E\left\{\left(\tilde{S}_j\tilde{S}_k^*|\tilde{a}|^2 + \tilde{S}_j\tilde{a}\tilde{n}_k^* + \tilde{S}_k^*\tilde{a}^*\tilde{n}_j + \tilde{n}_j\tilde{n}_k^*\right)\left(\tilde{S}_j^*\tilde{S}_k|\tilde{a}|^2 + \tilde{S}_j^*\tilde{a}^*\tilde{n}_k + \tilde{S}_k\tilde{a}\tilde{n}_j^* + \tilde{n}_j^*\tilde{n}_k\right)\right\}\\ &= E\left\{|\tilde{S}_j|^2|\tilde{S}_k|^2|\tilde{a}|^4 + |\tilde{S}_j|^2|\tilde{a}|^2|\tilde{n}_k|^2 + |\tilde{S}_k|^2|\tilde{a}|^2|\tilde{n}_j|^2 + |\tilde{n}_j|^2|\tilde{n}_k|^2\right\}\\ &\quad + \text{(products whose expectation goes to zero)}\\ &= |\tilde{S}_j|^2|\tilde{S}_k|^2\overline{|a|^4} + |\tilde{S}_j|^2\overline{|\tilde{a}|^2}\;\overline{|\tilde{n}_k|^2} + |\tilde{S}_k|^2\overline{|a|^2}\;\overline{|\tilde{n}_j|^2} + \overline{|\tilde{n}_j|^2}\;\overline{|\tilde{n}_k|^2}\end{aligned} \tag{31}$$

where the overbar denotes expectation. Letting $\overline{|\tilde{n}_j|^2} = 2\sigma_j^2$, $\overline{|\tilde{a}|^2} = 1$, and with $\overline{|\tilde{a}|^4} = 2$, the second moment becomes

$$E|\tilde{S}_j\tilde{S}_k^*|^2 = 2|\tilde{S}_j|^2|\tilde{S}_k|^2 + 2|\tilde{S}_j|^2\sigma_k^2 + 2|\tilde{S}_k|^2\sigma_j^2 + \sigma_k^2\sigma_j^2 \tag{32}$$

Subtracting the square of the expected value and dividing by L yields an expression for the variance:

$$\begin{aligned}\text{var}\left(\tilde{S}_j\tilde{S}_k^*\right) &= |\tilde{S}_j|^2|\tilde{S}_k|^2\\ &\quad + 2\left(|\tilde{S}_j|^2\sigma_k^2 + |\tilde{S}_k|^2\sigma_j^2\right) + 4\sigma_j^2\sigma_k^2\end{aligned} \tag{33}$$

If the estimation errors are sufficiently small, each estimate may be written as its true value plus a small random deviation. Assuming this to be the case, we have

$$\widehat{\tilde{S}_1^*\tilde{S}_k} = \tilde{S}_1^*\tilde{S}_k(1+\alpha) \tag{34a}$$

$$\widehat{|\tilde{S}_1|^2} = |\tilde{S}_1|^2(1+\beta) \tag{34b}$$

$$\widehat{\sigma_k^2} = \sigma_k^2(1+\gamma) \tag{34c}$$

Using Eqs. (24), (27), and (33), it follows that each error term is a zero-mean random variable with variance

$$\begin{aligned}\text{var}(\alpha) &= \frac{2}{L}\\ &\quad \times\left\{1 + \frac{4\sigma_1^2\sigma_k^2}{|\tilde{S}_1|^2|\tilde{S}_k|^2} + 2\left(\frac{\sigma_k^2}{|\tilde{S}_k|^2} + \frac{\sigma_1^2}{|\tilde{S}_1|^2}\right)\right\}\end{aligned} \tag{35a}$$

$$\begin{aligned}\text{var}(\beta) &= \frac{1}{|\tilde{S}_1|^4}\left\{\frac{2}{Q}\left(2\sigma_1^2 + |\tilde{S}_1|^2\right)^2 + \frac{8}{M}\sigma_1^4\right\};\\ Q &= L \text{ or } N\end{aligned} \tag{35b}$$

$$\text{var}\ (\gamma) = \frac{1}{M} \tag{35c}$$

The estimate of the rotated weight can now be written as

$$\tilde{w}_k \widehat{e^{-j\theta_1}} = \frac{\tilde{S}_1 \tilde{S}_k^*}{2\sigma_k^2 |\tilde{S}_1|} \frac{(1+\alpha)}{\sqrt{(1+\beta)}(1+\gamma)}$$

$$\approx \tilde{C}_k \frac{(1+\alpha)}{\left(1+\frac{\beta}{2}\right)\ (1+\gamma)} \tag{36}$$

where $\tilde{C}_k \underline{\Delta} \tilde{S}_1 \tilde{S}_k^* / 2\sigma_k^2 |\tilde{S}_1|$. Expanding the denominator, multiplying through, and keeping terms up to second order yields

$$\tilde{w}_k \widehat{e^{-j\theta_1}} = \tilde{C}_k \left[1 - \frac{\beta}{2} \left(1 - \frac{\beta}{2} + \alpha - \gamma \right) \right.$$

$$\left. + \alpha - \gamma\ (1 + \alpha - \gamma) \right] \tag{37}$$

The expected value of this expression is

$$E\left(\tilde{w}_k \widehat{e^{-j\theta_1}}\right) \cong \tilde{C}_k \left(1 + \frac{\overline{\beta^2}}{4} + \overline{\gamma^2} \right)$$

$$= \tilde{C}_k \left[1 + \text{var} \left(\frac{\beta}{2} \right) + \text{var}\ (\gamma) \right] \tag{38}$$

which shows that the estimate is biased, but becomes asymptotically unbiased as the number of samples grows without bound. Writing the rotated weight estimate as

$$\tilde{w}_k \widehat{e^{-j\theta_1}} = \tilde{C}_k (1 + \zeta) \tag{39}$$

where $\zeta = \alpha - \frac{\beta}{2} - \gamma - \alpha\gamma - \alpha\frac{\beta}{2} + \gamma\frac{\beta}{2} + \frac{\beta^2}{4} + \gamma^2$, it follows that

$$\text{var}\ \left(\tilde{w}_k \widehat{e^{-j\theta_1}}\right) = |\tilde{C}_k|^2\ \text{var}\ (\zeta) \tag{40}$$

Here ζ is a random variable with second-order statistics

$$E(\zeta) = \frac{\overline{\beta^2}}{4} + \overline{\gamma^2} \tag{41}$$

and

$$\text{var}\ (\zeta) = E\left[\alpha - \frac{\beta}{2} - \gamma - \alpha\frac{\beta}{2} - \alpha\gamma + \gamma\frac{\beta}{2} \right]^2$$

$$= \overline{\alpha^2} + \frac{\overline{\beta^2}}{4} + \overline{\gamma^2} + \overline{\gamma^2}\frac{\overline{\beta^2}}{4} + \overline{\alpha^2}\ \overline{\gamma^2} + \frac{\overline{\beta^2}}{4}\overline{\gamma^2}$$

$$+\ (\text{products whose expectation is zero}) \tag{42}$$

Since $E(\alpha) = E(\beta) = E(\gamma) = 0$, and α, β, and γ are statistically independent, it follows that all terms in Eq. (42) containing α, β, or γ to the first power go to zero. Thus, the normalized variance of the rotated weight may be expressed in symmetric form as

$$|\tilde{C}_k|^{-2}\ \text{var}\ \left(\tilde{w}_k \widehat{e^{-j\theta_1}}\right) =$$

$$\text{var}\ (\alpha) +\ \text{var} \left(\frac{\beta}{2} \right) +\ \text{var}\ (\gamma)$$

$$+\ \text{var}\ (\alpha)\ \text{var} \left(\frac{\beta}{2} \right) +\ \text{var}\ (\gamma)\ \text{var} \left(\frac{\beta}{2} \right)$$

$$+\ \text{var}\ (\alpha)\ \text{var}\ (\gamma) \tag{43}$$

The statistics of these rotated weight estimates for specific parameter values are examined in the next section.

VI. Numerical Results

The expressions for the normalized bias and variance of the rotated weights developed in Eqs. (41) and (42) are functions of the parameters M, N, and L, as well as of the signal powers and noise variances in the combiner channels. The noise variance is largely determined by the physical characteristics of the front-end amplifiers, and includes contributions from background radiation as well. The signal power in each channel depends on the strength of the source, the antenna aperture, and the amount of distortion suffered by the main reflector. However, the remaining parameters can be selected to achieve a desired level of estimator performance.

In a typical combining experiment, the antenna is first pointed off source, and the noise power in each complex channel is estimated according to Eq. (22). Denote the number of samples used to make this estimate M. Next, the antenna is pointed on source, and the signal in the central channel is measured by means of Eq. (25) or Eq. (28), using either L or N samples, where L is the number of samples per update. Of course, the signal levels in the other channels could also be determined, but that information is not used by this algorithm; instead, the rotated complex weights are estimated according to Eq. (19). Theoretically, some improvement could be obtained if independent signal power measurements were used to improve the magnitude estimates, but that issue will not be addressed here.

After the coefficients are determined, combining weight updates are obtained every L samples for use in the real-time combining operation. The inequality $(M, N) >> L$ is usually valid, since both signal and noise power levels tend to remain constant over a great many coefficient updates. However, we shall also consider the case $N = L$, corresponding to a situation where the signal power in the central channel changes fast enough to warrant its measurement with each update. This could occur if wind-induced dynamics or time-varying pointing errors were present.

Representative values were chosen for the signal power levels, normalized to the noise variance, which was assigned a value of 1 power unit. With a channel noise temperature of roughly 100 K, a strong Ka-band radio source (such as Venus or Jupiter) may produce a 10-K rise in the central channel when observed with the 34-m antenna at DSS 13. At low and high elevations, gravitationally induced distortions of the main reflector generally deflect as much as 10 percent of the total signal power to some of the outer channels. Thus, the values $\sigma_k^2 = 1, |\tilde{S}_1|^2 = 0.1$ and $|\tilde{S}_k|^2 = 0.01$, $k \neq 1$ will be assumed for the numerical examples that follow, meaning that the signal power in the central (reference) channel is one-tenth of the noise power, while typical signal powers in the outer channels are 10 times smaller than those in the central channel.

The normalized bias defined in Eq. (41) is shown in Fig. 3 as a function of N, with M as a parameter. For any N, the minimum achievable bias is a monotone decreasing function of M that approaches an asymptotic limit from above. Minimum values of M and N are clearly specified for any desired bias level: for example, if we wish to maintain a normalized bias of 0.001, then M must be greater than about 10^5 and N must be at least 3×10^5; at a sampling rate of 2×10^5 samples/sec, this would take a mere $2 \times 1.5 = 3$ sec, which is short compared to typical time scales encountered in practice. If we let M exceed 10^6, then the above value of N will suffice. Suppose we select this value of N in order to meet the bias requirements, and examine the normalized variance defined in Eq. (43).

The normalized variance of the rotated weight estimates is shown in Fig. 4 as a function of L. It is clear that a given value of N specifies a limit for the smallest attainable variance and, hence, limits the performance of the weight estimator. For the specified value of N, this limit is about 4×10^{-4}, even as M and L grow without bound. The dependence on N disappears if the signal power is recomputed with each update, using the previous L samples, corresponding to the case $N = L$. Now any desired level of performance can be achieved provided that both M and L are sufficiently great, as shown in Fig. 5. Given M and L, the corresponding normalized bias can be determined from Fig. 3 by substituting L for N. Note that for very small values of L, the variance increases rapidly when $N = L$, due to the greater error in the signal power estimate as a result of insufficient observations.

VII. Summary and Conclusions

A digital combining-weight estimation algorithm for use with broadband sources has been described and analyzed. Although the algorithm provides a biased estimate of the combining weights, the bias can be reduced to any desired level by observing enough samples. The normalized variance of the weight estimates can be similarly reduced; however, care must be taken to obtain accurate signal and noise power estimates, as these quantities ultimately limit the performance of the estimator at all update rates. With this algorithm, only three primitive estimates are needed to obtain each combining weight estimate: the noise variance in the kth channel, the signal power in the central channel, and the complex correlation coefficient between the central and kth channels. The first two are simple power measurements requiring magnitude squaring and accumulation, while the third is a complex multiply-and-accumulate operation; both operations can be carried out with current PC-based digital hardware, provided the sampling rates do not exceed roughly 250,000 samples/sec. Consequently, this approach is useful for reducing estimator complexity while greatly increasing the portability of the entire array feed compensation system, enabling the demonstration of combining gain on a variety of DSN antennas.

References

[1] V. A. Vilnrotter and E. R. Rodemich, "A Real-Time Signal Combining System for Ka-Band Feed Arrays Using Maximum Likelihood Weight Estimates," *The Telecommunications and Data Acquisition Progress Report 42-100, vol. October–December 1989*, Jet Propulsion Laboratory, Pasadena, California, pp. 81–99, February 15, 1990.

[2] V. A. Vilnrotter, E. R. Rodemich, and S. J. Dolinar, Jr., "Real-Time Combining of Residual Carrier Array Signals Using ML Weight Estimates," *IEEE Transactions on Communications*, vol. 40, no. 3, pp. 604–615, March 1992.

[3] S. Zohar and V. Vilnrotter, *Using a Focal-Plane Array to Estimate Antenna Pointing Errors*, JPL Publication 91-45, Jet Propulsion Laboratory, Pasadena, California, October 25, 1991.

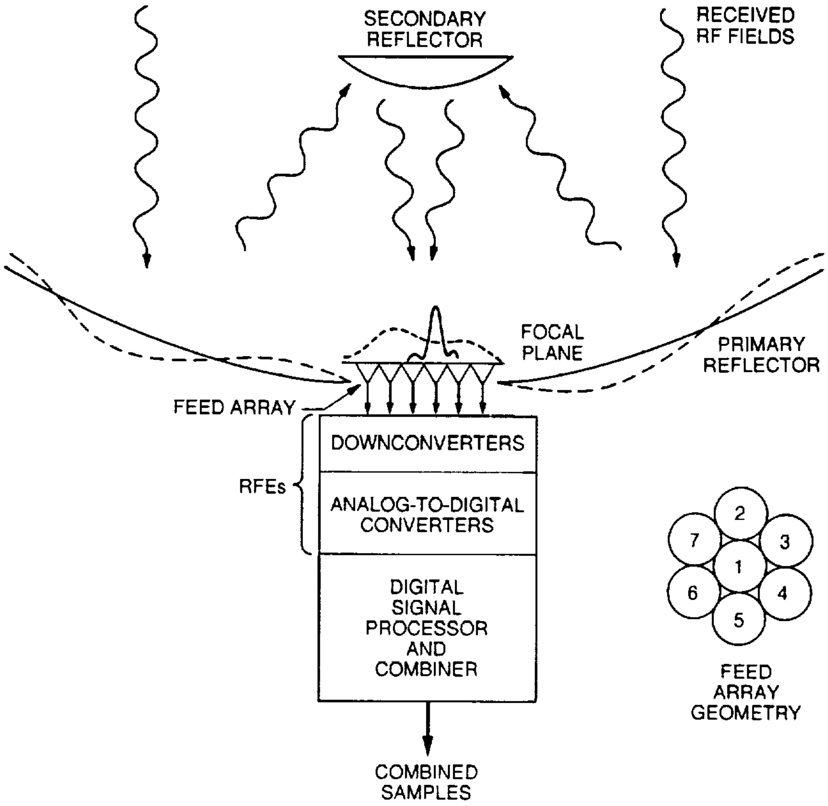

Fig. 1. Real-time antenna-compensation system conceptual design.

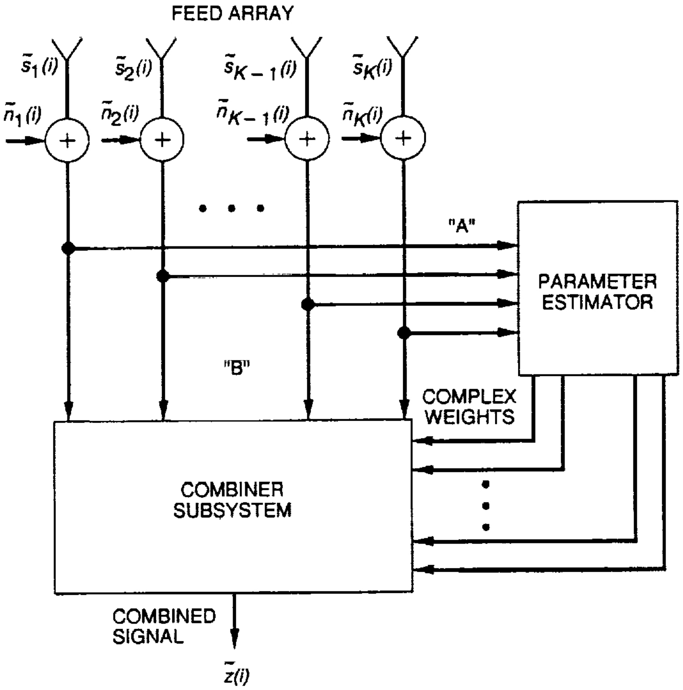

Fig. 2. Signal-combining system (baseband model).

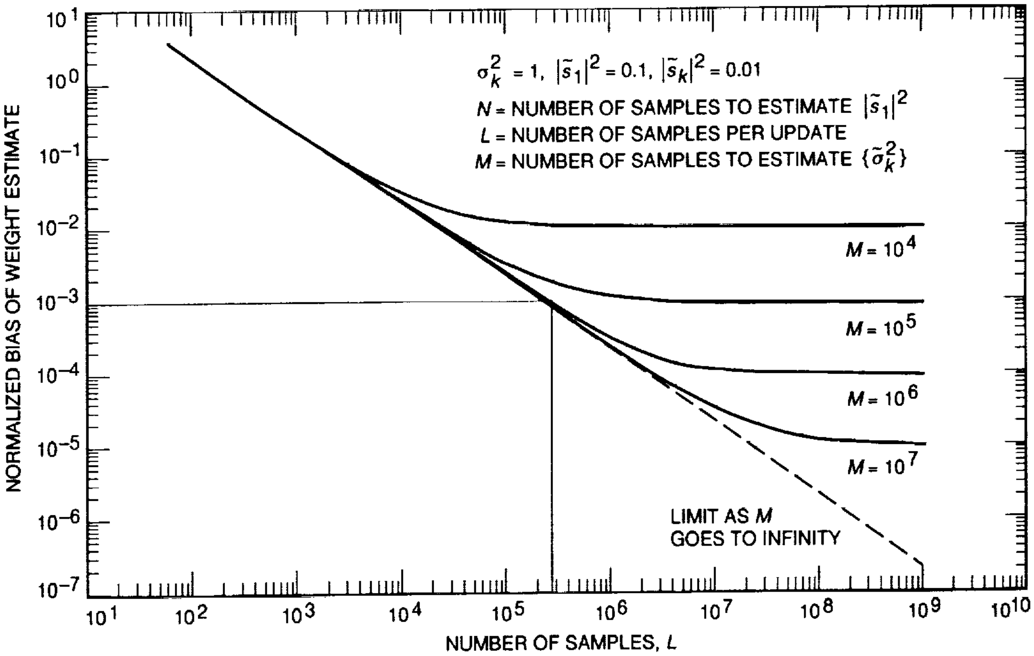

Fig. 3. Normalized bias versus number of samples (*N*).

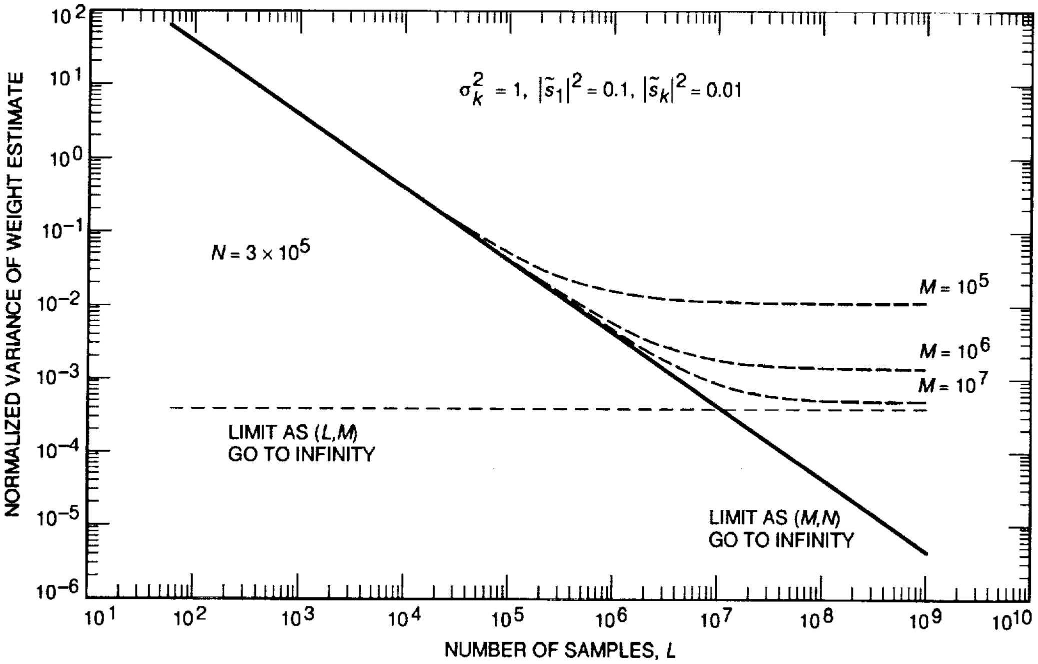

Fig. 4. Normalized variance versus number of samples (*L*).

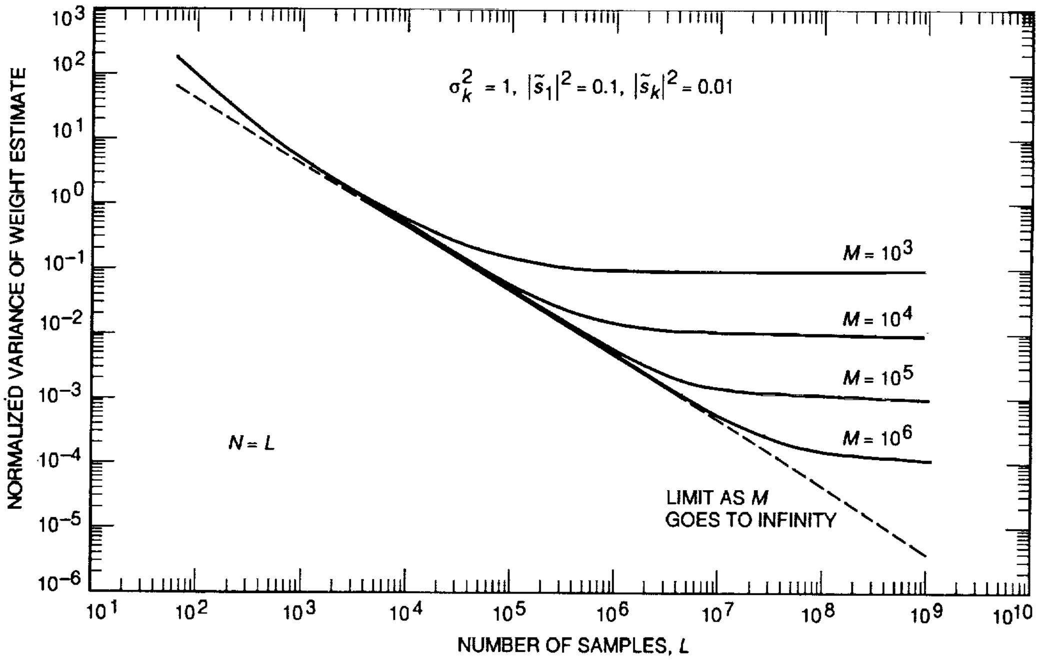

Fig. 5. Normalized variance versus number of samples ($N = L$).

N94- 29661

TDA Progress Report 42-116 February 15, 1994

Digital Combining-Weight Estimation for Broadband Sources Using Maximum-Likelihood Estimates

E. R. Rodemich
Robotic Systems and Advanced Computer Technology Section

V. A. Vilnrotter
Communications Systems Research Section

The algorithm described in [1] for estimating the optimum combining weights for the Ka-band (33.7-GHz) array feed compensation system is compared with the maximum-likelihood estimate. This provides some improvement in performance, with an increase in computational complexity. However, the maximum-likelihood algorithm is simple enough to allow implementation on a PC-based combining system.

I. Introduction

We consider the problem of estimating combining weights for a signal received by an antenna array. The signal is modeled as a Gaussian random variable, and independent Gaussian noise is added in each channel. An estimation method that has been proposed is treated in [1]. Here we compare that method with the method that uses maximum-likelihood (ML) estimates of the pertinent parameters. The computations required for these estimates, while more complex than the computations of [1], are well within the capabilities of a small on-site computer.

II. The Maximum-Likelihood Equations

The received signal in the kth channel at time i is assumed to be

$$\tilde{r}_k(i) = \tilde{S}_k \tilde{a}(i) + \tilde{n}_k(i), \qquad k = 1, 2, \ldots, K \tag{1}$$

where the $\tilde{n}_k(i)$ and $\tilde{a}(i)$ are independent complex Gaussian random variables, $\tilde{n}_k(i)$ is $N(0, 2\sigma_k^2)$, and $\tilde{a}(i)$ is $N(0,1)$. Then[1]

$$\tilde{c}_{jk} = E\left(\overline{\tilde{r}_j(i)}\tilde{r}_k(i)\right) = 2\sigma_k^2 \delta_{jk} + \overline{\tilde{S}_j}\tilde{S}_k \tag{2}$$

If $\tilde{\mathbf{C}}$ is the complex $K \times K$ matrix with entries $\tilde{c}_{jk}$, then the real and imaginary parts of the $\tilde{r}_k(i)$ (for $k = 1, \ldots, K$, i fixed) have a $2K$-dimensional distribution with density[2]

$$p_i = \frac{1}{\pi^K \det(\tilde{\mathbf{C}})} \exp\left[-\sum_{j,k=1}^{K} \tilde{r}_j(i)(\tilde{\mathbf{C}}^{-1})_{jk}\overline{\tilde{r}_k(i)}\right] \tag{3}$$

---

[1] The overbar denotes a complex conjugate.

[2] The arguments $\tilde{r}_1(i), \ldots, \tilde{r}_K(i)$ of p_i are not shown explicitly.

It is convenient to introduce the quantities

$$\tilde{T}_k = \frac{\tilde{S}_k}{\sqrt{2}\sigma_k} \tag{4}$$

Then

$$\tilde{c}_{jk} = 2\sigma_j\sigma_k\left(\delta_{jk} + \overline{\tilde{T}_j}\tilde{T}_k\right) \tag{5}$$

and the elements of the inverse matrix are

$$\tilde{b}_{jk} = (\tilde{\mathrm{C}}^{-1})_{jk} = \frac{1}{2\sigma_j\sigma_k}\left(\delta_{jk} - \frac{1}{\gamma}\overline{\tilde{T}_j}\tilde{T}_k\right) \tag{6}$$

where

$$\gamma = 1 + \sum_{k=1}^{K}|\tilde{T}_k|^2 \tag{7}$$

Also, we have

$$\det\,(\tilde{\mathrm{C}}) = 2^K\left(\prod_{k=1}^{K}\sigma_k^2\right)\gamma \tag{8}$$

Using these values in Eq. (3),

$$p_i = \frac{1}{(2\pi)^K\left(\prod_{k=1}^{K}\sigma_k^2\right)\gamma} \times \exp\left[-\frac{1}{2}\sum_{j,k=1}^{K}\frac{1}{\sigma_j\sigma_k}\tilde{r}_j(i)\left(\delta_{jk} - \frac{1}{\gamma}\overline{\tilde{T}_j}\tilde{T}_k\right)\overline{\tilde{r}_k(i)}\right] \tag{9}$$

We define the likelihood function as

$$\Lambda = \frac{1}{L}\sum_{i=1}^{L}\ln p_i \tag{10}$$

In terms of the sample covariances

$$\tilde{a}_{jk} = \frac{1}{L}\sum_{i=1}^{L}\overline{\tilde{r}_j(i)}\tilde{r}_k(i) \tag{11}$$

It follows from Eq. (9) that

$$\Lambda = -\sum_{k=1}^{K}\ln\,(2\pi\sigma_k^2) - \ln\,(\gamma) - \frac{1}{2}\sum_{j,k=1}^{K}\frac{1}{\sigma_j\sigma_k}\tilde{a}_{kj}\left(\delta_{jk} - \frac{1}{\gamma}\overline{\tilde{T}_j}\tilde{T}_k\right) \tag{12}$$

III. Cascaded Maximum-Likelihood Estimates

For maximum-likelihood estimates $\hat{\tilde{S}}_k$ and $\hat{\sigma}_k$, or equivalently $\hat{\tilde{T}}_k$ and $\hat{\sigma}_k$, we need to solve the equations obtained by setting the derivatives of Λ equal to zero. This system of equations must be solved iteratively. It need not have a unique solution, for the parameters are not even determined by the statistics of the signals [Eq. (1)] unless at least three of the $\tilde{S}_k$ are nonzero. For this reason, this approach is not pursued here. We assume that the σ_k are estimated from separate observations with the antenna pointed "off source." These noise estimates are themselves maximum-likelihood estimates obtained from the noise samples by differentiating Eq. (12) with respect to σ_j (assuming $\tilde{T}_k = 0$):

$$\hat{\sigma}_j = \sqrt{\frac{1}{2}\tilde{a}_{jj}}$$

where $\tilde{a}_{jj}$ is given by Eq. (11). The maximum-likelihood estimates of the $\tilde{T}_k$ use these noise estimates.

Differentiating Eq. (12) with respect to $\overline{\tilde{T}_j}$, we get

$$\left(-\frac{1}{\gamma} - \frac{1}{2\gamma^2}\sum_{k,m=1}^{K}\frac{1}{\sigma_k\sigma_m}\tilde{a}_{km}\overline{\tilde{T}_m}\tilde{T}_k\right)\tilde{T}_j + \frac{1}{2\gamma}\sum_{k=1}^{K}\frac{1}{\sigma_j\sigma_k}\tilde{a}_{kj}\tilde{T}_k = 0$$

It can be shown that this is equivalent to the simpler condition

$$\sum_{k=1}^{K} \frac{\tilde{a}_{kj}}{\sigma_k \sigma_j} \tilde{T}_k = 2\gamma \tilde{T}_j$$

Replacing the parameters by their estimates, we get

$$\sum_{k=1}^{K} \frac{\tilde{a}_{kj}}{\hat{\sigma}_k \hat{\sigma}_j} \hat{\tilde{T}}_k = 2\hat{\gamma} \hat{\tilde{T}}_j \tag{13}$$

This equation states that the complex K vector with components $\hat{\tilde{T}}_k$ is an eigenvector of the matrix composed of the elements $\tilde{a}_{kj}/(\hat{\sigma}_k \hat{\sigma}_j)$, with eigenvalue $2\hat{\gamma}$. If we replace the matrix elements by their mean values, using the true values of the σ_k, then this matrix has $K-1$ eigenvalues equal to 2, and one larger eigenvalue 2γ, corresponding to the eigenvector $\tilde{T}_k$. Hence, the estimates $\hat{\tilde{T}}_k$ can be found in terms of the σ_k by numerically finding the largest eigenvalue of the matrix in Eq. (13) and its eigenvector. The eigenvector must be scaled so that the eigenvalue $2\hat{\gamma}$ satisfies the relation [from Eq. (7)]

$$\hat{\gamma} = 1 + \sum_{k=1}^{K} |\hat{\tilde{T}}_k|^2 \tag{14}$$

The method for solving Eq. (13) is described briefly in Appendix A.

IV. Variance of the Cascaded ML Estimates for the $\tilde{T}_j$

For a large L, the sample covariances $\tilde{a}_{jk}$ are close to their mean values:

$$\tilde{a}_{jk} = \tilde{c}_{jk} + \delta\tilde{a}_{jk} \tag{15}$$

where the difference $\delta\tilde{a}_{jk}$ has a mean of zero and a small variance. It is easily shown that

$$E(\overline{\delta\tilde{a}_{jk}}\delta\tilde{a}_{lm}) = \frac{4}{L}\sigma_j\sigma_k\sigma_l\sigma_m$$

$$\times \left(\delta_{km} + \overline{\tilde{T}_k}\tilde{T}_m\right)\left(\delta_{lj} + \overline{\tilde{T}_l}\tilde{T}_j\right) \tag{16}$$

If the estimates $\hat{\sigma}_j$ are close to the correct values,

$$\hat{\sigma}_j = \sigma_j + \delta\sigma_j \tag{17}$$

Then the estimates $\hat{\tilde{T}}_j$ are close to the true values,

$$\hat{\tilde{T}}_j = \tilde{T}_j + \delta\tilde{T}_j \tag{18}$$

Expand Eq. (15), keeping only those terms which are of first order in the deviations $\delta\tilde{a}_{jk}$, $\delta\sigma_j$, and $\delta\tilde{T}_j$. We get

$$\sum_{k=1}^{K}\left[\frac{\delta\tilde{a}_{kj}}{2\sigma_k\sigma_j}\tilde{T}_k + \frac{\tilde{c}_{kj}}{2\sigma_k\sigma_j}\delta\tilde{T}_k - \frac{\tilde{c}_{kj}}{2\sigma_k\sigma_j}\tilde{T}_k\left(\frac{\delta\sigma_j}{\sigma_j} + \frac{\delta\sigma_k}{\sigma_k}\right)\right] =$$

$$\gamma\delta\tilde{T}_j + \tilde{T}_j\sum_{k=1}^{K}\left(\overline{\tilde{T}}_k\delta\tilde{T}_k + \tilde{T}_k\overline{\delta\tilde{T}}_k\right)$$

Using the formula in Eq. (5) and simplifying, the result is

$$(\gamma-1)\delta\tilde{T}_j + \tilde{T}_j\sum_{k=1}^{K}\tilde{T}_k\overline{\delta\tilde{T}}_k =$$

$$\sum_{k=1}^{K}\frac{\delta\tilde{a}_{kj}}{2\sigma_k\sigma_j}\tilde{T}_k - \tilde{T}_j\sum_{k=1}^{K}\frac{\delta\sigma_k}{\sigma_k}|\tilde{T}_k|^2$$

$$-(\gamma+1)\tilde{T}_j\frac{\delta\sigma_j}{\sigma_j} \tag{19}$$

If we multiply this equation by $\overline{\delta\tilde{T}}_j$ and sum over j, we get

$$(\gamma-1)\sum_{k=1}^{K}\left(\overline{\tilde{T}}_k\delta\tilde{T}_k + \tilde{T}_k\overline{\delta\tilde{T}}_k\right) =$$

$$\sum_{j,k=1}^{K}\frac{\delta\tilde{a}_{kj}}{2\sigma_k\sigma_j}\overline{\tilde{T}}_j\tilde{T}_k - 2\gamma\sum_{j=1}^{K}\frac{\delta\sigma_j}{\sigma_j}|\tilde{T}_j|^2 \tag{20}$$

This equation determines the real part of $\sum\overline{\tilde{T}}_k\delta\tilde{T}_k$. The imaginary part of this sum is undetermined, since the $\tilde{T}_k$ can be multiplied by an arbitrary common complex factor of absolute value 1. From Eq. (20), we can set

$$\sum_{k=1}^{K}\bar{\tilde{T}}_k\delta\tilde{T}_k = \frac{1}{2(\gamma-1)}\sum_{m,k=1}^{K}\frac{\delta\tilde{a}_{km}}{2\sigma_k\sigma_m}\bar{\tilde{T}}_m\tilde{T}_k - \frac{\gamma}{\gamma-1}\sum_{k=1}^{K}\frac{\delta\sigma_k}{\sigma_k}|\tilde{T}_k|^2 + jw \qquad (21)$$

where w is a real quantity not yet specified. Using this expression in Eq. (19), we get

$$(\gamma-1)\delta\tilde{T}_j = \sum_{k=1}^{K}\frac{\delta\tilde{a}_{kj}}{2\sigma_k\sigma_j}\tilde{T}_k - \frac{\tilde{T}_j}{2(\gamma-1)} \times \sum_{m,k=1}^{K}\frac{\delta\tilde{a}_{km}}{2\sigma_k\sigma_m}\bar{\tilde{T}}_m\tilde{T}_k + \frac{\tilde{T}_j}{\gamma-1}\sum_{k=1}^{K}\frac{\delta\sigma_k}{\sigma_k}|\tilde{T}_k|^2 - (\gamma+1)\frac{\delta\sigma_j}{\sigma_j}\tilde{T}_j - jw\tilde{T}_j \qquad (22)$$

In the following, we will take $w = 0$, since this turns out to give the best results. The estimate $\hat{\sigma}_j$, found with the signal absent, is

$$\hat{\sigma}_j = \sqrt{\frac{1}{2}\tilde{a}_{jj}}$$

Expanding as above,

$$\frac{\delta\sigma_j}{\sigma_j} = \frac{\delta\tilde{a}_{jj}}{4\sigma_j^2}$$

Using Eq. (16) (with no signal), we get

$$E\left(\frac{\delta\sigma_j\delta\sigma_k}{\sigma_j\sigma_k}\right) = \frac{1}{4M}\delta_{jk} \qquad (23)$$

where M is the number of samples used in the noise estimates.

Square Eq. (22) and take the expected value. We denote the deviation of Eq. (22) by the prefix δ_0 to distinguish it from that obtained by other methods below. Using Eqs. (16) and (23), the result is

$$E(|\delta_0\tilde{T}_j|^2) = \frac{1}{(\gamma-1)^2}\left\{\frac{1}{L}\gamma\left[\gamma-1-|\tilde{T}_j|^2+\frac{1}{4}\gamma|\tilde{T}_j|^2\right] + \frac{1}{4M}\left[\frac{|\tilde{T}_j|^2}{(\gamma-1)^2}\sum_{k=1}^{K}|\tilde{T}_k|^4 - 2\frac{\gamma+1}{\gamma-1}|\tilde{T}_j|^4 + (\gamma+1)^2|\tilde{T}_j|^2\right]\right\} \qquad (24)$$

The sum over j of this expression leads to

$$\sum_{j=1}^{K}E(|\delta_0\tilde{T}_j|^2) = \frac{1}{\gamma-1}\left\{\frac{1}{L}\gamma\left[K-1+\frac{1}{4}\gamma\right] + \frac{1}{4M} \times \left[(\gamma+1)^2 - \frac{2\gamma+1}{(\gamma-1)^2}\sum_{k=1}^{K}|\tilde{T}_k|^4\right]\right\} \qquad (25)$$

Now we consider another estimate, where the first channel is taken to be the one with maximum signal strength, and $\tilde{S}_1$ (or $\tilde{T}_1$) is estimated first. By Eq. (5),

$$E(\tilde{a}_{11}) = 2\sigma_1^2(1+|\tilde{T}_1|^2)$$

This leads to the estimate

$$|\hat{\tilde{T}}_1|^2 = \frac{\tilde{a}_{11}}{2\hat{\sigma}_1^2} - 1 \qquad (26)$$

The resulting error $\delta_2\tilde{T}_1$ has variance

$$E(|\delta_2\tilde{T}_1|^2) = \left(\frac{1}{L}+\frac{1}{M}\right)\frac{(1+|\tilde{T}_1|^2)^2}{4|\tilde{T}_1|^2} \qquad (27)$$

This estimate can be used to obtain an estimate for $\tilde{T}_j$ for $j \geq 2$ by using

$$\hat{\tilde{T}}_j = \frac{\tilde{a}_{1j}}{2\hat{\sigma}_1\hat{\sigma}_j\overline{\hat{\tilde{T}}_1}} \qquad (j \geq 2) \tag{28}$$

The variance of this estimate is

$$E(|\delta_2\tilde{T}_j|^2) =$$

$$\frac{1}{4L|\tilde{T}_1|^4}\left[|\tilde{T}_j|^2(1+|\tilde{T}_1|^2)^2 + 4|\tilde{T}_1|^2(1+|\tilde{T}_1|^2)\right]$$

$$+\frac{|\tilde{T}_j|^2}{4M|\tilde{T}_1|^4}(1+|\tilde{T}_1|^4) \tag{29}$$

V. Variance of the Combining-Weight Estimates

We now consider estimates for the weights

$$\tilde{w}_j = \frac{\overline{\tilde{S}_j}}{2\tilde{\sigma}_j^2} = \frac{\overline{\tilde{T}_j}}{\sqrt{2}\tilde{\sigma}_j}$$

obtained from the cascaded ML estimates of the signal-to-noise ratio (SNR) and noise parameters. The estimate

$$\hat{\tilde{w}}_j = \frac{\overline{\hat{\tilde{S}}_j}}{2\hat{\tilde{\sigma}}_j^{\,2}} = \frac{\overline{\hat{\tilde{T}}_j}}{\sqrt{2}\hat{\tilde{\sigma}}_j} \tag{30}$$

has a deviation $\delta\tilde{w}_j$ from the true value, given to the first order by

$$\delta\tilde{w}_j = \frac{1}{\sqrt{2}\sigma_j}\left(\overline{\delta\tilde{T}_j} - \overline{\tilde{T}_j}\frac{\delta\sigma_j}{\sigma_j}\right)$$

The mean-square value of this deviation can be computed for each of the estimation methods under consideration. We find

$$E(|\delta_0\tilde{w}_j|^2) = \frac{1}{2(\gamma-1)^2\sigma_j^2}\left\{\frac{1}{L}\gamma\left[\gamma - 1 - |\tilde{T}_j|^2 + \frac{1}{4}\gamma|\tilde{T}_j|^2\right]\right.$$

$$\left. + \frac{1}{4M}\left[\frac{|\tilde{T}_j|^2}{(\gamma-1)^2}\sum_{k=1}^{K}|\tilde{T}_k|^4 - \frac{4\gamma}{\gamma-1}|\tilde{T}_j|^4 + 4\gamma^2|\tilde{T}_j|^2\right]\right\} \tag{31}$$

$$E(|\delta_2\tilde{w}_j|^2) = \frac{1}{8L\sigma_j^2|\tilde{T}_1|^4}\left[|\tilde{T}_j|^2(1+|\tilde{T}_1|^2)^2 + 4(1-\delta_{j1})\right.$$

$$\left.\times |\tilde{T}_1|^2(1+|\tilde{T}_1|^2)\right] + \frac{|\tilde{T}_j|^2}{8M\sigma_j^2|\tilde{T}_1|^4}$$

$$\times (1 + 4\delta_{j1}|\tilde{T}_1|^2 + 4|\tilde{T}_1|^4) \tag{32a}$$

A modified form of this last method was considered in [1]. There, $\tilde{T}_1$ was estimated from Eq. (26) based on N samples, and the other $\tilde{T}_j$ were estimated by Eq. (28) for a later set of L samples. For this method, it can be shown that

$$E(|\delta\tilde{w}_j|^2) = \frac{|\tilde{T}_j|^2(1+|\tilde{T}_1|^2)^2}{8N\sigma_j^2|\tilde{T}_1|^4} + (1-\delta_{j1})$$

$$\times \frac{(1+|\tilde{T}_1|^2)(1+|\tilde{T}_j|^2)}{2L\sigma_j^2|\tilde{T}_1|^2} + \frac{|\tilde{T}_j|^2}{8M\sigma_j^2|\tilde{T}_1|^4}$$

$$\times (1 + 4\delta_{j1}|\tilde{T}_1|^2 + 4|\tilde{T}_1|^4) \tag{32b}$$

These values, divided by $|\tilde{w}_j|^2$, are plotted in Fig. 1. The values $|\tilde{T}_1|^2 = 0.05$ and $|\tilde{T}_j|^2 = 0.005$, $j \geq 2$, were used. M was fixed at the value 100,000, and $N = L$. There is no observable difference between the curves based on Eqs. (32a) and(32b). For a small L, the mean-square error from the maximum-likelihood formula is lower by 2.2 dB. For a large L, the other methods are better, but this is in an impractical range of the parameters. M should be at least as large as L, since the M samples provide noise estimates on which the subsequent estimates are based. The failure of the maximum-likelihood method in this range, which was applied only for estimating the $\tilde{T}_j$, shows that these estimates can be more strongly affected by errors in the noise estimates.

Figure 2 shows the maximum-likelihood curve for various values of M. These curves have the same general appearance as the corresponding curves for the method given in [1]. Again, on the right side of the figure, where the curves for various M are widely separated, the errors shown are higher than those shown in [1]. The significant points on these curves, with $M \geq L$, show an improvement over [1].

VI. Joint Maximum-Likelihood Estimates for the Equal Noise Case

An important special case which is seen in practice has all the σ_j equal. Here maximum-likelihood estimates can be used to simultaneously determine the noise and signal levels (the problems cited above no longer apply).

Denote the common value of the σ_j by σ. The formula in Eq. (12) for Λ becomes

$$\Lambda = -K \ln (2\pi\sigma^2) - \ln (\gamma)$$

$$- \sum_{j,k=1}^{K} \frac{\tilde{a}_{kj}}{2\sigma^2} \left(\delta_{jk} - \frac{1}{\gamma} \bar{\tilde{T}}_j \tilde{T}_k \right) \qquad (33)$$

To find the noise and signal amplitudes simultaneously by the maximum-likelihood method, set the derivative of Λ with respect to σ equal to zero, and solve this equation together with Eq. (13). Simplifying the derivative by using Eq. (13), the equation obtained is

$$2\hat{\sigma}^2(K - 1 + \hat{\gamma}) = \sum_{k=1}^{K} \tilde{a}_{kk} \qquad (34)$$

Eliminating $\hat{\sigma}$ from Eq. (13), we get

$$\sum_{k=1}^{K} \tilde{a}_{kj} \hat{\tilde{T}}_k = \frac{\hat{\gamma}}{K - 1 + \hat{\gamma}} \left(\sum_{k=1}^{K} \tilde{a}_{kk} \right) \hat{\tilde{T}}_j \qquad (35)$$

As before, this equation is solved by taking the vector with components $\hat{\tilde{T}}_j$ to be the eigenvector of the matrix $(\tilde{a}_{kj})$ corresponding to the largest eigenvalue. This eigenvalue must be the coefficient of $\hat{\tilde{T}}_j$ on the right, which determines $\hat{\gamma}$, and hence determines the $\hat{\tilde{T}}_j$ up to a common complex factor of absolute value 1. The noise estimate is then given by Eq. (34).

To get variance estimates, proceed as before. The equation analogous to Eq. (22) is

$$(\gamma - 1)\delta\tilde{T}_j = \sum_{k=1}^{K} \frac{\delta\tilde{a}_{kj}}{2\sigma^2} \tilde{T}_k - \frac{K - 1 - \gamma}{2(K - 1)(\gamma - 1)} \tilde{T}_j$$

$$\times \sum_{m,k=1}^{K} \frac{\delta\tilde{a}_{km}}{2\sigma^2} \bar{\tilde{T}}_m \tilde{T}_k - \frac{\gamma\tilde{T}_j}{2(K - 1)} \sum_{k=1}^{K} \frac{\delta\tilde{a}_{kk}}{2\sigma^2} - jw\tilde{T}_j \qquad (36)$$

where w is again an undetermined real quantity which will be set equal to 0. The noise error $\delta\sigma$ can be found from Eq. (34). Eliminating $\delta\tilde{T}_j$ by the use of Eq. (36), the result is

$$\frac{\delta\sigma}{\sigma} = \frac{1}{2(K - 1)}$$

$$\times \left(\sum_{k=1}^{K} \frac{\delta\tilde{a}_{kk}}{2\sigma^2} - \frac{1}{\gamma - 1} \sum_{m,k=1}^{K} \frac{\delta\tilde{a}_{km}}{2\sigma^2} \bar{\tilde{T}}_m \tilde{T}_k \right) \qquad (37)$$

To get variance estimates, square the expressions in Eqs. (36) and (37) and take the expected value. Denoting the deviation in $\tilde{T}_j$ by the prefix δ_4, we get

$$E(|\delta_4\tilde{T}_j|^2) =$$

$$\frac{1}{(\gamma - 1)^2} \left\{ \frac{1}{L}\gamma \left[\gamma - 1 - |\tilde{T}_j|^2 + \frac{1}{4}\frac{K}{K - 1}\gamma |\tilde{T}_j|^2 \right] \right\} \qquad (38)$$

$$E\left(\frac{\delta\sigma^2}{\sigma^2} \right) = \frac{1}{4L(K - 1)} \qquad (39)$$

Summing Eq. (38),

$$\sum_{j=1}^{K} E(|\delta_4\tilde{T}_j|^2) = \frac{\gamma}{L(\gamma - 1)} \left[K - 1 + \frac{1}{4}\frac{K}{K - 1}\gamma \right] \qquad (40)$$

Using the above formulas with Eq. (30),

$$E(|\delta_4\tilde{w}_j|^2) = \frac{1}{2\sigma^2(\gamma - 1)^2}$$

$$\times \left[\gamma(\gamma - 1 - |\tilde{T}_j|^2) + \frac{1}{4}\gamma^2|\tilde{T}_j|^2 \right.$$

$$\left. + \frac{(2\gamma - 1)^2}{4(K - 1)}|\tilde{T}_j|^2 \right] \qquad (41)$$

VII. Performance of the Weight Estimates

We now consider the combined signal, formed by taking the weighted sum

$$\tilde{z}(i) = \sum_{k=1}^{K} \hat{\tilde{w}}_k \tilde{r}_k(i) \tag{42}$$

where the weights are based on data before time i. If we use $\hat{\tilde{w}}_k = \tilde{w}_k + \delta\tilde{w}_k$ and express $\tilde{r}_k(i)$ by Eq. (1), we get four terms:

$$\begin{aligned}\tilde{z}(i) &= \sum_{k=1}^{K} \tilde{w}_k \tilde{S}_k \tilde{a}(i) + \sum_{k=1}^{K} \tilde{w}_k \tilde{n}_k(i) \\ &\quad + \sum_{k=1}^{K} \tilde{S}_k \tilde{a}(i) \delta\tilde{w}_k + \sum_{k=1}^{K} \tilde{n}_k(i) \delta\tilde{w}_k \\ &= \sum_{k=1}^{K} \tilde{w}_k \tilde{S}_k \tilde{a}(i) + E_1 + E_2 + E_3 \end{aligned} \tag{43}$$

The first term is the desired signal. The other terms are contributions to the error which can be considered separately, since their cross products have zero expectation.

Averaging over values of the current signal first, we have

$$E(|E_1|^2) = \sum_{k=1}^{K} 2\sigma_k^2 |\tilde{w}_k|^2 = \gamma - 1 \tag{44}$$

$$E(|E_2|^2) = \frac{1}{2} E\left(\left|\sum_{k=1}^{K} 2\sigma_k \tilde{T}_k \delta\tilde{w}_k\right|^2\right) \tag{45}$$

$$E(|E_3|^2) = E\left(\sum_{k=1}^{K} 2\sigma_k^2 |\delta\tilde{w}_k|^2\right) \tag{46}$$

These quantities are easily evaluated by using previous formulas.

The following estimation methods are referred to in Figs. 3 and 4:

(1) Method 1: the maximum-likelihood method of Section I.

(2) Method 2: the method based on Eqs. (26) and (28).

(3) Method 3: the modification of method 2 described in Section V.

In method 3, $\tilde{T}_1$ is estimated from Eq. (26) based on N samples, and the other $\tilde{T}_j$ are found from Eq. (28) using a later set of L samples. This is the method treated in [1].

The quantity $E(|E_2|^2 + |E_3|^2)/|\sum \tilde{w}_k \tilde{S}_k|^2$, the relative mean-square error caused by weight errors, is plotted for these three methods in Fig. 3. The formulas used are given in Appendix B. The values are plotted as a function of the signal-to-noise ratio, with the parameters L, M, and N fixed. (Throughout the curves, we take the SNR in every other channel to be one-tenth as large as the SNR in channel 1.) It is seen that method 2 for $N = L$ is better than method 3, although the difference is small at a low SNR. (For $N >> L$, method 3 would be better than method 2.) Of course, the ML value (method 1) is smallest, but the difference from method 2 is small at high SNR.

If we assume all channels have the same noise level, then method 4, the maximum-likelihood method of Section VI can also be considered. Comparing method 4 with the first three methods, it is seen that those methods can be improved by using a unified single noise estimate from the off-signal data. These improved methods are denoted by 1′, 2′, and 3′. The relative error for these four methods is shown in Fig. 4 (formulas are given in Appendix B). The behavior shown in Fig. 3 occurs here again, with the curves at a lower level, and method 4 is slightly better than method 1′.

VIII. Conclusions

Maximum-likelihood methods for combining weight estimation provide a consistent decrease in the mean-square error of the combined signal, as compared with other estimation methods, at the cost of a small increase in computational complexity. The part of the error which is caused by weight errors is decreased by over 2 dB, provided that at least as many samples are used to estimate the noise variance as the $\tilde{T}_k$. This can reduce the number of samples needed for equivalent performance to 30 percent less than the number needed by method 3.

Reference

[1] V. A. Vilnrotter and E. R. Rodemich, "A Digital Combining-Weight Estimation Algorithm for Broadband Sources With the Array Feed Compensation System," *The Telecommunications and Data Acquisition Progress Report 42-116, vol. October–December 1993,* Jet Propulsion Laboratory, Pasadena, California, pp. 86–97, February 15, 1994.

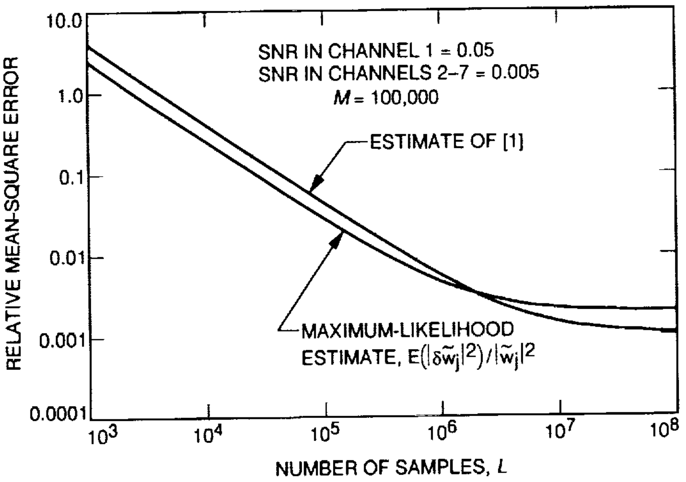

Fig. 1. Relative errors of the weight estimates.

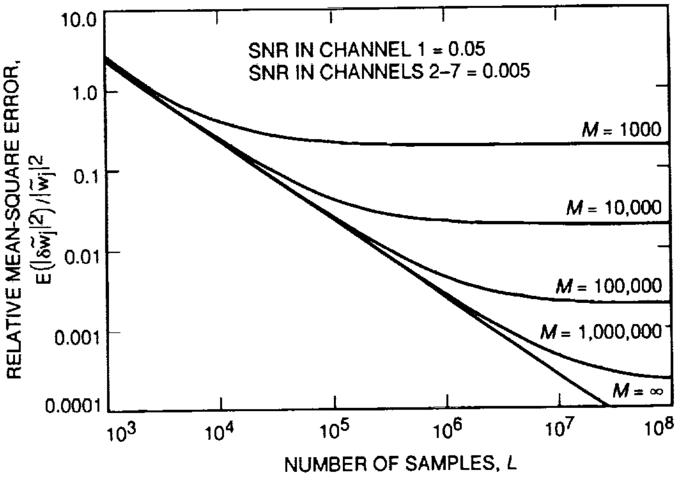

Fig. 2. Relative errors of the ML weight estimates.

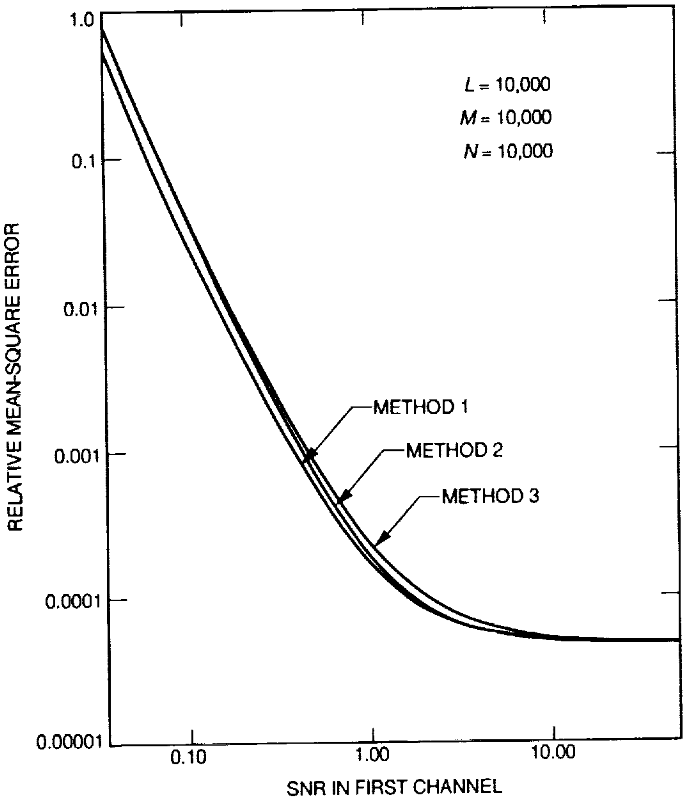

Fig. 3. Relative errors in the combined signal caused by weight errors (independent noise variances).

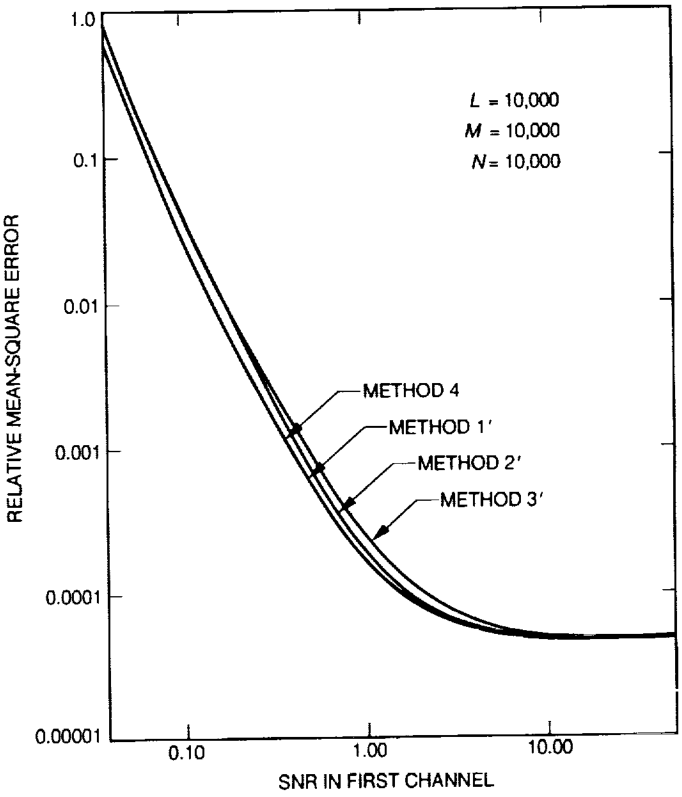

Fig. 4. Relative errors in the combined signal caused by weight errors (equal noise variances).

Appendix A

Method for Solving Eq. (13)

The mathematical problem posed by Eq. (13) is the following: Given a $K \times K$ Hermitian matrix $\tilde{\mathbf{A}}$, find its maximum eigenvalue and the corresponding eigenvector.

If the maximum eigenvalue is also the eigenvalue of maximum absolute value, then this can be accomplished by an iterative procedure. Choose any convenient starting vector $\tilde{\mathbf{x}}_0$.

If we take $\tilde{\mathbf{x}}_n = \tilde{\mathbf{A}}\tilde{\mathbf{x}}_{n-1}$ for $n \geq 1$, then $\tilde{\mathbf{x}}_n$, when normalized, approaches the eigenvector which is sought. Choose positive numbers c_n so that

$$\tilde{\mathbf{x}}_n = \frac{\tilde{\mathbf{A}}\tilde{\mathbf{x}}_{n-1}}{c_n}$$

has unit length. Then $\tilde{\mathbf{x}}_n$ approaches the eigenvector and c_n approaches the eigenvalue.

The rate of convergence of this procedure depends on the size of the next largest eigenvalue, as compared with the first. In our application, the convergence is slow for low SNR. However, the method can be modified to speed up the convergence. When suitably modified, the difference between $\tilde{\mathbf{x}}_n$ and the eigenvector decreases by a factor of the order of $(\gamma - 1)/\sqrt{L}$ at each step.

Appendix B

Formulas Used for Figs. 3 and 4

The formulas used for Figs. 3 and 4 are presented here.

For method 1,

$$E(|E_2|^2+|E_3|^2)=\frac{\gamma(\frac{1}{4}\gamma^2+K-1)}{L(\gamma-1)}+\frac{\gamma}{M(\gamma-1)}\left[\frac{1-8\gamma+4\gamma^2}{4(\gamma-1)^2}\sum_{k=1}^{K}|\tilde{T}_k|^4+\gamma\right] \tag{B-1}$$

For method 2,

$$\begin{aligned}E(|E_2|^2+|E_3|^2)=&\frac{1}{L}\left[\frac{\gamma(\gamma-1)}{4|\tilde{T}_1|^4}(1+|\tilde{T}_1|^2)^2+(K-1)\frac{1+|\tilde{T}_1|^2}{|\tilde{T}_1|^2}\right]\\&+\frac{1}{M}\left[\frac{\gamma(\gamma-1)}{4|\tilde{T}_1|^4}-\frac{\gamma-1}{|\tilde{T}_1|^2}+2+2|\tilde{T}_1|^2+\sum_{k=1}^{K}|\tilde{T}_k|^4\right]\end{aligned} \tag{B-2}$$

For method 3,

$$\begin{aligned}E(|E_2|^2+|E_3|^2)=&\frac{1}{4}\gamma(\gamma-1)\frac{(1+|\tilde{T}_1|^2)^2}{N|\tilde{T}_1|^4}+\frac{1}{L}\left[\frac{K-2+\gamma^2}{|\tilde{T}_1|^2}+K-\gamma-1\right]\\&+\frac{1}{M}\left[\frac{\gamma(\gamma-1)}{4|\tilde{T}_1|^4}-\frac{\gamma-1}{|\tilde{T}_1|^2}+2+2|\tilde{T}_1|^2+\sum_{k=1}^{K}|\tilde{T}_k|^4\right]\end{aligned} \tag{B-3}$$

For method 4,

$$E(|E_2|^2+|E_3|^2)=\frac{\gamma}{L(\gamma-1)}\left[\frac{1}{4}\gamma^2+K-1+\frac{(\gamma-\frac{1}{2})^2}{K-1}\right] \tag{B-4}$$

For method 1′,

$$E(|E_2|^2+|E_3|^2)=\frac{\gamma(\frac{1}{4}\gamma^2+K-1)}{L(\gamma-1)}+\frac{\gamma(\gamma-\frac{1}{2})^2}{MK(\gamma-1)} \tag{B-5}$$

For method 2′,

$$E(|E_2|^2+|E_3|^2)=\frac{1}{L}\left[\frac{\gamma(\gamma-1)}{4|\tilde{T}_1|^4}(1+|\tilde{T}_1|^2)^2+(K-1)\frac{1+|\tilde{T}_1|^2}{|\tilde{T}_1|^2}\right]+\frac{1}{MK}\left[\frac{\gamma(\gamma-1)}{4|\tilde{T}_1|^4}-\frac{\gamma^2-1}{|\tilde{T}_1|^2}+\gamma^2+\gamma+1\right] \tag{B-6}$$

For method 3′,

$$E(|E_2|^2 + |E_3|^2) = \frac{1}{4}\gamma(\gamma - 1)\frac{(1 + |\tilde{T}_1|^2)^2}{N|\tilde{T}_1|^4} + \frac{1}{L}\left[\frac{K - 2 + \gamma^2}{|\tilde{T}_1|^2} + K - \gamma - 1\right]$$

$$+ \frac{1}{MK}\left[\frac{\gamma(\gamma - 1)}{4|\tilde{T}_1|^4} - \frac{\gamma^2 - 1}{|\tilde{T}_1|^2} + \gamma^2 + \gamma + 1\right] \tag{B-7}$$

N94-29662

TDA Progress Report 42-116 February 15, 1994

Convolutional Encoding of Self-Dual Codes

G. Solomon[1]

There exist almost complete convolutional encodings of self-dual codes, i.e., block codes of rate 1/2 with weights w, $w = 0$ *mod 4. The codes are of length* $8m$ *with the convolutional portion of length* $8m-2$ *and the nonsystematic information of length* $4m-1$*. The last two bits are parity checks on the two* $(4m-1)$ *length parity sequences. The final information bit complements one of the extended parity sequences of length* $4m$*. Solomon and van Tilborg [1] have developed algorithms to generate these for the Quadratic Residue (QR) Codes of lengths 48 and beyond. For these codes and reasonable constraint lengths, there are sequential decodings for both hard and soft decisions. There are also possible Viterbi-type decodings that may be simple, as in a convolutional encoding/decoding of the extended Golay Code [2]. In addition, the previously found constraint length* $K = 9$ *for the QR (48, 24;12) Code is lowered here to* $K = 8$*. In future articles, we shall search for candidates with small* K *constraint lengths for the (80,40;16) Quadratic Residue Code or some isomorph.*

I. Technique

There exist almost complete convolutional encodings of self-dual codes, i.e., block codes of rate 1/2 with weights $w, w = 0 \bmod 4$. A new technique applied here is to generate convolutional codes of lengths $2(4m - 1)$ using specifically related irreducible polynomials to give a tail-bitten block code of distance $d-2$. Adjoining an additional information bit that complements one of the sequences of length $(4m - 1)$ and then appending two bits of parity on these individual $(4m - 1)$ sequences, one obtains an $(8m, 4m; d)$ code where all code words have weights that are multiples of 4. The minimum distance d will be optimal or near optimal for binary codes of rate 1/2 and length $8m$, if the polynomials have been chosen well.

Let $n = 4m - 1$. We choose the polynomials $p(x)$ and $q(x)$ to be taps of a convolutional encoder of K stages. We feed in a sequence of $n + K - 1$ information bits to the encoder with the first and last $(K - 1)$ bits the same. This generates a $(2n, n; d)$ block code. We append two additional parity checks on the two sequences of length

---

[1] Independent consultant to the Communications Systems Research Section.

n. A final information bit is modulo two added to the sequence generated by one of the polynomials, say $p(x)$. The final result is an $(8m, 4m; d)$ code.

Notice that this definition of the code differs from the one in the preceding paragraph. Clearly it does not matter in which order the parity checks are appended and the final information bit is added. For certain proofs, one definition will be preferable. The choice of $p(x)$ and $q(x)$ guarantees the even weights of the convolutionally encoded portion to be multiples of 4. The last two parity bits and the choice of the lengths guarantee that all weights of the code will be multiples of 4. This will be proven in the next section using the Solomon–McEliece Γ_2 formula. (See [3].)

In order to compute d, choose an irreducible polynomial $p(x)$ of degree $K - 1$ that is relatively prime to $x^n + 1$. Define $q(x) = x^{K-1}p(x^{-1})$. Find $p(x)/q(x) \equiv f(x)$ (mod $x^n + 1$). Test for the distance d relative to the total length of the convolutionally generated $(2n, n; d)$ code.

II. A Construction Theorem

For any positive integer $m \geq 3$, let $n = 4m - 1$. We may construct a block code of rate 1/2 of length $2(n+1) = 8m$ so that

(1) All of the weights are multiples of 4.

(2) The portion of length $2n$ is convolutionally generated by a K stage register $p(x)$ and $q(x)$ of degree $K - 1$ whose entries are $n + K - 1$ bits long with the first and last $(K - 1)$ bits identical. Two parity sequences, each of length n, are nonsystematically generated, one for each polynomial.

(3) The $(n + 1)$th information bit is added to each bit of the $p(x)$ parity sequence.

(4) The last 2 bits are overall parity checks on the n bit parity sequences.

(5) The minimum distance $d = 4d'$ is determined by the encoder polynomials $p(x)$ and $q(x)$ of degree $K - 1$. The polynomials are related thus: $q(x) = x^{K-1}p(x^{-1})$.

(6) $p(x)$ is chosen to give the maximum Hamming distance possible for the lengths $2(n+1)$. For example, it is shown in [1] that a $p(x)$ with $K = 9$ can be used to construct the (48,24;12) Quadratic Residue Code. This is improved to $K = 8$ here.

Proof: Let us examine the parity sequences of lengths $n = 4m - 1$ generated by $p(x)$ and $q(x)$ of degree $K - 1$. These are of the form $I(x)p(x)$ (mod $x^n + 1$) and $I(x)q(x)$ (mod $x^n + 1$). We shall obtain the Mattson–Solomon (MS) representation for the code word above. Let c_i be the MS coefficients of the information sequence $I(x)$ of length $n = 4m - 1$. For a suitably chosen z, $c_i = \sum_{j=0}^{(n-1)} a_j z^{-ij}$, where z is a primitive nth root of unity and a_i is the information sequence associated with $I(x)$. Then we get $c_i p(z^{-i})$ and $c_i q(z^{-i})$ for the MS coefficients of the parity sequences $I(x)p(x)$ (mod $x^n + 1$) and $I(x)q(x)$ (mod $x^n + 1$).

If $c_o = 0$, both the parity sequences have even weight and the even weights mod 4 are given by the Solomon–McEliece Γ_2 formula. If d_i are the MS coefficients, then $\Gamma_2 = \sum_{i=0}^{(n-1)/2} d_i d_{n-i}$. For the $p(x)$ parity sequence, this gives

$$\Gamma_2 = \sum_{i=0}^{(n-1)/2} c_i p(z^i) c_{-i} p(z^{-i})$$

For the $q(x)$ parity sequence, one obtains

$$\Gamma_2 = \sum_{i=0}^{(n-1)/2} c_i q(z^i) c_{-i} q(z^{-i})$$

Using the relationship of $p(x)$ to $q(x)$, one obtains equality of Γ_2 for the two sequences. Thus, the weights mod 4 are the same for the two parity sequences, and the sum of the weights mod 4 is therefore zero. This conclusion is unchanged when the two overall parity checks are appended to the convolutionally encoded parity sequences because, for this case, the parity checks are both zero. Finally, when the nth information bit is added to the $p(x)$ parity sequence of full length $4m$, the weight mod 4 is also unchanged. Thus, the total weight sum in this case is again a multiple of 4.

The odd weights of the parity sequences are generated by complementing the even-weight words. Consider the all-one $I(x)$ with only $c_0 = 1$. This yields two all-one parity sequences. Appending the overall parity checks to both gives two all-one vectors of length $2(n+1) = 8m$. All odd weights extended by even parity are thus transformed now to even weights divisible by 4.

From Solomon–van Tilborg [1], one obtains for $m = 3$ the Golay Code with $K = 4$ and $p(x) = x^3 + x + 1$. For

$m = 6$, one obtains the (48,24;12) Quadratic Residue Code with $K = 9$ and $p(x) = x^8 + x^4 + x^3 + x + 1$.

III. New Construction of the (48, 24;12) Quadratic Residue Code

In this section, we introduce an improved construction of the (48,24;12) Quadratic Residue (QR) Code that requires a convolutional encoding with $K = 8$ instead of $K = 9$.

Let $n = 23, K = 8$, $p(x) = x^7 + x^6 + x^5 + x^2 + 1$, and $q(x) = x^7 + x^5 + x^2 + x + 1$. One obtains the QR (48,24;12) Code in the following manner.

A. Encoding

Let the information bits be $i(0)$, $i(1)$, $i(2)$, $i(3)$, $\ldots$, $i(22)$, $i(\infty)$. Extend this sequence 7 bits backward by defining $i(-j) = i(23 - j); j = 1, 2, \ldots, 7$.

The encoded bits are $b(j)$, $c(j)$, $j = 0, 1, \ldots, 23$, where for $j = 0, 1, \ldots, 22$,

$$b(j) = i(j-7) + i(j-6) + i(j-5) + i(j-2) + i(j) + i(\infty)$$

$$c(j) = i(j-7) + i(j-5) + i(j-2) + i(j-1) + i(j)$$

$$b(23) = \sum_{j=0}^{22} b(j)$$

$$c(23) = \sum_{j=0}^{22} c(j)$$

Transmit the sequence $b(j), c(j); 0 \leq j \leq 23$.

Thus, a (46,22;10) tail-biting convolutional code is transmitted, initiated by a 7-bit sequence that repeats after 16 more. To these two parity sequences are adjoined overall parity checks. The 24th information bit of the QR Code determines whether the $b(j)$ sequence is complemented. The above sequence is the (48,24;12) Quadratic Residue Code.

To see this, let the additive recursion or check polynomial for the code be given in powers of x by 0, 1, 4, 6, 9, 12, 13, 15, 16, 19, 20, 24. This generates the (47,24;11) code, with the additional 48th bit the overall parity check. This gives the proper rate 1/2 and the distance = 12.

There exist a code word at coordinates 0, 2, 5, 6, 7, 13, 15, 22, 23, 28, 37 (in powers of, say, β, a 47th root of unity) and the overall parity check bit. Identify the quadratic residues with the trace one elements and the nonquadratic residues as the trace zero elements. If we take $x = 1$, the 0th power coordinate, as the overall parity check on the other 23 trace one elements, and $x = 0$, the additive identity in the field $GF(2^{23})$, as the overall parity check on the 23 trace zero elements, there are 5 coordinates in each set. In the trace one elements, choosing β so that $\mathrm{Tr}\beta = 1$, one has coordinates 2, 6, 7, 28, 37. In the trace zero elements, the powers or coordinates that occur are 5, 13, 1, 5, 22, 23. The powers of 2 are 1 2 4 8 16 32 17 34 21 42 37 27 7 14 28 9 18 36 25 3 6 12 24. In powers of 4, starting with 37, one gets (37 7 28 18 25 6 24 2 8 32 34 42 27 14 9 36 3 12 1 4 16 17 21). Similarly, the nonquadratic residues in powers of 4, starting with 22, are (22 41 23 45 39 15 13 5 20 33 38 11 44 35 46 43 31 30 26 10 40 19 29). Note that if we choose $p(x) = x^7 + x^5 + x^2 + x + 1$ and $q(x) = x^7 + x^6 + x^5 + x^2 + 1$, this will generate a convolutional portion of length 46 and, adding the overall parity checks, this will yield the QR Code. Thus, $K = 8$.

Note $p(x)/q(x) \pmod{x^{23} + 1} = x^{20} + x^{19} + x^{17} + x^{16} + x^{14} + x^{12} + x^{10} + x^6 + x^3$. This implies that the following positions form a code word: 37, 45, 13, 38, 44, 46, 31, 30, 10, 40, 0, $x = 0$ (the additive identity).

Cyclically shifting from 30 on, one obtains a code word in code coordinates starting from 0: [0, 1, 7, 8, 10, 14, 15, 16, 17, 27, 30].

IV. Viterbi Decoding

The following is a procedure for decoding the convolutionally encoded self-dual code based on Viterbi decoding. First, we decode assuming that the 24th information bit is 0, i.e., the received length 23 $(p(x), q(x))$ parity sequences are usable for the Viterbi decoding. One needs only to guess or know the initial 7 bits and one can apply Viterbi decoding using tail-biting techniques or try all 128 possible initial 7-tuples.

If one does not know the initial 7 bits, one may take the received encoded sequences (assuming that the 24th information bit is 0) and concatenate them until they form a chain of about 3 or 4 and then Viterbi decode as if starting in the middle. We use the parity information and take advantage of Hamming distance 12.

Alternatively, assume that the $p(x)$ sequence has been complemented and so concatenate the parity sequences $(1+p(x), q(x))$ to a length of 3 or 4, i.e., 69 or 92 bits, and Viterbi decode.

V. Future Work

In encoding and decoding the (80.40;16) extended QR Code, one uses the (78,39;14) tail-biting convolutional subcode. We shall try to find the smallest constraint length K for which our construction will work. If K is small enough, then a Viterbi decoding will do. Otherwise, a sequential decoding procedure or its modification may be necessary.

References

[1] G. Solomon and H. C. A. van Tilborg, "A Connection Between Block and Convolutional Codes," *SIAM J. Appl. Math*, vol. 37, no. 2, pp. 358–369, October 1979.

[2] R. W. D. Booth, M. A. Herro, and G. Solomon, "Convolutional Coding Techniques for Certain Quadratic Residue Codes," *International Telemetering Conference (XI) Proceedings*, Silver Springs, Maryland, pp. 168–177, October 1975.

[3] G. Solomon and R. J. McEliece, "Weights of Cyclic Codes," *Journal of Combinatorial Theory*, vol. 1, no. 4, pp. 459–475, December 1966.

N94-29663

TDA Progress Report 42-116 February 15, 1994

Optimizing the Galileo Space Communication Link

J. I. Statman
Communications Systems Research Section

The Galileo mission was originally designed to investigate Jupiter and its moons utilizing a high-rate, X-band (8415 MHz) communication downlink with a maximum rate of 134.4 kb/sec. However, following the failure of the high-gain antenna (HGA) to fully deploy, a completely new communication link design was established that is based on Galileo's S-band (2295 MHz), low-gain antenna (LGA). The new link relies on data compression, local and intercontinental arraying of antennas, a (14,1/4) convolutional code, a (255,M) variable-redundancy Reed–Solomon code, decoding feedback, and techniques to reprocess recorded data to greatly reduce data losses during signal acquisition. The combination of these techniques will enable return of significant science data from the mission.

I. Introduction

The Galileo spacecraft was launched in October 1989 for a 6-year cruise toward Jupiter [1]. Its Venus–Earth–Earth Gravity Assist (VEEGA) trajectory, shown in Fig. 1, includes encounters with Earth and two key asteroids, leading to its prime objective—long-term investigation of the Jovian system. During the investigation, Galileo will release a probe into the Jovian atmosphere, encounter Jupiter and its moon Io at close range, and conduct an 18-month, 10-encounter orbital tour of Europa, Ganymede, and Calisto. Throughout its travel, a variety of sensors will collect scientific data such as images, magnetic fields, and chemical composition for transmission to NASA's Deep Space Network (DSN) tracking stations.

The Galileo downlink was originally designed to utilize a 15-ft-diam (4.572 m) parabola-shaped HGA on the spacecraft. This antenna was folded during the launch and early flight awaiting an unfurling sequence that was scheduled for April 1991. However, the HGA did not open properly, resulting in a nonsymmetrical antenna pattern with wide gain fluctuations, rendering it ineffective for reliable communications. After repeated attempts to solve this anomaly, the mission was reoriented in March 1993 to use the S-band LGA.

Because of the great reduction of the power received at the ground stations, the Galileo project has teamed with TDA and the appropriate technical organizations to develop a communications plan that maximizes the data return for the LGA-based S-band link.[1] The remainder of this article describes in some detail the techniques utilized in this design and their applications to future space missions.

II. Link Design

In redesigning the link, the team searched for methods that maximize the "bang for the buck," i.e., those that

---

[1] L. Deutsch and J. Marr, *Low Gain Antenna S-Band Contingency Mission*, 1625-501 (internal document), Jet Propulsion Laboratory, Pasadena, California, April 10, 1992.

provide the most cost-effective increases in science return. This proved to be a delicate task—unlike measures like transmitter power or data rate that are objective and lend themselves to easy quantifying and comparison, "science return" is a subjective measure and depends on the end-user's preferences. The resulting design relies heavily on data compression, augmented by channel coding, arraying, and antenna improvement, to both increase the rate of the downlink and the "value" of each downlinked bit.

As shown in Fig. 2, when implementing this new design, JPL will be loading new software on the Galileo spacecraft, enhancing the Deep Space Communications Complexes (DSCCs) at Goldstone, California; Canberra, Australia; and Madrid, Spain, and upgrading other processing facilities. The DSCC improvements consist of a new subsystem, denoted DSCC Galileo Telemetry (DGT), that will be installed at the DSCCs in late 1995 and improvements to the Canberra antennas.

A. Data Compression

Galileo generates three types of data: images, low-rate science, and engineering. With a large number of algorithms available in the published literature, the overriding issue was to identify those algorithms that meet the spacecraft constraints and can be implemented in software in the spacecraft computers. Galileo, of a late 1970's design, uses what, at the time, was modern technology: 8-bit and 16-bit microprocessors with total memory of less than 1 MByte, well below what would be considered acceptable for a modern desktop workstation.

The design team has elected to compress the image data primarily with an integer cosine transform (ICT) [2,3], a derivative of the conventional discrete cosine transform (DCT) method. The ICT is an especially economical implementation for fixed point processors. In the past, lossy algorithms such as the DCT or ICT have been rejected from use in deep space probes due to the uniqueness of the data. With the Galileo predicament, a team of developers and scientists determined that with compression ratios as high as 10:1, the resulting images, though not ideal, are of acceptable quality.

The ICT implementation for Galileo is augmented with an error-containment capability. This is important because the deep space link often operates with reduced margins and is sensitive to data gaps. The ICT error containment is applied to minimize the impact of the gaps that could not be avoided.

For the low-rate science and engineering data, the design team considered lossless algorithms focusing on the Rice [4], Lempel–Ziv-Welsh (LZW) [5], and Huffman code [6] approaches. These approaches are still being evaluated, with emphasis on minimizing the additional loading on the restricted spacecraft computer resources.

B. Data Rate Averaging

Figure 3 shows qualitatively how the "science capture" and "downlink capacity" vary for a typical deep space mission. The downlink capacity varies primarily with the distance of the spacecraft from Earth. In contrast, science capture is often massive during short events (e.g., planetary encounters) with long "cruise" periods in between, when a much lower volume of science data is captured. Missions communications systems are designed to handle the peak science capture, resulting in excess link capacity during the "cruise" phases. Prior to the Galileo HGA anomaly, this was the planned Galileo strategy. However, with the anomaly, it became desirable to buffer data during peak science capture periods to reduce the variation in downlink rate.

Galileo has two such buffering areas: an onboard tape recorder and the resident memory. The tape recorder, with a total capacity of approximately 100 MBytes, is used to record images and other data at encounter periods and then replay the data at a much slower rate during cruise periods. The resident memory is used to store and replay the probe data and to add a further buffer between the tape recorder replay and the downlink transmitter.

This buffering allows for spreading of the data return to optimize the link utilization and minimize unused link capacity, in line with the low achievable data rates and the high goals of the Galileo mission. However, it also imposes a heavy burden on the ground receiving stations. As currently stated, Galileo requires continuous support (24 hours per day for almost 2 years) from the DSN 70-m network, plus augmentation from some 34-m antennas.

C. Improved Channel Coding

Galileo planned on utilizing a channel coding scheme similar to the standard Consultative Committee for Space Data Standards (CCSDS) channel coding: concatenated (7,1/2) convolutional code and (255,223) Reed–Solomon (R/S) code. To improve performance, a modified coding scheme [7], shown in Fig. 4, is implemented. Its key features are listed below:

(1) A (14,1/4) convolutional code that provides an approximate 1.2-dB coding gain over the (7,1/2) code. The selection of the (14,1/4) code is forced by the hardware configuration of Galileo—it is impossible

to bypass the hardware (7,1/2) encoder, hence the higher-constraint code is constructed by cascading an (11,1/2) software encoder to the (7,1/2) hardware encoder. Though not optimal among (14,1/4) convolutional codes, it provides remarkable coding gain.

(2) A variable redundancy R/S code. The particular implementation utilizes a four-redundancy code.

(3) A redecoding path, where data that have been decoded by the Viterbi decoder and R/S decoder are then passed a second time (and, if needed, additional times) through the Viterbi and R/S decoders. During each pass, the Viterbi decoder operation is "aided" by the knowledge that some bits were determined "true" in previous pass(es).

(4) An improved synchronization scheme [8] that accomplishes frame synchronization and Viterbi decoder node synchronization jointly.

Overall, the decoder provides a coding gain of approximately 1.8 dB as compared with the standard published by the CCSDS. Note that the decoder performance is measured at a bit error rate of 5×10^{-3}.

D. Minimization of Gaps

As described earlier, the downlink will operate continuously and transmit compressed data. Because of the compression and coding, even minute interruptions pose the risk of data being undecodable, with resulting severe damage to the decompression process. Such gaps occur in the deep space communications link due to receiver and decoder acquisition periods, pointing errors, and momentary equipment failures. Though it is impossible to fully prevent these gaps, the DGT incorporates two capabilities that greatly reduce their impact:

(1) The DGT's recording and buffering, as shown in Fig. 5, provides extensive recording of the signals, including those prior to any synchronization. This protects against data loses during acquisition.

(2) The DGT uses adaptive gap-closure algorithms consisting of software that attempts to recover data by reprocessing recorded data while adjusting the process parameters (e.g., tracking loop bandwidth) to recover data that were lost due to mismatches between the actual signal and the processing parameters.

Clearly, gaps caused by complete signal loss (e.g., large antenna pointing errors) are likely to be not recoverable. But, by and large, these techniques are expected to provide the decompressor with a minimal-gap bit stream.

E. Arraying

A popular technique for increasing the data rate is to array the signals from multiple antennas. For the weak Galileo signals, only large DSN antennas with diameters of 34 m and 70 m are used. Two arraying techniques are applied: full-spectrum combining [9,10] and complex-symbol combining [11].

Unfortunately, while arraying increases the overall ratio of antenna gain to system noise temperature (G/T), it also tends to reduce the overall reliability: the link, marginal as it is, becomes dependent on the correct operation of a number of antennas. In addition, the operational complexity of such a configuration, and the associated probability of human error, must be considered. Nevertheless, judicious application of arraying is expected to improve the overall science return.

F. Improved Antennas

Finally, the G/T of the individual antennas involved in the Galileo support was examined. It was observed that the DSN antennas were designed for multifrequency support, primarily at the S- and X-bands. The multifrequency support, as well as the extensive test capability, resulted in receiving systems with less-than-optimal S-band G/T. Since Galileo is visible primarily from the southern hemisphere, the DSN embarked on modifying the S-band receiving system in the Canberra 70-m antenna to improve its G/T by 0.97 dB. This is achieved, primarily, by reducing the system noise temperature from 15.6 to 12.5 K.

III. Future Uses

Is the approach taken in the improvement of the downlink suitable for Galileo only, or does it have a long-term payoff? The answer depends on the direction that the space program takes.

The DGT design is especially appropriate for the space program that NASA envisions, focusing on a large number of low-cost missions. For such missions, highly-directional antennas (mechanical or steered-beam) are costly; broad-beam antennas may be the norm. With these antennas, and the limited power offered by nonnuclear-based power supplies, the communications engineer must contend with lower data rates and tighter utilization of any communication link excess. The DGT approach provides an avenue to optimize the science return for a relatively low data rate.

Three classes of missions are of special interest:

(1) Multiple objects-in-a-beam missions. For missions that use several vehicles to land and/or orbit a

planet, a single antenna can be used for tracking. With the DGT approach, a single recorded stream can be processed sequentially to extract the data for the individual vehicles in near-real time. Transmissions for individual vehicles can be separated using any of the multiple-access techniques currently in use.

(2) Large uncertainty-in-predict missions. At times, spacecraft experience events where the characteristics of the downlink signal pose large uncertainties. Often these are associated with high dynamic events—change of trajectory, release of a probe, etc. The DGT, not requiring synchronization prior to the first recorder, allows capturing of the signal and postevent recovery.

(3) Short, intense, science-capture missions. For some missions, all the science data are captured during a short encounter period. The DGT enables the spacecraft to buffer the data on board and slowly downlink it, assuring the ability to close gaps and recover an uninterrupted science stream.

Overall, the DGT approach seems highly applicable to future missions. In fact, the only part of the DSCC augmentation that will find minor usage after this mission is the enhancement for the 70-m antenna. It will likely be dismantled after the end of Galileo support.

IV. Conclusions

A science-rich Galileo mission is being enabled through a concentrated effort to optimize the communications downlink with modifications both on Galileo and in NASA's ground tracking system. Much of the techniques, approach, and equipment can be applied to support other deep space missions.

Acknowledgments

The author is indebted to Dr. Sami Hinedi and Mr. Pat Beyer for reviewing this article and providing insightful comments. The author also thanks the many people on the design and implementation team whose hard work is reflected here.

References

[1] C. T. Russell, ed., *The Galileo Mission*, Boston: Kluwer Academic Press, 1992 (reprinted from *Space Science Review*, vol. 60, nos. 1–4, pp. 1–616, 1992).

[2] K. M. Cheung and K. Tong, "Proposed Data Compression Schemes for the Galileo S-Band Contingency Mission," in *Proceedings of the 1993 Space and Earth Science Data Compression Workshop*, Snowbird, Utah, April 2, 1993.

[3] W. Cham, "Development of Integer Cosine Transform by the Principles of Dyactic Symmetry," in *IEE Proceedings*, part 1, vol. 136, no. 4, pp. 276–282, August 1989.

[4] R. Rice, *Some Practical Universal Noiseless Coding Techniques*, JPL Publication 79-22, Jet Propulsion Laboratory, Pasadena, California, March 1979, and JPL Publication 83-17, Jet Propulsion Laboratory, Pasadena, California, March 1983.

[5] T. A. Welsh, "A Technique for High Performance Data Compression," *Computer*, vol. 17, no. 6, pp. 18–19, June 1984.

[6] D. A. Huffman, "A Method for the Construction of Minimum Redundancy Codes," in *Proceedings of the IRE*, vol. 40, pp. 1098–1101, 1952.

[7] T. Chauvin and K. M. Cheung, "A Parallel Viterbi Decoder for Shared Memory Multiprocessor Architecture," presented at the 3rd SIAM Conference on Linear Algebra in Signals, Systems, and Control, Seattle, Washington, August 1993.

[8] J. Statman, K. M. Cheung, T. Chauvin, J. Rabkin, and M. Belongie, "Decoder Synchronization for Deep Space Missions," *The Telecommunications and Data Acquisition Progress Report 42-116, vol. October–December 1993*, Jet Propulsion Laboratory, Pasadena, California, pp. 121–127, February 15, 1994.

[9] A. Mileant and S. Hinedi, "Overview of Arraying Techniques in the Deep Space Network," *The Telecommunications and Data Acquisition Progress Report 42-74, vol. April–June 1983*, Jet Propulsion Laboratory, Pasadena, California, pp. 13–28, August 15, 1983.

[10] D. H. Rogstad, "Suppressed Carrier Full-Spectrum Combining," *The Telecommunications and Data Acquisition Progress Report 42-107, vol. July–September 1991*, Jet Propulsion Laboratory, Pasadena, California, pp. 12–20, November 15, 1991.

[11] D. Divsalar, "Symbol Stream Combining Versus Baseband Combining for Telemetry Arraying," *The Telecommunications and Data Acquisition Progress Report 42-104, vol. October–December 1990*, Jet Propulsion Laboratory, Pasadena, California, pp. 109–115, February 15, 1991.

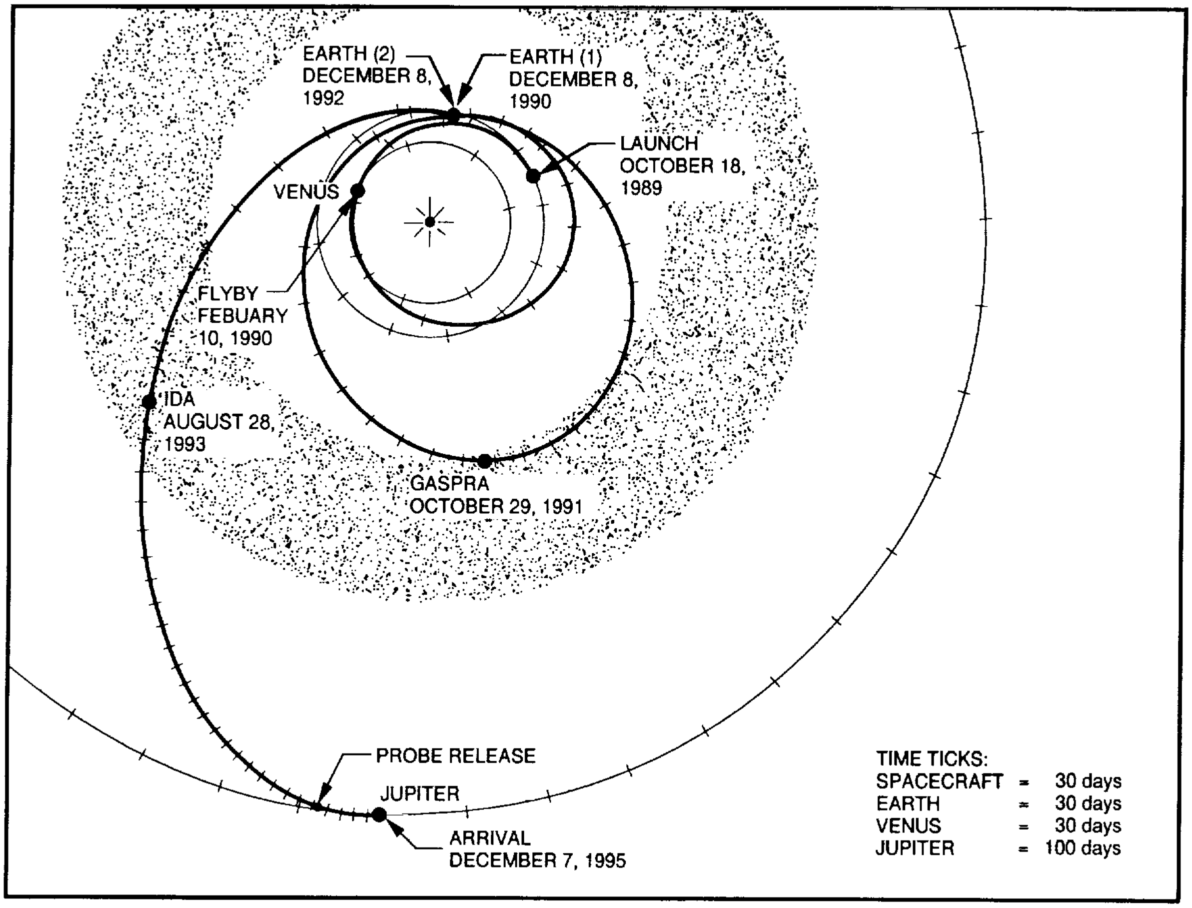

Fig. 1. The Galileo VEEGA trajectory.

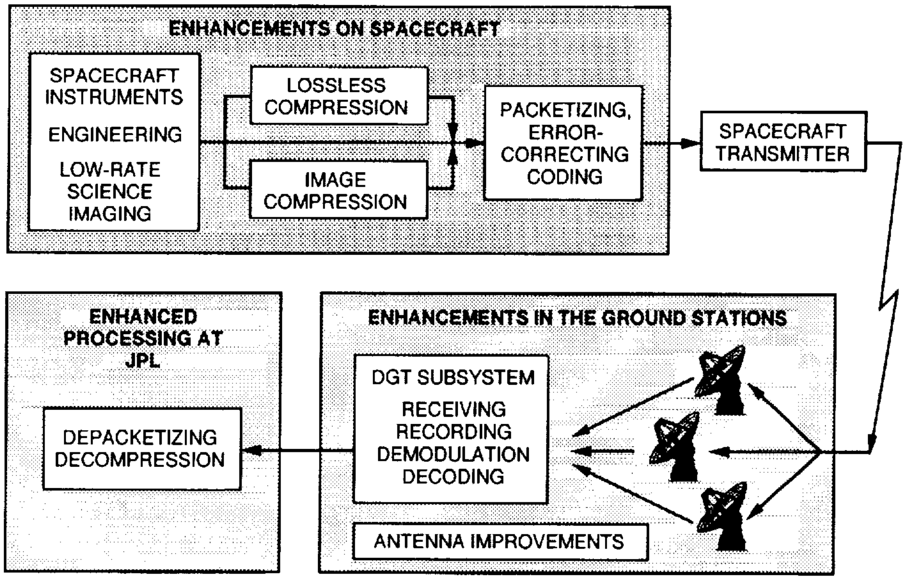

Fig. 2. End-to-end downlink flow.

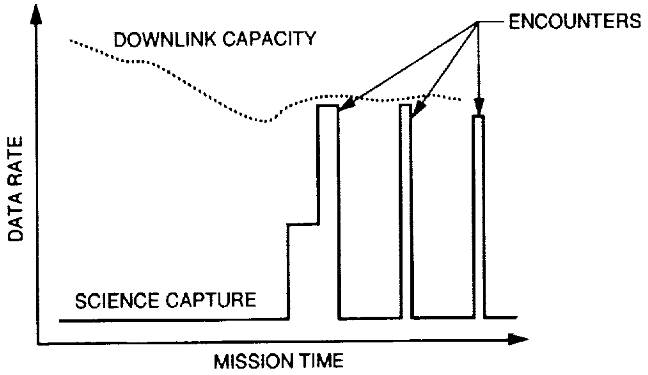

Fig. 3. "Science capture" versus "downlink capacity."

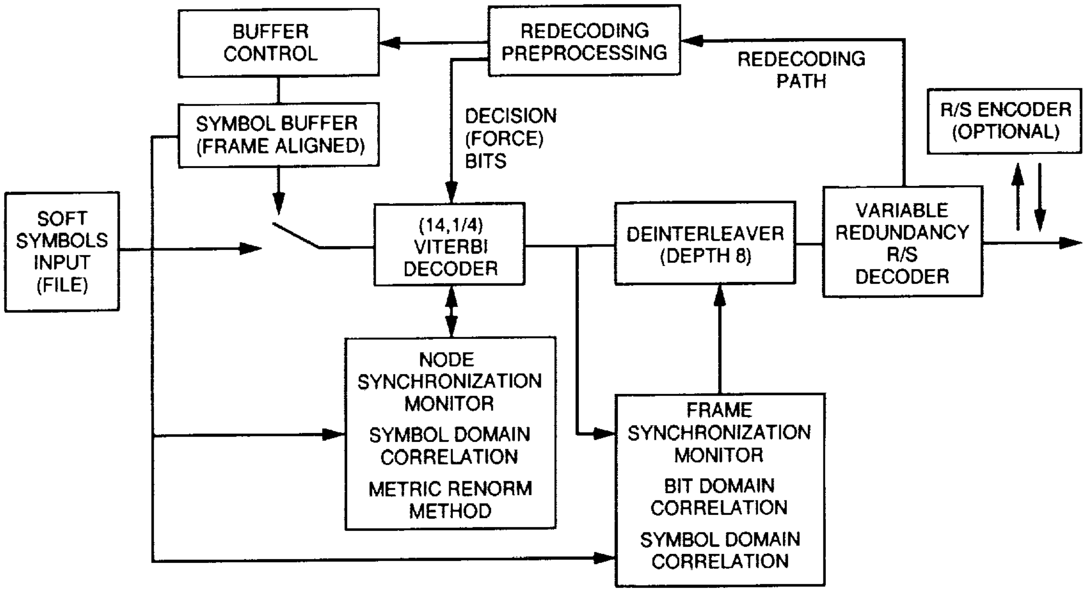

Fig. 4. The Galileo decoder.

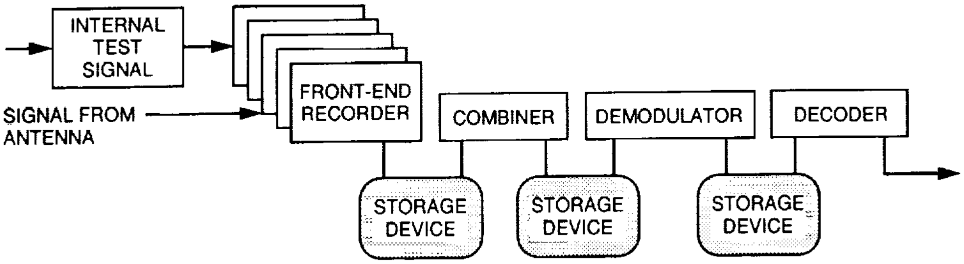

Fig. 5. DGT architecture.

N94-29664

Decoder Synchronization For Deep Space Missions

J. I. Statman, K.-M. Cheung, T. H. Chauvin, J. Rabkin, and M. L. Belongie
Communications Systems Research Section

The Consultative Committee for Space Data Standards (CCSDS) recommends that space communication links employ a concatenated, error-correcting, channel-coding system in which the inner code is a convolutional (7,1/2) code and the outer code is a (255,223) Reed–Solomon code. The traditional implementation is to perform the node synchronization for the Viterbi decoder and the frame synchronization for the Reed–Solomon decoder as separate, sequential operations. This article discusses a unified synchronization technique that is required for deep space missions that have data rates and signal-to-noise ratios (SNRs) that are extremely low. This technique combines frame synchronization in the bit and symbol domains and traditional accumulated-metric growth techniques to establish a joint frame and node synchronization. A variation on this technique is used for the Galileo spacecraft on its Jupiter-bound mission.

I. Introduction

The traditional approach to decoding the channel error-correcting coding in the space communication links [1] is for the implementation to follow the CCSDS functional model [2] shown in Fig. 1, i.e., establish a concatenated decoder consisting of two distinct stages: a Viterbi decoder and a Reed–Solomon decoder, with no feedback between the two stages. Each of the two decoders requires appropriate synchronization: the Viterbi decoder requires node synchronization (the grouping of n-tuplets of soft symbols that correspond to a single information bit), and the Reed–Solomon decoder requires frame synchronization (the detection of the transport frame and the extraction of Reed–Solomon words). In most applications, data received prior to the accomplishment of synchronization are lost; however, as long as the symbol-signal-to-noise ratio (SSNR, E_S/N_0) is relatively high, the synchronization time is short and the data loss is often ignored.

For a deep space communications environment, such an approach is often deficient—E_S/N_0 could be low, hence the synchronization time, measured in number of bits, would be longer. As the data rate decreases, the synchronization time, fixed in terms of number of bits, can result in loss of a significant percent of total data. Also, the sequential nature of the synchronization process compounds the data loss. To speed the synchronization process and reduce the data loss, we introduce here a joint synchronization technique that is being applied in the ground support for the Galileo deep space mission to Jupiter [3].

Section II introduces the core algorithms and the joint synchronization approach. Section III discusses the application of joint synchronization in several scenarios, and Section IV presents two specific cases where the joint synchronization approach is applied.

II. Description of Synchronization Algorithms

The structure of the general joint synchronization decoder is shown in Fig. 2. It consists of the traditional series of processing functions, namely a Viterbi decoder, a deinterleaver, and a Reed–Solomon decoder, preceded by a soft symbol buffer. The processing functions are controlled by a joint synchronization function, which in turn relies on several core synchronization algorithms. In this article, we select three such core synchronization algorithms: a frame-marker correlator in the symbol domain, a frame-marker correlator in the bit domain, and an accumulated-metric growth-rate indicator. It is worth noting that decoders often contain other synchronization indicators that can be integrated into a joint synchronizer using techniques similar to those described below.

A. Bit-Domain Correlation

This algorithm examines the Viterbi-decoded bits at the output of the Viterbi decoder for presence of the frame marker pattern. When the pattern is detected, it indicates that the node synchronization hypothesis is "true" and, by definition, frame synchronization was accomplished.

Let the transport frame be of length M, including a frame marker of length N at the beginning of each frame. Let the frame marker be $\langle d_o(i),\ i = 0, \ldots, N-1,\ d_o(i) = \pm 1 \rangle$. Then, the transmitted data stream can be represented as

$$D(i) = \left\langle \begin{matrix} d_o(i \ mod \ M), & i \ mod \ M < N \\ data, & i \ mod \ M \geq N \end{matrix} \right\rangle \qquad (1)$$

The bit-domain correlation algorithm computes the running correlation, $J_{bits}(k)$, between the frame marker and the received signal $s(i)$

$$J_{bits}(k) = \frac{1}{N} \sum_{i=0}^{N-1} d_o(i) s(i+k) \qquad (2)$$

where $s(i)$ is $D(i)$ contaminated by the effects of transmission, reception, and decoding. The expected value of $J_{bits}(k)$ is 1 when the received sequence is perfectly aligned with the frame marker. Elsewhere, for a properly selected frame marker, its autocorrelation properties ensure that the expected value of $J_{bits}(k)$ is near zero. In practice, there are two methods to implement the bit-domain correlation algorithm:

1. Testing for threshold, where the value of $J_{bits}(k)$ is compared against a threshold for a large number of k's. When the value of $J_{bits}(k)$ exceeds the threshold for the first time at k_0, the hypothesis that $s(i+k_0)$ is the beginning of the frame marker is declared true.
2. Testing for maximum, where the value $J_{bits}(k)$ is maximized over all $0 < k < M$, regardless of a threshold. Let k_0 be the location where $J_{bits}(k)$ reaches its highest value over the search range; then the hypothesis that $s(i + k_0)$ is the beginning of a frame marker is declared true.

In the special interest of *transparent* convolutional codes (i.e., if the soft symbols are inverted, the Viterbi-decoded bits are inverted as well), $J_{bits}(k)$ may take the values of +1 for "correct symbol phase correlation" or −1 for "inverted symbol phase correlation," indicating that the Viterbi decoder is synchronized but the soft symbols are inverted and must be returned to the correct phase (i.e., reinverted) prior to deinterleaving. For transparent codes, implementing the bit-domain correlation requires searching for both a maximum and a minimum of $J_{bits}(k)$, or alternatively employing high and low thresholds.

The bit-correlation approach is powerful and usually highly reliable. Its main disadvantage is that it requires hypothesis testing at all possible offsets of the soft symbol n-tuplets, as well as the correct and inverted symbol phases (only for nontransparent convolutional code). Thus, for a (15,1/6) nontransparent convolutional code, a large number of attempts (12 attempts in the worst case, 6 attempts on the average) are required before synchronization is accomplished.

B. Symbol-Domain Correlation

This algorithm examines the soft symbols prior to the Viterbi decoder for presence of an encoded version of the frame marker pattern. When the pattern is detected, it provides both the node and frame synchronization *prior to any decoding operation*. In this case, the symbol correlation function is

$$J_{sym}(k) = \frac{1}{N-(K-1)} \sum_{i=K}^{N} \frac{1}{n} F_e\left(d_0(i)\right) S(i+k) \qquad (3)$$

where $F_e\left(d_0(i)\right)$ is the n-tuplet of soft symbols corresponding to a single bit of the frame marker, $S(i+k)$ is an n-tuplet of received symbols, and the operation on the two

n-tuplets is a dot product. The main disadvantage of this algorithm is that correlation can be performed only over part of the frame marker. For a frame marker of N bits and convolutional code of length K, only the symbols corresponding to the last $N - (K - 1)$ bits are known in the symbol domain—the symbols that correspond to the first $K - 1$ bits of the frame marker are corrupted by the unknown previous contents of the encoder. Depending on N, K, and E_s/N_0, the partial correlation may degrade the correlation SNR sufficiently to make synchronization difficult.

To assess the performance of synchronization using symbol-domain correlation, let us compute the probability of false detection. Let the soft symbol be modeled as having a value of $\pm m + n_{sym(i)}$, where $\pm m$ has an equal probability of being $+m$ and $-m$ and $n_{sym(i)}$ is $N(0, \sigma_{sym})$.[1] Let us assume that the frame marker has been selected such that its autocorrelation is near ideal, i.e., no significant secondary correlation peaks exist. Let us further assume that the correlation between the frame marker and a noiseless set of received symbols contains no significant peaks. Then, when the received symbols are not aligned with the frame marker, $J_{sym}(k)$ can be modeled as $N(0, \sigma)$,

$$\sigma = \sigma_{sym} / \sqrt{n(N - (K - 1))} \tag{4}$$

while when the received symbols are aligned with the frame marker, $J_{sym}(k)$ is modeled as $N(m, \sigma)$. The probability of selecting an incorrect peak is given by

$$P_{FD} = \int_{-\infty}^{\infty} \frac{1}{\sqrt{2\pi}\sigma} e^{-\frac{(x-m)^2}{2\sigma^2}} \times \left[1 - \left(\int_{-\infty}^{x} \frac{1}{\sqrt{2\pi}\sigma} e^{-\frac{y^2}{2\sigma^2}} \, dy \right)^{M-1} \right] dx \tag{5}$$

If the effect of correlation between a random symbol pattern and the frame marker is included, the resulting probability of selecting an incorrect peak is given by Eq. (6) below. Figure 3 plots P_{FD} as a function of the correlation SNR, $10 \log \left(m^2 / 2\sigma^2 \right)$

$$P_{FD} = \frac{1}{\sqrt{2\pi}\sigma} \int_{-\infty}^{\infty} e^{-\frac{(x-m)^2}{2\sigma^2}} \times \left[1 - \left(\frac{1}{2^N} \sum_{i=0}^{N} \binom{N}{i} \times \int_{-\infty}^{x+N-2i} \frac{1}{\sqrt{2\pi}\sigma} e^{-\frac{y^2}{2\sigma^2}} \, dy \right)^{M-1} \right] dx \tag{6}$$

C. Accumulated Metric Growth Rate

This algorithm examines the accumulated metric at all the Viterbi decoder states, indicating the level of "mismatch" between the received soft symbol stream and the bit stream associated with the specific state. Even though the accumulated metric varies from state to state, its peak-to-peak variation is bounded by

(constraint length − 1)(max branch metric)

Because of this bound, implementors often monitor the growth rate of a single selected accumulated metric where at high Eb/N_0 there is a clear distinction between in-node-synchronization and out-of-node-synchronization conditions. The distinction between the two conditions becomes more blurry as Eb/N_0 decreases; the thresholds for detecting the in-lock and out-of-lock hypotheses must be chosen carefully to meet the probability-of-detection and false-alarm requirements. Unfortunately, threshold selection must be accomplished empirically, as the growth rate measurement does not lend itself to analytic expressions.

III. Unified Synchronization

The objective of the unified synchronization approach below is to realize the attractive benefits of the symbol-domain correlation; namely, accomplish node and frame synchronization prior to the Viterbi decoder, while mitigating the algorithm's degraded performance at low SNR.

Case 1: Independent frames, minimal restriction on latency. Let us first observe that many communications links consist of transport frames that are independently encoded as a result of the fact that the frame synchronization marker is longer than the constraint length of the convolutional code, therefore serving as an effective barrier between the frames, resetting the encoder to

---

[1] A zero-mean, normally distributed random variable with a standard deviation of σ_{sym}.

a known state. Let us also assume that there are minimal restrictions on latency.[2] In this case, a simple decoder architecture is possible,[3] as shown in Fig. 4.

In this architecture, no decoding is initiated until the input stream has been separated into frames, using frame-marker correlation in the symbol domain. Once the frame detection is verified, the frames are processed independently; the function labeled "Viterbi and Reed–Solomon decoders" is replicated as many times as needed to meet the required data rate and latency. This architecture is especially suitable for implementation with parallel processors and for cases where a "pool" of resources is available to cover the needs of many users with diverse needs.

Case 2: Independent frames, restriction on latency. The process of frame detection often requires performing the correlation over multiple frames and bridging "gaps" that eliminate frame markers, therefore introducing a substantial, and sometimes unacceptable, latency. In this case, the architecture can be modified as shown in Fig. 5, utilizing the symbol-domain frame-marker correlator only for tentative frame identification. Decoding of frames starts immediately following this tentative detection. However, results from the other synchronization algorithms are used to verify the synchronization and are fed back to allow correction of the synchronization, if needed.

The extent of input buffering and feedback depends on a trade-off between the latency requirement and the implementation restrictions on data rate and available storage.

Case 3: Nonindependent frames or tight latency requirements. This case occurs either when the frame marker is shorter than the convolutional code constraint length (hence, the encoding is not independent from frame to frame) or when the tight latency requirement dictates that Viterbi decoding must be initiated even prior to frame synchronization. The resulting decoder architecture is shown in Fig. 6—the Viterbi decoder relies on its internal measures, e.g., accumulated-metric-growth rate, to achieve node synchronization, but receives feedback from the symbol-domain and bit-domain frame-marker correlators. In this architecture, multiple Viterbi decoders could be employed to expedite the detection of the node synchronization over multiple symbol phase offsets.

IV. Examples

The joint synchronization approach has been applied in two decoder systems developed at JPL. The first decoder, the Maximum-Likelihood Convolutional Decoder Mark III (MCD III) [4,5], is a fully programmable $(K, 1/n)$ Viterbi decoder with $3 \leq K \leq 15$ and $2 \leq n \leq 6$. It is implemented in a fully parallel architecture using 64 identical, custom, very large-scale integrated circuit (VLSI) devices capable of operating at bit rates of up to 1.1 Mbits/sec. The MCD III incorporates all three synchronization algorithms described in Section II, resulting in a flexible synchronization architecture.

A more recent example is the Feedback Concatenated Decoder (FCD) developed specifically for the Galileo mission [6]. This decoder is implemented in software on a four-central-processing-unit (CPU) SUN workstation. It is capable of performing (14,1/4) Viterbi and four-redundancy $(255,x)$ Reed–Solomon decoding as well as the associated redecoding at 160 bits/sec. As an integrated decoder, it is oriented toward symbol-domain frame synchronization, while attempting to minimize latency (case 2 above).

V. Conclusions

We have presented a method of performing joint frame and node synchronization for a concatenated decoder. This approach enables a design that shortens the acquisition time and allows for parallel implementation of the decoder resource-demanding tasks, thus improving the overall decoder efficiency.

---

[2] Latency is the time delay between the signal arrival at the antenna and the time a fully decoded transport frame is available at the output of the decoder.

[3] E. Greenberg, JPL Interoffice Memorandum 3171-93-20 (internal document), Jet Propulsion Laboratory, Pasadena, California, April 6, 1993.

References

[1] S. Lin and D. Costello, *Error Control Coding*, Prentice–Hall Series on Computer Applications in Electrical Engineering, Englewood Cliffs, New Jersey: Prentice–Hall, 1983.

[2] Consultative Committee on Space Data Standards, *Recommendation for Space Data Systems Standards: Telementry Channel Coding*, Document 101-0-B-3 (blue book issue 3), Washington, DC: National Aeronautics and Space Administration, May 1992.

[3] J. Statman, "Optimizing the Galileo Space Communication Link," *The Telecommunications and Data Acquisition Progress Report 42-116, vol. October–December 1993*, Jet Propulsion Laboratory, Pasadena, California, pp. 114–120, February 15, 1994.

[4] J. Statman, G. Zimmerman, F. Pollara, and O. Collins, "A Long Constraint Length VLSI Viterbi Decoder for the DSN," *The Telecommunications and Data Acquisition Progress Report 42-95, vol. July-September 1988*, Jet Propulsion Laboratory, Pasadena, California, pp. 186–200, November 15, 1988.

[5] K. M. Cheung, L. Swanson, and S. Arnold, "Node Synchronization Schemes for the Big Viterbi Decoder," *The Telecommunications and Data Acquisition Progress Report 42-108, vol. October–December 1991*, Jet Propulsion Laboratory, Pasadena, California, pp. 134–142, February 15, 1992.

[6] T. Chauvin and K. M. Cheung, "A Parallel Viterbi Decoder for Shared Memory Multiprocessor Architecture," presented at the 3rd SIAM Conference on Linear Algebra in Signals, Systems, and Control, Seattle, Washington, August 1993.

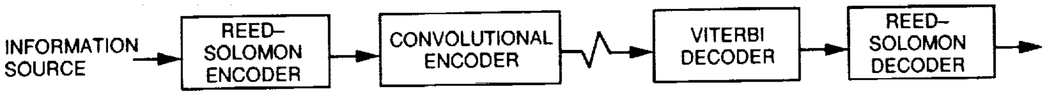

Fig. 1. Error-correcting encoder/decoder traditional configuration.

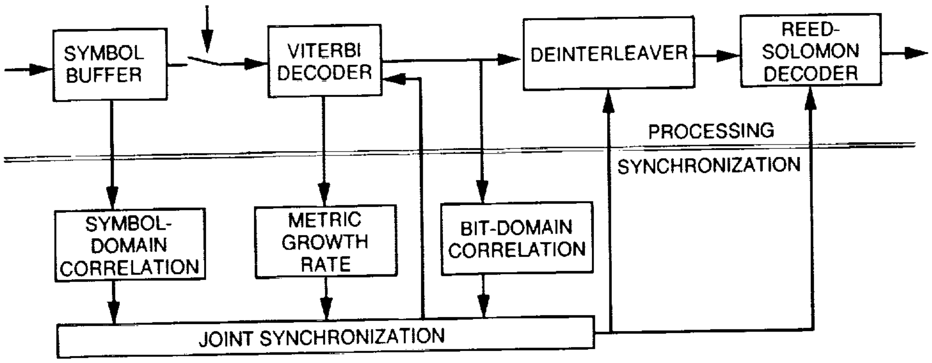

Fig. 2. Joint-synchronization decoder structure.

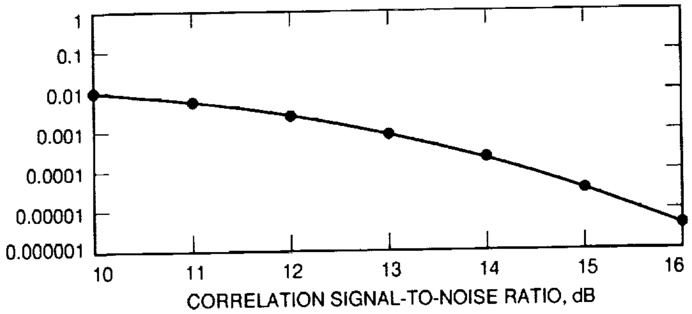

Fig. 3. Probability of false detection versus correlation SNR.

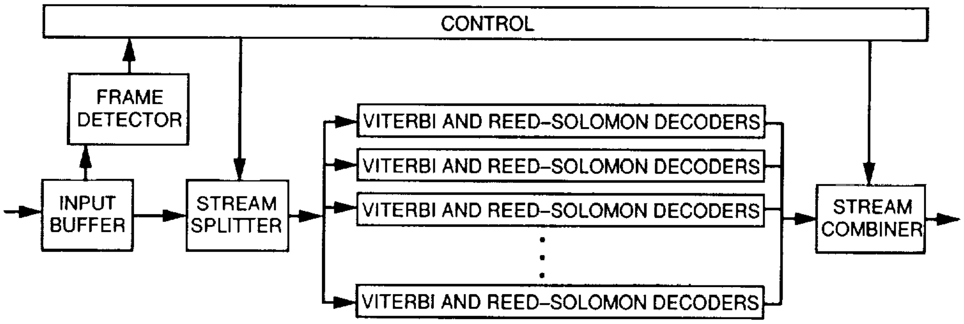

Fig. 4. Decoder architecture without synchronization feedback.

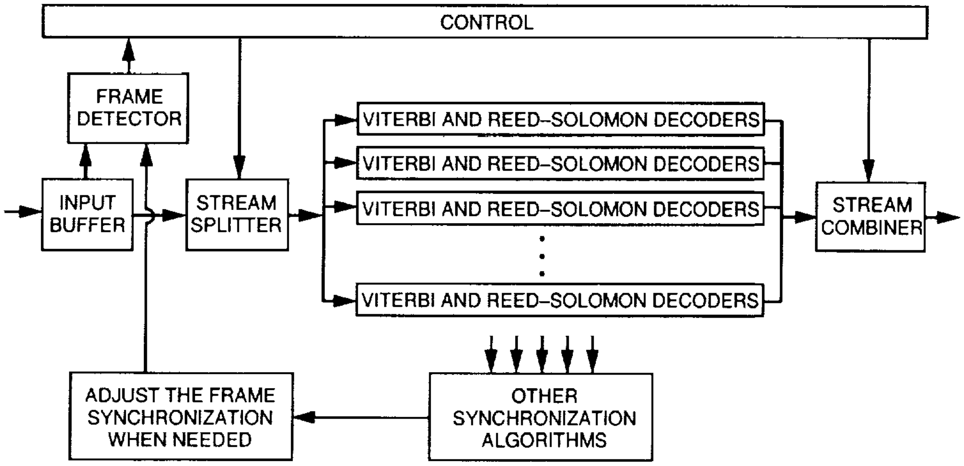

Fig. 5. Decoder architecture with feedback for synchronization correction.

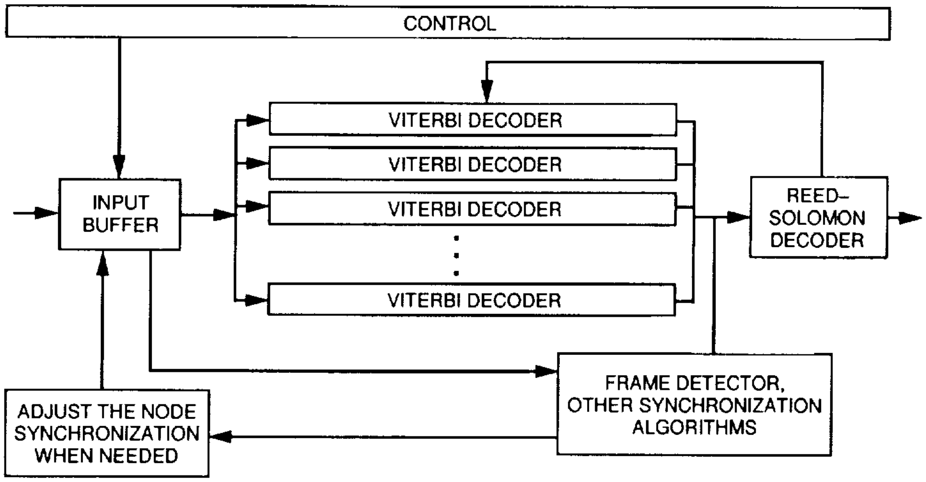

Fig. 6. Decoder architecture when the Viterbi decoder is self-synchronized.

N94- 29665

A Comparison of Full-Spectrum and Complex-Symbol Combining Techniques for the Galileo S-Band Mission

S. Million, B. Shah, and S. Hinedi
Communications Systems Research Section

Full-spectrum combining (FSC) and complex-symbol combining (CSC) are two antenna-arraying techniques being considered for the Galileo spacecraft's upcoming encounter with Jupiter. This article describes the performance of these techniques in terms of symbol signal-to-noise ratio (SNR) degradation and symbol SNR loss. It is shown that both degradation and loss are approximately equal at low values of symbol SNR but diverge at high SNR values. For the Galileo S-band (2.2 to 2.3 GHz) mission, degradation provides a good estimate of performance as the symbol SNR is typically below -5 dB.

For the following arrays—two 70-m antennas, one 70-m and one 34-m antenna, one 70-m and two 34-m antennas, and one 70-m and three 34-m antennas—it is shown that FSC has less degradation than CSC when the subcarrier and symbol window-loop bandwidth products are above 3.0, 10.0, 8.5, and 8.2 mHz at the symbol rate of 200 sym/sec, and above 1.2, 4.5, 4.0, and 3.5 mHz at a symbol rate of 400 sym/sec, respectively. Moreover, for an array of four 34-m antennas, FSC has less degradation than CSC when the subcarrier and symbol window-loop bandwidth products are above 0.32 mHz at the symbol rate of 50 sym/sec and above 0.8 mHz at the symbol rate of 25 sym/sec.

I. Introduction

In deep-space communications, combining signals from multiple antennas is commonly referred to as arraying. Arraying techniques are important because they can significantly enhance system performance. For example, if signal power-to-noise density ratio (P/N_0) is a measure of system performance, then the effective P/N_0 after arraying ideally should be equal to the sum of the P/N_0's corresponding to individual antennas. A typical arraying design trades complexity and gain (or improvement in system performance). Arraying is an attractive option for communication links operating near threshold. For instance, consider the Galileo spacecraft, which is currently on its way to Jupiter. Due to a malfunctioned high-gain antenna, Galileo must rely on its low-gain S-band antenna (and a much reduced link margin) for data transmission to Earth. The Galileo S-band mission will employ arraying, as well as other techniques such as suppressed carriers and data compression, to improve its link margin and maximize data return. The current plan is to implement an intercontinental array between antenna complexes in Australia, Spain, and the United States. Each complex has one 70-m and several 34-m antennas available for arraying. This article compares the full-spectrum combining (FSC) and complex-symbol combining (CSC) arraying techniques for the following five antenna combinations: two 70-m antennas; one 70-m and one 34-m antenna; one 70-m and two 34-m antennas; one 70-m and three 34-m antennas; and four 34-m antennas. Even when communication links are operating above threshold, arraying is an economically attractive option to increase the scientific return of a mission without having to build larger antennas. Smaller, inexpensive antennas (i.e., 34-m) can be built at less cost than a single larger antenna (i.e., 70-m), but with at least an equivalent performance after proper arraying.

A recent study [1], which presented an overview of several antenna-combining techniques, concluded that FSC resulted in the least degradation for weak signals. That study didn't consider the CSC arraying technique, which has been made possible by the advent of all-digital receivers in NASA's Deep Space Network (DSN) [2]. The CSC technique is an attractive arraying option because it requires little modification to existing systems. In FSC, depicted in Fig. 1(a), the received radio frequency (RF) signal at each antenna is downconverted to an intermediate frequency (IF), transmitted to a central location where it is aligned and combined with signals from other antennas, and then demodulated by a single receiver chain. The chain consists of one carrier loop, one subcarrier loop, one symbol-synchronization loop, and one matched filter. The RF/IF downconverter is assumed to output a complex IF signal (two IF signals that are orthogonal) denoted by the double lines in Fig. 1(a). The processing needed to align and combine the IF signals is shown in Fig. 1(b) for an array of two antennas. The details of this scheme are discussed in the section on FSC performance.

In CSC, depicted in Fig. 2(a), the received RF signal at each antenna is first open-loop downconverted to IF; it, in turn, is open-loop downconverted near baseband using a complex IF reference. The IF in-phase (I) and quadrature (Q) references are tuned to the predicted IF carrier frequency. The resulting complex signal near baseband, centered at the carrier predict error, is used for subcarrier tracking and symbol synchronization, which can be accomplished using either the I arm of the carrier alone or both the I and Q arms. The latter requires more complexity but results in an improved performance, as one would expect. After subcarrier demodulation, the signal is input to a pair of matched filters that output soft-quantized complex symbols that modulate a tone with frequency equal to the carrier-predict error. Since there are two channels in the down-conversion process (carriers I and Q), the symbols at the matched filter output modulate quadrature tones and can be viewed as complex symbols. The complex symbols from multiple antennas are then transmitted to a central location, aligned and combined at baseband, and demodulated using a baseband Costas loop. The CSC output is a single real-combined symbol stream. The combiner for CSC is shown in Fig. 2(b) and discussed in the section on CSC performance.

The key difference between FSC and CSC is the order of carrier-phase alignment between the antennas. In FSC, carrier-phase alignment precedes subcarrier demodulation, symbol synchronization, and matched filtering; in CSC, it follows. In both cases, the carrier phases are aligned and the signals are combined prior to carrier phase tracking and demodulation. As a result, for an array of two 70-m antennas, the effective P/N_0 at the input to the subcarrier and symbol loops in CSC is about 6 dB lower than FSC. Three of the 6 dB are due to the signals in CSC being combined after the subcarrier and symbol loops; the remaining 3 dB result from subcarrier and symbol synchronization that is performed without carrier lock.

Assuming the carrier is locked, the effective P/N_0 at the input to the subcarrier and symbol loops in CSC is about 3 dB lower than FSC. Another key difference between FSC and CSC arises when arraying a 70-m and 34-m antenna. In the Galileo case, the signal is so weak that it is harder for a stand-alone 34-m antenna to lock to the signal than a stand-alone 70-m antenna. Consequently, when implementing CSC between the two, the 70-m antenna needs to enable the 34-m antenna in tracking the subcarrier and symbols. When they are located within a few miles of each other, the 70-m antenna can transmit subcarrier and symbol-loop frequency and phase information to the 34-m antenna. However, when implementing FSC between a 70-m and 34-m antenna array, no aiding of the 34-m antenna is required since the carrier, subcarrier, and symbol-timing loops operate on the combined signal. Furthermore, since it is difficult for a single 34-m antenna to lock on to the signal by itself, an array of four 34-m antennas is less effective using CSC than FSC. These differences are summarized in Table 1.

In this article, the performances of FSC and CSC are measured both in terms of symbol SNR degradation and symbol SNR loss. Symbol SNR degradation is defined as the ratio of the SNR at the matched filter output in the presence of nonideal synchronization to the SNR in the presence of ideal synchronization. On the other hand, symbol SNR loss is defined as the additional symbol SNR needed in the presence of imperfect synchronization to achieve the same symbol error rate (SER) as in the presence of perfect synchronization. Mathematical representations of degradation and loss are given in the next section. Comparatively, loss gives the absolute, while degradation gives the relative, performance advantage of an arraying scheme. Moreover, since the calculation of degradation is less demanding than computation of loss [3], it is the preferred calculation method at low-symbol SNR's where it is approximately equal to loss. In the following sections, the degradation and loss for a single antenna, FSC, and CSC are derived and then illustrated via various numerical examples.

II. Single Receiver Performance

In deep-space communications, the downlink symbols are first modulated onto a square-wave subcarrier; the modulated subcarrier then modulates an RF carrier [4]. This allows transmission of a residual carrier component whose frequency does not coincide with the data spectrum. At the receiver, the deep-space signal is demodulated using a carrier-tracking loop, a subcarrier-tracking loop [5], and a symbol-synchronizer loop [6], as shown in Fig. 3. Depending on the modulation index, carrier tracking can be achieved by a phase-locked loop (PLL), Costas loop, or both [7]. The PLL or a combination of loops is used for modulation indices less than 90 deg, whereas a Costas loop is used when the modulation index is equal to 90 deg. The deep-space signal with the carrier fully suppressed[1] can be represented as [8]

$$r(t) = \sqrt{2P}d(t)\mathrm{Sqr}(\omega_{sc}t + \theta_{sc})\cos(\omega_c t + \theta_c) + n(t) \quad (1)$$

where P is the received data power in watts (W); ω_c and θ_c are the carrier angular frequency in radians per second (rads/sec) and phase in rads, respectively; and $\mathrm{Sqr}(\omega_{sc}t + \theta_{sc})$ is the square-wave subcarrier with subcarrier angular frequency ω_{sc} in rads/sec and subcarrier phase θ_{sc} in rads. The symbol stream $d(t)$ is given by

$$d(t) = \sum_{k=-\infty}^{\infty} d_k p(t - kT) \quad (2)$$

where d_k is the ±1 binary data for the kth symbol and T is the symbol period in seconds. The baseband pulse p(t) is unit power and limited to T seconds. The narrow-band noise $n(t)$ can be written as

$$n(t) = \sqrt{2}n_c(t)\cos(\omega_c t + \theta_c) - \sqrt{2}n_s(t)\sin(\omega_c t + \theta_c) \quad (3)$$

where $n_c(t)$ and $n_s(t)$ are statistically independent, stationary, band-limited, white Gaussian noise processes with one-sided spectral density level N_0 (W/Hz) and one-sided bandwidth W_n (Hz), which is large compared to 1/T. After signal demodulation, the symbol stream at the output of the matched filter in Fig. 3 can be written as [8]

$$v_k = \begin{cases} \sqrt{P}C_c C_{sc} d_k + n_k & d_k = d_{k-1} \\ \sqrt{P}C_c C_{sc}(1 - \frac{|\phi_{sy}|}{\pi})d_k + n_k & d_k \neq d_{k-1} \end{cases} \quad (4)$$

where the noise n_k is a Gaussian random variable with variance $\sigma_n^2 = N_0/2T$. The signal reduction functions C_c and C_{sc} are due to imperfect carrier and subcarrier synchronization and are given by [1]

$$C_c = \cos\phi_c \quad (5)$$

$$C_{sc} = 1 - \frac{2}{\pi}|\phi_{sc}| \quad (6)$$

where ϕ_c and ϕ_{sc} (in rads), respectively, denote the carrier- and subcarrier-phase tracking errors. The symbol timing error ϕ_{sy}, which affects the output only when there is a symbol transition, reduces the signal amplitude by $1 - |\phi_{sy}|/\pi$. Ideally, $\phi_c = \phi_{sc} = \phi_{sy} = 0$ and Eq. (4) reduce to the ideal matched filter output $v_k = \sqrt{P}d_k + n_k$, as expected. In writing Eq. (4), it is assumed that the carrier, subcarrier, and symbol loop bandwidths are much smaller than the symbol rate so that the phase errors ϕ_c, ϕ_{sc}, and ϕ_{sy} can be modeled as constant over several symbols. Throughout this article, ϕ_c is assumed to be Tikhonov distributed, and ϕ_{sc} and ϕ_{sy} are assumed to be Gaussian distributed. Let $p_c(\phi_c)$, $p_{sc}(\phi_{sc})$, and $p_{sy}(\phi_{sy})$ denote respectively the carrier, subcarrier, and symbol phase error density functions. Then

---

[1] This article considers the Galileo S-band scenario in which the carrier is fully suppressed.

$$p_c(\phi_c) = \begin{cases} \dfrac{\exp\left(\frac{1}{4}\rho_c \cos 2\phi_c\right)}{\pi I_o(\frac{1}{4}\rho_c)} & |\phi_c| \leq \frac{\pi}{2} \\ 0 & \text{otherwise} \end{cases} \tag{7}$$

where $I_k(x)$ denotes the modified Bessel function of order k, and ρ_c is the suppressed carrier or Costas loop SNR. Also, $p_{sc}(\phi_{sc})$ and $p_{sy}(\phi_{sy})$ are given by

$$p_i(\phi_i) = \frac{\exp\left(-\phi_i^2/2\sigma_i^2\right)}{\sqrt{2\pi}\sigma_i}, \quad \text{i = sc, sy} \tag{8}$$

where σ_{sc}^2 and σ_{sy}^2 are the reciprocals of the subcarrier and symbol loop SNR's, respectively, denoted as ρ_{sc} and ρ_{sy}. The carrier [8], subcarrier [8], and symbol [6] loop SNR's are respectively given as

$$\rho_c = \frac{P/N_0}{B_c}\left(1 + \frac{1}{2E_s/N_0}\right)^{-1} \tag{9}$$

$$\rho_{sc} = \left(\frac{2}{\pi}\right)^2 \frac{P/N_0}{W_{sc}B_{sc}}\left(1 + \frac{1}{2E_s/N_0}\right)^{-1} \tag{10}$$

$$\rho_{sy} = \frac{P/N_0}{2\pi^2 W_{sy}B_{sy}} \frac{\left(\text{erf}\left(\sqrt{\frac{E_s}{N_0}}\right) - \frac{W_{sy}}{2\sqrt{\pi}}\sqrt{\frac{E_s}{N_0}} \exp\left(-\frac{E_s}{N_0}\right)\right)^2}{\left(1 + \frac{E_s}{N_0}\frac{W_{sy}}{2} - \frac{W_{sy}}{2}\left[\frac{1}{\sqrt{\pi}} \exp\left(-\frac{E_s}{N_0}\right) + \sqrt{\frac{E_s}{N_0}} \text{ erf}\left(\sqrt{\frac{E_s}{N_0}}\right)\right]^2\right)} \tag{11}$$

---

where $E_s/N_0 = PT/N_0$ is the symbol SNR, erf $(x) = 2/\sqrt{\pi} \int_0^x \exp(-v^2)\, dv$ is the error function, and B_c, B_{sc}, and B_{sy} (in Hz) denote the single-sided carrier, subcarrier, and symbol loop bandwidths, respectively. The parameters W_{sc} and W_{sy}, which denote the subcarrier and symbol window, are unitless and limited to $(0, 1]$. The loop SNR's for the subcarrier and symbol loop are valid only when $\pi/2\ W_{sc} \gtrsim \sigma_{sc}$ and $\pi W_{sy} \gtrsim \sigma_{sy}$.

A useful quantity needed to compute degradation and loss is the symbol SNR conditioned on ϕ_c, ϕ_{sc}, and ϕ_{sy}. The conditional symbol SNR, denoted SNR', is defined as the square of the conditional mean of v_k divided by the conditional variance of v_k, i.e.,

$$SNR' = \frac{\overline{(v_k/\phi_c, \phi_{sc}, \phi_{sy})}^2}{\sigma_n^2}$$

$$= \begin{cases} \dfrac{2PT}{N_0} C_c^2 C_{sc}^2 & d_k = d_{k-1} \\ \dfrac{2PT}{N_0} C_c^2 C_{sc}^2 \left(1 - \dfrac{|\phi_{sy}|}{\pi}\right)^2 & d_k \neq d_{k-1} \end{cases} \tag{12}$$

where $\overline{(x/y)}$ denotes the statistical expectation of x conditioned on y, and v_k and σ_n^2 are defined earlier.

A. Degradation

The symbol SNR degradation is defined as the ratio of the unconditional SNR at the output of the matched filter in the presence of imperfect synchronization to the ideal matched filter output SNR. The unconditional SNR, denoted SNR, is found by first averaging Eq. (12) over the symbol transition probability, and then over the carrier, subcarrier, and symbol phases. Letting $\overline{x}$ denote the average of x, the unconditional SNR is given as

$$SNR = \frac{2PT}{N_0}\overline{C_c^2}\,\overline{C_{sc}^2}\,\overline{C_{sy}^2} \tag{13}$$

where the signal amplitude reduction due to symbol timing errors (averaged over the symbol transition probability) is denoted C_{sy}, and given as

$$C_{sy} = 1 - \frac{|\phi_{sy}|}{2\pi} \tag{14}$$

Averaging over the phases yields [1]

$$\overline{C_c^2} = \frac{1}{2}\left[1+\frac{I_1(\frac{1}{4}\rho_c)}{I_0(\frac{1}{4}\rho_c)}\right] \tag{15}$$

$$\overline{C_{sc}^2} = 1-\sqrt{\frac{32}{\pi^3}}\frac{1}{\sqrt{\rho_{sc}}}+\frac{4}{\pi^2}\frac{1}{\rho_{sc}} \tag{16}$$

$$\overline{C_{sy}^2} = 1-\sqrt{\frac{2}{\pi^3}}\frac{1}{\sqrt{\rho_{sy}}}+\frac{1}{4\pi^2}\frac{1}{\rho_{sy}} \tag{17}$$

Ideally, when there are no phase errors (i.e., when $\rho_c = \rho_{sc} = \rho_{sy} = \infty$), $\overline{C_c^2} = \overline{C_{sc}^2} = \overline{C_{sy}^2} = 1$ and Eq. (13) reduce to $SNR_{ideal} = 2PT/N_0$, as expected. The degradation, D, for a single antenna is thus given by

$$D = -10\ \log_{10}\left(\frac{SNR}{SNR_{ideal}}\right) = -10\ \log_{10}\overline{C_c^2}\ \overline{C_{sc}^2}\ \overline{C_{sy}^2} \tag{18}$$

B. Loss

For the single receiver shown in Fig. 3, the SER, denoted $P_s(E)$, is defined as

$$P_s(E) = \int_{-\frac{\pi}{2}}^{\frac{\pi}{2}}\int_{-\infty}^{\infty}\int_{-\infty}^{\infty} P_s'(E)p_c(\phi_c)p_{sc}(\phi_{sc})p_{sy}(\phi_{sy})$$

$$\times\ d\phi_{sy}d\phi_{sc}d\phi_c = f\left(\sqrt{\frac{E_s}{N_0}}\right) \tag{19}$$

where $f(\bullet)$ is the functional relationship between SER and $\sqrt{E_s/N_0}$ and $P_s'(E)$ is the SER conditioned on the phase errors ϕ_c, ϕ_{sc}, and ϕ_{sy}. Following similar steps as in [9], the conditional SER can be shown to be

$$P_s'(E) = \frac{1}{4}\ \text{erfc}\left(\sqrt{SNR'\ \text{when}\ d_k \neq d_{k-1}}\right)$$

$$+\ \frac{1}{4}\ \text{erfc}\left(\sqrt{SNR'\ \text{when}\ d_k = d_{k-1}}\right) \tag{20}$$

where

$$\text{erfc}\ (x) = \frac{2}{\sqrt{\pi}}\int_x^{\infty}\exp\ (-v^2)\ dv = 1-\text{erf}\ (x) \tag{21}$$

is the complementary error function. Substituting Eq. (12) for SNR' in Eq. (20) yields

$$P_s'(E) = \frac{1}{4}\text{erfc}\left[\sqrt{\frac{E_s}{N_0}}C_cC_{sc}\left(1-\frac{|\phi_{sy}|}{\pi}\right)\right]$$

$$+\ \frac{1}{4}\text{erfc}\left[\sqrt{\frac{E_s}{N_0}}C_cC_{sc}\right] \tag{22}$$

Ideally, when there are no timing errors (i.e., when $\rho_c = \rho_{sc} = \rho_{sy} = \infty$), $C_c = C_{sc} = (1-|\phi_{sy}|/\pi) = 1$ and Eq. (19) reduce to the well-known binary phase-shift keyed (BPSK) error rate, $P_s(E) = (1/2)$ erfc $(\sqrt{E_s/N_0})$.

Symbol SNR loss is defined as the additional symbol SNR needed in the presence of imperfect synchronization to achieve the same SER as in the presence of perfect synchronization. Mathematically, the SNR loss due to imperfect carrier, subcarrier, and symbol timing references is given in dB as

$$L_{dB} = -20\log\left[f^{-1}(P_s(E))\right]\ |_{[\text{infinite loop SNR}]}$$

$$+\ 20\log\left[f^{-1}(P_s(E))\right]\ |_{[\text{finite loop SNR}]} \tag{23}$$

where $P_s(E)$ is defined in Eq. (19). The first term in Eq. (23) is the value of E_s/N_0 required at a given value of $P_s(E)$ in the presence of perfect synchronization, whereas the second term is the value of E_s/N_0 required for imperfect synchronization. Note that loss defined in this way is a positive number.

III. FSC Performance

The FSC technique, depicted in Fig. 1(a), combines IF signals from multiple antennas and then demodulates the combined signal using the single receiver described in the previous section. The resulting gain is maximized by aligning the IF signals in time and phase prior to demodulation [1]. The alignment algorithm for an array of two antennas is shown in Fig. 1(b). Here signal 1 is assumed to be delayed by τ seconds, with respect to signal 2. The IF signal from antenna 2 is first delayed by $\hat{\tau}$ seconds, where $\hat{\tau}$ can be the output of the delay estimation loop, or it may be predicted from the geometric arrangement of the antennas and spacecraft. After delay compensation, both signals are input to the phase estimator, which outputs $\hat{\theta}_{21}$, the estimate of θ_{21}, which is the phase of signal 2 relative to signal 1 at the estimator input. Subsequently, signal 2 is phase shifted by an amount equal to $-\hat{\theta}_{21}$, scaled by[2] β_2, and then combined (or added) with signal 1. Notice in Fig. 1(b) that the phase estimator filters the IF signal so that only the L_{sc} harmonics of the IF spectrum are used for phase estimation. It is shown later that the accuracy of the estimates depends on B_{corr}, the bandwidth of the bandpass filter (BPF) centered at IF, and T_c, the estimation period.

The symbol SNR degradation and loss analysis for FSC closely follows the analysis of the previous section as the combined signal is demodulated by a single receiver. As before, imperfect carrier, subcarrier, and symbol synchronization are expected to reduce the symbol SNR. In addition to those effects, however, the reduction due to imperfect combining must be accounted for as well. Assuming that the IF signals in Fig. 1(b) are perfectly aligned in time ($\hat{\tau} = \tau$) but misaligned in phase,[3] the matched filter output for FSC is given by Eq. (4) with the modification that the one-sided noise power spectral density (PSD) level N_0 is now equal to the effective one-sided noise level $N_{0_{eff}}$ of the combined signal, and the data power P is now equal to the combined power P' conditioned on the phase-alignment error. The effective one-sided noise PSD level at the matched filter input is given by [1]

$$N_{0_{eff}} = N_{01} \sum_{n=1}^{L} \gamma_n \tag{24}$$

where

$$\gamma_n \triangleq \frac{P_n}{P_1} \frac{N_{01}}{N_{0n}} \tag{25}$$

and where P_n and N_{0n} denote, respectively, the signal power and one-sided noise PSD level of antenna n. Table 2 lists the γ_n factors[4] for several DSN antennas at both S-band (2.2 to 2.3 GHz) and X-band (8.4 to 8.5 GHz). Throughout this article, the ratio P_1/N_{01} is taken to be the signal power to one-sided noise PSD level of the reference antenna which, by convention, is taken to be the antenna with the highest gain. Consequently, in this article $\gamma_n \leq 1$. Table 2 lists the gamma values for 70-m and 34-m antennas assuming the 70-m antenna is the reference antenna. The same table can be reused for an arbitrary reference antenna as follows. Consider a three-element array consisting of one high-efficiency (HEF) 34-m antenna and two standard (STD) 34-m antennas operating at X-band. Let the 34-m HEF be the reference antenna with $\gamma_1 = 1$, then the 34-m STD antennas have $\gamma_2 = \gamma_3 = 0.13/0.26 = 0.5$.

Let the phase-alignment error between signal n and signal 1 be denoted by $\Delta\phi_{n1} = \theta_{n1} - \hat{\theta}_{n1}$; then the combined signal power conditioned on $\Delta\phi_{n1}$ is given as [1]

$$P' = P_1 \sum_{n=1}^{L} \sum_{m=1}^{L} \gamma_n \gamma_m C_{nm} \tag{26}$$

where

$$C_{nm} = e^{j(\Delta\phi_{n1} - \Delta\phi_{m1})} \tag{27}$$

is the complex signal-reduction function due to phase misalignment. To summarize, the matched filter output of FSC is given by Eq. (4) after replacing P by P' as given by Eq. (26) and replacing N_0 by $N_{0_{eff}}$ which is given by Eq. (24).

A useful quantity needed in later calculations is $\overline{C_{nm}}$. In Eq. (27), assuming the residual phase error for each antenna pair, $\Delta\phi_{n1}$ for $n = 2, ..., L$, to be Gaussian distributed with zero mean and variance $\sigma^2_{\Delta\phi_{n1}}$ and statistically independent from $\Delta\phi_{m1}$ for $n \neq m$, then it can be shown that [1]

$$\overline{C_{nm}} = \begin{cases} e^{-\frac{1}{2}[\sigma^2_{\Delta\phi_{n1}} + \sigma^2_{\Delta\phi_{m1}}]} & n \neq m \\ 1 & n = m \end{cases} \tag{28}$$

where the variance of the residual phase error can be related to the SNR of the correlator as follows:

$$\sigma^2_{\Delta\phi_{n1}} = \frac{1}{2SNR_{n1,fsc}} \tag{29}$$

Here, $SNR_{n1,fsc}$ denotes correlator SNR [or SNR of the complex signal $\tilde{x}$ in Fig. 1(b)], and it is shown in Appendix A to equal

---

[2] Here, $\beta_2 \triangleq \sqrt{(P_2/P_1)}(N_{01}/N_{02})$ is the weighting factor [3].

[3] This is a simplifying assumption consistent with the assumption in [1].

[4] *Deep Space Network/Flight Project Interface Design Handbook*, D-810-5, Rev. D, vol. I (internal document), Jet Propulsion Laboratory, Pasadena, California, Modules TCI-10, TCI-30, and TLM-10, 1988.

$$SNR_{n1,fsc} \triangleq \frac{E(\tilde{x})E(\tilde{x}^*)}{Var(\tilde{x})} = \frac{E(\tilde{x})E(\tilde{x}^*)}{E(\tilde{x}\tilde{x}^*) - E(\tilde{x})E(\tilde{x}^*)} \tag{30}$$

$$= \frac{T_c(\frac{4}{\pi})^2 \frac{P_1}{N_{01}} \left[\sum_{\substack{j=1 \\ j:odd}}^{L_{sc}} \frac{1}{j^2} \right]}{1 + \frac{1}{\gamma_n} + 2(\frac{\pi}{4})^2 B_{corr} \frac{1}{\sum_{\substack{j=1 \\ j:odd}}^{L_{sc}} \frac{1}{j^2}} \frac{N_{0n}}{P_n}} \tag{31}$$

where B_{corr} is the single-sided bandwidth of the IF filter preceeding the correlator, T_c is the averaging time of the correlator, and L_{sc} is the number of subcarrier harmonics at the BPF output. Note that if all the subcarrier harmonics pass unfiltered, then $\lim_{L_{sc}\to\infty} \sum_{j=1,j:odd}^{L_{sc}} 1/j^2 = 2(\pi/4)^2$.

The SNR conditioned on ϕ_c, ϕ_{sc}, ϕ_{sy}, $\Delta\phi_{n1}$ denoted SNR'_{fsc}, is defined as before to be the square of the conditional mean of v_k divided by the conditional variance of v_k, i.e.,

$$SNR'_{fsc} = \begin{cases} \frac{2P_1T}{N_{01}} C_c^2 C_{sc}^2 \left(\frac{\sum_{n=1}^{L} \gamma_n^2 + \sum_{n=1}^{L} \sum_{\substack{m=1 \\ n\neq m}}^{L} \gamma_n\gamma_m C_{nm}}{\sum_{n=1}^{L} \gamma_n} \right) & d_k = d_{k-1} \\ \frac{2P_1T}{N_{01}} C_c^2 C_{sc}^2 \left(1 - \frac{|\phi_{sy}|}{\pi}\right)^2 \left(\frac{\sum_{n=1}^{L} \gamma_n^2 + \sum_{n=1}^{L} \sum_{\substack{m=1 \\ n\neq m}}^{L} \gamma_n\gamma_m C_{nm}}{\sum_{n=1}^{L} \gamma_n} \right) & d_k \neq d_{k-1} \end{cases} \tag{32}$$

Comparing Eq. (32) with the single receiver conditional SNR in Eq. (12), it is clear that the term inside the large parentheses in Eq. (32) represents the less-than-ideal gain that results from phase misalignment of the IF signals prior to combining.

A. Degradation

The FSC SNR degradation is defined as the unconditional FSC SNR divided by the ideal SNR. The unconditional SNR is found by averaging Eq. (32) over the phases ϕ_c, ϕ_{sc}, ϕ_{sy}, and $\Delta\phi_{n1}$ and is given as

$$SNR_{fsc} = \frac{2P_1T}{N_{01}} \overline{C_c^2}\, \overline{C_{sc}^2}\, \overline{C_{sy}^2} \left(\frac{\sum_{n=1}^{L} \gamma_n^2 + \sum_{n=1}^{L} \sum_{\substack{m=1 \\ n\neq m}}^{L} \gamma_n\gamma_m \overline{C_{nm}}}{\sum_{n=1}^{L} \gamma_n} \right) \tag{33}$$

where $\overline{C_{nm}}$ is provided in Eq. (28). The quantities $\overline{C_c^2}$, $\overline{C_{sc}^2}$, and $\overline{C_{sy}^2}$ are given in Eqs. (15)–(17) with the modification that the loop SNR's ρ_c, ρ_{sc}, and ρ_{sy} presented in Eqs. (9)–(11) are now computed using the average combined power $P'/N_{0_{eff}}$, which is found by averaging Eq. (26) over the phase $\Delta\phi_{n1}$ and dividing by the effective noise level in Eq. (24). Ideally, when there are no phase errors, $\overline{C_c^2} = \overline{C_{sc}^2} = \overline{C_{sy}^2} = \overline{C_{nm}} = 1$ and Eq. (33) reduce to $\left(2P_1T/N_{01} \sum_{n=1}^{L} \gamma_n\right)$. Dividing Eq. (33) by the ideal FSC SNR yields the degradation in dB, namely,

$$D_{fsc} = -10\ \log_{10}\left(\overline{C_c^2}\,\overline{C_{sc}^2}\,\overline{C_{sy}^2}\left(\frac{\sum\limits_{n=1}^{L}\gamma_n^2 + \sum\limits_{n=1}^{L}\sum\limits_{\substack{m=1\\n\neq m}}^{L}\gamma_n\gamma_m\overline{C_{nm}}}{\left(\sum\limits_{n=1}^{L}\gamma_n\right)^2}\right)\right) \tag{34}$$

B. Loss

The FSC SER for an L antenna array, denoted $P_{fsc}(E)$, is defined as

$$P_{fsc}(E) = \int_{-\frac{\pi}{2}}^{\frac{\pi}{2}}\int_{-\infty}^{\infty}\int_{-\infty}^{\infty}\fint_{-\infty}^{\infty} P'_{fsc}(E)\left[p_c(\phi_c)p_{sc}(\phi_{sc})p_{sy}(\phi_{sy})\left(\prod_{n=2}^{L}p_{\Delta\phi_{n1}}(\Delta\phi_{n1})\right)\right]d\boldsymbol{\Delta}\phi\ d\phi_{sy}\ d\phi_{sc}\ d\phi_c \tag{35}$$

where $\fint_{-\infty}^{\infty}$ is the $(L-1)$-tuple integral over the residual phases $\boldsymbol{\Delta}\phi = (\Delta\phi_{21},\dots,\Delta\phi_{(L-1)1})$. Following similar steps as in the single antenna case, the conditional SER becomes

$$P'_{fsc}(E) = \frac{1}{4}\ \text{erfc}\left[\sqrt{\frac{E_{s1}}{N_{01}}\frac{\left(\sum\limits_{n=1}^{L}\gamma_n^2 + \sum\limits_{n=1}^{L}\sum\limits_{\substack{m=1\\n\neq m}}^{L}\gamma_n\gamma_m C_{nm}\right)}{\left(\sum\limits_{n=1}^{L}\gamma_n\right)}C_cC_{sc}\left(1-\frac{|\phi_{sy}|}{\pi}\right)}\right]$$

$$+\frac{1}{4}\ \text{erfc}\left[\sqrt{\frac{E_{s1}}{N_{01}}\frac{\left(\sum\limits_{n=1}^{L}\gamma_n^2 + \sum\limits_{n=1}^{L}\sum\limits_{\substack{m=1\\n\neq m}}^{L}\gamma_n\gamma_m C_{nm}\right)}{\left(\sum\limits_{n=1}^{L}\gamma_n\right)}C_cC_{sc}}\right] \tag{36}$$

where $E_{s1}/N_{01} = P_1T/N_{01}$ is the symbol SNR at antenna 1. Ideally, when there are no phase errors, $C_c = C_{sc} = (1-|\phi_{sy}|/\pi) = C_{nm} = 1$, and Eq. (35) reduces to $P_{fsc}(E) = (1/2)\ \text{erfc}\left(\sqrt{E_sL/N_0}\right)$ for an array of L antennas of the same size (i.e., when $\gamma_n = 1$ for all n). The symbol SNR loss for FSC is given by Eq. (23) after replacing $P_s(E)$ with $P_{fsc}(E)$, as presented in Eq. (35).

IV. CSC Performance

As depicted in Fig. 2(a), signals from multiple antennas in CSC are open-loop downconverted to baseband, partially demodulated using multiple subcarrier loops, multiple symbol loops, and multiple matched filters, then combined and demodulated using a single baseband carrier loop. The subcarrier and symbol loops used for CSC can be the same as those used in FSC, or they can be slightly modified versions that take advantage of both the I and Q components of the baseband signal. CSC implementations with the same loops as those in the FSC would use either the I or Q component of the baseband signal. In either case, the loop SNR's of the subcarrier and symbol loops need to be recomputed as the loop input can no longer be assumed to have carrier lock. Let $\rho^{I}_{sc_n,csc}$ denote the loop SNR of the nth subcarrier loop when either the I or Q arm is used (i.e., the unmodified loop), and let $\rho^{IQ}_{sc_n,csc}$ denote the subcarrier loop SNR when both the I and Q arms are used (i.e., the modified loop). Similarly, define $\rho^{I}_{sy_n,csc}$ and $\rho^{IQ}_{sy_n,csc}$ for the nth symbol loop. Then from Appendix B,

$$\rho^{I}_{sc_n,csc} = \left(\frac{2}{\pi}\right)^2 \frac{P_n/N_{0n}}{2W_{sc_n}B_{sc_n}} \left(1 + \frac{1}{P_nT/N_{0n}}\right)^{-1} \tag{37}$$

$$\rho^{I}_{sy_n,csc} = \frac{1}{2\pi^2} \frac{P_n/N_{0n}}{W_{sy_n}B_{sy_n}} \mathcal{L}_I \tag{38}$$

and

$$\rho^{IQ}_{sc_n,csc} = \left(\frac{2}{\pi}\right)^2 \frac{P_n/N_{0n}}{W_{sc_n}B_{sc_n}} \left(1 + \frac{1}{P_nT/N_{0n}}\right)^{-1} \tag{39}$$

$$\rho^{IQ}_{sy_n,csc} = \frac{1}{2\pi^2} \frac{P_n/N_{0n}}{W_{sy_n}B_{sy_n}} \mathcal{L}_{IQ} \tag{40}$$

where $W_{sc_n}B_{sc_n}$ and $W_{sy_n}B_{sy_n}$ are the window-loop bandwidth products of the nth subcarrier and symbol loops, respectively. The squaring loss $\mathcal{L}_I$ for the unmodified loop and $\mathcal{L}_{IQ}$ for the modified loop are defined in Appendix B, Section II. For the Galileo scenario, using the unmodified subcarrier and symbol loop reduces the loop SNR by 6 dB compared to the carrier-locked case, while using both the I and Q arms recovers 3 of the 6 dB. Consequently, since the modified subcarrier and symbol loops result in an improved performance, they will be used in this article when comparing CSC to FSC.[5]

Refering to Fig. 2(a), the combining gain is maximized by aligning the baseband signals in time and phase, prior to combining. The alignment algorithm for an array of two antennas is shown in Fig. 2(a). Here signal 1 is assumed to be delayed by m symbols with respect to signal 2. The signals are time aligned by delaying signal 2 by $\hat{m}$ symbols where $\hat{m}$ is an estimate of m. As in FSC, we assume perfect time alignment so that $\hat{m} = m$. After time alignment, the phase of signal 2 with respect to signal 1 is assumed to be θ_{21} rads. Hence, signal 2 is phase shifted by an amount equal to $-\theta_{21}$, scaled by β_2, and then combined with signal 1.

The analysis of CSC degradation and loss begins with the expression for the output of the matched filter in Fig. 2(a). Note that there are actually $2L$ matched filters per L antennas because after subcarrier demodulation, a real symbol stream is modulated by I and Q tones near baseband. Using complex notation, the matched-filter output stream corresponding to the kth symbol and the nth antenna, conditioned on ϕ_{sc_n} and ϕ_{sc_n}, can be written as

$$\tilde{v}_{k,n} = \begin{cases} \sqrt{P_n}C_{sc_n} d_k e^{[j(\Delta\omega_c t_k + \theta_{n1})]} + \tilde{n}_{k,n} \\ \qquad d_k = d_{k-1} \\ \sqrt{P_n}C_{sc_n} \left(1 - \frac{|\phi_{sy_n}|}{\pi}\right) d_k e^{[j(\Delta\omega_c t_k + \theta_{n1})]} + \tilde{n}_{k,n} \\ \qquad d_k \neq d_{k-1} \end{cases} \tag{41}$$

where the noise $\tilde{n}_{k,n}$ is a complex Gaussian random variable with variance N_0/T. The subcarrier reduction function, C_{sc_n}, is given by Eq. (6) after replacing ϕ_{sc} by ϕ_{sc_n}, the subcarrier phase error for loop n. In addition, the phase ϕ_{sy_n} denotes the symbol-synchronization phase error for loop n, and θ_{n1} is the phase relative to signal 1, i.e., $\theta_{11} = 0$. The baseband carrier frequency Δf_c or $\Delta\omega_c/2\pi$ is equal to the difference between the predicted and actual IF carrier frequency and is assumed to be much less than the symbol rate, i.e., $\Delta f_c << 1/T$. The degradation at the output of the matched filter when the carrier is open-loop downconverted is approximately given as

$$D_{\Delta f_c} = \left(\frac{\sin(\pi\Delta f_c T)}{(\pi\Delta f_c T)}\right)^2 \tag{42}$$

Figure 4 illustrates the matched-filter degradation as a function of $\Delta f_c T$, and it is clear that the degradation is less than 0.013 dB when $\Delta f_c T < 0.03$.

The combined signal after phase compensation, $\tilde{z}_k$ in Fig. 2(a), is given as

$$\tilde{z}_k = \sum_{n=1}^{L} \beta_n \tilde{v}_{k,n} e^{-j\hat{\theta}_{n1}} \tag{43}$$

where $\tilde{v}_{k,n}$ is given in Eq. (41) and $\hat{\theta}_{n1}$ is an estimate of θ_{n1}. The optimum combiner weights are given as [3]

$$\beta_n = \sqrt{\frac{P_n}{P_1}\frac{N_{01}}{N_{0n}}} \tag{44}$$

---

[5] The actual operating bandwidth for the modified and unmodified subcarrier and symbol loops are investigated in Appendix B.

After substituting Eq. (41) for $\tilde{v}_{k,n}$ in Eq. (43), the combined signal can be rewritten as follows (see Appendix C, Section I):

$$\tilde{z}_k = \sqrt{P'} d_k e^{j(\Delta\omega_c t_k + \theta_{\tilde{z}})} + \tilde{n}_k \tag{45}$$

where the variance of the combined complex noise is given as [3]

$$\sigma_{\tilde{n}}^2 = \frac{N_{01}}{T} \sum_{i=1}^{L} \gamma_i \tag{46}$$

The conditional combined signal power P' is given as

$$P' = \begin{cases} P_1 \sum\limits_{n=1}^{L} \sum\limits_{m=1}^{L} \gamma_n \gamma_m C_{sc_n} C_{sc_m} C_{nm} & d_k = d_{k-1} \\ P_1 \sum\limits_{n=1}^{L} \sum\limits_{m=1}^{L} \gamma_n \gamma_m C_{sc_n} C_{sc_m} \left(1 - \frac{|\phi_{sy_n}|}{\pi}\right) \left(1 - \frac{|\phi_{sy_m}|}{\pi}\right) C_{nm} & d_k \neq d_{k-1} \end{cases} \tag{47}$$

where C_{nm} is given by Eq. (27). The signal $\tilde{z}_k$ is then demodulated using a baseband Costas loop with output equal to $e^{-j(\Delta\omega_c t_k + \hat{\theta}_{\tilde{z}})}$, where $\hat{\theta}_{\tilde{z}}$ is an estimate of $\theta_{\tilde{z}}$. The demodulator output is a real combined symbol stream and can be represented as

$$z_k = \sqrt{P'} C_c d_k + n_k \tag{48}$$

where C_c and P' are respectively given by Eqs. (5) and (47). The noise n_k is a real Gaussian random variable with variance $\sigma_n^2 = 1/2\sigma_{\tilde{n}}^2$ where $\sigma_{\tilde{n}}^2$ is given by Eq. (46). The SNR conditioned on ϕ_c, ϕ_{sc_n}, ϕ_{sy_n}, $\Delta\phi_{n1}$, denoted SNR'_{csc}, is defined as the square of the conditional mean of z_k divided by the conditional variance of z_k, i.e,

$$SNR'_{csc} = \begin{cases} \frac{2P_1 T}{N_{01}} C_c^2 \left(\frac{\sum\limits_{n=1}^{L} \sum\limits_{m=1}^{L} \gamma_n \gamma_m C_{sc_n} C_{sc_m} C_{nm}}{\sum\limits_{n=1}^{L} \gamma_n} \right) & d_k = d_{k-1} \\ \frac{2P_1 T}{N_{01}} C_c^2 \left(\frac{\sum\limits_{n=1}^{L} \sum\limits_{m=1}^{L} \gamma_n \gamma_m C_{sc_n} C_{sc_m} \left(1 - \frac{|\phi_{sy_n}|}{\pi}\right) \left(1 - \frac{|\phi_{sy_m}|}{\pi}\right) C_{nm}}{\sum\limits_{n=1}^{L} \gamma_n} \right) & d_k \neq d_{k-1} \end{cases} \tag{49}$$

The last equation is useful in computing the symbol SNR degradation and loss for CSC as shown below.

A. Degradation

As before, the degradation is found by dividing the unconditional CSC SNR, which includes the effects of synchronization and alignment errors, by the ideal SNR. The unconditional SNR, denoted SNR_{csc}, is computed by taking the statistical expectation of Eq. (49) with respect to ϕ_c, ϕ_{sc_n}, ϕ_{sy_n}, and $\Delta\phi_{n1}$. The phase densities are assumed to be the same as before. In addition, ϕ_{sc_m} and ϕ_{sc_n} are assumed to be independent when $n \neq m$, and the same is true for ϕ_{sy_m} and ϕ_{sy_n}. Consequently,

$$SNR_{csc} = \frac{2P_1T}{N_{01}}\overline{C_c^2}\,\frac{\left(\sum\limits_{n=1}^{L}\gamma_n^2\overline{C_{sc_n}^2}\;\overline{C_{sy_n}^2} + \sum\limits_{n=1}^{L}\sum\limits_{\substack{m=1\\ n\neq m}}^{L}\gamma_n\gamma_m\overline{C_{sc_n}}\;\overline{C_{sc_m}}\;\overline{C_{sy_n}}\;\overline{C_{sy_m}}\;\overline{C_{nm}}\right)}{\sum\limits_{n=1}^{L}\gamma_n} \tag{50}$$

where the average signal reduction function due to phase misalignment between baseband signals n and m, denoted $\overline{C_{nm}}$, is given by Eq. (28) with $\sigma^2_{\Delta\phi_{n1}} = 1/(2SNR_{n1,csc})$. The CSC correlator SNR or $SNR_{n1,csc}$ is shown in Appendix C, Section II to be

$$SNR_{n1,csc} = \frac{P_1}{N_{01}}\,\frac{T_c\overline{C_{sc_1}}^2\,\overline{C_{sc_n}}^2\,\overline{C_{sy_1}}^2\,\overline{C_{sy_n}}^2}{\overline{C_{sc_n}^2}\;\overline{C_{sy_n}^2} + \overline{C_{sc_1}^2}\;\overline{C_{sy_1}^2}(\frac{1}{\gamma_n}) + \frac{N_{0n}}{P_nT}} \tag{51}$$

where T_c is the averaging time of the correlator and T is the symbol period. The loop reduction functions $\overline{C_{sc_n}^2}$ and $\overline{C_{sy_n}^2}$ for the nth subcarrier and symbol loops are respectively given by Eqs. (16) and (17) where the loop SNR's are given by Eqs. (39) and (40). Similarly, $\overline{C_{sc_n}}$ and $\overline{C_{sy_n}}$ can be computed using the same loop SNR as follows [1]:

$$\overline{C_{sc_n}} = 1 - \sqrt{\frac{8}{\pi^3}}\frac{1}{\sqrt{\rho_{sc_n}}} \tag{52}$$

$$\overline{C_{sy_n}} = 1 - \sqrt{\frac{1}{2\pi^3}}\frac{1}{\sqrt{\rho_{sy_n}}} \tag{53}$$

The carrier loop degradation $\overline{C_c^2}$ is given by Eq. (15), with the loop SNR ρ_c computed using the average combined power $P'/N_{0_{eff}}$, which is found by averaging Eq. (47) over all the phases and then dividing by the effective noise level, $N_{0_{eff}} = T\sigma_{\bar{n}}^2$. Ideally, when there are no phase errors, $\overline{C_c^2} = \overline{C_{sc}^2} = \overline{C_{sy}^2} = \overline{C_{sc}} = \overline{C_{sy}} = \overline{C_{nm}} = 1$ and Eq. (50) reduce to $\left[(2P_1T/N_{01})\sum_{n=1}^{L}\gamma_n\right]$ as expected. Degradation is defined as before and given as

$$D_{csc} = -10\,\log_{10}\left(\overline{C_c^2}\left(\frac{\left(\sum\limits_{n=1}^{L}\gamma_n^2\overline{C_{sc_n}^2}\;\overline{C_{sy_n}^2} + \sum\limits_{n=1}^{L}\sum\limits_{\substack{m=1\\ n\neq m}}^{L}\gamma_n\gamma_m\overline{C_{sc_n}}\;\overline{C_{sc_m}}\;\overline{C_{sy_n}}\;\overline{C_{sy_m}}\;\overline{C_{nm}}\right)}{\left(\sum\limits_{n=1}^{L}\gamma_i\right)^2}\right)\right) \tag{54}$$

B. Loss

The CSC SER for an L antenna array, denoted $P_{csc}(E)$, is defined as

$$P_{csc}(E) = \int_{-\frac{\pi}{2}}^{\frac{\pi}{2}}\int_{-\infty}^{\infty}\int_{-\infty}^{\infty}\int_{-\infty}^{\infty} P'_{csc}(E)\;p_c(\phi_c)\prod_{i=1}^{L}\left[p_{\phi_{sc_i}}(\phi_{sc_i})p_{\phi_{sy_i}}(\phi_{sy_i})\right]\prod_{n=2}^{L}\left[p_{\Delta\phi_{n1}}(\Delta\phi_{n1})\right]\;d\boldsymbol{\Delta\phi}\, d\boldsymbol{\phi_{sc}}\, d\boldsymbol{\phi_{sy}}\, d\phi_c \tag{55}$$

where the three $\int_{-\infty}^{\infty}$ are with respect to $\boldsymbol{\phi_{sc}} = (\phi_{sc_1}, ..., \phi_{sc_L}), \boldsymbol{\phi_{sy}} = (\phi_{sy_1}, ..., \phi_{sy_L})$, and $\boldsymbol{\Delta\phi} = (\Delta\phi_{21}, ..., \Delta\phi_{(L-1)1})$. The conditional SER, denoted P'_{csc}, is given as

$$P'_{csc} = \frac{1}{4}\operatorname{erfc}\left[\sqrt{\frac{E_{s1}}{N_{01}}\frac{\left(\sum_{n=1}^{L}\gamma_n^2 C_{sc_n}^2\left(1-\frac{|\phi_{sy_n}|}{\pi}\right)^2+\sum_{n=1}^{L}\sum_{\substack{m=1\\ n\neq m}}^{L}\gamma_n\gamma_m C_{sc_n}C_{sc_m}\left(1-\frac{|\phi_{sy_n}|}{\pi}\right)\left(1-\frac{|\phi_{sy_m}|}{\pi}\right)C_{nm}\right)}{\sum_{n=1}^{L}\gamma_n}C_c}\right]$$

$$+\frac{1}{4}\operatorname{erfc}\left[\sqrt{\frac{E_{s1}}{N_{01}}\frac{\left(\sum_{n=1}^{L}\gamma_n^2 C_{sc_n}^2+\sum_{n=1}^{L}\sum_{\substack{m=1\\ n\neq m}}^{L}\gamma_n\gamma_m C_{sc_n}C_{sc_m}C_{nm}\right)}{\sum_{n=1}^{L}\gamma_n}C_c}\right] \tag{56}$$

Ideally, when there are no losses, $C_c = C_{sc_n} = (1 - |\phi_{sy_n}|/\pi) = C_{nm} = 1$ and Eq. (55) reduce to $P(E)_{csc} = (1/2)\operatorname{erfc}\left(\sqrt{E_s L/N_0}\right)$, for an array of L antennas of the same size (i.e., when $\gamma_n = 1$ for all n). The loss for CSC is given by Eq. (23) with $P_s(E)$ now replaced by Eq. (55).

V. Numerical Results and Discussion

The discussion section is divided into two parts. The first part compares FSC and CSC for an array of two 70-m antennas when the symbol SNR at each antenna is very low (−11 dB) and very high (6 dB). The quantitative results obtained in Section I confirm that degradation and loss are equal at low SNR values, but show that degradation is a lower bound for loss at high symbol SNR values. The second part focuses on the Galileo S-band mission scenario, where the received SNR is expected to be very low. For this part, the FSC and CSC techniques are compared for several different antenna combinations with different symbol rates, using degradation as the performance measure.

A. Degradation Versus Loss

The FSC and CSC performance for an array of two 70-m antennas when the received signal is weak is shown in Fig. 5; results for a strong signal case are shown in Fig. 6(a) for $B_c = 70$ Hz and Fig. 6(b) for $B_c = 160$ Hz. The carrier bandwidth for the strong signal case was widened from 70 to 160 Hz to demonstrate the difference between degradation and loss as the carrier loop SNR becomes low. Inspection of these figures shows that degradation and loss are equal (within 0.01 dB) for weak signal levels, but degradation is a lower bound for loss at strong signal levels. Consequently, the generally relative performance measure of degradation can be used at low symbol SNR's to make an absolute assessment of the received system. It is shown later that the advantange of being able to use degradation instead of loss at low symbol SNR's is a significant savings in computation time. Clearly, if all harmonics of the subcarrier are used (see Section V-B), FSC outperforms CSC except at narrow $W_{sc}B_{sc} = W_{sy}B_{sy}$ where both curves converge.

The weak and strong signals are characterized as follows: weak signal is $P_1/N_{01} = P_2/N_{02} = 15$ dB-Hz, $R_{sym} = 1/T = 400$ sym/sec; strong signal is $P_1/N_{01} = P_2/N_{02} = 32$ dB-Hz, $R_{sym} = 1/T = 400$ sym/sec. Note that the weak signal's uncombined SNR $E_{s1}/N_{01} = E_{s2}N_{01} = -11$ dB, whereas the strong signal's $E_{s1}/N_{01} = E_{s2}/N_{01} = 6$ dB. For an ideal system, there is a 3-dB arraying gain so that the combined E_s/N_0 for the weak signal case is -8 dB, which corresponds[6] to an SER = 0.286942, and the combined E_s/N_0 in the strong signal case is 9 dB, for which the SER = 3.4×10^{-5}. The receiver parameters for FSC and CSC in the weak signal case are assumed to be as follows: $B_c = 0.1$ Hz, B_{sc} and B_{sy} are variable, $B_{corr} = 4$ kHz (FSC only), and $T_c = 120$ sec. The following parameters apply to the strong signal case: $B_c = 70$ Hz and $B_c = 160$ Hz, B_{sc} and B_{sy} are variable, $B_{corr} = 4$ kHz (FSC only), and $T_c = 120$ sec. Furthermore, the FSC correlator is assumed to operate only on fundamental subcarrier harmonics, i.e., $L_{sc} = 1$ in Eq. (31).

The degradation in these figures is found through Eq. (34) for FSC and Eq. (54) for CSC. The loss curves

---

[6] $P(E)_{ideal} = \frac{1}{2}\operatorname{erfc}\left(\sqrt{(E_s/N_0)L}\right)$ for L antennas of the same size.

are computed using Eqs. (23) and (35) for FSC and Eqs. (23) and (55) for CSC. The loss computation is an iterative process that uses a trial-and-error method as shown by the following example. Suppose the FSC loss for $W_{sc}B_{sc} = W_{sy}B_{sy} = 2$ mHz in Fig. 5 is to be computed. First, the FSC SER is computed[7] through Eq. (35) with $E_s/N_0 = -11$ dB. The resulting SER is 0.2916693, which is higher that the ideal SER of 0.286942. Consequently, a second computation of Eq. (35) is made with $E_s/N_0 = -11 \text{ dB} + \Delta E_s/N_0$. If the resulting SER is 0.286942, then the loss is said to be $\Delta E_s/N_0$. If the resulting SER is greater or less than 0.286942, then Eq. (35) is recomputed with different $\Delta E_s/N_0$ values until the SER is equal to the ideal SER. The value of $\Delta E_s/N_0$, which results in Eq. (35) equaling the ideal SNR, is by definition the loss. For this example, $\Delta E_s/N_0$ or the symbol SNR loss was found to be 0.2 dB. This method is clearly more difficult than degradation, which is a single computation devoid of integrals. Nevertheless, symbol SNR loss gives the absolute performance advantage of an arraying scheme, while symbol SNR degradation gives the relative performance advantage. The loop and correlator SNR's used in obtaining Figs. 5 and 6 are shown in Tables 3 and 4. The FSC loop SNR's are computed from Eqs. (9)–(11) using the average combined power found by averaging Eq. (26) over the residual phase and dividing by the effective noise level in Eq. (24). The CSC subcarrier and symbol loop SNR's are computed using Eqs. (39) and (40), respectively. However, the carrier loop SNR for CSC uses the average combined power $P'/N_{0_{eff}}$, which is found by averaging Eq. (47) over all the phases and then dividing by the effective noise level. Moreover, the correlation SNR's for FSC and CSC were computed using Eqs. (31) and (51), respectively.

B. Galileo S-Band Mission Scenario

The FSC and CSC performance for different combinations of 70-m and 34-m antennas is discussed in this section. Since Galileo has a weak signal, the performance measure used is degradation, although loss could have also been used, as demonstrated in Fig. 5. As pointed out in the introduction, the IF signals in FSC are typically transmitted to a central location before being combined and demodulated using a single receiver. However, since the retransmission channel is band-limited, signal energy may be lost prior to combining. Table 5 shows energy lost as a function of the number of subcarrier harmonics present at the central location (i.e., at the combiner input). For the Galileo scenerio, four subcarrier harmonics are present at the combiner input, and the energy lost is 0.22 dB. The retransmission of CSC signals to a central location, on the other hand, does not result in an energy loss because the symbol rates for Galileo (less than 640 sym/sec) can be easily supported by the retransmission channel.

1. Array of Two 70-m Antennas. With that background, consider first an array of two 70-m antennas when the signal characteristics and receiver parameters are the same as those in Fig. 5 with $R_{sym} = 400$ sym/sec. FSC performance for the Galileo scenerio is obtained by adding 0.22 dB to the FSC degradation in Fig. 5. The shifted FSC curve along with the CSC degradation (which is the same as in Fig. 5 since no energy is lost in CSC) is plotted in Fig. 7. Notice that both techniques have equal performance when $W_{sc}B_{sc} = W_{sy}B_{sy} = 1.2$ mHz. In addition, Fig. 7 shows results using the same parameters as in Fig. 5, but now with $R_{sym} = 200$ sym/sec (combined $E_s/N_0 = -5.0$ dB). In this case, FSC and CSC have equal performance when $W_{sc}B_{sc} = W_{sy}B_{sy} = 3.0$ mHz. The degradation due to individual components (carrier, subcarrier, symbol, and correlator) is discussed below, indicating the relative contribution of each to the total degradation shown in Fig. 7 for $R_{sym} = 400$ sym/sec.

The degradation due to a single component is defined as the degradation that would be observed when all but a single component are operating ideally. For example, in FSC the degradation due to the carrier loop is given as

$$D_{fsc}\big|_{[SNR_{n1,fsc}=\rho_{sc}=\rho_{sy}=\infty]} = -10 \ \log_{10} \overline{C_c^2} \tag{57}$$

which is derived by setting the correlation SNR, the subcarrier loop SNR, and the symbol loop SNR to infinity in Eq. (34). The degradation due to individual components is shown in Figs. 8(a), (b), (c), and (d). Table 6 lists the degradation breakdown for FSC and CSC at $W_{sc}B_{sc} = W_{sy}B_{sy} = 5$ mHz and $R_{sym} = 400$ sym/sec. It is evident that the combiner degradation for both schemes is negligible. Also, the carrier degradation is the same for FSC and CSC since the carrier loop SNR for both schemes is about the same. The subcarrier and symbol degradation, however, are significantly different for FSC and CSC, with CSC being greater because the carrier is not tracked nor the signal combined until after the subcarrier and symbol loops. Comparing the sum in Table 6 to Fig. 7 for $R_{sym} = 400$ sym/sec indicates that total degradation can be approximated as the sum of individual degradations.

2. Array of a 70-m and One 34-m STD Antenna. The performance of a 70-m with one 34-m STD

---

[7] Note that the SER in Eqs. (35) and (55) requires numerical integration. An approximation to SER can be derived, however, using the moments techniques described in [10].

antenna array is shown in Fig. 9(a) using the same parameters as in Fig. 5 except P_1/N_{01} = 15 dB-Hz and P_2/N_{02} = 7.3 dB-Hz, i.e., $\gamma_1 = 1$ and $\gamma_2 = 0.17$ as shown in Table 2. Figure 9(a) also shows the results when R_{sym} = 200 sym/sec. At these signal levels, the 34-m antenna is not expected to achieve subcarrier and symbol lock without being aided by the 70-m antenna. Consequently, the CSC arraying scheme is implemented by passing frequency and phase information from the 70-m to the 34-m antenna. As a result, the effective subcarrier and symbol loop SNR's of the 34-m are identical to that of the 70-m antenna. The modified CSC is called CSCA or complex-symbol combining with aiding. In this scenario, the practical FSC outperforms CSCA when $W_{sc}B_{sc} = W_{sy}B_{sy}$ is greater than 4.5 mHz at R_{sym} = 400 sym/sec and 10 mHz at R_{sym} = 200 sym/sec.

3. Array of a 70-m and Two 34-m STD Antennas. The result for an array of one 70-m and two 34-m antennas is shown in Fig. 9(b). Practical FSC, in this case, outperforms CSCA when $W_{sc}B_{sc} = W_{sy}B_{sy}$ is greater than 4.0 mHz at R_{sym} = 400 sym/sec and 8.5 mHz at R_{sym} = 200 sym/sec.

4. Array of a 70-m and Three 34-m STD Antennas. For an array of one 70-m and three 34-m antennas, practical FSC outperforms CSCA when $W_{sc}B_{sc} = W_{sy}B_{sy}$ is greater than 3.5 mHz at R_{sym} = 400 sym/sec and 8.2 mHz at R_{sym} = 200 sym/sec. See Fig. 9(c).

5. Array of Four 34-m STD Antennas. Figure 9(d) shows the result for an array of four 34-m antennas for R_{sym} = 50 sym/sec and R_{sym} = 25 sym/sec with B_{corr} = 400 Hz. For this array, FSC has less degradation than CSC when $W_{sc}B_{sc} = W_{sy}B_{sy}$ are above 0.32 mHz when R_{sym} = 50 sym/sec and above 0.8 mHz when R_{sym} = 25 sym/sec. Practical FSC is able to operate for the given $W_{sc}B_{sc} = W_{sy}B_{sy}$ without losing lock, assuming the subcarrier and symbol loops are able to lock to the signal if their respective loop SNR's are greater than 12 dB. For CSC, however, the maximum $W_{sc}B_{sc} = W_{sy}B_{sy}$ that can be supported without losing lock is about 0.9 mHz[8] at R_{sym} = 50 sym/sec and 2 mHz at R_{sym} = 25 sym/sec. Table 7 lists the break-even points for the different combinations of a 70-m and 34-m antennas mentioned.

VI. Conclusion

This article describes the performance of FSC and CSC in terms of symbol SNR degradation and symbol SNR loss. Both degradation and loss are approximately equal at low values of symbol SNR, but diverge at high SNR values. For arrays of two 70-m antennas, a 70-m and three 34-m antennas, a 70-m and two 34-m antennas, and a 70-m and one 34-m antenna, FSC has less degradation than CSC when $W_{sc}B_{sc} = W_{sy}B_{sy}$ are above 3.0, 10.0, 8.5, and 8.2 mHz at R_{sym} = 200 sym/sec, and 1.2, 4.5, 4.0, and 3.5 mHz at R_{sym} = 400 sym/sec, respectively. Moreover, for an array of four 34-m antennas, FSC has less degradation than CSC when $W_{sc}B_{sc} = W_{sy}B_{sy}$ are above 0.32 mHz at R_{sym}= 50 sym/sec and above 0.8 mHz at R_{sym} = 25 sym/sec.

Acknowledgments

The authors would like to thank Dr. W. J. Hurd for suggesting CSC as an arraying scheme. We also thank Dr. Van Snider and Dr. Fred Vance for their numerical integration comments. Finally, the various discussions with J. Statman, Pravin Vazirani, Steve Townes, Jeff Berner, Alexander Mileant, Mazen Shihabi, Mimi Aung-Goodman, and Scott Stephens are gratefully acknowledged.

---

[8] This point can be increased by using the average of the four phase estimates of the subcarrier and symbol loops to effectively improve the loop SNR by about 6 dB, so that the degradation is lessened.

References

[1] A. Mileant and S. Hinedi, "Overview of Arraying Techniques for Deep Space Communications," to be published in *IEEE Trans. Commun.*

[2] S. Hinedi, "NASA's Next Generation All-Digital Deep Space Network Breadboard Receiver," *IEEE Trans. on Commun.*, vol. 41, pp. 246–257, January 1993.

[3] D. Divsalar, "Symbol Stream Combining Versus Baseband Combining for Telemetry Arraying," *The Telecommunications and Data Acquisition Progress Report 42-74, vol. April–June 1983*, Jet Propulsion Laboratory, Pasadena, California, pp. 13–28, August 15, 1983.

[4] M. Shihabi, T. Nguyen, and S. Hinedi, "On the Use of Subcarrier in Future Space Missions," *IEEE Trans. on EMC*, February 1994.

[5] W. J. Hurd and S. Aguirre, "A Method to Dramatically Improve Subcarrier Tracking," *IEEE Trans. on Commun.*, vol. 36, pp. 238–243, February 1988.

[6] M. K. Simon, "Analysis of the Steady State Phase Noise Performance of a Digital Data-Transition Tracking Loop," *Space Programs Summary 37-55*, vol. 3, Jet Propulsion Laboratory, Pasadena, California, pp. 54–62, February 1969.

[7] R. Sfeir, S. Aguirre, and W. J. Hurd, "Coherent Digital Demodulation of a Residual Carrier Signal Using IF Sampling," *The Telecommunications and Data Acquisition Progress Report 42-78, vol. April–June 1984*, Jet Propulsion Laboratory, Pasadena, California, pp. 135–142, August 15, 1984.

[8] J. H. Yuen, *Deep Space Telecommunications Systems Engineering*, New York: Plenum Press, 1983.

[9] W. C. Lindsey and M. K. Simon, *Telecommunication Systems Engineering*, New Jersey: Prentice-Hall, Inc., 1973.

[10] J. K. Omura and M. K. Simon, *Satellite Communication Performance Evaluation: Computational Techniques Based on Moments,* JPL Publication 80-71, Jet Propulsion Laboratory, Pasadena, California, September 15, 1980.

Table 1. Comparison of FSC and CSC.

Parameter	FSC	CSC
Combining bandwidth	Sample rate	Sample rate
Carrier loop	Closed before subcarrier and symbol loops	Closed after subcarrier and symbol loops
Effective P/N_0 at input of subcarrier loop for two 70-m antennas		At least 6 dB lower than FSC when carrier is unlocked and 3 dB lower when carrier locked
Effective P/N_0 at input of symbol loop for two 70-m antennas		At least 6 dB lower than FSC when carrier is unlocked and 3 dB lower when carrier locked
Array of a 70- and 34-m antenna	Loops operate on the combined signal power	Phase and frequency information passed from 70- to 34-m antenna
Array of four 34-m antennas	Implementable	Harder to implement

Table 2. Gamma factors for DSN antennas.

Antenna size	Frequency band	γ_n
70 m	S-band	1.00
34 m STD	S-band	0.17
34 m HEF	S-band	0.07
70 m	X-band	1.00
34 m STD	X-band	0.13
34 m HEF	X-band	0.26

Table 3(a). FSC loop SNR's for SER = 0.286942.

$W_{sc}B_{sc} = W_{sy}B_{sy}$, mHz	Carrier loop SNR, dB	Subcarrier loop SNR, dB	Symbol loop SNR, dB	Correlator SNR, dB
0.01	21.8	57.9	46.0	15.9
0.1	21.8	47.9	36.0	15.9
0.3	21.8	43.1	31.3	15.9
0.5	21.8	40.9	29.0	15.9
0.7	21.8	39.4	27.6	15.9
0.9	21.8	38.3	26.5	15.9
2.0	21.8	34.9	23.0	15.9
4.0	21.8	31.8	20.0	15.9
6.0	21.8	30.1	18.2	15.9
8.0	21.8	28.8	17.0	15.9
10.0	21.8	27.9	16.0	15.9

Table 3(b). CSC loop SNR's for SER = 0.286942.

$W_{sc}B_{sc} = W_{sy}B_{sy}$, mHz	Carrier loop SNR, dB	Subcarrier loop SNR, dB	Symbol loop SNR, dB	Correlator SNR, dB
0.01	21.8	49.7	37.2	24.1
0.1	21.6	39.7	27.2	24.0
0.3	21.5	35.0	22.5	23.8
0.5	21.4	32.7	20.2	23.7
0.7	21.4	31.3	18.8	23.7
0.9	21.3	30.2	17.7	23.6
2.0	21.1	26.7	14.2	23.3
4.0	20.8	23.7	11.2	23.0
6.0	20.5	21.9	9.4	22.7
8.0	20.3	20.7	8.2	22.5
10.0	20.1	19.7	7.2	22.3

Table 4(a). FSC loop SNR's for SER = 3.4 × 10^{-5}.

$W_{sc}B_{sc} = W_{sy}B_{sy}$, mHz	Carrier loop SNR, dB		Subcarrier loop SNR, dB	Symbol loop SNR, dB	Correlator SNR, dB
	B_c = 160 Hz	B_c = 70 Hz			
0.01	12.7	16.3	80.8	72.1	47.8
0.1	12.7	16.3	70.8	62.1	47.8
1.0	12.7	16.3	60.8	52.1	47.8
10.0	12.7	16.3	50.8	42.1	47.8
100.0	12.7	16.3	40.8	32.1	47.8
1000.0	12.7	16.3	30.8	22.1	47.8

Table 4(b). CSC loop SNR's for SER = 3.4 × 10^{-5}.

$W_{sc}B_{sc} = W_{sy}B_{sy}$, mHz	Carrier loop SNR, dB		Subcarrier loop SNR, dB	Symbol loop SNR, dB	Correlator SNR, dB
	B_c = 160 Hz	B_c = 70 Hz			
0.01	12.7	16.3	77.1	67.3	49.3
0.1	12.7	16.3	67.1	57.3	49.3
1.0	12.7	16.3	57.1	47.3	49.3
10.0	12.7	16.3	47.1	37.3	49.2
100.0	12.6	16.2	37.1	27.3	49.1
1000.0	12.3	15.9	27.1	17.3	48.7

Table 5. Number of subcarrier harmonics versus loss in energy.

Number of subcarrier harmonics	Loss in energy, dB
1	0.91
2	0.45
3	0.30
4	0.22
5	0.18
6	0.15
7	0.13
8	0.11
9	0.10
10	0.07

Table 6. Degradation breakdown for two 70-m antennas at $W_{sc} B_{sc} = W_{sy} B_{sy} = 5$ mHz.

Degradation	FSC, dB	CSC, dB
Combiner	0.034	0.002
Carrier loop	0.029 $\rho_c = 21.8$	0.038 $\rho_c = 20.6$
Subcarrier loop	0.126 $\rho_{sc} = 30.8$	0.324 $\rho_{sc} = 22.7$
Symbol loop	0.124 $\rho_{sy} = 19.0$	0.342 $\rho_{sy} = 10.2$
Energy loss	0.22	0
Sum	0.533	0.708

Table 7. Break-even point for FSC and CSC.

Antenna array	Value of $W_{sy}B_{sy} = W_{sc}B_{sc}$ (mHz) where $D_{fsc} = D_{csc}$		Value of $W_{sy}B_{sy} = W_{sc}B_{sc}$ (mHz) where $D_{fsc} > D_{csc}$		Value of $W_{sy}B_{sy} = W_{sc}B_{sc}$ (mHz) where $D_{fsc} > D_{csc}$	
	$R_{sym} = 200$ Hz	$R_{sym} = 400$ Hz	$R_{sym} = 200$ Hz	$R_{sym} = 400$ Hz	$R_{sym} = 200$ Hz	$R_{sym} = 400$ Hz
Two 70-m	3.0	1.2	>3.0	>1.2	<3.0	<1.2
70- and three 34-m	8.2	3.5	>8.2	>3.5	<8.2	<3.5
70- and two 34-m	8.5	4.0	>8.5	>4.0	<8.5	<4.0
70- and one 34-m	10.0	4.5	>10.0	>4.5	<10.0	<4.4

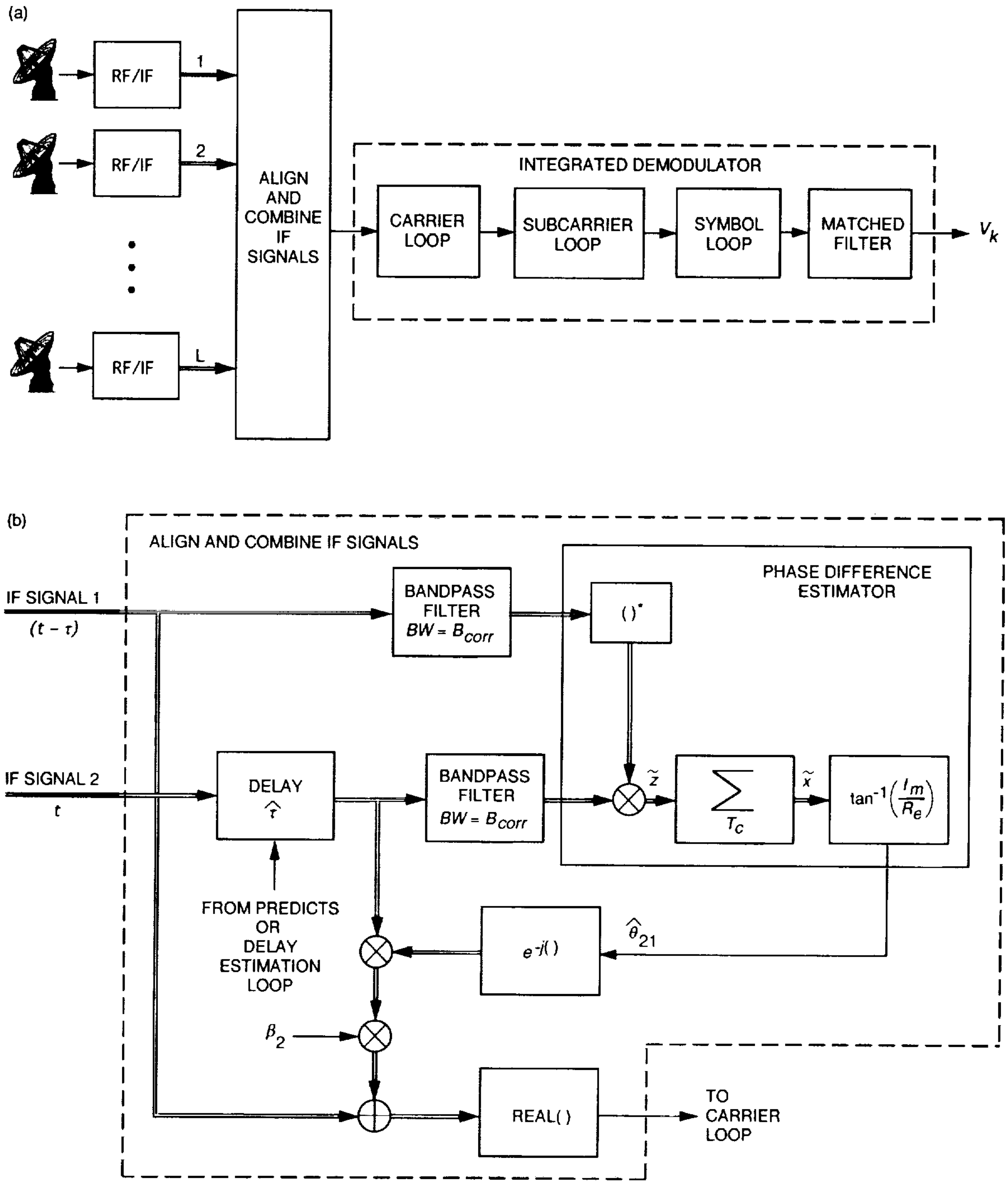

Fig. 1. Full-spectrum combining (FSC) algorithm: (a) *L* antenna array and (b) align-and-combine for an array of two antennas.

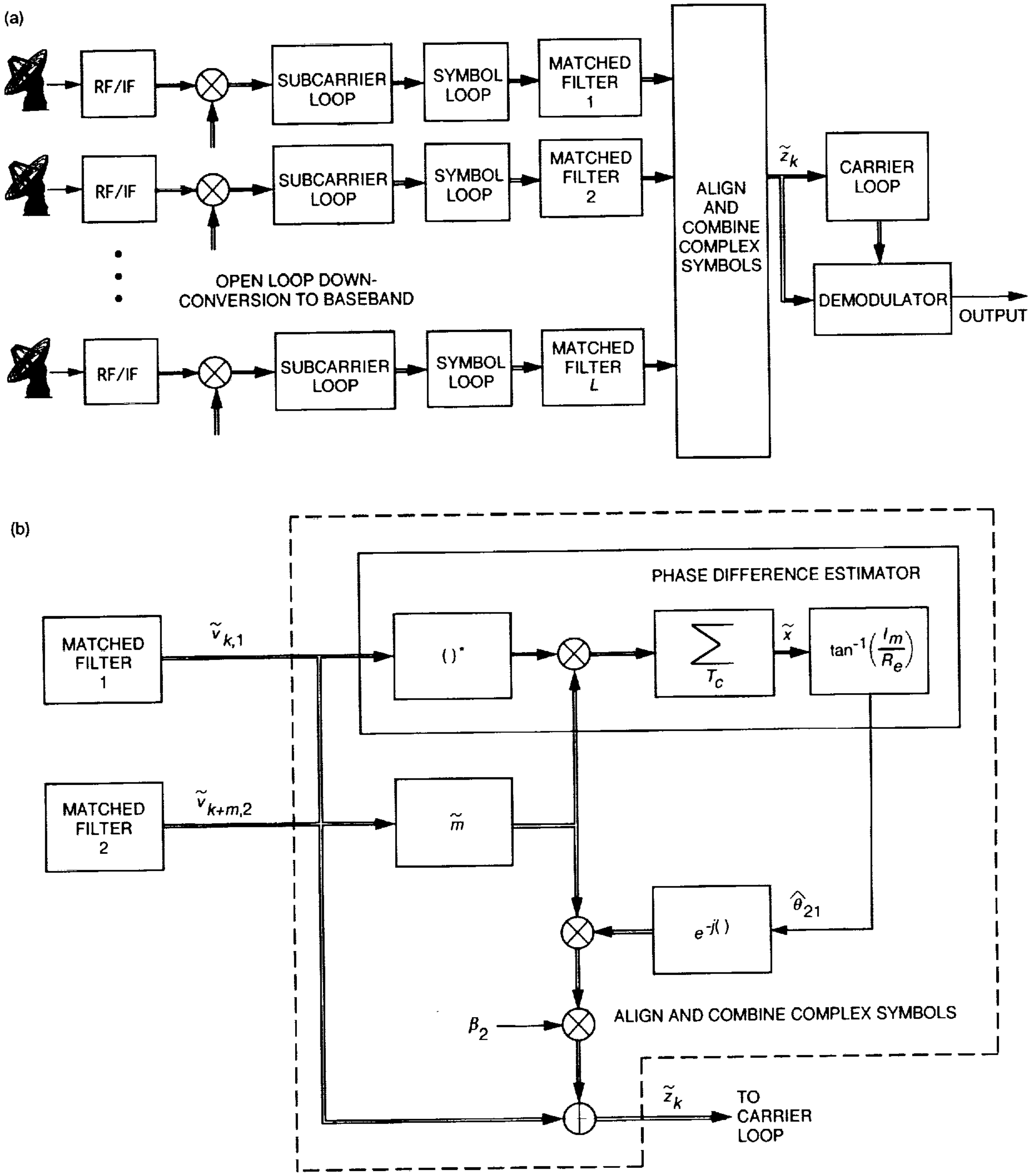

Fig. 2. Complex-symbol combining (CSC) algorithm: (a) *L* antenna array and (b) align-and-combine for an array of two antennas.

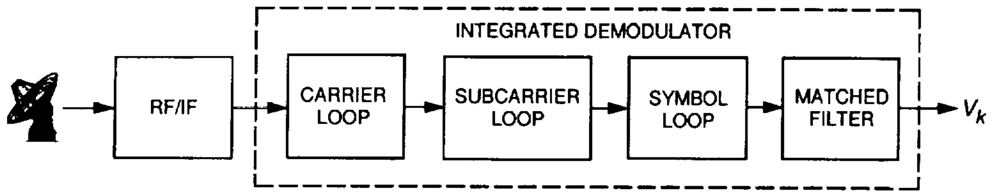

Fig. 3. A general coherent receiver model.

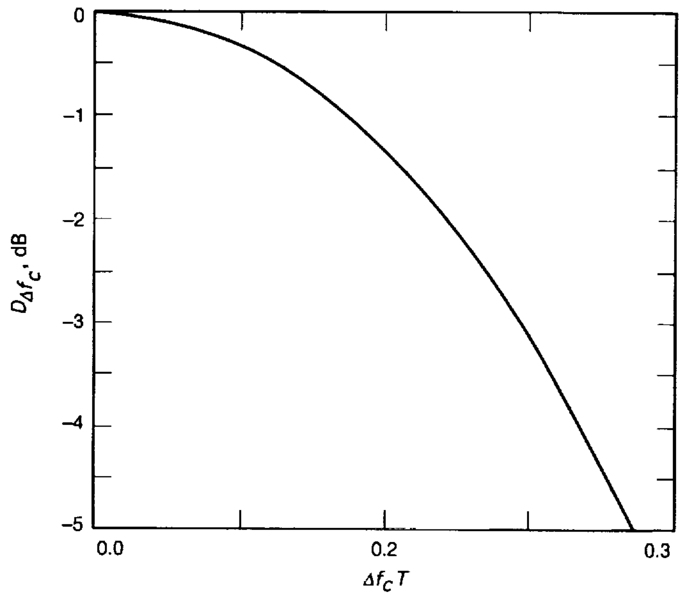

Fig. 4. Degradation at the matched filter output versus carrier frequency error-symbol time product.

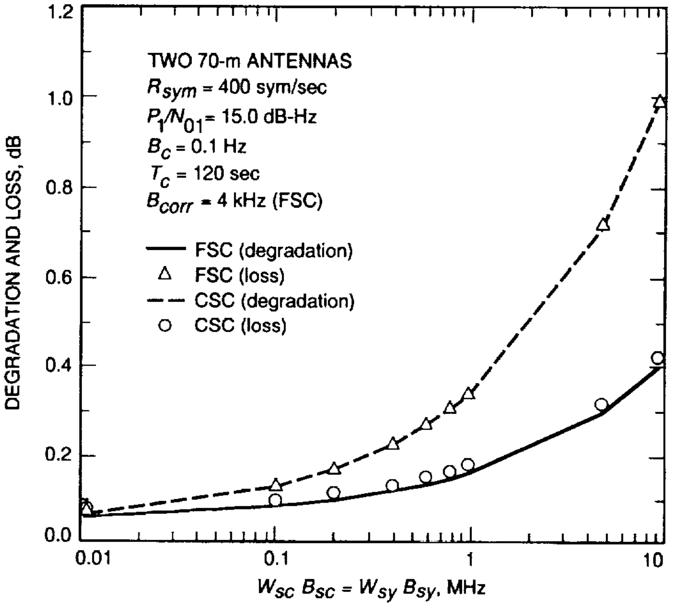

Fig. 5. Degradation and loss versus subcarrier and symbol window-loop bandwidth for SER = 0.286942.

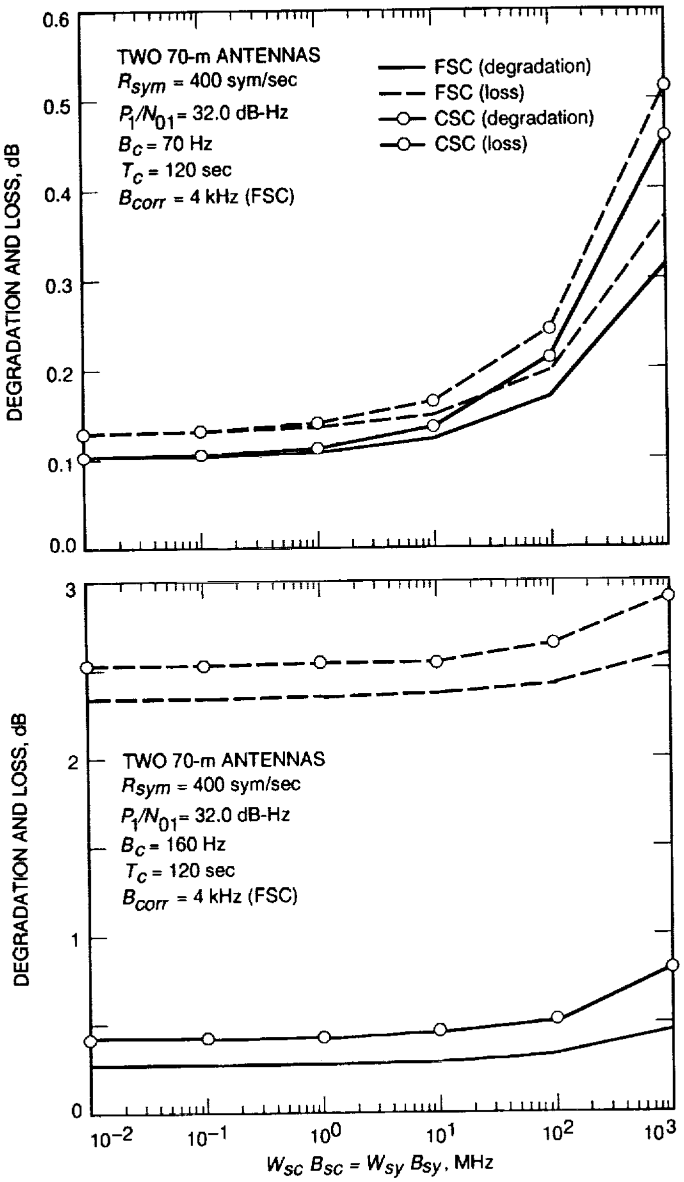

Fig. 6. A comparison of degradation and loss versus subcarrier and symbol window-loop bandwidth: (a) SER = 3.4 × 10^{-5} at Bc = 70 Hz and (b) SER = 3.4 × 10^{-5} at Bc = 160 Hz.

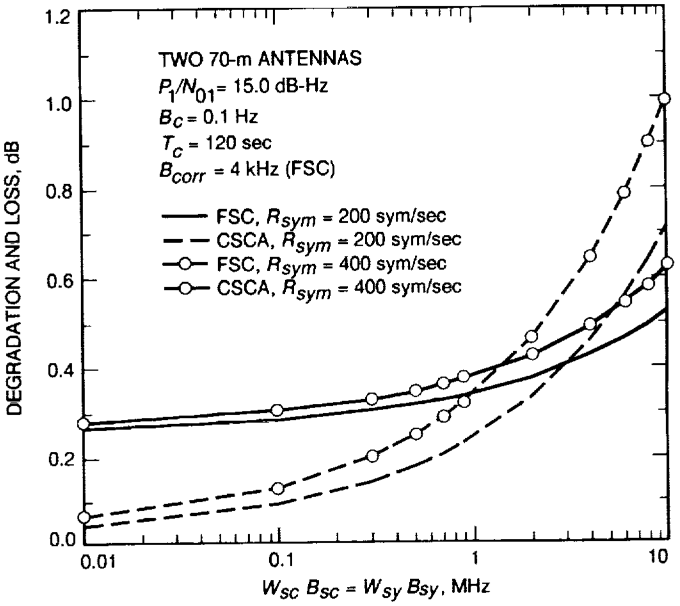

Fig. 7. Practical FSC and CSC degradation versus subcarrier and symbol window-loop bandwidth.

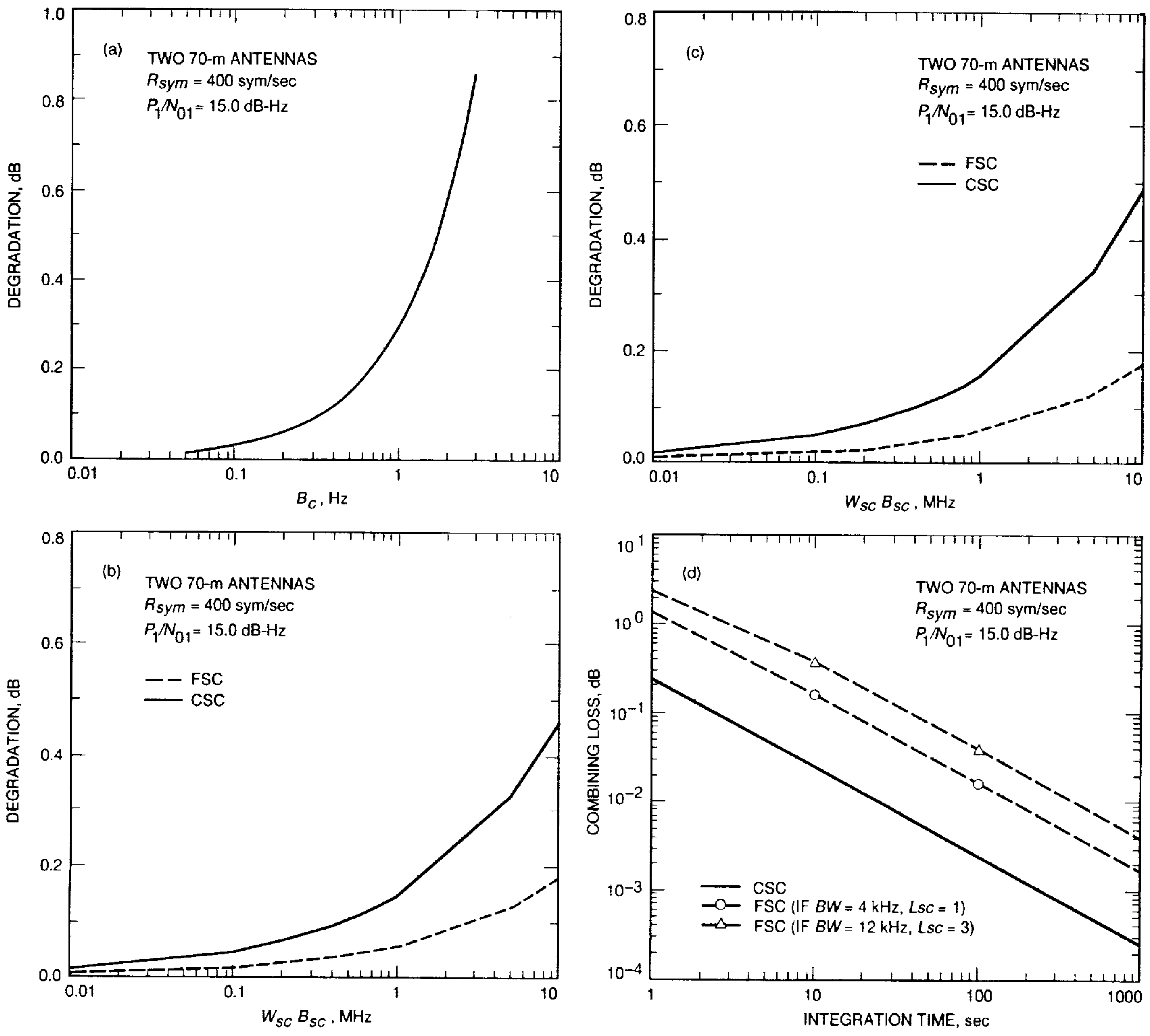

Fig. 8. Comparisons of degradation due to individual components: (a) carrier degradation versus carrier bandwidth; (b) subcarrier degradation versus subcarrier window-loop bandwidth; (c) symbol degradation versus symbol window-loop bandwidth; and (d) combining loss versus integration time.

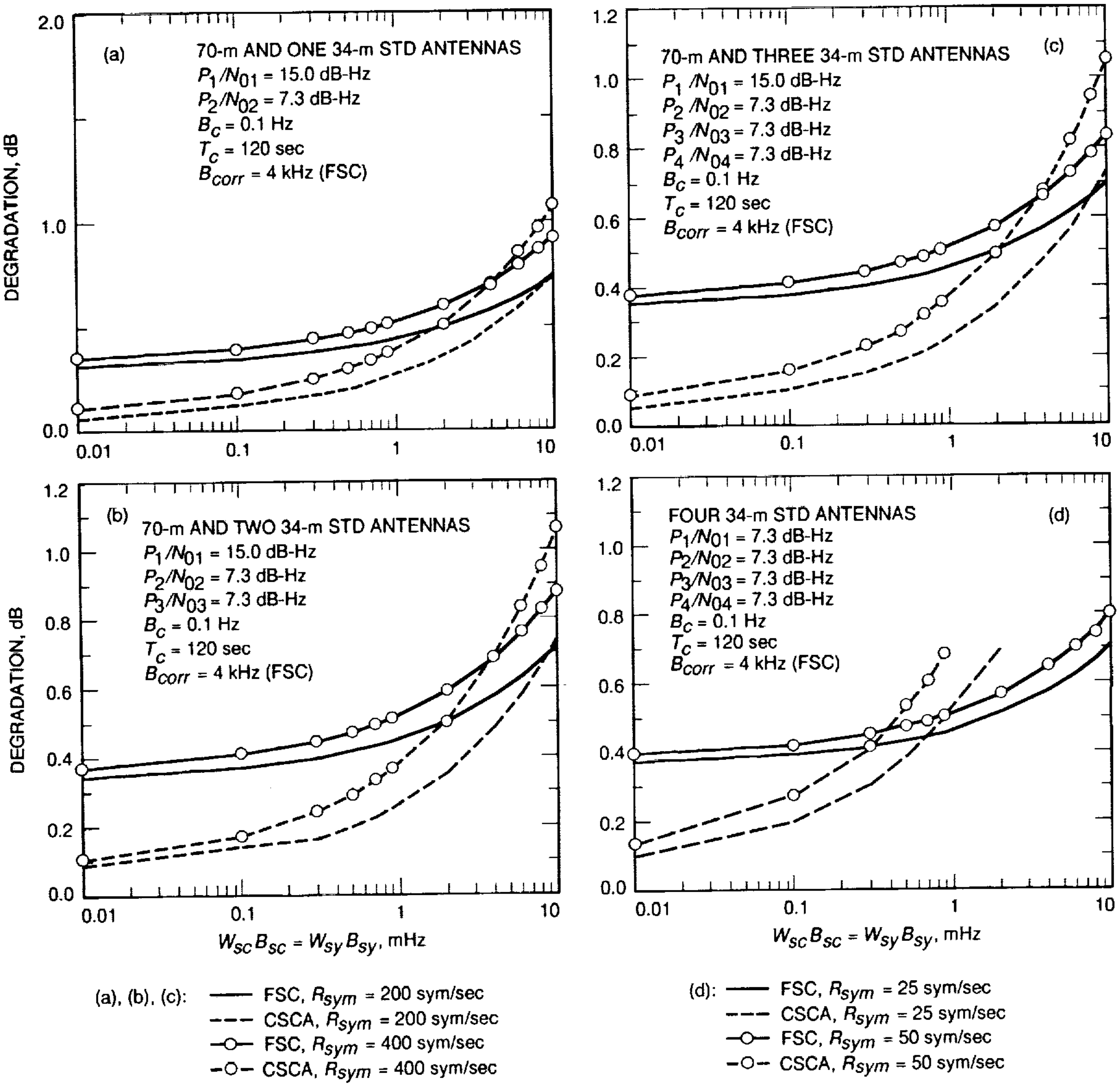

Fig. 9. Comparisons of degradation for various array configurations: (a) one 70-m and one 34-m STD antennas; (b) one 70-m and two 34-m STD antennas; (c) one 70-m and three 34-m STD antennas; and (d) four 34-m STD antennas.

Appendix A

The Performance of the FSC Correlator

The performance of the FSC correlator is derived here for the general case when total power is divided between data as well as the carrier. Once the general correlator SNR is derived, it will be simplified for the Galileo case, which operates with the carrier fully suppressed. As shown in Fig. 1(b), combining at IF requires both delay and phase adjustments in order to coherently add the signals. Here, perfect knowledge of the time delay is assumed and only phase compensation is needed before adding the IF signals. The IF signal at antenna n, denoted by the double lines in Fig. 1(b), consists of an in-phase (I) and quadrature (Q) component given as $r_{nI}(t)$ and $r_{nQ}(t)$, respectively, as follows:

$$r_{nI}(t) = \sqrt{2P_c}\cos(\omega_c t + \theta_{cn}) - \sqrt{2P_d}d(t)\mathrm{Sqr}(\omega_{sc}t + \theta_{sc_n})\sin(\omega_c t + \theta_{cn}) + n_{nI}(t) \tag{A-1}$$

$$r_{nQ}(t) = \sqrt{2P_c}\sin(\omega_c t + \theta_{cn}) + \sqrt{2P_d}d(t)\mathrm{Sqr}(\omega_{sc}t + \theta_{sc_n})\cos(\omega_c t + \theta_{cn}) + n_{nQ}(t) \tag{A-2}$$

where the total power P in watts (W) is divided between the residual carrier and data by controlling the modulation index, Δ. Specifically, the carrier power $P_c = P\cos^2\Delta$ and the data power[1] $P_d = P\sin^2\Delta$. Also, $n_{nI}(t)$ and $n_{nQ}(t)$ are statistically independent with a flat one-sided PSD level equal to N_0 W/Hz, and all other relevant parameters are defined in the main text. The square-wave subcarrier defined above can be expressed as follows:

$$\mathrm{Sqr}(\omega_{sc}t + \theta_{sc_n}) = \frac{4}{\pi}\sum_{\substack{j=1\\ j:odd}}^{L_{sc}} \frac{\sin[j(\omega_{sc}t + \theta_{sc_n})]}{j} \tag{A-3}$$

where L_{sc}, the number of subcarrier harmonics, is infinite. As shown in Fig. 1(b), the IF signal from antenna 1 and n are first bandpass filtered with single-sided bandwidth B_{corr}, and then complex correlated. The output of the correlation, denoted $\tilde{z}$, is a complex signal consisting of a real (I) and imaginary (Q) component, i.e.,

$$\tilde{z} = I + jQ \tag{A-4}$$

The correlator SNR at $\tilde{z}$, denoted as $SNR'_{n1,fsc}$, is defined as

$$\begin{aligned} SNR'_{n1,fsc} &\triangleq \frac{E(\tilde{z})E(\tilde{z}^*)}{Var(\tilde{z})} = \frac{E(\tilde{z})E(\tilde{z}^*)}{E(\tilde{z}\tilde{z}^*) - E(\tilde{z})E(\tilde{z}^*)} \\ &= \frac{E^2(I) + E^2(Q)}{Var(I) + Var(Q)} \end{aligned} \tag{A-5}$$

where $*$ represents the complex conjugate operation. Following the correlation, an averaging operation over T_c sec is performed to reduce the noise effect. In that period, $N = 2B_{corr}T_c$ independent samples are used to reduce the variance by a factor of N. The SNR at $\tilde{x}$, denoted $SNR_{n1,fsc}$, is thus given by

---

[1] For the Galileo case, $\Delta = 90$ deg so that $P_c = 0$ and $P = P_d$.

$$
\begin{aligned}
SNR_{n1,fsc} &= SNR'_{n1,fsc}N \\
&= SNR'_{n1,fsc}(2B_{corr}T_c)
\end{aligned}
\tag{A-6}
$$

For the general case of any L_{sc}, the correlator SNR using Eq. (A-5) can be shown to be

$$
SNR'_{n1,fsc} = \frac{4P_{c1}P_{cn} + 4\left(\frac{4}{\pi}\right)^2 \sqrt{P_{c1}P_{cn}P_{d1}P_{dn}}\left[\sum_{\substack{j=1\\ j odd}}^{L_{sc}}\left(\frac{1}{j}\right)^2\right] + \left(\frac{4}{\pi}\right)^4 P_{d1}P_{dn}\left[\sum_{\substack{j=1\\ j odd}}^{L_{sc}}\left(\frac{1}{j}\right)^2\right]^2}{4N_oB_{corr}\left[P_{c1} + P_{cn} + \frac{1}{2}\left(\frac{4}{\pi}\right)^2(P_{d1}+P_{dn})\left(\sum_{\substack{j=1\\ j odd}}^{L_{sc}}\left(\frac{1}{j}\right)^2\right) + B_{corr}\right]}
\tag{A-7}
$$

where B_{corr} is assumed to be sufficiently wide to pass the L_{sc} subcarrier harmonic unfiltered. The correlator SNR at the output of the accumulator is now obtained by using Eq. (A-6) and, after simplification, is given as

$$
SNR_{n1} = \frac{T_c\left(2\frac{P_{c1}}{N_{01}}\frac{P_{cn}}{N_{0n}} + 2\left(\frac{4}{\pi}\right)^2\sqrt{\frac{P_{c1}}{N_{01}}\frac{P_{cn}}{N_{0n}}\frac{P_{d1}}{N_{01}}\frac{P_{dn}}{N_{0n}}}\left(\sum_{\substack{j=1\\ j odd}}^{L}\left(\frac{1}{j}\right)^2\right) + \frac{1}{2}\left(\frac{4}{\pi}\right)^4\frac{P_{d1}}{N_{01}}\frac{P_{dn}}{N_{0n}}\left(\sum_{\substack{j=1\\ j odd}}^{L}\left(\frac{1}{j}\right)^2\right)^2\right)}{\frac{P_{c1}}{N_{01}} + \frac{P_{cn}}{N_{0n}} + \frac{1}{2}\left(\frac{4}{\pi}\right)^2\left(\frac{P_{d1}}{N_{01}} + \frac{P_{dn}}{N_{0n}}\right)\left(\sum_{\substack{j=1\\ j odd}}^{L}\left(\frac{1}{j}\right)^2\right) + B_{corr}}
\tag{A-8}
$$

For $\Delta = 90$ deg, Eq. (A-8) is reduced to Eq. (31). In addition, setting $\Delta = 0$ deg in Eq. (A-8) results in the same expression for the correlator SNR as that given in [1].

Appendix B

Subcarrier and Symbol Loop SNR Performance

I. Subcarrier Loop SNR Performance

Compared to the conventional unmodified subcarrier loop, which employs the I-arm as shown in Fig. B-1, the modified subcarrier loop, depicted in Fig. B-2, utilizes both the I and Q arms of the baseband signal for tracking. The loop SNR for both schemes is derived here and compared to the case when the carrier is locked. For CSC, the I and Q channels at the input of the subcarrier loop are respectively given as

$$I(t_n) = \sqrt{P}d(t_n)\mathrm{Sqr}(\omega_{sc}t_n + \theta_{sc})\cos(\Delta\omega_c t_n) + n_I(t_n) \tag{B-1}$$

$$Q(t_n) = \sqrt{P}d(t_n)\mathrm{Sqr}(\omega_{sc}t_n + \theta_{sc})\sin(\Delta\omega_c t_n) + n_Q(t_n) \tag{B-2}$$

where $n_I(t_n)$ and $n_Q(t_n)$ are independent Gaussian noise processes and all other parameters were previously defined. As shown in Fig. B-2, both the I and Q components are multiplied by the square-wave references and averaged over one symbol period (assuming perfect symbol synchronization), resulting in [5]

$$I_s(k) = \sqrt{P}d_k f(\phi_{sc})\cos(\Delta\omega_c t_k) + n_{Is}(k) \tag{B-3}$$

$$I_c(k) = \sqrt{P}d_k g(\phi_{sc})\cos(\Delta\omega_c t_k) + n_{Ic}(k) \tag{B-4}$$

$$Q_s(k) = \sqrt{P}d_k f(\phi_{sc})\sin(\Delta\omega_c t_k) + n_{Qs}(k) \tag{B-5}$$

$$Q_c(k) = \sqrt{P}d_k g(\phi_{sc})\sin(\Delta\omega_c t_k) + n_{Qc}(k) \tag{B-6}$$

where k denotes the symbol index, $f(\phi_{sc}) = 1 - 2/\pi|\phi_{sc}|$ for $|\phi_{sc}| \leq \pi$, $g(\phi_{sc}) = 2/\pi\ \phi_{sc}$ for $|\phi_{sc}| \leq \pi W_{sc}/2$, and $\mathrm{Var}[n_{Is}(k)] = \mathrm{Var}[n_{Ic}(k)] = \mathrm{Var}[n_{Qs}(k)] = \mathrm{Var}[n_{Qc}(k)] = \sigma_n^2 = N_0/2T$. The error signals of the conventional and modified subcarrier loops are respectively given as

$$e(k)_I = Pf(\phi_{sc})g(\phi_{sc})\cos^2(\Delta\omega_c t_k) + N_I(k) \tag{B-7}$$

$$e(k)_{IQ} = Pf(\phi_{sc})g(\phi_{sc}) + N_{IQ}(k) \tag{B-8}$$

where the variance of the noise terms respectively (after averaging over $\Delta\omega_c t_k$, assuming uniform distribution) are given as

$$\sigma_{N_{IQ}}^2 = P\sigma_n^2 + 2\sigma_n^4 \tag{B-9}$$

$$\sigma_{N_I}^2 = \frac{P\sigma_n^2}{2} + \sigma_n^4 \tag{B-10}$$

The slope of the S-curve can now be found by taking the first derivative of the average error signal with respect to ϕ_{sc}, and afterwards setting $\phi_{sc} = 0$. Accordingly, the slopes of the conventional and modified subcarrier loop are given as

$$K_{g,sc}^{I} = \frac{1}{\pi}P \tag{B-11}$$

$$K_{g,sc}^{IQ} = \frac{2}{\pi}P \tag{B-12}$$

Note the slope of the IQ-arm is identical to the slope of the I-arm when the carrier is locked [5]. Assuming linear theory, the loop SNR for the subcarrier loop is given as

$$\rho_{sc} = \frac{1}{2B_{sc}T}\frac{K_g^2}{\sigma_N^2} \tag{B-13}$$

where B_L is the one-sided noise bandwidth of the loop. Simplifying, the I- and IQ-arm loop SNR's are respectively given as

$$\rho_{sc}^{I} = \left(\frac{2}{\pi}\right)^2 \frac{P/N_0}{2B_L W_{sc}}\left(1 + \frac{1}{PT/N_0}\right)^{-1} \tag{B-14}$$

$$\rho_{sc}^{IQ} = \left(\frac{2}{\pi}\right)^2 \frac{P/N_0}{B_{sc} W_{sc}}\left(1 + \frac{1}{PT/N_0}\right)^{-1} \tag{B-15}$$

For comparison, the I-arm loop SNR when the carrier is locked is given in Eq. (10). Figure B-3 illustrates the subcarrier loop SNR's when the I-arm, IQ-arm, and the I-arm with the carrier locked are used. For low-symbol SNR's, the I-arm has a loop SNR that is 6 dB lower than when the carrier is locked. Using the IQ-arm recovers 3 of the 6 dB, but at the expense of more hardware. At high-symbol SNR's, the performance of the IQ-arm is identical to the I-arm when the carrier is locked.

The behavior of the I- and IQ-arm for the subcarrier loop is investigated when the carrier is actually locked. For the I-arm, the subcarrier is normalized by a slope that is less than the actual operating slope. Consequently, the operating bandwidth of the loop is actually narrower than the one specified. Fortunately, the subcarrier is normalized by the correct slope for the IQ-arm .

II. Digital Data Transition Tracking Loop SNR Performance

Similar to the subcarrier loop, the conventional digital data transition tracking loop (DTTL) shown in Fig. B-4 will be modified to utilize both the I and Q channels as depicted in Fig. B-5. Assuming perfect subcarrier demodulation, the I and Q components for CSC are given as

$$I_k = \sqrt{P}d_k \cos\left(\phi_c\right) + n_k^I \tag{B-16}$$

$$Q_k = \sqrt{P}d_k \sin\left(\phi_c\right) + n_k^Q \tag{B-17}$$

where n_k^I and n_k^Q are independent Gaussian random variables with variance $\sigma_n^2 = N_0/2T$, and $\phi_c = 2\pi\Delta f_c + \theta_c$ is the difference between the predicted and actual IF carrier frequency.

The performance of the DTTL has been derived in [6] assuming the carrier is locked ($\phi_c = 0$). When this is not the case, as in CSC, the loop suffers degradation; the objective is to quantify the decrease in performance for both the conventional and the modified DTTL. This analysis closely follows that of [6], except that the data are modulated by a slowly varying cosine function. Assuming the equivalent mathematical model of the DTTL in terms of a phase-locked loop, all the relevant parameters (slope of the S-curve and normalized equivalent noise spectrum) are derived conditioned on ϕ_c. Afterwards, these parameters are averaged over ϕ_c assuming ϕ_c is uniformly distributed from $-\pi$ to π.

The normalized mean of the error signal e_k conditioned on the normalized timing error λ (in cycles) and the carrier predict error ϕ_c is the normalized phase-detector characteristic $g_n(\lambda, \phi_c)$ commonly termed the loop S-curve. Following similar steps as in [6], $g_n^I(\lambda, \phi_c)$ and $g_n^{IQ}(\lambda, \phi_c)$, the S-curves of the conventional and the modified DTTL, are respectively given as

$$g_n^I(\lambda, \phi_c) = \lambda \;|\cos(\phi_c)|\; \text{erf}\,(B) - \frac{W_{sy} - 2\lambda}{8}\;|\cos(\phi_c)|\;[\text{erf}\,(A) - \text{erf}\,(B)] \tag{B-18}$$

$$\begin{aligned} g_n^{IQ}(\lambda, \phi_c) = {} & \lambda\;|\cos(\phi_c)|\;\text{erf}\,(B) + \lambda\;|\sin(\phi_c)|\;\text{erf}\,(B') - \frac{W_{sy} - 2\lambda}{8}\;|\cos(\phi_c)|\;[\,\text{erf}\,(A) - \text{erf}\,(B)] \\ & - \frac{w - 2\lambda}{8}\;|\sin(\phi_c)|\;[\,\text{erf}\,(A') - \text{erf}\,(B')] \end{aligned} \tag{B-19}$$

where $A = \sqrt{E_s/N_0}|\cos\phi_c|$, $A' = \sqrt{E_s/N_0}|\sin\phi_c|$, $B = \sqrt{E_s/N_0}(1-2\lambda)\;|\cos\phi_c|$, and $B' = \sqrt{E_s/N_0}(1-2\lambda)\;|\sin\phi_c|$. To compute, the S-curve conditioned only on λ, $g_n^I(\lambda, \phi_c)$ and $g_n^{IQ}(\lambda, \phi_c)$ are numerically integrated over ϕ_c assuming uniform distribution. Setting ϕ_c to zero in Eq. (B-18) results in the same S-curve as that in [6].

The first derivative of the S-curve at $\lambda = 0$ is given as

$$K_{g,sy}^I(\phi_c) = |\cos(\phi_c)|\;\text{erf}\,(A) - \frac{W_{sy}}{2}\cos^2(\phi_c)\sqrt{\frac{E_s}{N_0\pi}}\;\exp(-A^2) \tag{B-20}$$

$$\begin{aligned} K_{g,sy}^{IQ}(\phi_c) = {} & |\cos(\phi_c)|\;\text{erf}\,(A) - \frac{W_{sy}}{2}\cos^2(\phi_c)\sqrt{\frac{E_s}{\pi}}\;\exp(-A^2) \\ & + |\sin(\phi_c)|\;\text{erf}\,(A') - \frac{W_{sy}}{2}\sin^2(\phi_c)\sqrt{\frac{E_s}{\pi}}\;\exp(-A'^2) \end{aligned} \tag{B-21}$$

where $K_{g,sy}^I(\phi_c)$ and $K_{g,sy}^{IQ}(\phi_c)$ denote the slope of the S-curve for the conventional and modified DTTL conditioned on ϕ_c, respectively. Numerically integrating over the carrier phase ϕ_c results in the unconditional slopes denoted $K_{g,sy}^I$ and $K_{g,sy}^{IQ}$, respectively.

Setting ϕ_c in Eq. (B-20) to zero results in

$$K_{g,sy} = \text{erf}\left(\sqrt{\frac{E_s}{N_0}}\right) - \frac{W_{sy}}{2}\sqrt{\frac{E_s}{N_0\pi}}\;\exp\left(-\frac{E_s}{N_0}\right) \tag{B-22}$$

which is identical to the slope given in [6]. Figure B-6 lists the ratio of $K_{g,sy}^I/K_{g,sy}$ and $K_{g,sy}^{IQ}/K_{g,sy}$ for different symbol SNR's and window sizes. At low-symbol SNR, $K_{g,sy}$ and $K_{g,sy}^{IQ}$ are about the same, while $K_{g,sy}^I$ is about twice as large.

Also, the normalized noise spectrum at $\lambda = 0$ can be shown to be

$$\mathrm{h}^I(0,\phi_c) = 1 + 0.5W_{sy}\frac{E_s}{N_0}\cos^2(\phi_c) - \frac{W_{sy}}{2}\left[\frac{1}{\sqrt{\pi}}\exp(-A^2) + \sqrt{\frac{E_s}{N_0}}\,|\cos(\phi_c)|\,\mathrm{erf}(A)\right]^2 \tag{B-23}$$

$$\mathrm{h}^{IQ}(0,\phi_c) = 2 + 0.5W_{sy}\frac{E_s}{N_0} - \frac{W_{sy}}{2}\left[\frac{1}{\sqrt{\pi}}\exp(-A^2) + \sqrt{\frac{E_s}{N_0}}\,|\cos(\phi_c)|\,\mathrm{erf}(A)\right]^2$$

$$-\frac{W_{sy}}{2}\left[\frac{1}{\sqrt{\pi}}\exp(-A'^2) + \sqrt{\frac{E_s}{N_0}}\,|\sin(\phi_c)|\,\mathrm{erf}(A')\right]^2 \tag{B-24}$$

where $h^I(0,\phi_c)$ and $h^{IQ}(0,\phi_c)$ denote the normalized noise spectrum for the conventional and modified DTTL conditioned on ϕ_c, respectively. Numerically integrating over the carrier phase, ϕ_c, results in the unconditional normalized noise spectrum denoted as $h^I(0)$ and $h^{IQ}(0)$, respectively. Setting ϕ_c in Eq. (B-23) to zero results in

$$\mathrm{h}(0) = 1 + 0.5W_{sy}\frac{E_s}{N_0} - \frac{W_{sy}}{2}\left[\frac{1}{\sqrt{\pi}}\exp\left(-\frac{E_s}{N_0}\right) + \sqrt{R_s}\,\mathrm{erf}\left(\sqrt{\frac{E_s}{N_0}}\right)\right]^2 \tag{B-25}$$

which is the same as the normalized noise spectrum given in [6]. Figure B-7 lists values of $h(0)$, $h^I(0)$, and $h^{IQ}(0)$ for different symbol SNR's at $W_{sy} = 1$. It is evident that $h(0)$ is slightly greater than $h^I(0)$ but significantly less than $h^{IQ}(0)$.

Assuming linear theory, the loop SNR for the DTTL is given as [6]

$$\rho_{sy} = \frac{1}{2\pi^2}\frac{P}{N_0 W_{sy} B_{sy}}\mathcal{L} \tag{B-26}$$

where $\mathcal{L} = K^2_{g,sy}/h(0)$. Furthermore, the loop SNR for the conventional and modified DTTL, denoted ρ^I_{sy} and ρ^{IQ}_{sy}, are found by normalizing Eq. (B-26) by $\mathcal{L}^I = (K^I_{g,sy})^2/h^I(0)$ or $\mathcal{L}^{IQ} = (K^{IQ}_{g,sy})^2/h^{IQ}(0)$, respectively. Figure B-8 illustrates the loop SNR of the DTTL using the I-arm, IQ-arm, and I-arm when the carrier is locked. At low-symbol SNR, it is clear that using only the I-arm reduces the loop SNR by 6 dB compared to the case when the carrier is locked, and utilizing the IQ-arm recovers 3 of the 6 dB.

The behavior of the I- and IQ-arm for symbol loop is investigated when the carrier is actually locked. For the I-arm, the symbol loop is normalized by a slope that is less than the actual operating slope, as shown in Fig. B-6. Consequently, the operating bandwidth of the loop is actually narrower than the one specified. Fortunately, at low-symbol SNR, the symbol loop is normalized by the correct slope for the IQ-arm. For high-symbol SNR, however, the symbol loop for the IQ-arm is normalized by a slope that is greater than the actual operating slope and, consequently, the operating bandwidth of the loop is actually wider that the one specified.

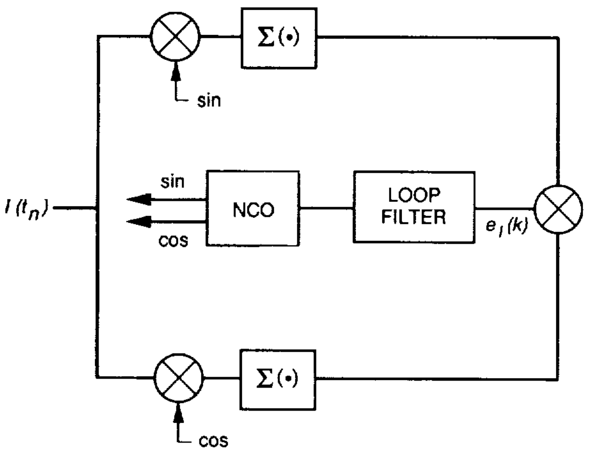

Fig. B-1. The unmodified subcarrier loop.

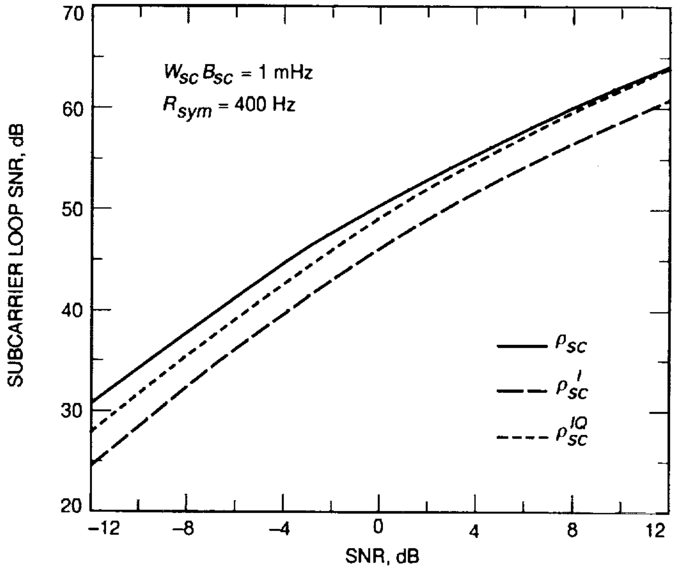

Fig. B-3. Subcarrier loop SNR versus symbol SNR.

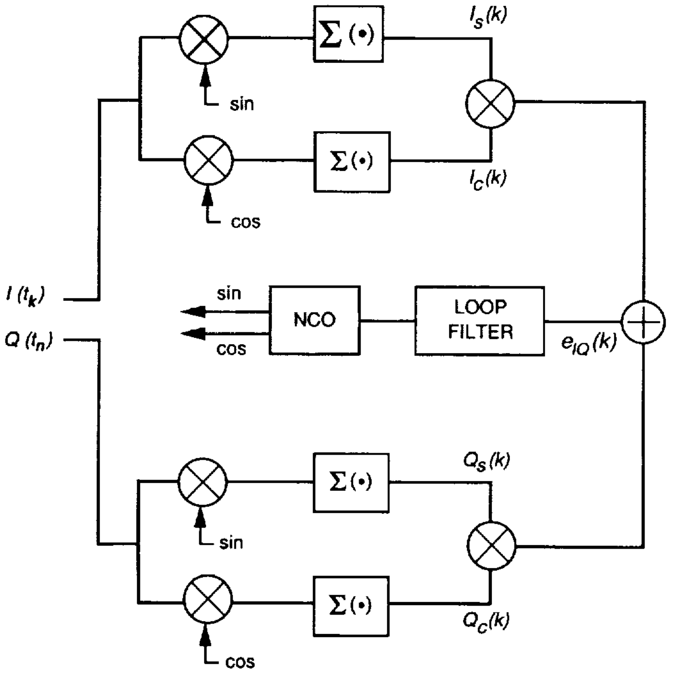

Fig. B-2. The modified subcarrier loop.

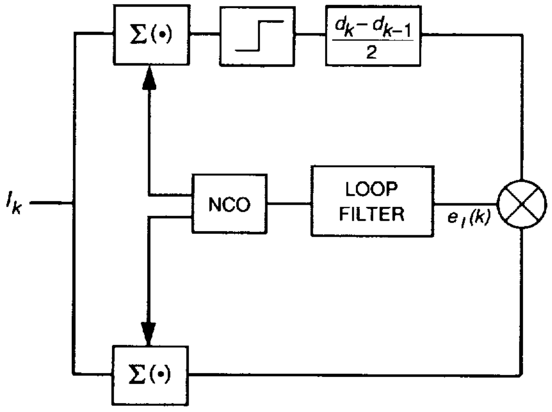

Fig. B-4. The unmodified digital data transition tracking loop (DTTL).

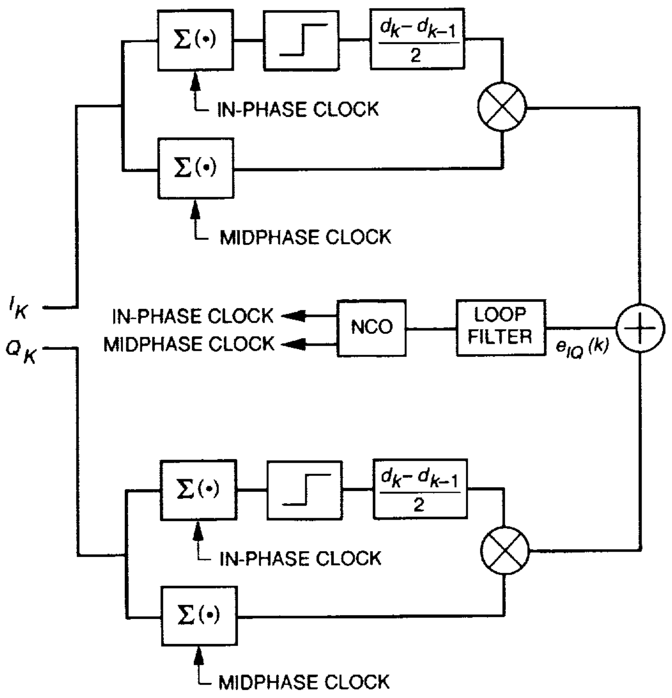

Fig. B-5. The modified digital data transition tracking loop.

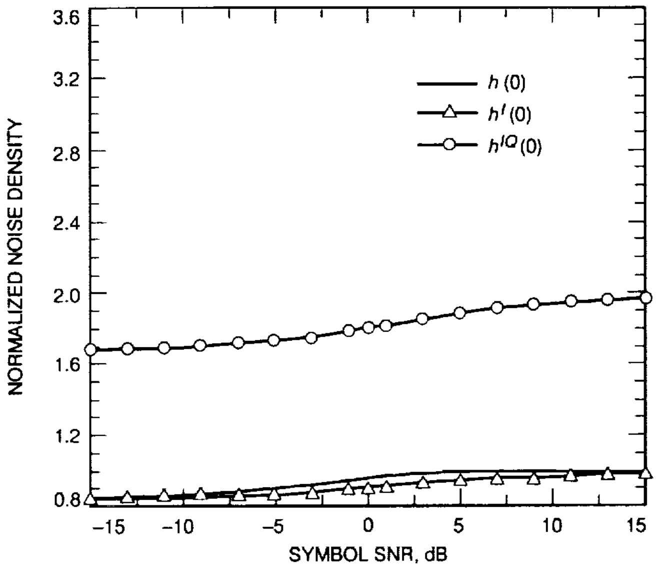

Fig. B-7. DTTL symbol SNR versus normalized noise density.

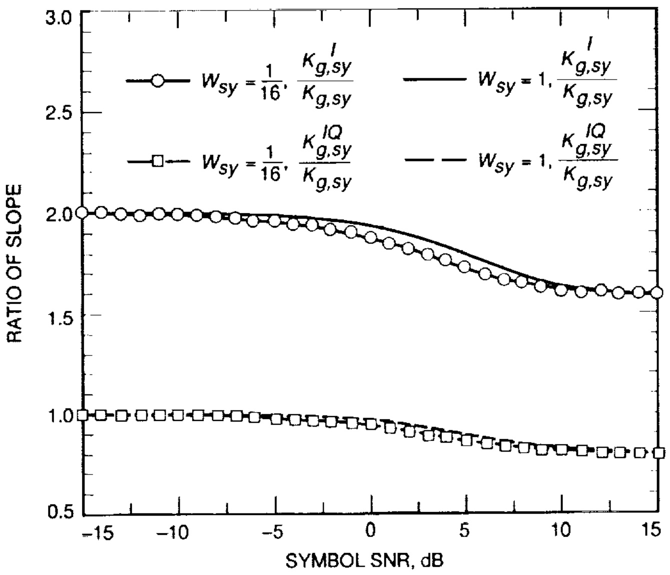

Fig. B-6. DTTL symbol versus ratio of slope.

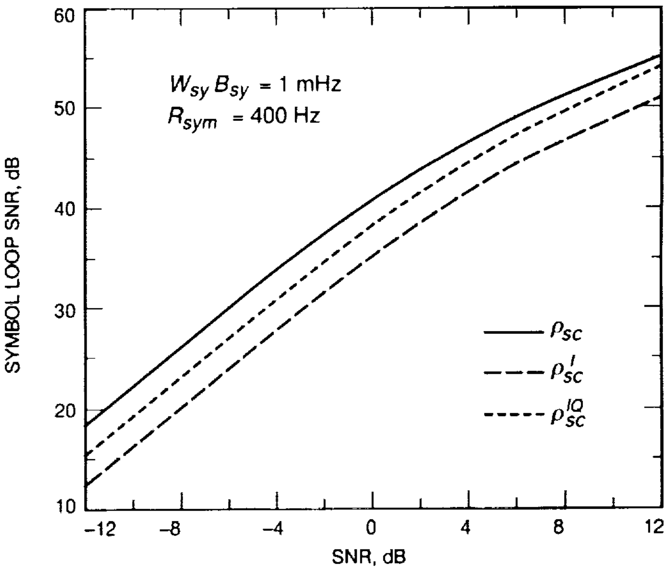

Fig. B-8. Symbol loop SNR versus symbol SNR.

Appendix C

Derivation of Equations

I. Derivation of Eq. (45)

Substituting Eq. (41) into Eq. (43) yields

$$\tilde{z}_k = \begin{cases} \sum\limits_{n=1}^{L} \beta_n \sqrt{P_n} C_{sc_n} d_k e^{[j(\Delta\omega_c t_k + \Delta\phi_{n1})]} + \tilde{n}_{k,n} e^{[-j(\hat{\theta}_{n1})]} & d = d_{k-1} \\ \sum\limits_{n=1}^{L} \beta_n \sqrt{P_n} C_{sc_n} \left(1 - \frac{|\phi_{sy_n}|}{\pi}\right) d_k e^{[j(\Delta\omega_c t_k + \Delta\phi_{n1})]} + \tilde{n}_{k,n} e^{[-j(\hat{\theta}_{n1})]} & d_k \neq d_{k-1} \end{cases} \tag{C-1}$$

where $\Delta\phi_{n1} = \theta_{n1} - \hat{\theta}_{n1}$ and all other symbols are defined in Eq. (41). The conditional combined power, denoted P', in Eq. (45) is found by deriving the conditional mean of $\tilde{z}_k$, i.e.,

$$P' = E(\tilde{z}_k/\phi_{sc_n}, \phi_{sy_n}, \Delta\phi_{n1}) E^*(\tilde{z}_k/\phi_{sc_m}, \phi_{sy_m}, \Delta\phi_{m1})$$

$$= \begin{cases} \sum\limits_{n=1}^{L} \sum\limits_{m=1}^{L} \beta_n \beta_m \sqrt{P_n} \sqrt{P_m} C_{sc_n} C_{sc_m} e^{j[\Delta\phi_{n1} - \Delta\phi_{m1}]} & d_k = d_{k-1} \\ \sum\limits_{n=1}^{L} \sum\limits_{m=1}^{L} \beta_n \beta_m \sqrt{P_n} \sqrt{P_m} C_{sc_n} C_{sc_m} \left(1 - \frac{|\phi_{sy_n}|}{\pi}\right) \left(1 - \frac{|\phi_{sy_m}|}{\pi}\right) e^{j[\Delta\phi_{n1} - \Delta\phi_{m1}]} & d_k \neq d_{k-1} \end{cases} \tag{C-2}$$

which simplifies to Eq. (47). In addition, the phase $\theta_{\tilde{z}}$ in Eq. (45) is given as

$$\theta_{\tilde{z}} = \begin{cases} \tan^{-1} \dfrac{\left(\sum\limits_{n=1}^{L} \beta_n \sqrt{P_n} C_{sc_n} \cos\left(\Delta\omega_c t_k + \Delta\phi_{n1}\right)\right)}{\left(\sum\limits_{n=1}^{L} \beta_n \sqrt{P_n} C_{sc_n} \sin\left(\Delta\omega_c t_k + \Delta\phi_{n1}\right)\right)} & d_k = d_{k-1} \\ \tan^{-1} \dfrac{\left(\sum\limits_{n=1}^{L} \beta_n \sqrt{P_n} C_{sc_n} \left(1 - \frac{|\phi_{sy_n}|}{\pi}\right) \cos\left(\Delta\omega_c t_k + \Delta\phi_{n1}\right)\right)}{\left(\sum\limits_{n=1}^{L} \beta_n \sqrt{P_n} C_{sc_n} \left(1 - \frac{|\phi_{sy_n}|}{\pi}\right) \sin\left(\Delta\omega_c t_k + \Delta\phi_{n1}\right)\right)} & d_k \neq d_{k-1} \end{cases} \tag{C-3}$$

II. Derivation of Eq. (51)

Let C_{sy_n} be the signal reduction function due to symbol timing errors in the nth symbol synchronization loop. Then the nth matched filter output in Eq. (41) can be rewritten as

$$\tilde{v}_{k,n} = \sqrt{P_n} C_{sc_n} C_{sy_n} d_k e^{[j(\Delta\omega_c t_k + \theta_{n1})]} + \tilde{n}_{k,n} \tag{C-4}$$

where

$$C_{sy_n} = \begin{cases} 1 & d_k = d_{k-1} \\ \left(1 - \frac{|\phi_{sy_n}|}{\pi}\right) & d_k \neq d_{k-1} \end{cases} \tag{C-5}$$

The relative phase difference between antenna n and the reference antenna is estimated by performing the correlation operation shown in Fig. 2(b). Assuming perfect time alignment, the correlation output $\tilde{x}$ is given as

$$\tilde{x} = \sum_{k=1}^{N} \tilde{v}_{k,n}\tilde{v}^{*}_{k,1} \tag{C-6}$$

where $N = T_c/T$ is the number of symbols used in the correlation. The correlation time and symbol time are respectively denoted as T_c and T. Substituting the expressions for $\tilde{v}_{k,n}$ and $\tilde{v}^{*}_{k,1}$ into Eq. (A-6) yields

$$\tilde{x} = \sqrt{P_1 P_n} C_{sc_1} C_{sc_n} C_{sy_1} C_{sy_n} e^{j(\theta_{n1})} + n_{\tilde{x}} \tag{C-7}$$

where

$$\mathrm{Var}(n_{\tilde{x}}) = 2P_1 \overline{C^2_{sc_1}}\,\overline{C^2_{sy_1}}\,\frac{N_{0n}}{2T_c} + 2P_n \overline{C^2_{sc_n}}\,\overline{C^2_{sy_n}}\,\frac{N_{01}}{2T_c} + 2\frac{N_{01}N_{0n}}{2TT_c} \tag{C-8}$$

Using the definition of SNR for complex signals as defined in Eq. (30), the correlator SNR between antenna n and antenna 1 for CSC is given as

$$SNR_{n1,csc} = \frac{\sqrt{P_1 P_n}\,\overline{C_{sc_1}}\,\overline{C_{sc_n}}\,\overline{C_{sy_1}}\,\overline{C_{sy_n}}}{2P_1 \overline{C^2_{sc_1}}\,\overline{C^2_{sy_1}}\,\frac{N_{0n}}{2T_c} + 2P_n \overline{C^2_{sc_n}}\,\overline{C^2_{sy_n}}\,\frac{N_{01}}{2T_c} + 2\frac{N_{01}N_{0n}}{2TT_c}} \tag{C-9}$$

and simplifying yields Eq. (51).

N94-29666

TOPEX/POSEIDON Operational Orbit Determination Results Using Global Positioning Satellites

J. Guinn, J. Jee, P. Wolff, F. Lagattuta, T. Drain, and V. Sierra
Navigation Systems Section

Results of operational orbit determination, performed as part of the TOPEX/POSEIDON (T/P) Global Positioning System (GPS) demonstration experiment, are presented in this article. Elements of this experiment include the GPS satellite constellation, the GPS demonstration receiver on board T/P, six ground GPS receivers, the GPS Data Handling Facility, and the GPS Data Processing Facility (GDPF). Carrier phase and P-code pseudorange measurements from up to 24 GPS satellites to the 7 GPS receivers are processed simultaneously with the GDPF software MIRAGE to produce orbit solutions of T/P and the GPS satellites. Daily solutions yield subdecimeter radial accuracies compared to other GPS, LASER, and DORIS precision orbit solutions.

I. Introduction

The Global Positioning System (GPS) Data Processing Facility (GDPF) was developed to demonstrate operational orbit determination and navigation support for TOPEX/POSEIDON. Orbit solutions are based on data collected by the GPS demonstration receiver (GPSDR) on board TOPEX/POSEIDON and six ground receivers. In addition, the GDPF is intended to evolve into a NASA resource for future low Earth-orbiting missions under the NASA Office of Space Communications.

An updated software set, based on the JPL institutional Orbit Determination Program (ODP), was created and named "MIRAGE." It stands for Multiple Interferometric Ranging Analysis using GPS Ensemble. MIRAGE maintains the complete interplanetary capability of the ODP software with the additional multisatellite and precision modelling features required for subdecimeter orbit determination. The GDPF scope of work includes preprocessing observations, performing orbit determination, producing predicted GPS and TOPEX/POSEIDON satellite almanacs for mission operations, and archiving raw and processed data. Figure 1 shows the interfaces of the GDPF.

II. Observation Preprocessing

Daily TOPEX/POSEIDON flight receiver raw data are collected from the TOPEX/POSEIDON ground system within 24 hours of the last observation. The raw data consist of carrier phase every second and P-Code pseudorange every 10 sec. In addition, the GPSDR onboard navigation solution (i.e., clock, position, and velocity) are provided every 10 sec. Descriptions of these observables can be found in many publications [1,2].

Automated reformatting and outlier and cycle slip editing are performed first. Next, the data are decimated to 5-min intervals, and a time-tag correction, based on a linear fit to the navigation clock solution, is applied. Finally, linear combinations of the pseudorange (P_1 and P_2) and carrier phase (L_1 and L_2) dual-frequency measurements are computed to produce ionosphere calibrations. These are applied to the raw P_1 and L_1 observations to produce the orbit determination observables P_C and L_C.

The ground GPS receiver observations are available from the GPS Data Handling Facility about 36 hr after the last data are collected. Both the carrier phase and pseudorange data are provided in receiver-independent exchange (RINEX) [3] format at 30-sec samples. The same editing and calibration steps are performed as described above for the GPSDR. Besides the six core ground sites, data from nine backup sites are also collected and processed. The primary and backup ground receiver locations are shown in Fig. 2.

For MIRAGE orbit determination processing, a merged file of edited GPSDR and ground receiver data is created in standard MIRAGE format. Two additional text files, in RINEX format, are produced for export. One is the raw GPSDR data while the other is the edited, calibrated, and compressed GPSDR measurements. All files are archived along with data collection and preprocessing statistics.

III. Orbit Determination Strategy

Thirty-hour data sets are constructed from the preprocessed observations to produce a 24-hr orbit solution. The additional data are fit to allow for internal consistency checks of the daily overlaps. Global GPS constellation coverage is realized by selecting a minimum of six ground station GPS receiver sites. Additional sites are selected to fill gaps during primary site outages.

Orbit determination using MIRAGE consists of three major steps. Iteration through each step is done until convergence of the state solutions and observation residuals is achieved. The three steps are

(1) Trajectory propagation.

(2) Observation processing.

(3) Filtering and smoothing.

A. Trajectory Propagation

To achieve subdecimeter accuracies, several dynamic force models are required. Tables 1 and 2 summarize the force models used in the numerical integration of the TOPEX/POSEIDON and GPS satellite trajectories. Reference frame, force, and measurement model parameters are based on TOPEX/POSEIDON and International Earth Rotation Service (IERS) standards [4].

B. Observation Processing

Both carrier phase and P-Code pseudorange data are processed. Table 3 lists the measurement models used for producing observation residuals. Again, these models are based largely on IERS standards.

C. Filtering and Smoothing

The filter and smoother generate corrections to the parameters affecting the trajectory propagation and the observation processing. MIRAGE employs a numerically stable square-root information filter that can compute smoothed estimates of time-varying stochastic parameters. Our orbit determination strategy employs a fiducial concept where three ground receivers, assumed to have well-known coordinates, are held fixed while the filter estimates the positions of three nonfiducial ground stations [5]. In addition, the states of the GPS satellites and TOPEX/POSEIDON are estimated along with the GPS satellite solar-pressure model parameters. The filtering strategy consists of a two-stage process—dynamic tracking followed by reduced dynamic tracking. In dynamic tracking, the accuracy of the orbit is limited by the precision of the dynamic models applied during trajectory propagation. In reduced dynamic tracking, the high-quality geometric information provided by the GPS measurement system is used to obtain a high-precision TOPEX/POSEIDON trajectory. Essentially, reduced dynamic tracking exploits the extreme precision of carrier phase tracking by using it to smooth the geometric solutions obtained from the less-precise pseudorange measurements. Although the success of the reduced dynamic technique is contingent on high-precision modeling of the GPS observations, the accuracies of the resultant trajectories are not degraded by deficiencies in the a priori dynamical models.

1. Data Weighting. The measurement precisions expected from the GPSDR and ground receiver observations were determined from ground tests before launch. Data weights consistent with these analyses and applied during filtering are shown in Table 4.

2. Stochastic Clock Estimation. To eliminate synchronization errors due to unstable oscillators, clock biases at the receivers and GPS transmitters are estimated at each measurement time. In the filter, one ground clock is chosen as a reference and a stochastic clock bias is estimated at each of the other receivers and GPS transmitters. A white noise stochastic process is employed with a batch length coinciding with the measurement intervals and the estimated smoothed clock biases are fed back to the observation processing module. As with standard double differencing techniques, the stochastic clock estimation strategy eliminates common clock errors. However, the stochastic method avoids both the difficulties of selecting a set of nonredundant double-difference combinations and the data noise correlations inherent in differenced measurements.

3. Stochastic Phase Bias Estimation. The continuously tracked GPS carrier phase precisely measures the relative range change between a GPS transmitter and its receiver. However, the carrier phase is ambiguous, which requires the estimation of a constant phase bias for each continuous pass between a transmitter and a receiver. In the filter, each phase bias is estimated as a white noise stochastic parameter that remains constant over a pass. At tracking discontinuities, the filter applies a white noise stochastic update for the bias parameter corresponding to an individual transmitter–receiver pair. The smoother generates a time profile of phase bias corrections that are applied during subsequent observation processing. This stochastic phase bias estimation strategy is efficient in terms of computation time and memory requirements, but does not attempt to resolve the integer nature of the phase biases.

4. Stochastic Estimation of Tropospheric Fluctuations. The model for troposphere delay is decomposed into a wet and a dry component.

$$\rho = \rho_{Z_d} R_d(\theta) + \rho_{Z_w} R_w(\theta)$$

where ρ_Z is the zenith delay and R is a mapping function that maps the zenith delay to the line of site at elevation θ. The fluctuations in the wet zenith delay are modeled as a stochastic random walk. The wet zenith delay is estimated at 5-min intervals (coincident with the measurement interval) using an a priori sigma of 5 cm and an effective batch-to-batch sigma of 3 mm for the noise driving the random walk process. As with the phase and clock biases, the smoothed time profiles of the stochastic fluctuations are fed back into the observation processing module on subsequent iterations of the orbit determination program.

5. Reduced Dynamic Tracking. The MIRAGE filter executes the reduced dynamic tracking strategy by modeling the three-dimensional accelerations on TOPEX/POSEIDON as exponentially time-correlated stochastic processes. The relative weighting of the dynamics and geometry may be adjusted by varying the time constant and the magnitude of the process noise uncertainty. A large time constant corresponds to a dynamic strategy while a short time constant emphasizes the geometry. In the orbit determination for TOPEX/POSEIDON, the three accelerations were updated at 5-min intervals; the time constant was 15 min with a corresponding batch-to-batch sigma of 7×10^{-9} m/sec^2 for the radial acceleration and 14×10^{-9} m/sec^2 for the spacecraft X and Y accelerations. This choice of filter parameters allowed deficiencies in the nongravitational force models to be compensated for by the stochastic accelerations; however, enough dynamical information is retained so that temporary degradation of the viewing geometry would not seriously reduce the accuracy of the output trajectory [6,7,8]. A summary of estimated parameters is given in Table 5.

IV. Orbit Determination Accuracy

Before launch, the MIRAGE software was intercompared with the GEODYN and UTOPIA software sets from the Goddard Space Flight Center (GSFC) and the University of Texas Center for Space Research (UTCSR), respectively. The intercomparison validated all dynamic trajectory models for TOPEX/POSEIDON and verified the laser range measurement models. For all cases, including the combined models case, the maximum radial differences were approximately 1 cm or less for a 10-day orbit. An additional intercomparison with the UTCSR GPS software MSODP to validate trajectory models for the GPS satellites was performed. All but the occulting solar radiation pressure produced subcentimeter, 10-day orbit comparisons. The solar radiation pressure intercomparison tests have been postponed due to the expected release of improved models.

After launch, the operational orbit determination accuracies have steadily improved as the procedures and techniques have been fine-tuned. Accuracy comparisons are broken into three distinct processing phases. The dates and groundtrack repeat cycles for each are presented in Table 6.

Data prior to cycle five were not considered for this analysis due to difficulties in the early days of the GPSDR plus the occurrence of several anti-spoofing days. Phase 1 processing was performed before most internal and external consistency checks (see below) were used; thus, it is not representative of the achievable accuracies. Phase 2 processing used 24-hr arcs with the dynamic technique augmented with empirical once- and twice-per-revolution parameters. Phase 3 consisted of 30-hr arcs with the additional reduced dynamic tracking strategy.

Statistics collected for the GPS carrier phase residuals (observations minus computed values) are presented in Fig. 3. These residuals are from phases 2 and 3 only. A marked reduction in the residuals is seen when the reduced dynamic technique is employed. Most of the gaps are due to GPS constellation anti-spoofing activity when no GPSDR data were available. Only 15 days of outage are associated with GPSDR software problems.

TOPEX/POSEIDON orbit comparisons have displayed subdecimeter agreements in the radial component with 1-day GPS precision orbit determination (POD) solutions and orbits derived from satellite LASER range (SLR) and Doppler orbitography and radiopositioning integrated by satellite (DORIS) data. Figures 4 and 5 show the three-dimensional and radial rms orbit differences during phases 2 and 3. The MIRAGE dynamic solutions are compared with dynamic solutions determined from laser data. These laser solutions are based on 10-day fits from GSFC's GEODYN program. In Fig. 5, the MIRAGE reduced dynamic solutions are compared. They are compared with another reduced dynamic solution from the GPS GIPSY–OASIS software that is part of the GPS Demonstration Experiment POD segment.

V. Processing Automation and Error Checking

One goal of the GDPF was to automate as much of the processing as possible. Beginning with the data collection through the delivery of final products, each aspect of the processing was examined and automated by means of standard Unix scripts and X-window interfaces to the scripts. Dashed lines in Fig. 1 denote automatic procedures that do not require human intervention. User inputs changing from day to day, such as the date, duration, and transmitting and receiving participants, are controlled via a graphical X-window interface that eliminates user input errors and ensures operational consistency. Error mail messages are generated to alert operators of malfunctions in the automated noninteractive scripts.

VI. Off-Nominal TOPEX/POSEIDON Attitude Modelling

Robust processing of off-nominal TOPEX/POSEIDON satellite attitude events is available in two ways. First, the actual attitude event change times (e.g., fixed to sinusoidal yaw steering event) are designed as user inputs. Secondly, the trajectory processing can use the attitude quaternions from telemetry. So far, all attitude events, except orbit maintenance maneuvers, have been accurately modelled with the user input overrides. The actual telemetry was required only for the maneuver.

VII. SLR and DORIS Data Types

In addition to the GPS P-code pseudorange and carrier phase observables, the MIRAGE software can process SLR and DORIS data. SLR and DORIS data types were incorporated to support TOPEX/POSEIDON verification activities. The SLR orbits are included in the Interim Geophysical Data Records (IGDR) science product [9]. Orbit file formats are identical for all data types (i.e., PFILE format); therefore, no interface changes are required for IGDR processing with MIRAGE GPS orbits. A utility has also been developed as part of the MIRAGE software to convert any MIRAGE orbit file into the precision orbit ephemeris (POE) format.

VIII. TOPEX/POSEIDON Mission Operations Support

A routine GDPF task is to produce GPSDR almanac predictions for initial acquisition operations. Almanac data are produced twice weekly as a contingency for rapid GPSDR failure recovery. The data are delivered to the Spacecraft Performance Analysis Team for reformatting and subsequent uplink to the GPSDR by the Flight Control Team.

IX. GPS Anti-Spoofing Results

During GPS constellation anti-spoofing activities, only Clear-Acquisition (CA) code pseudorange and L_1 carrier phase data are available from the GPSDR. However, an internal receiver calibration provides for an ionosphere correction to the ground receiver data. Preliminary tests have produced subdecimeter radial differences for limited sets of data by producing an approximate ionosphere calibration. This calibration is derived by subtracting the carrier phase measurements from the CA-code pseudorange measurements and smoothing the resulting signal to remove the multipath signal. This yields an ionosphere correction that can then be applied to both the CA-code pseudorange and carrier phase data.

X. GDPF Resources

Required GDPF resources in terms of personnel, computer time, and actual time to produce a 1-day (30-hr) solution are given in Table 7. Members of the operational orbit determination team work on a five-day-per-week schedule. Weekend backlogs are eliminated during this schedule. The totals given in Table 7 are for one team member per workstation. Continuous operation of the GDPF required a total of three members. The breakdown of tasks for the GDPF team is shown in Table 8. With the automation developed thus far, a single person could easily handle nominal production. The remainder of the team consists of backups, a lead, and sustaining hardware maintenance personnel.

XI. Conclusions

Operational orbit determination has been demonstrated for TOPEX/POSEIDON using the GPS constellation (20 to 24 satellites), the TOPEX/POSEIDON demonstration receiver, 6 ground receivers, the GPS Data Handling Facility, and the GPS Data Processing Facility. Comparisons between the MIRAGE orbit solutions and other precision orbit solutions based on LASER, DORIS, and GPS yield subdecimeter radial results. Both the GPS dynamic and reduced dynamic results from MIRAGE appear to exceed the original performance requirements (approximate 1-m radial position) and give results comparable to other geodetic quality software.

Acknowledgments

The authors would like to recognize the technical contributions of Bobby G. Williams to the overall design and development of the MIRAGE software. Also appreciated were other members of the software development team: Jim Collier, Vic Legerton, Rick Sunseri, and Mike Wang.

References

[1] L. Carson, L. Hailey, G. Geier, R. Davis, G. Huth, and T. Munson, "Design and Predicted Performance of the GPS Demonstration Receiver for the NASA TOPEX Satellite," *IEEE Transactions on Communications*, vol. CH-2675, pp. 422–454, July 1988.

[2] B. Hofmann-Wellenhof, H. Lichtenegger, and J. Collins, *GPS Theory and Practice*, 2nd ed., New York: Springer-Verlag, 1993.

[3] W. Gurtner and G. Mader, "RINEX: The Receiver Independent Exchange Format Version 2," *CSTG GPS Bulletin*, National Geodetic Survey, vol. 3, no. 3, September–October 1990.

[4] D. D. McCarthy, *IERS Standards*, IERS Technical Note 13, Paris: Observatoire de Paris, July 1992.

[5] B. G. Williams, K. C. McColl, and J. R. Guinn, "Navigation Accuracies for GPS Demonstration on TOPEX/POSEIDON," paper AIAA-90-2940, presented at the AIAA/AAS Astrodynamics Conference, Portland, Oregon, August 20–22, 1990.

[6] W. Bertiger, S. Wu, T. Yunck, R. Muellerschoen, P. Willis, Y. Bar-Sever, A. Davis, B. Haines, T. Munson, S. Lichten, and R. Sunseri, "Early Results From the TOPEX/POSEIDON GPS Precise Orbit Determination Demonstration," paper AAS-93-154, presented at the Third Annual AAS/AIAA Spaceflight Mechanics Meeting, Pasadena, California, February 22–24, 1993.

[7] B. G. Williams, "Precise Orbit Determination for NASA's Earth Observing System Using GPS," in *AAS Advances in the Astronautical Sciences*, vol. 65, San Diego, California: Univelt, Inc., pp. 83–100, 1988.

[8] S. C. Wu, T. P. Yunck, and C. L. Thornton, "Reduced-Dynamic Technique for Precise Orbit Determination of Low Earth Satellites," in *AAS Advances in the Astronautical Sciences*, vol. 65, San Diego, California: Univelt, Inc., pp. 101–113, 1988.

[9] B. G. Williams, E. J. Christensen, P. N. Yuan, K. C. McColl, and R. F. Sunseri, "Short Arc Orbit Determination for Altimeter Calibration and Validation on TOPEX/POSEIDON," in *AAS Advances in the Astronautical Sciences*, vol. 82, San Diego, California: Univelt, Inc., pp. 877–888, 1993.

Table 1. Force models for TOPEX/POSEIDON.

Model	Description
N-body	All planets, Sun, and Moon
Earth geopotential	50 x 50 truncated Joint Gravity Model-2 (JGM-2)
Indirect Earth–Moon Oblateness	2 x 2 lunar model
Solid Earth tides	IERS
Ocean tides	JGM-2
Rotational deformation	IERS
Relativity	Point mass Earth + Lense–Thirring
Solar radiation pressure	Conical shadow model
Atmospheric drag	Drag/temperature air density model
Albedo and infrared Earth radiation	2nd degree zonal model
Empirical accelerations	Once/rev and twice/rev models

Table 2. Dynamic force models for GPS satellites.

Model	Description
N-body	All planets, Sun, and Moon
Earth geopotential	12 x 12 truncated JGM-2
Indirect Earth–Moon oblateness	2 x 2 lunar model
Solid Earth tides	IERS
Ocean tides	JGM-2
Rotational deformation	IERS
Relativity	Point mass Earth + Lense–Thirring
Solar radiation pressure	Rock4 and Rock42 models

Table 3. Measurement models.

Model	Description
Solid Earth tides	0th-, 1st-, and 2nd-order corrections
Rotational deformation (pole tide)	IERS
Ocean loading	IERS
Polar motion	Daily values from University of Texas
Plate motion	Linear velocities
Earth center-of-mass offset	Currently zero

Table 4. GPS observation weights.

Data type	GPSDR	Ground station
Carrier phase, cm	2	1
Pseudorange, m	2	1

Table 5. Estimated parameters.

Parameter(s)	Number of parameters
TOPEX state	6
GPS states (24 satellites average)	144
Station locations (3 ground stations)	9
GPS solar pressure scale factors and Y-bias	72
Empirical dynamic parameters	9
Stochastics: (30-hr arcs with 5-min updates)	
Troposphere (six ground stations)	6
TOPEX and ground clocks (one master clock fixed)	30
Carrier phase biases	~160
TOPEX body-fixed accelerations (X, Y, Z)	3
Total	~439

Table 6. Dates for groundtrack repeat cycles.

Phase	Dates	Cycles
1	November 3, 1992–December 21, 1992	5–9
2	December 22, 1992–May 2, 1993	10–23
3	May 3, 1993–October 28, 1993	24–40

Table 7. GDPF processing performance.

Processing phase	CPU time, hr	Actual time, hr
Data preprocessing[a]		
Collection	0.1	0.1
TOPEX/POSEIDON editing	1.3	1.4
Ground station editing	0.4	0.5
Editing	0.1	0.1
Reformatting	0.1	0.1
Total	2.0	2.2
Orbit estimation (per iteration)		
Initialization	0.1	0.2
Trajectory propagation	0.3	0.3
Observation residual computation	0.5	0.5
Parameter estimation	0.1	0.1
Stochastic parameter smoothing	0.1	0.1
Three-iteration total	3.3	3.6
Archive	0.1	0.2
Total	5.4	6.0

[a] Automated processing performed prior to start of work day.

Table 8. GDPF personnel requirements.

Task	Personnel
Lead[a]	1
Data conditioning	1
Orbit conditioning	1
Hardware maintenance	0.5

[a] Lead will also assist and back up data-conditioning and orbit determination functions.

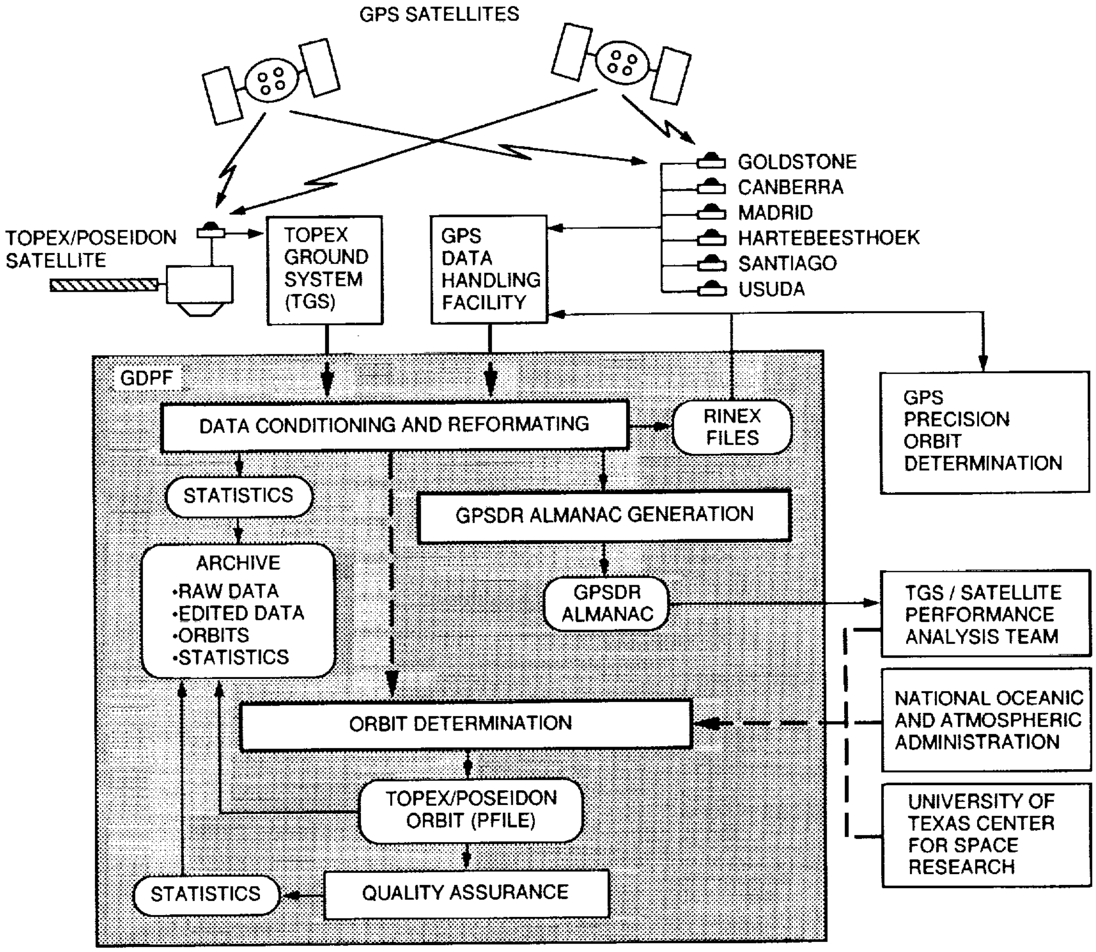

Fig. 1. GPS Data Processing Facility interfaces.

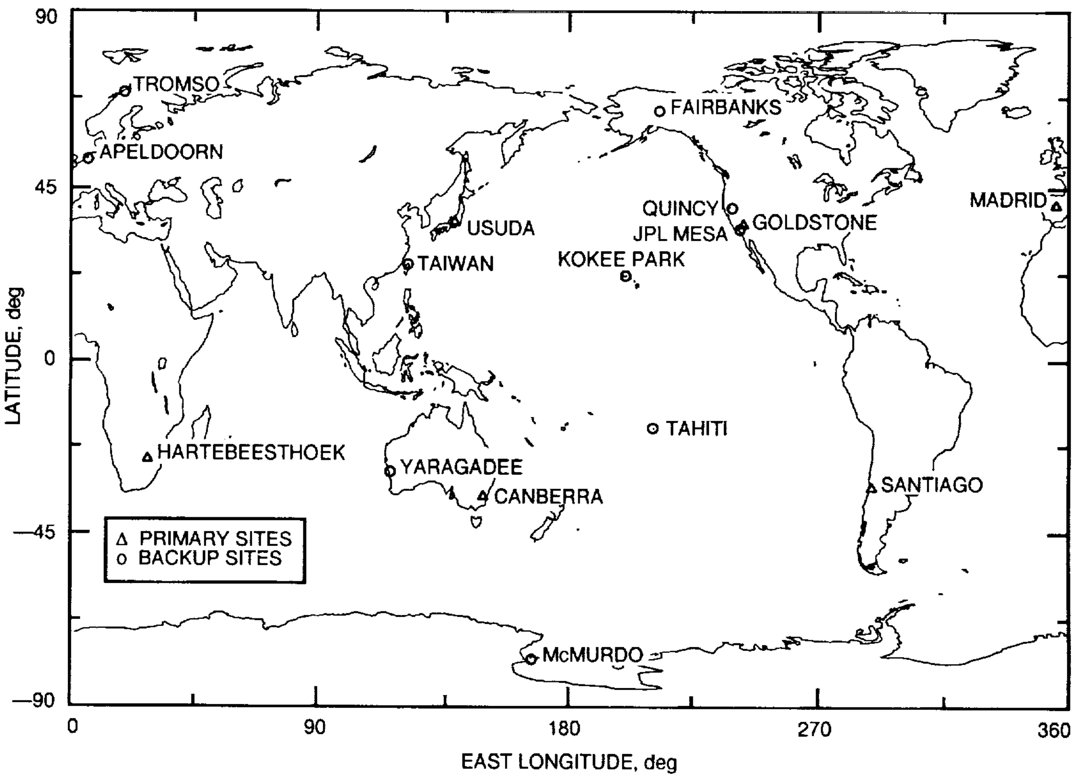

Fig. 2. TOPEX/POSEIDON GPS Ground Receiver Network.

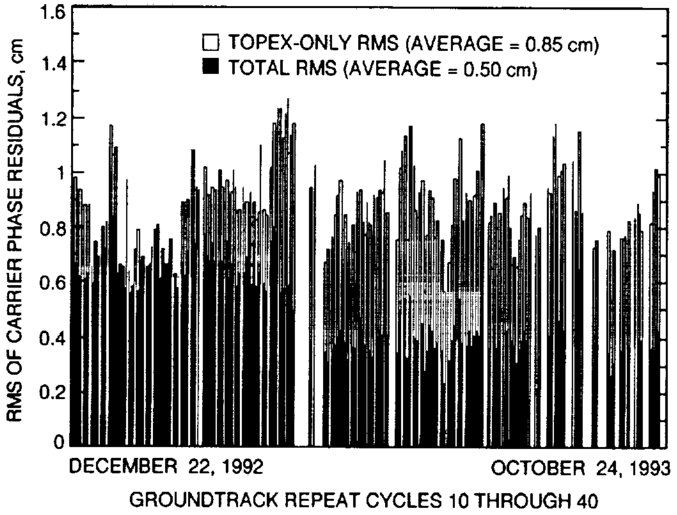

Fig. 3. MIRAGE observation residuals from TOPEX/POSEIDON flight receiver and six ground receivers.

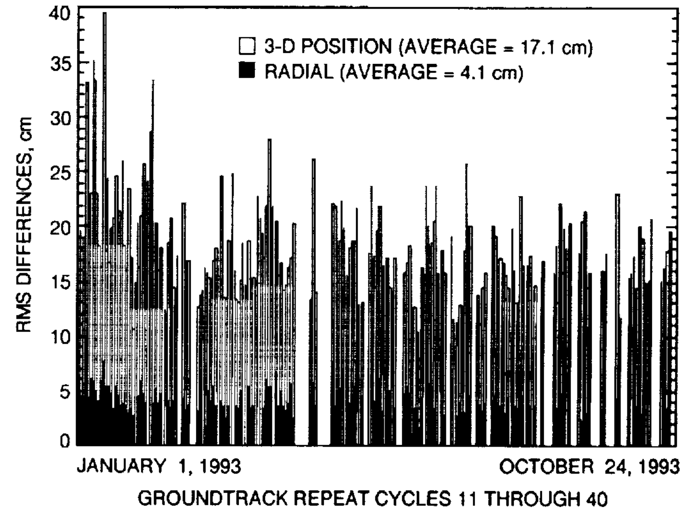

Fig. 4. MIRAGE GPS dynamic orbit solutions compared with laser and DORIS solutions.

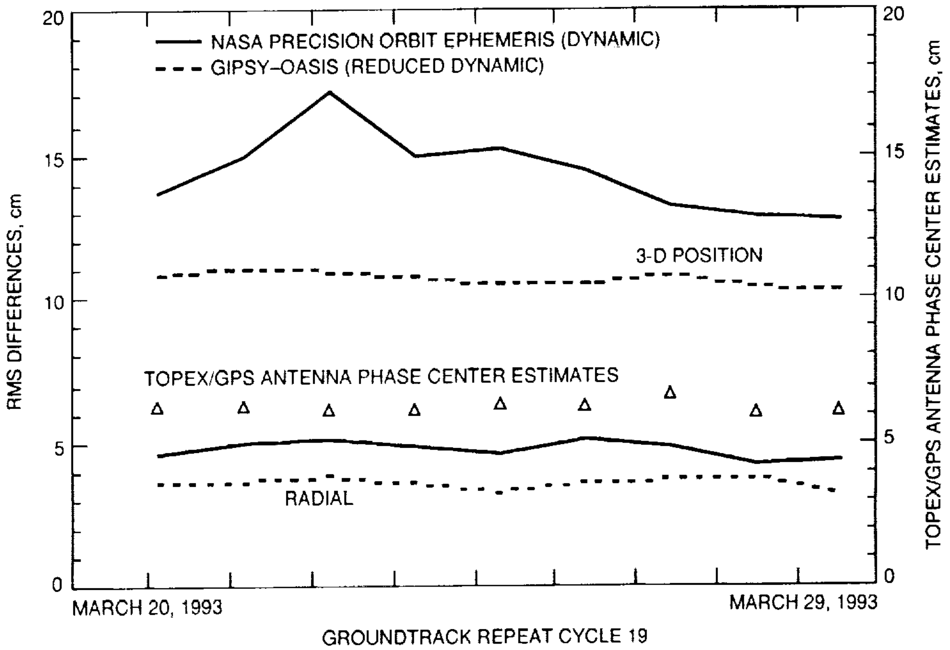

Fig. 5. MIRAGE GPS reduced dynamic orbit comparisons.

a-3.

N94- 29667

Design and Implementation of a Hybrid Digital Phase-Locked Loop With a TMS320C25—An Application to a Transponder Receiver Breadboard

H.-G. Yeh
Spacecraft Telecommunications Equipment Section

T. M. Nguyen
Communications Systems Research Section

Design, modeling, analysis, and simulation of a phase-locked loop (PLL) with a digital loop filter are presented in this article. A TMS320C25 digital signal processor (DSP) is used to implement this digital loop filter. In order to keep the compatibility, the main design goal was to replace the analog PLL (APLL) of the Deep-Space Transponder (DST) receiver breadboard's loop filter with a digital loop filter without changing anything else. This replacement results in a hybrid digital PLL (HDPLL). Both the original APLL and the designed HDPLL are Type I second-order systems. The real-time performance of the HDPLL and the receiver is provided and evaluated.

I. Introduction

Future NASA missions will require low-cost, small-sized, low-power-consumption spacecraft telecommunication equipment. To achieve the best design within mission resources, one must incorporate emerging technologies in the flight hardware. These requirements motivate the study of replacing a baseband analog loop filter with a digital filter in the phase-locked loop (PLL) of the existing X-band (7.145–7.19 MHz) transponder receiver breadboard.

Conventional spacecraft transponders employ analog circuits from the front-end antenna to the baseband carrier phase-tracking loop. With new digital technology, it is possible to build a very reliable all-digital IF and baseband circuit by using digital signal-processing techniques. However, before building a space-qualified all-digital transponder, it is preferable to experiment on a hybrid digital PLL (HDPLL) by using an existing X-band Deep-Space Transponder (DST) receiver breadboard as a first step in order to build confidence and obtain design experience. Furthermore, in order to keep the compatibility, the main design goal is limited to replacing an analog PLL (APLL) with an equivalent HDPLL without changing anything else. This implies a restricted design approach to the HDPLL. Modeling and computer simulation of the HDPLL are required to validate the algorithm and basic approach. This article describes the design, analysis, modeling, simulation, and real-time performance of a HDPLL of the X-band DST receiver breadboard.

The design specifications and functional description of the carrier tracking loop are summarized in Section II.

The conventional analog filter and APLL for various input signal levels are given in Section III. Section IV describes digital filter design, the HDPLL, and the analysis. Digital filter implementation and breadboard performance of the HDPLL are given in Section V. Finally, conclusions and recommendations are given in Section VI.

II. Design Requirements

The DST receiver specifications are listed as follows: The carrier signal tracking threshold is −157.3 dBm. The dynamic range is 88 dB (carrier threshold to −70 dBm). The noise figure at the DST receiver input is 1.4 dB nominal. The tracking range is ±250 kHz minimum at the assigned channel frequency. The steady-state tracking error at a carrier signal level greater than −110 dBm shall be less than 1 percent per 40 KHz. The capture range is ±1.3 KHz at a carrier signal level greater than −120 dBm. The acquisition and tracking rate is at least 550 Hz/sec at a carrier signal level greater than −110 dBm.

A DST receiver breadboard was built that met specifications [1], using all analog components in the APLL. The carrier phase-tracking APLL is a Type I second-order system with built-in characteristics, as follows:

1. The two-sided noise bandwidth ($2B_L$) of the carrier tracking loop at threshold is 18 Hz.
2. The signal-to-noise ratio (SNR) in the carrier tracking channel at the phase detector input is −25 dB.
3. The damping factor at threshold (−157.3 dBm) ranges from 0.4 to 0.6.
4. The loop predetection filter bandwidth is equal to 5000 Hz.

III. Analog Phase-Locked Loop

The basic block diagram of the receiver breadboard of the DST is given in Fig. 1(a). The simplified APLL which tracks carrier phase is given in Fig. 1(b). The equivalent HDPLL is obtained by replacing the analog loop filter with a digital filter, as shown in Fig. 1(b) and as will be discussed in the next section. A bandpass limiter is used in the APLL and HDPLL receivers to maintain a constant total power at the input to the loop [2,3]. This minimizes the total mean-square error of the loop over a wide range of input SNR's. It is also used to protect various loop components, the phase detector in particular, where signal and noise levels could otherwise vary over several orders of magnitude and exceed the dynamic range of these components.

By measuring the analog loop filter of the DST receiver breadboard, the loop filter parameters τ_1 and τ_2 are obtained and its transfer function is given as follows:

$$F(s) = \frac{A_0(1+\tau_2 s)}{1+\tau_1 s} \tag{1}$$

where $\tau_2 = 0.0464$ sec, $\tau_1 = 3655$ sec, and $A_0 = 43.4$ dB.

Because the bandwidth of the loop predetection bandpass filter is 5 kHz, the threshold level at the transponder input is −157.3 dBm. Consequently, the suppression factor α is 0.0531 at threshold and 1 at strong signal (50 dB above threshold) [2]. A detailed discussion on the suppression factor α is provided in Appendix A. The closed-loop transfer function of the linearized APLL is given in [3] with an open-loop dc gain parameter $k = 2.2(10^7)$. The parameter A_0 is included in parameter k [1].

$$H(s) = \frac{1+\tau_2 s}{1+\left[\tau_2 + \frac{1}{\alpha k}\right] s + \frac{\tau_1}{\alpha k} s^2} \tag{2}$$

For simulation purposes, the linearized APLL transfer function is computed for the input at threshold and strong signal. Computer simulations are conducted for both cases. The magnitude and phase responses of the APLL are shown in Figs. 2(a) and 2(b) at threshold and Figs. 3(a) and 3(b) at strong signal, respectively. The damping factor is 0.5 for threshold and 2.18 for strong signal. The two-sided equivalent loop noise bandwidth ($2B_L$) is 18 Hz at threshold and 160 Hz ($2B_L$) at strong input signal. Time domain responses of impulse, step, ramp error at both threshold and strong input signal cases are shown in Figs. 4(a–c) and 5(a–c), respectively.

The phase margins of the APLL are 44.5 deg and 85.6 deg at threshold and strong signal cases, respectively. Since phase is always greater than 180 deg, the gain margin is then not used. This APLL is a Type I second-order system with $\tau_1 >> \tau_2$ and $\tau_1 >> 1$. Therefore, $F(s)$ can be modelled as a perfect integrator, as follows:

$$F(s) \approx \frac{A_0(1+\tau_2 s)}{\tau_1 s} \tag{3}$$

This mathematical model of $F(s)$ will be used to develop the equivalent digital filter in the next section for easy DSP implementation.

IV. Digital Filter Design, the HDPLL, and Analysis

The analog filter $F(s)$ of the APLL is replaced by an equivalent digital filter and employed together with an analog-to-digital converter (ADC) and digital-to-analog converter (DAC) in the HDPLL as shown in Fig. 1(b). A sampling rate must be selected first for the HDPLL. Since the 3-dB bandwidth of the bandpass limiter is 5 kHz and the DSP board employed provides the best performance at a sampling rate of 50 kHz, the sampling rate selected is 50 kHz. The higher the sampling rate (50 >> 5 kHz), the more the HDPLL performs like the analog loop.

A. Digital Filter Design

Two design steps are required to obtain digital filters. In step one, a digital filter algorithm must be developed. In step two, the digital filter coefficients must be quantized and scaled properly for fixed-point arithmetic implementation of the HDPLL.

1. Digital Filter Algorithm. Based on the analog carrier loop filter transfer function, three digital filter design methods [4,5] are considered. These are bilinear transformation, hold equivalence (also known as step-invariant), and impulse-invariant methods. Since the sampling frequency is much higher than the APLL noise equivalent bandwidth, the bilinear transformation method can be applied directly without prewarping the analog frequency.

The bilinear transformation is

$$F_1(z) = F(s)\bigg|_{s = \frac{2(z-1)}{T(z+1)}} = \frac{bz+c}{z-1} \tag{4}$$

where

$$b = \frac{A_0(T+2\tau_2)}{2\tau_1}, \qquad c = \frac{A_0(T-2\tau_2)}{2\tau_1} \tag{5}$$

The hold equivalence is

$$F_2(z) = (1-z^{-1})\left(Z\left[\frac{F(s)}{s}\right]\right) = \frac{bz+c}{z-1} \tag{6}$$

where Z[.] represents a Z-transform of [.],

$$b = \frac{A_0\tau_2}{\tau_1}, \qquad c = \frac{A_0(T-\tau_2)}{\tau_1} \tag{7}$$

The impulse invariance is

$$F_3(z) = T\left(Z\left[F(s)\right]\right) = \frac{bz+c}{z-1} \tag{8}$$

where

$$b = \frac{A_0(T+\tau_2)}{\tau_1}, \qquad c = \frac{-A_0\tau_2}{\tau_1} \tag{9}$$

The parameters b, c, and associate zeros of the digital filters are obtained and given in Table 1.

Among these three digital filters, parameters b, c, and zero location are very close to each other. This is because the sampling frequency selected is much higher than the analog loop filter 3-dB bandwidth. Consequently, all three digital filters have nearly the same characteristics. However, the bilinear transformation is better than the other two transformations in preserving the phase response [10]. Hence $F_1(z)$ is chosen as the digital filter algorithm and will be quantized for fixed-point DSP implementation.

2. Quantization and Scaling [5]. Several simulations are conducted with fixed-point arithmetic in order to determine the number of bits of filter coefficients, digital gain, and scaling factor for implementation. It is found that the quantization causes a larger effect than which transformation is used. This is because the analog loop filter has an extremely narrow bandwidth in comparison to the sampling frequency. The pole and zero of the corresponding digital filter may cancel out each other if improper scaling and quantization are applied. Finally, 16-bit coefficients and a high digital gain ($g_d = 148$) are selected for the following reasons:

(1) Easy and fast acquisition.

(2) Accurate digital representation for parameters b and c and to avoid pole-zero cancellation due to quantization.

(3) Easy implementation by a TMS320C25.

(4) To preserve the noise equivalent bandwidth by choosing $g_d = 148$ for both strong signal and threshold. (More discussion on the g_d is provided in the analysis section.)

The 16-bit digital filter is obtained by

$$F_q(z) = \frac{[b_q z + c_q]\,2^{-8}}{z-1} \qquad (10)$$

where

$$b_q = \frac{\text{Int}\left[(g_d b/A_0)\left(2^8(2^{15})-1\right)+0.5\right]}{2^{15}-1} = 15764/32767$$

$$c_q = \frac{\text{Int}\left[(g_d c/A_0)\left(2^8(2^{15})-1\right)+0.5\right]}{2^{15}-1} = 15758/32767$$

$$g_d = \text{digital gain} = 148$$

Int [.] represents the integer portion of [.].

This digital filter exhibits similar performance to the analog carrier loop filter. However, an extra 8-bit gain (2^8) is applied to form b_q and c_q in Eq. (10) for maximizing numerical accuracy and results in 16-bit fixed-point coefficients for DSP implementation. This 8-bit gain is then compensated by 2^{-8} at the output of the digital filter. Hence the total filter gain remains the same as that of the analog filter. Notice that distortion due to quantization is very small and can be ignored.

B. The Hybrid Digital Phase-Locked Loop

The simplified block diagram of a HDPLL is shown in Fig. 1(b). By comparing Figs. 1(a) and 1(b), one notes that the analog filter of Fig. 1(a) is replaced by an equivalent digital filter with the 16-bit ADC and DAC in Fig. 1(b). We model the ADC plus digital filter plus DAC as an impulse modulator, a fixed-point digital filter algorithm, and a zero-order hold. By using the block diagram analysis of sampled data systems [4], the sampled (discrete-equivalent) transfer function, $H(z)$, of the linearized HDPLL is obtained. A detailed derivation is given in Appendix B. Again, computer simulations are conducted at both threshold and strong signal cases. The magnitude and phase responses of the HDPLL are shown in Figs. 2(a) and 2(b) at threshold, and Figs. 3(a) and 3(b) at strong signal, respectively. Notice that frequency responses of the APLL and HDPLL are approximately the same except for the phase response at frequencies above 1 kHz. This shows that the HDPLL preserves both magnitude and phase characteristics very well at frequencies less than 1 kHz. Consequently, the noise equivalent loop bandwidth of the HDPLL is the same as that of the APLL at both strong signal and threshold cases. Therefore, the phase jitter of the HDPLL is the same as that of the APLL.

The impulse, step responses, and ramp-error response of the HDPLL at both threshold and strong signal cases are shown in Figs. 6(a–c) and 7(a–c), respectively. The ramp-error response shows the dynamic phase error (DPE) in the acquisition. The digital gain is 148 at threshold in Figs. 6(a–c). Two different digital gains are used in Figs. 7(a–c). Notice that these time domain responses of the HDPLL are significantly different from counterparts of the APLL. Specifically, the impulse response of the HDPLL has a much smaller dynamic range than that of the APLL. On the other hand, the DPE of the HDPLL has a much larger dynamic range than that of the APLL. However, the impulse response of the HDPLL becomes larger with a larger digital gain, as shown in Fig. 7(a). The DPE becomes smaller with a larger digital gain, as shown in Fig. 7(c). It shows that digital gain significantly controls the dynamic range of the time domain response. These features indicate that the dynamic range of the accumulator of the processor must be large enough to accommodate the DPE during the acquisition process. We select $g_d = 148$ for having a B_L which meets the specification. It is observed that step responses of the HDPLL show that the damping factor is about 0.5 at threshold and larger than 1 at strong signal. Notice that there is a smoothing analog filter used after digital-to-analog (D/A) conversion in the HDPLL. Consequently, this HDPLL is a Type I, second-order closed-loop system.

C. Analysis

1. Digital Gain Versus Stability. It is well known that second-order, Type I APLLs are unconditionally stable. However, Type I HDPLLs are only conditionally stable and Type I second-order HDPLLs are unstable at high loop gains. The root locus plot of the HDPLL is shown in Fig. 8. Both poles are forced to remain on or near the real axis for the maximum possible range of loop gain, as shown in Fig. 8. The pole of the HDPLL moves outside the unit circle and becomes unstable when digital gain is larger than 50,465. By using $g_d = 148$, the phase margin and gain margin of the HDPLL are computed at both threshold and strong signal cases. Table 2 compares the phase margin between the APLL and the HDPLL. The phase margin of the HDPLL is about the same as that of the APLL. Consequently, the HDPLL is very stable at both threshold and strong signal cases.

2. Digital Gain Versus Noise Equivalent Bandwidth. In general, it does not matter whether the gain is in the digital or analog portion of the loop. However, since all analog parts of the HDPLL are fixed components in the receiver breadboard, only the digital filter gain can be easily adjusted as a flexible parameter. Consequently, the relationship between the digital gain and the noise equivalent bandwidth becomes important. The one-sided noise equivalent digital bandwidth B_{Ld} (Hz) of the HDPLL is given by

$$B_{Ld} = \frac{1}{2T\,(H^2(1))\,2\pi j} \oint_{|z|=1} H(z)H(z^{-1})\frac{dz}{z} \qquad (11)$$

where T is the update time in seconds and $H(z)$ is the transfer function of the HDPLL with $H(1) = 1$. The B_{Ld} can be calculated by using either numerical integration or Table III in [6]. At $g_d = 148$, the $2B_{Ld}$ is obtained as 156 Hz and 17 Hz at both strong signal and threshold, respectively. The noise equivalent bandwidth of the HDPLL is nearly the same as that of the APLL. Furthermore, the relationship between the g_d and the B_{Ld} is depicted in Fig. 9 at strong signal case. It is observed from Fig. 9 that the noise equivalent loop bandwidth increases when digital gain increases. However, the B_{Ld} will be greater than 25 kHz if the digital gain is greater than 26,400. Consequently, the g_d should be less than 26,400 to avoid aliasing errors.

3. Steady-State Phase Error. Under the assumption of linearity, the phase error (no noise) in the z-domain is given by the following expression:

$$\Theta(z) = \{1 - H(z)\}\,\theta_i(z) \qquad (12)$$

where $H(z)$ is the closed-loop transfer function of the HDPLL and $\theta_i(z)$ is the z-transform of the phase input. Furthermore, an instantaneous Doppler, denoted as $d(t)$, is assumed as follows:

$$d(t) = \frac{\omega_i(\Omega_o + \Lambda_o t)}{c} \qquad (13)$$

where

$\omega_i =$ carrier frequency (rad/sec)

$\Omega_o =$ spacecraft speed (m/sec)

$\Lambda_o =$ spacecraft acceleration (m/sec^2)

$c =$ speed of light (m/sec)

The input phase $\theta_i(t)$ of the HDPLL is the integration of the $d(t)$ with respect to time and is obtained by

$$\theta_i(t) = \frac{\omega_i(\Omega_o t + 0.5\Lambda_o t^2)}{c}$$

By applying the final value theorem to the phase-error equation, we get

$$\begin{aligned}\phi_{ss} &= \lim_{z\to 1}\,(z-1)(1-H(z))\theta_i(z)\\ &= \lim_{z\to 1}\,(1-H(z))\left(\frac{\omega_i}{c}\right)\\ &\quad\times\left[\frac{\Omega_o Tz}{(z-1)^2} + 0.5\Lambda_o T^2 z\left(\frac{z+1}{(z-1)^3}\right)\right]\\ &= \frac{(\omega_i/c)\Lambda_o T}{(k/A_0)(b_q + c_q)2^{-8}}\end{aligned} \qquad (14)$$

For the Voyager mission at an 8.4-GHz carrier frequency, we assume acceleration values of $\Lambda_o = 0.32$ m/sec^2 for Uranus [7]. The steady-state phase error at the strong signal case is obtained as 0.607 deg at encounter. Clearly, this HDPLL meets the specification that requires a steady-state error of 1 deg, as mentioned in Section II.

4. The Phase-Error Variance of the PLL. The phase-error variance of the linearized APLL after the bandpass limiter is calculated as

$$\sigma_e^2 = \left(\frac{N_0 B_L}{P_c}\right)\Gamma$$

where

$N_0 =$ the one-sided noise power spectral density

$P_c =$ the carrier power

$\Gamma =$ limiter performance factor $= (1+\rho_i)/(0.862+\rho_i)$

$\rho_i = P_c/N_0 W_i =$ the SNR input to the limiter

$W_i =$ the bandwidth of the bandpass filter = 5000 Hz

The limiter performance factor equation is obtained experimentally [8]. From the breadboard DST second IF gain distribution measurements,[1] parameters of both

---

[1] J. Perret, "Breadboard Uplink Command Channel Performance Analysis Calibration and Testing Accomplished in 1991," Interoffice Memorandum 3367-93-171 (internal document), Jet Propulsion Laboratory, Pasadena, California, May 1993.

threshold and strong signal cases are obtained with the automatic gain control (AGC) on (threshold) and off (strong signal), respectively. (See Table 3.)

Based on the parameters provided in Table 3, the SNR of both the APLL and HDPLL can be computed as follows:

$$
\begin{aligned}
\text{SNR of the APLL} &= 10 \ \log \ \frac{1}{\sigma_e^2} \ \text{dB} \\
&= 10 \ \log \ \left[\left(\frac{P_c}{N_0 W_i} \right) - \ \log \ (\Gamma) \ \text{dB} \right. \\
&\qquad \left. + \ \log \left(\frac{5000}{B_L} \right) \right] \ \text{dB}
\end{aligned}
$$

$$
\text{SNR of the HDPLL} = 10 \ \log \ \left[\frac{1}{\left(\frac{N_0 B_{Ld}}{P_c} \right) \Gamma} \right] \ \text{dB}
$$

The SNR of both APLL and HDPLL at both threshold and strong signal is provided in Table 4.

V. Digital Filter Implementation and Breadboard Performance

A PC board of the Ariel DSP-16 Plus is employed together with an X-band DST breadboard for real-time digital loop filter implementation. The bandwidth of both antialiasing (input) and smoothing (output) filters is 20 kHz. Both ADC and DAC are 16-bit with a selected sampling rate of 50 kHz for best board performance. A TMS320C25 digital signal processor is employed to implement this 16-bit digital loop filter. This DSP has a 32-bit-wide accumulator. However, a 40-bit equivalent accumulator is employed to accommodate the large dynamic range required during the acquisition process.

Transponder receiver experiment results are obtained in real-time operation. Evaluation experiments include receiver tracking threshold sensitivity and static phase errors for X-band uplink frequency offset. All measurements were made at room temperature (25 deg C). The theoretical equation used for the calculation of the carrier tracking threshold is given in Appendix A. The measured tracking threshold sensitivity at the receiver best lock frequency (7162.3125 MHz) is −155.3 dBm, which is higher than the design threshold value of −157.3 dBm. This is due to the dc bias at the analog-to-digital (A/D) converter of the DSP board. However, the measured hybrid digital receiver threshold characteristics show good correlation with the actual analog receiver performance and agree with theoretical performance over the tracking range, as shown in Fig. 10. Figure 11 shows a linear relationship between measured static phase error (SPE) voltage versus uplink frequency offset over the receiver tracking range. The measured SPE shows a good correlation with expected performance (Appendix C). The measured tracking ranges of APLL and HDPLL are ±270 and ±280 kHz, respectively, which is greater than the required tracking range value of ±250 kHz.

VI. Conclusion

This article presents the design, implementation, analysis, and performance testing of a HDPLL of the DST receiver breadboard. The baseband carrier loop filter has been successfully replaced by a 16-bit digital filter (digital integrator). A TMS320C25 DSP is employed to implement this filter in real time. All simulations show that the designed fixed-point digital filter works very well in the HDPLL. The simulated performance in the frequency domain of the HDPLL is nearly the same as the original APLL at both threshold and strong signal cases. However, time-domain responses of the HDPLL are controlled by the digital gain. To meet the B_L requirement, the g_d is chosen as 148. Hence, the HDPLL's dynamic range of time-domain responses is different than that of the APLL.

Testing results are in good agreement with predicted characteristics, with the exception of tracking threshold (about a 2-dB loss due to the dc bias of the A/D). This loss can be reduced if the digitization occurs at the IF signal, instead of the digitizing baseband signal. In conclusion, it has been demonstrated that the baseband carrier loop filter of the DST receiver can be replaced by a digital filter. By using this HDPLL as a basic model, an advanced digital receiver employing digital IF techniques is recommended for future deep-space transponders [9,10]. An adaptive scheme is also recommended to solve the high transient DPE problem as follows. First, to reduce the transient DPE in the acquisition mode, the digital gain of the digital filter should be increased. Consequently, the loop bandwidth is opened up. This operation will ensure a larger acquisition sweep rate. Secondly, after the phase is locked, the digital gain should be reduced. Hence, the loop bandwidth is reduced in the tracking mode. This operation will reduce phase noise and ensure a limited steady-state tracking error.

Acknowledgments

The authors gratefully acknowledge the valuable support of Charles Kyriacou, Arthur W. Kermode, John T. Meysenburg, and Selahattin Kayalar. Special thanks to William J. Hurd for his careful review, correction, and discussions.

References

[1] N. R. Mysoor, J. D. Perret, and A. W. Kermode, "An X-Band Spacecraft Transponder for Deep Space Applications—Design Concepts and Breadboard Performance," *IEEE Trans. MTT*, vol. 40, no. 6, pp. 1192–1198, June 1992.

[2] F. M. Gardner, *Phase-lock Techniques*, 2nd ed., New York: John Wiley and Sons, 1979.

[3] J. H. Yuen, *Deep Space Telecommunication Systems Engineering*, New York: Plenum, 1983.

[4] G. F. Franklin and J. D. Powell, *Digital Control of Dynamic Systems*, Reading, Massachusetts: Addison-Wesley, 1981.

[5] A. Oppenheim and R. Schafer, *Discrete-Time Signal Processing*, Englewood Cliffs, New Jersey: Prentice-Hall, 1990.

[6] E. I. Jury, *Theory and Application of the z-Transform Method*, Malabar, Florida: Krieger, 1964.

[7] S. Aguirre and W. J. Hurd, "Design and Performance of Sampled Data Loops for Subcarrier and Carrier Tracking," *The Telecommunications and Data Acquisition Progress Report 42-79, vol. July-September 1984*, Jet Propulsion Laboratory, Pasadena, California, pp. 81–95, November 15, 1984.

[8] R. C. Tausworthe,"Information Processing: Limiters in Phase-Locked Loops: A Correction to Previous Theory," *Space Program Summary 37-54*, vol. III, Jet Propulsion Laboratory, Pasadena, California, pp. 201–204, December 1968.

[9] T. M. Tien, S. Kayalar, H. G. Yeh, and C. Kyriacou, "Advanced Transponders for Deep Space Applications," *Proceedings of IEEE Conference on Aerospace Applications*, Steamboat Springs, Colorado, pp. 21–42, January 1993.

[10] T. M. Tien and H. G. Yeh, "Preliminary Design and Implementation of the Baseline Digital Baseband Architecture for Advanced Deep Space Transponder," *The Telecommunications and Data Acquisition Progress Report 42-114, vol. April-June 1993*, Jet Propulsion Laboratory, Pasadena, California, pp. 280–294, August 15, 1993.

Table 1. Parameters and zeros of digital filters.

Design method	Parameter b $(\times 10^{-3})$	Parameter c $(\times 10^{-3})$	Zero
Bilinear transformation	1.879256	−1.878446	0.999569
Hold equivalence	1.878851	−1.878041	0.999569
Impulse invariance	1.879661	−1.878851	0.999569

Table 2. A comparison of phase margin and gain margin between the APLL and HDPLL.

	Phase margin		Gain margin	
	APLL, deg	HDPLL, deg	APLL	HDPLL, dB
Threshold	44.5	47	N/A[a]	−77
Strong signal	85.6	86	N/A[a]	−51

[a] Gain margin is not used because the phase of the APLL is always greater than 180 deg.

Table 3. Measured signal and noise power input to the limiter and associated parameters ρ_i and Γ at threshold and strong signal.

	P_c, dBm	$N_0 W_i$, dBm	ρ_i	Γ
Threshold	−26.5	−1.5	0.003	1.16
Strong signal	−26.5	−87.5	1.2×10^6	1.0

Table 4. The SNR of both the APLL and HDPLL at both threshold[a] and strong signal.

SNR	APLL, dB	HDPLL, dB
Threshold	1.80	2.05
Strong signal	78.96	79.07

[a] Threshold is defined as the point where probability is 50-percent lock and 50-percent unlock.

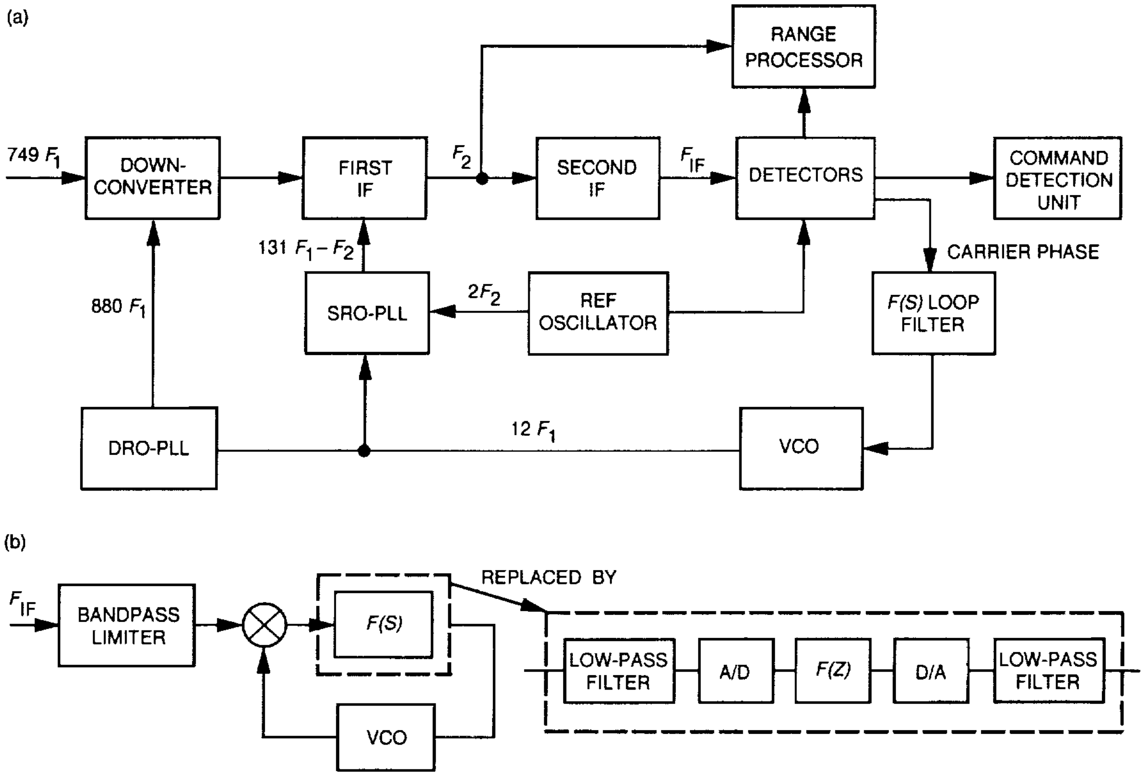

Fig. 1. Functional block diagrams of (a) the receiver of the DST breadboard and (b) the simplified carrier phase tracking loop with the analog loop filter replaced by a digital filter.

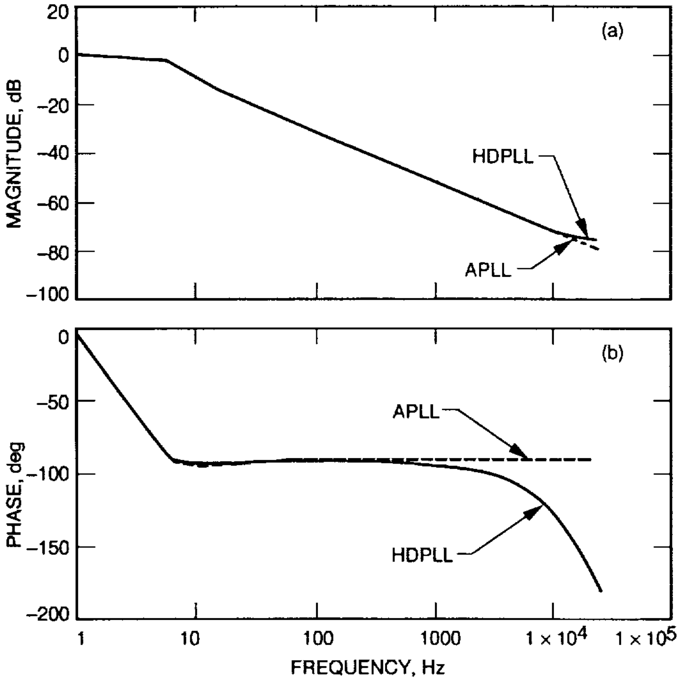

Fig. 2. Simulated responses of the APLL and HDPLL at the threshold: (a) magnitude and (b) phase.

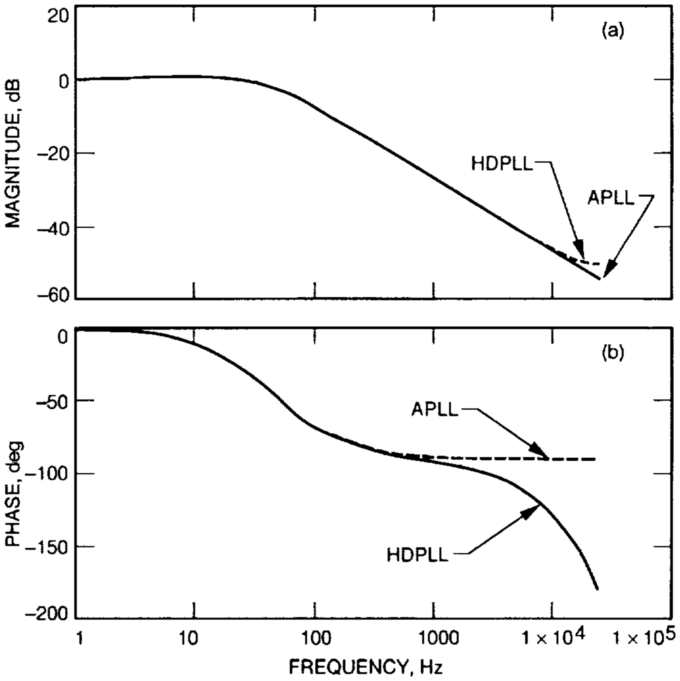

Fig. 3. Simulated responses of the APLL and HDPLL at the strong signal input: (a) magnitude and (b) phase.

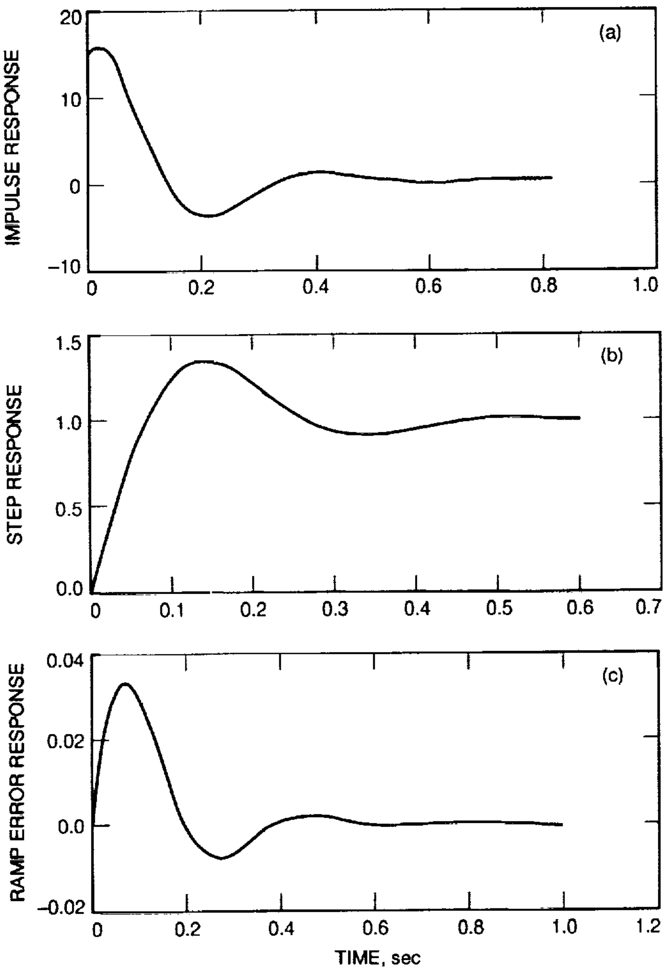

Fig. 4. Time-domain responses of the APLL at threshold: (a) impulse, (b) step, and (c) ramp error.

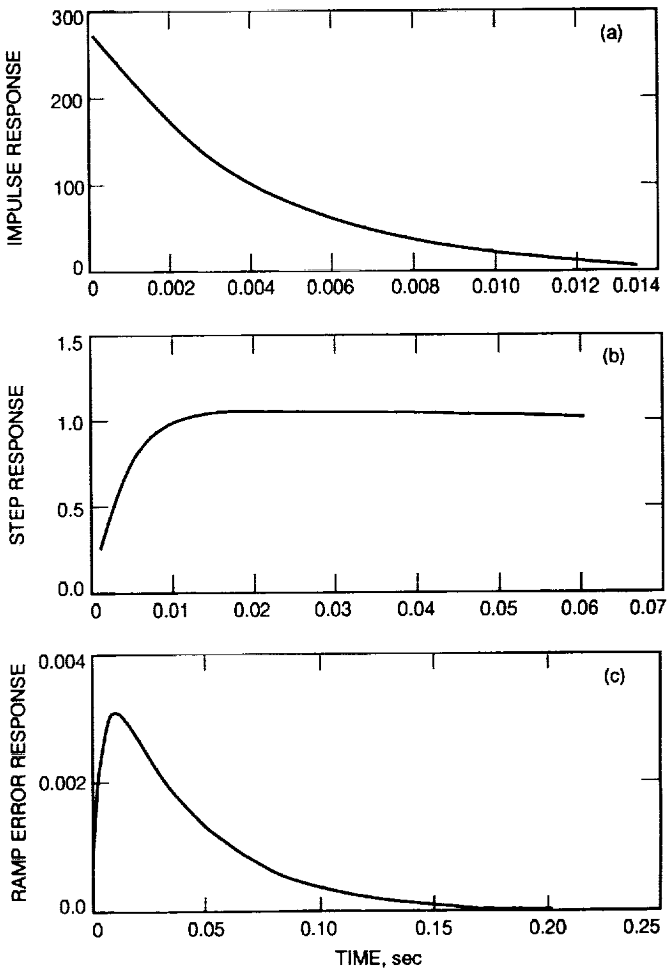

Fig. 5. Time-domain responses of the APLL at strong signal: (a) impulse, (b) step, and (c) ramp error.

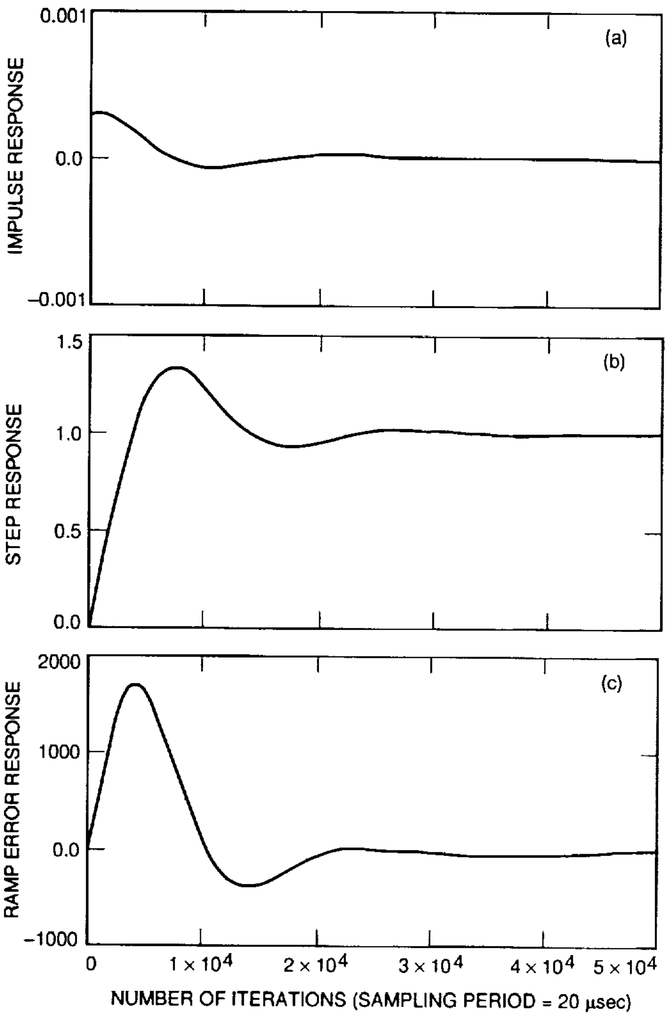

Fig. 6. Responses of the HDPLL at threshold: (a) impulse, (b) step, and (c) ramp error.

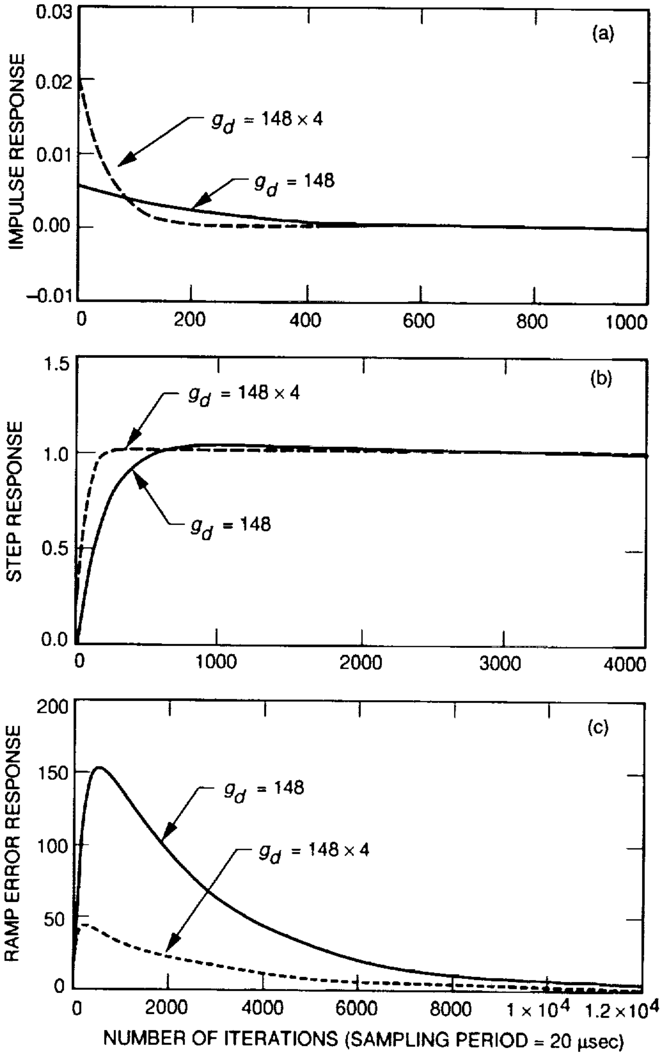

Fig. 7. Responses of the HDPLL at strong signal with two different digital gains: (a) impulse, (b) step, and (c) ramp error.

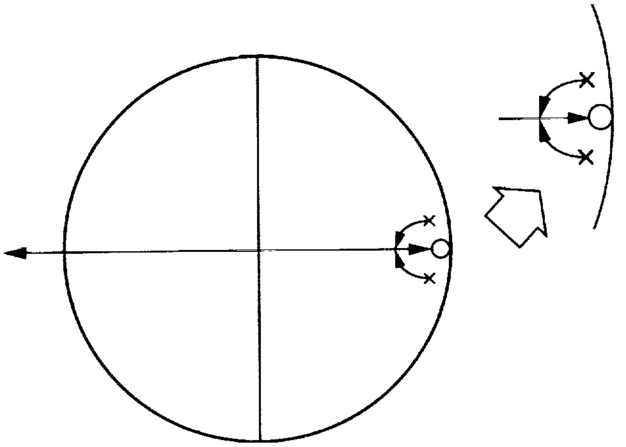

Fig. 8. The root locus plot of the HDPLL.

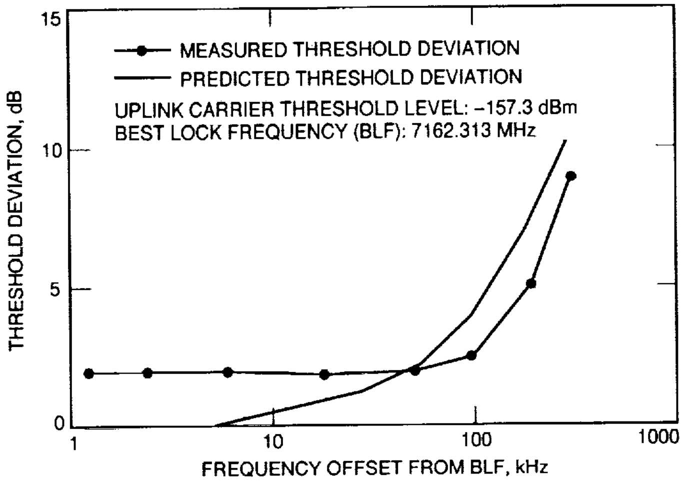

Fig. 10. The measured receiver carrier tracking threshold versus the offset frequency.

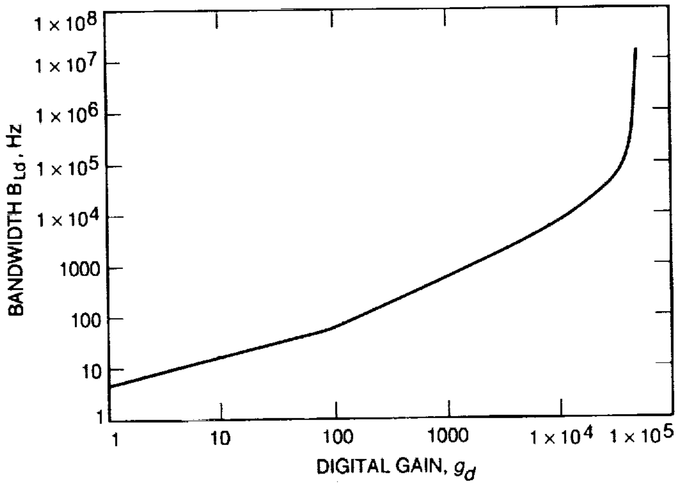

Fig. 9. Digital gain g_d versus one-sided noise equivalent bandwidth B_{Ld} at strong signal.

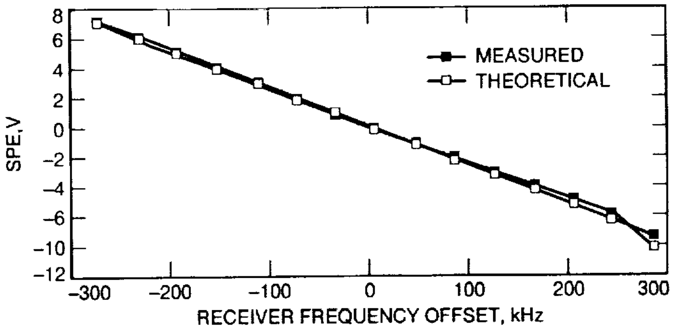

Fig. 11. The measured static phase error voltage of the HDPLL versus uplink frequency offset over the receiver tracking range.

Appendix A

A Mathematical Model of the Suppression Factor and Tracking Threshold Calculation

The mathematic model of the suppression factor α and calculation of the carrier tracking threshold of a PLL receiver are provided here.

The carrier tracking threshold of a PLL receiver is defined as the minimum uplink signal required to maintain a 50 percent probability of lock at any given offset from best lock frequency (BLF). The worst-case carrier tracking threshold signal level S_o at the transponder input port and at the BLF is determined from the following equations:

$$S_o = kT_oF(2B_L)L \tag{A-1}$$

where

$S_o =$ the received input signal level for tracking threshold at receiver BLF

$k =$ Boltzmann's constant

$T_o =$ the reference system temperature

$F =$ receiver noise figure at the transponder input

$L =$ the receiver carrier channel loss

The S_o is calculated and is equal to −157.5 dBm (the receiver carrier tracking threshold) for a $2B_L$ of 18 Hz, channel loss of 1 dB, and noise figure of 2.9 dB at 290 K.

The PLL receiver limiter suppression factor α is given by [3]

$$\alpha = 1/\sqrt{1 + \frac{2B_{LI}S_o}{\pi B_L S}} \tag{A-2}$$

where

$S =$ the receiver input signal power level

$B_{LI} =$ the noise equivalent predetection bandwidth

In the region near tracking threshold, the phase offset θ_e at the PLL phase detector can be estimated from an empirical equation

$$\begin{aligned} \theta_e &= 1 - \frac{\alpha_0}{\alpha} \\ \alpha_o &= \left(\frac{\pi B_L}{2B_{LI}}\right)^{0.5} \end{aligned} \tag{A-3}$$

Notice that α_0 is the limiter suppression factor at carrier threshold.

The phase-detector output voltage is given by an empirical equation

$$V_c = \alpha \sin(\theta_e)\cos(\theta_e) \tag{A-4}$$

The frequency offset at X-band is then obtained as

$$\Delta f = V_c k \tag{A-5}$$

where $k =$ open loop dc gain of the PLL.

Appendix B

Derivation of the HDPLL Closed-Loop Transfer Function

The HDPLL closed-loop transfer function derivation is provided here [4].

From Fig. 1(b), the DAC is modeled as $(1 - e^{-sT})/s$, and the voltage-controlled oscillator (VCO) is modeled as k/s. Then the output of the sampled-data system is obtained as

$$\theta_o^* = \frac{G^*}{1 + G^*}\,\theta_i^* \tag{B-1}$$

where

θ_o^* = the sampled output of the HDPLL

θ_i^* = the sampled input of the HDPLL

$$G^* = \alpha\left(1 - e^{-sT}\right) F_q^* \left(\frac{k/g}{s^2}\right)^*$$

$$= \alpha\left(1 - e^{-sT}\right) F_q \left[\frac{T(k/g)e^{sT}}{\left(e^{sT} - 1\right)^2}\right]$$

$$= \frac{AF_q(z)}{z - 1}$$

$$= \frac{A(b_q z + c_q)}{(z - 1)^2}$$

and

$$A = \frac{\alpha k T 2^{-8}}{g}$$

$$z = e^{sT}$$

b_q and c_q are 16-bit digital filter coefficients.

The closed-loop transfer function is then

$$H(z) = \frac{\theta_o^*}{\theta_i} = \frac{A(b_q z + c_q)}{z^2 + (Ab_q - 2)z + Ac_q + 1} \tag{B-2}$$

Appendix C

Relationship Between SPE and Uplink Frequency Offset

The relationship between the static phase error (SPE) and the uplink frequency offset over the receiver tracking range is found as follows.

The VCO receives SPE as input and provides output frequency at $12F_1$ with a gain of 628 Hz/V (measured). The frequency of the received uplink signal is $749F_1$, as shown in Fig. 1(a). Consequently, the uplink frequency offset from the best lock frequency is obtained as

$$\Delta f = -\text{SPE}(628)\left(\frac{749}{12}\right) \tag{C-1}$$

The minus sign is used for the negative feedback PLL.

N94- 29668

A 32-GHz Microstrip Array Antenna for Microspacecraft Application

J. Huang
Spacecraft Telecommunications Equipment Section

JPL/NASA is currently developing microspacecraft systems for future deep space applications. One of the frequency bands being investigated for microspacecraft is the Ka-band (32 GHz), which can be used with smaller equipment and provides a larger bandwidth. This article describes the successful development of a circularly polarized microstrip array with 28 dBic of gain at 32 GHz. This antenna, which is thin, flat, and small, can be surface-mounted onto the microspacecraft and, hence, takes very little volume and mass of the spacecraft. The challenges in developing this antenna are minimizing the microstrip antenna's insertion loss and maintaining a reasonable frequency bandwidth.

I. Introduction

JPL is currently considering the development of microspacecraft for future deep space missions in order to meet NASA's goal of having small and inexpensive spacecraft. The microspacecraft,[1] having sizes on the order of 0.5 m, will certainly require components that are small both in size and mass. One of the frequency bands under investigation for use with microspacecraft is the Ka-band (32 GHz). In this frequency range, components are smaller and larger bandwidths can be achieved as compared with a lower frequency range. A larger bandwidth will result in a higher data rate.

In microspacecraft development, antennas are one of the major components that warrant attention since they generally require significant amounts of real estate and mass. Conventional antennas such as horns and parabolic reflectors, although efficient radiators, are generally bulky in size and large in mass. As a result, three different types of flat antennas with very thin profiles have been proposed for the microspacecraft. Since they are flat, the antennas can be surface-mounted onto the spacecraft without additional supporting structures, such as those needed for curved parabolic reflectors. Therefore, they require very little volume and mass.

The first type is the microstrip array [1], in which many printed microstrip patch elements are combined by microstrip transmission lines. Due to the relatively high in-

---

[1] C. Salvo and C. Nunez, "Code R Microspacecraft Subsystem Technology Task," JPL Interoffice Memorandum 3132-92-099 (internal document), Jet Propulsion Laboratory, Pasadena, California, March 23, 1992.

sertion loss that generally exists in microstrip transmission lines, the microstrip array cannot be very large; otherwise the antenna will be very inefficient. At Ka-band, the microstrip array will have an acceptable insertion loss if its aperture dimension is less than 15 cm. The second type is the planar slotted waveguide array [2], which is generally bulky at low microwave frequencies, but which can be made low profile with a small mass at high frequencies, such as Ka-band. Because the slotted waveguide encounters very little insertion loss, its aperture size can be large. The upper limit of its size is governed by its metallic mass. At Ka-band, a reasonable dimension range for the planar slotted waveguide array is from 5 to 35 cm.

For antennas with dimensions larger than 35 cm, a third type of flat antenna, called the microstrip reflectarray or flat reflector [3], can be used. This antenna has similarities to the conventional parabolic reflector, in which both a feed and a reflecting surface are needed. However, for the microstrip reflectarray, the reflecting surface can be flat rather than curved. Many identical but isolated microstrip patches (which are not connected to each other by power dividers) with phase delay lines of different lengths are printed on this flat reflecting surface. It is these phase delay lines that will cause the reradiated energy originating from the feed to become coherent in the far field. Without power-division transmission lines, the insertion loss of the antenna will not increase as the size of the antenna increases. Consequently, the aperture size of the reflectarray can be very large while still maintaining good efficiency. Since they are flat, these reflecting surfaces can be surface-mounted onto the spacecraft without additional structure support, such as is needed for a curved parabola. Therefore, the spacecraft can have a lower mass and a lower volume by utilizing the reflectarray antenna.

Due to limited resources in fiscal year 1993, only the first type of antenna, the microstrip array, was developed. The other two types of antennas are planned to be developed in the following years. This article documents the development of the Ka-band microstrip array, which must be circularly polarized with 28 dBic of peak gain. The array employs a series feed technique [4] for its power-division transmission lines in order to reduce insertion loss, and it uses sequentially arranged [5] elements for its subarrays to improve the quality of the circular polarization (CP).

II. Antenna Requirements

The antenna technologies studied here are intended for a series of future JPL/NASA microspacecraft applications. The set of antenna requirements generated here, however, are for a particular application called Asteroid Comet Microspacecraft Explorer (ACME-II).[2] The ACME-II spacecraft, as illustrated in Fig. 1, has a hexagonal shape with dimensions on the order of 0.5 m. The bottom of the spacecraft is used for the propulsion adapter unit and does not have enough room for the antenna. The top is allocated for an optical camera, louvers, etc., and also does not have adequate space for the antenna. The only likely location for the antenna is on one of the six side panels, which are allocated for the solar arrays. It seems appropriate to mount a small and flat array antenna flush with the solar array. The antenna requirements for the ACME-II spacecraft are given in Table 1.

The antenna gain of 28 dBic is set for the microspacecraft's near-Earth encounter with an asteroid or a comet at a range of approximately 1 AU. This gain yields an antenna beamwidth of about 5 deg. With this relatively wide beamwidth, fine beam pointing at the Earth is not required. Therefore, an automatic antenna tracking capability is not required; rather, a fixed broadside beam is adequate for the antenna system. Coarse antenna pointing is to be done by the spacecraft's onboard system, such as the star tracker. The challenge in developing the proposed microstrip array antenna is to achieve the 28 dBic of gain with a minimal amount of insertion loss over a relatively wide bandwidth of 1 GHz. In other words, the efficiency of the microstrip array may need some attention. Low profile, small mass, and low cost are certainly the attractive features of the microstrip array antenna. Other antennas, such as horns and parabolic reflectors, although known to be efficient radiators, may have very poor efficiency in terms of antenna volume and mass for microspacecraft applications. For example, for a horn antenna to provide 28 dBic of gain, it will need approximately 9 cm x 9 cm of aperture with 20 cm of length. A significant amount of the spacecraft's volume is needed to accommodate the horn antenna since the spacecraft's dimension is only 50 cm across. Consequently, the horn antenna will have a volume at least 50 times and a mass at least 10 times as large as the microstrip array. To summarize, for microspacecraft applications, the salient physical features of the microstrip array can compensate for the antenna's relative inefficiency at Ka-band.

III. Antenna Development Background

To develop a high-gain microstrip array antenna, three major steps are generally required: the single patch el-

---

[2] Ibid.

ement development, a building-block subarray development, and the full array development. Since the microstrip patch is a narrow-band device (generally less than three-percent bandwidth), the development of the single patch is necessary to ensure its correct resonant frequency, polarization purity, bandwidth, etc. Currently, no mathematical tool can directly design a complete microstrip array to operate at the desired frequency. Although some mathematical tools are very accurate, one cannot ensure that the fabrication tolerance and the manufacturer's material specifications are all within the required accuracy. For example, the dielectric constant of the substrate is generally 1 percent off from the manufacturer's specification, which can cause a similar percentage of change in resonant frequency. The second step is the development of the building-block subarray, which means that the full array consists of many identical subarrays. This subarray should be developed prior to the full array to ensure good circular polarization and to minimize overall development risk. Once the single subarray is developed, many of these identical subarrays can then be combined by microstrip transmission lines to form the final array.

A. Single-Patch Element Development

For an array to generate CP, its element is generally required to be circularly polarized. However, when the radiation efficiency is not a concern, a CP array can be composed of linearly polarized (LP) elements [6,7]. Since the radiation efficiency is of concern, the patch element must be circularly polarized. There are basically two techniques for a single microstrip to generate CP. One is to have a square or circular patch excited by two orthogonally located feeds in time quadrature, as shown in Fig. 2(a). The other is to have a truncated-corner square patch, as shown in Fig. 2(b), excited by a single feed. Since the insertion loss of a microstrip array is mostly incurred in the microstrip power-distribution transmission lines, the lengths and complexity of these transmission lines should be minimized. As a result, the truncated-corner, single-feed patch rather than the orthogonally fed patch is selected for the array. There are several other techniques [8] to generate CP by a single-feed patch, such as using a tilted slot at the center of a square patch and a circular patch with two indented edges.

All these single-feed CP methods work as a result of the fields underneath the patch being perturbed by the small truncations. The perturbation splits the field into two orthogonal modes that are degenerate in frequency and in-phase quadrature. The amount of perturbation must be just right so that two orthogonally polarized fields with equal amplitudes and orthogonal phases can be formed. Consequently, the CP bandwidth is very narrow and generally is less than 1 percent. This narrow bandwidth will cause the resonant CP frequency to be very sensitive to fabrication tolerance, temperature change, etc. One technique for increasing the CP bandwidth is to arrange four neighboring elements sequentially in orientations and in phases. This technique is discussed in the next subsection.

The design of the truncated-corner square patch is assisted by both the cavity modal theory [9] and the variational method [10]. The cavity modal theory, used here to design an unperturbed square patch, assumes that the fields underneath the patch can be expanded in terms of trigonometric functions (modal functions). By solving for the unknown coefficients of these modal functions through known boundary conditions, the resonant frequency and input impedance can be determined. The amount of corner truncation for CP generation is then determined by the variational method with the simple close-form equation given below [10]:

$$f' = f\left(1 + \frac{S'}{2S}\right) \tag{1}$$

with

$$\frac{S'}{S} = \frac{1}{2Q}$$

where S' is the sum of the two truncated areas, S is the area of the unperturbed square patch, f is the resonant frequency of the unperturbed patch, f' is the frequency for the optimal axial ratio, and Q is the quality factor of the unperturbed patch.

The quality factor, Q, is a function of the substrate dielectric constant, thickness, and loss tangent. It can be obtained simply through a curve given in [10] or calculated from [8]. It can also be determined through the impedance bandwidth (in percent for a 2:1 voltage standing wave ratio [VSWR]) either calculated or measured for the unperturbed patch by the following simple relationship [11]:

$$Q = \frac{1}{\sqrt{2}(bandwidth)} \tag{2}$$

With the above formulations, the truncated-corner square patch was designed with the following dimensions (see

Fig. 2): $a = 0.038$ cm, $b = 0.297$ cm, the relative dielectric constant = 2.2, and the dielectric thickness = 0.025 cm. The measured input return loss at 32.0 GHz is −21 dB, which corresponds to a VSWR of 1.22:1. The measured axial ratio is best at 32 GHz but with a relatively large magnitude of 3 dB. This relatively large axial ratio is the result of the narrow-band characteristic with a high sensitivity to fabrication tolerance and the manufacturer's material specification tolerance. Nevertheless, it is expected that this large axial ratio can be reduced by the sequentially arranged subarray technique to be discussed in the next subsection. A photograph of this single patch with truncated corners is shown in Fig. 3, where the patch is fed by an impedance-matched microstrip transmission line and an end-launched OS-50 coax connector. The printed antenna circuit is etched on Duroid 5880 substrate material. Due to its extremely thin profile, the antenna is mounted on a brass plate for mechanical support.

B. Four-Element Subarray Development

It has been known that the CP quality and bandwidth can be improved if four elements, each being a narrow-band CP element, can be arranged sequentially [5,6] in orientation and in phase, as shown in Fig. 4. The four elements are arranged in 0-, 90-, 180-, and 270-deg fashion to achieve symmetry and to cancel undesirable higher-order modes (explained in [6]) and, thus, to achieve purer polarization. Figure 5 presents the photograph of the sequentially arranged four-element subarray with each single element having dimensions identical to those presented in Fig. 3. The element spacing is 0.73 free-space wavelength, and the required differential phases between elements are achieved by designing transmission lines of different lengths. A vertically launched OS-50 coax connector is used to feed the microstrip-transmission-line power-dividing circuit. The measured input return loss at 32 GHz is −17.4 dB (VSWR = 1.31:1). Its 1.5:1 VSWR bandwidth is about 0.5 GHz. The radiation pattern measured with a spinning dipole is shown in Fig. 6, where an axial ratio of less than 0.25 dB is demonstrated in the broadside direction. This axial ratio is significantly better than that of the single element. This four-element subarray is used as the building block in the full array, where all the subarrays are identical and are combined by microstrip power distributing lines, as discussed in the next section.

IV. Full Array Design

To provide the required antenna gain of 28 dBic, an aperture size of approximately 10 cm × 10 cm is needed at 32 GHz. The number of radiating elements needed is about 200. When combining such a relatively large number of elements by microstrip transmission lines at Ka-band, the insertion loss becomes significant. One technique to minimize this insertion loss is to employ the series-feed method in which all the four-element subarrays are combined serially by the power distributing circuit. This series-feed method is illustrated in Fig. 7. The input/output coax connector, located at the center of the array, feeds the microstrip transmission line with a two-way power division that splits the power parallel to the left and right identical halves. Each half array is then fed serially in columns by the microstrip line. The upper and lower halves of the array are fed in parallel at the array's horizontal center line and then fed serially at each subarray location.

Figure 8 illustrates the difference between the series-feed and the parallel-feed techniques for a four-element array having uniform power distribution. A series-fed array means that a certain amount of power is used to feed the first element; then a certain amount from the remaining power is used to feed the second element at a delayed time; and this continues until the fourth element is reached. At the fourth element, only one-quarter of the total power remains to be transmitted. In other words, full power goes through the transmission line at the first element location, and the power diminishes as it travels toward the last element. Consequently, the largest loss in total power for the transmission line occurs at the first element, and this power loss reduces as the power travels down the series-fed line. For this reason, most of the insertion loss occurs at the center region of the array, shown in Fig. 7. For a parallel-fed array, all elements are fed equally at the same time by parallel transmission lines. Therefore, the insertion loss exists almost uniformly from the beginning of the transmission line all the way to the end of the line. Thus, the series-fed array will encounter significantly less insertion loss than will the parallel-fed array.

Note that at each power division point in Fig. 7 the microstrip line changes width. This was uniquely designed to ensure uniform power distribution with proper impedance matches throughout the array. It should be noted that the microstrip lines are impedance matched at every junction point throughout the array so that multiple reflections of the signal are minimized to reduce insertion loss. Furthermore, the bandwidth of this array is slightly larger than the conventional "resonant" array, in which impedances are not matched and multiply reflected signals are significant. For the array in Fig. 7, the spacings between adjacent columns in the horizontal direction and between adjacent subarrays in the vertical direction are all integral multiples of the "guide" wavelength, so that the far-field radiation from all patches is in phase in the broadside direction. Here the guide wavelength is the effective wavelength of the transmission line in a dielectric substrate. Two guide wavelengths are used here so that they are long enough to physically accommodate the subarrays and yet short enough to avoid excess insertion loss. Because of this guide wavelength requirement for phase coherence, the spacing between two adjacent patch elements becomes approximately 0.74 free-space wavelength. Also, because the guide wavelengths are slightly different for different transmission line widths, the spacing between adjacent patches is slightly different throughout the array (not all exactly equal to 0.74 free-space wavelength). This is why not all the patch elements in any given vertical column or horizontal row are precisely aligned. In the array, there are a total of 8 vertical columns with 6 subarrays in each column, and, therefore, there are a total of 48 sequentially arranged subarrays with a total of 192 microstrip patch elements.

Due to the fact that the array must have integral multiple numbers of subarrays and preferably be symmetrically fed from the center, it is not possible to have a square aperture and yet still fully utilize the required 10-cm × 10-cm area (see Fig. 7). Consequently, a rectangular aperture is formed. The overall antenna physical size is 11.4 cm × 8.9 cm. The microstrip patches and lines are etched on a 0.025-cm-thick dielectric substrate (Duroid 5880), which in turn is mounted on a 0.16-cm-thick supporting aluminum plate. The total antenna thickness is 0.185 cm. The array's actual radiating aperture size (10.8 cm × 8.3 cm) is slightly smaller than its physical size. This is because additional ground planes on the edges of the array are needed to accommodate the transmission lines.

The power distribution circuit for the full array is a combination of parallel- and series-feed [4] transmission lines. It will not be a good design if a sole series-feed technique is used. This is because a sole series-fed array will cause its main beam to be scanned away from the intended direction as frequency is changed due to accumulated phase change. With a relatively wide band signal, the composite transmit beam of all the frequencies within the band will appear to be wider and the gain at the receiver direction will thus be lower. Viewed another way, the spectrum of the antenna filter response will be distorted. For the array shown in Fig. 7, the right and left halves of the array are fed in parallel, while within each half array, the columns are fed serially. As frequency changes, the beam of each half array will scan. However, the two half arrays will scan in opposite directions, leaving the composite beam pointed in the broadside direction with a lower gain. Because the beamwidth of each half array is wider than the complete array, its beam scan due to frequency changes will result in smaller gain changes than that of a narrowbeam, solely series-fed array. To summarize, this combined parallel and series feed technique will result in a stable beam direction over a relatively wide bandwidth with a relatively low insertion loss.

V. Experimental Results

The full array, as sketched in Fig. 7, has been fabricated and tested and is shown in Fig. 9. The input is a perpendicularly launched OS-50 coax connector. Its measured input return loss is given in Fig. 10, where a return loss of −23.6 dB (1.14:1 VSWR) is noted at 32 GHz. The 1.5:1 VSWR bandwidth is about 2 GHz, which is significantly wider than the four-element subarray's bandwidth of 0.5 GHz. This is partly because the full array's input match is better designed and partly due to the fact that the full array has a much larger resistive insertion loss in the transmission lines to lower the returned energy. One can note that in Fig. 9 there are two tuning stubs located a quarter-wavelength away from the input connector and that there is none for the four-element subarray. These tuning stubs can eliminate a large portion of the mismatch over a significant bandwidth.

Both the measured narrowbeam and broadbeam principal plane patterns of the rectangular aperture array are shown in Figs. 11 and 12, respectively. The 3-dB beamwidths are 4.5 deg in one principal plane and 5.7 deg in the orthogonal plane. These patterns, measured at 32 GHz, show a peak side-lobe level of −12 dB and a peak cross-pol level of −18 dB (corresponding to a 2-dB axial ratio). It is believed that the 2-dB axial ratio, which is worse than that of the four-element subarray, is mostly caused by the accumulated phase errors in the series-fed microstrip lines and is partly due to the leakage radiation from these lines. The measured 3-dB axial ratio bandwidth of the full array is 1.3 GHz. The array's peak gain is 28.4 dBic, which was measured using a standard gain horn by the comparison method. Based on the radiating aperture size of 10.8 cm × 8.3 cm, the calculated directivity of a uniformly distributed array should be 31.0 dBic. This implies that the array has an overall efficiency of 55 percent with a total loss of 2.6 dB. The loss is mostly the result of the microstrip transmission line's ohmic losses (1.0 to 1.5 dB), which occurred in the substrate dielectric and in the copper conductor. The remaining portions of the loss are mismatch loss, cross-pol loss, side-lobe loss, patch element loss, and input connector loss. The cross-pol and side-lobe losses are partly due to imperfect design and partly caused by radiation leakage from the transmission lines. It is expected that the overall loss would be significantly higher if the series-fed technique and the single-fed CP patch were not used. The antenna gain was also measured across a frequency bandwidth, which demonstrated that the array has a bandwidth of 0.95 GHz with 1 dB of maximum gain drop. The antenna's total mass, including the aluminum supporting plate, is 0.053 kg (1.88 oz). The characteristics and performance of the array antenna are summarized in Table 2.

VI. Conclusions

A 32-GHz circularly polarized microstrip array with 192 patch elements has been successfully developed for the microspacecraft application. It is intended as a downlink telecommunication spacecraft antenna. Each patch element is circularly polarized with a single feed and two truncated corners.

The stability and quality of the circular polarization is improved by arranging four adjacent elements in a sequential fashion. Thus, the full array consists of 48 identical four-element subarrays. To minimize the insertion loss, these subarrays are combined primarily by series-feed microstrip transmission lines, and impedances are matched throughout the array. The antenna achieved the required gain of 28 dBic with a physical size of 11.4 cm × 8.9 cm and a thickness of 0.18 cm. Due to its low profile, the array antenna is to be surface-mounted along with the solar panels. The total antenna mass is only 0.053 kg (1.88 oz). The antenna has achieved the goal of occupying very little of the volume and mass of the spacecraft.

Acknowledgments

The author gratefully acknowledges John Cardone and Greg Boreham for layout and fabrication of the array and Cosme Chavez for testing the array. Special thanks are given to Dr. Hugh Smith for reviewing and editing this article.

References

[1] R. J. Mailloux, J. F. McIlvenna, and N. P. Kernweis, "Microstrip Array Technology," *IEEE Transactions on Antennas and Propagation*, vol. AP-29, pp. 25–37, January 1981.

[2] R. S. Elliott, *Antenna Theory and Design*, Englewood Cliffs, New Jersey: Prentice-Hall, Inc., pp. 414–425, 1981.

[3] J. Huang, "Microstrip Reflectarray," *IEEE AP-S Symposium Digest*, vol. 2, pp. 612–615, June 1991.

[4] J. Huang, "A Parallel/Series Fed Microstrip Array with High Efficiency and Low Cross-Pol," *Microwave and Optical Technology Letters*, vol. 5, no. 5, pp. 230–233, May 1992.

[5] T. Teshirogi, M. Tanaka, and W. Chujo, "Wideband Circularly Polarized Array Antenna with Sequential Rotations and Phase Shifts of Elements," *Proc. Int. Symposium on Antennas and Propagation*, Japan, pp. 117–120, 1985.

[6] J. Huang, "A Technique for an Array to Generate Circular Polarization With Linearly Polarized Elements," *IEEE Transactions on Antennas and Propagation*, vol. AP-34, pp. 1113–1124, September 1986.

[7] P. S. Hall, J. Huang, E. Rammos, and A. Roederer, "Gain of Circularly Polarized Arrays Composed of Linearly Polarized Elements," *IEEE Electronics Letters*, vol. 25, January 1989.

[8] J. R. James and P. S. Hall, *Handbook of Microstrip Antennas*, London: Peter Pergrinus Ltd., pp. 219–272, 1989.

[9] Y. T. Lo, D. Solomon, and W. F. Richards, "Theory and Experiment on Microstrip Antennas," *IEEE Transactions on Antennas and Propagation*, vol. AP-27, pp. 137–145, March 1979.

[10] M. Haneishi and S. Yoshida, "A Design Method of Circularly Polarized Rectangular Microstrip Antenna by One-Point Feed," *Electronics and Communications in Japan*, vol. 64-B, no. 4, pp. 46–54, 1981.

[11] I. J. Bahl and P. Bhartia, *Microstrip Antennas*, Dedham, Massachusetts: Artech House, Inc., pp. 60–64, 1980.

Table 1. ACME-II antenna requirements.

Parameter	Requirement
Frequency, GHz	32
Operation	Downlink transmit only
Gain, dBic	≥28
Polarization	Right-hand circular
Side-lobe level, dB	≤−13
Cross-pol level, dB	≤−15
Beam direction	Fixed broadside
Input VSWR at 32 GHz	≤1.5:1
Bandwidth, GHz	≥1
Power handling, W	5
Antenna mass, kg	≤0.5
Aperture size, cm	10 x 10

Table 2. Characteristics and performance of the array antenna.

Parameter	Characteristic or performance	Requirement
Center frequency, GHz	32	32
Input VSWR at 32 GHz	1.14:1	1.5:1
1.5:1 VSWR bandwidth, GHz	2	1
Peak gain, dBic	28.4	28.0
−1-dB gain bandwidth, GHz	0.95	1.0
Beamwidth, deg	5.7 x 4.5	~5 x 5
Peak side-lobe level, dB	−12	−13
Polarization	Right-hand CP	Right-hand CP
3-dB axial ratio bandwidth, GHz	1.3	1
Radiating aperture size, cm	10.8 x 8.3	≤10 x 10
Physical size, cm	11.4 x 8.9	≤10 x 10
Antenna thickness, cm	0.18	Not specified
Antenna mass, kg	0.053	≤0.5
Power handling, W	Expected 10	5

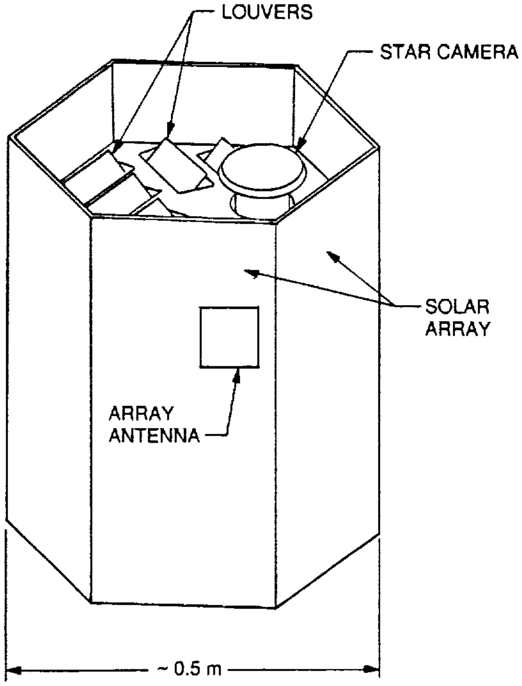

Fig. 1. ACME-II microspacecraft configuration.

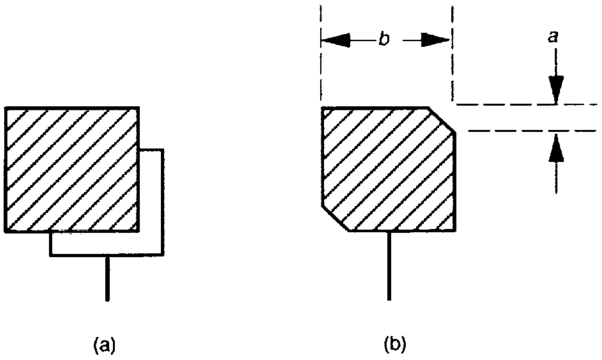

Fig. 2. Circularly polarized single-patch antenna with (a) orthogonal dual feeds and (b) single feed with truncated corners.

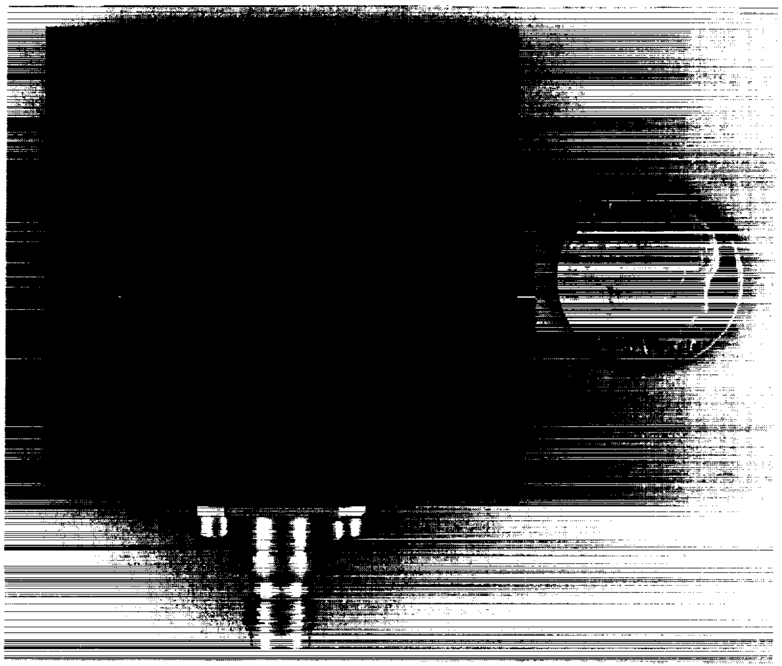

Fig. 3. The circularly polarized single-feed patch.

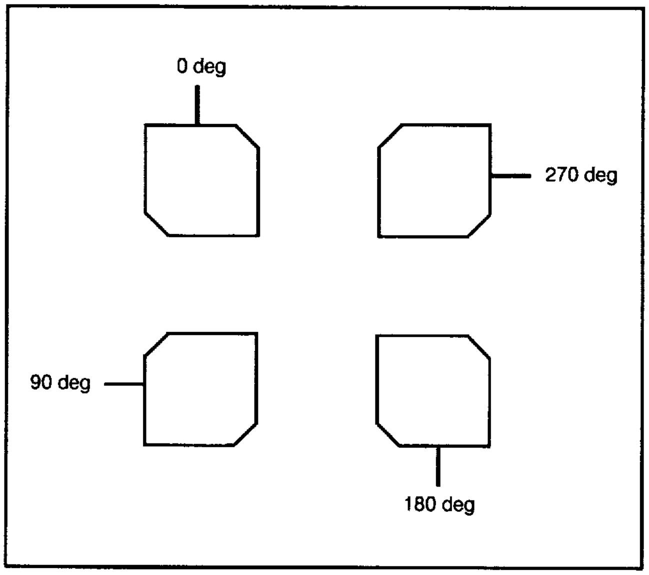

Fig. 4. The circularly polarized four-element subarray with sequential arrangement.

Fig. 5. The sequentially arranged four-element subarray.

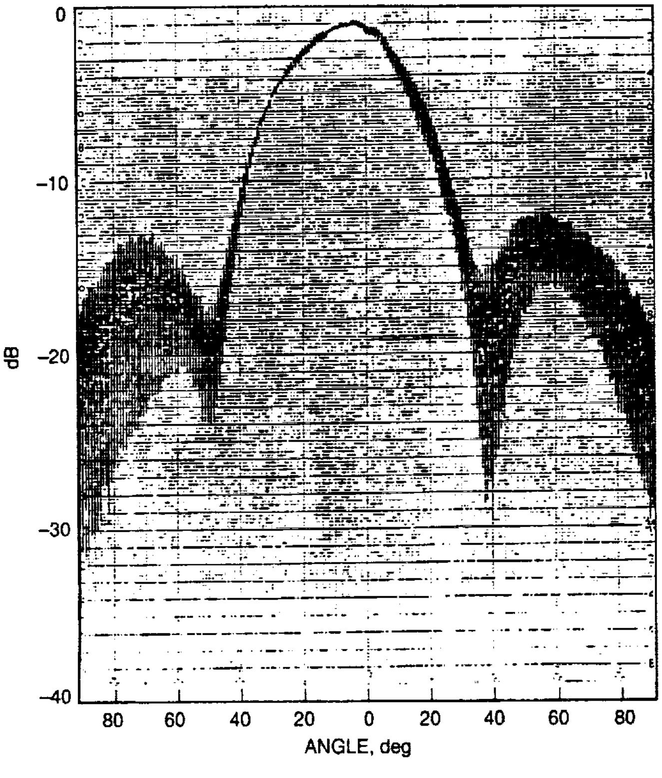

Fig. 6. Measured spinning-linear pattern of the four-element subarray.

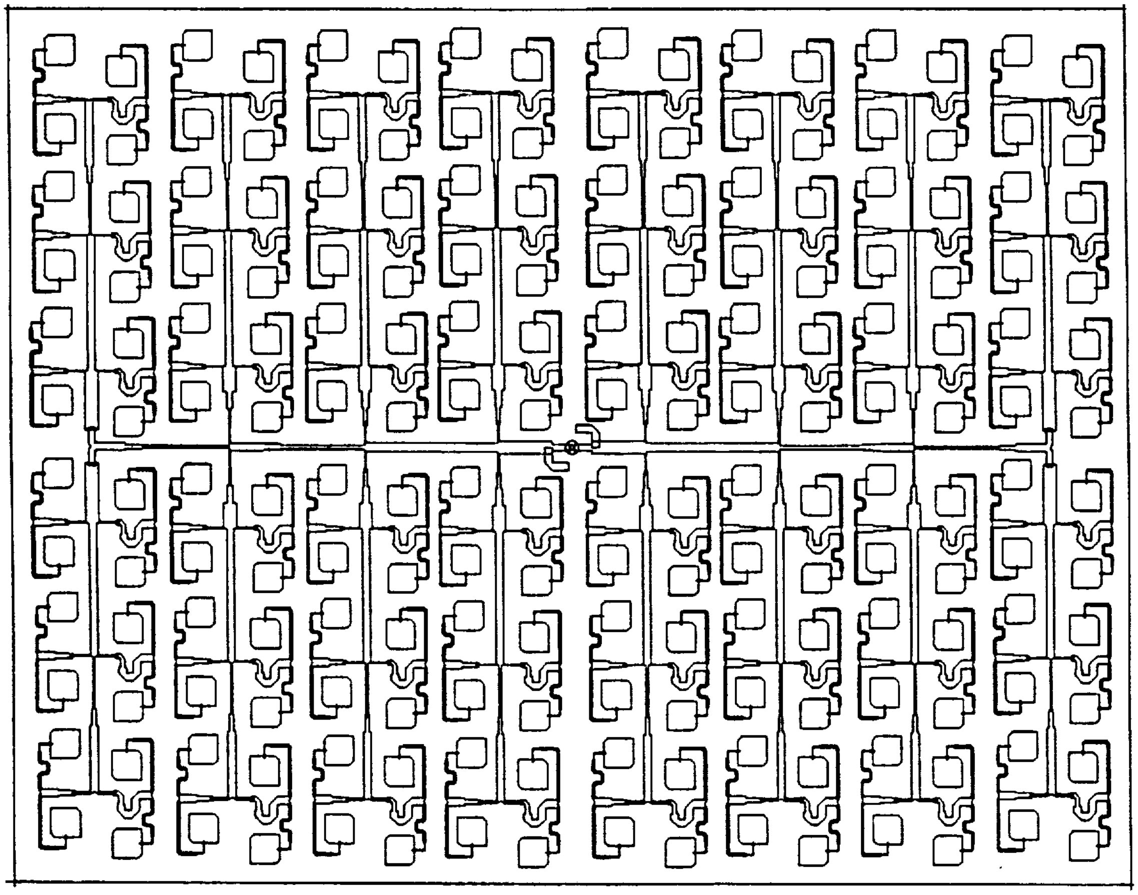

Fig. 7. The full array design.

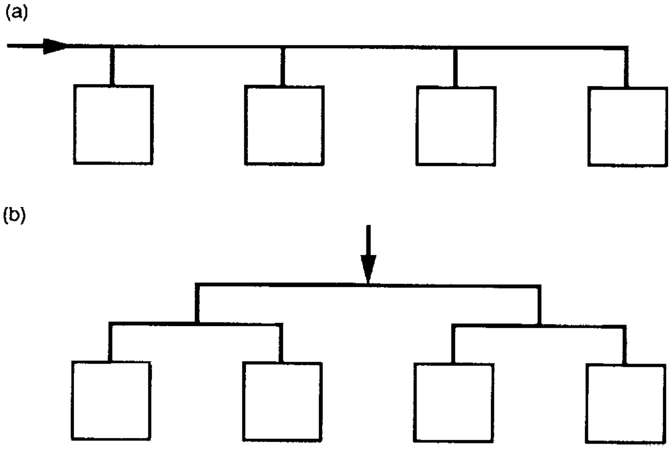

Fig. 8. Comparison of the microstrip (a) series-feed and (b) parallel-feed techniques with a four-element array.

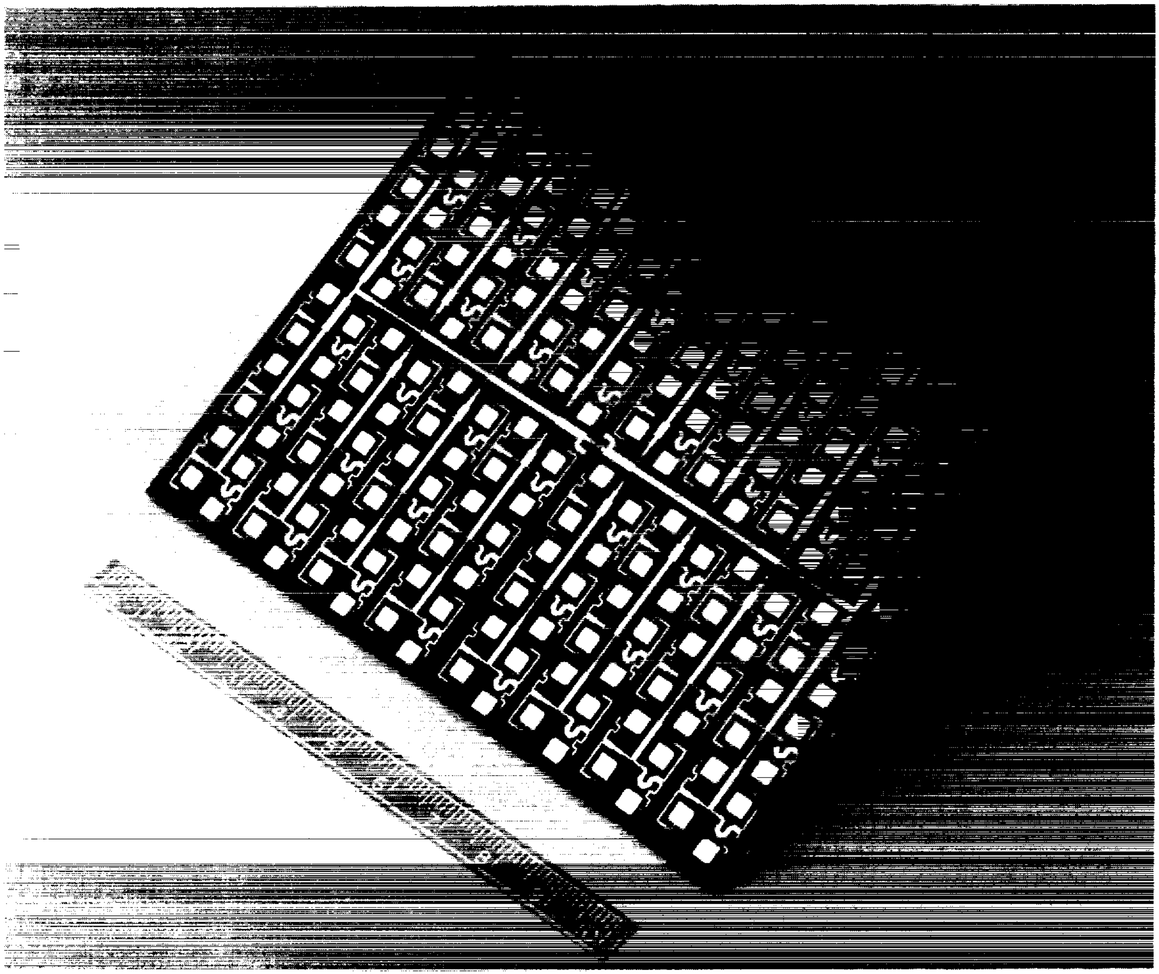

Fig. 9. The 32-GHz full array with 192 patch elements.

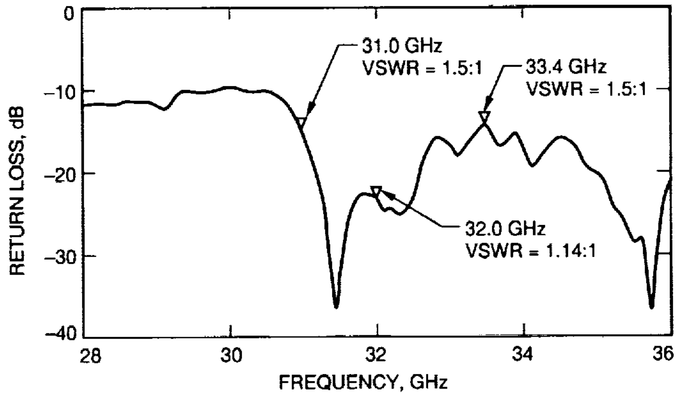

Fig. 10. Measured input return loss of the full array.

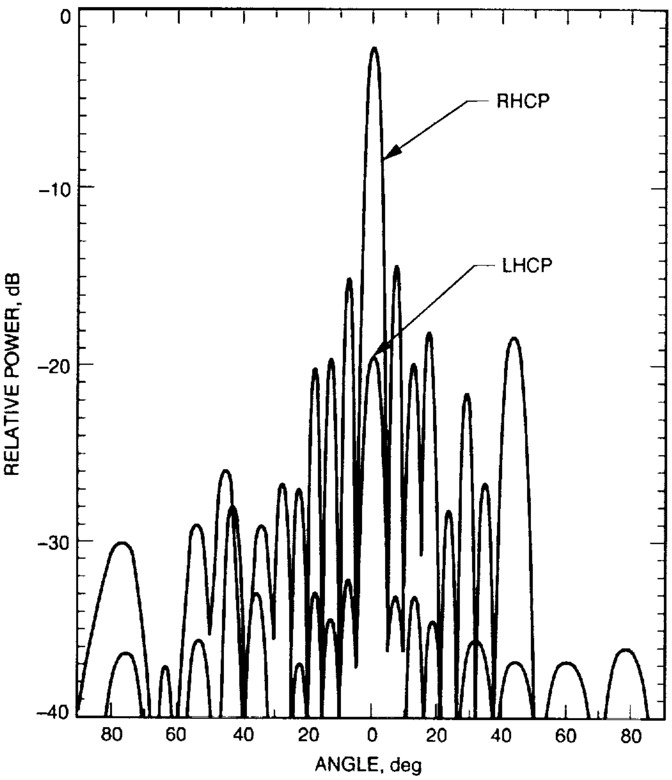

Fig. 11. Measured narrow-beam principal-plane pattern of the full array.

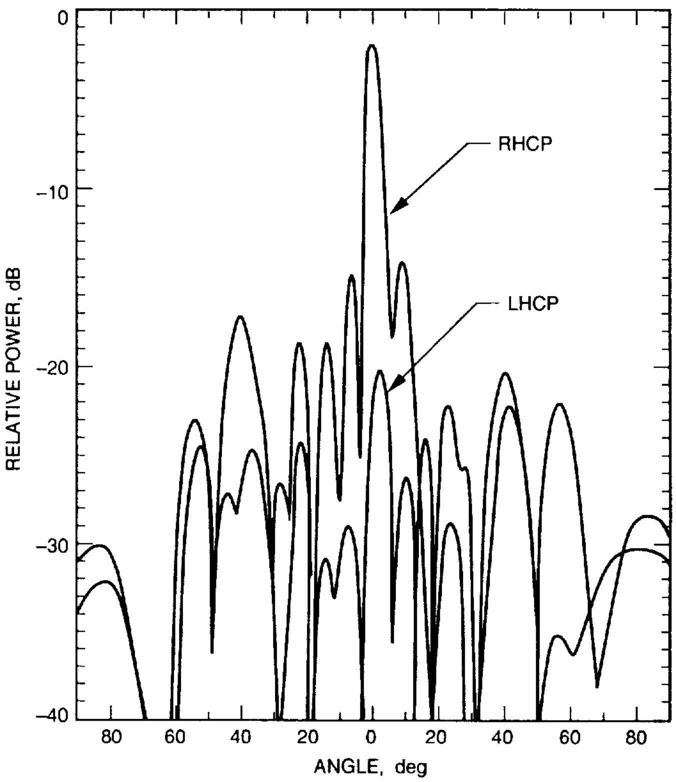

Fig. 12. Measured broad-beam principal-plane pattern of the full array.

N94- 29669

TDA Progress Report 42-116 February 15, 1994

Effects of Low Sampling Rate in the Digital Data-Transition Tracking Loop

A. Mileant
Telecommunications Systems Section

S. Million and S. Hinedi
Communications Systems Research Section

This article describes the performance of the all-digital data-transition tracking loop (DTTL) with coherent and noncoherent sampling using nonlinear theory. The effects of few samples per symbol and of noncommensurate sampling and symbol rates are addressed and analyzed. Their impact on the probability density and variance of the phase error are quantified through computer simulations.

It is shown that the performance of the all-digital DTTL approaches its analog counterpart when the sampling and symbol rates are noncommensurate (i.e., the number of samples per symbol is an irrational number). The loop signal-to-noise ratio (SNR) (inverse of phase error variance) degrades when the number of samples per symbol is an odd integer but degrades even further for even integers.

I. Introduction

In modern digital communication systems, analog-to-digital (A/D) conversion is performed as far toward the front end as possible using available technology. Usually, the received signal is amplified and then downconverted to the appropriate frequency for digital conversion. Thereafter, various system functions are performed digitally, including carrier, subcarrier, and symbol synchronization, as well as signal detection and decoding. Depending on the application, one can either sample the baseband signals (in-phase and quadrature) or sample the intermediate frequency (IF) signal. Furthermore, the sampling clock can be free running or controlled by the symbol synchronization loop. In the former case, the sampling rate is noncommensurate with the symbol rate. In the latter case, the sampling clock can be adjusted to obtain an integer number of samples per received symbol. All of these issues affect the final architecture and design of a receiver and influence the amount of cross-coupling among the various loops.

A receiver called the Advanced Receiver (ARX) has been developed for Deep Space Network (DSN) applications [1,2]. In the ARX, the signal is sampled at the IF, and the various tracking loops are implemented digitally, e.g., the "classical" analog integrate-and-dump filters, which are typically part of the loop arms (in-phase and quadrature), are replaced by digital accumulators. This article investigates the performance of the all-digital data-transition tracking loop (DTTL), used for symbol synchronization, for any number of samples per symbol. In the previous version of the Advanced Receiver (ARX I) [1], the sampling was performed synchronously with the symbol rate, and an integer number of samples per symbol were available. In the current version of the Advanced Receiver (ARX II) [2], the sampling is performed asynchronously, and the sampling clock is fixed and independent of the symbol rate. At the highest desired data rate of 6.6 Msymbols/sec and with a fixed 20-MHz processing rate for the ARX II, only about 3 samples per symbol can be obtained. We are interested in the all-digital DTTL response and performance with a small number of samples per symbol.

Some analytical results for the phase error variance of the analog DTTL were derived in [3], where the input is an analog signal and symbol and midphase detection were performed with analog integrate-and-dump filters. Later, the analysis was extended in [4], taking into account variations of the equivalent noise spectrum with respect to normalized phase error. In this article, we extend the previous results for the analog DTTL to the all-digital DTTL. We first note that there are two sampling models. One is to sample the signal instantaneously and the other is to obtain the sample by integration-and-dump (I & D) sampling of the signal. The instantaneous sampling technique can be used when the sampling rate is significantly higher than the symbol rate. The I & D sampling technique should be used when the number of samples per symbol is small [7]. In the absence of prefiltering and noise, the received symbol pulse is a perfect square wave, and instantaneous sampling provides voltage values of equal value. In the I & D case, all samples also have equal value except for the first one after a transition boundary of two symbols with different polarity. The all-digital DTTL can operate on either type of sample.

To illustrate the differences between analog and all-digital DTTLs, we consider the noiseless case first. Note that if the input is an analog signal, the midphase integrator can produce a nonzero error voltage no matter how small the phase error is. Thus, a correction voltage can be generated at every symbol transition whenever a phase error exists. Therefore, the analog DTTL has infinite resolution for phase detection.

The all-digital DTTL, in contrast, has only finite resolution for phase detection. This is illustrated in the following: Suppose that there are an even number of samples per symbol. When a symbol transition occurs, the digital midphase accumulator will produce a nonzero voltage only if the phase error causes sample slipping (assuming equal amplitude samples). As long as the phase error stays within a range of values that avoids sample slipping, the loop always generates a zero error signal. This range of undetectable phase errors accounts for the finite resolution of the all-digital DTTL. The more samples per symbol we use, the higher the resolution we can achieve and the closer the all-digital DTTL is to its analog counterpart. A key question is the impact of the all-digital DTTL's finite resolution on the S-curve and the phase error variance for few samples per symbol (say, three or four samples).

Another issue in an all-digital implementation is the effect of a noninteger number of samples per symbol. If the sampling clock is driven by the symbol synchronization loop, the number of samples per symbol can be made an exact even integer, which reduces the self-noise generated in the midphase accumulator, as will be discussed later. Under that sampling scenario, the sampling clock is constantly adapting as the data rate changes due to Doppler or other effects. One disadvantage of that scheme is that no fixed time base is available in the system. On the other hand, if the sampling clock is free running and is derived from a fixed frequency standard, the sampling period is fixed although the symbol rate may change. This may result in a noninteger number of samples per symbol. A model is derived in this article to analyze the performance of the all-digital DTTL for any sampling and symbol rates. In Section II, a nonlinear analysis of the loop is presented to handle all scenarios along with simulation results. The conclusion is presented in Section III.

II. Analysis

The performance of the all-digital data-transition tracking loop with coherent and noncoherent sampling is analyzed here. The block diagram of the all-digital DTTL is shown in Fig. 1. The input $r(i)$ to the DTTL can be obtained by instantaneous sampling or by I & D sampling. In the subsequent derivation, closed form solutions will be obtained assuming samples of equal value, and results will be verified by simulation assuming samples of both equal and unequal value.

Noncoherent sampling means that the sampling clock runs independently of the estimated symbol phase, i.e., the sampling time is independent of the estimated symbol phase. This has minimal impact if there are many samples per symbol. As the number of samples per symbol decreases, the S-curve becomes more and more coarse, and self-noise (to be explained later) increases. Our goal is to quantify the effects of a small number of samples per symbol on the phase error variance. A theory is presented for a first-order DTTL using Markov chains. The approach is to derive the S-curve and to solve the Chapman–Kolmogorov (C–K) equation to get the density function of the phase error. The closed-loop phase error variance and the degradation of the symbol detection can be evaluated from the phase error density function.

To illustrate the phenomenon of self-noise, we consider a simple example shown in Fig. 2, where we have five samples per symbol. We assume no thermal noise and perfect tracking at a particular moment. The output of the symbol transition detector is not zero because it either sums three samples from the first symbol and two samples from the second symbol [Fig. 2(a)] or sums two samples from the first symbol and three samples from the second symbol [Fig. 2(b)]. Notice that this situation occurs for every symbol interval as long as the loop maintains perfect tracking. The nonzero output of the loop filter will drag the loop away from the perfect tracking condition.

In order to quantify this phenomenon, we first introduce three useful parameters. Let β denote the number of samples per symbol, which may not be an integer, and $\alpha(1)$ denote the offset of the first sample mark in a received symbol from the symbol boundary. By convention, $\alpha(k)$ is normalized and is measured as a fraction of the sampling interval. We observe that $\alpha(k)$ remains constant if β is an integer, and it varies from symbol to symbol if β is not an integer. Let us number the received symbols by 1, 2, 3, ... and denote the value of $\alpha(k)$ at the first symbol as $\alpha(1)$, which is referred to as the initial sampling offset. The values of $\alpha(k)$ at the subsequent symbols, namely, $\alpha(2)$, $\alpha(3)$, ..., can be computed from β and $\alpha(1)$. The number of sample marks in a transition detection window and the number of sample marks in a symbol detection window are all functions of $\alpha(k)$. Thus, the output of the symbol detector and that of the transition detector fluctuate from symbol to symbol as $\alpha(k)$. This subject will be discussed later in more detail.

Another important observation about the all-digital DTTL with a low number of samples per symbol is that it can have an irreducible phase error due to a finite number of samples per symbol. To illustrate this phenomenon, let us consider the example shown in Fig. 3, where every symbol contains four samples. We can see that as long as the estimated phase lies between t_1 and t_2, the error signal is always zero (or nearly zero if the received symbol does not have a perfect square waveform or if we have unequal amplitude samples) and the DTTL continues tracking. However, we see that there still exists unresolved phase ambiguity within the interval from t_1 to t_2. Mathematically, this phase ambiguity can be explained by a staircase S-curve. This phenomenon might have little effect on symbol detection performance if we use straight accumulation to detect the symbols. However, if we use weighted accumulation to detect the symbols, the phase ambiguity can introduce misweighting and thus degrade performance [5,6].

Before we proceed to the mathematical analysis, let us examine the all-digital DTTL block diagram again. The error signal accumulator between the loop filter $F(z)$ and the multiplier performs an averaging function so that the subsequent loop filter can operate at a slower speed. The loop bandwidth is determined primarily by the loop filter $F(z)$. Thus, the presence of the accumulator is simply for hardware convenience. In the following analysis, we consider the DTTL without the error-signal accumulator.

A. Mathematical Model

Assuming that the carrier and subcarrier (if any) have been removed in an ideal fashion, the received baseband waveform is given by

$$r(t) = \sqrt{S}\sum_k a_k p(t - kT) + n(t) \tag{1}$$

where S is the signal power, T is the symbol time, $n(t)$ is white Gaussian noise with one-sided power spectral density N_0 W/Hz, $a_k = \pm 1$ represents the polarity of the kth symbol, and $p(t)$ is the square-wave function having a value of 1 for $0 \le t < T$, and having a value of 0 elsewhere. The ith sample can be expressed after normalizing by $1/\sqrt{S}$ as

$$r(i) = a_k + n(i) \tag{2}$$

where we assume the sample is derived from the kth symbol, $n(i)$ is a zero-mean Gaussian random variable with variance $\sigma^2 = N_0/(2ST_S)$, and T_S is the sampling interval. Let the phase error λ (in cycles) be defined as

$$\lambda = \frac{\theta - \widehat{\theta}}{2\pi} \tag{3}$$

where θ is the actual received symbol phase and $\widehat{\theta}$ is the estimated symbol phase. Note that λ should have a value between -0.5 and 0.5. The error signal is affected by the locations of samples within their respective received symbols. In order to quantify this effect, we define a set of four Δ_k integer-valued functions. They represent the number of sample marks contained in their respective intervals, as illustrated in Fig. 4. The output of the in-phase accumulator $x(k)$ and the midphase accumulator $y(k)$ can be expressed in terms of the Δ_k functions, namely

$$x(k) = \begin{cases} \Delta_1(k)a_k + \Delta_2(k)a_{k+1} + n_1(k) + n_2(k) \\ \quad \text{for } \lambda \geq 0 \\ \\ \Delta_1(k)a_k + \Delta_2(k)a_{k-1} + n_1(k) + n_2(k) \\ \quad \text{for } \lambda < 0 \end{cases}$$

$$x(k+1) = \begin{cases} \Delta_1(k+1)a_{k+1} + \Delta_2(k+1)a_{k+2} + n_3(k) \\ +n_4(k) \quad \text{for } \lambda \geq 0 \\ \\ \Delta_1(k+1)a_{k+1} + \Delta_2(k+1)a_k + n_3(k) \\ +n_4(k) \quad \text{for } \lambda < 0 \end{cases}$$

$$y(k+1) = \Delta_3(k)a_k + \Delta_4(k)a_{k+1} + n_2(k) + n_3(k) \tag{4}$$

where $n_j(k), j = 1, 2, 3, 4$ are zero-mean Gaussian random variables with variances

$$\text{Var}\{n_1(k)\} = \begin{cases} (\Delta_1(k) - \Delta_3(k))\sigma^2 \text{ for } \lambda \geq 0 \\ \\ (\Delta_1(k) + \Delta_2(k) + \Delta_2(k+1) - \Delta_3(k))\sigma^2 \\ \quad \text{for } \lambda < 0 \end{cases}$$

$$\text{Var}\{n_2(k)\} = \begin{cases} (\Delta_3(k) + \Delta_2(k))\sigma^2 \text{ for } \lambda \geq 0 \\ \\ (\Delta_3(k) - \Delta_2(k+1))\sigma^2 \text{ for } \lambda < 0 \end{cases}$$

$$\text{Var}\{n_3(k)\} = \begin{cases} (\Delta_4(k) - \Delta_2(k))\sigma^2 \text{ for } \lambda \geq 0 \\ \\ (\Delta_4(k) + \Delta_2(k+1))\sigma^2 \text{ for } \lambda < 0 \end{cases}$$

$$\text{Var}\{n_4(k)\} = \begin{cases} (\Delta_2(k) + \Delta_1(k+1) + \Delta_2(k+1) \\ -\Delta_4(k))\sigma^2 \text{ for } \lambda \geq 0 \\ \\ (\Delta_1(k+1) - \Delta_4(k))\sigma^2 \text{ for } \lambda < 0 \end{cases} \tag{5}$$

and the Δ_j functions are computed from

$$\Delta_1(k) = \begin{cases} \lfloor 2\beta - \alpha(k-1) \rfloor - \lfloor (1+\lambda)\beta - \alpha(k-1) \rfloor \\ \quad \text{for } \lambda \geq 0 \\ \\ \lfloor (2+\lambda)\beta - \alpha(k-1) \rfloor - \lfloor \beta - \alpha(k-1) \rfloor \\ \quad \text{for } \lambda < 0 \end{cases}$$

$$\Delta_2(k) = \begin{cases} \lfloor (1+\lambda)\beta - \alpha(k) \rfloor - \lfloor \beta - \alpha(k) \rfloor \\ \quad \text{for } \lambda \geq 0 \\ \\ \lfloor \beta - \alpha(k-1) \rfloor - \lfloor (1+\lambda)\beta - \alpha(k-1) \rfloor \\ \quad \text{for } \lambda < 0 \end{cases}$$

$$\Delta_3(k) = \lfloor \beta - \alpha(k) \rfloor - \left\lfloor \left(1 + \lambda - \frac{w}{2}\right)\beta - \alpha(k) \right\rfloor$$

$$\Delta_4(k) = \left\lfloor \left(1 + \lambda + \frac{w}{2}\right)\beta - \alpha(k) \right\rfloor - \left\lfloor \beta - \alpha(k) \right\rfloor \tag{6}$$

with w denoting the width of the transition window and $w \leq 1$. As previously mentioned, $\alpha(k+1)$ is the sampling offset and is computed recursively from $\alpha(k)$ using

$$\alpha(k+1) = \lfloor \beta - \alpha(k) + 1 \rfloor - (\beta - \alpha(k)) \tag{7}$$

and $\lfloor y \rfloor$ denotes the greatest integer strictly less than y (i.e., $\lfloor 4.2 \rfloor = 4$, $\lfloor 4 \rfloor = 3$). The derivation of the Δ_i functions are similar and we illustrate only one example here, $\Delta_2(k)$. To derive $\Delta_2(k)$, we use the beginning of the kth received symbol as the reference point. The number of samples in the kth received symbol is $\lfloor \beta - \alpha(k) \rfloor + 1$. The number of samples from the beginning of the kth symbol to the end of the kth estimated symbol is $\lfloor (1+\lambda)\beta - \alpha(k) \rfloor + 1$. Equation (5) follows by observing that the number of samples from the end of the kth received symbol to the end of the kth estimated symbol is $\Delta_2(k)$. The error signal $e(k+1)$ is given by

$$e(k+1) = z(k+1)y(k+1) \tag{8}$$

where $z(k+1)$ denotes the output of the transition detector and $\text{sgn}(x)$ denotes the "signum" function, i.e.,

$$z(k+1) = \frac{\text{sgn}\,[x(k+1)] - \text{sgn}\,[x(k)]}{2} \tag{9}$$

The conditional S-curve is defined by

$$g(\lambda | \alpha(k)) = E_{s,n}\{e(k+1) | \lambda, \alpha(k)\} \tag{10}$$

where $E_{s,n}$ represents the conditional expectation with respect to both the signal (s) and the noise (n), assuming fixed λ and $\alpha(k)$. Following mathematical manipulation similar to that in [4], we get

$$E_{s,n}\{e(k+1)|\lambda,\alpha(k)\} =$$

$$\begin{cases} 0.25[\Delta_4(k)(\mathrm{erf}\,[r_1(k)] - \mathrm{erf}\,[r_2(k)] + \mathrm{erf}\,[r_1(k+1)] \\ +\ \mathrm{erf}\,[r_2(k+1)]) - \Delta_3(k)(\mathrm{erf}\,[r_1(k)] + \mathrm{erf}\,[r_2(k)]) \\ -\ r_3(k)(\Delta_3(k) + \Delta_2(k))(\exp[-r_1^2(k)] + \exp[-r_2^2(k)]) \\ +\ r_3(k)(\Delta_4(k) - \Delta_2(k))(\exp[-r_1^2(k+1)] \\ +\ \exp[-r_2^2(k+1)])] \quad \text{for } \lambda \geq 0 \\ 0.25[\Delta_4(k)(\mathrm{erf}\,[r_1(k+1)] + \mathrm{erf}\,[r_2(k+1)]) - \Delta_3(k) \\ (\mathrm{erf}\,[r_1(k+1)] - \mathrm{erf}\,[r_2(k+1)] \\ +\ \mathrm{erf}\,[r_1(k)] + \mathrm{erf}\,[r_2(k)]) \\ -\ r_3(k)(\Delta_3(k) - \Delta_2(k))(\exp[-r_1^2(k)] + \exp[-r_2^2(k)]) \\ +\ r_3(k)(\Delta_4(k) + \Delta_2(k))(\exp[-r_1^2(k+1)] \\ +\ \exp[-r_2^2(k+1)])] \quad \text{for } \lambda < 0 \end{cases} \tag{11}$$

where

$$r_1(k) = \sqrt{\frac{R_s(\Delta_1(k) - \Delta_2(k))^2}{\beta(\Delta_1(k) + \Delta_2(k))}}$$

$$r_2(k) = \sqrt{\frac{R_s(\Delta_1(k) + \Delta_2(k))}{\beta}}$$

$$r_3(k) = \sqrt{\frac{\beta}{\pi R_s(\Delta_1(k) + \Delta_2(k))}}$$

$$R_s = \frac{2ST}{N_0}$$

$$\mathrm{erf}\,(x) = \frac{2\int_0^x e^{-t^2}dt}{\sqrt{\pi}} \tag{12}$$

We observe that $g(\lambda|\alpha(k))$ is the (unconditional) S-curve if $\alpha(k)$ is a constant. If $\alpha(k)$ changes from symbol to symbol, its effect will be smoothed in the loop as long as the loop time constant (inverse of loop bandwidth) is larger than MT. M denotes the number of distinct $\alpha(k)$'s and is discussed in the subsequent section. Therefore, the S-curve is obtained by averaging Eq. (11) over the M values of $\alpha(k)$, which is determined by the initial sampling offset and the number of samples per symbol β, that is,

$$g(\lambda) = \frac{1}{M}\sum_{k=1}^{M} g(\lambda|\alpha(k)) \tag{13}$$

The S-curve $g(\lambda)$ is a function of λ, β, and $\alpha(k)$. In general, β can be any real number. When β is an irrational number, then $\alpha(k)$ is nonperiodic. However, when β is a rational number, then $a(k)$ becomes periodic and assumes a finite number of possible values. For example, if β is of the form $X.0000\ldots$, where X is any nonzero integer, then $\alpha(k)$ will have only one value all the time; if β is of the form $X.X000\ldots$, then $\alpha(k)$ will have at most 10 different values; if β is of the form $X.XX000\ldots$, then $\alpha(k)$ will have at most 100 different values, and so forth. For example, consider $\beta = 4.1$ and suppose the initial sampling offset $\alpha(1) = 0.7$. Clearly, $\alpha(2) = 0.6$, $\alpha(3) = 0.5$, $\alpha(4) = 0.4$, $\alpha(5) = 0.3$, $\alpha(6) = 0.2$, $\alpha(7) = 0.1$, $\alpha(8) = 0$, $\alpha(9) = 0.9$, $\alpha(10) = 0.8$, $\alpha(11) = 0.7\ldots$. The more values $\alpha(k)$ takes, the smoother will be the S-curve of the tracking loop.

For a large β, $r_i(k+1) = r_i(k)$ and $i = 1,2,3$; for $\lambda \geq 0$, $\Delta_1(k) \rightarrow (1-\lambda)\beta$, $\Delta_2(k) \rightarrow \lambda\beta$, $\Delta_3(k) \rightarrow (w/2 - \lambda)\beta$, $\Delta_4(k) \rightarrow (w/2 + \lambda)\beta$; and, as a result, $r_1(k) \rightarrow (1 - 2\lambda)\sqrt{R_s}$, $r_2(k) \rightarrow \sqrt{R_s}$, $r_3(k) \rightarrow 1/\sqrt{\pi R_s}$. Substituting back in Eq. (11) and simplifying, one obtains

$$\begin{aligned} \frac{E_{s,n}\{e(\lambda)\}}{\beta} &= \lambda\,\mathrm{erf}\left(\sqrt{R_s}(1-2\lambda)\right) \\ &\quad - \frac{1}{8}[w - 2\lambda]\left[\mathrm{erf}\left(\sqrt{R_s}\right)\right. \\ &\quad \left.-\mathrm{erf}\left(\sqrt{R_s}(1-2\lambda)\right)\right] \end{aligned} \tag{14}$$

which agrees with the S-curve derived by Simon [4] for the analog loop. For $\lambda \leq 0$, similar steps can be taken to show that the resulting S-curve also agrees with the analog case, with slope at the origin given by

$$m = \beta \left(\operatorname{erf}\left(\sqrt{R_s}\right) - \frac{w}{2}\sqrt{\frac{R_s}{\pi}}e^{-R_s} \right) \tag{15}$$

Figure 5 depicts the theoretical and simulated S-curves as a function of the phase error for various values of β, namely 4, 5, 10, 4.5, and 4.74, with $w = 1$. Note the staircase shape of the S-curve for all β, with step size proportional to $1/M\beta$. In this case, the phase detector is insensitive to variations of the input phase which occur in the flat regions of the S-curve. For small integers, the steps are large, while for large integers, the steps are small. In general, the S-curve is not symmetric and has a bias (i.e., $g(0) \neq 0$) proportional to $1/M\beta$, except for the case when β is an exact even integer. The sign of the asymmetry depends on $\alpha(1)$, which was set to 0.5 in Fig. 5(e). As β approaches an irrational number, the S-curve becomes smooth due to the averaging over a large set of values and it converges to the S-curve encountered in analog systems. In all these figures, the S-curve has a zero slope at the origin, which prevents a linear analysis because it requires a nonzero slope. Also depicted in Fig. 5(a) are two cases: when the signal and noise ($s + n$) are filtered prior to the loop and when only the signal is filtered but not the noise. The first scenario represents the case where the main contribution of the filtering is occurring at the receiver, while the latter scenario is representative of filtering at the transmitter. The filter used in the simulations is a first-order lowpass with transfer function $H(z) = h_0/(1 + h_1 z^{-1})$. Note from Fig. 5(a) that the filtering introduces a bias and a slight asymmetry in the S-curve which is mainly due to the signal filtering. The asymmetry in the S-curve can be reduced by using a raised cosine or square-root raised cosine filter [7] that results in a symmetrical pulse shape around the data transition point. In the remaining figures, simulations with both signal and noise filtering are shown to assess the impact of imperfect square pulses.

One way to linearize the loop and, hence, to smooth the shape of the S-curve is to randomly shift by an amount the position of the window relative to the symbol transition point. The effect of this random back and forth shifting is to produce on the average the same amount of samples in both halves of the symbol transition detector, so that β would appear to have an irrational value to the mid-phase detector. The performance of the DTTL with such a detector can be the topic of future work.

We will proceed to perform a nonlinear analysis of the loop using the C–K equation. However, we will need the open-loop variance of the error signal at the input to the loop filter to compute the transitional probability density. The second moment of the error signal is given by

$$\begin{aligned} e_2(\lambda) &= E_{s,n}\left\{ \left(\frac{1}{M}\sum_{k=1}^{M} e(k,\lambda) \right)^2 \right\} \\ &= \frac{1}{M}\sum_{k=1}^{M} E_{s,n}\{e(k,\lambda)^2\} + \frac{2}{M-1}\sum_{k=1}^{M-1} E_{s,n}\{e(k,\lambda) \\ &\quad \times e(k+1,\lambda)\} \\ &\triangleq \frac{1}{8M}\sum_{k=1}^{M}\left[v_1(k) + v_2(k)\right] + \frac{2}{16(M-1)}\sum_{k=1}^{M-1} \\ &\quad \times \left[v_3(k) + v_4(k) + v_5(k)\right] \end{aligned} \tag{16}$$

where the variables $v_i(k)$, $i = 1,2,3,4,5$ are defined in the Appendix. The open-loop variance is then computed using

$$\sigma_e^2(\lambda) = e_2(\lambda) - g^2(\lambda) \tag{17}$$

The open loop variance $\sigma_e^2(\lambda)$ is depicted in Fig. 6 for various values of β as a function of λ. Again, note the staircase shape of the variance which approaches a smooth function for $\beta = 4.74$. The analysis agrees very well with the simulation points for all values of β.

B. Probability Density Function of the Phase Error

When the number of samples per symbol, β, is low and the decimal part of β has only a few nonzero digits, the S-curve takes a coarse staircase shape, as discussed previously. In this case, the loop behaves nonlinearly, and the phase jitter of the loop cannot be predicted from the loop's noise-equivalent bandwidth. However, when the statistics of the driving noise process are known, the C–K equation permits one to derive the probability density function (pdf) of the closed-loop phase jitter even for a highly nonlinear loop. Once this pdf is found, all the moments of the phase jitter process can be computed, and the noise performance of the loop can be predicted.

In general, an all-digital phase-locked loop can be described by a stochastic difference equation of the form

$$\lambda(k) = u(k) - [g(\lambda(k)) + n(k)]N(z)F(z) \tag{18}$$

where $\lambda(k)$ is the phase error at the instant k, $u(k)$ is the input signal sequence, $F(z)$ and $N(z)$ are the discrete transfer functions of the loop filter and the numerically controlled oscillator (NCO), respectively, the function $g(\lambda(k))$ represents the nonlinearity of the phase detector, and $n(k)$ is the open-loop noise process. In digital phase-locked loops, this noise process consists of both thermal and quantization noise. For the all-digital DTTL under consideration, the noise $n(k)$ is zero-mean with the variance given by Eq. (17). In general, the product $F(z)N(z)$ is of the form

$$F(z)N(z) = \frac{b_0 + b_1 z^{-1} + \ldots + b_N z^{-N}}{a_0 + a_1 z^{-1} + \ldots + a_N z^{-N}} \qquad (19)$$

Here in the context of the stochastic difference equations, z^{-1} should be thought of as the unit delay operator. Using Eq. (19), Eq. (18) can be rewritten as

$$\begin{aligned}\lambda(k) = {} & [a_0 u(k) + b_0(g(\lambda(k)) + n(k))] \\ & + z^{-1}[a_1 u(k) - a_1\lambda(k) - b_1 g(\lambda(k)) - b_1 n(k)] \\ & + z^{-2}[a_2 u(k) - a_2\lambda(k) - b_2 g(\lambda(k)) - b_2 n(k)] \\ & + \quad \cdots \quad \cdots \quad \cdots \\ & + z^{-N}[a_N u(k) - a_N\lambda(k) - b_N g(\lambda(k)) - b_N n(k)]\end{aligned} \qquad (20)$$

Defining x_1 as the row with z^{-1}, x_2 as the row with z^{-2}, etc., the above equation can now be expressed in terms of the following state and output equations:

$$\begin{aligned}\underline{x}(k+1) &= \mathbf{A}\underline{x}(k) - \underline{b}\,g(\lambda(k)) + \underline{a}\,u(k) - \underline{b}\,n(k) \\ \lambda(k) &= x_1(k) + [a_0 u(k) + b_0 g(\lambda(k)) + b_0 n(k)]\end{aligned} \qquad (21)$$

where $\underline{x}$ is the state vector, $[x_1\, x_2 \cdots x_N]^t$, $\mathbf{A}$ is the transition matrix

$$\mathbf{A} = \begin{bmatrix} -a_1 & 1 & 0 & 0 & \cdot \\ -a_2 & 0 & 1 & 0 & \cdot \\ \cdot & 0 & 0 & \cdot & \cdot \\ -a_N & 0 & 0 & 0 & 0 \end{bmatrix} \qquad (22)$$

$\underline{a} = [a_1\, a_2 \cdots a_N]^t$, and $\underline{b} = [b_1\, b_2 \cdots b_N]^t$ (the superscript t denotes transpose). The need to rewrite the original stochastic difference in vector form stems from the fact that the original equation does not represent a Markov process while its new form is a vector Markov process. For a vector Markov process, the C–K equation relates the probability density function of the state vector $\underline{\mathbf{x}}$ at time $(k+1)$, $p_{k+1}(\underline{\mathbf{x}}(k+1))$, to its probability density function at time k through the following integral:

$$p_{k+1}(\underline{\mathbf{x}}(k+1) = \underline{x}|\,\underline{x}_0) = \underbrace{\int_{-\infty}^{\infty}\cdots\int}_{N-dim} q[\underline{\mathbf{x}}(k+1) = \underline{x}|\,\underline{\mathbf{x}}(k) = \underline{v}]p_k(\underline{\mathbf{x}}(k) = \underline{v}|\,\underline{x}_0)\,dv_1 \cdots dv_N \qquad (23)$$

where $\underline{x}_0$ is the initial condition vector and $q(\cdot)$ is the transition probability density function.

We will now focus on solving the above equation for the steady-state case (large k) and a periodic phase detector. In steady state, the initial condition vector $\underline{x}_0$ is washed out and can be dropped from the C–K equation, $p_{k+1}(\cdot) \rightarrow p_k(\cdot) \overset{\Delta}{=} p(\cdot)$, so that the index k can be dropped also. With a periodic phase detector $g(\cdot)$, each state variable takes values only between $0.5 < x_i \leq 0.5$ $(i = 1 \ldots N)$. This requires the "folding" (or collapsing) of the transitional pdf $q[\cdot]$ to the bounded region. We define this new transitional pdf as $\xi[\cdot]$ and rewrite the C–K as follows:

$$\acute{p}(\underline{\mathbf{y}} = \underline{y}) = \underbrace{\int_{-0.5}^{0.5}\cdots\int}_{N-dim} \xi[\underline{\mathbf{y}}(k+1) = \underline{y}|\,\underline{\mathbf{y}}(k) = \underline{w}]\,\acute{p}(\underline{\mathbf{y}} = \underline{w})dw_1 \cdots dw_N \qquad (24)$$

where the primed p represents the new pdf restricted to the $\{-0.5, 0.5\}$ region. Even in this simplified form of the C–K equation, closed form solutions can be obtained only for a few special cases. In general, the C–K equation has to be solved numerically, and solutions for N larger than 1 can become very computationally demanding.

In order to proceed, we will restrict our attention to the case of $N = 1$ with $F(z) = b_1$ and $N(z) = z^{-1}/1 - z^{-1}$ (ideal summer), which corresponds to a type-I loop with no computational delay. Rewriting Eq. (19) for this restricted case, we get

$$F(z)N(z) = \frac{b_1 z^{-1}}{a_0 + a_1 z^{-1}} \tag{25}$$

With $N = 1$, the variables in Eq. (20) are $a_0 = 1$ and $a_1 = -1$ with all others being zero. Since we are not considering any static phase error, we set the input signal $u_k \rightarrow 0$ so that the loop is driven by noise only. Next, we discretize the continuous variable y into $L + 1$ y_i values and, thus, approximate the Markov process by a Markov chain [8]. The larger the value of L, the better is the approximation. The continuous pdf on both sides of the C–K equation can be replaced by discrete probabilities $P(y_i) = \delta p(y = y_i)$ where $\delta = 1/L$, and the transition pdf $\xi[i,j]$ is replaced by transition probability mass distribution $Q[i,j] = \delta^2 \xi[i,j]$. With this substitution, the C–K equation becomes

$$P(y = y_i) = \sum_{j=-\frac{L}{2}}^{\frac{L}{2}} Q[y(k+1) = y_i \,|\, y(k) = w_j]\, P(y = w_j) \tag{26}$$

where $x_i = i\delta$, $i = -L/2, \cdots L/2$. The above equation has to be true for all i. Let $\underline{P}(\cdot)$ be the $(L + 1)$ dimensional vector with elements $P(y = y_i)$ and $\mathbf{Q}$ be the $(L + 1) \times (L+1)$ matrix with elements $Q[i,j]$; then the C–K equation can be written in the compact form $\underline{P} = \mathbf{Q}\underline{P}$, which can be solved by various techniques used in systems of linear equations [9]. For example, one can write the above matrix equation as

$$[\mathbf{Q} - \mathbf{I}]\underline{P} = \underline{0} \tag{27}$$

with $\mathbf{I}$ being the identity matrix and $\underline{0}$ the zero vector. This matrix $\mathbf{Q} - \mathbf{I}$ will have at most $(L + 1)$ distinct eigenvalues, and the desired solution, the $\underline{P}$ vector, will be the eigenvector corresponding to the zero eigenvalue. The last step in solving for $\underline{P}$ is to assume a suitable transition probability density function which will generate the elements $Q[i,j]$ of the matrix $\mathbf{Q}$. When thermal noise dominates, the noise process $n(k)$ can be assumed to be Gaussian, for which

$$Q[i,j] = \delta^2 \frac{1}{\sqrt{2\pi\sigma_j^2}} \sum_{l=-\infty}^{\infty} \exp\left[\frac{(x_i + l - \mu_j)^2}{2\sigma_j^2}\right] \tag{28}$$

where $\sigma_j^2 = b_1^2 \sigma_e^2(\lambda)$, $\sigma_e^2(\lambda)$ is the variance given by Eq. (17) at $\lambda = x_j$, and $\mu_j = -a_1 x_j - b_1 g(x_j)$.

However, the Gaussian assumption becomes less accurate when the quantization noise starts to dominate over the thermal noise (the high-SNR case). Our simulations have shown that, at high SNRs, the pdf on the phase error process becomes highly irregular and difficult to describe mathematically. So a trapezoidal or a uniform distribution function with mean and variance as used for the Gaussian gives results close to the ones obtained by simulation. In our computations, the singular value decomposition (SVD) algorithm was used, and L was set to 1100 to achieve acceptable resolution at a high SNR. The computed and simulated pdfs are depicted in Fig. 7 for the case of $\beta = 4, 5, 10, 4.5$, and 4.74. When $\beta = 4$, the pdf exhibits a significant flat region, as expected. However, for $\beta = 5$, the flat region disappears due to the effect of the odd number of samples per symbol. The simulations were carried out with one-sided loop bandwidth B_L set to 0.01 Hz and a symbol rate of 1 symbol/sec. For $\beta = 10$, the flat region is present again but is significantly reduced compared to the case of $\beta = 4$. For $\beta = 4.5$ or 4.74, the pdf is a smooth function, as one would expect. Note the nonzero mean in Fig. 7(e), which is due to the asymmetric S-curve in Fig. 5(e).

The corresponding variances for all cases are shown in Table 1. In Table 1(a), the loop SNR (inverse of tracking variance) is higher at $\beta = 5$ than at $\beta = 4$ and 10 due to the averaging process over the various offsets, $\alpha(k)$'s. Note that the simulations and predictions agree well in all cases, with the largest deviation, of about 0.7 dB, obtained with $\beta = 5$. Table 1(b) depicts the effect of the self-noise which is dominant at high symbol SNRs (such as 25 dB). The model predicts the contribution of the self-noise very accurately for integer as well as noninteger β. This noise is the limiting factor in the tracking performance in any all-digital DTTL implementation and is nonexistent in an analog design.

III. Conclusion

Nonlinear analysis of the all-digital DTTL is used to quantify its performance as a function of the number of samples per symbol β. It is shown that the probability density function of the closed-loop phase error can vary significantly depending upon the number of samples per symbol, β, and the symbol SNR.

The performance of the all-digital DTTL approaches its analog counterpart as β increases and the sampling and symbol rates are noncommensurate (i.e., β is irrational). The loop SNR (inverse of phase error variance) degrades when β is an odd integer and degrades even further when β is an even integer. In general, the S-curve has a bias proportional to $1/(M\beta)$, but for an even-integer β the bias goes to zero.

Acknowledgment

Credit should be given to Dr. J. B. Thomas at JPL, who suggested the advantage of noncommensurate sampling in systems where the number of samples per symbol is small.

References

[1] D. H. Brown and W. J. Hurd, "DSN Advanced Receiver: Breadboard Description and Test Results," *The Telecommunications and Data Acquisition Progress Report 42-89, vol. January-March 1987*, Jet Propulsion Laboratory, Pasadena, California, pp. 48–66, May 15, 1987.

[2] S. Hinedi, "NASA's Next Generation Deep Space Network Breadboard Receiver," *IEEE Trans. on Comm.*, vol. 41, no. 1, pp. 246–257, January 1993.

[3] W. C. Lindsey and T. O. Anderson, "Digital-Data Transition Tracking Loop," International Telemetry Conference, October 8–10, 1968, Los Angeles, California.

[4] M. K. Simon, "An Analysis of the Steady-State Phase Noise Performance of a Digital Data-Transition Tracking Loop," *Jet Propulsion Laboratory Space Programs Summary 37-55*, vol. III, Jet Propulsion Laboratory, Pasadena, California, pp. 54–62, February 1969.

[5] R. Sadr and W. J. Hurd, "Detection Of Signals by the Digital Integrate-and-Dump Filter with Offset Sampling," *The Telecommunications and Data Acquisition Progress Report 42-91, vol. July-September 1987*, Jet Propulsion Laboratory, Pasadena, California, pp. 158–173, November 15, 1987.

[6] R. Sadr, "Detection Of Signals by Weighted Integrate-and-Dump Filter," *The Telecommunications and Data Acquisition Progress Report 42-91, vol. July-September 1987*, Jet Propulsion Laboratory, Pasadena, California, pp. 174–185, November 15, 1987.

[7] E. A. Lee and D. G. Messerschmitt, *Digital Communication*, Boston, Massachusetts: Kluwer Academic Publishers, 1988.

[8] W. B. Davenport and W. L. Root, *Random Signals and Noise*, New York: McGraw-Hill Book Co., 1958.

[9] G. Strang, *Linear Algebra and Its Applications*, 3rd ed., Florida: Harcourt Brace Jovanovich, Inc., 1988.

Table 1. Predicted and simulated variances: (a) white noise dominated region and (b) self-noise dominated region.

(a)

β	Symbol SNR, dB	Variance, simulation	Variance, theory
4.0	3	0.00635	0.006324
5.0	3	0.000954	0.00114
10.0	3	0.00234	0.002434
10.0	10	0.000925	0.000972
4.5	3	0.00235	0.0026
4.74	3	0.00253	0.002720

(b)

β	Symbol SNR, dB	Variance, simulation	Variance, theory
4.0	25	0.004448	0.004578
5.0	25	0.000028	0.000030
10.0	25	0.000910	0.000972
4.5	25	0.000021	0.000024
4.75	25	0.002633	0.002750

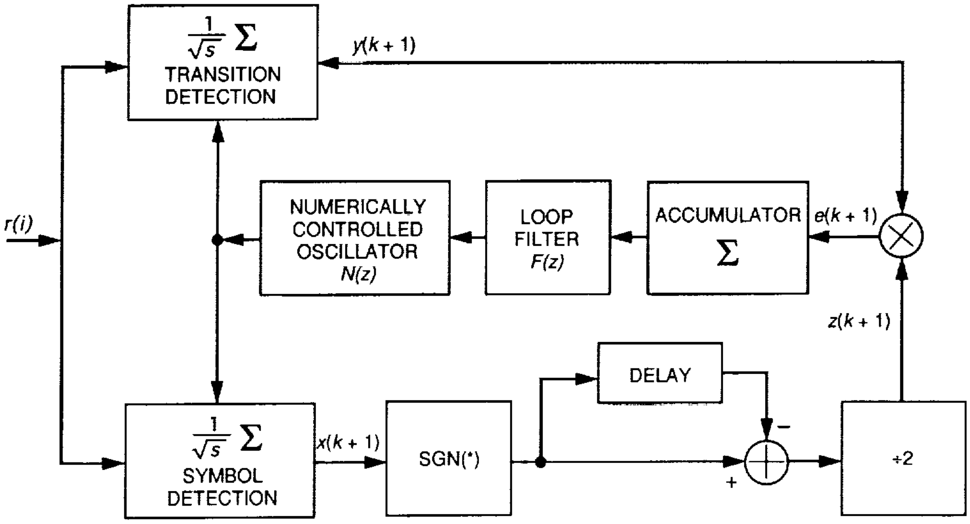

Fig. 1. Block diagram of the all-digital DTTL.

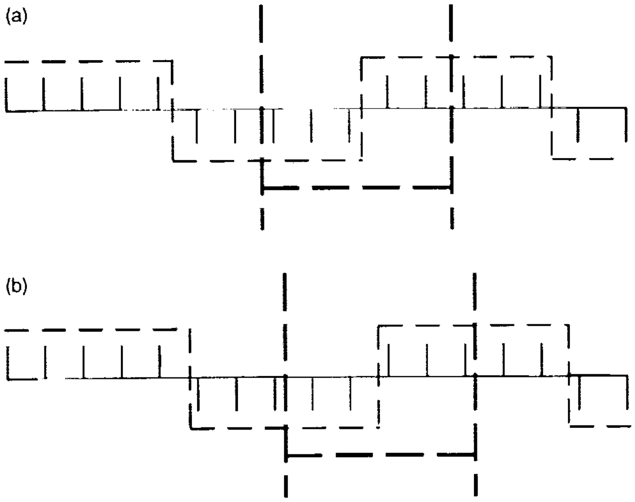

Fig. 2. The effect of an odd number of samples per symbol: (a) three samples from the first symbol and two samples from the second symbol and (b) two samples from the first symbol and three samples from the second symbol.

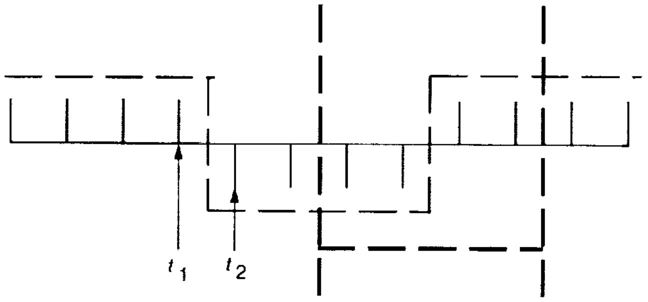

Fig. 3. The phase ambiguity phenomenon.

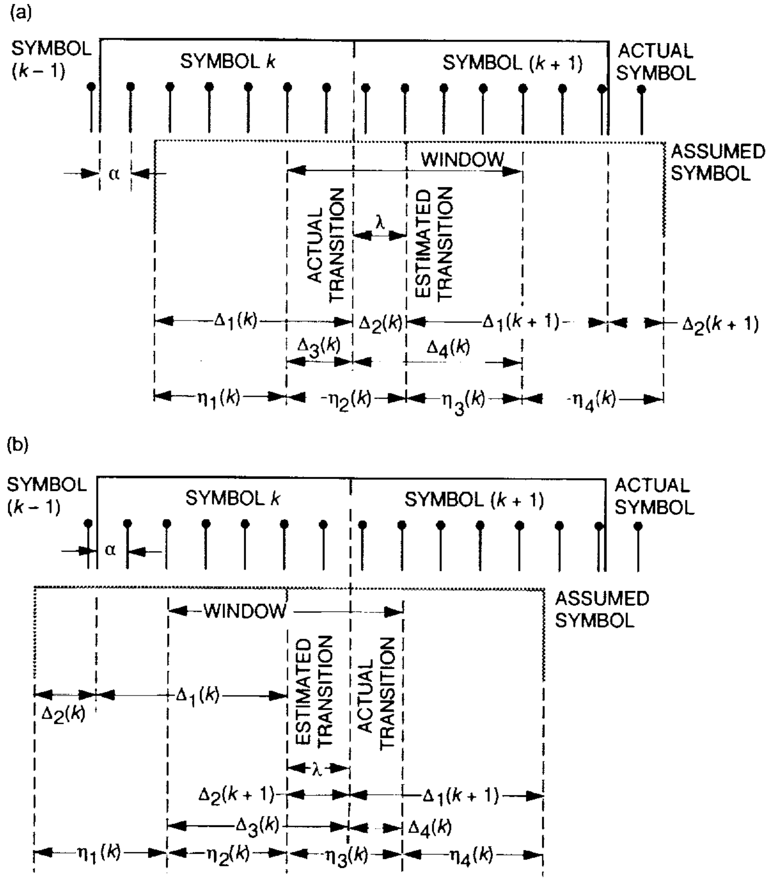

Fig. 4. Definitions of Δ_i functions: (a) $\lambda \geq 0$ and (b) $\lambda \leq 0$.

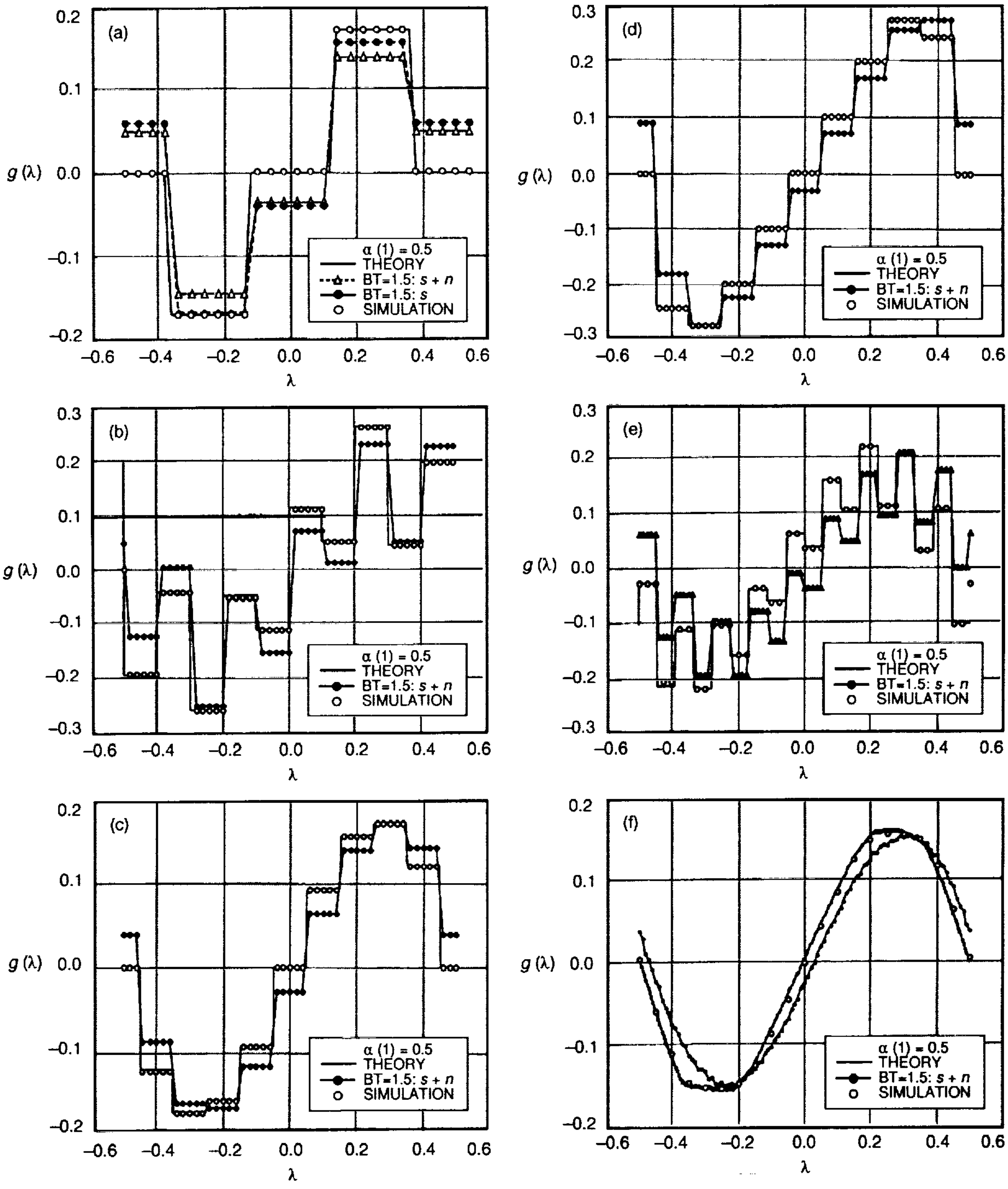

Fig. 5. S curves for various β's: (a) $\beta = 4$, symbol SNR = 3 dB, (b) $\beta = 5$, symbol SNR = 3 dB, (c) $\beta = 10$, symbol SNR = 3 dB, (d) $\beta = 10$, symbol SNR = 10 dB, (e) $\beta = 4.5$, symbol SNR = 3 dB, and (f) $\beta = 4.74$, symbol SNR = 3 dB.

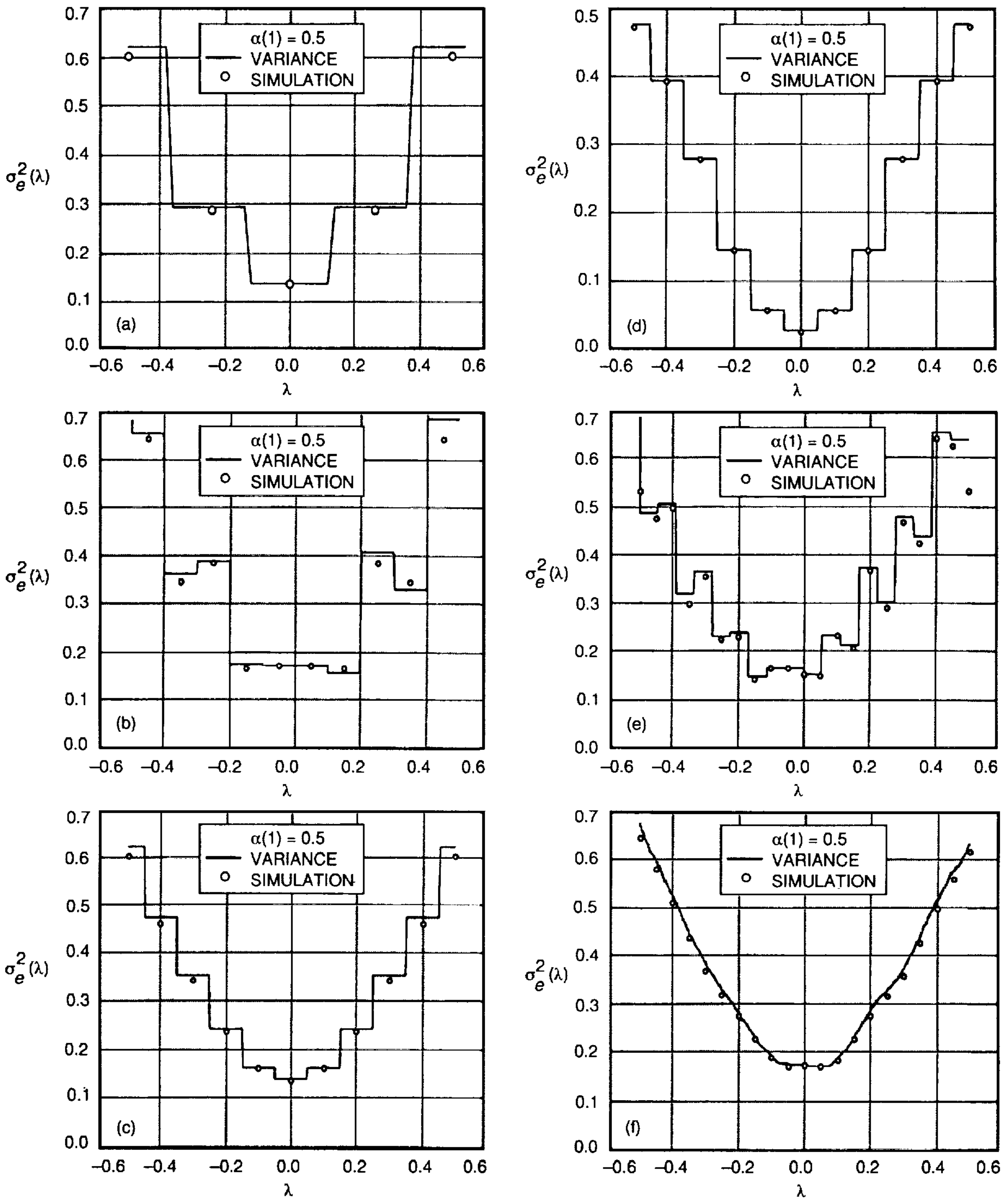

Fig. 6. Open-loop variance $\sigma_e^2(\lambda)$: (a) $\beta = 4$, symbol SNR = 3 dB, (b) $\beta = 5$, symbol SNR = 3 dB, (c) $\beta = 10$, symbol SNR = 3 dB, (d) $\beta = 10$, symbol SNR = 10 dB, (e) $\beta = 4.5$, symbol SNR = 3 dB, and (f) $\beta = 4.74$, symbol SNR = 3 dB.

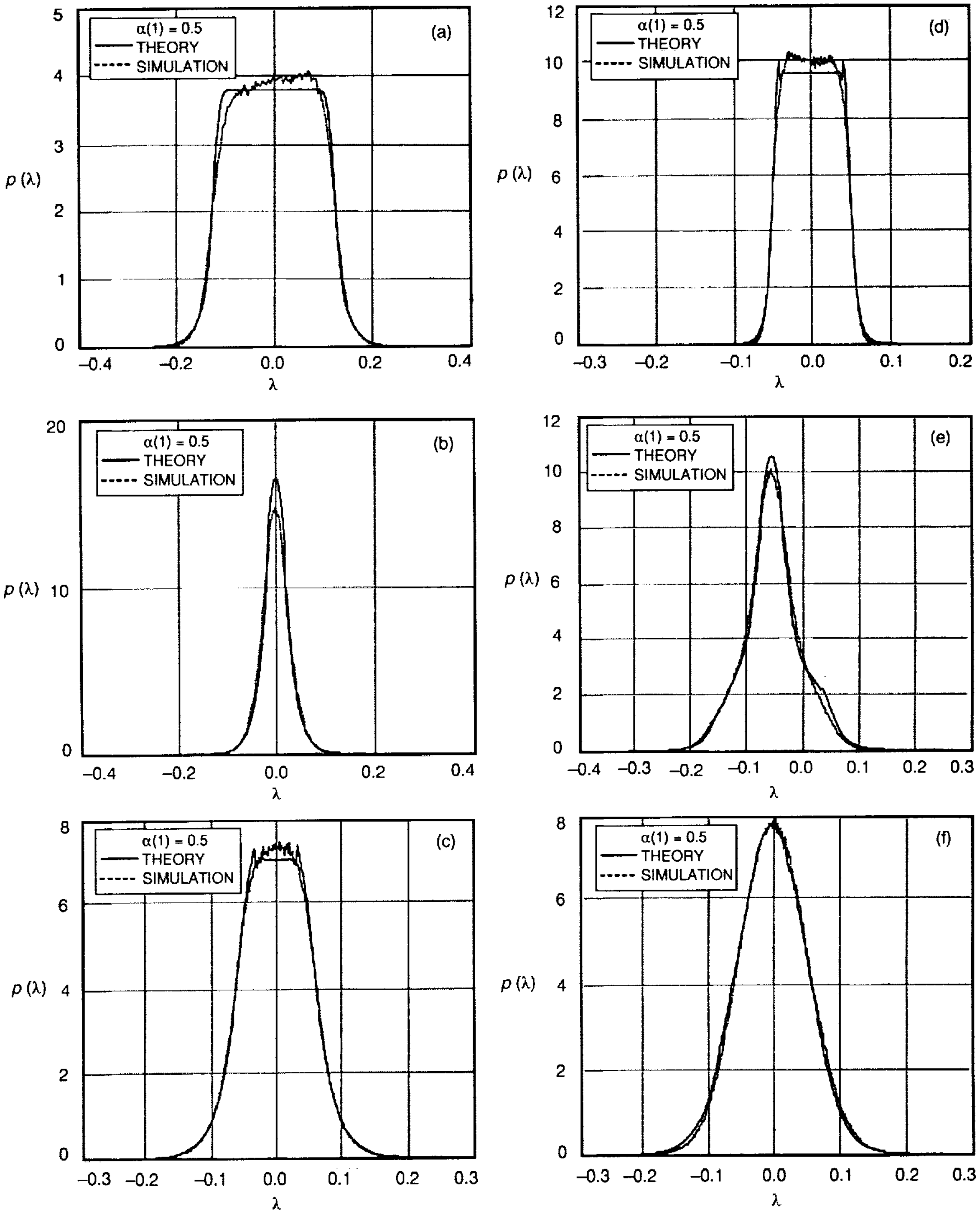

Fig. 7. Probability density function $p(\lambda)$: (a) $\beta = 4$, symbol SNR = 3 dB, (b) $\beta = 5$, symbol SNR = 3 dB, (c) $\beta = 10$, symbol SNR = 3 dB, (d) $\beta = 10$, symbol SNR = 10 dB, (e) $\beta = 4.5$, symbol SNR = 3 dB, and (f) $\beta = 4.74$, symbol SNR = 3 dB.

Appendix

Definition of Variables $v_1(k)$, $v_2(k)$, $v_3(k)$, $v_4(k)$, and $v_5(k)$

$$\begin{aligned}
v_1(k) = {} & \Bigg(\left[\Delta_3^2(k) + \Delta_4^2(k) + \frac{\beta[\Delta_3(k) + \Delta_4(k)]}{2R_s}\right] \\
& \times [4 + (\operatorname{erf}[r_1(k)] - \operatorname{erf}[r_2(k)])(\operatorname{erf}[r_1(k+1)] + \operatorname{erf}[r_2(k+1)])]\Bigg) \\
& - 2\Delta_3(k)\Delta_4(k)(\operatorname{erf}[r_1(k)] + \operatorname{erf}[r_2(k)])(\operatorname{erf}[r_1(k+1)] + \operatorname{erf}[r_2(k+1)]) \\
& + (\Delta_3(k) + \Delta_2(k))^2 r_3(k)\Bigg((\operatorname{erf}[r_1(k+1)] + \operatorname{erf}[r_2(k+1)]) \\
& \times \left(-\frac{\Delta_1(k) - \Delta_2(k)}{\Delta_1(k) + \Delta_2(k)} \exp[-r_1^2(k+1)] + \exp[-r_2^2(k+1)]\right)\Bigg) \\
& - (\Delta_4(k) - \Delta_2(k))^2 r_3(k+1)\Bigg((\operatorname{erf}[r_1(k)] - \operatorname{erf}[r_2(k)]) \\
& \times \frac{\Delta_1(k+1) - \Delta_2(k+1)}{\Delta_1(k+1) + \Delta_2(k+1)}(\exp[-r_1^2(k+1)] + \exp[-r_2^2(k+1)])\Bigg) \quad \text{for } \lambda \geq 0
\end{aligned} \tag{A-1}$$

$$\begin{aligned}
v_1(k) = {} & \Bigg(\left[\Delta_3^2(k) + \Delta_4^2(k) + \frac{\beta[\Delta_3(k) + \Delta_4(k)]}{2R_s}\right] \\
& \times [4 + (\operatorname{erf}[r_1(k)] - \operatorname{erf}[r_2(k)])(\operatorname{erf}[r_1(k+1)] + \operatorname{erf}[r_2(k+1)])]\Bigg) \\
& - 2\Delta_3(k)\Delta_4(k)(\operatorname{erf}[r_1(k)] + \operatorname{erf}[r_2(k)])(\operatorname{erf}[r_1(k+1)] + \operatorname{erf}[r_2(k+1)]) \\
& + (\Delta_3(k) - \Delta_2(k))^2 r_3(k)\Bigg((\operatorname{erf}[r_1(k+1)] + \operatorname{erf}[r_2(k+1)]) \\
& \times \left(-\frac{\Delta_1(k) - \Delta_2(k)}{\Delta_1(k) + \Delta_2(k)} \exp[-r_1^2(k+1)] + \exp[-r_2^2(k+1)]\right)\Bigg) \\
& - (\Delta_4(k) + \Delta_2(k))^2 r_3(k+1)\Bigg((\operatorname{erf}[r_1(k)] - \operatorname{erf}[r_2(k)]) \\
& \times \left(\frac{\Delta_1(k+1) - \Delta_2(k+1)}{\Delta_1(k+1) + \Delta_2(k+1)} \exp[-r_1^2(k+1)] + \exp[-r_2^2(k+1)]\right)\Bigg) \quad \text{for } \lambda < 0
\end{aligned} \tag{A-2}$$

$$\begin{aligned}
v_2(k) = {} & 2\Delta_3(k)(r_3(k)[\Delta_3(k) + \Delta_2(k)](\mathrm{erf}\,[r_1(k+1)] + \mathrm{erf}\,[r_2(k+1)]) \\
& \times (\exp\,[-r_1^2(k+1)] - \exp\,[-r_2^2(k+1)]) - r_3(k+1)[\Delta_4(k) - \Delta_2(k)] \\
& \times (\mathrm{erf}\,[r_1(k)] + \mathrm{erf}\,[r_2(k)])(\exp\,[-r_1^2(k+1)] + \exp\,[-r_2^2(k+1)])) \\
& + 2\Delta_4(k)(-r_3(k)[\Delta_3(k) + \Delta_2(k)](\mathrm{erf}\,[r_1(k+1)] + \mathrm{erf}\,[r_2(k+1)]) \\
& \times (\exp\,[-r_1^2(k+1)] + \exp\,[-r_2^2(k+1)]) + r_3(k+1)[\Delta_4(k) - \Delta_2(k)] \\
& \times (\mathrm{erf}\,[r_1(k)] - \mathrm{erf}\,[r_2(k)])(\exp\,[-r_1^2(k+1)] + \exp\,[-r_2^2(k+1)])) \quad \text{for } \lambda \geq 0
\end{aligned} \tag{A-3}$$

$$\begin{aligned}
v_2(k) = {} & 2\Delta_3(k)(r_3(k)[\Delta_3(k) + \Delta_2(k)](\mathrm{erf}\,[r_1(k+1)] - \mathrm{erf}\,[r_2(k+1)]) \\
& \times (\exp\,[-r_1^2(k+1)] + \exp\,[-r_2^2(k+1)]) - r_3(k+1)[\Delta_4(k) - \Delta_2(k)] \\
& \times (\mathrm{erf}\,[r_1(k)] + \mathrm{erf}\,[r_2(k)])(\exp\,[-r_1^2(k+1)] + \exp\,[-r_2^2(k+1)])) \\
& + 2\Delta_4(k)(-r_3(k)[\Delta_3(k) + \Delta_2(k)](\mathrm{erf}\,[r_1(k+1)] + \mathrm{erf}\,[r_2(k+1)]). \\
& \times (\exp\,[-r_1^2(k+1)] + \exp\,[-r_2^2(k+1)]) + r_3(k+1)[\Delta_4(k) - \Delta_2(k)] \\
& \times (\mathrm{erf}\,[r_1(k)] + \mathrm{erf}\,[r_2(k)])(\exp\,[-r_1^2(k+1)] - \exp\,[-r_2^2(k+1)])) \quad \text{for } \lambda < 0
\end{aligned} \tag{A-4}$$

$$\begin{aligned}
v_3(k) = {} & \Delta_3(k)\Delta_3(k+1)[(\mathrm{erf}\,[r_1(k)] + \mathrm{erf}\,[r_2(k)])(\mathrm{erf}\,[r_1(k+1)] + \mathrm{erf}\,[r_2(k+1)])] \\
& - (\Delta_3(k)\Delta_4(k+1)(\mathrm{erf}\,[r_1(k)] + \mathrm{erf}\,[r_2(k)])((\mathrm{erf}\,[r_1(k+1)] - \mathrm{erf}\,[r_2(k+1)]) \\
& + (\mathrm{erf}\,[r_1(k+2)] + \mathrm{erf}\,[r_2(k+2)]))) \\
& - \Delta_3(k+1)\Delta_4(k)(4 + [(\mathrm{erf}\,[r_1(k)] - \mathrm{erf}\,[r_2(k)])(\mathrm{erf}\,[r_1(k+1)] \\
& + \mathrm{erf}\,[r_2(k+1)])] + (\mathrm{erf}\,[r_1(k+1)] - \mathrm{erf}\,[r_2(k+1)]) \\
& \times (\mathrm{erf}\,[r_1(k+2)] + \mathrm{erf}\,[r_2(k+2)])) \\
& + \Delta_4(k)\Delta_4(k+1)((\mathrm{erf}\,[r_1(k)] - \mathrm{erf}\,[r_2(k)])((\mathrm{erf}\,[r_1(k+1)] - \mathrm{erf}\,[r_2(k+1)]) \\
& + (\mathrm{erf}\,[r_1(k+2)] + \mathrm{erf}\,[r_2(k+2)])) + (\mathrm{erf}\,[r_1(k+1)] + \mathrm{erf}\,[r_2(k+1)]) \\
& \times (\mathrm{erf}\,[r_1(k+2)] + \mathrm{erf}\,[r_2(k+2)])) \quad \text{for } \lambda \geq 0
\end{aligned} \tag{A-5}$$

$$
\begin{aligned}
v_3(k) = {} & \Delta_4(k)\Delta_4(k+1)[(\operatorname{erf}[r_1(k+1)] + \operatorname{erf}[r_2(k+1)]) \\
& \times (\operatorname{erf}[r_1(k+2)] + \operatorname{erf}[r_2(k+2)])] \\
& - (\Delta_3(k)\Delta_4(k+1)(\operatorname{erf}[r_1(k+2)] + \operatorname{erf}[r_2(k+2)])((\operatorname{erf}[r_1(k)] + \operatorname{erf}[r_2(k)]) \\
& + (\operatorname{erf}[r_1(k+1)] - \operatorname{erf}[r_2(k+1)]))) \\
& - \Delta_3(k+1)\Delta_4(k)(4 + [(\operatorname{erf}[r_1(k)] + \operatorname{erf}[r_2(k)])(\operatorname{erf}[r_1(k+1)] \\
& - \operatorname{erf}[r_2(k+1)])] + (\operatorname{erf}[r_1(k+2)] - \operatorname{erf}[r_2(k+2)]) \\
& \times (\operatorname{erf}[r_1(k+1)] + \operatorname{erf}[r_2(k+1)])) \\
& + \Delta_3(k)\Delta_3(k+1)((\operatorname{erf}[r_1(k)] + \operatorname{erf}[r_2(k)])((\operatorname{erf}[r_1(k+2)] - \operatorname{erf}[r_2(k+2)]) \\
& + (\operatorname{erf}[r_1(k+1)] + \operatorname{erf}[r_2(k+1)])) + (\operatorname{erf}[r_1(k+1)] - \operatorname{erf}[r_2(k+1)]) \\
& \times (\operatorname{erf}[r_1(k+2)] - \operatorname{erf}[r_2(k+2)])) \quad \text{for } \lambda < 0
\end{aligned}
\tag{A-6}
$$

$$
\begin{aligned}
v_4(k) = {} & (r_3(k)[\Delta_3(k) + \Delta_2(k)]r_3(k+1)[\Delta_3(k+1) + \Delta_2(k+1)](\exp[-r_1^2(k+1)] \\
& + \exp[-r_2^2(k+1)])(\exp[-r_1^2(k+1)] + \exp[-r_2^2(k+1)])) \\
& + (\Delta_3(k)[\Delta_4(k) - \Delta_2(k)]r_3(k+1)[\Delta_4(k+1) - \Delta_2(k+1)] \\
& \times (\exp[-r_1^2(k+1)] + \exp[-r_2^2(k+1)])(\exp[-r_1^2(k+2)] + \exp[-r_2^2(k+2)])) \\
& - (r_3(k)[\Delta_3(k) + \Delta_2(k)]r_3(k+1)[\Delta_4(k+1) - \Delta_2(k+1)](\exp[-r_1^2(k+1)] \\
& + \exp[-r_2^2(k+1)])(\exp[-r_1^2(k+2)] + \exp[-r_2^2(k+2)])) \\
& - (\operatorname{erf}[r_1(k)] - \operatorname{erf}[r_2(k)])\sqrt{\frac{\beta(\Delta_4(k) - \Delta_2(k))^4}{\pi R_s}} \\
& \times \Bigg(\Bigg(\frac{(\Delta_1(k+1) - \Delta_2(k+1))}{(\Delta_4(k) - \Delta_2(k) + \Delta_3(k+1) - \Delta_2(k+1))^{1.5}} \exp\Bigg[-(\Delta_1(k+1) - \Delta_2(k+1))^2\frac{R_s}{\beta} \\
& \times \left|\frac{1}{[\Delta_3(k) + \Delta_2(k)]\left[1 + \dfrac{[\Delta_3(k+1) + \Delta_2(k+1)]}{[\Delta_4(k) - \Delta_2(k)]}\right]} - \frac{1}{[\Delta_4(k) - \Delta_2(k)]}\right|\Bigg]\Bigg) \\
& + \Bigg(\frac{(\Delta_1(k+1) + \Delta_2(k+1))}{(\Delta_4(k) - \Delta_2(k) + \Delta_3(k+1) - \Delta_2(k+1))^{1.5}} \exp\Bigg[-(\Delta_1(k+1) + \Delta_2(k+1))^2\frac{R_s}{\beta}
\end{aligned}
$$

$$\times \left|\frac{1}{[\Delta_3(k)+\Delta_2(k)]\left[1+\frac{[\Delta_3(k+1)+\Delta_2(k+1)]}{[\Delta_4(k)-\Delta_2(k)]}\right]}-\frac{1}{[\Delta_4(k)-\Delta_2(k)]}\right\|\Bigg]\Bigg)\Bigg)$$

$$+ (\operatorname{erf}\ [r_1(k+2)] + \operatorname{erf}\ [r_2(k+2)])\sqrt{\frac{\beta(\Delta_4(k)-\Delta_2(k))^4}{\pi R_s}}$$

$$\times \Bigg(-\Bigg(\frac{(\Delta_1(k+1)-\Delta_2(k+1))}{(\Delta_4(k)-\Delta_2(k)+\Delta_3(k+1)-\Delta_2(k+1))^{1.5}}\exp\ \Bigg[-(\Delta_1(k+1)-\Delta_2(k+1))^2\frac{R_s}{\beta}$$

$$\times \left|\frac{1}{[\Delta_3(k)+\Delta_2(k)]\left[1+\frac{[\Delta_3(k+1)+\Delta_2(k+1)]}{[\Delta_4(k)-\Delta_2(k)]}\right]}-\frac{1}{[\Delta_4(k)-\Delta_2(k)]}\right\|\Bigg]\Bigg)$$

$$+ \Bigg(\frac{(\Delta_1(k+1)+\Delta_2(k+1))}{(\Delta_4(k)-\Delta_2(k)+\Delta_3(k+1)-\Delta_2(k+1))^{1.5}}\exp\ \Bigg[-(\Delta_1(k+1)+\Delta_2(k+1))^2\frac{R_s}{\beta}$$

$$\times \left|\frac{1}{[\Delta_3(k)+\Delta_2(k)]\left[1+\frac{[\Delta_3(k+1)+\Delta_2(k+1)]}{[\Delta_4(k)-\Delta_2(k)]}\right]}-\frac{1}{[\Delta_4(k)-\Delta_2(k)]}\right\|\Bigg]\Bigg)\Bigg) \tag{A-7}$$

$$v_5(k) = r_3(k)\ [\Delta_3(k)+\Delta_2(k)](\exp\ [-r_1^2(k+1)] + \exp\ [-r_2^2(k+1)])(\Delta_3(k+1)(\operatorname{erf}\ [r_1(k+1)] + \operatorname{erf}\ [r_2(k+1)])$$

$$- \Delta_4(k+1)[(\operatorname{erf}\ [r_1(k+1)] - \operatorname{erf}\ [r_2(k+1)]) + (\operatorname{erf}\ [r_1(k+2)] + \operatorname{erf}\ [r_2(k+2)])]) + \Delta_3(k+1)$$

$$\times [\Delta_3(k+1)+\Delta_2(k+1)](\Delta_3(k)(\operatorname{erf}\ [r_1(k)] + \operatorname{erf}\ [r_2(k)])(\exp\ [-r_1^2(k+1)] + \exp\ [-r_2^2(k+1)])$$

$$- \Delta_4(k)[(\operatorname{erf}\ [r_1(k+2)] + \operatorname{erf}\ [r_2(k+2)])(\exp\ [-r_1^2(k+1)] - \exp\ [-r_2^2(k+1)])$$

$$+ (\operatorname{erf}\ [r_1(k)] - \operatorname{erf}\ [r_2(k)])(\exp\ [-r_1^2(k+1)] + \exp\ [-r_2^2(k+1)])])$$

$$+ r_3(k)[\Delta_4(k)-\Delta_2(k)](\Delta_4(k+1)[(\operatorname{erf}\ [r_1(k)] - \operatorname{erf}\ [r_2(k)])$$

$$\times (\exp\ [-r_1^2(k+1)] - \exp\ [-r_2^2(k+1)]) + (\operatorname{erf}\ [r_1(k+2)] + \operatorname{erf}\ [r_2(k+2)])$$

$$\times (\exp\ [-r_1^2(k+1)] + \exp\ [-r_2^2(k+1)])] - \Delta_3(k+1)[(\operatorname{erf}\ [r_1(k+2)] + \operatorname{erf}\ [r_2(k+2)])$$

$$\times (\exp\ [-r_1^2(k+1)] - \exp\ [-r_2^2(k+1)]) + (\operatorname{erf}\ [r_1(k)] - \operatorname{erf}\ [r_2(k)])$$

$$\times (\exp\ [-r_1^2(k+1)] + \exp\ [-r_2^2(k+1)])])$$

$$+ r_3(k+1)[\Delta_4(k+1)-\Delta_2(k+1)](\exp\ [-r_1^2(k+2)] + \exp\ [-r_2^2(k+2)])$$

$$\times (\Delta_4(k)[(\operatorname{erf}\ [r_1(k)] - \operatorname{erf}\ [r_2(k)]) + (\operatorname{erf}\ [r_1(k+1)] + \operatorname{erf}\ [r_2(k+1)])]$$

$$- \Delta_3(k)(\operatorname{erf}\ [r_1(k)] + \operatorname{erf}\ [r_2(k)])) \tag{A-8}$$

N94- 29670

An Improved Conscan Algorithm Based on a Kalman Filter

D. B. Eldred
Guidance and Control Section

Conscan is commonly used by DSN antennas to allow adaptive tracking of a target whose position is not precisely known. This article describes an algorithm that is based on a Kalman filter and is proposed to replace the existing fast Fourier transform-based (FFT-based) algorithm for conscan. Advantages of this algorithm include better pointing accuracy, continuous update information, and accommodation of missing data. Additionally, a strategy for adaptive selection of the conscan radius is proposed. The performance of the algorithm is illustrated through computer simulations and compared to the FFT algorithm. The results show that the Kalman filter algorithm is consistently superior.

I. Introduction

The objective of conscan is to improve the estimate of the target location; the target location is defined as the direction of maximum carrier power as received on the ground. During conscan, the antenna is rotated in a circle about a point we call the conscan center at a constant rate ω. Figure 1 shows the variables used in the analysis.

Without loss of generality the origin is placed at the conscan center. We define $\mathbf{x} \equiv \mathbf{x}(t)$ as the 2-vector which specifies what we seek to estimate: the unknown actual target at time t, and we define $\hat{\mathbf{x}} \equiv \hat{\mathbf{x}}(t)$ as the estimate of the target's location. We assume that discrete measurements are taken at times $t = t_i$. Let the subscript "i" denote a quantity taken at time t_i; for example, $\mathbf{x}_i \equiv \mathbf{x}(t_i)$. Lack of the "$i$" subscript implies that the affected quantity is constant over a conscan period. We refer to $\mathbf{x}_i$ as the state of the system, and thus $\hat{\mathbf{x}}_i$ is the state estimate. The known instantaneous location of the antenna boresight is defined by $\mathbf{x}_{ai}$, which during conscan is given by

$$\mathbf{x}_{ai} = \begin{bmatrix} R\cos(\omega t_i) \\ R\sin(\omega t_i) \end{bmatrix} \tag{1}$$

Here, R is referred to as the conscan radius, and ω is the conscan frequency.

The output of the antenna receiver is the carrier power P_{0i}. Assuming a circularly symmetric antenna gain function, the carrier power can be approximated as a quadratic function of the offset angle:[1]

$$P_{ci} = P_{0i}\left(1 - \mu\frac{\beta_i^2}{h^2}\right) + \eta_i \quad (2)$$

where P_{0i} is the maximum carrier power which occurs when the antenna is pointed directly at the target, h is the antenna half-power beamwidth, $\mu = 4\ln(2)$, β_i is the offset angle between the antenna boresight and the target, and η_i is the signal noise, or error. We assume that the signal noise is random with zero mean and is Gaussian distributed with a standard deviation of σ_η. From Fig. 1, we have

$$\beta_i = \sqrt{(\mathbf{x}_i - \mathbf{x}_{ai})^\mathsf{T}(\mathbf{x}_i - \mathbf{x}_{ai})} \quad (3)$$

and thus

$$P_{ci}(\mathbf{x}_i) = P_{0i}\left(1 - \frac{\mu}{h^2}(\mathbf{x}_i - \mathbf{x}_{ai})^\mathsf{T}(\mathbf{x}_i - \mathbf{x}_{ai})\right) + \eta_i \quad (4)$$

If we assume that $P_{0i} = P_0$ and $\mathbf{x}_i = \mathbf{x}$ are constant throughout a conscan period, then from Eq. (1) it is easily shown that the ensemble average of the carrier power over the conscan period is approximately

$$\langle P_{ci}\rangle \approx P_0\left(1 - \frac{\mu}{h^2}(\mathbf{x}^\mathsf{T}\mathbf{x} + R^2)\right) \quad (5)$$

Subtracting Eq. (5) from Eq. (4) yields

$$P_{ci}(\mathbf{x}_i) - \langle P_{ci}\rangle \approx \frac{2P_0\mu}{h^2}\mathbf{x}_{ai}^\mathsf{T}\mathbf{x}_i + \eta_i \quad (6)$$

Equation (6) constitutes the measurement equation for the purposes of the estimators. It is important to note that the measurement equation is linear with respect to the unknown state $\mathbf{x}_i$, as this makes it possible to apply linear estimation theory to estimate $\mathbf{x}_i$.

We define $\mathbf{z}_i$ as

$$\mathbf{z}_i \equiv P_{ci}(\mathbf{x}_i) - \langle P_{ci}\rangle \quad (7)$$

and thus

$$\mathbf{z}_i = \frac{2P_0\mu}{h^2}\mathbf{x}_{ai}^\mathsf{T}\mathbf{x}_i + \eta_i \quad (8)$$

In the subsequent analysis, we refer to $\mathbf{z}_i$ as our *measurement.*

II. FFT Estimator

A brief discussion of the existing fast Fourier transform (FFT) estimator is given below so that it can be compared to the Kalman filter estimator. We assume that $P_{0i} = P_0$ and $\mathbf{x}_i = \mathbf{x}$ are constant over a conscan period. Multiplying Eq. (8) by $\mathbf{x}_{ai}$ and averaging both sides over a conscan period yields, after some algebra,

$$\langle \mathbf{z}_i\mathbf{x}_{ai}\rangle = \frac{P_0\mu R^2}{h^2}\mathbf{x} + \langle \eta_i\mathbf{x}_{ai}\rangle \quad (9)$$

Utilizing the fact that η_i is assumed to be zero mean, we obtain an estimate for the state:

$$\hat{\mathbf{x}} = \frac{h^2\langle \mathbf{z}_i\mathbf{x}_{ai}\rangle}{P_0\mu R^2} \quad (10)$$

We define $\mathbf{M}$ to be the covariance of the state estimate:

$$\mathbf{M} \equiv E\left((\hat{\mathbf{x}}_i - \mathbf{x})(\hat{\mathbf{x}}_i - \mathbf{x})^\mathsf{T}\right) \quad (11)$$

where E denotes expectation, or ensemble average. After further manipulation it can be shown that

$$\mathbf{M} = \frac{h^4\sigma_\eta^2}{2P_0^2\mu^2R^2n}\mathbf{I} \quad (12)$$

where $\mathbf{I}$ is the 2 × 2 identity matrix and n is the number of samples taken over a single conscan period. This result is consistent with results described elsewhere.[2]

In practice, an FFT is used to estimate $\mathbf{x}$ [1]; this yields the same result as Eq. (10) but also yields harmonics above the fundamental frequency. Hence, we call this the FFT algorithm. Use of an FFT imposes several constraints on the algorithm: n must be an integer power of 2; there must be no missing measurements; and the measurements must be evenly spaced in time. Theoretically, failure in

---

[1] L. Alvarez, "Open Loop Conscan Pointing Error Estimation Accuracy at Ka-band," JPL Interoffice Memorandum 3328-93-044 (internal document), Jet Propulsion Laboratory, Pasadena, California, July 8, 1993.

[2] Ibid.

the estimator can be detected by the presence of significant amplitudes in the harmonics above the fundamental frequency, but in practice, detection of the harmonics above the fundamental frequency has been only partially implemented, partly because it is readily apparent when conscan has failed.

III. Kalman Filter Estimator

A detailed general description of a Kalman filter is given in [2]. However, square root algorithms in which the Cholesky factors of the covariance matrix are propagated are widely recognized to have superior numerical properties, and hence we implement the square root covariance filter described in [3]. We assume that between time intervals t_i and t_{i+1}, $\mathbf{x}_i$ drifts according to

$$\mathbf{x}_{i+1} = \mathbf{x}_i + \mathbf{n}_i \tag{13}$$

where $\mathbf{n}_i$ is a random 2-vector with covariance $\mathbf{Q} \equiv E(\mathbf{n}_i\mathbf{n}_i^{\mathsf{T}})$. We assume that at time t_i the state estimate is known with covariance $\mathbf{M}_i \equiv E\left((\hat{\mathbf{x}}_i - \mathbf{x}_i)(\hat{\mathbf{x}}_i - \mathbf{x}_i)^{\mathsf{T}}\right)$. Our measurements take the form

$$\mathbf{z}_i = \mathbf{H}_i\mathbf{x}_i + \mathbf{v}_i \tag{14}$$

where $\mathbf{v}_i$ is a random vector with zero mean and whose covariance is given by $\mathbf{R} \equiv E\left(\mathbf{v}_i\mathbf{v}_i^{\mathsf{T}}\right)$. From Eq. (8), we can make the identifications

$$\left.\begin{aligned}
\mathbf{H}_i &= \frac{2P_0\mu}{h^2}\mathbf{x}_{ai}^{\mathsf{T}} \\
\mathbf{v}_i &= \eta_i \\
\mathbf{R} &= \sigma_\eta^2
\end{aligned}\right. \tag{15}$$

With these preliminaries completed, we are ready to construct the Kalman filter estimator, which requires execution of the following updates at each time interval t_i:

$$\left.\begin{aligned}
\left\langle \hat{P}_c \right\rangle_i &= \frac{1}{n}\sum_{k=i-n+1}^{i} P_{ck} \\
\hat{P}_{0i} &= \frac{\left\langle \hat{P}_c \right\rangle_i}{1 - \frac{\mu}{h^2}(R^2 + \hat{\mathbf{x}}_i^{\mathsf{T}}\hat{\mathbf{x}}_i)} \\
\mathbf{z}_i &= P_{ci} - \left\langle \hat{P}_c \right\rangle_i \\
\mathbf{x}_{ai} &= \begin{bmatrix} R\cos(\omega t_i) \\ R\sin(\omega t_i) \end{bmatrix} \\
\mathbf{H}_i &= \frac{2\hat{P}_{0i}\mu}{h^2}\mathbf{x}_{ai}^{\mathsf{T}} \\
\mathbf{T} &= \begin{bmatrix} \mathbf{R}^{1/2} & \mathbf{H}_i\mathbf{S}_i & 0 \\ 0 & \mathbf{S}_i & \mathbf{Q}^{1/2} \end{bmatrix} \\
\mathbf{T} \times \mathbf{U}_i &= \begin{bmatrix} \mathbf{V}_i^{1/2} & 0 & 0 \\ \mathbf{G}_i & \mathbf{S}_{i+1} & 0 \end{bmatrix} \\
\mathbf{K}_i &= \mathbf{G}_i\mathbf{V}_i^{-1/2} \\
\mathbf{M}_i &= \mathbf{S}_i\mathbf{S}_i^{\mathsf{T}} \\
\hat{\mathbf{z}}_i &= \mathbf{H}_i\hat{\mathbf{x}}_i \\
\hat{\mathbf{x}}_{i+1} &= \hat{\mathbf{x}}_i + \mathbf{K}_i(\mathbf{z}_i - \hat{\mathbf{z}}_i)
\end{aligned}\right\} \tag{16}$$

Here, n is the number of samples in a complete conscan period. $\mathbf{U}_i$ is an orthogonal transformation that triangularizes $\mathbf{T}$ and may be obtained, for example, using Householder transformations. Quantities such as $\mathbf{R}^{1/2}$ are "matrix square roots" or Cholesky factors. The Kalman filter algorithm is straightforward except for the estimation of the average carrier power, $\left\langle \hat{P}_c \right\rangle_i$, which is computed as a running average of the n most recent outputs from the antenna receiver, and estimation of the maximum carrier power, $\hat{P}_{0i}$, which is computed using Eq. (5). Thus, the Kalman filter requires that at least n measurements have been accumulated before the filter can be started. This results in a delay of a single conscan period before the Kalman filter begins producing estimates. A similar delay also occurs in the FFT algorithm.

IV. Selection of the Conscan Radius

An algorithm for selecting the conscan radius was developed as part of this study. We again assume a constant target offset $\mathbf{x}_i = \mathbf{x}$. Recall from Eq. (5) that the average carrier power over a conscan period is given by

$$\langle P_c \rangle = P_0 \left(1 - \frac{\mu}{h^2}(\mathbf{x}^T\mathbf{x} + R^2)\right) \tag{17}$$

Obviously, the average carrier power is maximized for $\mathbf{x} = 0$, which can be attained by repointing the antenna until the conscan center coincides with the target location. However, the best that can be done in practice is to repoint the antenna to place the conscan center at the *estimated* target location $\hat{\mathbf{x}}$. In the newly pointed antenna, the average carrier power becomes

$$\langle P_c \rangle = P_0 \left(1 - \frac{\mu}{h^2}\left((\mathbf{x} - \hat{\mathbf{x}})^T(\mathbf{x} - \hat{\mathbf{x}}) + R^2\right)\right) \tag{18}$$

and the average-carrier-power expectation, using the definition of $\mathbf{M}$ given in Eq. (11), becomes

$$E\left(\langle P_c \rangle\right) = P_0 \left(1 - \frac{\mu}{h^2}(\mathrm{trace}(\mathbf{M}) + R^2)\right) \tag{19}$$

A necessary condition for the average power to be maximized is for the expectation of the carrier power given by Eq. (19) to be stationary with respect to R; taking a differential and setting it to zero requires

$$\frac{\partial}{\partial R}\mathrm{trace}(\mathbf{M}) = -2R \tag{20}$$

An analytic expression for $\mathbf{M}(R)$ for the Kalman filter would be difficult if not impossible to obtain. In principle it would be possible to propagate $\partial\mathbf{M}/\partial R$ along with the Kalman filter equations, but this more than doubles the number of computations performed at each iteration and excessively complicates the algorithm. Instead we use Eq. (12), developed from FFT principles, as an approximation for $\mathbf{M}$, with the reasoning that this result is an upper bound on $\mathbf{M}$ because it is based on data from only a single conscan period. In this case, solving Eq. (20) yields the optimal conscan radius:

$$R_{opt} = \sqrt[4]{\frac{h^4\sigma_\eta^2}{P_0^2\mu^2 n}} \tag{21}$$

Typically the conscan radius is set to result in 0.1 dB gain loss in the carrier power. The set of parameters summarized in Table 1 yields an optimal conscan radius of $R_{opt} = 1.86$ mdeg for a 34-m antenna. The conscan radius for 0.1-dB gain loss is 5.9 mdeg. This suggests that the conscan radius is currently larger than it needs to be, at least for this set of parameters.

V. Implementation Details

The behavior of the Kalman filter depends heavily on the selection of the process noise and measurement noise covariances and also on the covariance of the state estimate used to initiate the algorithm. The following criteria are used to select these values.

The measurement noise variance $\mathbf{R}$ is assumed to be provided by the RF receiver. (See [4,5] and other material[3,4] for information.) For the simulations, a model developed elsewhere[5] is used. Though $\mathbf{R}$ is not independent of offset angle, it can be considered to be constant for the small offset angles used during conscan.

The process noise covariance $\mathbf{Q}$ can be established by considering the maximum anticipated drift in the offsets within one sample period. We select

$$\mathbf{Q} = (\text{drift rate} \times \text{sample time})^2\mathbf{I} \tag{22}$$

where $\mathbf{I}$ is the 2×2 identity matrix. The drift rate used in the simulations is

$$\text{drift rate} = \frac{1}{5} \times \frac{R}{\text{conscan period}} \tag{23}$$

An alternative, which we suggest for implementation, would be to use the reciprocal of the antenna gimbal servo bandwidth.

The initial covariance $\mathbf{M}_0$ of the state estimate is given by the expected uncertainty of the initial target location. This should be based on the known open loop (blind)

---

[3] M. Aung and S. Stephens, "Statistics of the P_c/N_0 Estimator in the Block V Receiver," JPL Interoffice Memorandum 3338-92-089 (internal document), Jet Propulsion Laboratory, Pasadena, California, April 29, 1992.

[4] R. E. Scheid, "Statistical Analysis of the Antenna Carrier Power," JPL Interoffice Memorandum 343-92-1291 (internal document), Jet Propulsion Laboratory, Pasadena, California, October 9, 1992.

[5] Ibid.

pointing performance of the antenna. For the simulations, we assume that the target can be located anywhere within the conscan circle; thus we choose

$$\mathbf{M}_0 = R^2\mathbf{I} \tag{24}$$

VI. Computer Simulations

The parameters used in the computer simulations are typical for a 34-m DSN antenna operating at Ka-band (32 GHz) and are summarized in Table 1. A random-number generator was used to simulate noise in the carrier power. Each simulation used a different seed to start the random-number generator, which ensures that a reasonable cross section of cases is represented. The Kalman filter estimator was then propagated through the data, starting with a zero initial estimate. For comparison to the existing algorithm, the FFT estimator was also propagated. The FFT estimator is easily distinguished from the Kalman filter because updates are produced only once per conscan period. The simulations were written in Matlab, which allows symbolic manipulation of matrices and vectors within an interpretive programming environment.

The first simulation is shown in Figs. 2-4 and illustrates the convergence of both Kalman filter and FFT estimators to a constant target offset. The simulated carrier power is shown in Fig. 2. The sinusoidal modulation of the carrier power resulting from the nonzero offset is readily apparent. Figure 3 shows the output of the Kalman filter and the FFT estimator. The dashed line on the plot indicates the true target location. The Kalman filter estimator begins by collecting carrier power over a single conscan period so that an estimate of the average carrier power $\langle P_{ci} \rangle$ can be obtained. Propagation of the Kalman filter begins immediately thereafter. Convergence of the estimate is virtually complete within a fraction of a conscan period. The Kalman filter estimates are consistently better than the FFT estimates. In fact, in steady state the standard deviation of the Kalman filter estimates is about one-third that of the FFT estimates.

A measure of the convergence of the Kalman filter is given by the norm of the estimate covariance $\mathbf{M}_i$. Figure 4 shows the time history of $|\mathbf{M}_i|$ and demonstrates that the Kalman filter converges very rapidly at first and then reaches steady state after about 100 sec, or about 3 conscan periods. This is an important observation because it assures us that running the simulations longer will not reveal any different behavior of the algorithm.

In the simulation shown in Fig. 5, the measurement noise has been doubled to investigate the relative sensitivities of the two algorithms to measurement noise. Convergence of the Kalman filter algorithm is changed very little, though close examination reveals a larger amplitude in the high-frequency component of the Kalman filter estimates. Errors in the FFT estimates are pronounced, being roughly doubled when the measurement noise is doubled. As before, the Kalman filter estimates are about three times more accurate than the FFT estimates, as measured by the standard deviations in steady state.

The simulation shown in Fig. 6 shows the ability of both algorithms to successfully estimate a relatively large initial offset. Despite the fact that the initial offset was set at more than three times the conscan radius, both algorithms quickly converge to the correct value. In general, convergence is improved in both algorithms as R grows larger.

In Fig. 7, a data dropout between 100 and 150 sec was simulated. The measurement covariance update and state update steps in the Kalman filter algorithm are not applied for each missing measurement. The most recent estimate is used throughout the dropout period, and then when data become available again, the Kalman filter gracefully continues. Recall that this FFT algorithm is incapable of accommodating missing data, so there is no corresponding plot showing FFT estimates.

The ability of the algorithms to accommodate a drifting parameter is illustrated in Fig. 8. For this simulation, the offset is taken to be a constant drift at a rate of 2 mdeg per 100 sec. Both algorithms successfully track the offset, though they consistently underestimate the offset slightly.

The performance of the algorithms in the presence of a gradually changing maximum carrier power P_0 is shown in Fig. 9. In this simulation, the nominal carrier power is increased by 2 percent over each conscan period. The Kalman filter algorithm behaves roughly as before, though some oscillation is apparent in the estimates. Numerical experiments have shown that the amplitude of these oscillations increases with the drift rate $\dot{P}_0$, but degradation of the Kalman filter estimates is gradual and, in this case, is comparable to the FFT algorithm estimates.

VII. Summary, Conclusions, and Future Work

A sequential estimator for executing conscan on the DSN antennas has been described. The algorithm, based on a Kalman filter, has important advantages over the existing FFT algorithm, including better accuracy of the estimates, nearly continuous updates, and the ability to accommodate missing data. It also has many of the desirable properties of the FFT algorithm, particularly robustness and the ability to track large initial offsets. In addition, an algorithm that is used for selecting the optimal con-scan radius and is based on maximizing carrier power is proposed. The performance and behavior of the Kalman filter algorithm as compared to the FFT algorithm have been analyzed extensively through computer simulations, which have shown that the Kalman filter algorithm is consistently superior.

Future work on the Kalman filter algorithm should concentrate on a field implementation to demonstrate that it can work as well with real data as it works in an idealized computer simulation.

References

[1] J. E. Ohlson and M. S. Reid, *Conical-Scan Tracking with the 64-m Diameter Antenna at Goldstone*, Technical Report 32-1605, Jet Propulsion Laboratory, Pasadena, California, October 1, 1976.

[2] A. E. Bryson and Y. Ho, *Applied Optimal Control*, New York: Hemisphere Publishing Corporation, 1975.

[3] M. Verhaegen and P. Van Dooren, "Numerical Aspects of Different Kalman Filter Implementations," *IEEE Transactions on Automation and Control*, vol. AC-31, no. 10, pp. 907–917, October 1986.

[4] T. J. Brunzie, "The Parkes Front-End Controller and Noise-Adding Radiometer," *The Telecommunications and Data Acquisition Progress Report 42-102, vol. April–June 1990*, Jet Propulsion Laboratory, Pasadena, California, pp. 119–137, August 15, 1990.

[5] A. M. Monk, "Carrier-to-Noise Power Estimation for the Block V Receiver," *The Telecommunications and Data Acquisition Progress Report 42-106, vol. April–June 1991*, Jet Propulsion Laboratory, Pasadena, California, pp. 353–363, August 15, 1991.

Table 1. Selected parameters used in the simulations.

Quantity	Value	Description
n	32	Number of samples in a conscan period
t	1 sec	Sample period
σ_η	5.3×10^{-15} W	Standard deviation of P_0
$\mathbf{R}$	σ_η^2	Measurement covariance
R	5.9 mdeg	Conscan radius for 0.1-dB gain loss
$\mathbf{M}_0$	$R^2\mathbf{I}$	Starting state covariance
$\mathbf{Q}$	$\left(\frac{R}{5n}\right)^2$	Process noise covariance
$\hat{\mathbf{x}}_0$	$\begin{bmatrix} 0 \\ 0 \end{bmatrix}$	Starting estimate
h	65 mdeg	Half-power beamwidth
P_0	4.14×10^{-13} W	Maximum carrier power

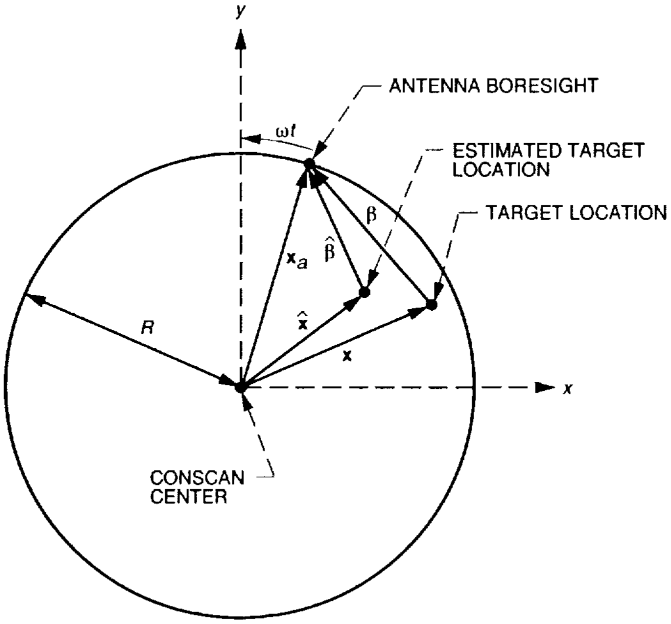

Fig. 1. Definition of variables.

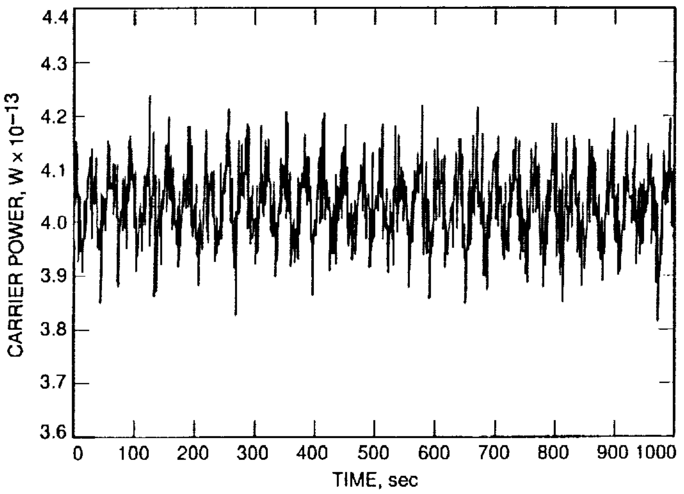

Fig. 2. Simulated carrier power used for testing conscan algorithms.

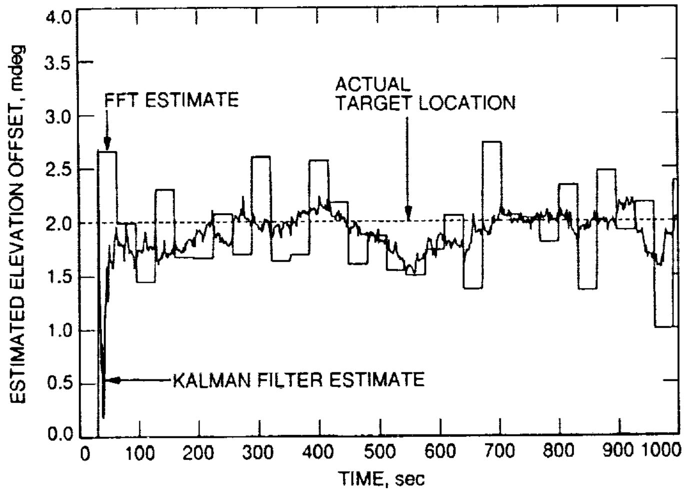

Fig. 3. Convergence of Kalman filter and FFT estimates to a constant offset.

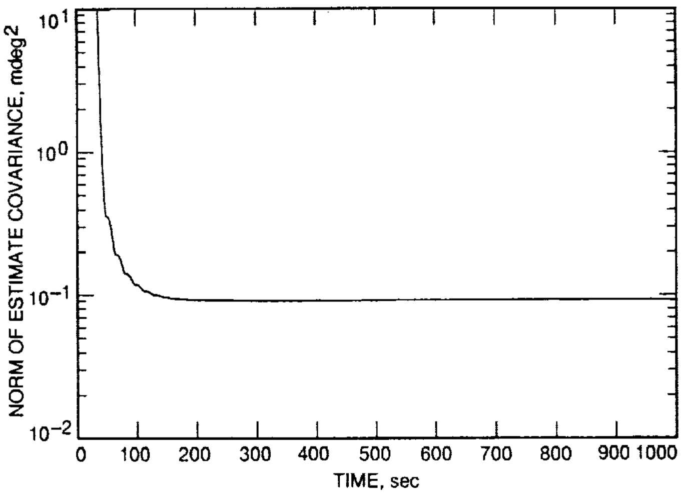

Fig. 4. Convergence of the estimate covariance for a constant offset.

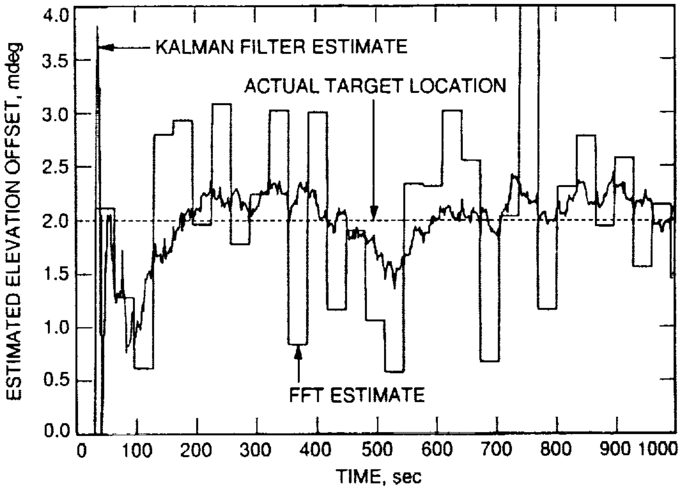

Fig. 5. Performance of the estimators for doubled measurement noise.

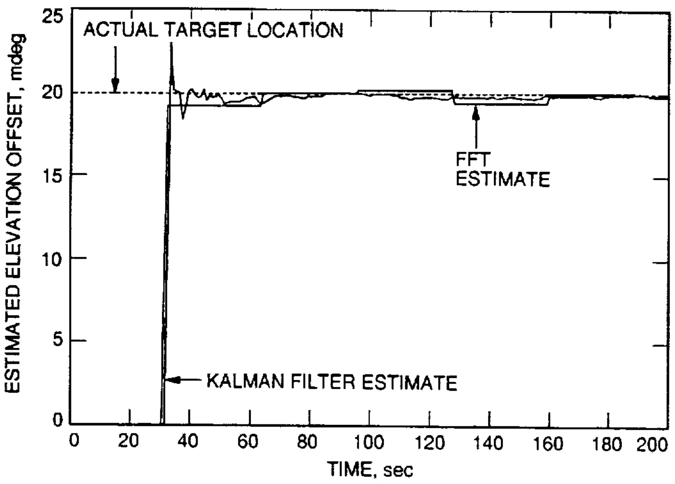

Fig. 6. Tracking of a large offset.

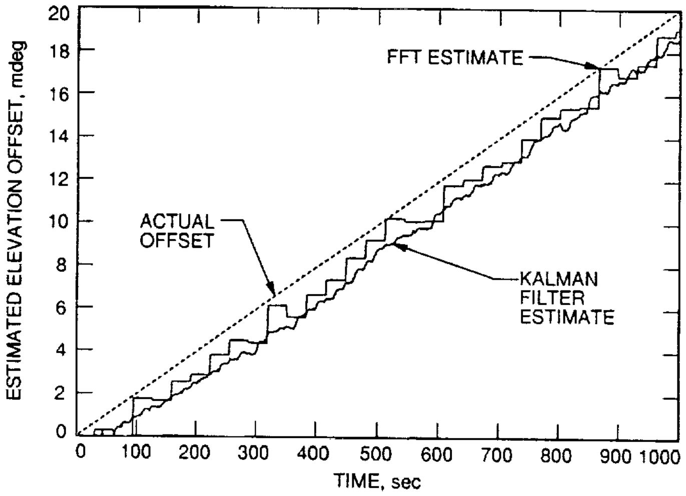

Fig. 8. Tracking a constant rate drift in the offset.

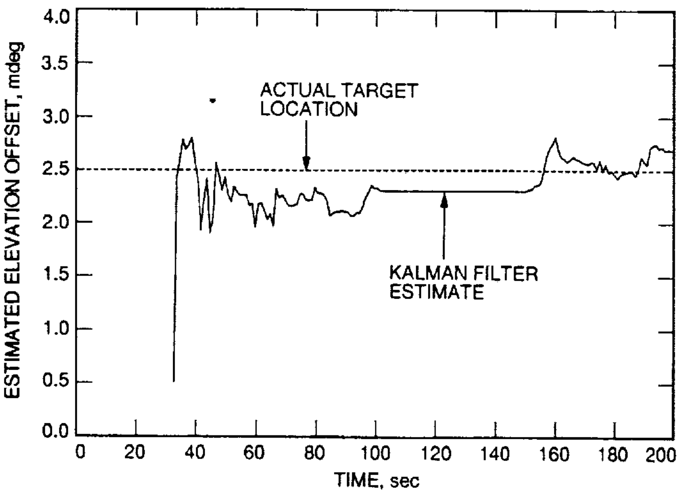

Fig. 7. Demonstration of the Kalman filter algorithm with a data dropout.

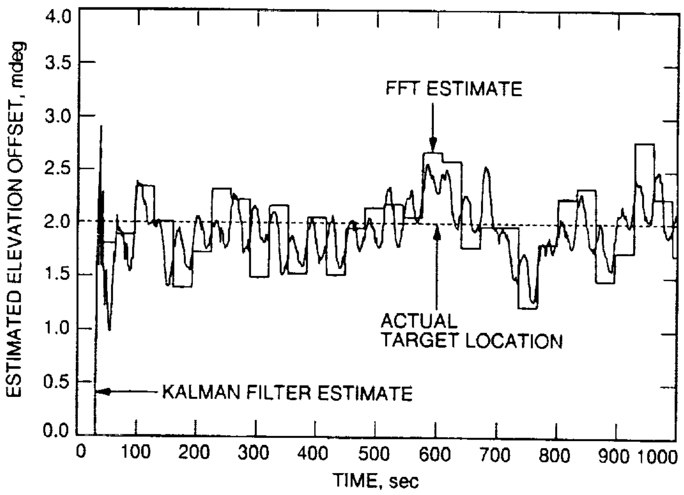

Fig. 9. Effect of maximum carrier power drift on estimator performance.

N94- 29671

TDA Progress Report 42-116

February 15, 1994

A Complex Symbol Signal-to-Noise Ratio Estimator and Its Performance

Y. Feria
Communications Systems Research Section

This article presents an algorithm for estimating the signal-to-noise ratio (SNR) of signals that contain data on a downconverted suppressed carrier or the first harmonic of a square-wave subcarrier. This algorithm can be used to determine the performance of the full-spectrum combiner for the Galileo S-band (2.2- to 2.3-GHz) mission by measuring the input and output symbol SNR. A performance analysis of the algorithm shows that the estimator can estimate the complex symbol SNR using 10,000 symbols at a true symbol SNR of -5 dB with a mean of -4.9985 dB and a standard deviation of 0.2454 dB, and these analytical results are checked by simulations of 100 runs with a mean of -5.06 dB and a standard deviation of 0.2506 dB.

I. Introduction

Current plans are for the performance of the full-spectrum recorder (FSR) and full-spectrum combiner (FSC) for the Galileo S-band (2.2- to 2.3-GHz) mission to be measured by running symbol-error-rate (SER) curves on the demodulated data. To do so, one needs to generate test signals at various points of the system, and the test signals must be consistent from one point to the other, which may be difficult. The measurement can only be done at the output of the demodulator, which means that if the demodulator is malfunctioning, other modules (e.g., the FSR or FSC) cannot be tested. Also, since test signals are needed, online testing is impossible.

To overcome the disadvantages of measuring the performance from the SER curves, one would like to directly measure the symbol signal-to-noise ratio (SNR) at various points of the system. This means that the symbol SNR has to be estimated through complex symbols. By complex symbols, we mean the real symbols at an offset frequency with in-phase (I) and quadrature (Q) components. This article presents a complex symbol SNR estimator that estimates the symbol SNR of data with I and Q components of a carrier and/or the first harmonic of a square-wave subcarrier. This SNR estimator can be used to measure the performance of the FSC as well as that of the complex symbol combiner for the Galileo S-band mission.

The technique of the complex symbol SNR estimator is similar to that of the split-symbol moments estimator [1,2], except with complex symbols rather than real ones. The idea behind splitting a real symbol into two halves and correlating them (originally suggested by Larry Howard [2]), is to get the signal power by correlating two halves of a symbol, where the signal parts of the two halves of the same symbol are correlated but the noises on the two halves of the symbol are uncorrelated.

The same idea is applied here to the complex symbols, with the assumption that the offset frequency is known. The idea is to correlate the first half of a symbol with the complex conjugate of the second half of the same symbol, and then to take the real part to get the signal power multiplied by a factor that is a function of the offset frequency. This factor can be divided out if the offset frequency is known. The same step is repeated for N symbols, and the results are averaged to get a better estimate of the signal power.

The signal power plus the noise power can be obtained by averaging the magnitudes squared of the sums of the samples in a complex symbol over N symbols. The estimate of the SNR ratio is then readily obtained. In the next section, a brief description of the complex symbol SNR estimator is given.

Some practical problems are not considered here. For instance, the frequency offset may not be known and may not be a constant. Also, if the symbol synchronization is off, say by a sample, the performance of the estimator will be affected, and in the future, the effect needs to be quantified.

II. Brief Description of the Estimator

For given samples of I and Q components of baseband data with an offset frequency ω_o, we wish to estimate the symbol SNR. The I and Q components of the lth sample in the kth symbol are expressed as follows:

$$y_{I_{lk}} = \frac{m}{N_s} d_k \cos\ (\omega_o l T_s + \phi_o) + n_{I_{lk}} \tag{1}$$

$$y_{Q_{lk}} = \frac{m}{N_s} d_k \sin\ (\omega_o l T_s + \phi_o) + n_{Q_{lk}} \tag{2}$$

where

$$\begin{aligned} l &= 0, \ldots, N_s - 1 \\ k &= 1, \ldots, N \end{aligned}$$

Here N_s is the number of samples per symbol and is assumed to be an even integer, T_s is the sample period, and $d_k = \pm 1$ is the kth symbol. The noise samples in the I and Q channels are assumed to be independent with zero mean and equal variance σ_n^2/N_s. The true symbol SNR is

$$\text{SNR} = \frac{m^2}{2\sigma_n^2} \tag{3}$$

Presented here is an algorithm to estimate this symbol SNR. First, add all samples in the first half of a symbol for I and Q separately,

$$Y_{\alpha I_k} = \sum_{l=0}^{N_s/2-1} y_{I_{lk}} \tag{4}$$

$$Y_{\alpha Q_k} = \sum_{l=0}^{N_s/2-1} y_{Q_{lk}} \tag{5}$$

Repeat the first step for the second half of the symbol

$$Y_{\beta I_k} = \sum_{l=N_s/2}^{N_s-1} y_{I_{lk}} \tag{6}$$

$$Y_{\beta Q_k} = \sum_{l=N_s/2}^{N_s-1} y_{Q_{lk}} \tag{7}$$

Multiply the I component of the first half of a symbol by that of the second half; do the same for the Q components; and add the results. This is equivalent to taking the real part of the product of the first half and the complex conjugate of the second half of a symbol. Repeat the same procedure for N symbols, and average the results to obtain the parameter m_p

$$\begin{aligned} m_p &= \frac{1}{N} \sum_{k=1}^{N} (Y_{\alpha I_k} Y_{\beta I_k} + Y_{\alpha Q_k} Y_{\beta Q_k}) \\ &= \frac{1}{N} \sum_{k=1}^{N} \Re \left\{ Y_{\alpha_k} Y_{\beta_k}^* \right\} \end{aligned} \tag{8}$$

where

$$Y_{\alpha_k} = Y_{\alpha I_k} + j Y_{\alpha Q_k} \tag{9}$$

$$Y_{\beta_k} = Y_{\beta I_k} + j Y_{\beta Q_k} \tag{10}$$

Take the magnitude squared of the complex sum of the two symbol halves, repeat for N symbols, and average the results to obtain m_{ss}

$$m_{ss} = \frac{1}{N} \sum_{k=1}^{N} |Y_{\alpha_k} + Y_{\beta_k}|^2 \qquad (11)$$

Mathematical expressions for the complex symbol halves Y_{α_k} and Y_{β_k} and the parameters m_p and m_{ss} are given in Appendix A in terms of the underlying model parameters of Eqs. (1) and (2). Finally, use m_p and m_{ss} to obtain the estimated symbol SNR

$$\text{SNR}^* = \frac{4m_p \,\text{sinc}^2\,(\omega_o T_s/2) \,/\, \left[\text{sinc}^2\,(\omega_o T_{sy}/4)\cos\,(\omega_o T_{sy}/2)\right]}{m_{ss} - m_p\,(2 + 2/\cos\,(\omega_o T_{sy}/2))} \qquad (12)$$

where ω_o is the offset angular frequency, and T_{sy} is the symbol duration,

$$T_{sy} = N_s T_s$$

The estimate, SNR*, defined in Eq. (12) is shown in the next section to have an expected value equal to the true symbol SNR defined in Eq. (3), plus some bias that decreases with the number of symbols averaged. The variance of SNR* is also derived in the next section as a function of the number of symbols averaged and the true symbol SNR.

III. Mean and Variance of Symbol SNR Estimates

In Eq. (12), the estimate of the complex symbol SNR, SNR*, is a function of the random variables m_p and m_{ss}. Let g denote that function

$$\text{SNR}^* = g(m_p, m_{ss}) \qquad (13)$$

Assume that $g(m_p, m_{ss})$ is "smooth" in the vicinity of the point $(\overline{m}_p, \overline{m}_{ss})$, where $\overline{m}_p$ and $\overline{m}_{ss}$ are the means of m_p and m_{ss}, respectively. The expectation of the estimate, SNR*, can then be approximated by [3, p. 212]

$$E\{\text{SNR}^*\} \simeq g(\overline{m}_p, \overline{m}_{ss}) + \frac{1}{2} \times \left(\sigma^2_{mp} \frac{\partial^2 g}{\partial m_p^2} + 2\,\text{cov}\,(m_p, m_{ss}) \frac{\partial^2 g}{\partial m_p \partial m_{ss}} + \sigma^2_{mss} \frac{\partial^2 g}{\partial m_{ss}^2}\right) \qquad (14)$$

where σ^2_{mp} and σ^2_{mss} are the variances of m_p and m_{ss}, respectively, and cov (m_p, m_{ss}) is their covariance. The variance of the estimate, SNR*, can be approximated by [3, p. 212]

$$\sigma^2_{\text{SNR}^*} \simeq \left(\frac{\partial g}{\partial m_p}\right)^2 \sigma^2_{m_p} + \left(\frac{\partial g}{\partial m_{ss}}\right)^2 \sigma^2_{m_{ss}} + 2 \frac{\partial g}{\partial m_p} \frac{\partial g}{\partial m_{ss}}\,\text{cov}\,(m_p, m_{ss}) \qquad (15)$$

In Eqs. (14) and (15), all the partial derivatives and the covariance are evaluated at $(\overline{m}_p, \overline{m}_{ss})$. Expressions for the mean and variance of m_p, the mean and variance of m_{ss}, the covariance of m_p and m_{ss}, and the partial derivatives are derived in Appendices B through E, respectively. Substituting all the terms from the appendices into Eqs. (14) and (15), the mean and variance of SNR* are obtained,

$$E\{\text{SNR}^*\} = \text{SNR} + \frac{1}{N\cos^2\,(z/2)} \times \left[\frac{1}{C_1^2} + \text{SNR}\left(\frac{5}{4} - \frac{1}{4}\cos\,(z)\right) + \text{SNR}^2 \frac{C_1^2}{4}\,(1 - \cos\,(z))\right] \qquad (16)$$

and

$$\sigma^2_{\text{SNR}^*} = \frac{1}{N\cos^2(z/2)} \left[\frac{2}{C_1^4} + \text{SNR}\frac{4}{C_1^2} + \text{SNR}^2 \times \left(\frac{7}{4} - \frac{3}{4}\cos\,(z)\right) \text{SNR}^3 \frac{C_1^2}{4}\,(1 - \cos\,(z))\right] \qquad (17)$$

where

$$z = \omega_o T_{sy}$$

and

$$C_1 = \frac{\text{sinc } (\omega_o T_{sy}/4)}{\text{sinc } (\omega_o T_s/2)}$$

IV. Analysis Verification

Two methods are used to verify the analytical results of the mean and the variance in the complex symbol SNR estimation:

(1) Compare the numerical results of the analysis to simulation results.

(2) Set the offset frequency to zero and compare the performance of the complex symbol SNR estimator and that of the real symbol SNR estimator.

A. Simulation Results

Simulation results for the mean and variance of SNR* are shown in Figs. (1) and (2), and are compared to the theoretical results of Eqs. (16) and (17). The analytical and simulation results are also compared in Table 1. In all cases, the offset frequency, $f_o = \omega_o/(2\pi)$, is set at 20 Hz. The simulation results are based on 100 runs each, and the simulated means and variances are obtained by averaging over the 100 runs.

B. Special Case

A special case is when the offset frequency $\omega_o = 0$. In this case, the performance of the complex symbol SNR estimator should reduce to that of the real symbol SNR estimator given in [1] and [5], with N samples of pure noise and N samples of the signal plus noise.

For this special case, the mean and variance of the complex symbol SNR estimates reduce to

$$E\{\text{SNR}^*\} = \text{SNR} + \frac{1}{N}(1 + \text{SNR}) \tag{18}$$

$$\sigma^2_{\text{SNR}^*} = \frac{1}{N}(2 + 4\text{SNR} + \text{SNR}^2) \tag{19}$$

The analysis in [1], which assumed a constant signal level for all the samples, is easily extended to cover the case of a signal in only half the samples. The real symbol SNR and the real estimate, $E\{\text{SNR}^*\}$, in Eqs. (17a) and (17b) of [1] are simply replaced by values $\overline{\text{SNR}}$ and $\overline{\text{SNR}^*}$, respectively, representing averages over the $2N$ real samples. These average values are one-half the corresponding complex SNR and complex estimate SNR* defined here. With these correspondences, the mean of the real estimate in [1] reduces to

$$E\{\text{SNR}^*\} = \text{SNR} + \frac{1}{N-1}(1 + \text{SNR}) \tag{20}$$

and the variance of the real estimate is

$$\sigma^2_{\text{SNR}^*} = \left(\frac{N}{N-1}\right)^2 \frac{1}{N-2} \times \left[(\text{SNR}^2 + 2\text{SNR} + 1) + \frac{N-1}{N}(2\text{SNR} + 1)\right] \tag{21}$$

For a large N, Eq. (20) is equivalent to

$$E\{\text{SNR}^*\} = \text{SNR} + \frac{1}{N}(1 + \text{SNR}) \tag{22}$$

and Eq. (21) approximates to

$$\sigma^2_{\text{SNR}^*} = \frac{1}{N}(\text{SNR}^2 + 4\text{SNR} + 2) \tag{23}$$

Comparing Eq. (18) with Eq. (22), and Eq. (19) with Eq. (23), it is clear that the special case of the complex symbol SNR estimator has the same performance as the real symbol SNR with N signal-plus-noise samples and N pure noise samples.

V. Conclusions

A complex symbol signal-to-noise ratio estimator is presented in this article. This estimator modifies the split-symbol moments estimator for estimating the real symbol SNR [2] in order to accommodate complex symbols, with the assumption that the offset frequency is known. This estimator can be used to measure the performance of the full spectrum combiner as well as the complex symbol combiner for the Galileo S-band mission.

Acknowledgments

The author would like to thank Sam Dolinar for his valuable contributions to this work and Steve Townes for his many valuable suggestions and helpful discussions. Special thanks are also due to Tim Pham for his great support of this work. The author is grateful to Jay Rabkin for drawing her attention to this problem.

Table 1. Simulation results of the complex symbol SNR estimation.

SNR, dB	Mean of SNR*, dB		σ of SNR*, dB		N	N_s	Runs
	Theory	Simulation	Theory	Simulation			
−2	−1.9968	−2.0039	0.2956	0.2834	2,500	10	100
−2	−1.9984	−2.0136	0.2112	0.1937	5,000	10	100
−5	−4.9985	−5.0589	0.2454	0.2506	10,000	10	100
−8	−7.9986	−8.0437	0.3056	0.2787	20,000	10	100

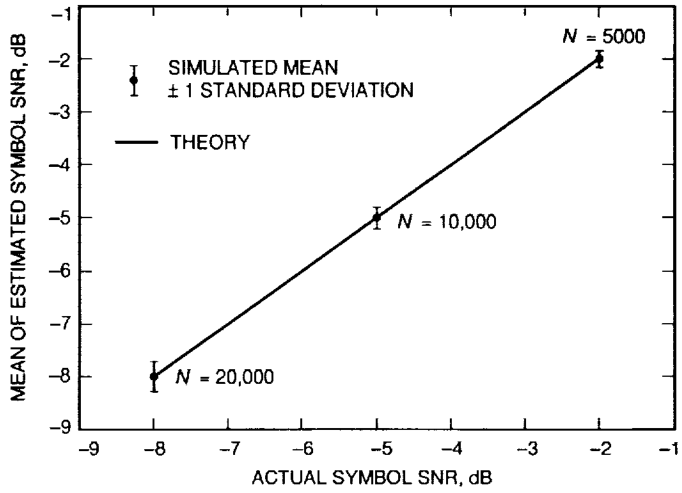

Fig. 1. Means and standard deviations of the symbol SNR estimates.

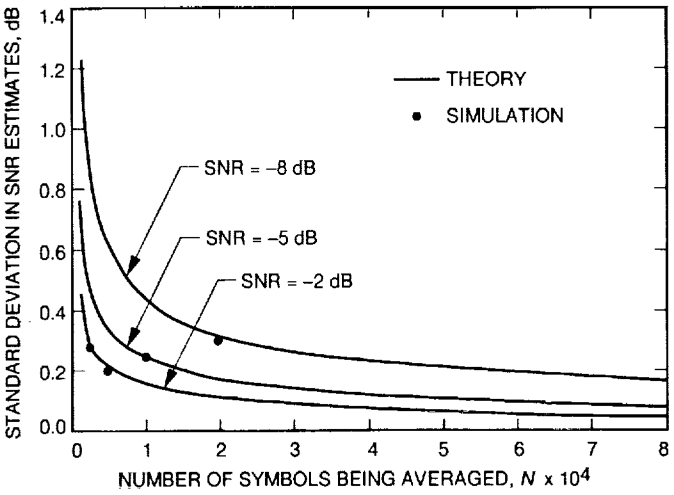

Fig. 2. Standard deviations of the complex symbol SNR estimates.

Appendix A

Sums of the Halves of a Symbol and Definitions of m_p and m_{ss}

The sum of the first half of the kth symbol is

$$Y_{\alpha_k} = \sum_{l=0}^{N_s/2-1} \frac{m}{N_s} d_k e^{j(\omega_o T_s l \; + \; \phi_o)} + n_{\alpha_k}$$

$$= \frac{m}{N_s} d_k e^{j\phi_o} \frac{1 - e^{j\omega_o T_s N_s/2}}{1 - e^{j\omega_o T_s}} + n_{\alpha_k}$$

$$= \frac{1}{2} m d_k e^{j(1/4\omega_o T_{sy} \; - \; 1/2\omega_o T_s \; + \; \phi_o)} \frac{\text{sinc } (\omega_o T_{sy}/4)}{\text{sinc } (\omega_o T_s/2)}$$

$$+ n_{\alpha_k} \qquad \text{(A-1)}$$

and the sum of the second half of the kth symbol is

$$Y_{\beta_k} = \sum_{l=N_{s/2}}^{N_s-1} \frac{m}{N_s} d_k c^{j(\omega_o T_s l \; + \; \phi_o)} + n_{\beta_k}$$

$$= \frac{m}{N_s} d_k e^{j(\omega_o T_s N_s/2 \; + \; \phi_o)} \frac{1 - e^{j(\omega_o T_s N_s/2)}}{1 - e^{j\omega_o T_s}} + n_{\beta_k}$$

$$= \frac{1}{2} m d_k e^{j(3/4\omega_o T_{sy} \; - \; 1/2\omega_o T_s \; + \; \phi_o)} \frac{\text{sinc } (\omega_o T_{sy}/4)}{\text{sinc } (\omega_o T_s/2)}$$

$$+ n_{\beta_k} \qquad \text{(A-2)}$$

where the noise terms, n_{α_k} and n_{β_k}, are complex Gaussian noises, with each of the components (real and imaginary) having a variance of $\sigma_n^2/2$. In terms of the in-phase and quadrature noise samples in Eqs. (1) and (2), the complex noise terms, n_{α_k} and n_{β_k}, are

$$n_{\alpha_k} = \sum_{l=0}^{N_s/2-1} (n_{I_{lk}} + j n_{Q_{lk}}) \qquad \text{(A-3)}$$

and

$$nn_{\beta_k} = \sum_{l=N_{s/2}}^{N_s-1} (n_{I_{lk}} + j n_{Q_{lk}}) \qquad \text{(A-4)}$$

where $j = \sqrt{-1}$.

Let s_{α_k} and s_{β_k} denote the signal parts of Y_{α_k} and Y_{β_k}, respectively. Then Y_{α_k} and Y_{β_k} can be expressed as

$$Y_{\alpha_k} = s_{\alpha_k} + n_{\alpha_k} \qquad \text{(A-5)}$$

and

$$Y_{\beta_k} = s_{\beta_k} + n_{\beta_k} \qquad \text{(A-6)}$$

The product of the sum of the first half of the kth symbol and the conjugate of the sum of the second half of the same symbol is

$$Y_{\alpha_k} Y_{\beta_k}^* = s_{\alpha_k} s_{\beta_k}^* + s_{\alpha_k} n_{\beta_k}^* + n_{\alpha_k} s_{\beta_k}^* + n_{\alpha_k} n_{\beta_k}^*$$

$$= \frac{1}{4} m^2 e^{j(-\omega_o T_{sy}/2)} \frac{\text{sinc}^2(\omega_o T_{sy}/4)}{\text{sinc}^2(\omega_o T_s/2)}$$

$$+ s_{\alpha_k} n_{\beta_k}^* + n_{\alpha_k} s_{\beta_k}^* + n_{\alpha_k} n_{\beta_k}^* \qquad \text{(A-7)}$$

Taking the real part of the product, one obtains

$$\Re\{Y_{\alpha_k} Y_{\beta_k}^*\} = \frac{1}{4} m^2 \cos\left(\frac{\omega_o T_{sy}}{2}\right) \frac{\text{sinc}^2 \; (\omega_o T_{sy}/4)}{\text{sinc}^2(\omega_o T_s/2)}$$

$$+ \Re\{s_{\alpha_k} n_{\beta_k}^* + n_{\alpha_k} s_{\beta_k}^* + n_{\alpha_k} n_{\beta_k}^*\} \qquad \text{(A-8)}$$

Define m_p as

$$m_p = \sum_{k=1}^{N} \Re\{Y_{\alpha_k} Y_{\beta_k}^*\} \qquad \text{(A-9)}$$

The sum of the whole kth symbol is

$$Y_k = \sum_{l=0}^{N_s-1} \frac{m}{N_s} d_k e^{j(\omega_o T_s l \; + \; \phi_o)} + n_k$$

$$= \frac{m}{N_s} d_k e^{j\phi_o} \frac{1 - e^{j\omega_o T_s N_s}}{1 - e^{j\omega_o T_s}} + n_k$$

$$= m d_k e^{j\left(1/2\omega_o T_{sy} \; - \; 1/2\omega_o T_s \; + \; \phi_o\right)} \frac{\text{sinc}\ (\omega_o T_{sy}/2)}{\text{sinc}\ (\omega_o T_s/2)} + n_k$$

$$= s_k + n_k \tag{A-10}$$

where s_k is the signal part of the whole symbol and n_k is a complex Gaussian noise with a variance of σ_n^2 in each component (real and imaginary), and

$$s_k = s_{\alpha_k} + s_{\beta_k}$$

$$n_k = n_{\alpha_k} + n_{\beta_k}$$

Note that the signal and noise parts of a whole complex symbol, s_k and n_k, can also be expressed in terms of their in-phase and quadrature components, that is,

$$s_k = s_{I_k} + js_{Q_k} \tag{A-11}$$

$$n_k = n_{I_k} + jn_{Q_k} \tag{A-12}$$

where s_{I_k}, s_{Q_k} and n_{I_k}, n_{Q_k} denote the I and Q components of the signal and the noise in the kth symbol. Furthermore, Y_k can be expressed as

$$Y_k = s_{I_k} + js_{Q_k} + n_{I_k} + jn_{Q_k} \tag{A-13}$$

The sum squared of the kth symbol is

$$|Y_k|^2 = m^2 \frac{\text{sinc}^2\ (\omega_o T_{sy}/2)}{\text{sinc}^2\ (\omega_o T_s/2)} + |n_k|^2 + 2\Re\{n_k s_k^*\}$$

$$= m^2 C_2^2 + |n_k|^2 + 2\Re\{n_k s_k^*\} \tag{A-14}$$

where

$$C_2^2 = \frac{\text{sinc}^2\ (\omega_o T_{sy}/2)}{\text{sinc}^2(\omega_o T_s/2)}$$

Define m_{ss} as

$$m_{ss} = \sum_{k=1}^{N} |Y_k|^2 \tag{A-15}$$

Appendix B

Evaluation of the Mean and Variance of m_p

All the expectations in the following are conditional on knowing the symbol synchronization.

$$E\{m_p\} = \frac{1}{N}\sum_{k=1}^{N} E\{U_k\}$$

$$= \frac{1}{4}m^2\frac{\text{sinc}^2\ (\omega_o T_{sy}/4)}{\text{sinc}^2\ (\omega_o T_s/2)}\cos\left(\frac{\omega_o T_{sy}}{2}\right)$$

$$+\frac{1}{N}\sum_{k=1}^{N} E\{\Re\{s_{\alpha_k}n^*_{\beta_k} + n_{\alpha_k}s^*_{\beta_k} + n_{\alpha_k}n^*_{\beta_k}\}\}$$

$$= \frac{1}{4}m^2\frac{\text{sinc}^2\ (\omega_o T_{sy}/4)}{\text{sinc}^2\ (\omega_o T_s/2)}\cos\left(\frac{\omega_o T_{sy}}{2}\right) \qquad \text{(B-1)}$$

where

$$U_k = \Re\{Y_{\alpha_k}Y^*_{\beta_k}\}$$

$$= \Re\{(s_{\alpha_k} + n_{\alpha_k})(s^*_{\beta_k} + n^*_{\beta_k})\}$$

and s_{α_k} and s_{β_k} denote the signal part of Y_{α_k} and Y_{β_k}, respectively, as in Eqs. (A-5) and (A-6). The last step in Eq. (B-1) follows from the independence of the noises with zero mean in the two halves of each symbol. Note that $T_{sy} = N_s T_s$.

Because the $\{U_k\}$ are independent, the variance of m_p can be computed as [4, p. 352]

$$\sigma^2_{m_p} = \frac{1}{N^2}\sum_{k=1}^{N}\sigma^2_{U_k} \qquad \text{(B-2)}$$

Now let subscripts I and Q denote the in-phase and quadrature components of the signals. The second moment of U_k can be expressed as

$$E\{U_k^2\} = \frac{\sigma_n^2}{2}E\left\{s^2_{\beta I_k} + s^2_{\alpha I_k} + s^2_{\beta Q_k} + s^2_{\alpha Q_k}\right\}$$

$$+\frac{\sigma_n^4}{2} + E\{(s_{\alpha I_k}s_{\beta I_k} + s_{\alpha Q_k}s_{\beta Q_k})^2\}$$

$$= \frac{m^2}{2}\frac{\text{sinc}^2(\omega_o T_{sy}/4)}{\text{sinc}^2(\omega_o T_s/2)}\frac{\sigma_n^2}{2} + \frac{\sigma_n^4}{2}$$

$$+ E\{(s_{\alpha I_k}s_{\beta I_k} + s_{\alpha Q_k}s_{\beta Q_k})^2\} \qquad \text{(B-3)}$$

Combining Eqs. (B-1), (B-3), and (B-2) yields

$$\sigma^2_{m_p} = \frac{1}{N}\left(\frac{1}{4}m^2\frac{\text{sinc}^2\ (\omega_o T_{sy}/4)}{\text{sinc}^2\ (\omega_o T_s/2)}\sigma_n^2 + \frac{\sigma_n^4}{2}\right) \qquad \text{(B-4)}$$

Appendix C

Evaluation of the Mean and Variance of m_{ss}

The mean of m_{ss} is

$$E\{m_{ss}\} = E\left\{\frac{1}{N}\sum_{k=1}^{N}|Y_k|^2\right\}$$

$$= m^2C_2^2 + \frac{1}{N}\sum_{k=1}^{N}E\,|n_k|^2 + \frac{1}{N}\sum_{k=1}^{N}E\{\Re\{n_k s_k^*\}\}$$

$$= m^2C_2^2 + 2\sigma_n^2 \qquad \text{(C-1)}$$

To find the variance of m_{ss}, let

$$V_k = |Y_k|^2$$

$$= Y_{I_k}^2 + Y_{Q_k}^2$$

$$= (s_{I_k} + n_{I_k})^2 + (s_{Q_k} + n_{Q_k})^2 \qquad \text{(C-2)}$$

where Y_{I_k}, Y_{Q_k}, s_{I_k}, s_{Q_k}, n_{I_k}, and n_{Q_k} are defined in Appendix A. Because the $\{V_k\}$ are independent, the variance of m_{ss} can be expressed in terms of the variance of V_k [4, p. 352],

$$\sigma_{m_{ss}}^2 = \frac{1}{N^2}\sum_{k=1}^{N}\sigma_{V_k}^2 \qquad \text{(C-3)}$$

$$\sigma_{V_k}^2 = E\{V_k^2\} - (E\{V_k\})^2 \qquad \text{(C-4)}$$

where

$$E^2\{V\} = E^2\{m_{ss}\}$$

$$= (m^2C_2^2 + 2\sigma_n^2)^2 \qquad \text{(C-5)}$$

Expanding V_k^2, take the expectation of V_k^2; apply $E\{n_{I_k}^2\} = E\{n_{Q_k}^2\} = \sigma_n^2$, $E\{n_{I_k}^3\} = E\{n_{Q_k}^3\} = 0$, and $E\{n_{I_k}^4\} = E\{n_{Q_k}^4\} = 3\sigma_n^4$ [3, p. 147]; and use the independence of n_{I_k} and n_{Q_k}, and one will obtain

$$E\{V_k^2\} = 8\sigma_n^4 + 8\sigma_n^2(s_{I_k}^2 + s_{Q_k}^2) + (s_{I_k}^2 + s_{Q_k}^2)^2$$

$$\times\ 8\sigma_n^4 + 8m^2C_2^2\sigma_n^2 + m^4C_2^4 \qquad \text{(C-6)}$$

The variance of V_k becomes

$$\sigma_{V_k}^2 = 4m^2C_2^2\sigma_n^2 + 4\sigma_n^4 \qquad \text{(C-7)}$$

Finally, the variance of m_{ss} can be written as

$$\sigma_{m_{ss}}^2 = \frac{1}{N}\left[4m^2C_2^2\sigma_n^2 + 4\sigma_n^4\right] \qquad \text{(C-8)}$$

Appendix D

Evaluation of the Covariance of m_p and m_{ss}

The covariance of m_p and m_{ss} is defined as

$$\text{cov}\ (m_p, m_{ss}) = E\{(m_p - \overline{m}_p)(m_{ss} - \overline{m}_{ss})\}$$

$$= E\{m_p m_{ss}\} - \overline{m}_p \overline{m}_{ss} \qquad \text{(D-1)}$$

As in Appendices B and C, let

$$U_k = \Re\{Y_{\alpha_k} Y^*_{\beta_k}\}$$

$$= Y_{\alpha I_k} Y_{\beta I_k} + Y_{\alpha Q_k} Y_{\beta Q_k}$$

$$= (s_{\alpha_{I_k}} + n_{\alpha_{I_k}})(s_{\beta_{I_k}} + n_{\beta_{I_k}})$$

$$+ (s_{\alpha_{Q_k}} + n_{\alpha_{Q_k}})(s_{\beta_{Q_k}} + n_{\beta_{Q_k}}) \qquad \text{(D-2)}$$

and

$$V_k = |Y_k|^2$$

$$= s_{I_k}^2 + 2s_{I_k} n_{I_k} + n_{I_k}^2 + s_{Q_k}^2 + 2s_{Q_k} n_{Q_k} + n_{Q_k}^2 \qquad \text{(D-3)}$$

The expectation of the product of $U_k V_k$ can be expressed as

$$E\{U_k V_k\} =$$

$$\sigma_n^4 + 2\sigma_n^2 E\{s_{\alpha_{I_k}} s_{\beta_{I_k}} + s_{\alpha_{Q_k}} s_{\beta_{Q_k}}\} + E\{s_{I_k}^2 + s_{Q_k}^2\}\sigma_n^2$$

$$+ E\{(s_{I_k}^2 + s_{Q_k}^2)(s_{\alpha_{I_k}} s_{\beta_{I_k}} + s_{\alpha_{Q_k}} s_{\beta_{Q_k}})\}$$

$$= \sigma_n^4 + 2\sigma_n^2 \left(\frac{1}{4} m^2 C_1^2 \cos\frac{z}{2}\right)$$

$$+ \sigma_n^2 (m^2 C_2^2) + m^2 C_2^2 \left(\frac{1}{4} m^2 C_1^2 \cos\frac{z}{2}\right) \qquad \text{(D-4)}$$

where

$$C_1 = \frac{\text{sinc}\ (\omega_o T_{sy}/4)}{\text{sinc}\ (\omega_o T_s/2)}$$

$$C_2 = \frac{\text{sinc}\ (\omega_o T_{sy}/2)}{\text{sinc}\ (\omega_o T_s/2)}$$

and

$$z = \omega_o T_{sy}$$

Note that

$$C_2^2 = \frac{1}{2} C_1^2 \left[1 + \cos\left(\frac{\omega_o T_{sy}}{2}\right)\right]$$

Then

$$E\{m_p m_{ss}\} =$$

$$E\left\{\frac{1}{N}\sum_{k=1}^{N} U_k \frac{1}{N}\sum_{l=1}^{N} V_l\right\}$$

$$= \frac{1}{N^2}\left[\sum_{k=1}^{N} E\{U_k V_k\} + \sum_{k=1}^{N} E\{U_k\} \sum_{l=1, l\neq k}^{N} E\{V_l\}\right]$$

$$= \frac{1}{N^2}\left[N E\{U_k V_k\} + N \overline{m}_p (N-1) \overline{m}_{ss}\right] \qquad \text{(D-5)}$$

Finally, the covariance of m_p and m_{ss} is

$$\text{cov}\ (m_p, m_{ss}) = \frac{1}{N}[E\{U_k V_k\} - \overline{m}_p \overline{m}_{ss}]$$

$$= \frac{1}{N}\left[m^2 C_2^2 \sigma_n^2 + \sigma_n^4\right] \qquad \text{(D-6)}$$

Appendix E

Evaluation of the Partial Derivatives

Denote the following parameters in a convenient form,

$$K_1 = \frac{4\text{sinc}^2\,(\omega_o T_s/2)}{\text{sinc}^2\,(\omega_o T_{sy}/4)\,\cos\,(\omega_o T_{sy}/2)}$$

$$K_2 = \frac{2}{\cos\,(\omega_o T_{sy}/2)} + 2$$

and

$$C_1 = \frac{\text{sinc}\,(\omega_o T_{sy}/4)}{\text{sinc}\,(\omega_o T_s/2)}$$

$$z = \omega_o T_{sy}$$

In terms of K_1 and K_2, the estimate SNR* defined in Eq. (12) is given by

$$\text{SNR}^* = g(m_p, m_{ss})$$

$$= \frac{K_1 m_p}{m_{ss} - K_2 m_p} \qquad \text{(E-1)}$$

Then $g(\overline{m}_p, \overline{m}_{ss}) = \text{SNR}$, and the partial derivatives of this estimator function are

$$\left.\frac{\partial g}{\partial m_p}\right|_{\overline{m}_p,\overline{m}_{ss}} = \frac{K_1 K_2 \overline{m}_p}{(\overline{m}_{ss} - K_2\overline{m}_p)^2} + \frac{K_1}{\overline{m}_{ss} - K_2\overline{m}_p} =$$

$$\frac{1}{\sigma_n^2 \cos\,(z/2)}\left[\text{SNR}\left(1 + \cos\frac{z}{2}\right) + \frac{2}{C_1^2}\right] \qquad \text{(E-2)}$$

$$\left.\frac{\partial^2 g}{\partial m_p^2}\right|_{\overline{m}_p,\overline{m}_{ss}} = \frac{2K_1 K_2^2 \overline{m}_p}{(\overline{m}_{ss} - K_2\overline{m}_p)^3} + \frac{2K_1 K_2}{(\overline{m}_{ss} - K_2\overline{m}_p)^2} =$$

$$\frac{2}{\sigma_n^4}\frac{\cos^2(z/4)}{\cos^2(z/2)}\left[2\text{SNR}\left(1 + \cos\frac{z}{2}\right) + \frac{4}{C_1^2}\right] \qquad \text{(E-3)}$$

$$\left.\frac{\partial g}{\partial m_{ss}}\right|_{\overline{m}_p,\overline{m}_{ss}} = -\frac{K_1\overline{m}_p}{(\overline{m}_{ss} - K_2\overline{m}_p)^2}$$

$$= -\frac{1}{2\sigma_n^2}\text{SNR} \qquad \text{(E-4)}$$

$$\left.\frac{\partial^2 g}{\partial m_{ss}^2}\right|_{\overline{m}_p,\overline{m}_{ss}} = \frac{2K_1\overline{m}_p}{(\overline{m}_{ss} - K_2\overline{m}_p)^3}$$

$$= \frac{1}{2\sigma_n^4}\text{SNR} \qquad \text{(E-5)}$$

$$\left.\frac{\partial^2 g}{\partial m_p \partial m_{ss}}\right|_{\overline{m}_p,\overline{m}_{ss}} =$$

$$-\frac{2K_1 K_2\overline{m}_p}{(\overline{m}_{ss} - K_2\overline{m}_p)^3} - \frac{K_1}{(\overline{m}_{ss} - K_2\overline{m}_p)^2} =$$

$$-\frac{1}{\cos(z/2)\sigma_n^4}\left[\text{SNR}\left(1 + \cos\frac{z}{2}\right) + \frac{1}{C_1^2}\right] \qquad \text{(E-6)}$$

where the second lines of Eqs. (E-2) through (E-6) are obtained by substituting the expressions for $\overline{m}_p = E\{m_p\}$ and $\overline{m}_{ss} = E\{m_{ss}\}$ from Appendices B and C.

References

[1] S. Dolinar, "Exact Closed-Form Expressions for the Performance of the Split-Symbol Moments Estimator of Signal-to-Noise Ratio," *The Telecommunications and Data Acquisition Progress Report 42-100, vol. October–December 1989,* Jet Propulsion Laboratory, Pasadena, California, pp. 174–179, February 15, 1990.

[2] L. Howard, "Signal and Noise Measurements in the NASA Deep Space Network," *20th URSI Conference,* Washington, DC, August 10–19, 1981.

[3] A. Papoulis, *Probability, Random Variables, and Stochastic Processes,* New York: McGraw–Hill, 1965.

[4] R. Fante, *Signal Analysis and Estimation,* New York: John Wiley and Sons, 1988.

[5] M. Simon and A. Mileant, "SNR Estimation for the Baseband Assembly," *The Telecommunications and Data Acquisition Progress Report 42-85, vol. January–March 1986,* Jet Propulsion Laboratory, Pasadena, California, pp. 118–126, May 15, 1986.

N94- 29672

X-Band Ultralow-Noise Maser Amplifier Performance

G. W. Glass and G. G. Ortiz
Radio Frequency and Microwave Subsystems Section

D. L. Johnson
Applied Mechanics Technologies Section

Noise temperature measurements of an 8440-MHz ultralow noise maser amplifier (ULNA) have been performed at subatmospheric, liquid-helium temperatures. The traveling-wave maser was operated while immersed in a liquid helium bath. The lowest input noise temperature measured was 1.43 ± 0.16 K at a physical temperature of 1.60 K. At this physical temperature, the observed gain per centimeter of ruby was 4.9 dB/cm. The amplifier had a 3-dB bandwidth of 76 MHz.

I. Introduction

NASA's Deep Space Network uses low-noise ruby maser amplifiers for deep space telecommunications and to support radio and radar astronomy. Many deep-space mission communication links would not be possible without the low noise temperature performance that masers provide.

Currently, typical specifications of a DSN X-band (8420 MHz) maser system under normal operating conditions are 45 dB of net gain (1.4 dB/cm), over 100 MHz of instantaneous bandwidth, and a noise temperature at the input of 3.5 K, referenced to the room temperature flange. The required 4.5 K physical temperature of the maser is provided by a three-stage closed-cycle refrigerator (CCR). These maser-CCR packages are normally mounted near the vertices of large, tippable, parabolic antennas. The work presented in this article uses these specifications as a baseline for comparison.

Further cooling of a maser amplifier results in significant improvements in noise temperature and gain. At X-band, the input noise temperature is proportional to the physical temperature, while the electronic gain in decibels (excluding circuit losses) is inversely proportional to the physical temperature (both to a first-order approximation). Thus, immersing a maser amplifier in a bath of superfluid helium (below 2.17 K) will result in a threefold increase in the gain in decibels and a threefold decrease in the noise temperature (e.g., from 3.5 to 1.2 K at 8400 MHz).

Several 34-m beam waveguide (BWG) antennas are being implemented in the DSN that will provide, in contrast to present DSN antennas, a relatively large nontipping location for the maser and feed components. For these antennas, the use of a superfluid helium cryostat becomes very practical as a means to cool the maser (and its feed components). This is necessary in order to achieve a very low system noise temperature, while simultaneously increasing maser gain.

In order to provide the lowest front-end system noise temperature for its deep space telecommunications downlink, the Jet Propulsion Laboratory has developed and demonstrated superfluid helium-cooled maser amplifiers for the DSN. This article describes laboratory noise temperature and gain measurements made on an ULNA maser centered at 8440 MHz in subatmospheric liquid helium. A brief discussion on the limits of X-band ULNA technology is also presented.

II. Theory

The noise power of a maser amplifier at a given physical temperature is discussed by Siegman in [1]. An extension of this discussion by Shell, et al. in [2] yields the following equation for the theoretical noise temperature of a maser amplifier:

$$T_{amp} =$$

$$\frac{\left(G_{net}^{ratio}-1\right)}{G_{net}^{ratio}} \frac{hf}{k} \left[\frac{G_{elect}^{(dB)}}{G_{net}^{(dB)}} \frac{r}{r-1} + \frac{L_0^{(dB)}}{G_{net}^{(dB)}} \frac{1}{\left(e^{\frac{hf}{kT_0}}-1\right)} \right] \tag{1}$$

where

G_{net}^{ratio} = net electronic gain ratio, unitless

h = Planck constant = $6.6262 \times 10^{-34}\ J-s$

f = operating frequency, Hz

k = Boltzmann constant = $1.3806 \times 10^{-23}\ J/K$

$G_{elect}^{(dB)}$ = electronic gain, dB

r = inverted spin population ratio, unitless

$L_0^{(dB)}$ = forward insertion loss, dB

T_0 = maser physical temperature, K

Using Eq. (1), the expected noise temperature of a maser at the input to the cryogenic system can be calculated. Assuming an electronic gain of 39 dB, a net gain of 34 dB, a forward insertion loss of 5.0 dB, an inverted spin population ratio of 2.32, and a maser amplifier physical temperature of 1.6 K, the expected noise temperature is 1.02 K.

The maser noise temperature in Eq. (1) consists primarily of two noise-generating mechanisms. The first term is related to the spontaneous emission of photons by the ruby spin system, while the second is due to dissipative losses in the microwave circuitry. It is interesting to note that as the maser physical temperature (and the ruby spin temperature) approaches zero, the gain and inverted spin population ratio terms each approach unity, while the conductor loss term goes to zero. Thus, Eq. (1) takes the limiting form of the equivalent quantum-noise temperature as discussed by Oliver in [3]

$$T_{MQL} = \frac{h}{k} f \tag{2}$$

At 8400 MHz, the quantum-noise temperature limit is 0.40 K. Thus, quantum noise accounts for almost half of the total noise associated with this maser amplifier.

Maser gain expressions are also given in [1]. Considering only first-order temperature-dependent terms, the decibel gain is

$$G_{dB} = 27 \frac{SN}{Q_m} \tag{3}$$

where S is the slowing factor (the ratio of the velocity of light to the group velocity), N is the length of the circuit in free-space wavelengths, and Q_m is the magnetic Q. The Q_m term is directly proportional to temperature. Thus, the gain of a maser amplifier is inversely porportional to temperature. Assuming that the gain of a maser amplifier at a physical temperature of 4.2 K is 10 dB, then the expected gain of this amplifier at 1.6 K is 26 dB.

III. System Description

A diagram of the noise and gain measurement setup with the maser amplifier in place is shown in Fig. 1. The system is housed within a liquid-helium-filled dewar with the maser immersed in superfluid liquid helium. The input and output waveguides are cooled by the discharging helium vapors. The upper halves of the maser input and output waveguides are made of thin-walled stainless steel to minimize heat leak into the helium bath. These stainless steel waveguide sections are copper plated to a minimum thickness of three skin depths to ensure a low radio frequency loss. The lower halves of these waveguide sections are made of copper.

The most economical and expedient means of providing a maser amplifier for this system demonstration was to use an available Block IIA maser structure, described in [4]. This structure was modified for stable operation at 1.5 K. The principal modification was to increase the reverse loss provided by the resonant yttrium iron garnet (YIG) isolator from 37.5 to 74 dB. Further details about the existing X-band ULNA structure and its modifications can be found in [5].

The bath temperature is reduced below 4.2 K by decreasing the vapor pressure above the helium bath in the dewar. Vapor pressure control is provided by two pumping ports at the top of the dewar connected to two helium-tight, single-stage Leybold-Hereaus S65B TRIVAC vacuum pumps. A combined pumping speed of 2600 lpm (92 cfm) evacuates the dewar to a pressure of 800 Pa. Once a stable operating temperature (vacuum pressure) is maintained, as monitored on high-precision carbon-glass resistors, noise and gain measurements can be performed.

Maser gain-bandpass measurements were made as the helium bath was slowly cooled from 2.20 to 1.60 K. Noise temperature measurements were made over a range of frequencies at a variety of temperatures by cooling the cryostat to its lowest temperature and then allowing the cryostat temperature to gradually increase.

The maser noise temperature and gain were measured using the Y-factor technique [6,7]. A cooled attenuator (20 dB) in front of the maser was used as the cold load (T_{cold}), while the hot load (T_{hot}), referenced at the maser input, was a noise diode with an excess noise ratio (ENR) value of 13 dB [8]. The attenuator is supercooled within the helium bath while the noise diode resides outside the dewar. This technique has the advantage of reducing the value of T_{hot} and T_{cold}, while maintaining a large Y-factor. An added benefit is that the pad presents a good input match to the noise source and the maser. The maser under test did not have sufficient gain for the receiver. So, a follow-up amplifier was connected at the output of the system to increase the gain. The follow-up amplifier was chosen such that the power meter could read the low noise powers of T_{cold} and yet have enough dynamic range to accommodate a measurement of T_{hot}.

The equation that defines the noise temperature of the entire system, referenced to the input flange of the cryostat, is given by

$$T_{eff} = \phi + L(L_p - 1)T_p + LL_pT_e + \frac{(\phi + T_rL)}{G_e} \qquad (4)$$

The last term in Eq. (4) is negligible compared to the preceding terms, so to a first-order approximation it may be excluded. The noise temperature of the maser at the input flange, T_e, was solved for in Eq. (4), yielding,

$$T_e = \frac{[T_{eff} - \phi - L(L_p - 1)T_p]}{LL_p} \qquad (5)$$

where T_{eff} is a measurable quantity; ϕ is the thermal noise contribution due to the input line; L is the line loss; L_p is the cryogenic 20-dB attenuator loss; and T_p is the physical temperature of the pad. All must be accurately measured. These quantities are obtained by performing three separate measurements of the noise and loss (or gain) contributions at the same physical operating temperatures.

Two assumptions were made in the derivation of Eq. (4). The first is that the components are all linear, and the second is that $h\nu << kT$, where ν is the frequency of interest. The maser amplifier and all other components in the three measurements were linear. However, $h\nu/kT = 0.32$ is not negligible with respect to unity; therefore, a correction term, $T_c^{'} \cong 0.024\nu$ (GHz), as explained in [9], may be added to T_e to determine the corrected amplifier noise temperature, T_c. For this measurement, $T_c^{'} = 0.20$ K and $T_c = T_e + T_c^{'} = 0.20$ K.

IV. Measurements and Results

The first measurement determined the RF loss ($2L$) and noise temperature contribution (2ϕ) of the input and output waveguide lines. The setup of the first measurement consisted of a through coaxial line between the input and output waveguide lines. At a constant physical temperature of 1.60 K, noise and loss measurements were performed. At 8400 MHz, the noise temperature contribution of the input line (ϕ) and the input line loss (L) were measured to be 29.26 ± 1.22 K and −0.89 ± 0.02 dB, respectively.

A 20-dB attenuator was installed between the input and output waveguide lines for the second measurement. A precision carbon-glass thermometer was attached to the attenuator to accurately monitor its temperature. This measurement determined the pad loss (L_p) at a known temperature (T_p). At 1.60 ± 0.05 K and 8400 MHz, the attenuator loss measured −20.09 ± 0.03 dB.

The maser was installed behind the 20-dB attenuator for the third measurement. Measured values of T_{eff} and the associated gain, G_e, were 382 K and 41.8 dB, respectively. Substituting data from the previous measurements and the value of T_{eff} from this third procedure into Eq. (4), the maser input noise temperature, T_e, equals 1.23 ± 0.16 K. Adding the correction term $T_c^{'}$ gives a corrected maser input noise temperature of 1.43 ± 0.16 K.

The theoretical estimate of the error in T_e is obtained by taking the differential of Eq. (5), which yields

$$dT_e = \frac{\partial T_e}{\partial T_{eff}} dT_{eff} + \frac{\partial T_e}{\partial \phi} d\phi + \frac{\partial T_e}{\partial L} dL + \frac{\partial T_e}{\partial L_p} dL_p + \frac{\partial T_e}{\partial T_p} dT_p \qquad (6)$$

The most significant error contribution in these measurements is in T_p, the attenuator physical temperature. Thus, the better the bath temperature is known, the more accurate the noise temperature measurement.

For each of these measurements, the temperature of the liquid helium bath was lowered below the normal boiling point (4.2 K) by pumping on the bath to reduce the vapor pressure of the liquid helium. In each case, the minimum bath temperature achieved was 1.60 K. The physical temperature was measured with a carbon-glass thermometer and verified with a vacuum pressure gauge. The lowest temperature achieved was limited by the helium boil-off rate and the pumping speed of the high-vacuum equipment.

Tables 1 and 2 present noise temperature and gain per unit length results, respectively, for a range of frequencies between 8350 and 8500 MHz and for a range of superfluid temperatures. Maser noise temperature measurements at 8400 MHz are plotted as a function of physical temperature in Fig. 2. In this plot, it is satisfying to note that a least-squares line through the data passes close to the maser noise temperature quantum limit at a physical temperature of 0 K.

Maser gain was measured at several different temperatures as the bath temperature was cooled to 1.6 K. The 8400-MHz results are shown graphically in Fig. 3. A 7-dB increase (from 28 to 35 dB at 8400 MHz) in maser gain was measured upon cooling from 2.2 to 2.17 K. This result, shown graphically in Fig. 4, is due to the onset of superfluidity at 2.17 K. Superfluid helium has a very high effective thermal conductivity, ensuring that the maser ruby temperature is equal to the bath temperature. This effect is due to an increase by three orders of magnitude in the thermal conductivity at temperatures below the lambda point. The test results suggest that above 2.17 K the ruby operates at a temperature about 0.5 K higher than that of the bath.

At the lowest temperature of 1.6 K, the maser exhibited a net gain of 41.8 dB, with a bandwidth of 76 MHz centered at 8400 MHz, as shown in Fig. 5. The maser's ruby bar was 8.5 cm long, giving a maser net gain per centimeter of 4.9 dB/cm. Figure 6 shows a close comparison between measured data and the theoretical gain as a function of physical temperature.

V. Conclusion

The noise performance of an 8400-MHz maser amplifier has been measured in superfluid helium. The measured results agree closely with theory. A value of 1.43 ± 0.16 K was measured, while the theoretical value is 1.02 K. The associated maser gain measurement at the same frequency and physical temperature was 4.9 dB/cm, agreeing closely with theoretical predictions.

The telemetry needs of the DSN for outer planet missions, as well as for Mars surface exploration, can only be met with the lowest noise amplifiers. This maser technology, used in conjunction with beam waveguide antennas, will assist the DSN in meeting its needs into the next century.

Acknowledgments

The X-band maser in this article is the product of the combined effort of the Advanced Cryo-Electronics Group under the supervision of Javier Bautista. In addition, the authors wish to thank Jason Kovatch, Ted Hanson, and Steve Montanez for their technical support during this effort.

References

[1] A. E. Siegman, *Microwave Solid State Masers*, New York: McGraw-Hill, 1964.

[2] J. S. Shell, R. C. Clauss, S. M. Petty, G. W. Glass, M. S. Fiore, J. J. Kovatch, J. R. Loreman, D. E. Neff, R. B. Quinn, and D. T. Trowbridge, "Ruby Masers for Maximum G/T_{op}," accepted for a special issue of the *Proceedings of the IEEE on the Design and Instrumentation of Antennas for Deep Space Telecommunications and Radio Astronomy*, scheduled to be published in February 1994.

[3] B. M. Oliver, "Thermal and Quantum Noise," *Proceedings of the IEEE*, vol. 53, no. 5, p. 436, May 1965.

[4] D. L. Trowbridge, "Block IIA Traveling-Wave Maser," *The Telecommunications and Data Acquisition Progress Report 42-87, vol. July–September 1986*, Jet Propulsion Laboratory, Pasadena, California, pp. 158–164, November 15, 1986.

[5] D. L. Johnson, S. M. Petty, J. J. Kovatch, G. W. Glass, "Ultralow Noise Performance of an 8.4-GHz Maser-Feedhorn System," *The Telecommunications and Data Acquisition Progress Report 42-100, vol. October–December 1989*, Jet Propulsion Laboratory, Pasadena, California, pp. 100–110, Febuary 15, 1990.

[6] C. T. Stelzried, "Microwave Thermal Noise Standards," *IEEE Trans. on MTT*, vol. MTT-16, no. 9, pp. 646–655, 1968.

[7] N. Kuhn, "Accurate and Automatic Noise Figure Measurements with Standard Equipment," *IEEE MTT-S Int. Microwave Symp. Digest*, pp. 425–427, 1980.

[8] M. W. Pospieszalski, "On the Noise Measurement of Noise Parameters of Microwave Two-Ports," *IEEE Trans. on MTT*, vol. MTT-34, pp. 456–458, 1986.

[9] C. T. Stelzried, *The Deep Space Network-Noise Temperature Concepts, Measurements, and Performance*, JPL Publication 82-33, Jet Propulsion Laboratory, Pasadena, California, September 15, 1982.

Table 1. Maser noise temperature results.

Physical temperature, K	Frequency, MHz						
	8350	8375	8400	8425	8450	8475	8500
	Noise temperature, K						
1.600	1.47	1.47	1.42	1.70	2.13	2.55	3.82
1.700	1.50	1.62	1.53	1.76	2.26	3.00	11.42
1.800	1.62	1.81	1.61	2.01	2.50	3.30	13.81
1.900	1.74	1.92	1.66	2.26	2.74	3.59	17.03
2.000	2.01	2.16	1.80	2.55	3.04	4.12	19.37
2.101	2.28	2.38	1.96	2.83	3.24	4.29	18.99

Table 2. Maser gain per unit length results.

Physical temperature, K	Frequency, MHz						
	8350	8375	8400	8425	8450	8475	8500
	Maser gain per unit length, dB/cm						
1.600	4.67	4.86	4.92	5.18	4.43	4.48	2.45
1.700	4.24	4.32	4.28	4.16	3.58	2.44	1.06
1.800	3.97	4.05	3.99	3.90	3.36	2.29	0.96
1.900	3.72	3.79	3.72	3.65	3.14	2.12	0.83
2.000	3.45	3.53	3.49	3.44	2.95	1.94	0.73
2.101	3.22	3.31	3.29	3.22	2.77	1.81	0.64

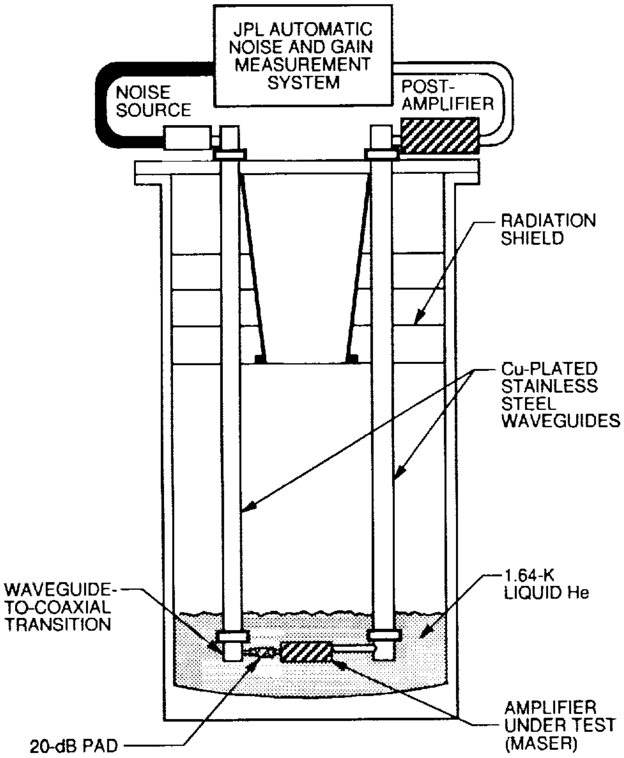

Fig. 1. The noise and gain measurement system with the maser installed.

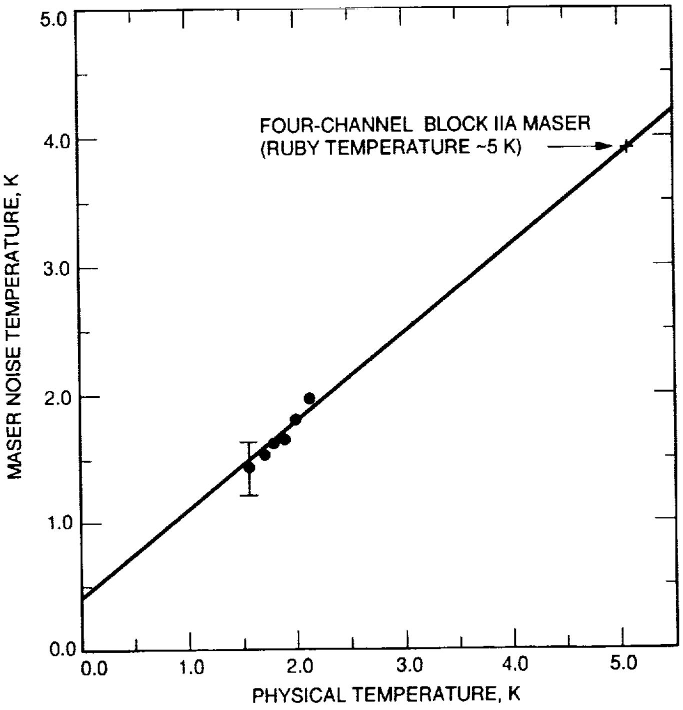

Fig. 2. Measured noise temperature for an 8400-MHz maser ULNA as a function of physical temperature.

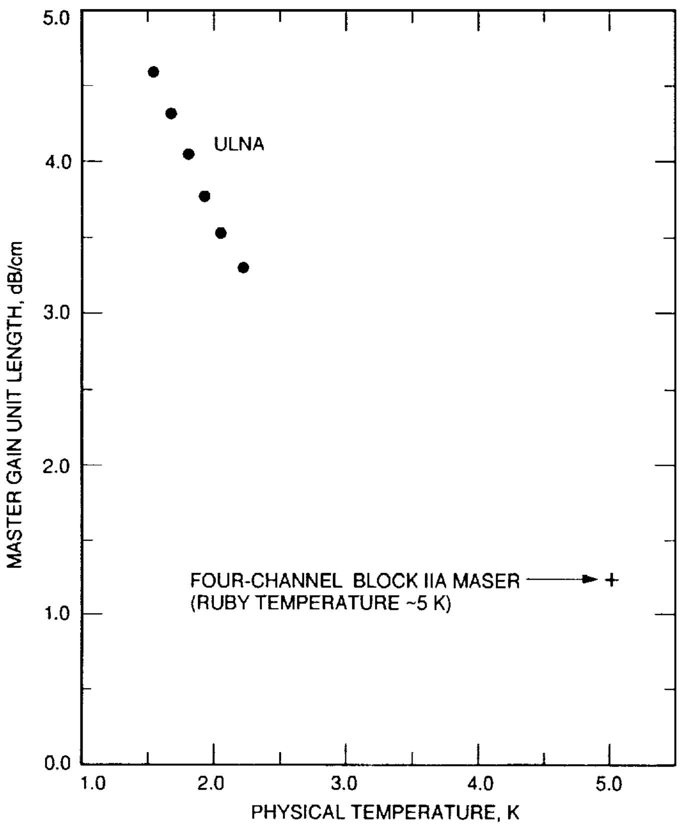

Fig. 3. Maser gain at 8400 MHz with respect to physical temperature.

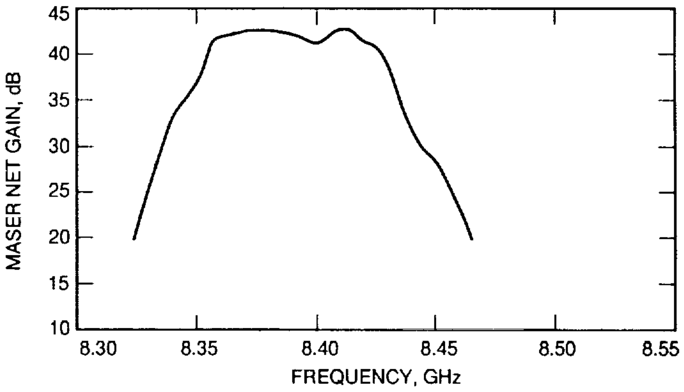

Fig. 5. Maser gain-bandpass curve at 1.6 K.

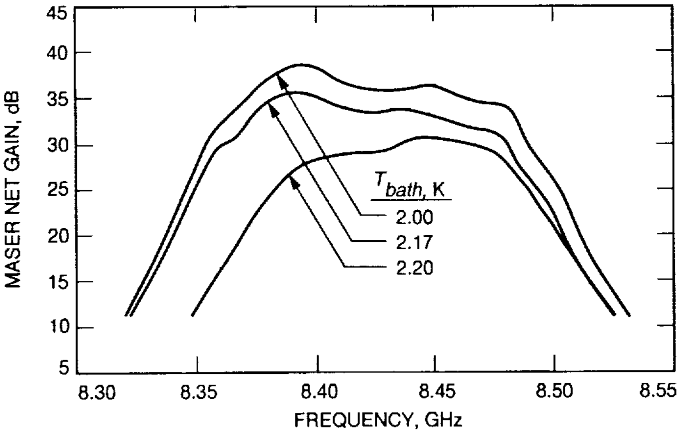

Fig. 4. Maser gain-bandpass as a function of temperature about the helium lamda point.

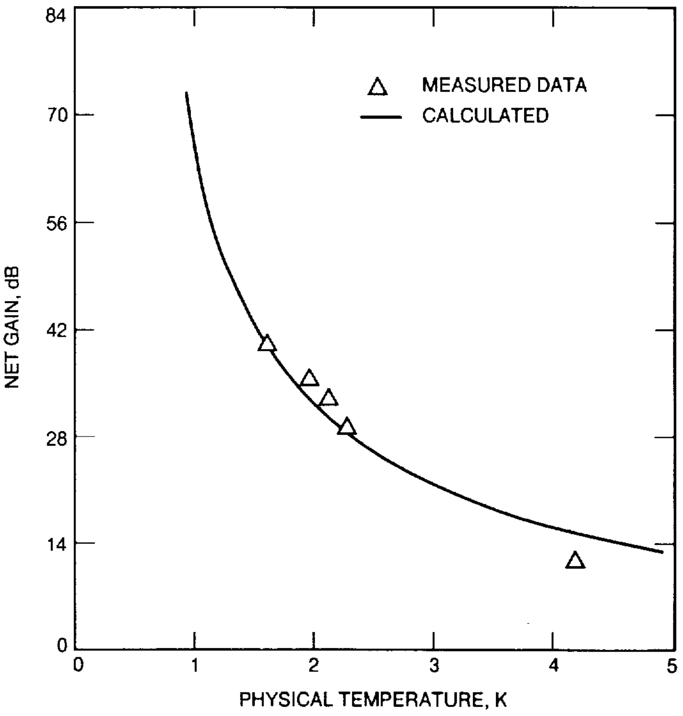

Fig. 6. Comparison of theoretical and measured maser net gain as a function of physical temperature.

N94-29673

TDA Progress Report 42-116

February 15, 1994

Simulation of Interference Between Earth Stations and Earth-Orbiting Satellites

D. F. Bishop
Telecommunications Systems Section

It is often desirable to determine the potential for radio frequency interference between Earth stations and orbiting spacecraft. This information can be used to select frequencies for radio systems to avoid interference or it can be used to determine if coordination between radio systems is necessary. A model is developed that will determine the statistics of interference between Earth stations and elliptical orbiting spacecraft. The model uses orbital dynamics, detailed antenna patterns, and spectral characteristics to obtain accurate levels of interference at the victim receiver. The model is programmed into a computer simulation to obtain long-term statistics of interference. Two specific examples are shown to demonstrate the model. The first example is a simulation of interference from a fixed-satellite Earth station to an orbiting scatterometer receiver. The second example is a simulation of interference from Earth-exploration satellites to a deep-space Earth station.

I. Theory and Models

Figure 1 contains an illustration of the interference geometry for Earth orbiters and an Earth station. Spacecraft 1 may be transmitting or receiving. Its antenna is pointed toward an arbitrary location on Earth. The Earth station may be transmitting or receiving. Its antenna is pointed toward spacecraft 2 or toward an arbitrary point described by the Earth station antenna azimuth and elevation.

Two interference scenarios are considered. In the first scenario, the Earth station is transmitting a signal toward spacecraft 2. This signal is unintentionally received by spacecraft 1. In the second scenario, spacecraft 1 is transmitting a signal that is unintentionally received by the Earth station.

The interference geometry shown in Fig. 1 is common to many interference scenarios that occur between two different radio systems. The level of interference that occurs at a victim receiver depends on angles γ_g and γ_{rg} and the distance D_{sf} that are shown in Fig. 1. The primary emphasis of the first part of this article is to show how to compute these parameters as a function of time. The antenna gain of spacecraft 1 in the direction of the Earth station is a function of angle γ_g. The path loss between spacecraft 1 and the Earth station is a function of the distance D_{sf}. Lastly, the antenna gain of the Earth station in the direction of spacecraft 1 is a function of angle γ_{rg}. The antenna gains and path loss are used to determine interference levels at the victim receiver as a function of time.

The interference angles and path distance in Fig. 1 may be computed with standard orbit determination methods [1]. The appendix contains detailed derivations of the angles and path distance.

The International Telecommunication Union (ITU) antenna pattern is used to calculate the Earth station antenna gain [2].

$$G(\gamma_{rg}) = G_p - 2.5 \times 10^{-3}\left(\frac{D\gamma_{rg}}{\lambda}\right)^2 \text{ (dBi)},$$

$$0 \text{ deg} \le \gamma_{rg} < \phi_m$$

$$= G_1, \quad \phi_m \le \gamma_{rg} < \phi_r$$

$$= 32 - 25 \times \log(\gamma_{rg}), \quad \phi_r \le \gamma_{rg} < 48 \text{ deg}$$

$$= -10, \quad 48 \text{ deg} \le \gamma_{rg} < 180 \text{ deg} \tag{1}$$

where

$G_p =$ peak antenna gain, dBi
$D =$ antenna diameter, m
$\lambda =$ wavelength $= c/f$, m
$G_1 = 2 + 15 \times \log(D/\lambda)$, dBi
$\phi_m = 20\lambda(G_p - G_1)^{1/2}/D$, deg
$\phi_r = 15.85(D/\lambda)^{-0.6}$, deg
$c =$ speed of light $= 3 \times 10^8$, m/sec
$f =$ frequency, Hz

This equation is valid for $D/\lambda \ge 100$. For $D/\lambda < 100$, a different pattern is used.

$$G(\gamma_{rg}) = G_p - 2.5 \times 10^{-3}\left(\frac{D\gamma_{rg}}{\lambda}\right)^2 \text{ (dBi)},$$

$$0 \text{ deg} \le \gamma_{rg} < \phi_m$$

$$= G_1, \quad \phi_m \le \gamma_{rg} < \frac{100\lambda}{D}$$

$$= 52 - 10 \log\left(\frac{D}{\lambda}\right) - 25 \times \log(\gamma_{rg}),$$

$$\frac{100\lambda}{D} \le \gamma_{rg} < 48 \text{ deg}$$

$$= 10 - 10 \log\left(\frac{D}{\lambda}\right),$$

$$48 \text{ deg} \le \gamma_{rg} < 180 \text{ deg} \tag{2}$$

The path loss from spacecraft 1 to the Earth station is computed.

$$PL = 20 \times \log\left(\frac{c}{[4\pi D_{sf} f]}\right) \text{ (dB)} \tag{3}$$

The angle γ_g in Fig. 1 is used to compute the antenna gain of spacecraft 1 in the direction of the Earth station. The spacecraft gain pattern is mission dependent.

II. Application 1: Simulation of Interference From a Fixed-Satellite Earth Station to a Scatterometer Receiver and Calculation of Scatterometer Power Flux Density

A. Introduction

The World Administrative Radio Conference of 1992 (WARC-92) allocated the 13.75- to 14-GHz frequency band to fixed-satellite (Earth-to-space) service on a primary basis. NASA scatterometers are permitted to use this band under the category of space research (spacecraft radiolocation) service on a secondary basis. The International Radio Consultative Committee (CCIR) formulated Task Group 7/3 (TG 7/3) to study the use of the 13.4- to 14-GHz frequency band by science services. One of the goals of TG 7/3 was to determine the effect that the new allocation (to fixed-satellite service) would have on NASA scatterometers near 14 GHz. The models developed in Section I and the appendix were used to generate a simulation of interference from a fixed-satellite Earth station to a scatterometer in Earth orbit. The scatterometer is represented by spacecraft 1 and the fixed-satellite spacecraft is represented by spacecraft 2 in Fig. 1. The fixed-satellite Earth station is represented by the Earth station in Fig. 1.

B. Analysis

The computation of the scatterometer antenna gain in the direction of the fixed-satellite Earth station depends on components of the angle γ_g in Fig. 1. The scatterometer antenna coordinate and spacecraft coordinate systems are illustrated in Fig. 2. There are six antenna beams, whose positions are defined by angles α, β, and γ. A vector in the antenna coordinate system can be transformed into a vector in the spacecraft coordinate system.

$$\mathbf{x_s} = \mathbf{A}\mathbf{x_a} \tag{4}$$

where

$$\mathbf{A} = \begin{bmatrix} A & D & G \\ B & E & H \\ C & F & I \end{bmatrix}$$

$$
\begin{aligned}
A &= \cos(\gamma)\cos(\alpha)\\
B &= \cos(\gamma)\cos(90-\alpha)\\
C &= \cos(90-\gamma)\\
D &= -\cos(90-\alpha)\cos(\beta)+\cos(90-\beta)\cos(90-\gamma)\cos(\alpha)\\
E &= \cos(\alpha)\cos(\beta)+\cos(90-\beta)\cos(90-\gamma)\cos(90-\alpha)\\
F &= -\cos(90-\beta)\cos(\gamma)\\
G &= -[\cos(90-\alpha)\cos(90-\beta)+\cos(90-\gamma)\cos(\beta)\cos(\alpha)]\\
H &= \cos(\alpha)\cos(90-\beta)-\cos(90-\gamma)\cos(\beta)\cos(90-\alpha)\\
I &= \cos(\beta)\cos(\gamma)
\end{aligned}
$$

A vector in the spacecraft coordinate system can be transformed into a vector in the orbit-plane coordinate system.

$$\mathbf{x_{wa}} = \mathbf{B}\mathbf{x_s} \tag{5}$$

where

$$\mathbf{B} = \begin{bmatrix} -\frac{y_w}{a} & 0 & -\frac{x_w}{a} \\ \frac{x_w}{a} & 0 & -\frac{y_w}{a} \\ 0 & -1 & 0 \end{bmatrix}$$

a = semimajor axis (Earth radii)

A vector in the orbit-plane coordinate system can be transformed into the right ascension–declination coordinate system.

$$\mathbf{x_{an}} = \mathbf{P}\mathbf{x_{wa}} \tag{6}$$

where **P** is defined in Eq. (A-3) in the appendix.

The vector (from the scatterometer spacecraft to the fixed-satellite Earth station) is transformed from the right ascension–declination coordinate system into the antenna-coordinate system. This is done by converting from the right ascension–declination system to the orbit-plane system, to the spacecraft system, and to the antenna system.

$$\mathbf{x_{sfa}} = -\mathbf{A}^T\mathbf{B}^T\mathbf{P}^T\mathbf{x_{fs}} = (x_{sfa}, y_{sfa}, z_{sfa})^T \tag{7}$$

These components are used to determine the off-axis angles in the narrow-beam plane and wide-beam plane of the fan beam antenna (Fig. 3). The antenna boresight points in the **k** direction.

$$
\begin{aligned}
\cos(\beta_g) &= \frac{z_{sfa}}{(x_{sfa}^2 + z_{sfa}^2)^{1/2}}\\
\cos(\alpha_g) &= \frac{z_{sfa}}{(y_{sfa}^2 + z_{sfa}^2)^{1/2}}
\end{aligned}
\tag{8}
$$

These angles are used to compute the narrow-beam and wide-beam components of the fan beam antenna gain.

$$
\begin{aligned}
G_1(\beta_g) &= -3\left(\frac{\beta_g}{0.173}\right)^2, \quad 0 \text{ deg} \le \beta_g < 0.5 \text{ deg}\\
&\quad \text{(narrow-beam component, dBi)}\\
&= -23.9 - 2.16\beta_g, \quad 0.5 \text{ deg} \le \beta_g < 5.6 \text{ deg}\\
&= -48, \quad 5.6 \text{ deg} \le \beta_g < 180 \text{ deg}\\
G_2(\alpha_g) &= 34 - 3\left(\frac{\alpha_g}{13.9}\right)^2, \quad 0 \text{ deg} \le \alpha_g < 20 \text{ deg}\\
&\quad \text{(wide-beam component, dBi)}\\
&= 35.83 - 0.402\alpha_g, \quad 20 \text{ deg} \le \alpha_g < 114 \text{ deg}\\
&= -14.5, \quad 114 \text{ deg} \le \alpha_g < 180 \text{ deg}
\end{aligned}
\tag{9}
$$

The fan beam antenna gain in the direction of the fixed-satellite Earth station is the summation of the narrow-beam and wide-beam components.

$$G_{fb} = G_1(\beta_g) + G_2(\alpha_g) \tag{10}$$

where the minimum value of G_{fb} is -14 dBi. At this point, there is enough information to compute the level of interference from the fixed-satellite Earth station to the scatterometer.

$$I = P_T + G(\gamma_{rg}) + SL + PL + G_{fb} \tag{11}$$

where

I = interference power spectral density (dBW/Hz)

P_T = fixed-satellite Earth station transmitter power

= 85 – 53.4 dBW

$G(\gamma_{rg})$ = fixed-satellite Earth station antenna gain in direction of scatterometer [Eq. (1)]

G_p = 53.4 dBi

D = 4.5 m

f = 13.995 GHz

SL = 10 × log (1/BW) (dBW/Hz)

BW = bandwidth = 2 MHz

PL = path loss from fixed-satellite Earth station to scatterometer [Eq. (3)], dB

G_{fb} = fan beam antenna gain in direction of fixed-satellite Earth station [Eq. (10)], dBi

The threshold level where interference is considered harmful to the scatterometer is −207 dBW/Hz.[1] The ground track of the scatterometer is computed to provide a visual indication of where the scatterometer is interfered with. The latitude of the ground track is computed first.

$$L_{agt} = 90 - \cos^{-1}\left(\frac{z}{a}\right) \tag{12}$$

Then, the longitude is computed by

$$\begin{aligned} L_{ogt} &= L_{o1} - \frac{360t}{1436.1}, \quad y \geq 0 \\ &= -L_{o1} - \frac{360t}{1436.1}, \quad y < 0 \end{aligned} \tag{13}$$

where

$$L_{o1} = \cos^{-1}\left[\frac{x}{a(\sin[90 - L_{agt}])}\right]$$

The longitude is transformed to obtain values between −180 and 180 deg.

C. Statistics and Probability of Interference

When the scatterometer is visible to the fixed-satellite Earth station, it is possible for interference to occur. The duration of these interference episodes varies with each orbit of the scatterometer. The scatterometer-simulation program computes the maximum and average times of an interference episode for the complete simulation period. Then histograms of these interference episodes are generated and the distribution of interference episodes may be estimated.

The scatterometer measures wind speed over the ocean. Taking this measurement requires that three antenna beams (beams 1–3 or beams 4–6) have no interference. The effect of interference from a fixed-satellite Earth station to the scatterometer is to create certain areas on the ocean where measurements of the wind speed cannot be taken by the scatterometer. It is possible that the scatterometer will have interference on the ascending portion of the orbit over a particular area of the Earth. When the scatterometer passes over this area on a descending portion of the orbit, it is possible that there will be no interference. Therefore, it is desirable to compute the statistics of interference for areas of the Earth.

For a simple example, the Earth is divided into areas of 100 km × 100 km near the equator. To facilitate programming, this is done by dividing the Earth into areas that are 0.89833-deg longitude in width and 0.89833-deg latitude in height. The width of these areas is 100 km at the equator, tapering off to a width of 0 km at the north and south poles. The antenna beams are very narrow in one direction and wide in the orthogonal direction. Therefore, the beams are approximated with 31 vectors in the wide-beam plane of the antenna. These vectors are spaced 1 deg apart, yielding a total coverage of 30 deg in the wide-beam plane. The point of intersection of an antenna vector with the Earth is determined.

Figure 4 shows the geometry. The unit vector $\mathbf{v}/|\mathbf{v}|$ is converted from antenna coordinates to the right ascension declination coordinate system. Then angle α_v can be calculated. The magnitude of $\mathbf{v}$ and the vector $\mathbf{R}$ can be determined by

$$\begin{aligned} -\mathbf{x} \bullet \frac{\mathbf{v}}{|\mathbf{v}|} &= a(\cos[\alpha_v]) \\ |\mathbf{R}|^2 &= a^2 + |\mathbf{v}|^2 - 2a|\mathbf{v}|\cos(\alpha_v) \\ \mathbf{R} &= \mathbf{x} + \mathbf{v} \end{aligned} \tag{14}$$

where

$$\frac{\mathbf{v}}{|\mathbf{v}|} = (v_x, v_y, v_z)^T$$

---

[1] M. Spencer, "Interference Criterion for Ku-Band Scatterometer," JPL Interoffice Memorandum (internal document), Jet Propulsion Laboratory, Pasadena, California, December 8, 1992.

This vector location is converted to latitude and longitude [Eqs. (12) and (13)]. Then, the area to which this point belongs is determined.

Wind-speed measurements on the right side of the scatterometer are taken by combining signals from beams 1–3 and, on the left side, by combining signals from beams 4–6. An area on the right side is considered to be covered if a vector from beams 1–3 intersects the area on the same orbit and the interference is below the receiver interference threshold for beams 1–3. Likewise, an area on the left side is considered to be covered if a vector from beams 4–6 intersects the area on the same orbit and the interference is below the receiver interference threshold for beams 4–6. The probability of interference is estimated as

$$p = \frac{n}{d} \tag{15}$$

where

$p =$ estimate of probability of area interference

$n =$ the number of times that an area is covered and interfered with

$d =$ the number of times that an area is covered

where the definitions of "covered" and "interfered with" are provided in the paragraph above.

D. Power Flux Density of the Scatterometer

Compatibility between terrestrial and spacecraft radio systems is often determined from the power flux density of the spacecraft on the surface of the Earth. Therefore, the power flux density of the scatterometer is computed. Figure 5 contains an illustration of the geometry.

$$P_{fd} = P_t + G_2(\alpha_g) + FSS \tag{16}$$

where

$P_{fd} =$ power flux density of scatterometer at surface of the Earth, dBW/m^2

$P_t =$ scatterometer transmit power, dBW

$G_2(\alpha_g) =$ scatterometer transmit antenna gain as a function of angle (α_g) in the wide-beam plane (Fig. 3), dBi

$FSS =$ free space spreading loss, dB/m^2

$= 10 \times \log\left(1/[4\pi(6378 \times 10^3 D_{se})^2]\right)$

The direction of the antenna gain vector is computed in the antenna coordinate system (Fig. 3).

$$\mathbf{x_{va}} = (0, \cos[90 - \alpha_g], \cos[\alpha_g])^T \tag{17}$$

This vector is transformed into the right ascension–declination coordinate system with Eqs. (4–6).

$$\mathbf{x_{vr}} = \mathbf{PBA}\mathbf{x_{va}} = (x_{vr}, y_{vr}, z_{vr})^T \tag{18}$$

Then, the angle (α_{se}) is computed by

$$\mathbf{x} \bullet \mathbf{x_{vr}} = -a[\cos(\alpha_{se})] \tag{19}$$

The distance between the scatterometer and the point of intersection with the Earth can be computed by

$$D_{se} = a[\cos(\alpha_{se})] - [(a[\cos(\alpha_{se})])^2 - (a^2 - 1)]^{1/2} \tag{20}$$

The vector to the point of intersection of the antenna gain vector and the Earth is computed by

$$\mathbf{x_{cr}} = \mathbf{x} + D_{se}\mathbf{x_{vr}} \tag{21}$$

The latitude and longitude of this point, L_{ae}, and L_{oe}, are computed with Eqs. (12) and (13).

It is desirable to know the power flux density as a function of elevation angle on the Earth. Therefore, the elevation of the vector $-\mathbf{x_{vr}}$ is computed.

$$E_l = \sin^{-1}(-\mathrm{x}_{vr}\cos[L_{ae}]\cos[L_{oe}] - y_{vr}\cos[L_{ae}]$$

$$\times \cos[90 - L_{oe}] - z_{vr}\cos[90 - L_{ae}]) \tag{22}$$

E. Simulation

Table 1 shows the results of a sample simulation. Interference is considered harmful if it exceeds the threshold shown on the table. The fixed-satellite Earth station and geostationary satellite are arbitrarily located. Interference is computed at 1-sec intervals. The estimated probability of interference is the number of interference minutes divided by simulation minutes. The scatterometer orbital period is approximately 100 min. Because the position of the orbit changes relative to the fixed-satellite Earth station, some orbits have no interference and other orbits have episodes of interference for varying amounts of time. The maximum and mean of these interference episodes are provided.

III. Application 2: Simulation of Interference from an Earth-Exploration Satellite to a Deep-Space Earth Station

A. Introduction

The Deep Space Network (DSN) uses the 8400- to 8450-MHz band for space-to-Earth transmissions. Earth-station receivers are protected by interference criteria that have been negotiated in international forums. Other radio services that use this band are aware of the interference criteria and limit their transmissions accordingly. However, radio services that transmit in adjacent bands may not be fully aware of their emissions in the DSN band. If these out-of-band emissions are strong enough, they can disrupt DSN communications.

B. Power Spectral Density of Adjacent Band Interferers

The power spectral density from an Earth-orbiting spacecraft is computed with the following equation:

$$P_{SD} = P_T + SD(f) + G_T + PL_1 + G_R \qquad (23)$$

where

P_{SD} = power spectral density of interfering spacecraft at a deep-space Earth station receiver, dBW/Hz

P_T = spacecraft transmitter power, dBW

$SD(f)$ = spectral density of spacecraft transmitter (Table 2), dB/Hz

G_T = peak transmit antenna gain, dBi

PL_1 = path loss, dB

$= 20 \times \log [c/(4\pi A_m f)]$

c = speed of light = 3×10^5 km/s

A_m = minimum orbit altitude, km

f = frequency, Hz

G_R = DSN receive antenna gain = 74 dBi

The spectral density is computed from the equations shown in Table 2 [3].[2]

In particular, the Earth Observing System (EOS) program is planning the launch of several spacecraft [4] that will have spectral emissions in the 8400- to 8450-MHz band. Using Eq. (23), the emission of an EOS spacecraft is determined to exceed the DSN interference criterion of -220.9 dBW/Hz by about 45 dB in the 8400- to 8450-MHz band. Equation (23) produces a worst-case power spectral density at the deep-space Earth station because it uses peak antenna gains and the minimum orbit altitude to compute the path loss. Statistics of the interference power spectral density are provided next.

C. Simulation of Interference to a Deep-Space Earth Station from Low Earth-Orbiting Spacecraft in an Adjacent Band

It is useful to know the amount of time that the power spectral density from an adjacent-band spacecraft exceeds the interference criteria of the deep-space Earth station. Figure 6 shows a plot of satellite visibility to an Earth station versus orbit altitude. It is assumed that the satellite passes directly over the Earth station with a circular orbit. The geometry is illustrated in Fig. 7. Visibility time is computed as

$$T_{vis} = \frac{3600 T_o \theta}{\pi} (\text{sec}) \qquad (24)$$

where

T_o = orbital period, hr [5]

$= 2\pi(A + R)^{3/2}/\mu^{1/2}$

A = orbit altitude, km

R = Earth radius = 6378 km

μ = Earth gravitation, mass product

$= 5.17 \times 10^{12}$ km^3/hr^2

θ = central angle, rad

$= \cos^{-1}(R/[R + A])$

If the satellite has sufficient power, it can produce line-of-sight interference to the Earth station during its orbit visibility time. This can be a significant amount of time even for a low-altitude spacecraft. Interference times for

---

[2] B. Tunstall, "Transmit Filtering for EOS Direct Access System Downlink," Memorandum to J. Scott (internal document), Goddard Space Flight Center, Greenbelt, Maryland, July 10, 1992.

actual spacecraft systems depend on transmitter power, orbits, antenna gains, etc. Figure 1 can be used to illustrate the interference geometry. The EOS spacecraft is represented with spacecraft 1. The deep-space Earth station points at a specified azimuth and elevation. The EOS spacecraft is in a circular orbit around the Earth with its antenna pointing toward the center of the Earth. The angle γ_{rg} between the boresight of the deep-space Earth station and the vector to the EOS spacecraft is computed with Eqs. (A-15) and (A-17) in the appendix. The deep-space Earth station (70-m) antenna gain in the direction of the EOS spacecraft is computed with Eq. (1).

$$\begin{aligned} G(\gamma_{rg}) &= 74 - 0.0025\ (1960\gamma_{rg})^2 (\text{dBi}), \\ &\qquad 0 \text{ deg} \le \gamma_{rg} < 0.0485 \text{ deg} \\ &= 51.4, \quad 0.0485 \text{ deg} \le \gamma_{rg} < 0.168 \text{ deg} \\ &= 32 - 25\ \log\ (\gamma_{rg}), \quad 0.168 \text{ deg} \le \gamma_{rg} < 48 \text{ deg} \\ &= -10, \quad 48 \text{ deg} \le \gamma_{rg} \le 180 \text{ deg} \end{aligned} \tag{25}$$

The angle γ_g between the antenna boresight of the EOS spacecraft and the vector to the deep-space Earth station is computed with Eqs. (A-19) and (A-20) in the appendix. The EOS spacecraft antenna gain in the direction of the deep-space Earth station is computed. The model is a set of straight line segments that approximates the actual pattern.[3]

$$\begin{aligned} G_e(\gamma_g) &= -3.5 + \frac{2.5\gamma_g}{3} (\text{dBi}), \quad 0 \text{ deg} \le \gamma_g < 3 \text{ deg} \\ &= 0.091 - \frac{4\gamma_g}{11}, \quad 3 \text{ deg} \le \gamma_g < 14 \text{ deg} \\ &= -8.5 + \frac{14\gamma_g}{56}, \quad 14 \text{ deg} \le \gamma_g < 70 \text{ deg} \\ &= 84.25 - \frac{21.5\gamma_g}{20}, \quad 70 \text{ deg} \le \gamma_g < 90 \text{ deg} \\ &= -14.5, \quad 90 \text{ deg} \le \gamma_g \le 180 \text{ deg} \end{aligned} \tag{26}$$

The interference power spectral density level at the deep-space Earth station receiver is computed by

$$I_o = SD(f) + P_e + G_e(\gamma_g) + PL + G(\gamma_{rg}) \tag{27}$$

where P_e = EOS transmitter power = 11.8 dBW.

The first simulation on Table 3 is for one EOS spacecraft transmitting in the direct playback mode (QPSK, 150 MSPS per channel). Statistics of the interference are provided. The second simulation in Table 3 is for five different spacecraft. The antenna pattern for the last four spacecraft is the same as for the EOS antenna [Eq. (26)] except for additive constants to provide the correct peak antenna gain for each spacecraft. Each interference event is composed of a number of interference samples that occur at 0.5-sec intervals. Samples are plotted on Fig. 8 for the second simulation in Table 3. At each sample interval, the amount of interference exceeding the −220.9 dBW/Hz criterion [6] is plotted. Some events have only one sample (0.5 sec of interference) and some have up to 20 samples (10 sec of interference). The simulation ran on a Sun workstation.

The antenna pattern of the deep-space Earth station provided in Eq. (25) was developed a number of years ago for generalized Earth stations. More accurate gain data have been made available for the 70-m antennas of the DSN.[4] These data have been fitted with a number of equations.

$$\begin{aligned} G_m(\gamma_{rg}) &= 74.15 - 0.0025(2400\gamma_{rg})^2 (\text{dBi}), \\ &\qquad 0 \text{ deg} \le \gamma_{rg} < 0.0376 \text{ deg (dBi)} \\ &= 53.7, \\ &\qquad 0.0376 \text{ deg} \le \gamma_{rg} < 0.04 \text{ deg} \\ &= 57.4 - 0.025(1350[\gamma_{rg} - 0.049])^2, \\ &\qquad 0.04 \text{ deg} \le \gamma_{rg} < 0.0626 \text{ deg} \\ &= 49, \\ &\qquad 0.0626 \text{ deg} \le \gamma_{rg} < 0.0905 \text{ deg} \\ &= 25 - 23\ \log\ (\gamma_{rg}), \\ &\qquad 0.0905 \text{ deg} \le \gamma_{rg} < 33.2 \text{ deg} \\ &= -10, \\ &\qquad 33.2 \text{ deg} \le \gamma_{rg} < 180 \text{ deg} \end{aligned} \tag{28}$$

---

[3] J. Hart, "Interference Analysis for EOS AM Direct Access System," Interoffice Memorandum (internal document), Stanford Telecom, Seabrook, Maryland, July 7, 1992.

[4] D. Bathker, personal communication, DSN International Frequency Management Program, TDA Planning Section, Jet Propulsion Laboratory, Pasadena, California, October 1993.

Figure 9 contains plots of antenna data, curve fits from Eq. (28), and the ITU pattern [2]. Equation (28) fits the data quite well for this application. The ITU model overestimates the gain data in every region except that from 0.04 to 0.06 deg. It is expected that the interference from low-Earth-orbit spacecraft would be reduced when the DSN Earth station antenna is modeled with Eq. (28).

The computer simulation was conducted with $G_m(\gamma_{rg})$ replacing $G(\gamma_{rg})$ in Eq. (27). In the first simulation, one EOS spacecraft transmitted in the direct playback mode. In the second simulation, five different spacecraft were transmitting. The interference percentage is one-fourth of that in Table 3 with the new antenna model for one EOS spacecraft. For five spacecraft, the interference percentage is approximately one-fourth of that in Table 3 with the new antenna model.

All of the simulations use an elevation of 5 deg and an azimuth of 100 deg for the deep-space Earth station antenna. When larger elevation angles are used, the interference percentages are decreased. This is because the spacecraft spends less time within the same Earth station antenna beamwidth at higher elevations. The interference levels are computed at 0.5-sec intervals in all simulations.

IV. Summary and Conclusions

A model is developed that will determine the statistics of interference between Earth stations and elliptical orbiting spacecraft. Detailed models of the geometry of Earth orbiters and Earth stations are shown. It is possible to determine antenna gains and path distances quite accurately with these models. Interference levels at the victim receiver are determined by antenna gains, path distances, and radio system characteristics. The models may be used to predict interference in a wide variety of scenarios that involves Earth stations and Earth orbiters. Two examples that make use of these models are shown.

The first example is a simulation of interference from a fixed-satellite Earth station to an orbiting scatterometer receiver. Table 1 contains a summary of a simulation that was performed. Models were developed to estimate the probability that certain areas of the Earth would not have accurate measurements due to interference. Also, the power flux density on Earth of the scatterometer signal as a function of elevation angle is determined. Results from the simulation showed that the scatterometer should use a different frequency to avoid interference from several fixed-satellite Earth stations. Simulation results compared favorably with other simulation programs.[5]

The second example is a simulation of interference from an Earth-exploration satellite to a deep-space Earth station. Worst-case levels of power spectral density from low Earth orbiters at the station are computed. These levels exceed the interference criteria of the deep-space Earth station in the 8400- to 8450-MHz band. A simulation of interference from low Earth orbiters to a deep-space Earth station is conducted. This simulation computes the path loss and off-axis antenna gains as a function of orbital position of the low Earth orbiter. It can be used to predict the statistics of interference to the deep-space Earth station. Table 3 contains a summary of two different simulations that were performed. Results from the simulation showed that excessive coordination could be avoided if Earth-exploration satellites reduced their emissions by 20 dB in the 8400- to 8450-MHz band. The interference statistics are in close agreement with other simulations.[6]

The simulations are programmed in Fortran and run on a Sun workstation. The author may be contacted for instructions on the operation of the simulation programs.

---

[5] J. Hart, personal communication, Stanford Telecom, Seabrook, Maryland, April 1993.

[6] J. Hart, "Compliance of EOS Direct Access System with DSN Protection Criteria," Interoffice Memorandum (internal document), Stanford Telecom, Seabrook, Maryland, May 17, 1993.

Acknowledgments

The author gratefully acknowledges the help of Dan Bathker, Benito G.-Luaces, J. Hart (Stanford Telecom), Mike Spencer, and Carroll Winn in the development and testing of the models and simulations. Charles Ruggier is acknowledged for review of the manuscript.

Table 1. Example of an interference simulation from a fixed-satellite Earth station to an orbiting scatterometer receiver.

Parameter	Value
Scatterometer interference threshold, dBW/Hz	−207
Scatterometer altitude, km	797
Fixed-satellite Earth station	85-dBW EIRP, 2-MHz bandwidth 4.5-m antenna 34 deg N, 128 deg W
Geostationary satellite	196 deg W
Simulation minutes	10,000
Number of interference computations per minute	60
Antenna beam element	1
Number of interference minutes	2.067
Estimated probability of interference	2.067×10^{-4}
Maximum period of an interference episode, min	0.567
Mean period of an interference episode, min	0.129

Table 2. Spectral density equations.

Modulation	Spectral density (baseband)[a]
Quadriphase-shift keying	$(2/SR) \times [\sin(2\pi f/SR)]^2/(2\pi f/SR)^2$
Unbalanced quadriphase-shift keying	$(r_I/SR_I) \times [\sin(\pi f/SR_I)]^2/(\pi f/SR_I)^2$ $+(r_Q/SR_Q) \times [\sin(\pi f/SR_Q)]^2/(\pi f/SR_Q)^2$
Phase-shift keying	$(1/SR) \times [\sin(\pi f/SR)]^2/(\pi f/SR)^2$
Minimum-shift keying	$[16/(\pi^2 SR)] \times [\cos(2\pi f/SR)]^2/(1 - 16f^2/SR^2)^2$

SR = total output symbol rate
f = frequency[a]
r_I = ratio of power in I channel to total power
SR_I = symbol rate of I channel
r_Q = ratio of power in Q channel to total power
SR_Q = symbol rate of Q channel

---

[a] Replace f with $f - f_c$ (where f_c is the center frequency) to obtain the spectral density at the center frequency.

Table 3. Simulation results comparing one EOS spacecraft to five other spacecraft—EOS (DP), SPOT-4, IRS-1B, POEM 1, and RADARSAT-1.

Parameter	EOS spacecraft	Five spacecraft
Duration of simulation, min	525,600 (1 year)	525,600 (1 year)
Interference events	37	128
Interference percentage	8.89×10^{-4}	2.39×10^{-3}
Interference duration, sec		
Shortest	3.5	0.5
Longest	10	10
Average	7.58	5.90
Time between interference events, days		
Shortest	1.99	0.08
Longest	13.44	12.83
Average	10.11	2.87

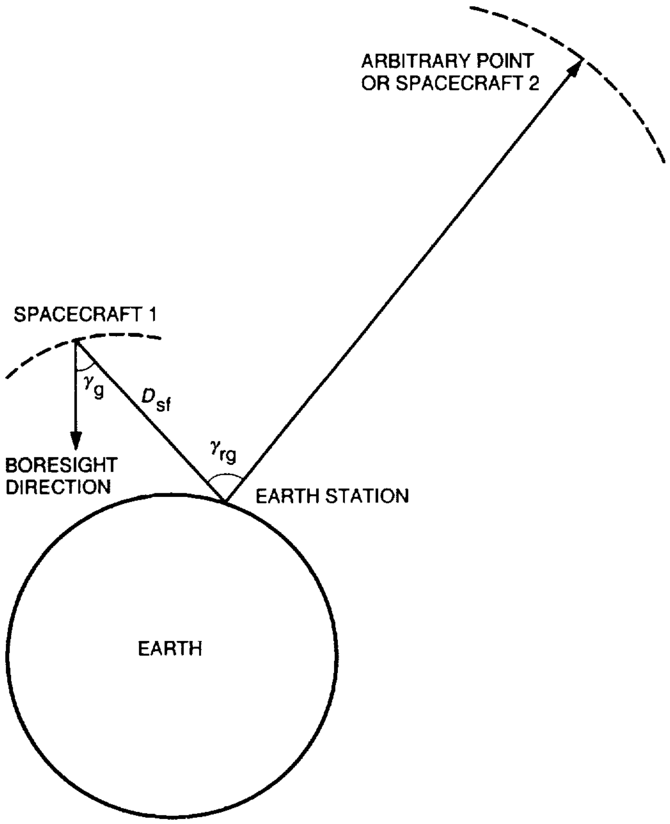

Fig. 1. Interference geometry for Earth orbiters and an Earth station.

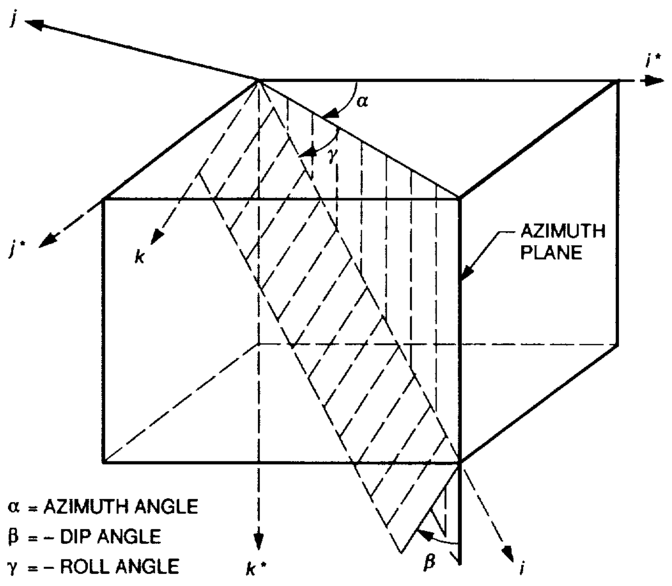

Fig. 2. Antenna and spacecraft coordinate systems.

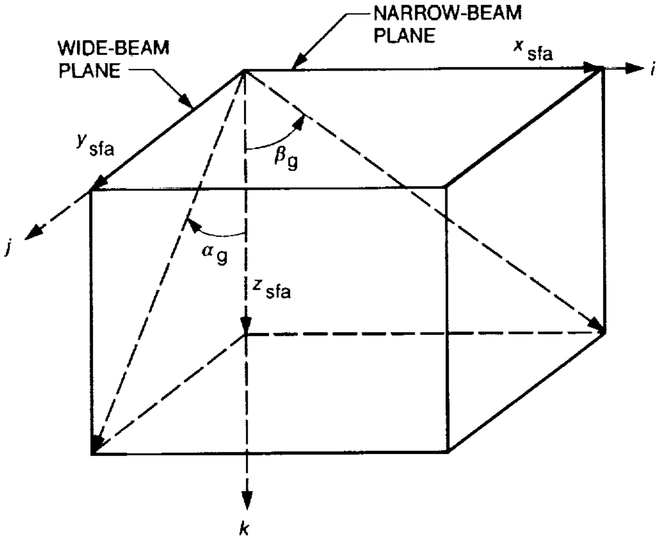

Fig. 3. Off-axis angles in the wide-beam and narrow-beam planes.

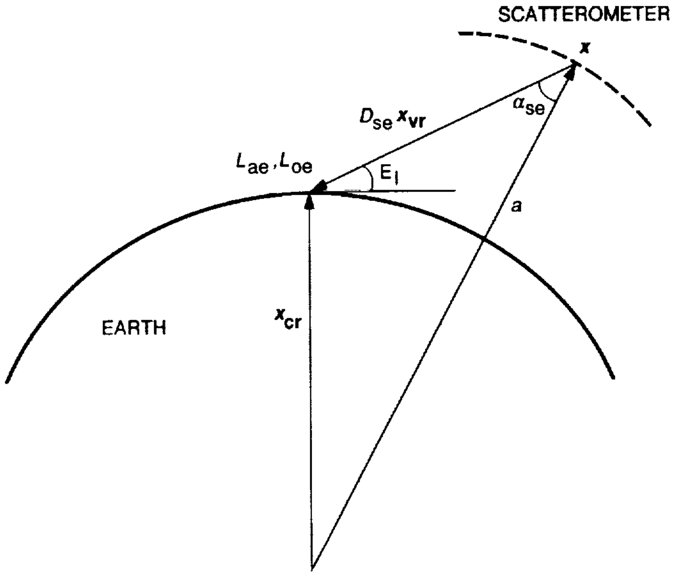

Fig. 5. Geometry for scatterometer power flux density calculation.

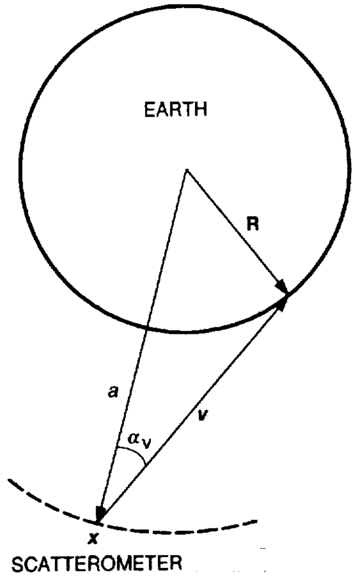

Fig. 4. Intersection of antenna beam with Earth.

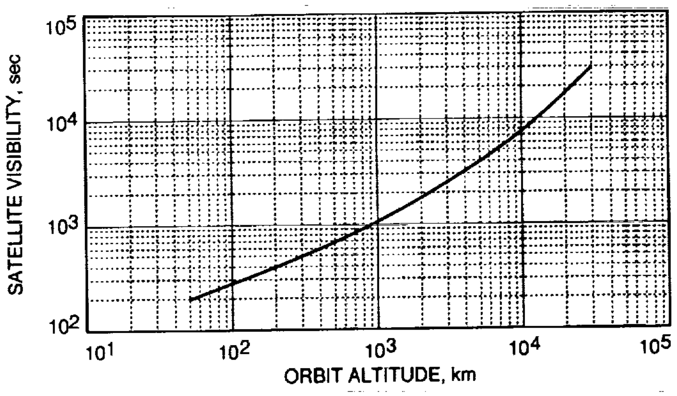

Fig. 6. Satellite visibility to an Earth station versus orbit altitude for circular satellite orbits.

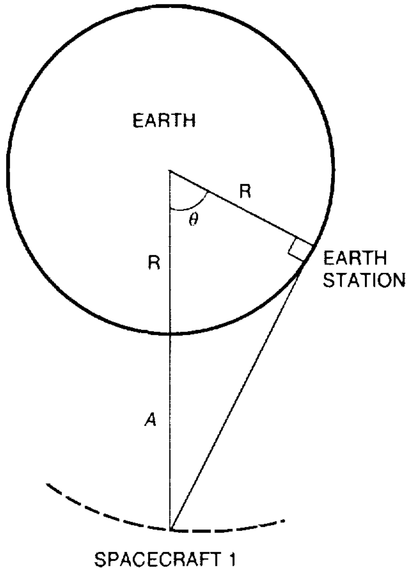

Fig. 7. Geometry for spacecraft visibility time calculation.

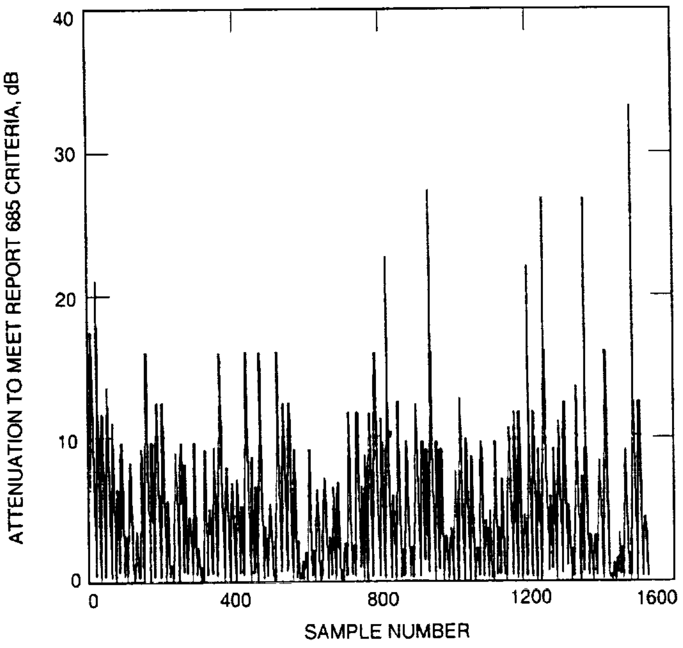

Fig. 8. Interference samples exceeding Report 685 for five other spacecraft: EOS (DP), SPOT-4, IRS-1B, POEM 1, and RADARSAT-1.

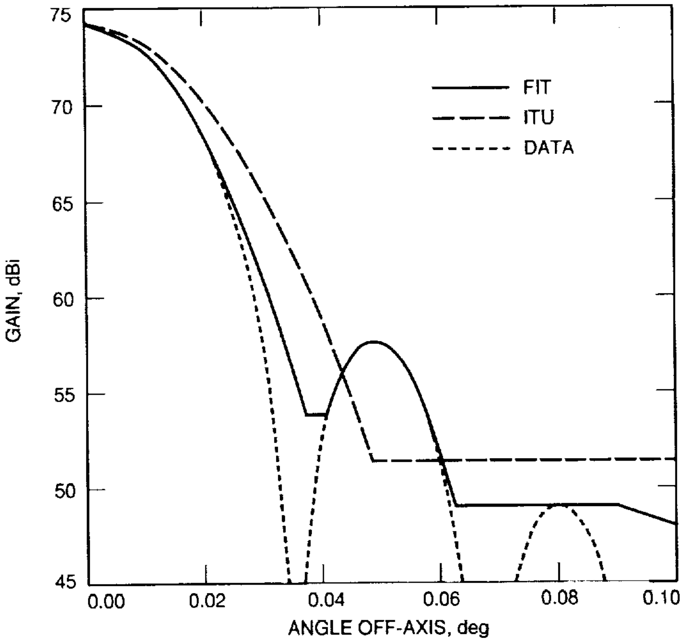

Fig. 9. Gain pattern for DSN 70-m antenna.

Appendix

Interference Geometry and Orbital Dynamics Models

The spacecraft orbit plane is illustrated in Fig. A-1. The position of spacecraft 1 in its orbit plane is computed first.

$$\mathbf{x_w} = (a[\cos(E)] - ae, a[1-e^2]^{1/2}[\sin(E)], 0)^T \quad \text{(A-1)}$$

where

$a =$ semimajor axis, Earth radii

$E =$ eccentric anomaly, rad

$M = E - e(\sin[E]) =$ mean anomaly, rad

$= \mathrm{nt}$

$e =$ orbit eccentricity

$n = 0.07437/a^{3/2}$, rad/min

$t =$ time, min

Newton's iteration [7] may be used to solve for the eccentric anomaly, as follows:

$$E_0 = M + \frac{e(\sin[M])}{1 - \sin[M+e] + \sin[M]}$$

$$M_k = E_k - e(\sin[E_k])$$

$$E_{k+1} = E_k + \frac{M - M_k}{1 - e[\cos(E_k)]} \quad \text{(A-2)}$$

where

$$k = 0, 1, 2, \ldots$$

The position of spacecraft 1 in the orbit plane is converted to its position in the right ascension–declination coordinate system.

$$\mathbf{x} = \mathbf{P}\mathbf{x_w} = (x, y, z)^T \quad \text{(A-3)}$$

where

$$\mathbf{P} = \begin{bmatrix} P_x & Q_x & W_x \\ P_y & Q_y & W_y \\ P_z & Q_z & W_z \end{bmatrix}$$

$$\begin{aligned}
P_x &= \cos(\omega)\cos(\Omega) - \sin(\omega)\sin(\Omega)\cos(i) \\
P_y &= \cos(\omega)\sin(\Omega) + \sin(\omega)\cos(\Omega)\cos(i) \\
P_z &= \sin(\omega)\sin(i) \\
Q_x &= -\sin(\omega)\cos(\Omega) - \cos(\omega)\sin(\Omega)\cos(i) \\
Q_y &= -\sin(\omega)\sin(\Omega) + \cos(\omega)\cos(\Omega)\cos(i) \\
Q_z &= \cos(\omega)\sin(i) \\
W_x &= \sin(\Omega)\sin(i) \\
W_y &= -\cos(\Omega)\sin(i) \\
W_z &= \cos(i)
\end{aligned}$$

$\omega =$ argument of perigee

$\Omega =$ longitude of the ascending node

$i =$ orbital inclination

The location of the Earth station is determined in the right ascension–declination coordinate system.

$$\begin{aligned}
\mathbf{x_g} &= (\sin[\Theta]\cos[\theta], \sin[\Theta]\sin[\theta], \cos[\Theta])^T \\
&= (x_g, y_g, z_g)^T \quad \text{(A-4)}
\end{aligned}$$

where

$\Theta = 90 - l_a$

$\theta = l_o + k + 360t/1436.1$

$k =$ an arbitrary constant used to rotate the Earth station relative to the orbit plane

$l_a =$ Earth station latitude

$l_o =$ Earth station longitude

The Earth station may be pointed at another satellite (spacecraft 2) or its boresight direction may be described with azimuth and elevation notation. If it is pointed at spacecraft 2, that satellite's position may be described with Eqs. (A-1) to (A-3).

$$\mathbf{x_2} = (x_2, y_2, z_2)^T \tag{A-5}$$

A special case exists when spacecraft 2 is in a geostationary orbit. It may be assumed that it is located in the equatorial plane. The location is determined in the right ascension–declination coordinate system.

$$\mathbf{x_2} = \mathbf{x_{gg}} = 6.6257(\sin{[\Theta_g]}\cos{[\theta_g]}, \sin{[\Theta_g]}\sin{[\theta_g]}, 0)^T \tag{A-6}$$

where

$\Theta_g = 90$

$\theta_g =$ geostationary longitude $+k + 360t/1436.1$

If the Earth station is pointed at a specific elevation and azimuth, its boresight direction may be converted from azimuth–elevation coordinates to Earth-centered coordinates as

$$\mathbf{x_{ec}} = \mathbf{C}\mathbf{x_{ae}} = (x_{ec}, y_{ec}, z_{ec})^T \tag{A-7}$$

where

$$\mathbf{C} = \begin{bmatrix} C_1 & C_2 & C_3 \\ C_4 & C_5 & C_6 \\ C_7 & C_8 & C_9 \end{bmatrix}$$

$C_1 = \cos{(l_o)}\cos{(90 - l_a)}$

$C_2 = -\cos{(90 - l_o)}$

$C_3 = \cos{(l_a)}\cos{(l_o)}$

$C_4 = \cos{(90 - l_o)}\cos{(90 - l_a)}$

$C_5 = \cos{(l_o)}$

$C_6 = \cos{(l_a)}\cos{(90 - l_o)}$

$C_7 = -\cos{(l_a)}$

$C_8 = 0$

$C_9 = \cos{(90 - l_a)}$

$\mathbf{x_{ae}} = (-\cos{[el]}\cos{[az]}, \cos{[el]}\sin{[az]}, \sin{[el]})^T$

el = elevation of Earth station antenna

az = azimuth of Earth station antenna

These coordinates are converted to spherical coordinates, as follows:

$$\Theta_b = \cos^{-1}\left(\frac{z_{ec}}{r_{ec}}\right) \text{ (deg)}$$

$$\theta_b = \cos^{-1}\left(\frac{x_{ec}}{r_{xy}}\right) + k + \frac{360t}{1436.1}, y_{ec} \geq 0 \text{ (deg)}$$

$$= 360 - \cos^{-1}\left(\frac{x_{ec}}{r_{xy}}\right) + k + \frac{360t}{1436.1}, y_{ec} < 0 \tag{A-8}$$

where

$r_{ec} = (x_{ec}^2 + y_{ec}^2 + z_{ec}^2)^{1/2}$

$r_{xy} = (x_{ec}^2 + y_{ec}^2)^{1/2}$

Finally, these coordinates are converted to the right ascension–declination coordinate system by

$$\mathbf{x_{bor}} = r_{ec}(\sin{[\Theta_b]}\cos{[\theta_b]}, \sin{[\Theta_b]}\sin{[\theta_b]}, \cos{[\Theta_b]})^T \tag{A-9}$$

The line-of-sight visibility of the Earth station to spacecraft 1 is determined. Figure A-2 illustrates the central angle between the two. The central angle between spacecraft 1 and the Earth station is computed as

$$\mathbf{x} \bullet \mathbf{x_g} = |\mathbf{x}|\cos{(\gamma)} \tag{A-10}$$

where γ = central angle between spacecraft 1 and the Earth station.

Figure A-2 also illustrates the limit of visibility. The constraint is that the line between spacecraft 1 and the Earth station is tangent to the Earth. Central angles that are less than or equal to this angle indicate that spacecraft 1 is visible to the Earth station.

$$\gamma_v = \cos^{-1}\left(\frac{1}{|\mathbf{x_v}|}\right) \tag{A-11}$$

The visibility condition is stated as

$$\gamma \leq \gamma_v \tag{A-12}$$

Interference between spacecraft 1 and the Earth station can occur only if they are visible. If spacecraft 1 is visible, additional computations are necessary. The angle γ_{rg} on Fig. 1 is used to compute the antenna gain of the Earth station in the direction of spacecraft 1. The vector from the Earth station to spacecraft 2 is computed as

$$\mathbf{x_{fg}} = \mathbf{x_2} - \mathbf{x_g} \tag{A-13}$$

A special case occurs when spacecraft 2 is a geostationary satellite, as follows:

$$\mathbf{x_2} = \mathbf{x_{gg}} \tag{A-14}$$

If the pointing of the Earth station antenna is described in terms of azimuth and elevation, then

$$\mathbf{x_{fg}} = \mathbf{x_{bor}} \tag{A-15}$$

The vector from the Earth station to spacecraft 1 is computed as

$$\mathbf{x_{fs}} = \mathbf{x} - \mathbf{x_g} \tag{A-16}$$

The angle between these two vectors [Eqs. (A-13) and (A-16)] can be used to determine the antenna gain of the Earth station in the direction of spacecraft 1.

$$\mathbf{x_{fg}} \bullet \mathbf{x_{fs}} = |\mathbf{x_{fg}}||\mathbf{x_{fs}}| \cos\,(\gamma_{rg}) \tag{A-17}$$

The distance between the Earth station and spacecraft 1 is computed as

$$D_{sf} = 6378|\mathbf{x_g} - \mathbf{x}|(km) \tag{A-18}$$

The angle between the antenna boresight of spacecraft 1 and the direction to the Earth station is computed as

$$\mathbf{x_{b1}} \bullet (-\mathbf{x_{fs}}) = |\mathbf{x_{b1}}||\mathbf{x_{fs}}| \cos\,(\gamma_g) \tag{A-19}$$

where $\mathbf{x_{b1}}$ = antenna boresight vector of spacecraft 1.

A special case occurs when the antenna of spacecraft 1 points toward the center of the Earth.

$$\mathbf{x_{b1}} = -\mathbf{x} \tag{A-20}$$

References

[1] P. R. Escobal, *Methods of Orbit Determination*, New York: Wiley, 1976.

[2] *International Telecommunication Union Radio Regulations*, ISBN 92-61-01221-3, vol. 2, 1982.

[3] S. Pasupathy, "Minimum Shift Keying: A Spectrally Efficient Modulation," *IEEE Communications Society Magazine*, vol. 17, no. 4, pp. 14–22, July 1979.

[4] Goddard Space Flight Center, *Mission Requirements and Data Systems Support Forecast*, Greenbelt, Maryland, pp. 18–23, April–May 1993.

[5] *Reference Data for Radio Engineers*, New York: Howard W. Sams & Co., Inc., 1982.

[6] CCIR, "Protection Criteria and Sharing Considerations Relating to Deep-Space Research," *Reports of the CCIR, annex to vol. II, Space Research and Radioastronomy Services*, CCIR Report 685-3, Geneva, Switzerland, pp. 281–302, 1990.

[7] R. H. Battin, *Introduction to the Mathematics and Methods of Astrodynamics*, New York: American Institute of Aeronautics and Astronautics, 1987.

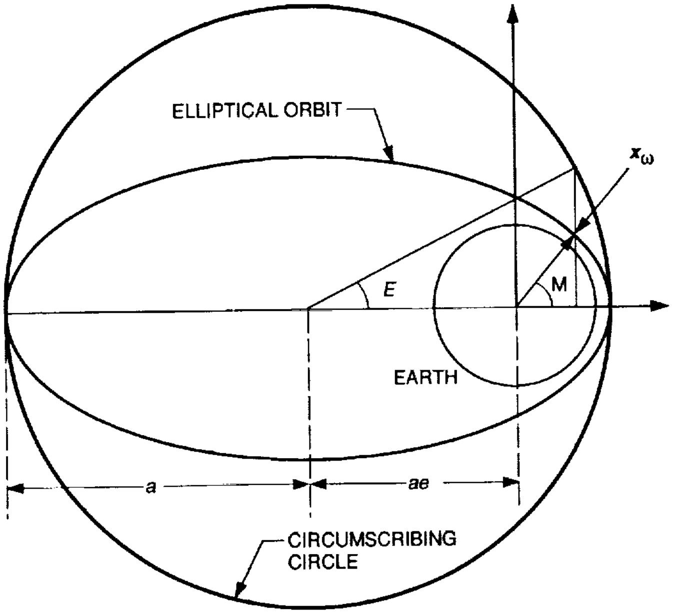

Fig. A-1. Spacecraft orbit plane geometry.

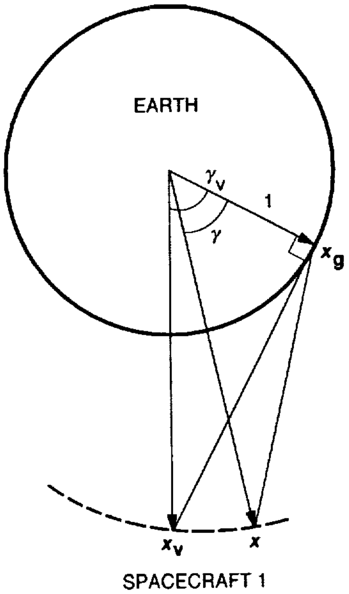

Fig. A-2. Visibility between a spacecraft and an Earth station.

Author Index,[1] 1993

The Telecommunications and Data Acquisition Progress Report

42-113, January–March, May 15, 1993
42-114, April–June, August 15, 1993
42-115, July–September, November 15, 1993
42-116, October–December, February 15, 1994

Abbate, S. F.

42-114 Stability Measurements of the Radio Science System at the 34-m High-Efficiency Antennas, pp. 112–139.

See Pham, T. T.

Abusali, P. A. M.

42-115 Improved Thermal Force Modeling for GPS Satellites, pp. 32–41.

See Vigue, Y.

Alvarez, L. S.

42-115 Analysis of Open-Loop Conical Scan Pointing Error and Variance Estimators, pp. 81–90.

42-116 The Rb 780-Nanometer Faraday Anomalous Dispersion Optical Filter: Theory and Experiment, pp. 71–85.

See Yin, B.

Andrews, M. M.

42-113 Galileo Post-Gaspra Cruise and Earth-2 Encounter, pp. 106–117.

See Beyer, P. E.

Asmar, S. W.

42-113 The Flight Performance of the Galileo Orbiter USO, pp. 184–202.

See Morabito, D. D.

42-114 The Flight Performance of the Galileo Orbiter USO, pp. 327–345.

See Morabito, D. D.

Bartos, R. D.

42-113 An Analysis of the 70-Meter Antenna Hydrostatic Bearing by Means of Computer Simulation, pp. 147–173.

Bautista, J. J.

42-114 Insertion Loss and Noise-Temperature Contribution of High-Temperature Superconducting Bandpass Filters Centered at 2.3 and 8.45 GHz, pp. 61–67.

See Prater, J. L.

42-115 Cryogenic, Low-Noise High Electron Mobility Transistor Amplifiers for the Deep Space Network, pp. 65–80.

Belongie, M.

42-114 Enhanced Decoding for the Galileo S-Band Mission, pp. 96–111.

See Dolinar, S.

---

[1] In the case of joint authorship, the reader is referred to the citation under the first author, where all the authors of the article are listed.

Flanagan, M. J.

42-115 Spur-Reduced Digital Sinusoid Synthesis, pp. 91–104.

G. A. Zimmerman

Folkner, W. M.

42-113 Precise Tracking of the Magellan and Pioneer Venus Orbiters by Same-Beam Interferometry—Part II: Orbit Determination Analysis, pp. 22–36.

J. S. Border, S. Nandi, and K. S. Zukor

Franco, M.

42-116 Determining Noise Temperatures in Beam Waveguide Systems, pp. 42–52.

See Imbriale, W.

Fugate, R. Q.

42-114 GOPEX at the Starfire Optical Range, pp. 255–279.

Gawronski, W. K.

42-115 Beam-Waveguide Antenna Servo Design Issues for Tracking Low-Earth-Orbiting Satellites, pp. 135–152.

J. A. Mellstrom

42-115 Experimental Modification and Identification of the DSS-13 Antenna Control System Model, pp. 42–53.

See Racho, C. S.

Glass, G. W.

42-116 X-Band Ultralow-Noise Maser Amplifier Performance, pp. 246–253.

G. G. Ortiz and D. L. Johnson

Goddard, R. E.

42-113 Gravity Referenced Elevation Encoder Development, pp. 63–73.

Guinn, J.

42-116 TOPEX/POSEIDON Operational Orbit Determination Results Using Global Positioning Satellites, pp. 163–174.

J. Jee, P. Wolff, F. Lagattuta, T. Drain, and V. Sierra

Gutierrez-Luaces, B. O.

42-114 Performance Results of a Digital Test Signal Generator, pp. 140–153.

M. Marina and B. Parham

Haines, B. J.

42-115 New Approaches for Tracking Earth Orbiters Using Modified GPS Ground Receivers, pp. 17-31.

See Lichten, S. M.

42-115 A Review of GPS-Based Tracking Techniques for TDRS Orbit Determination, pp. 1–16.

S. M. Lichten, R. P. Malla, and S.-C. Wu

Heflin, M. B.

42-114 Improved Treatment of Global Positioning System Force Parameters in Precise Orbit Determination Applications, pp. 14–20.

See Vigue, Y.

Hinedi, S.

42-116 A Comparison of Full-Spectrum and Complex-Symbol Combing Techniques for the Galileo S-Band Mission, pp. 128–162.

See Million, S.

42-116 Effects of Low Sampling Rate in the Digital Data-Transition Tracking Loop, pp. 204–222.

See Mileant, A.

Hops, J. M.

42-114 Formal Functional Test Designs With a Test Representation Language, pp. 154–169

Huang, J.

42-116 A 32-GHz Microstrip Array Antenna for Microspacecraft Application, pp. 190–203.

Imbriale, W.

42-116 Determining Noise Temperatures in Beam Waveguide Systems, pp. 42–52.

W. Veruttipong, T. Otoshi, and M. Franco

Jee, J.

42-116 TOPEX/POSEIDON Operational Orbit Determination Results Using Global Positioning Satellites, pp. 163–174.

See Guinn, J.

Jin, Y.

42-115 Box Codes of Lengths 48 and 72, pp. 105–109.

See Solomon, G.

Johnson, D. L.

42-116 X-Band Ultralow-Noise Maser Amplifier Performance, pp. 246–253.

See Glass, G. W.

Kayalar, S.

42-113 Acoustic Charge Transport Technology Investigation for Advanced Development Transponder, pp. 174–183.

Krisher, T. P.

42-113 The Flight Performance of the Galileo Orbiter USO, pp. 184–202.

See Morabito, D. D.

42-114 The Flight Performance of the Galileo Orbiter USO, pp. 327–345.

See Morabito, D. D.

Lagattuta, F.

42-116 TOPEX/POSEIDON Operational Orbit Determination Results Using Global Positioning Satellites, pp. 163–174.

See Guinn, J.

Lee, L. F.

42-115 Link Monitor and Control Operator Assistant: A Prototype Demonstrating Semiautomated Monitor and Control, pp. 124–134.

L. P. Cooper

Lee, P. R.

42-114 HRMS Sky Survey Wideband Feed System Design for DSS 24 Beam Waveguide Antenna, pp. 316–326.

See Stanton, P. H.

Lesh, J. R.

42-114 An Overview of the Galileo Optical Experiment (GOPEX), pp. 192–204.

See Wilson, K. E.

Levine, B. M.

42-114 Data Analysis for GOPEX Image Frames, pp. 213–229.

K. S. Shaik and T.-Y. Yan

Levy, R.

42-113 DSS-14 Subreflector Actuator Dynamics During the Landers Earthquake, pp. 130–146.

D. Strain

42-113 A Note on the Computation of Antenna-Blocking Shadows, pp. 74–79.

42-114 Cammatic: An Approach to Improve DSS 13 Antenna Gravity-Loading Performance, pp. 43–50.

D. Strain

Lichten, S. M.

42-114 Improved Treatment of Global Positioning System Force Parameters in Precise Orbit Determination Applications, pp. 14–20.

See Vigue, Y.

42-114 Use of Global Positioning System Measurements to Determine Geocentric Coordinates and Variations in Earth Orientation, pp. 21–33.

See Malla, R. P.

42-115 New Approaches for Tracking Earth Orbiters Using Modified GPS Ground Receivers, pp. 17–31.

L. E. Young, S. Nandi, B. J. Haines, C. E. Dunn, and C. D. Edwards

Morabito, D. D.

42-113 The Flight Performance of the Galileo Orbiter USO, pp. 184–202.

T. P. Krisher and S. W. Asmar

42-114 The Flight Performance of the Galileo Orbiter USO, pp. 327–345.

T. P. Krisher and S. W. Asmar

Muellerschoen, R. J.

42-114 Improved Treatment of Global Positioning System Force Parameters in Precise Orbit Determination Applications, pp. 14–20.

See Vigue, Y.

Nandi, S.

42-113 Precise Tracking of the Magellan and Pioneer Venus Orbiters by Same-Beam Interferometry—Part II: Orbit Determination Analysis, pp. 22–36.

See Folkner, W. M.

42-115 New Approaches for Tracking Earth Orbiters Using Modified GPS Ground Receivers, pp. 17–31.

See Lichten, S. M.

Neff, D.

42-114 A Cryogenic Seven-Element HEMT Front End for DSS 13, pp. 51–60.

See Bowen, J.

Nguyen, T. M.

42-114 Preliminary Design and Implementation of the Baseline Digital Baseband Architecture for Advanced Deep Space Transponders, pp. 280–294.

H.-G. Yeh

42-116 Design and Implementation of a Hybrid Digital Phase-Locked Loop With a TMS320C25—An Application to a Transponder Receiver Breadboard, pp. 175–189.

See H.-G. Yeh

Okamoto, G.

42-114 GOPEX Laser Transmission and Monitoring Systems, pp. 248–254.

K. Masters

Ortiz, G. G.

42-116 X-Band Ultralow-Noise Maser Amplifier Performance, pp. 246–253.

See Glass, G. W.

Otoshi, T. Y.

42-113 Maximum and Minimum Return Losses From a Passive Two-Port Network Terminated With a Mismatched Load, pp. 80–88

42-116 Determining Noise Temperatures in Beam Waveguide Systems, pp. 42–52.

See Imbriale, W.

Owen, Jr., W. M.

42-114 Telescope Pointing for GOPEX, pp. 230–235.

Palmatier, T. H.

42-114 Estimating the Size of Huffman Code Preambles, pp. 90–95.

See McEliece, R. J.

Parham, B.

42-114 Performance Results of a Digital Test Signal Generator, pp. 140–153.

See Gutierrez–Luaces, B. O.

Peng, T. K.

42-114 Stability Measurements of the Radio Science System at the 34-m High-Efficiency Antennas, pp. 112–139.

See Pham, T. T.

Pham, T. T.

42-114 Stability Measurements of the Radio Science System at the 34-m High-Efficiency Antennas, pp. 112–139.

J. C. Breidenthal, T. K. Peng, S. F. Abbate, and S. T. Rockwell

Pollara, F.

42-114 Coding Performance of the Probe–Orbiter–Earth Communication Link, pp. 68–83.

See Divsalar, D.

Shay, T. M.

42-116 The Rb 780-Nanometer Faraday Anomalous Dispersion Optical Filter: Theory and Experiment, pp. 71–85.

See Yin, B.

Shell, J.

42-116 A Dual-Cavity Ruby Maser for the Ka-Band Link Experiment, pp. 53–70.

R. B. Quinn

Sierra, V.

42-116 TOPEX/POSEIDON Operational Orbit Determination Results Using Global Positioning Satellites, pp. 163–174.

See Guinn, J.

Solomon, G.

42-115 Box Codes of Lengths 48 and 72, pp. 105–109.

Y. Jin

42-116 Convolutional Encoding of Self-Dual Codes, pp. 110–113.

Stanley, R. P.

42-113 The General Theory of Convolutional Codes, pp. 89–98.

See McEliece, R. J.

Stanton, P. H.

42-113 Experimental and Modal Verification of an Integral Equation Solution for a Thin-Walled Dichroic Plate With Cross-Shaped Holes, pp. 46–62.

See Epp, L. W.

42-114 HRMS Sky Survey Wideband Feed System Design for DSS 24 Beam Waveguide Antenna, pp. 316–326.

P. R. Lee and H. F. Reilly

42-115 Performance of the X-/Ka-/KABLE-Band Dichroic Plate in the DSS-13 Beam Waveguide Antenna, pp. 54–64.

See Chen, J. C.

Statman, J. I.

42-113 Signal-to-Noise Ratio Losses in Full Spectrum Combining of Signals With a Downconverted Subcarrier, pp. 123–129.

See Feria, Y.

42-116 Decoder Synchronization for Deep Space Missions, pp. 121–127.

K.-M. Cheung, T. H. Chauvin, J. Rabkin, and M. L. Belongie

42-116 Optimizing the Galileo Space Communication Link, pp. 114–120.

Strain, D.

42-113 DSS-14 Subreflector Actuator Dynamics During the Landers Earthquake, pp. 130–146.

See Levy, R.

42-114 Cammatic: An Approach to Improve DSS 13 Antenna Gravity-Loading Performance, pp. 43–50.

See Levy, R.

Swanson, L.

42-113 Uncorrectable Sequences and Telecommand, pp. 99–105.

See Ekroot, L.

Thurman, S. W.

42-116 Enhanced Orbit Determination Filter: Inclusion of Ground System Errors as Filter Parameters, pp. 37–41.

See Masters, W. C.

Townes, C. H.

42-116 Toward Astrometric Tracking With the Infrared Spatial Interferometer, pp. 1–9.

See Treuhaft, R. N.

Traxler, M. R.

42-113 DSN Support of Mars Observer, pp. 118–122.

TECHNICAL REPORT STANDARD TITLE PAG

1. Report No. 42-116

2. Government Accession No.

3. Recipient's Catalog No.

4. Title and Subtitle
The Telecommunications and Data Acquisition Progress Report

5. Report Date
February 15, 1994

6. Performing Organization Code

7. Author(s)
Editor: Joseph H. Yuen

8. Performing Organization Report No
42-116

9. Performing Organization Name and Address

JET PROPULSION LABORATORY
California Institute of Technology
4800 Oak Grove Drive
Pasadena, California 91109

10. Work Unit No.

11. Contract or Grant No.
NAS7-918

12. Sponsoring Agency Name and Address

NATIONAL AERONAUTICS AND SPACE ADMINISTRATION
Washington, D.C. 20546

13. Type of Report and Period Covered
TDA Progress Report, vol.
October-December 1993

14. Sponsoring Agency Code

15. Supplementary Notes

16. Abstract

This quarterly publication provides archival reports on developments in programs managed by JPL's Office of Telecommunications and Data Acquisition (TDA). In space communications, radio navigation, radio science, and ground-based radio and radar astronomy, it reports on activities of the Deep Space Network (DSN) in planning, supporting research and technology, implementation, and operations. Also included are standards activity at JPL for space data and information systems and reimbursable DSN work performed for other space agencies through NASA. The preceding work is all performed for NASA's Office of Space Communications (OSC). The TDA Office also performs work funded by another NASA program office through and with the cooperation of OSC. This is the Orbital Debris Radar Program with the Office of Space Systems Development.

The TDA Office is directly involved in several tasks that directly support the Office of Space Science (OSS), with OSC funding DSN operational support. In radio science, *The TDA Progress Report* describes the spacecraft radio science program conducted using the DSN. For the High-Resolution Microwave Survey (HRMS), the report covers implementation and operations for searching the microwave spectrum. In solar system radar, it reports on the uses of the Goldstone Solar System Radar for scientific exploration of the planets, their rings and satellites, asteroids, and comets. In radio astronomy, the areas of support include spectroscopy, very long baseline interferometry, and astrometry.

Finally, tasks funded under the JPL Director's Discretionary Fund and the Caltech President's Fund that involve the TDA Office are included.

17. Key Words (Selected by Author(s))
Astronautics
Communications
Mathematical and Computer Sciences
Space Sciences

18. Distribution Statement
Unlimited/Unclassified

19. Security Classif. (of this report)
Unclassified

20. Security Classif. (of this page)
Unclassified

21. No. of Pages
281

22. Price

JPL 0184 R 9/83